

The background of the cover features a technical line drawing of multiple robotic arms. The top half of the image has an orange background, while the bottom half has a white background. The robotic arms are depicted with various joints, sensors, and actuators, rendered in a purple line-art style. The title is centered in the orange section.

INTERFACING HUMANS AND MACHINES FOR REHABILITATION AND ASSISTIVE DEVICES

EDITED BY: Carlos A. Cifuentes, Jan Veneman, Eduardo Rocon and
Carlos Rodriguez-Guerrero
PUBLISHED IN: Frontiers in Robotics and AI



frontiers

Frontiers eBook Copyright Statement

The copyright in the text of individual articles in this eBook is the property of their respective authors or their respective institutions or funders. The copyright in graphics and images within each article may be subject to copyright of other parties. In both cases this is subject to a license granted to Frontiers.

The compilation of articles constituting this eBook is the property of Frontiers.

Each article within this eBook, and the eBook itself, are published under the most recent version of the Creative Commons CC-BY licence.

The version current at the date of publication of this eBook is CC-BY 4.0. If the CC-BY licence is updated, the licence granted by Frontiers is automatically updated to the new version.

When exercising any right under the CC-BY licence, Frontiers must be attributed as the original publisher of the article or eBook, as applicable.

Authors have the responsibility of ensuring that any graphics or other materials which are the property of others may be included in the CC-BY licence, but this should be checked before relying on the CC-BY licence to reproduce those materials. Any copyright notices relating to those materials must be complied with.

Copyright and source acknowledgement notices may not be removed and must be displayed in any copy, derivative work or partial copy which includes the elements in question.

All copyright, and all rights therein, are protected by national and international copyright laws. The above represents a summary only. For further information please read Frontiers' Conditions for Website Use and Copyright Statement, and the applicable CC-BY licence.

ISSN 1664-8714

ISBN 978-2-88971-843-6

DOI 10.3389/978-2-88971-843-6

About Frontiers

Frontiers is more than just an open-access publisher of scholarly articles: it is a pioneering approach to the world of academia, radically improving the way scholarly research is managed. The grand vision of Frontiers is a world where all people have an equal opportunity to seek, share and generate knowledge. Frontiers provides immediate and permanent online open access to all its publications, but this alone is not enough to realize our grand goals.

Frontiers Journal Series

The Frontiers Journal Series is a multi-tier and interdisciplinary set of open-access, online journals, promising a paradigm shift from the current review, selection and dissemination processes in academic publishing. All Frontiers journals are driven by researchers for researchers; therefore, they constitute a service to the scholarly community. At the same time, the Frontiers Journal Series operates on a revolutionary invention, the tiered publishing system, initially addressing specific communities of scholars, and gradually climbing up to broader public understanding, thus serving the interests of the lay society, too.

Dedication to Quality

Each Frontiers article is a landmark of the highest quality, thanks to genuinely collaborative interactions between authors and review editors, who include some of the world's best academicians. Research must be certified by peers before entering a stream of knowledge that may eventually reach the public - and shape society; therefore, Frontiers only applies the most rigorous and unbiased reviews. Frontiers revolutionizes research publishing by freely delivering the most outstanding research, evaluated with no bias from both the academic and social point of view. By applying the most advanced information technologies, Frontiers is catapulting scholarly publishing into a new generation.

What are Frontiers Research Topics?

Frontiers Research Topics are very popular trademarks of the Frontiers Journals Series: they are collections of at least ten articles, all centered on a particular subject. With their unique mix of varied contributions from Original Research to Review Articles, Frontiers Research Topics unify the most influential researchers, the latest key findings and historical advances in a hot research area! Find out more on how to host your own Frontiers Research Topic or contribute to one as an author by contacting the Frontiers Editorial Office: frontiersin.org/about/contact

INTERFACING HUMANS AND MACHINES FOR REHABILITATION AND ASSISTIVE DEVICES

Topic Editors:

Carlos A. Cifuentes, Escuela Colombiana de Ingenieria Julio Garavito, Colombia

Jan Veneman, Hocoma (Switzerland), Switzerland

Eduardo Rocon, Spanish National Research Council (CSIC), Spain

Carlos Rodriguez-Guerrero, Vrije University Brussel, Belgium

Dr Jan Veneman is employed by Hocoma AG. All other Topic Editors declare no competing interests with regards to the Research Topic subject.

Citation: Cifuentes, C. A., Veneman, J., Rocon, E., Rodriguez-Guerrero, C., eds. (2022). Interfacing Humans and Machines for Rehabilitation and Assistive Devices. Lausanne: Frontiers Media SA. doi: 10.3389/978-2-88971-843-6

Table of Contents

- 05 Editorial: Interfacing Humans and Machines for Rehabilitation and Assistive Devices**
Carlos A. Cifuentes, Jan F. Veneman, Eduardo Rocon and Carlos Rodriguez-Guerrero
- 08 Using Multiple Decomposition Methods and Cluster Analysis to Find and Categorize Typical Patterns of EEG Activity in Motor Imagery Brain–Computer Interface Experiments**
Alexander Frolov, Pavel Bobrov, Elena Biryukova, Mikhail Isaev, Yaroslav Kerechanin, Dmitry Bobrov and Alexander Legin
- 21 Mobility Skills With Exoskeletal-Assisted Walking in Persons With SCI: Results From a Three Center Randomized Clinical Trial**
EunKyoung Hong, Peter H. Gorman, Gail F. Forrest, Pierre K. Asselin, Steven Knezevic, William Scott, Sandra Buffy Wojciehowski, Stephen Kornfeld and Ann M. Spungen
- 34 Robotic Cane Controlled to Adapt Automatically to Its User Gait Characteristics**
Andrés Trujillo-León, Ragou Ady, David Reversat and Wael Bachta
- 47 Compact Gearboxes for Modern Robotics: A Review**
Pablo López García, Stein Crispel, Elias Saerens, Tom Verstraten and Dirk Lefeber
- 67 A Novel User Control for Lower Extremity Rehabilitation Exoskeletons**
Kiran K. Karunakaran, Kevin Abbruzzese, Ghaith Androwis and Richard A. Foulds
- 81 Portable Take-Home System Enables Proportional Control and High-Resolution Data Logging With a Multi-Degree-of-Freedom Bionic Arm**
Mark R. Brinton, Elliott Barcikowski, Tyler Davis, Michael Paskett, Jacob A. George and Gregory A. Clark
- 93 Benchmarking Wearable Robots: Challenges and Recommendations From Functional, User Experience, and Methodological Perspectives**
Diego Torricelli, Carlos Rodriguez-Guerrero, Jan F. Veneman, Simona Crea, Kristin Briem, Bigna Lenggenhager and Philipp Beckerle
- 100 Occurrence and Type of Adverse Events During the Use of Stationary Gait Robots—A Systematic Literature Review**
Jule Bessler, Gerdienke B. Prange-Lasonder, Robert V. Schulte, Leendert Schaake, Erik C. Prinsen and Jaap H. Buurke
- 117 Bioinspired Postural Controllers for a Locked-Ankle Exoskeleton Targeting Complete SCI Users**
Jemina Fasola, Romain Baud, Tristan Vouga, Auke Ijspeert and Mohamed Bouri
- 129 Effective Multi-Mode Grasping Assistance Control of a Soft Hand Exoskeleton Using Force Myography**
Muhammad Raza Ul Islam and Shaoping Bai

- 143** *Inertial-Robotic Motion Tracking in End-Effector-Based Rehabilitation Robots*
Arne Passon, Thomas Schauer and Thomas Seel
- 162** *ExoNet Database: Wearable Camera Images of Human Locomotion Environments*
Brock Laschowski, William McNally, Alexander Wong and John McPhee
- 168** *Dynamic Margins of Stability During Robot-Assisted Walking in Able-Bodied Individuals: A Preliminary Study*
Arvind Ramanujam, Kamyar Momeni, Manikandan Ravi, Jonathan Augustine, Erica Garbarini, Peter Barrance, Ann M. Spungen, Pierre Asselin, Steven Knezevic and Gail F. Forrest
- 179** *Applicability of an Active Back-Support Exoskeleton to Carrying Activities*
Tommaso Poliero, Maria Lazzaroni, Stefano Toxiri, Christian Di Natali, Darwin G. Caldwell and Jesús Ortiz
- 192** *Evaluation of Motor Primitive-Based Adaptive Control for Lower Limb Exoskeletons*
Polyana F. Nunes, Icaro Ostan and Adriano A. G. Siqueira
- 205** *Analysis of Compensatory Movements Using a Supernumerary Robotic Hand for Upper Limb Assistance*
Martina Rossero, Andrea S. Ciullo, Giorgio Grioli, Manuel G. Catalano and Antonio Bicchi
- 219** *Suitability of the Openly Accessible 3D Printed Prosthetic Hands for War-Wounded Children*
John-John Cabibihan, Farah Alkhatib, Mohammed Mudassir, Laurent A. Lambert, Osama S. Al-Kwafi, Khaled Diab and Elsadig Mahdi
- 233** *3D Scanning of the Forearm for Orthosis and HMI Applications*
Joel C. Perry, Jacob R. Brower, Robert H. R. Carne and Melissa A. Bogert



Editorial: Interfacing Humans and Machines for Rehabilitation and Assistive Devices

Carlos A. Cifuentes^{1*}, Jan F. Veneman², Eduardo Rocon³ and Carlos Rodriguez-Guerrero⁴

¹Department of Biomedical Engineering, Colombian School of Engineering Julio Garavito, Bogota, Colombia, ²Hocoma AG, Volketswil, Switzerland, ³Centro de Automática y Robótica, Consejo Superior de Investigaciones Científicas-Universidad Politécnica de Madrid (CSIC-UPM), Madrid, Spain, ⁴Robotics and Multibody Mechanics Research Group, Department of Mechanical Engineering, Vrije Universiteit Brussel and Flanders Make, Brussels, Belgium

Keywords: prosthetics and orthotics, exoskeletons, human-robot interfaces, brain-machine interfaces, sensors and actuators for human-robot interaction

Editorial on the Research Topic

Interfacing Humans and Machines for Rehabilitation and Assistive Devices

INTRODUCTION

Currently, around 10% of the world's population, or roughly 650 million people, live with some type of disability. In countries with life expectancies over 70 + years, people spend on average about 8 years, or 11.5 percent of their lifetime, living with disabilities (Disabled World (2021). Di, 2021).

In response to this need scientists from different fields, together with engineers and clinicians have been working on developing robotic solutions for a wide variety of rehabilitation and assistive scenarios. Robotic exoskeletons are now commonly found tools used at neurorehabilitation centers, treating stroke and spinal cord injury survivors. Occupational exoskeletons are now alleviating a big part of the harmful body loading, responsible for widely common musculoskeletal disorders found in industrial settings. Bionic prostheses are now making their way through the markets and getting attention by the social security systems around the world and will most likely become widely adopted in the near future. All the aforementioned technologies require interfacing humans and robots to assure a safe and efficient cognitive and physical interaction. Here, the interface refers to any hardware or software link that connects two dissimilar systems: humans and robots.

The topic “*Interfacing Humans and Machines for Rehabilitation and Assistive Devices*” was opened to gather professionals and researchers from various backgrounds and discuss the pertinence and feasibility of new human-robot interfaces in the field of rehabilitation and assistance. The community's outstanding response to the call led to 18 contributions by 97 different authors that address the requirements and challenges of implementing and deploying rehabilitation and assistive robotics (see **Figure 1**). The contributions proposed new control and modeling strategies for orthotic and prosthetic devices (for both upper and lower limbs), explored methodologies to detect human intention, and assess quantitative and qualitative measurements of the behavior and outcomes when interfacing humans and machines.

The research topic comprises promising state-of-the-art developments in a broad spectrum of devices. There are many ways to address and classify rehabilitation and assistive devices, not forgetting the differences between them. A rough categorization could be whether 1) they are worn or integrated on the body, or 2) they are external tools either handled by the user or by the therapist. The first group can then be subdivided into whether 1) they replace (or add) a body structure, what are

OPEN ACCESS

Edited and reviewed by:

Noman Naseer,
Air University, Pakistan

*Correspondence:

Carlos A. Cifuentes
carlos.cifuentes@escuelaing.edu.co

Specialty section:

This article was submitted to
Biomedical Robotics,
a section of the journal
Frontiers in Robotics and AI

Received: 16 October 2021

Accepted: 17 November 2021

Published: 03 January 2022

Citation:

Cifuentes CA, Veneman JF, Rocon E and Rodriguez-Guerrero C (2022) Editorial: Interfacing Humans and Machines for Rehabilitation and Assistive Devices. *Front. Robot. AI* 8:796431. doi: 10.3389/frobt.2021.796431

known as prostheses, or 2) they support body functions by supporting existing body structures, known as orthoses.

Prosthetics can derive from different technological sources. One that has gained significant attention is innovations in desktop 3D printers and open-source designs that lead to creating body-powered, 3D printed prosthetic hands. Based on the additive deposition of material in a layer-by-layer manner to construct parts from a 3D computer-aided design (CAD) model, these devices have disrupted the field of rehabilitation and assistive devices and are every day more available to be implemented as functional low-cost alternatives. However, there are fundamental interfacing issues that need to be addressed for long-term usage. In this case, Cabibihan et al. evaluated them to benefit children with congenital missing limbs and the war-wounded.

On the other side, there are more advanced electro-mechanical prostheses, also called bionic arms or hands. These devices have been designed to approximate the natural limb in both form and function. They have continuously achieved a better range of functional grip, power, and precision. However, they do not match the dexterity of natural hands yet, and several challenges arise from the human-machine interaction (HMI) comprising sensing, control, and actuation. Accurate and efficient interaction includes the implementation of biological signals such as EMG recordings from the residual limb and EEG and various clever control strategies (Brinton et al.); (Frolov et al.).

In the field of orthoses, which are mechanical structures that correct, support, restore and enhance the function of a part of the body instead of replacing it, the contributions here presented focused on their robotic counterparts: the robotic exoskeletons. In this case, exoskeletons for different parts of the body and varying configurations of material are studied.

Upper limb exoskeletons are commonly used in the industry by workers during long-hour tasks and in robotic-assisted rehabilitation therapies, in both cases to support repetitive movements. The use of soft technology has gained significant attention in upper limbs as compliant interaction with the subject favors its purpose. The detection of the human intention of motion is fundamental to controlling these robotic devices to assist humans according to their needs. Similar to strategies presented with orthotic devices, novel approaches for detecting hand motion intention and controlling the exoskeletons are based on EMG signals (Islam and Bai). In addition to the development of robotic kinematics and control, the study of proper methods to design physical HMI plays a fundamental role in the comfort and usability of the device, as presented by Perry et al. Just like some upper limb exoskeletons, occupational back-support exoskeletons are every day, more commonly used to mitigate work-related pain. Poliero et al. evaluated the impact of carrying activities on lower-back loading than lifting to select different assistive strategies.

The exoskeletons that have been more intensely studied are, without a doubt, lower limb exoskeletons. The actuation system implemented in them is one of the essential factors in their design as it generally determines the performance, efficiency, and portability. There are mainly three types of actuators used in

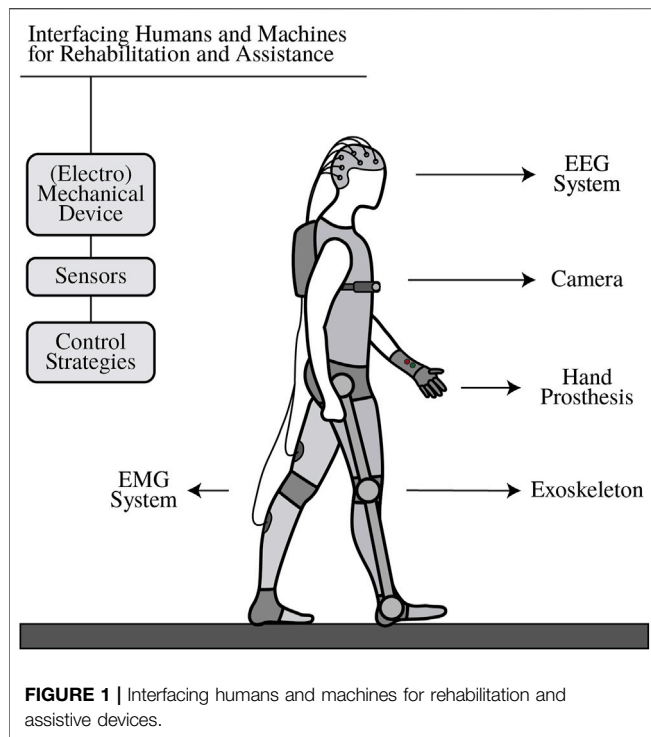
modern exoskeletons: 1) electrical motors, 2) pneumatic actuators, and 3) hydraulic actuators. Even though some researchers choose pneumatic or hydraulic actuators due to their higher power/weight ratio or better compliance, most exoskeletons use electric motors due to their precision and ease of control. Therefore, the analysis of components as gearboxes, elastic elements, and transmission systems is critical in developing lower limb exoskeletons (García et al.). There are many commercially available examples with various technologies implemented in the market. However, researchers are constantly in the quest for new, more natural ways of controlling these devices. From bio-inspired controllers 1) based on motor primitives (Nunes et al.) or 2) developed to allow dynamic standing balance (Fasola et al.) to approaches that naturally decodes a neuromuscular surrogate (Karunakaran et al.), contributions explore the development of strategies to match a healthy gait pattern better. (Laschowski et al.), for example, introduced an environment recognition system to improve the control of robotic lower-limb exoskeletons and prostheses during human locomotion.

As the new exoskeletons are developed and tested in the market and the research centers, the need for standardized assessment measures and characterization increases. Methods such as analyzing the dynamic margins of stability during robot-assisted gait are a way to robustly and objectively measure such devices' performance (Ramanujam et al.). However, other more clinically related parameters that could help to assess the impact of their use could be 1) to determine the number of training sessions necessary to achieve adequate exoskeletal-assisted walking skills and velocity milestones (through the implementation of well-known walking tests as presented by Hong et al. or 2) to keep track of adverse events and associated risks when performing robot-assisted gait training (Bessler et al.). Since there is a wide range of possibilities to correctly assesses lower limb exoskeletons, a benchmarking framework becomes more and more necessary. Benchmarking wearable robots is then a vital task to quantify both the technical performance of the devices and the physical impact they have on the users (Torricelli et al.).

Additionally, somewhere between prostheses and orthoses are the Supernumerary Robotic Limbs (SRL), also called extra theses. They consist of additional robotic body parts (e.g., limbs and fingers) to augment the user's abilities. SRL function together with an intact musculoskeletal system, but add an utterly functional body structure, not a replacement, but still as a structure and not as a support of an existing structure.

They have been initially proposed for industrial purposes and differ from exoskeletons, as they do not request any joint-to-joint alignment. The analysis of compensatory movements performed by this SRL determines the future usability of this type of system moving forward into assistive applications, as presented by Rossero et al.

Even though this first big group of devices worn or integrated on the body is the most renowned device in the field, rehabilitation, and assistive technology, either handled by the user or by the therapist, offer patients with disabilities other opportunities.



To this second group belong devices for functional gait compensation such as crutches, walkers, and wheelchairs, and each of them represents a whole area of research and development. Among them, canes are the devices more commonly used to increase gait stability. A simple single-point cane may prevent or reduce falls in patients with imbalance. Similar to orthosis, robotic counterparts for each of the devices mentioned above exist. Smart walkers, robotic wheelchairs, and robotic cane embrace the same challenge of interfacing with humans for optimal performance (Trujillo-León et al.).

Other rehabilitation robots, not necessarily in the field of orthosis, are also used in training setups. End-effector-based systems are robotic systems that are only attached to the distal segments of the limbs and belong to this group. They include, for example, cable-driven motion support robots. Compared to

exoskeletons, these systems require more minor adjustments to each patient. However, they need the motion of all adjacent segments to be inferred using mechanical models or additional sensors, such as inertial units presented by Passon et al.

Interfacing humans and machines for rehabilitation and assistive devices evidently encompasses many possible devices and design choices that directly affect the living conditions of people who have suffered from motor impairments or amputations. In pursuit of practical functionality, these solutions require robust interfaces that allow natural and compliant control. Possibilities are endless, and the contributions gathered in this topic invite professionals and researchers from various backgrounds to collaborate and share promising developments where humans and machines are interfaced in rehabilitation or assistive environments. The editors and authors of this affluent and evolving research topic believe that this space, with all its different rehabilitation and assistive devices, can mutually inspire developers in their quest for a better quality of life.

AUTHOR CONTRIBUTIONS

All authors contributed to the conception and design of this article. CC wrote the first draft of the manuscript, and all authors commented on previous versions of the manuscript. All authors read and approved the final manuscript.

FUNDING

This work was supported by the Ministry of Science, Technology, and Innovation of Colombia (Grant 801-2017) and (Grant 845-2020). This Research Topic is recommended by the COST Action CA16116 “Wearable Robots for Augmentation, Assistance or Substitution of Human Motor Functions” and by the Iberoamerican Network on Rehabilitation and Assistance of Patients with Neurologic Damage using Low-Cost Robotic Exoskeletons, REASISTE, supported by CYTED (216RT0504).

REFERENCES

Disabled World (2021). *Disabled World, Disability Statistics: Information, Charts, Graphs and Tables*. Available at: <https://www.disabled-world.com/disability/statistics/> (Accessed 02, 09, 2021).

Conflict of Interest: JV was employed by the company Hocoma AG, manufacturer of devices for functional movement therapy.

The remaining authors declare that the research was conducted in the absence of any commercial or financial relationships that could be construed as a potential conflict of interest.

Publisher’s Note: All claims expressed in this article are solely those of the authors and do not necessarily represent those of their affiliated organizations, or those of the publisher, the editors and the reviewers. Any product that may be evaluated in this article, or claim that may be made by its manufacturer, is not guaranteed or endorsed by the publisher.

Copyright © 2022 Cifuentes, Veneman, Rocon and Rodriguez-Guerrero. This is an open-access article distributed under the terms of the Creative Commons Attribution License (CC BY). The use, distribution or reproduction in other forums is permitted, provided the original author(s) and the copyright owner(s) are credited and that the original publication in this journal is cited, in accordance with accepted academic practice. No use, distribution or reproduction is permitted which does not comply with these terms.



Using Multiple Decomposition Methods and Cluster Analysis to Find and Categorize Typical Patterns of EEG Activity in Motor Imagery Brain–Computer Interface Experiments

Alexander Frolov^{1,2}, Pavel Bobrov^{1,2*}, Elena Biryukova^{1,2}, Mikhail Isaev^{1,2}, Yaroslav Kerechanin^{1,2}, Dmitry Bobrov¹ and Alexander Legin¹

¹ Research Institute of Translational Medicine, Pirogov Russian National Research Medical University, Moscow, Russia,

² Institute of Higher Nervous Activity and Neurophysiology, Russian Academy of Science, Moscow, Russia

OPEN ACCESS

Edited by:

Eduardo Rocon,
Consejo Superior de Investigaciones
Científicas (CSIC), Spain

Reviewed by:

Enrique Hortal,
Maastricht University, Netherlands
Javier Gomez-Pilar,
University of Valladolid, Spain

*Correspondence:

Pavel Bobrov
p-bobrov@yandex.ru

Specialty section:

This article was submitted to
Biomedical Robotics,
a section of the journal
Frontiers in Robotics and AI

Received: 28 April 2020

Accepted: 02 June 2020

Published: 30 July 2020

Citation:

Frolov A, Bobrov P, Biryukova E,
Isaev M, Kerechanin Y, Bobrov D and
Legin A (2020) Using Multiple
Decomposition Methods and Cluster
Analysis to Find and Categorize
Typical Patterns of EEG Activity in
Motor Imagery Brain–Computer
Interface Experiments.
Front. Robot. AI 7:88.
doi: 10.3389/frobt.2020.00088

In this study, the sources of EEG activity in motor imagery brain–computer interface (BCI) control experiments were investigated. Sixteen linear decomposition methods for EEG source separation were compared according to different criteria. The criteria were mutual information reduction between the source activities and physiological plausibility. The latter was tested by estimating the dipolarity of the source topographic maps, i.e., the accuracy of approximating the map by potential distribution from a single current dipole, as well as by the specificity of the source activity for different motor imagery tasks. The decomposition methods were also compared according to the number of shared components found. The results indicate that most of the dipolar components are found by the Independent Component Analysis Methods AMICA and PWCICA, which also provided the highest information reduction. These two methods also found the most task-specific EEG patterns of the blind source separation algorithms used. They are outperformed only by non-blind Common Spatial Pattern methods in terms of pattern specificity. The components found by all of the methods were clustered using the Attractor Neural Network with Increasing Activity. The results of the cluster analysis revealed the most frequent patterns of electrical activity occurring in the experiments. The patterns reflect blinking, eye movements, sensorimotor rhythm suppression during the motor imagery, and activations in the precuneus, supplementary motor area, and premotor areas of both hemispheres. Overall, multi-method decomposition with subsequent clustering and task-specificity estimation is a viable and informative procedure for processing the recordings of electrophysiological experiments.

Keywords: brain–computer interface, motor imagery, blind source separation, independent component analysis, common spatial patterns, cluster analysis, EEG pattern extraction

INTRODUCTION

A brain–computer interface (BCI) is a system for controlling a device using registered brain activity. To control the device, the BCI operator is usually required to perform different mental tasks and does not need to use any muscles. In practice, BCI systems are intended to create new means of communication between the operator and his/her environment, which is essential for the paralyzed. Recently, BCI technology has been used not to create a new communication channel but rather to enhance the resting one lost due to stroke or trauma. BCI rehabilitation applications are a growing field, with more clinical data reported every year (Ang et al., 2011, 2015; Ramos-Murguialday et al., 2013; Ono et al., 2014; Frolov et al., 2017b; Mane et al., 2019; Bai et al., 2020). Aside from in the clinic, these systems can be used in fundamental research. The feedback provided by BCI system operation makes its user highly concentrated on performing the tasks required to control it. The user has to produce stable and repeatable patterns of the brain activity recorded, greatly facilitating the investigation of the task-specific patterns of brain activity (Frolov et al., 2012).

Although there are numerous BCI classifiers, i.e., algorithms for brain activity pattern classification, these algorithms typically do not provide pattern features that have clear physiological interpretation. In this work, we have decided to investigate the EEG recordings of our BCI experiments with different source separation methods. Methods such as Principal and Independent Component Analysis (ICA, Hyvärinen et al., 2004), as well as other Blind Source Separation (BSS, Cichocki and Amari, 2002) techniques and non-blind Common Spatial Patterns (CSP, Bashashati et al., 2007), are widely used in EEG research both in the BCI and non-BCI fields. As will be described later, all of the methods considered decompose the signal into the sum of sources, or components, each characterized by its topographic map of weights and temporal activity.

Our experiments are mainly focused on the investigation of the performance of different motor imagery tasks while controlling the BCI (Frolov et al., 2012, 2017a,b). Earlier, we showed that ICA can be effectively used to find the sources of task-related sensorimotor mu-rhythm desynchronization (Frolov et al., 2012) as well as to extract the patterns of activity of three other brain areas involved in motor imagery (Frolov et al., 2017a). However, these results were obtained using a single ICA method. In this paper, we investigate the results of the application of several source separation methods for processing our records. The methods are compared in terms of how many shared components they provide as well as the task specificity of EEG patterns they find. We are mainly focused on studying sources that have clear physiological interpretations.

In Delorme et al. (2012), it was shown that physiologically meaningful components are dipolar. Results were obtained by using several ICA methods to decompose EEG recordings corresponding to visual memory tasks performed. A component being dipolar means that its topographic weight map, which can be looked upon as a scalp potential distribution, is adequately approximated by the distribution resulting from a single current dipole. Note that EEG being a result of the superposition of

multiple dipolar source potentials at a time is an accepted model of the EEG origin (Niedermeyer and Da Silva, 2005). The fact that a component is dipolar implies that it results from well-localized changes of electric activity in the brain, allowing it to be attributed to a certain brain area activation or deactivation.

Although the areas the activity of which results in the appearance of dipolar components are typically rather small (about several millimeters in diameter), they significantly impact the EEG signal recorded by all of the electrodes. That is why the main task of the decomposition method is to unmix the signal components. The unmixing done by the ICA and other BSS methods is often based on reducing the mutual information between the components (Hyvärinen et al., 2004). That is why mutual information reduction (MIR) is another criterion of method comparison.

Another indication of a component's relevance is the repeatability of its occurrence among all the subjects and records. The components reflecting common or task-specific EEG phenomena are expected to be found in most of the recordings. That is why a cluster analysis was applied to the topographic maps and power spectral densities of the components found. The results allow the evaluation of the rate at which a certain phenomenon can be discovered by the methods tested.

The paper is organized as follows. The next section provides information on the dataset and participants, as well as details of the 16 blind and non-blind signal decomposition methods used in this work. The measures of both similarity between the methods and similarity of the extracted components are described. The algorithms for estimating the task-specificity of the components and for cluster analysis are given. The results of the method comparison are then represented, and clusters of the most frequently encountered components are shown together with the cluster statistics. The results obtained are discussed, and possible physiological interpretation of the extracted components is given.

METHODS

We used the data from the BCI experiments carried out at the Institute for the Higher Nervous Activity and Neurophysiology of the Russian Academy of Science. The study was approved by the Institute's ethical committee.

Participants

Twenty-three volunteers (7 females and 16 males) aged from 21 to 36 (26 ± 4) participated in the experiments. The volunteers were right-handed according to the Edinburgh Handedness Inventory and had no reported neurological or other disorders. All of them gave written informed consent.

None of the participants had an experience of controlling a BCI. The ability of the participants to perform motor imagery was not assessed prior to the experiments.

Experimental Procedure

The original EEG dataset for the work was obtained using the same procedure as described in earlier works (Frolov et al., 2012, 2017a). Each subject had to sit relaxed, looking at the center of

the screen or had to imagine flexion of either his left or right hand according to visual cue presented on the screen. Each task had to be performed for 10 s, with a 2 s preparation period. There were 20 cue presentations for each hand motor image, which were split into blocks containing 2 cues for each hand. In each block, the cues were given in a random order. Each motor imagery task was preceded by the relaxation period.

There were from 10 to 20 experimental days (14 ± 3) for each subject, with 1–3 day gaps possible between the sessions.

The EEG data were recorded using the NVX52 acquisition device (Medical Computer Systems, Russia) with 32 electrodes placed according to the 10–10 system. The data were band-pass filtered with a 5–30 Hz Butterworth filter as well as a 50 Hz notch filter to suppress power line interference.

EEG Classification

The EEG data were classified with a Bayesian classifier under the assumption that the signal has a multivariate Gaussian distribution with a zero mean and a different covariance matrix for each task classified:

$$P(\mathbf{x}|i) = \frac{1}{\sqrt{2\pi} \det \mathbf{C}_i} \exp\left(-\frac{\mathbf{x}^T \mathbf{C}_i^{-1} \mathbf{x}}{2}\right), \quad (1)$$

where \mathbf{C}_i is a covariance matrix of the EEG corresponding to the i th task, and \mathbf{x} is an EEG sample. According to the Bayes rule, the probability that a given sample will correspond to the i th class is proportional to $P(\mathbf{x}|i)P(i)$, where $P(i)$ is the probability of the i th task being cued. Thus, for a signal epoch logarithm of the probability of all its samples to correspond to the i th class is proportional to $\frac{1}{n_t} (-\sum_t \mathbf{x}_t^T \mathbf{C}_i^{-1} \mathbf{x}_t) - \ln \det \mathbf{C}_i + \ln P(i) + \text{const}$, where summation is performed over all the epoch samples, n_t is the epoch length in samples, and the constant term is independent of both the signal and the class number. Since $\frac{1}{n_t} (-\sum_t \mathbf{x}_t^T \mathbf{C}_i^{-1} \mathbf{x}_t)$ can be substituted with $\text{trace}(\text{cov}(\mathbf{X})\mathbf{C}_i^{-1})$, where $\text{cov}(\mathbf{X})$ is the epoch covariance estimate under the assumption of a zero mean, the class number is

$$i_{\text{class}}(\mathbf{X}) = \underset{i}{\operatorname{argmax}} (\ln P(i) - \text{trace}(\text{cov}(\mathbf{X})\mathbf{C}_i^{-1}) - \ln \det \mathbf{C}_i) \quad (2)$$

We used a window of 1 s length sliding with a 100 ms shift to present the feedback during the sessions. The probabilities $P(i)$ were estimated based on the cue durations. The classifier was updated after each block of cues, with no feedback during the first block.

Signal Decomposition

All of the blind and non-blind source separation methods used can be, in general, represented in the form of multivariate linear decomposition with an optional noise term.

$$\mathbf{X} = \mathbf{a}_1 \xi_1 + \dots + \mathbf{a}_n \xi_n + \mathbf{N} = \mathbf{A} \Xi + \mathbf{N}, \quad (3)$$

where \mathbf{X} is the decomposed signal in matrix form, \mathbf{a}_i , $i = 1, \dots, n$, are columns of \mathbf{A} that define the source (component) weights representing the source topographic maps, ξ_i , $i = 1, \dots, n$, are

row vectors of the source activities, n is the number of EEG channels, and is the optional noise term. Matrix \mathbf{A} is called the mixing matrix, and its inverse, \mathbf{W} , is called the unmixing matrix. The invertibility of \mathbf{A} is based on the assumptions that there are as many components as there are signal channels and that the signal correlation matrix has full rank. These assumptions are in general not required but are common for linear source separation methods (Cichocki and Amari, 2002; Hyvärinen et al., 2004), and all of the decomposition methods used in the paper were derived under these assumptions.

Usually, the signal is whitened before searching for decomposition (3) so that the covariance matrix of \mathbf{X} becomes an identity matrix. Also, it is well-known that the component activity variances are not defined, thus requiring the application of some constraints when the decomposition is computed. That is why we shall further consider the decomposed signal to be whitened, i.e.

$$\mathbf{X} = \mathbf{VZ}, \quad (4)$$

where \mathbf{V} is a matrix such that $\mathbf{V} \text{cov}(\mathbf{X}) \mathbf{V}^T = \mathbf{I}$. If we also suppose that all ξ_i , $i = 1, \dots, n$, have unit variance, then the mixing matrix for \mathbf{Z} is orthogonal, $\mathbf{Z} = \mathbf{U}\Xi$, $\mathbf{U}\mathbf{U}^T = \mathbf{I}$, and the EEG mixing matrix is \mathbf{A} equals $\mathbf{V}\mathbf{U}$.

We used 16 source separation methods to obtain the decomposition (3).

PCA, or Principle Component Analysis, is a classic example of a technique for obtaining the decomposition (3). It uses Singular Value Decomposition to diagonalize the signal covariance matrix. Usually, the components with too much or too little variance are discarded. If one rather chooses to keep all of the components under the constraints that their variances are equal to 1, this will become signal whitening. In this case, $\mathbf{U} = \mathbf{I}$, and the unmixing matrix is not orthonormal.

KURT is an ICA method based on maximizing the difference of the component distributions from normal. The difference is measured by the absolute value of the component excess kurtosis, which serves as a cost function for iterative component search (Delfosse and Loubaton, 1995; Hyvärinen et al., 2004), i.e., the columns of unmixing matrix \mathbf{W} are estimated sequentially by maximizing the excess kurtosis for $\mathbf{w}_i^T \mathbf{Z}$ under the assumption that \mathbf{W} is orthogonal.

CUMUL is an ICA method using the signal non-stationarity as the criterion of statistical independence (Hyvärinen, 2001). The non-stationarity is measured by the fourth-order cumulant:

$$\text{cum}_4(x) = E\{x^2(t)x^2(t-\tau)\} - E\{x^2(t)\}E\{x^2(t-\tau)\} - 2E\{x(t)x(t-\tau)\}^2. \quad (5)$$

The decomposition seeks to maximize the sum of the source cumulants. The proof of non-stationarity maximization being a criterion of component independence can be found in Hyvärinen et al. (2004), chapter 18. The time lag τ serves as the method parameter. In our experiment, it was set to 100 ms to extract the components with dominant alpha-band frequencies.

FastICA is an ICA method in which mutual information reduction between the components serves as the statistical

independence criterion. The mutual information between the components $\xi_i, i = 1, \dots, n$, is defined as

$$I(\xi_1, \dots, \xi_n) = \sum_i H(\xi_i) - H(\Xi), \quad (6)$$

where $H(\cdot)$ denotes entropy. The entropy of linear transformation is $H(\mathbf{WZ}) = H(\mathbf{Z}) + |\det(\mathbf{W})|$. Under the assumption of \mathbf{Z} being whitened and the components having unit variance, \mathbf{W} is orthogonal, which implies that $\det(\mathbf{W}) = 1$ and $H(\mathbf{WZ})$ does not depend on $\det(\mathbf{W})$. As a result, $H(\mathbf{w}_i^T \mathbf{Z})$ can be used as a cost function for sequential search of the unmixing matrix columns \mathbf{w}_i .

Since computing the entropy requires knowledge on the signal distribution, different parametric approximations are used. FastICA uses approximation in the form

$$H(x) \propto \text{const} - [E\{g(x)\} - E\{g(v)\}]^2, \quad (7)$$

where $g(x)$ is a non-linear function and v is a random normally distributed variable with unit variance. FastICA can be computed using different non-linearities (Bingham and Hyvärinen, 2000; Hyvärinen et al., 2004). In this work, we used two functions, namely, $\tanh(x)$ and $x \exp(-x^2/2)$. The corresponding methods are denoted as FastICAT and FastICAG.

RunICA, or extended infomax, is an ICA method that is similar to FastICA. The method takes into account both super- and sub-Gaussian distributions by applying two different non-linearities, $g_+(x) = -2 \log \cosh(x)$ and $g_-(x) = \log \cosh(x) - x^2/2$, and switching between them. Originally, the infomax algorithm was introduced by Bell and Sejnowski (1995) based on a neural network approach to maximize the entropy of the neural network output. It was later reformulated in terms of parametric non-linearities for source entropy estimation (Lee et al., 1999).

AMICA, which stands for Adaptive Mixture Independent Component Analysis, is an ICA method based on the assumption that all EEG components have generalized Gaussian mixture distributions

$$p(\xi_i) = \sum_{j=1, \dots, k} \alpha_{ij} q(\xi_i, \rho_{ij}, \mu_{ij}, \beta_{ij}), \quad (8)$$

$$q(\xi, \rho, \mu, \beta) = \frac{\rho}{2\beta\Gamma(1/\rho)} \exp\left(-\left|\frac{\xi - \mu}{\beta}\right|^\rho\right). \quad (9)$$

AMICA can also segment the signal into several parts corresponding to different models (8) when the number of the models is set to higher than 1. All distribution parameters, unmixing matrix coefficients, and model scores (in the case of several models) are estimated using the expectation-maximization algorithm (Palmer et al., 2006, 2008, 2012). In our work, we compared AMICA with the default settings (2 models, 2 distributions in mixture) to AMICA with two models and Gaussian distributions with means fixed to zero (2 models, 2 distributions in mixture, $\rho_{ij}^l = 2, \mu_{ij}^l = 0$, where l indicates the model, $l = 1, 2$, and $i = 1, \dots, n, j = 1, 2$), and to AMICA with a single model and Gaussian distributions with means fixed

to zero (1 model, 2 distributions in mixture, $\rho_{ij} = 2, \mu_{ij} = 0, i = 1, \dots, n, j = 1, 2$). The two latter cases will be denoted as AMICA1 and AMICA2, respectively.

PWCICA is an ICA method mapping the signal into a complex domain using the first derivative (rate) of the signal as its imaginary part. The algorithm is described in Ball et al. (2016). It uses the complex variant of FastICA in order to find decomposition (3) in the complex domain (Bingham and Hyvärinen, 2000). After that, the real-valued unmixing matrix is computed using the algorithm provided in Ball et al. (2016).

SOBI, or Second Order Blind Identification, is a blind source separation method that uses joint diagonalization to remove signal cross-covariance for a set of defined time lags (Belouchrani et al., 1997). Particularly, a set of time lags δ_k is specified, and corresponding cross-covariance matrices are estimated:

$$\mathbf{C}_k = E(\mathbf{X}(t), \mathbf{X}(t - \delta_k)), \quad (10)$$

Next, the unmixing matrix \mathbf{W} is found by joint diagonalization of the estimated cross-covariance matrices:

$$\mathbf{W} = \underset{\mathbf{M}}{\operatorname{argmin}} \left(\sum_k \|\mathbf{M}\mathbf{C}_k\mathbf{M}^T\|_{\text{off}} \right) \quad (11)$$

where $\|\cdot\|_{\text{off}}$ denotes the Euclidean norm of the off-diagonal part of a matrix. The norm of the unmixing matrix column is constrained to be equal to 1. There exist several algorithms for solving the problem (11). We used one proposed in Ziehe et al. (2004) to obtain the solution.

CSP, or Common Spatial Patterns (Ramoser et al., 2000; Bashashati et al., 2007, 2015), is a non-blind decomposition method, in contrast to the source separation techniques described above. This method utilizes the information on signal segmentation with respect to the experimental tasks in order to find the decomposition (3). The method is used for feature extraction in two-class separation problems. The decomposition is sought that maximizes the component variance ratio for the states classified under the assumption that total component variance is fixed. This is equivalent to finding matrix \mathbf{W} such that

$$\begin{cases} \mathbf{W}\mathbf{C}_1\mathbf{W}^T = \mathbf{D}_1 \\ \mathbf{W}(\mathbf{C}_1 + \mathbf{C}_2)\mathbf{W}^T = \mathbf{I} \end{cases}, \quad (12)$$

where \mathbf{C}_i is the i -th class covariance matrix and \mathbf{D}_1 is a diagonal matrix. The equations (12) have an explicit solution where \mathbf{W} and \mathbf{D}_1 result from singular-value decomposition (SVD) of the matrix $\mathbf{D}^{-1/2} \mathbf{U}^T \mathbf{C}_1 \mathbf{U} \mathbf{D}^{-1/2}$ with orthogonal matrix \mathbf{U} and diagonal matrix \mathbf{D} given by SVD of $\mathbf{C}_1 + \mathbf{C}_2$. We used several CSP decompositions in this work, namely, CSP12 comparing relaxation and left hand motor imagery, CSP13 comparing relaxation and right hand motor imagery, CSP23 comparing left with right hand motor imagery, and CSP1X comparing relaxation and both left and right hand motor imagery. Although equations (12) are solved using signal epochs corresponding to the selected tasks only, the unmixing matrix was used to estimate the activity of the components at all other time moments.

MCSP is a generalization of the CSP method for multiple-class problems. There are several methods of generalization

(Lee et al., 2005; Bashashati et al., 2015). The most frequent approaches are to either compute all pairwise CSP and combine the corresponding components into a new signal to be classified or to use classifier voting or a tree of some sort when only two classes are compared at each step (e.g., relaxation vs. motor imagery with subsequent discrimination between the hands if the motor imagery was recognized). However, these techniques would not give us any additional information in terms of sources, as we have already considered all pairwise CSP decompositions for our experimental tasks, as well as the CSP1X comparing relaxation and motor imagery. That is why we have decided to use a different approach. Problem (12) was generalized so as to find \mathbf{W} such that

$$\begin{cases} \mathbf{W}\mathbf{C}_1\mathbf{W}^T = \mathbf{D}_1 \\ \mathbf{W}\mathbf{C}_2\mathbf{W}^T = \mathbf{D}_2 \\ \mathbf{W}(\mathbf{C}_1 + \mathbf{C}_2 + \mathbf{C}_3)\mathbf{W}^T = \mathbf{I} \end{cases}$$

The equations are written for the case of three tasks, but the generalization for the case of an arbitrary number of classes is straightforward. The problem in general has no explicit solution and can be solved numerically using any joint diagonalization technique. The joint diagonalization algorithm was the same as was used to perform the SOBI decomposition (Ziehe et al., 2004). It should be noted that unlike the two-class CSP, component variance ratio maximization (or minimization) for different classes is not guaranteed, but if any component has high (small) variance for a certain class, it will have small (high) variance for other classes.

Mutual Information Reduction

The mutual information reduction (MIR) provided by the decomposition methods is defined as

$$\text{MIR} = I(x_1, \dots, x_n) - I(\xi_1, \dots, \xi_n), \quad (13)$$

where the mutual signal information I is given by equation (6). Using (6), we get

$$\text{MIR} = \sum_i H(x_i) - H(\mathbf{X}) - \sum_i H(\xi_i) + H(\Xi) \quad (14)$$

Since $\mathbf{X} = \mathbf{A}\Xi$,

$$H(\mathbf{X}) = H(\Xi) + \log |\det \mathbf{A}| \quad (15)$$

and thus

$$\text{MIR} = \sum_i H(x_i) - \sum_i H(\xi_i) + \log |\det \mathbf{A}| \quad (16)$$

The entropy of each individual channel and component was estimated and bias-corrected as in Delorme et al. (2012).

Dipolar Component Selection

The decomposition (3) shows that the contribution of each component to the signal registered by the EEG electrodes is given by the weight vector, which can be treated as potential distribution over the scalp surface. This allows the source of electrical activity represented by the component to be localized.

As has been shown for the case of visual memory tasks, the physiologically meaningful components tend to have dipolar distributions of their weights, i.e., the distributions that could be adequately approximated by a single current dipole inside a head model (Delorme et al., 2012). We had neither anatomical magnetic resonance imagery (MRI) scans nor digitized electrode positions for most of our subjects. This is why a standardized head model based on the ICBM MNI atlas (Fonov et al., 2009, 2011) was used for estimating the dipolarity of the component weights. The dipolarity was computed as a residual variance of the best single dipole fit for the corresponding distribution. The fit was considered acceptable if the residual variance did not exceed 10%.

Shared Components

The number of the same components found by different decomposition methods can be used as a measure of similarity between the methods. On the other hand, the more methods reveal the component, the less likely it is that the component is an artifact of a certain mathematical procedure underlying the decomposition algorithm. That is why we focused our attention on the components found by different methods.

Two component similarity measures were used to determine which components were shared between the methods. The first measure was the absolute value of the cosine between normalized component weight vectors given by the corresponding mixing matrix columns. The second one was the absolute value of the Pearson correlation between the component activities. Two thresholds were chosen for the measures. The components were considered the same when both measures exceeded the corresponding thresholds. We have chosen 0.9 as the threshold for the topographic map similarity and 0.8 as the threshold for activity correlation.

When the number of shared components is obtained, the similarity between the decomposition methods can be measured as

$$\text{sim}_{ij} = \frac{n_s}{n_i + n_j - n_s}, \quad (17)$$

where n_s is the number of shared components, and n_i and n_j are the numbers of components obtained by the i -th and j -th methods, respectively. The similarity measure varies from 0, when there are no shared components, to 1, when the methods have provided identical decomposition. Also, only the dipolar components can be considered when the similarity (17) is calculated, allowing non-dipolar components that are unlikely to have physiological meaning to be discarded. The number of methods that found a component minus one will be called the component rank. The component rank equals 0 when it is found by only one method and 15 when it is found by all of the 16 methods considered.

Classification Accuracy and the Component Specificity

Given a set of the EEG components, their activity can be used for estimating the accuracy of discriminating between the experimental tasks. This estimate can serve as a measure of

components' specificity for the performed tasks, allowing the task-specific EEG patterns to be extracted and both artifacts and irrelevant EEG activity to be removed.

We used a greedy algorithm to find the task-specific components as follows. Only the dipolar components were considered. At the first step, classification accuracy was estimated for each set containing one or two components. The best set was then selected. The remaining components were added to the set one by one so that the new set would provide the highest classification accuracy. The components from the set for which the classification accuracy was maximal (over all of the steps) were considered as the task-specific components. The classification was tested by 120 trials of cross-validation where 7 blocks were chosen for the training set and the 3 remaining blocks were used as the testing set.

The accuracy of task classification was measured by Cohen's kappa index, κ (Vieira et al., 2010), which was calculated from the elements of the confusion matrix (g_{ij}) resulting from the cross-validation. The element g_{ij} counts how many times the i -th task was recognized by the classifier under the condition that the classified EEG epoch corresponded to the j -th cue. Given g_{ij} , the κ index is

$$\kappa = \frac{g_0 \sum_i g_{ii} - \sum_j g_j^2}{g_0^2 - \sum_j g_j^2}, \quad (18)$$

where g_0 is the sum of all of the elements of the confusion matrix, $\sum_i g_{ii}$ is the sum of all diagonal elements of the confusion matrix, and g_j is the sum of all of the elements of the j -th column of the confusion matrix. The index varies from -1 to 1 (perfect classification) and equals 0 in case of random classification.

Component Clustering

The decomposition (3) gives at least as many components as there are electrodes for each of the methods used. Consequently, the number of components computed for all experimental recordings is too high to check the components manually. In order to investigate EEG patterns most typical for our experimental tasks, we used cluster analysis to group the components according to their similarity. The clustering was performed using the Attractor Neural Network with Increasing Activity (ANNIA), which was originally proposed for Boolean factor analysis (Frolov et al., 2007). Adaptation of the technique for cluster analysis is described in Bobrov et al. (2014). When the ANNIA is used for clustering, the strength of synaptic connections between the neurons of the network is determined by the similarity between the corresponding elements rather than by Hebbian learning. The stopping criterion is based on a threshold that specifies the minimal average similarity between the elements of a cluster. In Bobrov et al. (2014), the ANNIA was used to group the components with respect to their topographic map similarity. In this paper, we have also accounted for the component activity similarity using the correlation coefficient between the components' activity power spectral densities estimated for each of the experimental tasks. Spectral analysis was used since the components obtained from different recordings were compared, in contrast with the

TABLE 1 | Percentage of dipolar components found and the method MIR.

Method	% of dipolar components	MIR, bits/(sec-chan)
PCA	4.35 [2.17; 7.50]	63.56 [51.89; 77.34]
KURT	15.39 [6.98; 27.50]	70.15 [58.97; 83.69]
CUMUL	12.77 [6.38; 22.61]	70.96 [59.21; 84.81]
FastICAT	15.63 [8.51; 27.50]	68.24 [57.28; 82.96]
FastICAG	15.22 [8.33; 27.33]	67.58 [56.60; 83.75]
RunICA	10.87 [3.54; 25.00]	74.92 [65.21; 86.47]
AMICA	25.53 [11.11; 38.96]	68.98 [57.47; 83.99]
AMICA1	21.74 [12.50; 32.55]	69.23 [58.11; 83.95]
AMICA2	27.50 [15.38; 40.00]	66.74 [55.88; 80.30]
PWCICA	19.57 [6.38; 31.25]	67.42 [56.00; 81.38]
SOBI	15.22 [6.67; 26.67]	71.52 [58.80; 84.88]
CSP12	4.26 [1.37; 13.68]	62.99 [50.11; 78.13]
CSP13	4.17 [2.08; 12.74]	63.24 [48.94; 77.74]
CSP1X	4.26 [1.91; 14.97]	63.72 [50.34; 77.87]
CSP23	2.22 [1.23; 10.00]	63.18 [48.82; 78.13]
MCSP	6.90 [2.17; 17.95]	63.89 [51.40; 77.78]

shared components search described earlier. Both the component similarity measures considered vary from 0 to 1 , and their mean was taken as the similarity measure for ANNIA.

RESULTS

Comparison of the Decomposition Methods

The methods were compared according to the criteria described in the previous section. The percentage of dipolar components found by each method is presented in **Table 1** (median values and quartiles are presented). The table also contains average values of mutual information reduction values for each of the methods. The p -values resulting from pairwise comparison of the percentage of the dipolar components found are presented in the upper diagonal part of **Table 2**. The values were obtained using a Wilcoxon test of the values pooled from all of the participants and sessions with subsequent Benjamini-Hochberg correction (initial significance level: 0.05 ; resulting critical value: 0.0429). The results indicate that the PWCICA and AMICA methods provide more dipolar components than the other methods. The difference is significant for the AMICA methods and insignificant when PWCICA is compared to other BSS methods. The PCA and CSP methods extracted significantly fewer dipolar components than the other methods.

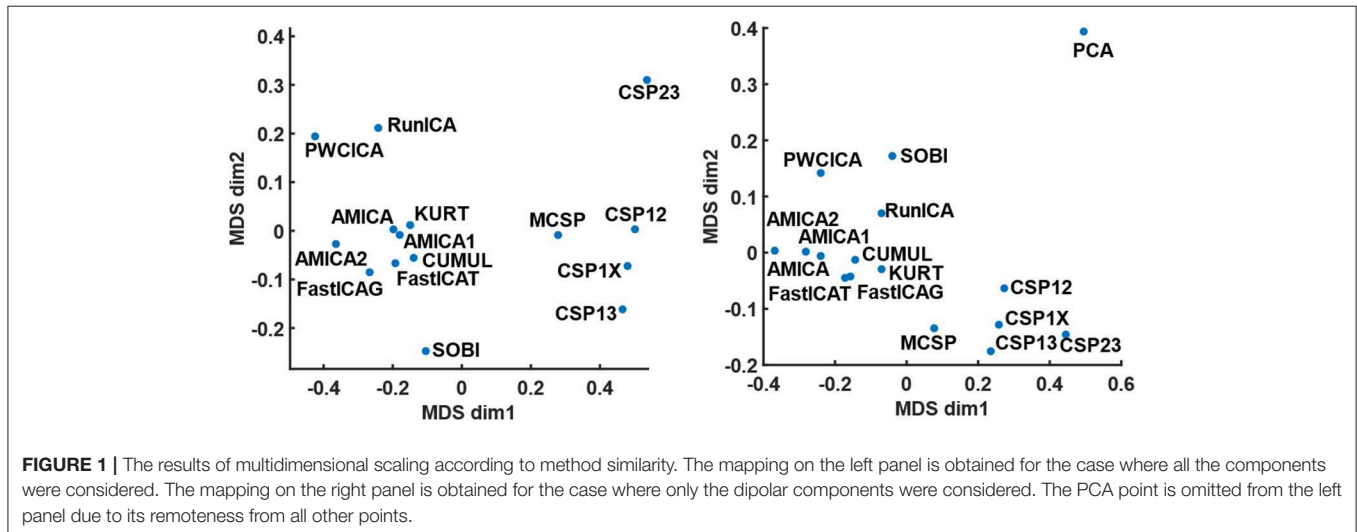
Pairwise Wilcoxon comparison of the MIR values with Benjamini-Hochberg correction (initial significance level: 0.05 ; resulting critical value: 0.0275) shows that the ICA methods provide significantly higher mutual information reduction than the PCA and CSP methods. The difference between ICA and other methods in terms of MIR was insignificant, as was the difference between the PCA and CSP methods.

The method similarity was estimated by the fraction of shared components according to (17), providing a method similarity

TABLE 2 | The p -values of pairwise Wilcoxon testing of the percentage of the dipolar components found (upper triangle part) and the pattern classification accuracy (lower triangle part).

	MCSP	CSP23	CSP12	CSP1X	CSP13	AMICA1	AMICA	AMICA2	PWCICA	SOBI	FastICAT	KURT	FastICAG	CUMUL	RunICA	PCA
MCSP		<1e-4	<1e-4	<1e-4	<1e-4	<1e-4	<1e-4	<1e-4	<1e-4	<1e-4	<1e-4	<1e-4	<1e-4	<1e-4	0.0053	<1e-4
CSP23	0.0463		0.0312	0.0053	0.0045	<1e-4	<1e-4	<1e-4	<1e-4	<1e-4	<1e-4	<1e-4	<1e-4	<1e-4	<1e-4	0.0037
CSP12	0.1150	0.6045		0.5743	0.5525	<1e-4	<1e-4	<1e-4	<1e-4	<1e-4	<1e-4	<1e-4	<1e-4	<1e-4	<1e-4	0.8583
CSP1X	0.0352	0.9696	0.5822		0.9963	<1e-4	<1e-4	<1e-4	<1e-4	<1e-4	<1e-4	<1e-4	<1e-4	<1e-4	<1e-4	0.3943
CSP13	0.0094	0.6366	0.3041	0.6029		<1e-4	<1e-4	<1e-4	<1e-4	<1e-4	<1e-4	<1e-4	<1e-4	<1e-4	<1e-4	0.5076
AMICA1	<1e-4	0.0231	0.0056	0.0175	0.0628		0.0323	<1e-4	0.0004	<1e-4	<1e-4	<1e-4	<1e-4	<1e-4	<1e-4	<1e-4
AMICA	<1e-4	0.0056	0.0015	0.0046	0.0181	0.6061		0.0673	<1e-4	<1e-4	<1e-4	<1e-4	<1e-4	<1e-4	<1e-4	<1e-4
AMICA2	0.0682	0.7721	0.5554	0.8452	0.8395	0.0940	0.0457		<1e-4	<1e-4	<1e-4	<1e-4	<1e-4	<1e-4	<1e-4	<1e-4
PWCICA	<1e-4	0.0007	<1e-4	0.0005	0.0027	0.2870	0.6421	0.0076		0.0937	0.5838	0.1890	0.2345	0.0008	<1e-4	<1e-4
SOBI	<1e-4	0.0006	<1e-4	0.0003	0.0016	0.2197	0.5266	0.0055	0.8586		0.2654	0.7172	0.6611	0.0350	0.0003	<1e-4
FastICAT	<1e-4	<1e-4	<1e-4	<1e-4	0.0002	0.0825	0.2646	0.0012	0.4937	0.6218		0.4582	0.5342	0.0013	<1e-4	<1e-4
KURT	<1e-4	<1e-4	<1e-4	<1e-4	<1e-4	0.0758	0.2594	0.0009	0.4703	0.5728	0.9670		0.9049	0.0158	<1e-4	<1e-4
FastICAG	<1e-4	<1e-4	<1e-4	<1e-4	<1e-4	0.0515	0.2027	0.0007	0.3798	0.5108	0.8375	0.9007		0.0094	<1e-4	<1e-4
CUMUL	<1e-4	<1e-4	<1e-4	<1e-4	<1e-4	0.0145	0.0839	<1e-4	0.1834	0.2308	0.5076	0.5392	0.6238		0.0526	<1e-4
RunICA	<1e-4	<1e-4	<1e-4	<1e-4	<1e-4	0.0024	0.0202	<1e-4	0.0391	0.0659	0.1537	0.1792	0.2098	0.4488		<1e-4
PCA	<1e-4	<1e-4	<1e-4	<1e-4	<1e-4	<1e-4	<1e-4	<1e-4	<1e-4	<1e-4	<1e-4	<1e-4	<1e-4	0.0002	0.0100	
On-line	<1e-4	<1e-4	<1e-4	<1e-4	<1e-4	<1e-4	<1e-4	<1e-4	<1e-4	<1e-4	<1e-4	<1e-4	<1e-4	<1e-4	<1e-4	<1e-4

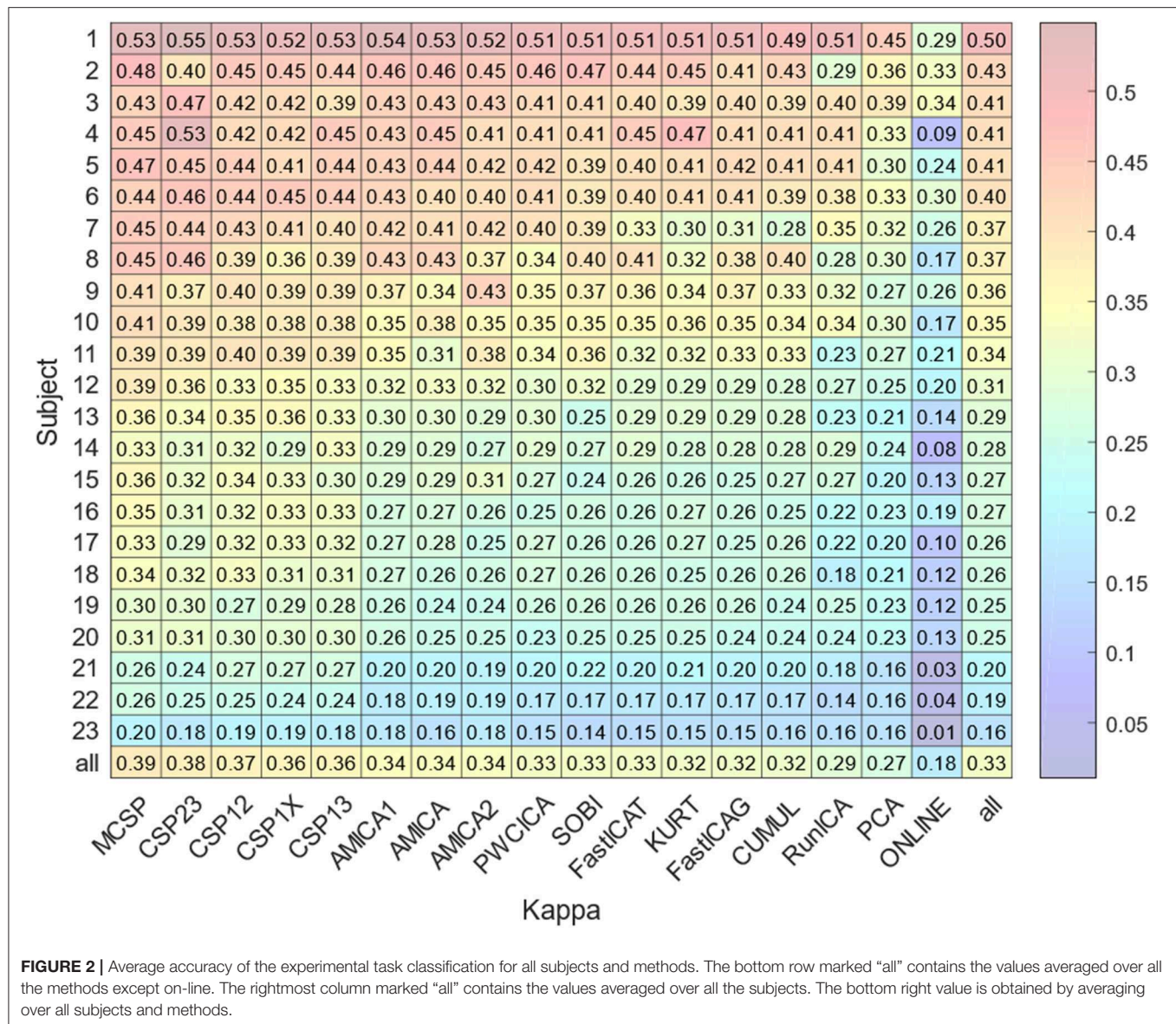
The values indicating insignificant difference are in bold.



matrix. The similarity matrices for the cases when either all or only dipolar components were considered were used for mapping the method onto a 2D plane with a multidimensional scaling technique. The results of the mapping are shown in **Figure 1**. Apparently, the methods tend to group according to the decomposition criteria, one group containing the ICA methods except PWCICA, and another group containing the CSP methods. SOBI and PWCICA are distant from both groups, while the PCA is as an outlier.

The results for classification accuracy, obtained after searching for the task-specific components, are shown in **Figure 2**. Mean κ values are shown for each subject and each method. The methods are sorted according to the κ value averaged over

all the subjects. The subjects are sorted according to the κ value averaged over all the methods. The lower diagonal part of **Table 2** contains p -values resulting from the pairwise comparison of the κ values for different methods. The values were obtained using Wilcoxon test of the values pooled from all of the participants and sessions with Benjamini-Hochberg correction (initial significance level: 0.05; resulting critical value: 0.320). The CSP methods provide patterns that are significantly better classified than those found by the other methods. The PCA patterns are significantly worse-classified than the patterns found by the other methods. The task-specific component search yielded accuracy values significantly exceeding those obtained during on-line BCI operation,



which is likely due to discarding irrelevant, artifact, and noisy components.

Component Clustering

The clusters obtained using the ANNIA were sorted according to their component occurrence, i.e., the percentage of the experimental session in which the components of the cluster were found. **Figure 3** shows topographic maps and activity power spectral densities (PSD) for the components of the first 12 clusters. The maps and PSDs were obtained by averaging over all of the cluster components regardless of the subject or session. **Table 3** presents the occurrence, average dipolarity, average rank, and specificity of the components of each cluster. As stated above, the component dipolarity was measured by the residual variance of the topographic map fit with a potential distribution resulting from a single current dipole, and the component rank is the

number of methods that found the component minus one. The specificity was calculated as the percentage of cases when the component was included in the best set of components (the set search is described in the Methods section) among the cases when the component was found.

It should be mentioned that AMICA restricted to only Gaussian distributions in mixtures performed as well as AMICA with the generalized super-Gaussian mixtures, suggesting that dipolar components obtained from band-pass filtered EEG signal have activity the distribution of which can be adequately approximated with a mixture of two Gaussians.

DISCUSSION

In the EEG\MEG field, and, particularly, in BCI research, ICA methods are mostly used for artifact removal during signal

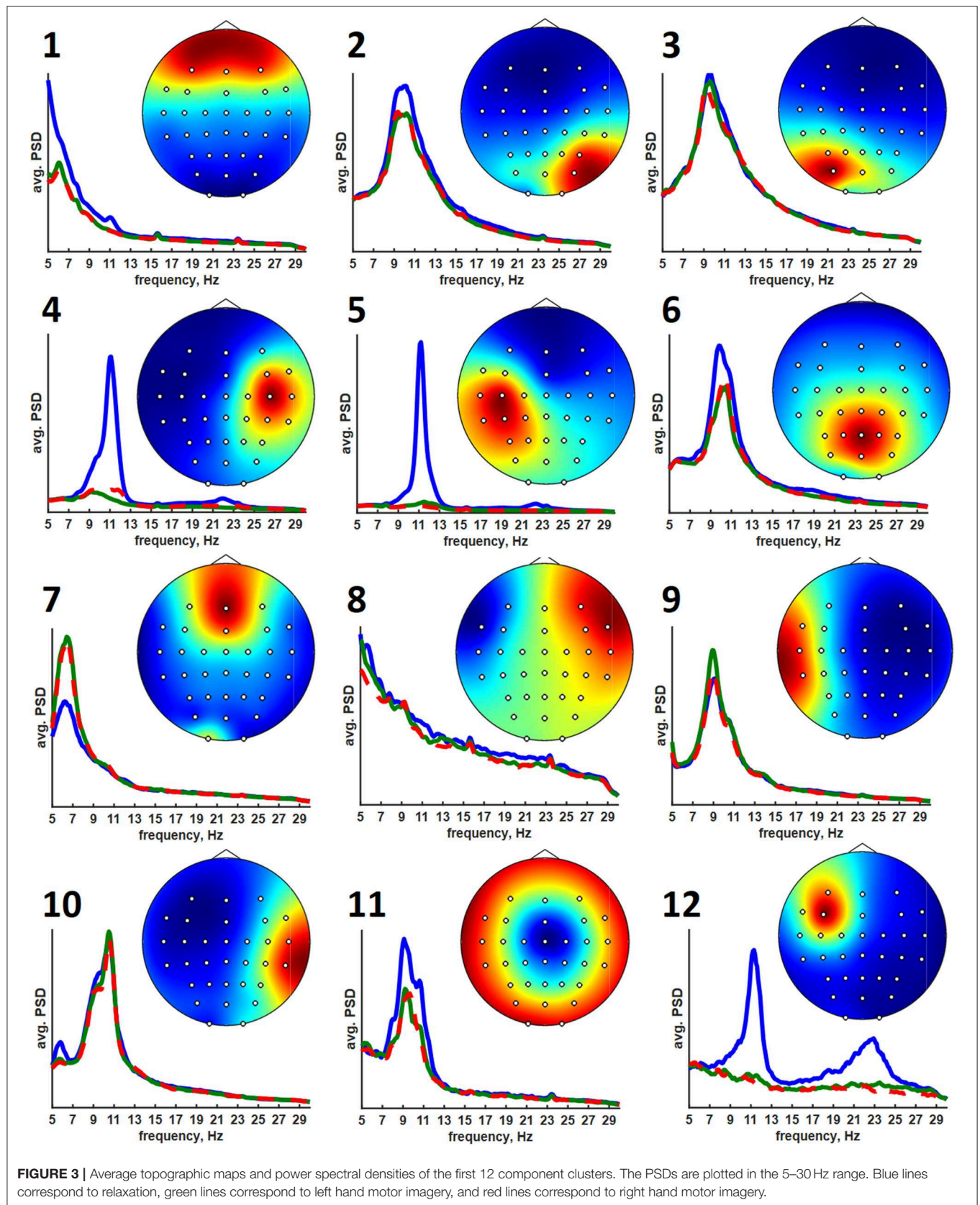


TABLE 3 | The cluster statistics.

Cluster	1	2	3	4	5	6	7	8	9	10	11	12
Occurrence, %	71	70	61	52	52	48	39	38	35	30	26	22
Dipolarity, %	2	9	8	8	4	3	2	3	9	8	3	4
Rank	3.74	2.24	1.78	1.62	3.53	2.83	2.66	1.48	1.06	1.78	1.92	2.23
Specificity, %	21	10	8	24	59	61	34	10	16	18	26	41

preprocessing or epoch classification. They are applied for eliminating ocular (Höller et al., 2013; Dharmapalani et al., 2016; Sarin et al., 2020), motion (Zhou et al., 2016; Kobler et al., 2019), and muscle (Höller et al., 2013; Dharmapalani et al., 2016) artifacts. The most popular method used for artifact suppression is RunICA (extended infomax), likely due to its incorporation into EEGLAB (Delorme and Makeig, 2004) and BrainStorm (Tadel et al., 2011) software. The ICA methods are also believed to provide effective spatial filters for BCI feature selection (Kachenoura et al., 2007; Lotte et al., 2018; Xiaopei et al., 2019). The main limitation to using the methods is that they require a substantial amount of data to converge to meaningful decomposition, and many of the algorithms have high computational costs to implement on-line. These issues, as well as the nature of the algorithm used to automatically select the most specific components, limit the on-line implementation of the procedure proposed in this paper. The procedure is rather intended for assessing the overall task-specificity of the EEG signal and adequately arranging experimental recordings and subjects with respect to the BCI control efficiency. Performing the cluster analysis allows the most frequent and typical EEG patterns in the processed recordings to be extracted with no need to choose a single decomposition method. The best method may differ when different criteria are applied, such as the number of the dipolar components found, the mutual information reduction, or the accuracy of classification of the extracted patterns.

The method comparison shows that ICA methods provide results similar to each other despite the difference in the independence criteria underlying the algorithms. These methods find significantly more dipolar components and provide significantly higher MIR than CSP or PCA, with the best results being for AMICA and PWCICA. PCA also has the lowest number of components shared with the other methods, as indicated by the results of multidimensional scaling. The maximal similarity between the PCA and other methods, estimated according to (17), was five times less than the minimal similarity between the other methods when all of the components were considered and two times less when only the dipolar components were considered. On the other hand, our results indicate that non-blind CSP methods find more of the separable activity patterns, much like in Xiaopei et al. (2019), where three ICA methods were compared to CSP in terms of providing the best spatial filters for a BCI classifier. However, unlike our case, no significant difference between RunICA and CSP was observed in Xiaopei et al. (2019). CSP outperformed the ICA methods, likely due to accounting for the signal segmentation with respect to the experimental tasks.

Thus, CSP decomposition is likely to find the dipolar components with task-specific activity, while it is poor at extracting other task-irrelevant dipolar sources. However, finding irrelevant but physiologically plausible sources may be useful for proving that BCI works based on the activity of the targeted brain areas. E.g., it may be important to establish that motor imagery BCI used for post-stroke rehabilitation worked because of the activity of the motor areas and not just due to eye movements or differences in concentration level.

The results of cluster analysis agree with those obtained earlier for fewer healthy subjects and patients with subcortical lesions (Frolov et al., 2017a). In previous work, the components relevant to controlling a hand exoskeleton via BCI were found to correspond to the sources of sensorimotor mu-rhythm located at the bottom of the central sulci of the left (SIL) and right (SIR) hemispheres, alpha-rhythmic activity in the precuneus (Prc), and alpha- and beta- activity in both the supplementary motor area (SMA) and in the premotor cortex of the left hemisphere (PrmL). These sources correspond to clusters 5 (SIL), 6 (SIR), 3 (Prc), 11 (SMA), and 8 (PrmL). We have also found clusters corresponding to blinking (1) and eye movements (7), which sometimes exhibited task-relevant activity, e.g., the subjects often blinked more frequently during relaxation. Clusters 2 and 3 correspond to the occipital alpha rhythm, which has low task-specificity. Interestingly, the source symmetrical to PrmR was more frequent compared to the earlier results (Frolov et al., 2017a). Source 12 exhibited activity similar to the mu-rhythm, but unfortunately, the subjects for whom it was observed had no individual anatomical MRI scans, so the source could not be reliably localized. However, the SIL source was found for more than half of the recordings for which source 12 was extracted. Also, sources SIL and 12 were found together by the same method in 35% cases. These findings suggest that source 12 might have localization different from that of the SIL sources.

The average PSDs of the clustered component activities reflect the specificity presented in Table 2. The most specific components of the 5-th, 6-th, and 12-th clusters exhibit prominent rhythm desynchronization during the motor imagery. Notably, there is no evident lateralization in the average level of desynchronization between the hemispheres. There are different results on the mu-rhythm behavior in the ipsilateral hemisphere during the hand motor imagery. Our results agree with those obtained in Vasilyev et al. (2016), where ipsilateral rhythm suppression was observed. However, ipsilateral rhythm synchronization was observed in Nam et al. (2011). We suppose that the reason for the result disagreement lies in the BCI protocol. It seems that active motor imagery, when maintained

for a long time (from 10 s in these experiments to 20 s in our earlier NIRS study (Bobrov et al., 2016), involves activation of both hemispheres, either due to high concentration and the complexity of the task or due to the person's intention to "check" whether the requested hand movement has been imagined. The first explanation is supported by the results of Nam et al. (2011), where the ipsilateral rhythm synchronization was observed mainly in the end phase of brief motor imagery (1 s) trials, suggesting that brief and prolonged motor imagery may require different strategies. The latter explanation comes from some of the participants reporting that they had sometimes switched attention to the other hand to "make sure it isn't moving". Note, that both phenomena (different strategy and attention switch) may be present during prolonged motor imagery and underlie the absence of the asymmetry of rhythm suppression.

Unlike the SIL, SIR, and 12th sources, other sources do not exhibit such prominent rhythm desynchronization or synchronization during the motor imagery. However, the Prm, SMA, and Prc sources are often marked as being task-specific. These areas are often reported to be relevant to motor planning, execution, and imagery. The Prm sources are likely to reflect mirror neuron system activation when the image of the motion to be executed or imagined is generated to be compared to the incoming sensory information (Rizzolatti et al., 2014). The SMA source is likely to correspond to the supplementary motor area activation. This area is considered to be involved in the motion timing, motion sequence generation, or motion suppression (Rizzolatti et al., 2014). It was reported to be more active during the motor imagery than during real motion execution, suggesting that its main role is to suppress the actual movement when motor imagery is performed (Guillot et al., 2014). The occurrence of the Prm and SMA sources is not as high as that of the Prc and SI sources. Nevertheless, we believe that these areas are activated in all of the participants but that the activations are not often prominent in the electroencephalogram and thus are harder to find, even when using advanced techniques. This supposition

is supported by the results of numerous fMRI studies (Héту et al., 2013) that report up to 34 areas being active during motor imagery.

In conclusion, we suggest the use of multi-method decomposition with subsequent component specificity estimation and clustering, focusing on the shared components. The primary methods to be used are PWCICA, AMICA, and MCSP, but utilizing other algorithms to support the findings seems to be reasonable.

DATA AVAILABILITY STATEMENT

The raw data supporting the conclusions of this article will be made available upon request by the authors, without undue reservation.

ETHICS STATEMENT

The studies involving human participants were reviewed and approved by Ethics committee of Institute of Higher Nervous Activity and Neurophysiology of Russian Academy of Sciences. The patients/participants provided their written informed consent to participate in this study.

AUTHOR CONTRIBUTIONS

MI, YK, DB, and AL performed the experiments and collected the data. DB and AL designed the experimental software. PB, MI, and YK analyzed EEG data. AF and PB contributed to the interpretation of the data. AF, PB, and EB contributed to writing the manuscript. All authors approved the final version of the manuscript for submission.

FUNDING

This work was supported by the Russian Ministry of Education and Science, grant RFMEFI60519X0184.

REFERENCES

- Ang, K. K., Chua, K. S. G., Phua, K. S., Wang, C., Chin, Z. Y., Kuah, C. W. K., et al. (2015). A randomized controlled trial of EEG-based motor imagery brain-computer interface robotic rehabilitation for stroke. *Clin. EEG Neurosci.* 46, 310–320. doi: 10.1177/1550059414522229
- Ang, K. K., Guan, C., Chua, K. S. G., Ang, B. T., Kuah, C. W. K., Wang, C., et al. (2011). A large clinical study on the ability of stroke patients to use an EEG-based motor imagery brain-computer interface. *Clin. EEG Neurosci.* 42, 253–258. doi: 10.1177/155005941104200411
- Bai, Z., Fong, K. N., Zhang, J. J., Chan, J., and Ting, K. (2020). Immediate and long-term effects of BCI-based rehabilitation of the upper extremity after stroke: a systematic review and meta-analysis. *J. Neuroeng. Rehabil.* 17, 1–20. doi: 10.1186/s12984-020-00686-2
- Ball, K., Bigdely-Shamlo, N., Mullen, T., and Robbins, K. (2016). PWC-ICA: a method for stationary ordered blind source separation with application to EEG. *Comput. Intell. Neurosci.* 2016:20. doi: 10.1155/2016/9754813
- Bashashati, A., Fatourehchi, M., Ward, R. K., and Birch, G. E. (2007). A survey of signal processing algorithms in brain-computer interfaces based on electrical brain signals. *J. Neural Eng.* 4, R32–R57. doi: 10.1088/1741-2560/4/2/R03
- Bashashati, H., Ward, R. K., Birch, G. E., and Bashashati, A. (2015). Comparing different classifiers in sensory motor brain computer interfaces. *PLoS ONE* 10:e0129435. doi: 10.1371/journal.pone.0129435
- Bell, A. J., and Sejnowski, T. J. (1995). An information-maximization approach to blind separation and blind deconvolution. *Neural Comput.* 7, 1129–1159. doi: 10.1162/neco.1995.7.6.1129
- Belouchrani, A., Abed-Meraim, K., Cardoso, J.-F., and Moulines, E. (1997). A blind source separation technique using second-order statistics. *IEEE Transac. Signal Proc.* 45, 434–444. doi: 10.1109/78.554307
- Bingham, E., and Hyvärinen, A. (2000). A fast fixed-point algorithm for independent component analysis of complex valued signals. *Int. J. Neural Syst.* 10, 1–8. doi: 10.1142/S0129065700000028
- Bobrov, P., Frolov, A., Husek, D., and Snael, V. (2014). Clustering the sources of EEG activity during motor imagery by Attractor Neural Network with Increasing Activity (ANNIA). *Proc. Fifth Int. Conf. Innov. Bio Inspir. Comput. Appl.* 303, 183–191. doi: 10.1007/978-3-319-08156-4_19
- Bobrov, P., Isaev, M., Korshakov, A., Oganessian, V., Kerechanin, J., Popodko, A., et al. (2016). Sources of electrophysiological and foci of hemodynamic

- brain activity most relevant for controlling a hybrid brain-computer interface based on classification of EEG patterns and near-infrared spectrography signals during motor imagery. *Hum. Physiol.* 42, 241–251. doi: 10.1134/S036211971603004X
- Cichocki, A., and Amari, S.-I. (2002). *Adaptive Blind Signal and Image Processing: Learning Algorithms and Applications*. Chichester: John Wiley and Sons.
- Delfosse, N., and Loubaton, P. (1995). Adaptive blind separation of independent sources: a deflation approach. *Signal Proc.* 45, 59–83. doi: 10.1016/0165-1684(95)00042-C
- Delorme, A., and Makeig, S. (2004). EEGLAB: an open source toolbox for analysis of single-trial EEG dynamics including independent component analysis. *J. Neurosci. Methods* 134, 9–21. doi: 10.1016/j.jneumeth.2003.10.009
- Delorme, A., Palmer, J., Onton, J., Oostenveld, R., and Makeig, S. (2012). Independent EEG sources are dipolar. *PLoS ONE* 7:e30135. doi: 10.1371/journal.pone.0030135
- Dharmapran, D., Nguyen, H. K., Lewis, T. W., Delosangeles, D., Willoughby, J. O., and Pope, K. J. (2016). “A comparison of independent component analysis algorithms and measures to discriminate between EEG and artifact components,” in *2016 38th Annual International Conference of the IEEE Engineering in Medicine and Biology Society (EMBC)* (Orlando, FL: IEEE), 825–828.
- Fonov, V., Evans, A. C., Botteron, K., Almli, C. R., McKinstry, R. C., Collins, D. L., et al. (2011). Unbiased average age-appropriate atlases for pediatric studies. *Neuroimage* 54, 313–327. doi: 10.1016/j.neuroimage.2010.07.033
- Fonov, V. S., Evans, A. C., McKinstry, R. C., Almli, C. R., and Collins, D. L. (2009). Unbiased nonlinear average age-appropriate brain templates from birth to adulthood. *Neuroimage* 47:S102. doi: 10.1016/S1053-8119(09)70884-5
- Frolov, A., Aziatskaya, G., Bobrov, P., Luykmanov, R. K., Fedotova, I., Húsek, D., et al. (2017a). Electrophysiological brain activity during the control of a motor imagery-based brain-computer interface. *Hum. Physiol.* 43, 501–511. doi: 10.1134/S036211971705005X
- Frolov, A., Husek, D., Bobrov, P., Korshakov, A., Chernikova, L., Konovalov, R., et al. (2012). Sources of EEG activity most relevant to performance of brain-computer interface based on motor imagery. *Neural Netw. World* 22, 21–37. doi: 10.14311/NNW.2012.22.002
- Frolov, A.A., Husek, D., Muraviev, I.P., and Polyakov, P.Y. (2007). Boolean factor analysis by attractor neural network. *IEEE Trans. Neural Netw.* 18, 698–707. doi: 10.1109/TNN.2007.891664
- Frolov, A.A., Mokienko, O., Lyukmanov, R., Biryukova, E., Kotov, S., Turbina, L., et al. (2017b). Post-stroke rehabilitation training with a motor-imagery-based brain-computer interface (BCI)-controlled hand exoskeleton: a randomized controlled multicenter trial. *Front. Neurosci.* 11:400. doi: 10.3389/fnins.2017.00400
- Guillot, A., Di Rienzo, F., and Collet, C. (2014). “The neurofunctional architecture of motor imagery,” in *Advanced Brain Neuroimaging Topics in Health and Disease-Methods and Applications*, eds T. D. Papageorgiou, G. I. Christopoulos, and S. M. Smirnakis (Rijeka: Intech), 433–456.
- Héту, S., Grégoire, M., Saimpont, A., Coll, M.-P., Eugène, F., Michon, P.-E., et al. (2013). The neural network of motor imagery: an ALE meta-analysis. *Neurosci. Biobehav. Rev.* 37, 930–949. doi: 10.1016/j.neubiorev.2013.03.017
- Höller, Y., Bergmann, J., Thomschewski, A., Kronbichler, M., Höller, P., Crone, J. S., et al. (2013). Comparison of EEG-features and classification methods for motor imagery in patients with disorders of consciousness. *PLoS ONE* 8:e80479. doi: 10.1371/journal.pone.0080479
- Hyvarinen, A. (2001). Blind source separation by nonstationarity of variance: a cumulant-based approach. *IEEE Transac. Neural Netw.* 12, 1471–1474. doi: 10.1109/72.963782
- Hyvärinen, A., Karhunen, J., and Oja, E. (2004). *Independent Component Analysis*. New York, NY: John Wiley and Sons.
- Kachenoura, A., Albera, L., Senhadji, L., and Comon, P. (2007). ICA: a potential tool for BCI systems. *IEEE Signal Process. Mag.* 25, 57–68. doi: 10.1109/MSP.2008.4408442
- Kobler, R., Hirata, M., Hashimoto, H., Dowaki, R., Sburlea, A. I., and Müller-Putz, G. (2019). “Simultaneous decoding of velocity and speed during executed and observed tracking movements: an MEG study,” in *Proceedings of the 8th Graz Brain-Computer Interface Conference 2019: Bridging Science and Application*. Graz: Verlag der Technischen Universität Graz. 100–105.
- Lee, F., Scherer, R., Leeb, R., Neuper, C., Bischof, H., and Pfurtscheller, G. (2005). “A comparative analysis of multi-class EEG classification for brain computer interface,” in *Proceedings of the 10th Computer Vision Winter Workshop* (Graz), 195–204.
- Lee, T.-W., Girolami, M., and Sejnowski, T. J. (1999). Independent component analysis using an extended infomax algorithm for mixed subgaussian and supergaussian sources. *Neural Comput.* 11, 417–441. doi: 10.1162/089976699300016719
- Lotte, F., Bougrain, L., Cichocki, A., Clerc, M., Congedo, M., Rakotomamonjy, A., et al. (2018). A review of classification algorithms for EEG-based brain-computer interfaces: a 10 year update. *J. Neural Eng.* 15:031005. doi: 10.1088/1741-2552/aab2f2
- Mane, R., Chew, E., Phua, K. S., Ang, K. K., Robinson, N., Vinod, A., et al. (2019). Prognostic and monitoring EEG-biomarkers for BCI upper-limb stroke rehabilitation. *IEEE Transac. Neural Syst. Rehabil. Eng.* 27, 1654–1664. doi: 10.1109/TNSRE.2019.2924742
- Nam, C. S., Jeon, Y., Kim, Y.-J., Lee, I., and Park, K. (2011). Movement imagery-related lateralization of event-related (de) synchronization (ERD/ERS): motor-imagery duration effects. *Clin. Neurophysiol.* 122, 567–577. doi: 10.1016/j.clinph.2010.08.002
- Niedermeyer, E., and Da Silva, F. L. (2005). *Electroencephalography: Basic Principles, Clinical Applications, and Related Fields*. Philadelphia, PA: Lippincott Williams and Wilkins.
- Ono, T., Shindo, K., Kawashima, K., Ota, N., Ito, M., Ota, T., et al. (2014). Brain-computer interface with somatosensory feedback improves functional recovery from severe hemiplegia due to chronic stroke. *Front. Neuroeng.* 7:19. doi: 10.3389/fneng.2014.00019
- Palmer, J.A., Kreutz-Delgado, K., and Makeig, S. (2006). “Super-Gaussian mixture source model for ICA,” in *International Conference on Independent Component Analysis and Signal Separation* (Charleston, SC: Springer), 854–861.
- Palmer, J.A., Kreutz-Delgado, K., and Makeig, S. (2012). *AMICA: An Adaptive Mixture of Independent Component Analyzers With Shared Components*. Swartz Center for Computational Neuroscience, University of California San Diego, Technical Report.
- Palmer, J. A., Makeig, S., Kreutz-Delgado, K., and Rao, B. D. (2008). “Newton method for the ICA mixture model,” in *Acoustics, Speech and Signal Processing. 2008. ICASSP 2008 (IEEE International Conference on: IEEE)* (Las Vegas, NV), 1805–1808.
- Ramoser, H., Müller-Gerking, J., and Pfurtscheller, G. (2000). Optimal spatial filtering of single trial EEG during imagined hand movement. *IEEE Trans. Rehabil. Eng.* 8, 441–446. doi: 10.1109/86.895946
- Ramos-Murguialday, A., Broetz, D., Rea, M., Laer, L., Yilmaz, O., Brasil, F.L., et al. (2013). Brain-machine interface in chronic stroke rehabilitation: a controlled study. *Ann. Neurol.* 74, 100–108. doi: 10.1002/ana.23879
- Rizzolatti, G., Cattaneo, L., Fabbri-Destro, M., and Rozzi, S. (2014). Cortical mechanisms underlying the organization of goal-directed actions and mirror neuron-based action understanding. *Physiol. Rev.* 94, 655–706. doi: 10.1152/physrev.00009.2013
- Sarin, M., Verma, A., Mehta, D. H., Shukla, P. K., and Verma, S. (2020). “Automated ocular artifacts identification and removal from eeg data using hybrid machine learning methods,” in *2020 7th International Conference on Signal Processing and Integrated Networks (SPIN)* (Noida: IEEE), 1054–1059.
- Tadel, F., Baillet, S., Mosher, J. C., Pantazis, D., and Leahy, R. M. (2011). Brainstorm: a user-friendly application for MEG/EEG analysis. *Comput. Intell. Neurosci.* 2011:879716. doi: 10.1155/2011/879716
- Vasilyev, A., Liburkina, S., and Kaplan, A. Y. (2016). Lateralization of EEG patterns in humans during motor imagery of arm movements in the brain-computer interface. *Zhurnal Vyshei Nervnoi Deiatelnosti Imeni I.P. Pavlova*. 66, 302–312.
- Vieira, S. M., Kaymak, U., and Sousa, J. M. (2010). “Cohen’s kappa coefficient as a performance measure for feature selection,” in *International Conference on Fuzzy Systems* (Barcelona: IEEE), 1–8.

- Xiaopei, W., Zhou, B., Lv, Z., and Zhang, C. (2019). To explore the potentials of independent component analysis in brain-computer interface of motor imagery. *IEEE J. Biomed. Health Inform.* 24, 775–787. doi: 10.1109/JBHI.2019.2922976
- Zhou, B., Wu, X., Lv, Z., Zhang, L., and Guo, X. (2016). A fully automated trial selection method for optimization of motor imagery based brain-computer interface. *PLoS ONE* 11:e0162657. doi: 10.1371/journal.pone.0162657
- Ziehe, A., Laskov, P., Nolte, G., and MäZler, K.-R. (2004). A fast algorithm for joint diagonalization with non-orthogonal transformations and its application to blind source separation. *J. Mach. Learn. Res.* 5, 777–800. Available online at: <http://www.jmlr.org/papers/v5/ziehe04a.html>

Conflict of Interest: The authors declare that the research was conducted in the absence of any commercial or financial relationships that could be construed as a potential conflict of interest.

Copyright © 2020 Frolov, Bobrov, Biryukova, Isaev, Kerechanin, Bobrov and Legin. This is an open-access article distributed under the terms of the Creative Commons Attribution License (CC BY). The use, distribution or reproduction in other forums is permitted, provided the original author(s) and the copyright owner(s) are credited and that the original publication in this journal is cited, in accordance with accepted academic practice. No use, distribution or reproduction is permitted which does not comply with these terms.



Mobility Skills With Exoskeletal-Assisted Walking in Persons With SCI: Results From a Three Center Randomized Clinical Trial

EunKyoung Hong^{1,2}, Peter H. Gorman³, Gail F. Forrest^{4,5}, Pierre K. Asselin^{1,2}, Steven Knezevic¹, William Scott⁶, Sandra Buffy Wojciehowski^{4,7}, Stephen Kornfeld^{1,2} and Ann M. Spungen^{1,2,8*}

¹ Spinal Cord Damage Research Center, James J. Peters VA Medical Center, Bronx, NY, United States, ² Department of Rehabilitation and Human Performance, Icahn School of Medicine at Mount Sinai, New York, NY, United States, ³ Department of Neurology, University of Maryland School of Medicine and Chief, Division of Rehabilitation Medicine, University of Maryland Rehabilitation and Orthopaedic Institute, Baltimore, MD, United States, ⁴ Center for Spinal Stimulation and Center for Mobility and Rehabilitation Engineering, Kessler Foundation, West Orange, NJ, United States, ⁵ Physical Medicine & Rehabilitation, Rutgers New Jersey Medical School, Newark, NJ, United States, ⁶ Department of Neurology, University of Maryland School of Medicine and VA Maryland Healthcare System, Baltimore, MD, United States, ⁷ Performance Exercise Attitude and Knowledge Center, Craig Hospital, Englewood, CO, United States, ⁸ Department of Medicine, Icahn School of Medicine at Mount Sinai, New York, NY, United States

OPEN ACCESS

Edited by:

Jan Veneman,
Hocoma, Switzerland

Reviewed by:

Matteo Lancini,
University of Brescia, Italy
Solaiman Shokur,
École Polytechnique Fédérale de
Lausanne, Switzerland

*Correspondence:

Ann M. Spungen
Ann.Spungen@va.gov

Specialty section:

This article was submitted to
Biomedical Robotics,
a section of the journal
Frontiers in Robotics and AI

Received: 01 May 2020

Accepted: 09 June 2020

Published: 04 August 2020

Citation:

Hong E, Gorman PH, Forrest GF, Asselin PK, Knezevic S, Scott W, Wojciehowski SB, Kornfeld S and Spungen AM (2020) Mobility Skills With Exoskeletal-Assisted Walking in Persons With SCI: Results From a Three Center Randomized Clinical Trial. *Front. Robot. AI* 7:93. doi: 10.3389/frobt.2020.00093

Background: Clinical exoskeletal-assisted walking (EAW) programs for individuals with spinal cord injury (SCI) have been established, but many unknown variables remain. These include addressing staffing needs, determining the number of sessions needed to achieve a successful walking velocity milestone for ambulation, distinguishing potential achievement goals according to level of injury, and deciding the number of sessions participants need to perform in order to meet the Food and Drug Administration (FDA) criteria for personal use prescription in the home and community. The primary aim of this study was to determine the number of sessions necessary to achieve adequate EAW skills and velocity milestones, and the percentage of participants able to achieve these skills by 12 sessions and to determine the skill progression over the course of 36 sessions.

Methods: A randomized clinical trial (RCT) was conducted across three sites, in persons with chronic (≥ 6 months) non-ambulatory SCI. Eligible participants were randomized (within site) to either the EAW arm first (Group 1), three times per week for 36 sessions, striving to be completed in 12 weeks or the usual activity arm (UA) first (Group 2), followed by a crossover to the other arm for both groups. The 10-meter walk test seconds (s) (10MWT), 6-min walk test meters (m) (6MWT), and the Timed-Up-and-Go (s) (TUG) were performed at 12, 24, and 36 sessions. To test walking performance in the exoskeletal devices, nominal velocities and distance milestones were chosen prior to study initiation, and were used for the 10MWT (≤ 40 s), 6MWT (≥ 80 m), and TUG (≤ 90 s). All walking tests were performed with the exoskeletons.

Results: A total of 50 participants completed 36 sessions of EAW training. At 12 sessions, 31 (62%), 35 (70%), and 36 (72%) participants achieved the 10MWT, 6MWT, and TUG milestones, respectively. By 36 sessions, 40 (80%), 41 (82%), and 42 (84%) achieved the 10MWT, 6MWT, and TUG criteria, respectively.

Conclusions: It is feasible to train chronic non-ambulatory individuals with SCI in performance of EAW sufficiently to achieve reasonable mobility skill outcome milestones.

Keywords: exoskeletal-assisted walking, mobility walking tests, 10MWT, 6MWT, TUG, Food and Drug Administration

INTRODUCTION

Paralysis resulting from spinal cord injury (SCI) often leads to a reduction in mobility and an associated decrease in daily physical activity. In addition, SCI also leads to other secondary adverse consequences related to body composition (Wilmet et al., 1995; Spungen et al., 1999, 2000), cardiovascular function (Wahman et al., 2010; LaVela et al., 2012), autonomic integrity (Wecht et al., 2000, 2001), and bowel function (Glickman and Kamm, 1996; Stiens et al., 1997; Korsten et al., 2004). The combination of reduced mobility and secondary consequences of SCI leads to a reduced quality of life (Costa et al., 2001; Tate et al., 2002; Jensen et al., 2007; Wilson et al., 2011; Munce et al., 2013).

Devices classified by the Food and Drug Administration (FDA) as “powered exoskeletons” (Product Classification U. S. Food Drug Administration, 2019) have become commercially available and enable individuals with motor paralysis to stand and walk over ground. These devices employ use of a ridged external frame for bracing the lower extremities and trunk. Rechargeable battery powered motors are then used to power movement of the hip and knee joints. Just as able bodied walking requires the ability to maintain balance and perform weight shifting (Tapio, 2016), powered exoskeleton assisted ambulation requires the same. These movements are measured by sensors in the device that trigger motors to power movement at the hip and knee joints. Consecutive weight shifting must be completed by actively maintaining balance on the stance leg so that the swing leg can clear the floor appropriately. Subsequent weight shift onto the contralateral side continues to trigger the device to take steps. Over ground balance maintenance and weight shifting are assisted through use of crutches or a walker. The execution of this exoskeletal-assisted walking (EAW) movement places demands on the neuromuscular and sensory systems of the user, increasing oxygen consumption when compared to able bodied ambulation (Asselin et al., 2015; Evans et al., 2015). The additional metabolic activity required to ambulate with these devices has the potential to provide a cardiovascular exercise challenge and thereby improve cardiovascular health (Escalona et al., 2018). However, since this technology remains relatively new, many aspects of its use by persons with SCI have yet to be determined.

Due to limitations with current available systems, not all persons with SCI are able to successfully achieve EAW (walking velocity of ≥ 0.40 m/s over 10 meters and 6-min walk distance ≥ 110 m with minimal assistance or less). Some users may manage

to take steps but require a significant amount of assistance to accomplish this. Therefore, identification of basic skills during early sessions in order to predict who would be potential responders, that is successful and independent users of the device in the home and community after completing a training program, would be important. The purpose of this study was to document the number of sessions necessary to achieve adequate EAW skills and velocity milestones, to document the proportion of participants who achieved successful EAW skills by 12 sessions, and to determine the skill progression over the course of 36 sessions.

METHOD

Recruitment

This study was approved by the Institutional Review Boards (IRB) of the three collaborating clinical sites, namely the James J. Peters VA Medical Center (JJPVAMC), Bronx, NY, Kessler Institute for Rehabilitation/Kessler Foundation (KIR/KF), West Orange, NJ, and the University of Maryland, Baltimore IRB for the University of Maryland Rehabilitation and Orthopedic Institute (UM Rehab and Ortho), Baltimore, MD). In addition, the Department of Defense Congressionally Directed Medical Research Program (DOD CDMRP) IRB approved the total study. Several recruitment strategies were employed. The study physicians at each site were the primary source of identifying potential participants. In-services at each site were provided to educate other staff physicians about this study for referrals. Additionally, at each site IRB-approved flyers and brochures were distributed. Physician-referred potential participants, as well as those responding to IRB approved advertisements or the clinicaltrials.gov website listing (NCT02314221), were informed about the details and eligibility for the study. The targeted study population included persons with chronic SCI (≥ 6 months) who were non-ambulatory and therefore used wheelchairs for mobility. The inclusion/exclusion criteria of this study are described below (Table 1).

Protocol

Participants were screened for eligibility after signing the informed consent form. Screening tests for eligibility included a complete history and physical examination incorporating the following: the International Standards for Neurological Classification of SCI (ISNCSCI) examination to determine level and completeness of injury, range of motion at the hips, knees

TABLE 1 | Enrollment criteria.**Enrollment criteria***Inclusion criteria:*

1. Males and females, between 18 and 65 years old;
2. Traumatic or non-traumatic tetraplegia or paraplegia >6 months in duration;
3. Unable to ambulate faster than 0.17 m/s on level ground with or without an assistive device and are wheelchair-dependent for mobility;
4. Height 160 to 190 cm (63–75 in or 5'3" to 6'3" ft)
5. Weight <100 kg (<220 lb)
6. Able to hold the Lofstrand crutches or wheeled walker; and
7. Able to sign informed consent.

Exclusion criteria:

1. Diagnosis of neurological injury other than SCI including:
 - a Multiple sclerosis, Stroke, Cerebral Palsy, Amyotrophic lateral sclerosis, Traumatic Brain injury, Spina bifida, Parkinson's disease, or
 - b Other neurological condition that the study physician considers in his/her clinical judgment to be exclusionary;
2. Severe concurrent medical disease, illness or condition;
3. Lower extremity fracture within the past 2 years;
4. Dual Energy X-ray Absorptiometry (DXA) results indicating a t-score below -3.5 at the femoral neck or the total proximal femur bone and knee bone mineral density (BMD) <0.60 gm/cm²;
5. Diagnosis of heterotopic ossification of the lower extremities which affect range of motion or proper BMD measurements;
6. Significant contractures defined as flexion contracture limited to 35° at the hip and 20° at the knee;
7. Untreated hypertension (SBP>140, DBP>90 mmHg);
8. Symptomatic orthostatic hypotension during standing that does not resolve after attempts at upright posture that were made over several days, and standing by the participant is deemed to pose a health risk, as determined by a physician, because of symptomatic orthostatic hypotension;
9. Systemic or peripheral infection;
10. A medical diagnosis in the patient chart of atherosclerosis, congestive heart failure, or history of myocardial infarction;
11. Trunk and/or lower extremity pressure ulcers;
12. Severe spasticity (defined by an Ashworth score of 4.0 across a lower extremity joint or clinical impression of the study physician or physical therapist);
13. Significant contractures defined as flexion contracture limited to 25° at the hip and knee;
14. Diagnosis of heterotopic ossification of the lower extremities which affect range of motion or proper measurement of BMD measurements;
15. Psychopathology documentation in the medical record or history of that may conflict with study objectives;
16. Pregnancy and/or lactating females.
17. Brain injury with score on mini-mental status examination <26
18. Diagnosis of coronary artery disease that precludes moderate to intense exercise;
19. Deep vein thromboses in lower extremities of <6 months duration;
20. Other illness that the study physician considers in his/her clinical judgment to be exclusionary.

and ankles bilaterally, Ashworth spasticity examination in the lower extremities, standing orthostatic tolerance test, and bone mineral density (BMD) scanning of bilateral knees (proximal tibia and distal femur) and hips (femoral neck and total hip) by Dual Energy X-ray Absorptiometry (DXA). Exclusion criteria for the BMD measurements have been described (Table 1).

Eligible participants were randomized within site to one of two groups for 12 weeks (3 months): Group 1 received EAW first for 12 weeks then crossover to usual activity (UA) for a second 12 weeks; Group 2 received UA first for 12 weeks then crossover

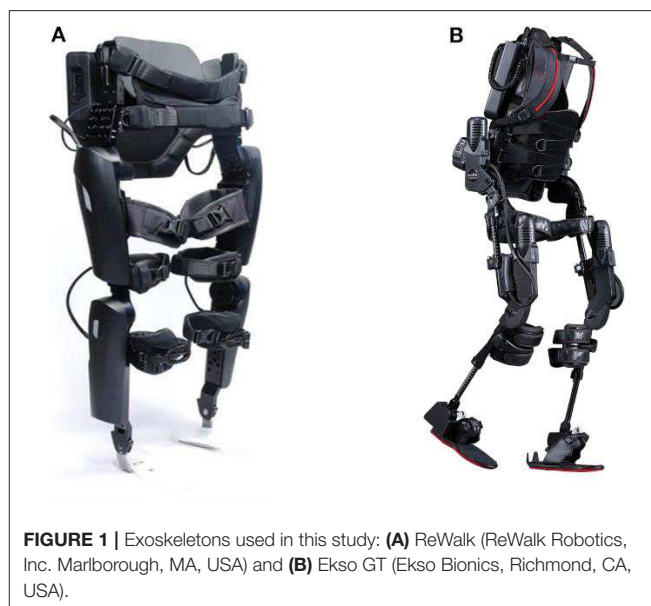


FIGURE 1 | Exoskeletons used in this study: (A) ReWalk (ReWalk Robotics, Inc. Marlborough, MA, USA) and (B) Ekso GT (Ekso Bionics, Richmond, CA, USA).

to EAW for 12 weeks of training. The EAW arm consisted of EAW training, three sessions per week (4–6 h/week) for 36 sessions. The UA arm consisted of identification of usual activities for each participant and encouragement to continue with these activities throughout the 12-week UA arm. This study employed a randomized, crossover design with an EAW intervention arm and an UA arm which was designed to serve as a control arm for the secondary outcomes of the clinical/medical variables. The results of the medical variables are beyond the scope of the present manuscript and will be presented in a future work. As such, the UA arm was not intended to be used as a control comparison for the mobility outcome measures.

Two powered exoskeleton devices (Figure 1) were used in this study, namely the ReWalkTM (ReWalk Robotics, Marlborough, MA)¹ and the EksoTM (Ekso Bionics, Richmond, CA)². These powered exoskeletons were chosen because they were the only devices commercially available and FDA approved for use within rehabilitation centers at the time of study development. In addition, the ReWalk has been FDA approved for home and community use based on certain user characteristics and achievements within a supervised rehabilitation center (spinal injury level T7 to L5, walking velocity of ≥0.4 m/s over 10 meters and 6 min walk distance ≥110 m) (Hoffmann, 2016). Both devices have functional similarities, such as the required concurrent use of Lofstrand crutches or a wheeled walker in the case of the Ekso, and the need for the user to shift their weight in order to trigger sensors that in turn motorized the hip. However, there are some notable differences in the specifications of the devices such as the stepping pattern and the design such as the footplate in the Ekso. The maximum documented velocities for the devices are 0.80 m/s for the ReWalk¹ and 0.45 m/s for the Ekso². The Ekso device has a rigid back that provides

¹ReWalk. Available online at: <https://rewalk.com/>.

²Ekso Bionics. Available online at: <https://eksobionics.com/ekshealth/>.

thoracic support to accommodate participants who have less trunk stability such as those with a low cervical (C) or high thoracic (T) level of injury. The footplate of Ekso has a sensor to detect weight shifts and assist with triggering the hip motors. The foot trajectory of the Ekso follows a semi-elliptical trajectory with a higher step height for foot clearance, leading to a marching style gait pattern. In the Ekso, depending on the functional abilities of the user, the level of device assist could be selected from the adaptive, maximal or fixed mode. In response to the participants' functional abilities, variable assistance constantly adapts motor output or a fixed level of assistance could be set for participants. The ReWalk gait paradigm is more of a swing pattern minimizing the step height but requiring more controlled balance to successfully achieve reciprocal stepping (Asselin et al., 2016). Thus, the ReWalk powered exoskeleton was chosen primarily for participants with injury levels at T3 and below who could perform weight shifting and clear each foot during stepping. Those with higher cord lesions and less trunk stability were better able to utilize the Ekso powered exoskeleton. Although choice of which device was commonly distributed based on level and completeness of injury, device selection was somewhat variable depending on the participant's preference and the clinical judgment of the study team. Both devices were used at JJPVAMC and Kessler, and the ReWalk was only used at UM Rehab and Ortho. Study-related serious adverse event (SAE) and adverse event (AE) tracking occurred throughout the study.

Training Sessions

Generally, within the first two sessions, standing balance skills were practiced and achieved prior to progression to walking skills. Walking skills began with unloading the right foot (both devices use the right leg to take the first step). Shifting weight onto the right foot and unweighting the left foot was the next step in the progression of walking. Continuous walking resulted from serial performance of the anterior-lateral diagonal shift onto the contralateral limb. Because this was an entirely new skill for the participants, mobility outcomes were not measurable at time 0 (baseline). It was important to determine how many participants could achieve successful EAW skills by 12 sessions to prove or disprove clinical relevance and to project progression by 36 sessions. Participants were asked to perform EAW sessions three times/week for 12 weeks. During each session, heart rate (HR), blood pressure (BP), total steps and rating of perceived exertion (RPE, by the Borg scale: from 6 to 20) (Escalona et al., 2018)³ were monitored. Additional details of the training program were presented previously (Asselin et al., 2016; Baunsgaard et al., 2018). Missed sessions (due to transportation, weather, etc.) were added on to the length of the training period when possible in order to achieve a total of 36 sessions. A modified Functional Independence Measure (FIM) was used to assess how much physical assistance from the trainer was provided to participants in order to complete mobility skills. The FIM scale (7: Complete Independence, 6: Modified Independence, 5: Supervision, 4:

Minimal Assist, 3: Moderate Assist, 2: Maximal Assist, 1: Total Assist, 0: Activity does not occur) (Dodds et al., 1993; FIM, 2019) for level of assistance during EAW was used and ranged from 0 to 6. While a score of 7, complete independence, is a part of the FIM scale, it is not applicable for this study as all participants required the use of the exoskeleton, thus negating the ability of complete independence (Dodds et al., 1993; FIM, 2019).

Outcome Measures

A variety of walking assessments were employed to assess an individual's functional independence (Shinkai et al., 2000; Middleton et al., 2015). The 10-meter walk test (10MWT), which measures the time in seconds (s) taken to walk 10 meters, is a short distance performance measurement to determine functional mobility and vestibular function (Van Hedel et al., 2008)⁴. The 6 min walk test (6MWT) is a submaximal exercise test that measures the distance in meters (m) traversed over 6 min and provides cardiopulmonary and musculoskeletal functional capacity information (Van Hedel et al., 2008; Bittner and Singh, 2017). The timed-up-and-go (TUG) is the time from the starting in a seated position to stand-up, walk ten feet, turn around, walk back ten feet, and sit down. This measurement was performed to assess fall risk and ability to balance and maneuver the device during the sit-to-stand and stand-to-sit procedures (Podsiadlo and Richardson, 1991; Van Hedel et al., 2008). During all walking tests, level of assistance, balance maintenance, weight shifts, reciprocal stepping and functional mobility were observed and recorded. The three walking test measurements were performed during the 12th, 24th, and 36th sessions.

Data Analysis

All statistical tests were set *a priori* at alpha = 0.05. Descriptive statistics and frequency distributions were used to describe the demographic data. All statistical analyses were completed using SPSS 23.00 or higher. The continuous variables were reported in mean plus or minus standard deviation. Total steps over 36 sessions and average of steps were calculated to determine participants' overall performance during this study. Because of differences in characteristics of devices, number of steps and velocity were categorized by devices. With each walking outcome (10MWT, 6MWT, and TUG), achievement of the hypothesized goals during the EAW intervention were reported as categorical data and presented as percent occurrence. The hypotheses for significant positive changes at session 12 verses session 36 for the EAW walking tests were as follows: at session 12, 10% of participants would complete the 10MWT in ≤ 40 s and 20% of the participants would complete the 6MWT of ≥ 80 m and TUG in ≤ 90 s; at session 36, 70% of participants would complete the 10MWT in ≤ 40 s and 6MWT of ≥ 80 m and 60% of participants would perform the TUG in ≤ 90 s. Additional analyses were performed according to skill level of completing the 10MWT, 6MWT and TUG categorized by slow, medium, and fast velocity sub-groups. The velocity sub-groups were defined *post hoc* after the review of data starting with using

³ Perceived Exertion (Borg Rating of Perceived Exertion Scale): Centers for Disease Control and Prevention. Available online at: <https://www.cdc.gov/physicalactivity/basics/measuring/exertion.htm>.

⁴ 10 Meter Walking Test: Physiopedia. Available online at: https://www.physio-pedia.com/10_Metre_Walk_Test.

TABLE 2 | Exoskeletal-assisted walking velocity categories for each of the walking tests.

EAW category	10MWT	6MWT	TUG
Slow	<0.25 m/s	<80 m	≥120 s
Medium	≥0.25 and <0.40 m/s	≥80 and <110 m	≥90 and <120 s
Fast	≥0.40 m/s	≥110 m	<90 s

10MWT, 10-minute walk test; 6MWT, six-meter walk test; TUG, timed up and go; m/s, meters per second; m, meters; s, seconds.

the FDA criteria as the minimum velocity for “fast” and thus representing those with the greatest skill level in the devices. The “medium” velocity was defined as those who could walk at speed and distance ranges that demonstrated some proficiency with the devices, and “slow” were those who were minimally able to use the devices. The velocities and distances by category for each walking test are provided (Table 2). To determine significant main effects, the mobility skills were evaluated for the three different time points using a repeated measure analysis of variance (ANOVA). *Post hoc* analysis were performed using paired *t*-tests to determine significance between sessions 12 and 36 for progression of participant performances on the mobility outcomes. Additionally, the TUG criterion was analyzed further and compared to the established FDA criteria for the 10MWT (speed ≥0.40 m/s) and 6MWT (distance ≥110 m).

Due to differences in characteristics of level of injury with residual muscle function, participants were sub-grouped according to the International Standards for Neurological Classification of Spinal Cord Injury (ISNCSCI): motor complete tetraplegia (C1-C8; American Spinal Injury Association impairment scale (AIS) A&B); motor incomplete tetraplegia (C1-C8; AIS C&D); motor complete paraplegia (T1-T12; AIS A&B); and motor incomplete paraplegia (T1-T12; AIS C&D). A mixed model ANOVA was performed to determine significant main and interaction effects for the neurological classifications with respect to time (12, 24, and 36 sessions) and number of steps per session block by mobility test (10MWT, 6MWT, and TUG). *Post hoc* analyses were performed using a paired *t*-test to compare performances of walking assessments from 12 to 36 sessions within the level and completeness sub-groups.

RESULTS

Participants

A total of 50 individuals (average age 39 ± 14 years) completed 36 sessions of EAW training. Demographic information for gender, height, weight, duration of injury, level of injury, ISNCSCI classification, and device used are summarized (Table 3).

The proportion of males (76%) and females included in this study corresponds with reported proportion of males (about 78%) and females in the United States SCI population (NSCISC, 2019). More individuals with paraplegia participated in this study mainly due to the need of arm and hand function in order to safely use crutches or a walker to maintain balance. Most

participants with injury level of T3 or lower used the ReWalk and participants with injury level higher than T3 used the Ekso. However, there were some participants that were thought to be better suited for the other device. This resulted in a total of 28 participants that trained in the ReWalk and 22 that trained with the Ekso (Table 3).

There were no “probably study-related” SAEs, but there were four “possibly study-related” SAEs. There were 49 total study-related AEs which included 39 skin abrasions/bruising, eight musculoskeletal/edema, and two falls. All study-related skin abrasions and musculoskeletal AEs were resolved, and participants continued in study. There were two falls during EAW, but no injuries occurred. Participants had appropriate HR and BP responses throughout the training sessions. RPE's during training ranged from very, very light to very hard (Tapio, 2016). There were no HR or BP-related AEs during EAW.

Total Steps Results

There were no order effects for Group 1 (immediate) vs. Group 2 (delayed therapy) for total steps and for any of the walking test results. Descriptive statistics were used to determine mean and standard deviation for the cumulative total number of steps for all sessions. The average number of steps per session by session 36 for all participants ($N = 50$) regardless of the device were $51,065 \pm 17,836$ and the average steps per session were $1,420 \pm 491$. The cumulative total number of steps taken across all sessions for all participants split by device is presented in relation to the fastest walking velocity achieved by 36 sessions (Figure 2A). The number of steps taken per session increased overall sessions for both devices. Participants who used the ReWalk took significantly less steps per session during the first 12 sessions than participants who used the Ekso. However, during the last 12 sessions (sessions 25–36) participants who used the ReWalk were able to take more steps per session than those who used the Ekso. Ultimately, participants who used the Ekso took more total overall steps than those who used the ReWalk. The first 6 sessions were pilot sessions where the participants were introduced to the device and had the actual training. The linear regressions of ReWalk ($r^2 = 0.0956$, $y = 27.90x + 931.24$) and Ekso ($r^2 = 0.082$, $y = 16.62x + 1267.96$) were performed with steps only on sessions 7–36 (Figure 2B, Table 4).

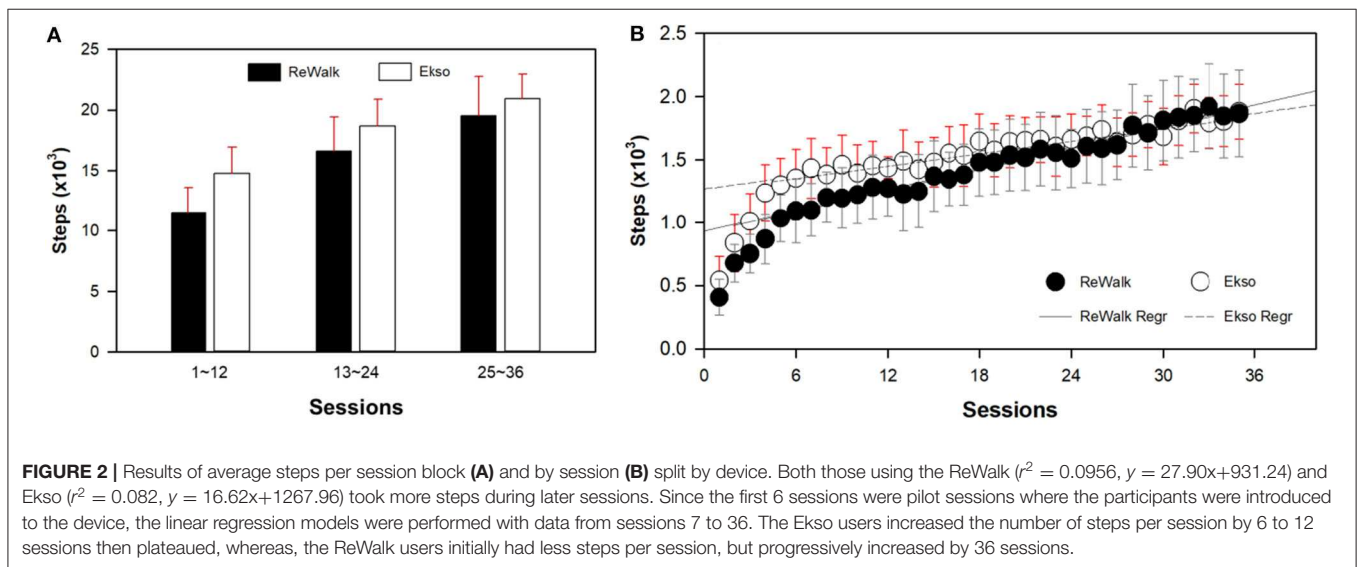
10 Meter Walk Test (10MWT) Results

At session 12, 92% of the participants performed the 10MWT in ≤ 60 s (≥ 0.17 m/s). Participants were able to perform the 10MWT with an average of 38.6 ± 14.8 s by 12 sessions. The fastest 10MWT at 12 sessions was 20.0 s and the slowest was 83.4 s. By 36 sessions, 82% of the participants (compared with 62% at session 12) were able to perform the 10MWT in ≤ 40 s (≥ 0.25 m/s). The average 10MWT across all participants was 36.3 ± 14.6 s by 24 sessions and 32.1 ± 12.6 by 36 sessions. With 36 sessions of EAW training, 17 of 50 participants (34%) fulfilled the FDA 10MWT requirement (≥ 0.40 m/s) for personal use prescription (Tables 5, 6).

TABLE 3 | Demographic and spinal cord injury characteristics of the total study group.

Count (N) and percent (%)			Demographic characteristics				SCI characteristics					
			Age	Height	Weight	Body mass index	Duration of injury	Motor complete		Motor incomplete		
								(AIS A/B)		(AIS C/D)		
Category	N	%	Years	cm	kg	kg/m²	Years	n	%	n	%	
All	50	100	38.68 ± 14.15	174.14 ± 10.33	72.80 ± 13.44	23.94 ± 3.65	4.69 ± 5.18	31	62	19	38	
Males	38	76	39.87 ± 14.78	178.00 ± 8.52	76.80 ± 11.67	24.24 ± 3.44	5.37 ± 5.63	26	52	12	24	
Females	12	24	34.9 ± 11.68	161.93 ± 4.07	60.14 ± 10.80	22.97 ± 4.25	2.55 ± 2.46	5	10	7	14	
Para	36	72	37.44 ± 12.68	173.85 ± 10.08	72.16 ± 13.40	23.83 ± 3.80	4.99 ± 5.78	27	54	9	18	
Tetra	14	28	41.86 ± 17.50	174.90 ± 11.31	74.45 ± 13.93	24.22 ± 3.36	3.93 ± 3.22	4	8	10	20	
Males-Para	28	56	39.21 ± 13.31	177.53 ± 8.04	74.92 ± 12.53	23.74 ± 3.58	5.77 ± 6.27	22	44	6	12	
Males-Tetra	10	20	41.70 ± 19.01	179.32 ± 10.10	82.06 ± 6.88	25.64 ± 2.72	4.25 ± 3.31	4	8	6	12	
Female-Para	8	16	31.25 ± 8.01	160.97 ± 3.83	62.48 ± 12.41	24.12 ± 4.75	2.26 ± 2.16	5	10	3	6	
Females-Tetra	4	8	42.25 ± 15.59	163.83 ± 4.40	55.45 ± 4.93	20.66 ± 1.74	3.12 ± 3.28	0	0	4	8	
DOI > 2 years	26	52	38.15 ± 13.39	174.97 ± 8.60	74.79 ± 12.98	24.37 ± 3.67	7.85 ± 5.55	16	32	10	20	
DOI ≤ 2 years	24	48	39.25 ± 15.20	173.25 ± 12.05	70.65 ± 13.87	23.47 ± 3.65	1.28 ± 0.54	15	30	9	18	
ReWalk para	27	54	35.63 ± 11.07	174.32 ± 9.77	72.59 ± 13.38	23.88 ± 4.04	5.73 ± 6.43	20	4	7	14	
ReWalk tetra	1	2	31	188.96	84.37	23.88	5.00	0	0	1	2	
Ekso para	9	18	42.89 ± 16.15	172.44 ± 11.46	70.86 ± 14.16	23.67 ± 3.14	2.79 ± 2.14	7	14	2	4	
Ekso tetra	13	26	42.69 ± 17.92	173.89 ± 11.10	73.69 ± 14.19	24.24 ± 3.49	3.85 ± 3.33	4	8	9	18	

Values represent means and (standard deviations); SCI, spinal cord injury; AIS, American Spinal Injury Association Impairment Scale; cm, centimeters; kg, kilograms; m, meters; G1, Group 1; G2, Group 2; Para, paraplegia; and Tetra, tetraplegia; EAW, exoskeletal-assisted walking; UA, usual activities; DOI, duration of SCI; ReWalk or Ekso user for the study as indicated.



Six Minute Walk (6MWT) Test Results

Thirty-five participants (70%) were able to walk a distance ≥ 80 meters for the 6MWT by 12 sessions. Twenty-six participants (52%) achieved successful EAW training with or without minimal assistance by 12 sessions. Forty-eight participants (96%) were able to walk more than 50 meters (≥ 0.14 m/s) in the 6MWT and the average 6MWT was 99.8

± 35.1 m at 12 sessions. By 24 sessions, about half of the participants (24 participants, 48%) were able to meet FDA requirements for the 6MWT (≥ 110 m). By 36 sessions, 41 (82%) participants accomplished a 6MWT of ≥ 80 m (≥ 0.22 m/s). The average 6MWT was 111.9 ± 42.6 m by 24 sessions and 125.3 ± 40.4 m by 36 sessions. At 36 sessions of EAW training, 33 of 50 participants (66%) fulfilled the FDA

TABLE 4 | Walking test results by devices (ReWalk and Ekso).

Walking test	Unit	Session 12		Session 24		Session 36	
		ReWalk	Ekso	ReWalk	Ekso	ReWalk	Ekso
10MWT	Mean \pm SD (s)	29.51 \pm 7.80	50.08 \pm 13.59	26.89 \pm 7.53	48.37 \pm 12.41	25.61 \pm 7.89	40.02 \pm 12.87
	Min–Max (s)	19.98–46.17	29.90–83.43	17.80–46.60	24.70–70.58	16.58–47.50	21.03–63.68
	Mean \pm SD (m/s)	0.36 \pm 0.09	0.21 \pm 0.06	0.40 \pm 0.10	0.22 \pm 0.06	0.42 \pm 0.11	0.27 \pm 0.08
6MWT	Mean \pm SD (m)	119.50 \pm 32.68	74.78 \pm 18.01	136.85 \pm 38.50	80.05 \pm 20.93	148.44 \pm 32.99	96.79 \pm 28.94
	Min–Max (m)	59.70–168.40	43.75–112.70	40.70–196.40	46.53–141.80	65.40–206.60	54.60–162.00
	Mean \pm SD (m/s)	0.33 \pm 0.09	0.21 \pm 0.05	0.38 \pm 0.11	0.22 \pm 0.06	0.41 \pm 0.09	0.27 \pm 0.08
TUG	FIM 1 to 3 (n, %)	10 (38%)	9 (47%)	8 (30%)	4 (18%)	2 (7%)	2 (9%)
	FIM 4 to 5 (n, %)	14 (54%)	10 (53%)	14 (52%)	18 (82%)	15 (56%)	19 (86%)
	FIM 6 (n, %)	2 (8%)	–	5 (18%)	–	10 (37%)	1 (5%)
	Mean \pm SD (s)	67.17 \pm 15.25	90.33 \pm 18.33	69.69 \pm 33.82	81.95 \pm 24.11	53.41 \pm 11.24	72.22 \pm 20.47
	Min–Max (s)	43.72–108.78	64.90–134.37	34.59–155.24	39.05–144.60	35.15–81.50	42.61–103.38
Total Steps by Sessions	FIM 1 to 3 (n, %)	12 (52%)	17 (89%)	14 (58%)	12 (54%)	7 (27%)	7 (33%)
	FIM 4 to 5 (n, %)	10 (43%)	2 (11%)	8 (33%)	10 (46%)	12 (46%)	13 (62%)
	FIM 6 (n, %)	1 (5%)	–	2 (9%)	–	7 (27%)	1 (5%)
	Mean \pm SD (#)	11,789 \pm 5,421	14,357 \pm 5,186	28,788 \pm 12,441	32,760 \pm 9,892	50,475 \pm 19,393	53,685 \pm 13,645
	Min–Max (#)	3,620–21,459	4,963–21,516	8,925–47,493	13,163–48,352	21,005–85,125	22,633–74,772
Grouped Total Steps ^a	Mean \pm SD (#)	11,789 \pm 5,421	14,357 \pm 5,186	16,999 \pm 7,455	18,403 \pm 5,078	209,52 \pm 8,246	20,925 \pm 4,544
	Min–Max (#)	3,620–21,459	4,963–21,516	5,025–28,820	8,200–28,431	9,338–38,677	9,470–27,767
Steps within Session	Mean \pm SD (#)	1,173 \pm 594	1,256 \pm 345	1,426 \pm 593	1,538 \pm 430	1,718 \pm 731	1,601 \pm 349
	Min–Max (#)	210–2,300	423–1,835	427–2,511	389–2,556	143–3,689	745–2,108

10MWT, ten meter walk test in meters (m); 6MWT, six-minute walk test in seconds (s); TUG, timed up and go in seconds (s); SD, standard deviation; m/s, meters per second; Min, minimum values achieved; Max, maximum value achieved; n, number and %, percent of participants who achieved the criteria; Com, motor complete; Tetra, tetraplegia; Inc, motor incomplete; Para, paraplegia; FDA, Food and Drug Administration; and FIM, Functional Independence Measure. Shaded areas indicate the FIM scores (FIM definitions are reported in **Table 5** legend) for 6MWT and TUG walking tests at 12, 24, and 36 sessions. Not all participants had a FIM score recorded during Sessions 12, 24, and 36.

^aGrouped Total Steps were defined as grouped sessions: 1–12, 13–24, and 25–36.

requirement for the 6MWT (110 m) for personal use prescription (**Tables 5, 6**).

Timed Up and Go (TUG) Test Results

At session 12, 46 participants (92%) performed the TUG in 120 s and 36 participants (72%) performed the TUG in <90 s. By Session 36, 84% of the participants were able to perform the TUG in <90 s (**Tables 5, 6**).

Combined Walking Test Result Reporting

The number and percent of participants who were categorized by slow, medium, and fast walkers, their progression into the more skillful category over the three timepoints (sessions 12, 24, and 36) and number of participants who met FDA velocity criteria, stratified by level of injury are presented (**Table 5**). With 36 sessions of EAW training, 15 of 50 participants (30%) who used the ReWalk succeeded in achieving both of FDA speed requirements for personal use prescription (10MWT within 25 s or ≥ 0.40 m/s and 6MWT ≥ 110 m or ≥ 0.31 m/s). Those fifteen participants met the FDA requirement by 24 sessions (**Table 5**).

The overall performance results from the different walking assessments at the three time points, the change in performance with additional training sessions and the range of speeds achieved, respectively, are presented (**Table 6**). A repeated measures ANOVA with a Greenhouse-Geisser correction

determined that the mean of 10MWT, 6MWT, and TUG differed statistically between time points (10MWT: ($F_{(1.841, 88.372)} = 13.921$, $p < 0.0005$), 6MWT ($F_{(1.849, 88.734)} = 34.830$, $p < 0.0005$), and TUG ($F_{(1.597, 68.665)} = 13.749$, $p < 0.0005$)). Paired-sample t -tests were conducted to compare the performance of tasks with the number of sessions. There were no significant differences in the 10MWT and the TUG from 12 to 24 sessions. However, there were significant differences in all mobility assessments, 10MWT, 6MWT, and TUG from 24 to 36 sessions. There were also significant differences from 12 to 36 sessions. The mean values for the 10MWT (s), 6MWT (m), and TUG (s) walking assessments are presented (**Table 6**). The average results of all participants' walking velocities and distances from 12 to 36 sessions were significantly improved (**Table 6**).

Using the walking velocity, participants were divided into three sub-groups: slow, medium, and fast. The results of the TUG showed most of participants (82%) falling into the medium and fast velocity sub-groups at session 12. This improved with further training, as 86% of participants fell in the fast category at session 36. It was hypothesized that 20% of participants at 12 sessions and 60% of participants at 36 sessions would be able to perform the TUG in ≤ 90 s. However, more than two thirds of participants (72%) accomplished TUG criterion at session 12 and 90% of participants did at session 36 in

TABLE 5 | Number and percent of participants by walking velocity categories.

	Outcomes	Velocity and distance categories	12 sessions n (%)	24 sessions n (%)	36 sessions n (%)
10MWT	Primary	≥0.17 m/s	46 (92%)		
	Primary	≥0.25 m/s	31 (62%)		41 (82%)
		Slow: <0.25 m/s	21 (42%)	16 (32%)	10 (20%)
		Medium: ≥0.25 to <0.40 m/s	16 (32%)	18 (36%)	22 (44%)
		Fast: ≥0.40 m/s	13 (26%)	16 (32%)	17 (34%)
	ReWalk (only) users who met FDA velocity and distance criteria (10MWT: ≥ 0.40 m/s and 6MWT: ≥ 110 m)	Total (n = 28)	9 (32%)	15 (54%)	15 (54%)
		Com Tetra (n = 0)	n/a	n/a	n/a
		Inc Tetra (n = 1)	1 (100%)	1 (100%)	1 (100%)
		Com Para (n = 20)	6 (30%)	11 (55%)	11 (55%)
		Inc Para (n = 7)	2 (29%)	3 (43%)	3 (43%)
6MWT	Primary	≥50 m	48 (96%)		
	Primary	≥80 m	35 (70%)		41 (82%)
		Slow: <80 m	16 (32%)	14 (28%)	8 (16%)
		Medium: ≥80 to <110 m	18 (36%)	12 (24%)	8 (16%)
		Fast: ≥110 m	16 (32%)	24 (48%)	33 (66%)
		FIM ≥4	26 (52%)	37 (74%)	45 (90%)
TUG	Primary	≤120 s	48 (96%)		
	Primary	≤90 s	36 (72%)		45 (90%)
		Slow: ≥120 s	1 (2%)	5 (10%)	0 (0%)
		Medium: ≥90 to <120 s	10 (20%)	5 (10%)	5 (10%)
		Fast: <90 s	36 (72%)	38 (76%)	43 (86%)
		FIM ≥4	13 (26%)	20 (40%)	33 (66%)

10MWT, ten meter walk test in meters (m); 6MWT, six-minute walk test in seconds (s); TUG, timed up and go in seconds (s); SD, standard deviation; m/s, meters per second; Min, minimum values achieved; Max, maximum value achieved; n, number and %, percent of participants who achieved the criteria; Com, motor complete; Tetra, tetraplegia; Inc, motor incomplete; Para, paraplegia; and FDA, Food and Drug Administration. slow, medium, and fast velocity sub-groups. The velocity sub-groups were defined post hoc after the review of data.

Shaded areas indicate the Primary outcome results for each of the walking tests at 12 and 36 sessions. The FDA criteria was applied only to the ReWalk users because the Ekso is not indicated for personal use.

Modified Functional Independence Measurement (FIM) Scoring Key:

1, Total Assist (performs <25% of task); 2, Maximal Assist (performs 25 to 49% of task); 3, Moderate Assist (performs 50–74% of task); 4, Minimal Assist (performs 75% or more of task); 5, Supervision (cuing, coaxing, prompting); 6, Modified Independence (no assistance, user may require extra time); 7, Complete Independence (timely, safely, no assistance, no devices), albeit, not applicable in this study.

TABLE 6 | Walking test assessment results.

Sessions		12	24	36
10MWT	Mean ± SD (s)	38.56 ± 14.80	36.34 ± 14.60	32.08 ± 12.59 ^{¥T}
	Mean ± SD (m/s)	0.30 ± 0.11	0.32 ± 0.12	0.36 ± 0.12 ^{¥T}
	Min–Max (s)	20.0–83.4	17.8–70.6	16.6–63.7
6MWT	Mean ± SD (s)	99.83 ± 35.07	111.86 ± 42.61*	125.25 ± 40.37 ^{¥°}
	Mean ± SD (m/s)	0.28 ± 0.10	0.31 ± 0.12*	0.35 ± 0.11 ^{¥°}
	Min–Max (s)	43.8–168.4	40.7–196.4	54.6–206.6
TUG	Mean ± SD (s)	78.01 ± 20.28	75.31 ± 30.10	62.03 ± 18.55 ^{¥°}
	Min–Max (s)	43.72–134.37	34.59–155.24	35.15–103.38

SD, standard deviation; m, meters; WT, walk test; min, minutes; TUG, timed up and go; sec, seconds; and m/s, meters per second. Sessions 12 vs. 24: * $p < 0.0001$; Sessions 12 vs. 36: [¥] $p < 0.0001$; and Sessions 24 vs. 36: [°] $p = 0.0008$, [°] $p < 0.0001$.

≤90 s. Using the walking velocity from the 10MWT, the average TUG was calculated for the three velocity sub-groups and presented (Table 7).

Comparison Between Devices

Due to the different characteristics between the ReWalk and Ekso, the results from the 10MWT, 6MWT, and TUG were

TABLE 7 | Average TUG by velocity sub-groups of 10MWT speed.

			TUG					
			Session 12		Session 24		Session 36	
			N	Mean \pm SD	N	Mean \pm SD	N	Mean \pm SD
10 MWT	≤ 0.25 m/s	Slow	20	89.61 \pm 19.75	16	87.84 \pm 24.43	10	83.25 \pm 16.76
	$0.25 \leq \text{Speed} \leq 0.4$	Medium	15	74.93 \pm 18.40	17	76.24 \pm 32.01	23	59.48 \pm 16.43
	≥ 0.4 m/s	Fast	12	62.53 \pm 9.84	15	60.88 \pm 28.77	15	51.80 \pm 10.32

10MWT, ten-meter walk test in meters; TUG, timed up and go in seconds; SD, standard deviation; m/s, meters per second.
TUG was defined/calculated by the velocity sub-groups of 10MWT at 12, 24, and 36 sessions.

significantly different by device. By session 36, the fastest participant in the ReWalk performed the 10MWT in 16.6 s and slowest in 47.5 s, whereas in the Ekso the fastest was 21.0 s and the slowest was 63.7 s (Table 4, Figure 3A).

Effect of Neurological Deficit

Change in walking test performance was independent of neurological deficit. As mentioned previously, participants were divided by four neurological deficit sub-groups: motor complete tetraplegia ($n = 4$); motor incomplete tetraplegia ($n = 10$); motor complete paraplegia ($n = 27$); and motor incomplete paraplegia ($n = 9$). There were no significant differences between groups in terms of improvements from 12 to 36 sessions on the 10MWT [one-way ANOVA ($F_{(3, 45)} = 2.555$, $p = 0.067$)], 6MWT [one-way ANOVA ($F_{(3, 45)} = 1.150$, $p = 0.339$)], and TUG [one-way ANOVA ($F_{(3, 41)} = 1.115$, $p = 0.354$)]. Within level and completeness sub-groups, paired t -tests were used to compare the performance of tasks from 12 to 36 sessions. Overall, those with complete tetraplegia walked shorter distances in the 6MWT and took more time for the 10MWT and TUG at session 12. Participants with complete paraplegia performed the best among the sub-groups for 10MWT and 6MWT at session 12. From sessions 12 to 36, those with complete tetraplegia demonstrated no significant change in the 10MWT and 6MWT, however, there was significant improvement on TUG ($p = 0.019$). All walking assessments were significantly improved from 12 to 36 sessions in the sub-groups of incomplete tetraplegia (10MWT: $p = 0.020$, 6MWT: $p = 0.011$, TUG: 0.046) and complete paraplegia (10MWT: $p = 0.001$, 6MWT: $p < 0.000$, TUG: $p = 0.002$). Both those with incomplete tetraplegia and complete paraplegia demonstrated improvement in the TUG ($p = 0.015$). Each sub-group's results of the walking tests are reported at 12, 24, and 36 sessions (Figure 3B).

Using the average of the highest achieved number of steps per session block (between 1 and 12, 13 and 24, 25 and 36) split by tetraplegia/paraplegia and device, a repeated measures ANOVA with a Greenhouse-Geisser correction determined that the number of steps differed statistically between session blocks ($F_{(1.336, 66.477)} = 39.868$, $p < 0.0001$). However, there were no significant differences among sub-groups (tetraplegia/paraplegia and device) in terms of number of steps from session block 1–12 [one-way ANOVA ($F_{(3, 46)} = 0.507$, $p = 0.679$)], session block 13–24 [one-way ANOVA ($F_{(3, 46)} = 0.364$, $p = 0.779$)],

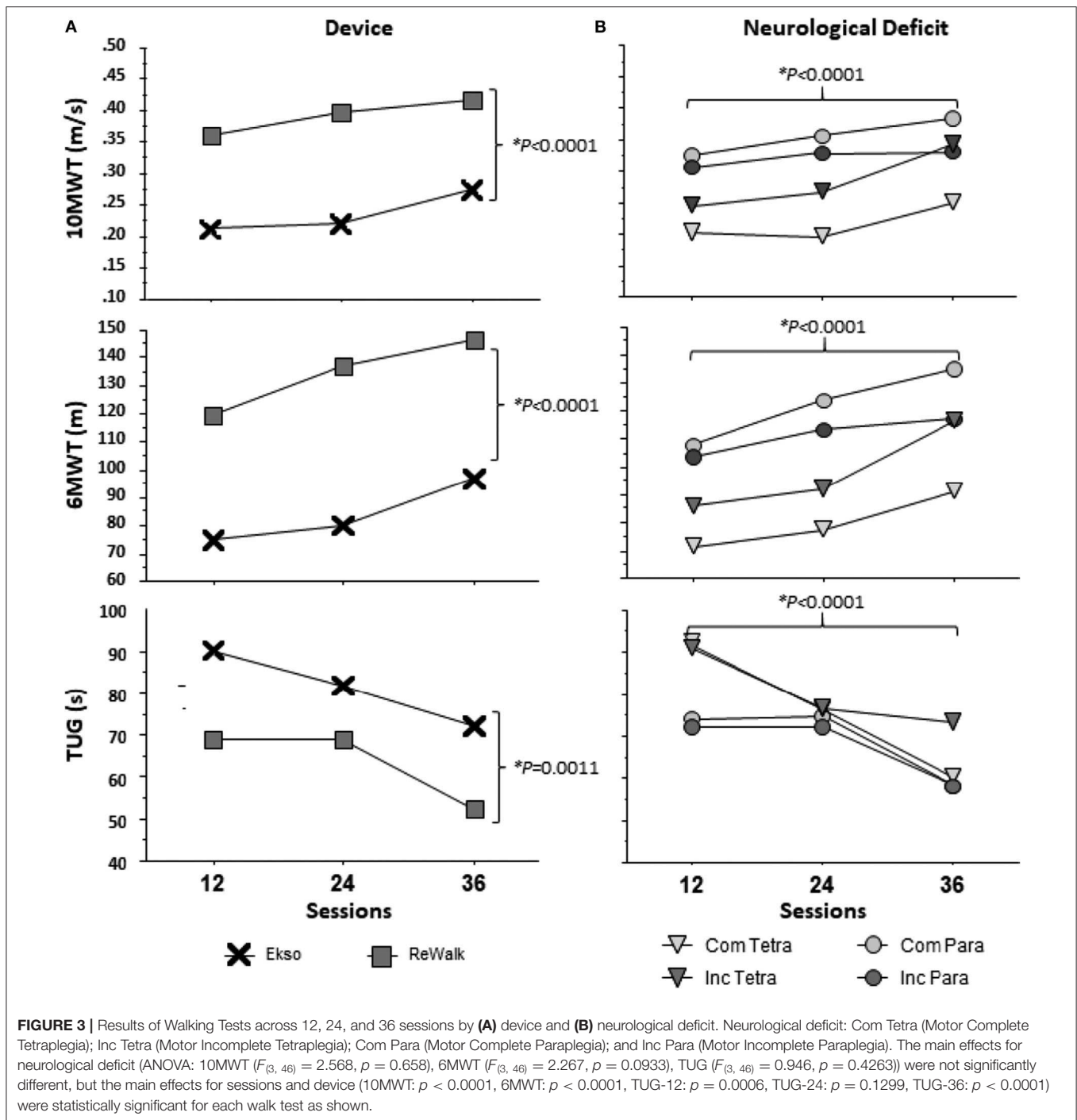
and session block 25–36 [one-way ANOVA ($F_{(3, 46)} = 0.437$, $p = 0.728$)] (Figure 4).

Regardless of device there was a positive relationship between the total cumulative number of steps taken during the 36 sessions and the maximum 10MWT velocity achieved. ReWalk users had a stronger relationship than those who used the Ekso ($p = 0.0028$ vs. $p = 0.093$, respectively) (Figure 5).

DISCUSSION

More than half of the participants succeeded in achieving hypothesized milestones of ≤ 40 s for the 10MWT, ≥ 80 m for the 6MWT and ≤ 90 s for TUG using EAW by session 12 and more than 80% of the participants achieved them by session 36. The rate of improvement in the walking tests was unrelated to the level, completeness, or duration of SCI. These findings indicate that improving the skill level of using these devices as measured by walking velocity and distance is achievable across a broad spectrum of SCI level and completeness. Among neurological sub-groups, there were no significant differences in improvements on walking assessments. Participants with complete paraplegia performed better than participants with complete tetraplegia for all walking assessments (10MWT, 6MWT, and TUG) during all time points, but there were no differences between incomplete tetraplegia and incomplete paraplegia by session 36. This was expected, as those with lower levels of injury retain more residual motor control over their body, allowing them to control thoracic movements in the device, and translating into a better ability to perform exoskeletal ambulation. All participants in the complete tetraplegia sub-group used the Ekso for this study. Participants with lower level injury more often were placed in the ReWalk group. The study was not designed to determine differences in the mobility test outcomes between the Ekso and ReWalk groups. However, the faster walking velocities in the ReWalk may have been due to differences in level and completeness of injury as well as differences between the devices' engineering characteristics.

It may not be practical for clinicians to provide 36 sessions of EAW training due to limitations in payment for physical therapy visits, especially for personal prescription (i.e., use in the home and community). However, participants who met FDA criteria (10MWT: speed ≥ 0.40 m/s and 6MWT: distance ≥ 110 m) mastered weight shifting while standing and clearing the foot for



stepping within 24 sessions. Nine participants achieved this by session 12, and 15 achieved it by session 24, and continued to meet these criteria at session 36. Future investigations focused on the different characteristics of the participants that would eventually obtain the skill needed to pass the FDA criteria should be explored. This could then be used to formulate a basic screening test to identify participants most likely to achieve the skills needed to pass the FDA criteria. Although the number of

covered physical therapy visits vary depending on insurance, in general there is a cap at about 20 visits for Medicare and Medicaid patients. Our data suggest that the “sweet spot” for achieving the FDA criteria for most individuals falls between 12 and 24 visits, and is in alignment with current Center for Medicare and Medicaid Services (CMS) reimbursement guidelines.

There was high variability in the total number of steps taken in both devices. This may be accounted for by participant

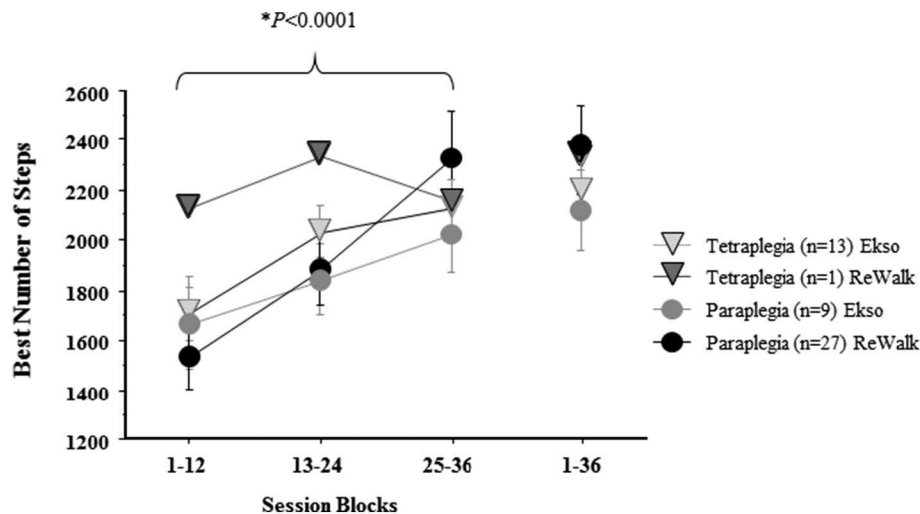


FIGURE 4 | The average best number of total steps in a session block by level of SCI by device. The mean \pm standard error of the best number of total steps/sessions achieved during each 12-session block by Tetra (Tetraplegia), Para (Paraplegia) and by device (ReWalk, Ekso) are reported. The overall best number of steps in a single session is reported for 1–36. The number of steps significantly increased by session block, but no significant effects were found for combination of Tetra/Para and Device.

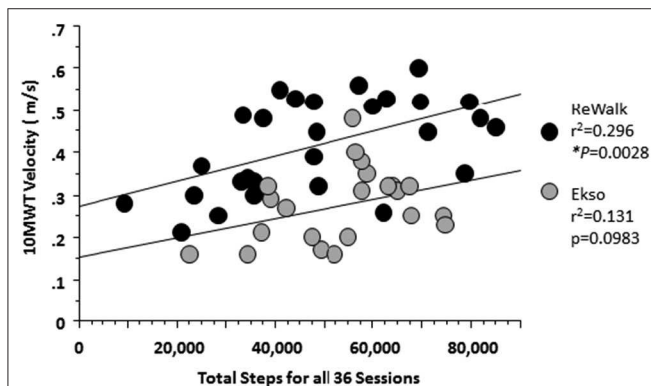


FIGURE 5 | Relationship between the total steps and 10MWT velocity at 36 session by Device. At 36 sessions, participants using either device showed that with more steps taken there was an associated increase in 10MWT velocity. A significant relationship was noted for those who used the ReWalk ($r^2 = 0.296$, $p = 0.0028$) and a trend for those who used the Ekso ($r^2 = 0.131$; $p = 0.0983$).

motivation, confidence in the device, stamina, and/or total time attended per session. All participants walked more steps with the progression of sessions. On average, Ekso users took more total cumulative steps than ReWalk users. However, the average number of steps during later sessions and within session 36 for ReWalk users were higher than those for Ekso users. Overall, the ReWalk users were faster than the Ekso users. While the participants who used the ReWalk were generally able to walk faster, this device was limited to those individuals with a greater amount of trunk stability (based on ISNCSCI level) and strong enough hand grasp to use crutches without any type of assistance. Greater trunk stability and strength likely improved balance and

made the performance of weight shifting easier. Our findings suggest that the Ekso is easier to learn to use than the ReWalk initially, but once learned, the ReWalk user has more flexibility to control velocity and achieve faster walking speeds. The Ekso users increased the number of steps per session early in training with many reaching near their peak steps by session 12, and then they plateaued. On the other hand, the ReWalk users initially had less steps per session, but progressively increased by 36 sessions. This is likely a design feature, since the Ekso can provide more hip and knee flexion assistance than the ReWalk, making it easier to learn to use the device. Ekso users were able to achieve higher number of steps early and continue to steadily increase stepping throughout session progression. ReWalk use required more trunk control over the device to successfully take steps and has a higher initial learning curve to achieve proper posture, weight shifting and stepping for many participants.

Even with the limitation of the device characteristics, there were two Ekso users in the sub-group of incomplete tetraplegia who met the fast walking velocity criteria. While these two Ekso users were daily power wheelchair users and had cervical levels of SCI, they were functionally able to take a few steps without the exoskeleton but with an assistive device such as a walker and with physical assistance from another person. Remarkably, these two Ekso users met all hypothesized criteria of nominal velocity and distance by session 12. Although the ReWalk requires trunk stability and strong enough hand grip to use the crutches, in the incomplete tetraplegia sub-group, there was one person who used the ReWalk and met the fast walking criteria (i.e., the FDA personal use criteria). In contrast, only three of the nine participants with low paraplegia made the FDA criteria in the sub-group of incomplete paraplegia who used the ReWalk. One participant with low paraplegia who used the ReWalk was partially able to meet FDA criteria (6MWT: distance ≥ 110 m), although the person had performed all

hypothesized study criteria of nominal velocity and distance by session 12.

In summary, most participants who were unable to meet the fast walking velocity criteria were individuals with high level paraplegia or were Ekso users. Unexpectedly, three participants with tetraplegia achieved the FDA criteria even with the severity of their neurological deficit. Based on these results, selection of the proper device should not solely be defined by neurological deficit, but other factors such as user preference, comfort and fit, and skill ability as determined by a short trial of devices. Although it is recognized that the number of sessions during training may be limited to policies of third-party payers or government insurance coverage, when possible, the duration and number of individualized EAW mobility training sessions should be determined by participants' stamina, motivation, residual function, and strength, and not just the level or completeness of the SCI.

To minimize trainer support and help the user gain reasonable independence, it is important to establish appropriate goal setting and time management for EAW mobility training. When personal prescription is the goal, an efficient EAW mobility skills training should be implemented. Following guidelines already established by our group, an effective exoskeleton training program necessitates all components of appropriate candidate selection, proper fitting of the device, a steady skill progression plan, and provision of participant assistance on areas of the body with intact sensation (Asselin et al., 2016). As was the case in a previous report, we used these guidelines for this study. For the effective training program, sufficient education of the elements of EAW must be included. Upon completion of a training program, the user should be able to identify the safe environments for device use and operate the device in simulated or actual use environments representative of indicated environments and use⁵. One of the most important elements is using the devices in actual environments such as noisy or crowded hallways, door navigation, and in spaces where turning is required. The EAW walking tests have been previously reported as reliable for testing achievements in mobility during the walking sessions and were accurate predictors of functional independence in the home and community (Louie et al., 2015). Our data confirm the reliability of these tests. There are no specific FDA criteria for the TUG although it is important to measure. The TUG is an essential skill because users must be proficient at standing up, walking, turning and sitting down. Our hypothesized minimal criteria for TUG success were ≤ 120 s by session 12 and ≤ 90 s by session 36 sessions. These criteria were easy to achieve compared to 10MWT and 6MWT. According to our average TUG data set of 10MWT, the TUG criterion to ≤ 75 s by session 12 and ≤ 60 s by session 36 sessions would be more discriminative. Thus, TUG ≤ 60 s would be suggested as a benchmark for skill proficiency. This more stringent TUG criterion could be used to support a skill level needed to take the device home, as it encompasses additional skills and is not solely focused on walking speed.

⁵Electronic Code of Federal Regulations. Available online at: https://www.ecfr.gov/cgi-bin/text-idx?SID=9b627fd1822b8fcd87ad660db602de1candmc=true&node=pt21.8.890&rgn=div5%E2%80%9D%5C1%E2%80%9Cse21.8.890_13480#se21.8.890_13480.

CONCLUSIONS

EAW training was demonstrated to be safe, feasible, and effective within a 36-session training timeline. Most participants improved their walking velocity and distances with the progression of sessions. The observed combination of how the Ekso triggers stepping and higher step clearance allowed participants to walk more successfully during the earlier sessions. Whereas, ReWalk users usually needed more sessions to learn appropriate weight shifting to better trigger stepping and to clear the foot during the swing phase, but once they learned this skill, they walked at faster velocities. More than half of the ReWalk users were able to meet FDA velocity criteria for personal prescription. Our data suggests that clinical programs can expect success rates of 58% by 12 sessions, 68% by 24 sessions and 78% by 36 session to achieve walking velocity medium and fast milestones of ≥ 0.25 m/s and ≥ 0.40 m/s, respectively, regardless of level and completeness of injury or device used. The results from this study provide guidelines for estimating the potential of individuals with SCI to achieve proficient and safe EAW mobility skills for institutional and personal use of these devices.

DATA AVAILABILITY STATEMENT

All datasets generated for this study are included in the article/supplementary material.

ETHICS STATEMENT

The studies involving human participants were reviewed and approved by Institutional Review Boards (IRB) of James J. Peters VA Medical Center (JJPVAMC), Bronx, NY, Kessler Institute for Rehabilitation/Kessler Foundation (KIR/KF), University of Maryland, Baltimore IRB for the University of Maryland Rehabilitation and Orthopaedic Institute (UM Rehab and Ortho, Baltimore, MD), and Department of Defense Congressionally Directed Medical Research Program (DOD CDMRP) IRB. The patients/participants provided their written informed consent to participate in this study.

AUTHOR CONTRIBUTIONS

AS, PG, GF, and PA designed the study. AS, PG, GF, EH, PA, SKn, SKo, WS, and SW contributed to the implementation of the research, to the analysis of the results, and to the writing of the manuscript. All authors contributed to the article and approved the submitted version.

FUNDING

This study was supported by the Department of Defense/CDMRP SC130234 Award: W81XWH-14-2-0170 and National Center for the Medical Consequences of SCI (B9212-C and B2020-C) at the James J. Peters Veterans Affairs Medical Center. Additional financial support was provided by the James Lawrence Kernan Endowment Fund and a philanthropic gift from Dr. Bert Glaser at the Baltimore site and the Bronx Veterans Medical Research Foundation at the Bronx site.

ACKNOWLEDGMENTS

The authors would like to acknowledge the efforts of therapist Marni Kallins, PT and research coordinators

Michael Elliot, Denis Doyle Green, Rebecca Webb, and Leigh Casey. The contents of this paper do not represent the views of the Department of Veterans Affairs or the United States Government.

REFERENCES

- Asselin, P., Knezevic, S., Kornfeld, S., Ciriogliaro, C., Agranova-Breyer, I., and Bauman, W. A. (2015). Heart rate and oxygen demand of powered exoskeleton-assisted walking in persons with paraplegia. *J. Rehabil. Res. Dev.* 52:147. doi: 10.1682/JRRD.2014.02.0060
- Asselin, P. K., Avedissian, M., Knezevic, S., Kornfeld, S., and Spungen, A. M. (2016). Training persons with spinal cord injury to ambulate using a powered exoskeleton. *J. Vis. Exp.* 16:e54071. doi: 10.3791/54071
- Baunsgaard, C. B., Nissen, U. V., Brust, A. K., Frotzler, A., Ribeill, C., Kalke, Y.-B., et al. (2018). Gait training after spinal cord injury: safety, feasibility and gait function following 8 weeks of training with the exoskeletons from Ekso Bionics. *Spinal Cord.* 56:106. doi: 10.1038/s41393-017-0013-7
- Bittner, V., and Singh, S. (2017). The 6 Minute Walk Test: Cardiology Advisor. Available online at: <https://www.thecardiologysupport.com/home/decision-support-in-medicine/cardiology/the-6-minute-walk-test/> (accessed July 1, 2020).
- Costa, P., Perrouin-Verbe, B., Colvez, A., Didier, J., Marquis, P., Marrel, A., et al. (2001). Quality of life in spinal cord injury patients with urinary difficulties. *Eur. Urol.* 39, 107–113. doi: 10.1159/000052421
- Dodds, T. A., Martin, D. P., Stolov, W. C., and Deyo, R. A. (1993). A validation of the functional independence measurement and its performance among rehabilitation inpatients. *Arch. Phys. Med. Rehabil.* 74, 531–536. doi: 10.1016/0003-9993(93)90119-U
- Escalona, M. J., Brosseau, R., Vermette, M., Comtois, A. S., Duclos, C., Aubertin-Leheudre, M., et al. (2018). Cardiorespiratory demand and rate of perceived exertion during overground walking with a robotic exoskeleton in long-term manual wheelchair users with chronic spinal cord injury: a cross-sectional study. *Ann. Phys. Rehabil. Med.* 61, 215–223. doi: 10.1016/j.rehab.2017.12.008
- Evans, N., Hartigan, C., Kandilakis, C., Pharo, E., and Clesson, I. (2015). Acute cardiorespiratory and metabolic responses during exoskeleton-assisted walking overground among persons with chronic spinal cord injury. *Top. Spinal Cord Inj. Rehabil.* 21, 122–132. doi: 10.1310/sci2102-122
- FIM (2019). *Functional Independence Measure (FIM): Physiopedia*. Available online at: [https://www.physio-pedia.com/Functional_Independence_Measure_\(FIM\)](https://www.physio-pedia.com/Functional_Independence_Measure_(FIM)) (accessed July 1, 2020).
- Glickman, S., and Kamm, M. A. (1996). Bowel dysfunction in spinal-cord-injury patients. *Lancet* 347, 1651–1653. doi: 10.1016/S0140-6736(96)91487-7
- Hoffmann, M. J. (2016). *Indications for use: ReWalk [letter]* 2016. Available online at: https://www.accessdata.fda.gov/cdrh_docs/pdf16/K160987.pdf
- Jensen, M. P., Kuehn, C. M., Amtmann, D., and Cardenas, D. D. (2007). Symptom burden in persons with spinal cord injury. *Arch. Phys. Med. Rehabil.* 88, 638–645. doi: 10.1016/j.apmr.2007.02.002
- Korsten, M. A., Fajardo, N. R., Rosman, A. S., Creasey, G. H., Spungen, A. M., and Bauman, W. A. (2004). Difficulty with evacuation after spinal cord injury: colonic motility during sleep and effects of abdominal wall stimulation. *J. Rehabil. Res. Dev.* 41, 95–100. doi: 10.1682/JRRD.2004.01.0095
- LaVela, S. L., Evans, C. T., Prohaska, T. R., Miskevics, S., Ganesh, S. P., and Weaver, F. M. (2012). Males aging with a spinal cord injury: prevalence of cardiovascular and metabolic conditions. *Arch. Phys. Med. Rehabil.* 93, 90–95. doi: 10.1016/j.apmr.2011.07.201
- Louie, D. R., Eng, J. J., and Lam, T. (2015). Gait speed using powered robotic exoskeletons after spinal cord injury: a systematic review and correlational study. *J. Neuroeng. Rehabil.* 12:82. doi: 10.1186/s12984-015-0074-9
- Middleton, A., Fritz, S. L., and Lusardi, M. (2015). Walking speed: the functional vital sign. *J. Aging Phys. Act.* 23, 314–322. doi: 10.1123/japa.2013-0236
- Munce, S. E., Perrier, L., Tricco, A. C., Straus, S. E., Fehlings, M. G., Kastner, M., et al. (2013). Impact of quality improvement strategies on the quality of life and well-being of individuals with spinal cord injury: a systematic review protocol. *Syst. Rev.* 2:14. doi: 10.1186/2046-4053-2-14
- NSCISC (2019). Facts and Figures at a Glance Birmingham, AL: University of Alabama at Birmingham: National Spinal Cord Injury Statistical Center. Available online at: <https://www.nscisc.uab.edu/Public/Facts%20and%20Figures%202019%20-%20Final.pdf> (accessed July 1, 2020).
- Podsiadlo, D., and Richardson, S. (1991). The timed “Up and Go”: a test of basic functional mobility for frail elderly persons. *J. Am. Geriatr. Soc.* 39, 142–148. doi: 10.1111/j.1532-5415.1991.tb01616.x
- Product Classification U. S. Food and Drug Administration (2019). Available online at: <https://www.accessdata.fda.gov/scripts/cdrh/cfdocs/cfPCD/classification.cfm?ID=PHL> (accessed December 30, 2019)
- Shinkai, S., Watanabe, S., Kumagai, S., Fujiwara, Y., Amano, H., Yoshida, H., et al. (2000). Walking speed as a good predictor for the onset of functional dependence in a Japanese rural community population. *Age Ageing* 29, 441–446. doi: 10.1093/ageing/29.5.441
- Spungen, A., Adkins, R., Bauman, W., Kemp, B., and Waters, R. (1999). The effect of level and completeness of lesion on body composition in subjects with spinal cord injury. *J. Spinal Cord Med.* 22:43.
- Spungen, A. M., Wang, J., Pierson, R. N., and Bauman, W. A. (2000). Soft tissue body composition differences in monozygotic twins discordant for spinal cord injury. *J. Appl. Physiol.* 88, 1310–1315. doi: 10.1152/jap.2000.88.4.1310
- Stiens, S. A., Bergman, S. B., and Goetz, L. L. (1997). Neurogenic bowel dysfunction after spinal cord injury: clinical evaluation and rehabilitative management. *Arch. Phys. Med. Rehabil.* 78, S86–S102. doi: 10.1016/S0003-9993(97)90416-0
- Tapio, S. (2016). *What is Mobility? (And why it's so important)*. Available online at: <https://www.vahvafitness.com/what-is-mobility/> (accessed July 1, 2020).
- Tate, D. G., Kalpakjian, C. Z., and Forchheimer, M. B. (2002). Quality of life issues in individuals with spinal cord injury. *Arch. Phys. Med. Rehabil.* 83, S18–S25. doi: 10.1053/apmr.2002.36835
- Van Hedel, H., Wirz, M., and Dietz, V. (2008). Standardized assessment of walking capacity after spinal cord injury: the European network approach. *Neurol. Res.* 30, 61–73. doi: 10.1179/016164107X230775
- Wahman, K., Nash, M. S., Westgren, N., Lewis, J. E., Seiger, Å., and Levi, R. (2010). Cardiovascular disease risk factors in persons with paraplegia: the Stockholm spinal cord injury study. *J. Rehabil. Med.* 42, 272–278. doi: 10.2340/16501977-0510
- Wecht, J. M., de Meersman, R. E., Weir, J. P., Bauman, W. A., and Grimm, D. R. (2000). Effects of autonomic disruption and inactivity on venous vascular function. *Am. J. Physiol. Heart Circ. Physiol.* 278, H515–H520. doi: 10.1152/ajpheart.2000.278.2.H515
- Wecht, J. M., De Meersman, R. E., Weir, J. P., Spungen, A. M., Bauman, W. A., and Grimm, D. R. (2001). The effects of autonomic dysfunction and endurance training on cardiovascular control. *Clin. Auton. Res.* 11, 29–34. doi: 10.1007/BF02317799
- Wilmet, E., Ismail, A., Heilporn, A., Welraeds, D., and Bergmann, P. (1995). Longitudinal study of the bone mineral content and of soft tissue composition after spinal cord section. *Spinal Cord.* 33, 674–677. doi: 10.1038/sc.1995.141
- Wilson, J. R., Hashimoto, R. E., Dettori, J. R., and Fehlings, M. G. (2011). Spinal cord injury and quality of life: a systematic review of outcome measures. *Evid. Based Spine Care J.* 2, 37–44. doi: 10.1055/s-0030-1267085

Conflict of Interest: The authors declare that the research was conducted in the absence of any commercial or financial relationships that could be construed as a potential conflict of interest.

Copyright © 2020 Hong, Gorman, Forrest, Asselin, Knezevic, Scott, Wojciehowski, Kornfeld and Spungen. This is an open-access article distributed under the terms of the Creative Commons Attribution License (CC BY). The use, distribution or reproduction in other forums is permitted, provided the original author(s) and the copyright owner(s) are credited and that the original publication in this journal is cited, in accordance with accepted academic practice. No use, distribution or reproduction is permitted which does not comply with these terms.



Robotic Cane Controlled to Adapt Automatically to Its User Gait Characteristics

Andrés Trujillo-León*, Ragou Ady, David Reversat and Wael Bachta

CNRS, UMR 7222, INSERM, U1150, Institut des Systèmes Intelligents et de Robotique, Sorbonne Université, Paris, France

OPEN ACCESS

Edited by:

Carlos Rodriguez-Guerrero,
Vrije University Brussel, Belgium

Reviewed by:

Anselmo Frizera Neto,
Federal University of Espirito Santo,
Brazil

Danielle Marie Stramel,
Columbia University, United States

*Correspondence:

Andrés Trujillo-León
atrujilloleon@uma.es

Specialty section:

This article was submitted to
Biomedical Robotics,
a section of the journal
Frontiers in Robotics and AI

Received: 21 January 2020

Accepted: 06 July 2020

Published: 12 August 2020

Citation:

Trujillo-León A, Ady R, Reversat D and
Bachta W (2020) Robotic Cane
Controlled to Adapt Automatically to
Its User Gait Characteristics.
Front. Robot. AI 7:105.
doi: 10.3389/frobt.2020.00105

Research on robotic assistance devices tries to minimize the risk of falls due to misuse of non-actuated canes. This paper contributes to this research effort by presenting a novel control strategy of a robotic cane that adapts automatically to its user gait characteristics. We verified the proposed control law on a robotic cane sharing the main shape features of a non-actuated cane. It consists of a motorized telescopic shaft mounted on the top of two actuated wheels driven by the same motor. Cane control relies on two Inertial Measurement Units (IMU). One is attached to the cane and the other to the thigh of its user impaired leg. During the swing phase of this leg, the motor of the wheels is controlled to enable the tracking of the impaired leg thigh angle by the cane orientation. The wheels are immobilized during the stance phase to provide motionless mechanical support to the user. The shaft length is continuously adjusted to keep a constant height of the cane handle. The primary goal of this work is to show the feasibility of the cane motion synchronization with its user gait. The control strategy looks promising after several experiments. After further investigations and experiments with end-users, the proposed control law could pave the road toward its use in robotic canes used either as permanent assistance or during rehabilitation.

Keywords: assistive devices, robotic cane, gait cycle, synchronization, mobility

1. INTRODUCTION

Falls are a major health, societal and economic problem, resulting in 424,000 annual fatalities around the world (World Health Organization, 2012). When they are not fatal, they cause high traumas and morbidity. Indeed, falling may result in damages ranging from minor bruises to more serious brain injuries and hip fractures (Sterling et al., 2001). In Europe, falls related costs are estimated at 25 billion euros each year (European Public Health Association, 2015).

The most common response to falls is the use of assistive devices. Even though they are perceived positively by the patients (Tyson and Rogerson, 2009), the improper use of these devices is among the extrinsic causes leading to falls (Liu et al., 2011).

In the last two decades, many lines of research have been dedicated to improving the assistance provided by assistive devices. Mainly, instrumented and robotic devices have been developed. For instance, instrumented canes, which consist in canes equipped with strain gauges, inertial measurement units (IMUs), embedded computers and other equipment have been designed to enable an unobtrusive monitoring of cane use (Au et al., 2008; Mercado et al., 2014; Trujillo-León et al., 2015; Wade et al., 2018). Normally, the cane orientation and the forces applied to it are measured and collected to enable their later analysis by the medical staff.

Robotic canes, on the other hand, aim to provide additional assistive functionalities and they generally share the same mechanical architecture. They consist in a basic cane mounted on the top of a statically stable wheeled mobile robot. The additional functions provided by robotic canes include navigation assistance, user intention detection or fall prevention. In Spenko et al. (2006), navigation assistance functions are provided. The mobile platform consists of two driving and one castor wheels. It encloses a camera and a sonar array used for localization purposes. The cane mounted on the top of this platform is equipped with a force and torque sensor that measures the load applied by the user. In the first navigation mode, the robotic cane, using its localization system, moves autonomously to guide the user toward a desired position. In the second mode, a shared control is implemented, i.e., the user moves the robotic cane but the latter can correct his deviations from a pre-planned path.

Robotic canes come with extra weight resulting mainly from the integrated batteries and structure. Some robotic canes detect the walking direction and move accordingly, thus alleviating the user muscular effort. In Wakita et al. (2013), a cane enclosing a force and torque sensor is mounted on the top of an omnidirectional mobile platform. The device is controlled through an on-line estimation of the Intentional Direction (ITD). The ITD is estimated using the direction of the horizontal force applied to the cane by its user. In order to secure the user gait, the cane controller is tuned to make it move easily along the detected direction and to be difficult to maneuver in the other directions.

To prevent falls, robotic canes adapt their motion to their user balance. In Suzuki et al. (2009), a cane is mounted on a mobile base that consists of two wheels with servo brakes and two castor wheels. The platform is equipped with laser range finders. Indeed, the brake control is adapted to the distance between the user feet position and the robotic cane. In Di et al. (2016), a robotic cane is controlled in a way that avoids its users tipping over when holding it. A recent work is presented in Phi and Fujimoto (2019); an innovative robotic cane incorporating an omnidirectional motorized wheel has been proposed.

In previous works (Ady et al., 2013, 2014), we proposed a prototype of robotic cane that avoided the common bulky and cumbersome structure of robotics canes and walkers, and that shared the compactness and longitudinal shape that characterize the conventional ones. In this paper, we focus on the control strategy using a revisited version of the robotic cane. The control law is aimed at providing safe and proper support in the very instants it is required. For that purpose, the cane motion is automatically synchronized with its user gait, without requiring any specific intervention.

1.1. Synchronization of a Cane With the Gait Cycle

People use their arm to synchronize their basic cane motion with their gait cycle during straight forward walking. This synchronization can be analyzed in the sagittal plane. Only one stride is required since walking straight forward is cyclic. As depicted in **Figure 1** top, starting from a standing position (a),

the weak leg (grayed in the figure) leaves the ground and starts its swing phase (b), the cane is lifted and moved forward in synergy with the leg motion. The cane tip is put on the ground a step further and synchronously with the impaired leg heel strike (c). The maximum tangential forces applied to the cane occur during the heel-strike (c) and the push off (e) of the impaired leg. The maximum normal force applied to the cane occurs during the phase (d) (Chen et al., 2001).

The robotic cane, which design is detailed in the next section, is aimed at making this synchronization automatic, i.e., the user no longer needs to lift the cane at each step. Instead, it should adapt automatically its motion to the gait cycle. To provide the same assistance of a conventional cane, its wheels should move forward during the impaired leg swing phase and stop when the latter touches the ground. At the same time, the shaft length should vary continuously to keep a constant height of the cane handle in order to avoid pushing or pulling the user hand. The intended synchronization scheme of the robotic cane is depicted in **Figure 1** bottom.

1.2. Synchronization of the Cane Wheels With the Impaired Leg Motion

If the step size and its duration are learned offline, the motion of the wheels can be achieved in open loop, i.e., a predefined trajectory could be programmed. In this case, the cane motion cannot adapt to changes of the gait parameters. However, the objective here is to enable the cane adapting to its user's gait characteristics.

An alternative choice, consisting in a closed loop control of the displacements of the wheels based on motion synergies, is preferred. Motion synergies have already been used in rehabilitation robotics to generate reference trajectories for exoskeletons. For instance, the authors of Vallery et al. (2009) took advantage from the existing synergy between lower limb joints to provide reference trajectories to an exoskeleton assisting an impaired limb based on the motion of the sound leg. Synchronizing robotic motion with respect to a cane assisted gait cycle has been studied in Hassan et al. (2012), Hassan et al. (2018). In their study, the authors used the existing cane-lower limbs synergy to control a single leg version of the HAL exoskeleton. Firstly, they assessed the existence of a coordination between the lower limb joints trajectories and the cane angle (the cane rotation in the sagittal plane). Then, they implemented a limb motion estimation method, i.e., the cane angle and that of the sound leg joints were used to generate the reference motion of the exoskeleton assisting the impaired leg.

In our work, the aim is to control the robotic cane motion based on the impaired leg motion. Moreover, unlike the setup used in Hassan et al. (2012), we would like to reduce the required components by equipping the user with only one IMU.

The paper is organized as follows. In section 2, the current prototype is presented. The synchronization strategy is presented and supported by experimental results in section 3. In section 4, the control law of the cane is derived. In section 5, the experimental results, obtained using the prototype and its

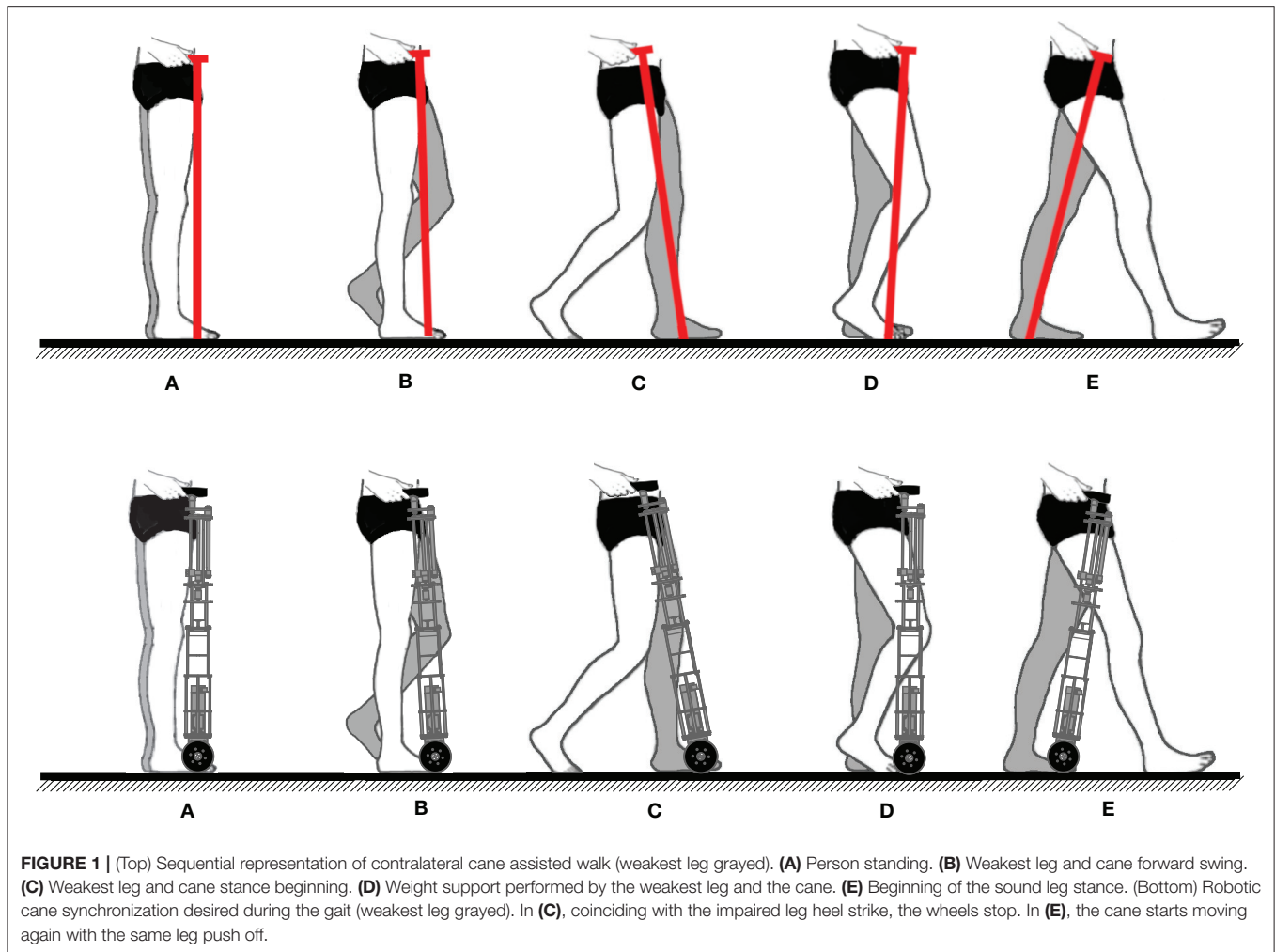


FIGURE 1 | (Top) Sequential representation of contralateral cane assisted walk (weakest leg grayed). **(A)** Person standing. **(B)** Weakest leg and cane forward swing. **(C)** Weakest leg and cane stance beginning. **(D)** Weight support performed by the weakest leg and the cane. **(E)** Beginning of the sound leg stance. (Bottom) Robotic cane synchronization desired during the gait (weakest leg grayed). In **(C)**, coinciding with the impaired leg heel strike, the wheels stop. In **(E)**, the cane starts moving again with the same leg push off.

associated control law, are discussed. A conclusion ends the paper by giving some future research directions.

2. ROBOTIC CANE PRESENTATION

In this section, the design objectives of the robotic cane are given. Its mechanical architecture, as well as its embedded electronics, are then presented.

2.1. Design Objectives

From a mechanical point of view, the goal is providing a lightweight compact cane able to follow the pace of people with balance troubles. The prototype, presented hereafter, is based on requirements expressed in terms of the cane forward velocity and support forces.

In Chen et al. (2001), the mean pace of 20 post-stroke hemiplegic patients has been reported to vary between 0.04 and 0.35 m/s. As the gait cycle includes double support phases, where both feet are touching the ground, the speed of one leg during its swing phase may be greater than the mean walking pace. To take this fact into account, the cane forward speed has been

designed to be equal to 1 m/s, which is approximately twice the pace reported in Peel et al. (2012). In Murray et al. (1969), the authors collected data from 53 disabled people, and analyzed the load they were applying along the axis of their canes. They reported a mean vertical force of 147 N. In Chen et al. (2001), a decomposition of the load applied to canes by post-stroke hemiplegic patients has been achieved. The results show that the cane bears $\sim 13\%$ of the body weight in the vertical direction and $<1\%$ in the posterior-anterior and lateral directions. For a weight of 70 kg, this corresponds to 91 and 1 N, respectively. This gives an idea about the cane design needs in terms of forward velocity and payload.

2.2. Mechanical Architecture

The cane is shown in Figure 2. It is composed of a telescopic shaft and two wheels; all of them are actuated. Its base consists in a 10 cm square, and the shape becomes thinner while approaching the handle. Its height is adjustable and can vary between 0.85 and 1 m. The shaft translation is ensured by a 100 W EC-i40 Maxon driving a 2.5 mm ball screw mechanism. This ensures nominal velocity and force of 0.16 m/s and 82 N, respectively. The wheels,

of 10 cm diameter each, are located at the tip of the cane and are driven together. They are actuated by a 50 W Maxon EC-45 flat motor associated with GP42C gear-head. This gives rise to a nominal velocity and a nominal torque of 1.15 m/s and 40 Nm, respectively. Note that the velocity and force at the cane tip are dependent on the normal force applied to the cane and the friction between the wheels and the ground.

The whole cane prototype weights 5.7 kg. Thus, it is lighter than common robotic walking aid devices or even other stick-like robotic canes, such as that in Phi and Fujimoto (2019). Besides, the batteries, which are the heaviest components, are placed in the lower part. This way, the center of mass of the structure is near the floor allowing to operate the cane from the handle in a light and comfortable way. Note as well that the cane is not lifted from the ground during its operation.

The telescopic shaft is designed based on a reversible ball-screw mechanism. As explained above, the force supported by the latter is 82 N, and thus not sufficient to bear the maximal vertical load applied by a user when leaning on the cane, which approximately equals to 91 N (see previous subsection). Thus, the arching mechanism (see **Figure 2** left) is crucial to ensure gait safety. If the user applies a force on the handle, the resulting moment yields friction and prevents any downward motion of the shaft. The arching mechanism makes the upper part of the cane irreversible, without adding any additional weight or bulkiness.

2.3. Control Electronics and Sensors

The control architecture is implemented as follows: the cane control is carried out by a BeagleBone board with a sampling frequency of 50 Hz. It communicates via WIFI with two IMUs from X-IO Technologies. One is attached to the cane and

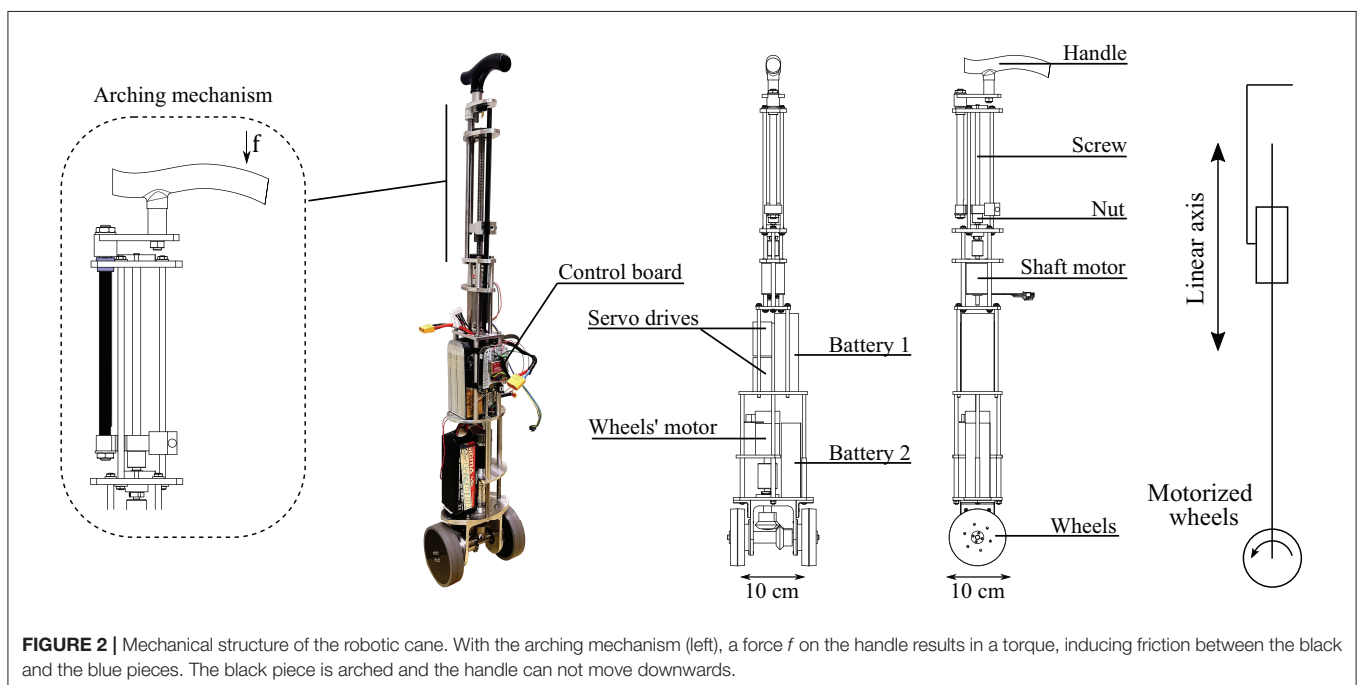
provides its angle. The other is attached to the participant impaired leg, providing both its angle and angular velocity. The IMUs provide angles in an Euler representation. Using serial communication, the board acquires the positions of the shaft and the wheels. It then computes and sends the reference velocities to the servo drives. The latter are Solo-Whistle from Elmo. The whole system is powered thanks to two LIPO batteries of a 18.5 V, 7 Ah and a 22.2 V, 4.2 Ah, respectively. They allow a operating time from 1 to 2 days, depending on the frequency of the cane usage. However, the batteries of the IMUs can not withstand more than half a day. This issue is simple to fix. The IMU attached to the cane can be powered by the cane batteries. The one worn by participants can be powered by an external USB charger.

3. SYNCHRONIZATION STRATEGY

Our synchronization strategy is based on the slaving of the cane angle on the impaired leg during its swing, and on the cane immobilization during the stance phase. First, a simple method to detect online the gait phases is provided. Then, experimental evidence is given about the soundness of the method and about the coupling between of the impaired thigh and a conventional cane angle.

3.1. Gait Phase Detection Algorithm

When the detection of the gait phase is needed, motion capture and force platforms are appealing solutions if the gait takes place in clinical laboratories. When outdoor motion capture is required, affordable sensors, like accelerometers and gyroscopes, are often used (Mayagoitia et al., 2002). For example, a 3-axis accelerometer held against the sacrum has been used in Evans



et al. (1991) to detect heel strikes. In Willemsen et al. (1990), 3-axis accelerometers have been attached to the shank of hemiplegic individuals' impaired legs in order to detect swing phases. The authors of Dai et al. (1996) use tilt sensors in the lower leg to detect the swing phase and deliver electric stimulation. Moreover, in Maqbool et al. (2017) the authors present an approach to real-time detection of mid-swing phase, toe off and initial contact using peaks in the shank angular speed with a wireless gyroscope. In Hwang et al. (2018), the authors propose a method for real-time gait analysis based on a head-worn IMU. The user head vertical acceleration is processed to peak detection since the impact of the foot on the ground at heel strike, and the upward motion during toe off, are transmitted to the head along the body axis. In Martinez-Hernandez et al. (2018), swing and stance phases are detected with a method based on simultaneous Bayesian recognition. The authors use three IMUs attached to the thigh, the shank and the foot, respectively.

In our case, the distinction between the stance and swing phase is accomplished with the gyroscope included in the wireless IMU placed on the assisted leg thigh. The angular velocity sign allows to detect whether the leg is in a stance or in a swing phase. The thigh performs an anti-clockwise rotation during the swing phase, and a clockwise rotation during the stance phase. Hence, a threshold on the thigh angle angular velocity in the sagittal plane allows a distinction between them. The detection scheme is showed in **Figure 3** left. Once the angular speed has exceeded the threshold during three consecutive samples, a swing phase is detected. Otherwise, the phase is considered to be stance. The number of samples exceeding the threshold to identify the change of phase has been experimentally determined and the measure is aimed to avoid false positives due to noise peaks.

3.2. Experimental Validation

The experiments involved six healthy individuals, three males and three females, aged in average 27.7 years old. The study was

carried out in conformity with the Declaration of Helsinki of the World Medical Association, and all the participants gave their informed consent. Their gait was altered with a hands free crutch aimed to immobilize injured legs. The impaired leg was simulated by equipping the crutch. They were asked to use a conventional cane in a contralateral way. The participants were equipped with a set of optical markers, so that the motion of their limbs was captured by an OptiTrack system. The cane position and orientation were also captured through the use of extra markers. The experiments began after a 5 min familiarization period. The experiments were composed of series of 3.5-m forward assisted-gait, corresponding to slow, normal, and fast walking paces. The volunteers undergone three tests at each speed.

The mean values (\pm standard deviations) of these speeds across all the trials and the subjects were respectively 0.23 m/s (± 0.06), 0.36 m/s (± 0.08), and 0.52 m/s (± 0.12).

3.2.1. Validation of the Coupling Between the Impaired Leg Thigh and the Cane Orientation

For each trial, Pearson correlation between the angles of the simulated impaired leg and the cane was computed. For each walking pace, the average of the correlation coefficients across all the trials and participants was computed. The obtained values were $r = 0.92$ (± 0.04), $r = 0.91$ (± 0.03), and $r = 0.9$ (± 0.07) for respectively the slow, normal and fast paces. This shows that the cane angle is strongly correlated with the thigh orientation of the impaired leg.

3.2.2. Validation of the Gait Detection Phases

For each trial, the heel strike and the toe-off ground-truth instants were extracted thanks to the capture motion markers attached to the participants feet. At the same time, the detection technique showed in **Figure 3** was used to determine if the impaired leg was in its stance or swing phase. The impaired leg angular speed was obtained by deriving the angle acquired by the motion

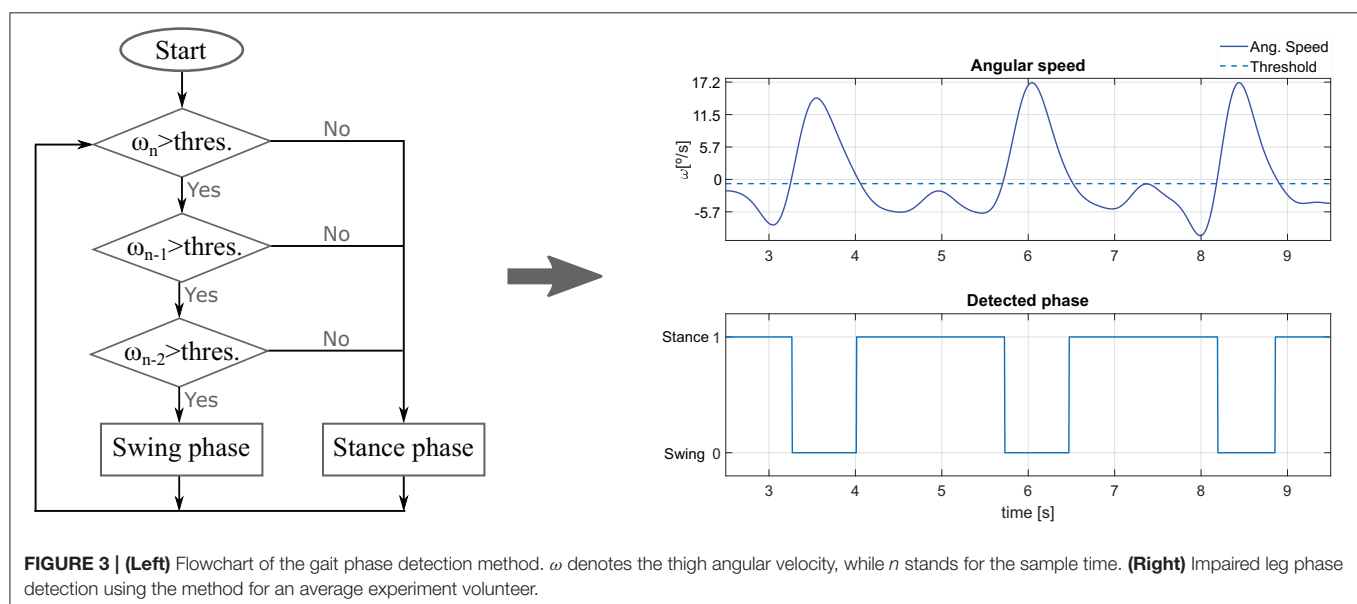


FIGURE 3 | (Left) Flowchart of the gait phase detection method. ω denotes the thigh angular velocity, while n stands for the sample time. **(Right)** Impaired leg phase detection using the method for an average experiment volunteer.

capture system. The results show that both the heel strike and toe off are detected with reasonable accuracy with respect to the considered ground-truth instants. Thus, the user balance is not threatened (the worst reported difference was in the order of 0.2 s). The method gives good results but can still be tuned more specifically (e.g., by varying the detection threshold) for each user and walking pace to improve the accuracy. **Figure 3** right shows an example of the gait phase detection for an average experiment participant.

4. CONTROL IMPLEMENTATION

As previously mentioned, the robotic cane should be controlled in order to maintain a constant height of its handle during the whole gait cycle. Moreover, during the assisted leg swing phase, the cane angle should track this leg thigh orientation. In the sequel, the kinematic model of the device is given. Then, the control laws associated to the height and angle servoing are detailed.

4.1. Robotic Cane Kinematic Model

A sagittal plane kinematic representation of the robotic cane is given in **Figure 4**. Three coordinate frames are attached to the three bodies composing the cane. $\mathfrak{R}_R = \{O_R, \vec{x}_R, \vec{y}_R, \vec{z}_R\}$ is attached to the wheel. $\mathfrak{R}_C = \{O_C, \vec{x}_C, \vec{y}_C, \vec{z}_C\}$ and $\mathfrak{R}_H = \{O_H, \vec{x}_H, \vec{y}_H, \vec{z}_H\}$ are attached, respectively, to the lower and upper parts of the chassis. O_R and O_H represent the centers of, respectively, the cane wheels and handle. O_C is a point belonging to the lower part of the chassis. The length l of the chassis is made variable thanks to the motorized axis. The cane orientation in the sagittal plane is defined by the angle θ representing the rotation of \mathfrak{R}_H with respect to the world frame $\mathfrak{R}_0 = \{O_0, \vec{x}_0, \vec{y}_0, \vec{z}_0\}$ around \vec{y}_0 . The radius of the wheels and the handle center height are denoted, respectively r and h .

The cane is assumed to remain in contact with the ground and the wheels to roll without slipping. These two assumptions give rise to mechanical constraints that allow establishing kinematic relationships between the velocity of O_H , the cane orientation θ and the wheel rotation speed ω . To establish these relationships, the velocity of O_H is first derived:

$$\vec{V}_{O_H \in \mathfrak{R}_H / \mathfrak{R}_0} = \vec{V}_{O_H \in \mathfrak{R}_H / \mathfrak{R}_C} + \vec{V}_{O_H \in \mathfrak{R}_C / \mathfrak{R}_0} \quad (1)$$

Since the upper part of the chassis is translating with respect to the lower part, the following equation holds:

$$\vec{V}_{O_H \in \mathfrak{R}_H / \mathfrak{R}_C} = l \vec{z}_C = l \sin \theta \vec{x}_0 + l \cos \theta \vec{z}_0 \quad (2)$$

Moreover, it can be written that:

$$\begin{aligned} \vec{V}_{O_H \in \mathfrak{R}_C / \mathfrak{R}_0} &= \vec{V}_{O_R \in \mathfrak{R}_C / \mathfrak{R}_0} + \overrightarrow{O_H O_R} \wedge \vec{\Omega}_{\mathfrak{R}_C / \mathfrak{R}_0} \\ &= \vec{V}_{O_R \in \mathfrak{R}_C / \mathfrak{R}_0} - l \vec{z}_H \wedge \dot{\theta} \vec{y}_0 \\ &= \vec{V}_{O_R \in \mathfrak{R}_C / \mathfrak{R}_0} + l \dot{\theta} \cos \theta \vec{x}_0 - l \dot{\theta} \sin \theta \vec{z}_0 \end{aligned} \quad (3)$$

As the wheels are rolling without slipping, it comes that:

$$\vec{V}_{O_R \in \mathfrak{R}_C / \mathfrak{R}_0} = r(-\omega + \dot{\theta}) \vec{x}_0 \quad (4)$$

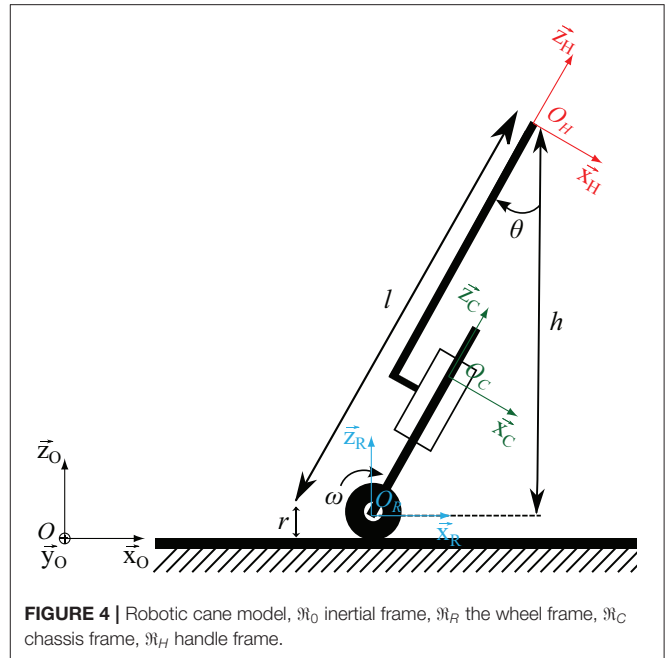


FIGURE 4 | Robotic cane model, \mathfrak{R}_0 inertial frame, \mathfrak{R}_R the wheel frame, \mathfrak{R}_C chassis frame, \mathfrak{R}_H handle frame.

Putting together equations (1), (2), (3), and (4) gives:

$$\begin{aligned} \vec{V}_{O_H \in \mathfrak{R}_H / \mathfrak{R}_0} &= \underbrace{(l \sin \theta + r(-\omega + \dot{\theta}) + l \dot{\theta} \cos \theta)}_{\dot{x}_{O_H}} \vec{x}_0 + \\ &\quad \underbrace{(l \cos \theta - l \dot{\theta} \sin \theta)}_{\dot{z}_{O_H}} \vec{z}_0 \end{aligned} \quad (5)$$

Equation (5) shows that, as expected, any variation the telescopic shaft length and any rotation of the cane wheels give rise to a displacement of the cane handle.

The control law, that will be given in the sequel, will ensure that \dot{z}_{O_H} and \dot{x}_{O_H} are equal to zero in order to avoid moving the subject hand and threatening balance.

4.2. Control Law Structure

To provide the necessary assistance, the cane controller has to fulfill two main tasks: zeroing the tracking angular error between the cane and the impaired leg while keeping an almost constant height of the handle. The cane kinematics are governed by Equation (5). Thus, this equation constrains the control law.

The controller is composed of two loops: an inner loop aiming at keeping a constant height, and an outer loop dedicated to the tracking of the impaired leg angle. The inner loop should have a shorter response time. This structure allows an easy tuning while respecting the cane kinematics governing law.

The two components of the control law are described below.

4.2.1. Cane Handle Height Control

The cane telescopic axis is controlled to maintain a constant height of the cane handle during the assisted gait. The axis length

variation should verify the following equation ($\dot{z}_{OH} = 0$):

$$\dot{z}_{OH} = \frac{d}{dt}(l \cos \theta + r) = \dot{l} \cos \theta - l \dot{\theta} \sin \theta = 0 \quad (6)$$

Let us assume that, at the beginning of the gait, the cane handle height is defined by z_{OH0} in the \mathfrak{N}_0 frame.

At the beginning to the experiment, the cane is held vertically. z_{OH0} is then equal to $l_0 + r$ in the considered cane orientation. This way, $l_0 = z_{OH0} - r$, where l_0 is the initial telescopic axis length, at the vertical cane orientation, and r the radius of the wheels.

To maintain a constant height regardless of the cane orientation θ , and considering a motionless contact point of the cane, the telescopic axis length must satisfy:

$$l_d = \frac{z_{OH0} - r}{\cos \theta} \quad (7)$$

where l_d is a varying set point.

To maintain a constant height, the following control law is implemented:

$$\ddot{l} = K_a \left(\underbrace{\frac{z_{OH0} - r}{\cos \theta}}_{l_d} - l \right) \quad (8)$$

where \ddot{l} is the reference velocity sent to the servo drive of the linear axis. K_a is a proportional gain. If $\theta \notin \{-\frac{\pi}{2}, \frac{\pi}{2}\}$, the continuous-time asymptotic convergence of the height adjustment is ensured if K_a is strictly >0 . Two K_a values could be assigned depending on the weak leg phase in the gait cycle. The gain is small during the weak leg stance phase in order to limit the linear axis motion and provide a safe support. Moreover, if the force applied by the user is sufficient, the axis may be arched. The gain is higher during the swing phase in order to comply more efficiently with the user hand motion. Hereafter, K_a was chosen equal 3 and 5 s^{-1} during the stance and swing phase, respectively.

4.2.2. Cane Orientation Control

The control of the cane orientation is achieved through the modulation of the velocity of the wheels. Their rotation influences the velocity of the handle as can be seen in Equation (5). To cancel this influence, the velocity of the wheels should satisfy \dot{x}_{OH} :

$$\omega = \frac{(r + l \cos \theta)}{r} \dot{\theta} + \frac{\sin \theta}{r} \dot{l} \quad (9)$$

Since $z_{OH} = l \cos \theta + r$, and $\dot{z}_H = 0$ (this is the objective of the telescopic axis control), it comes that:

$$\dot{l} = \frac{l \sin \theta}{\cos \theta} \dot{\theta}$$

Equation (9) writes:

$$\begin{aligned} \omega &= \frac{(r + l \cos \theta)}{r} \dot{\theta} + \frac{l \sin^2 \theta}{r \cos \theta} \dot{\theta} \\ &= \frac{(r \cos \theta + l)}{r \cos \theta} \dot{\theta} \end{aligned} \quad (10)$$

The control law of the wheels established to reduce the motion of the cane handle is:

$$\tilde{\omega} = K_r \frac{(r \cos \theta + l)}{r \cos \theta} (\theta_d - \theta) \quad (11)$$

with $\tilde{\omega}$ representing the speed input sent to the servo-drive driving the cane wheels and θ_d the assisted limb thigh orientation to be followed. Assuming a correct estimation of the wheels radius, and $\theta \notin \{-\frac{\pi}{2}, \frac{\pi}{2}\}$, the continuous-time asymptotic stability is ensured by choosing K_r strictly positive. During our experiments, K_r was equal to 3.8 s^{-1} .

5. EXPERIMENTAL RESULTS

In this section, an experimental evaluation of the cane adaptive motion with the gait cycle is carried out. In subsections 5.1 and 5.2, the different tests were performed by a member of the team. In subsection 5.3, the robotic cane was evaluated by a group of volunteers. The experimental context is shown in **Figure 5**. The participant left leg (that to be assisted) and the cane were equipped with wireless IMUs, so the latter was synchronized with the gait cycle based on the leg motion. The rear and the front of the base of the hands free crutch attached to the left leg were equipped with optical markers. It emulated the foot of the impaired leg. The right hand and the cane tip were as well-equipped with markers. The data recorded by the BeagleBone board were the left thigh orientation and its angular speed, the cane orientation, the velocity of the wheels, the telescopic shaft velocity and the detected gait phase. The cane synchronization with the gait has been assessed using the experimental data

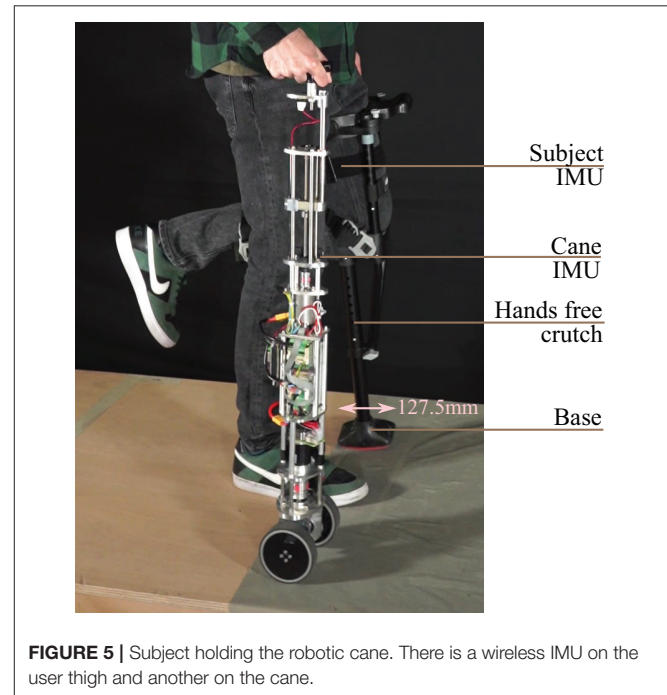


FIGURE 5 | Subject holding the robotic cane. There is a wireless IMU on the user thigh and another on the cane.

obtained thanks to the Optitrack motion capture system in addition to the data logged into cane board memory.

5.1. Assessment of the Support Provided by the Robotic Cane

In order to assess the ability of the arching mechanism and the wheels' motor to withstand the forces applied on it, the cane was placed on a force platform and the participant was asked to lean on it. The force platform allowed the monitoring of the forces along the axis of the cane frame (see **Figure 6**). The wheels' motor velocity was set to zero, which is the case when a stance phase of the impaired leg is detected. The shaft motor reference velocity was also set to zero. This setting is the most challenging and corresponds to the phase (d) of **Figure 1** bottom. The cane is vertical so the shaft velocity is supposed to be equal

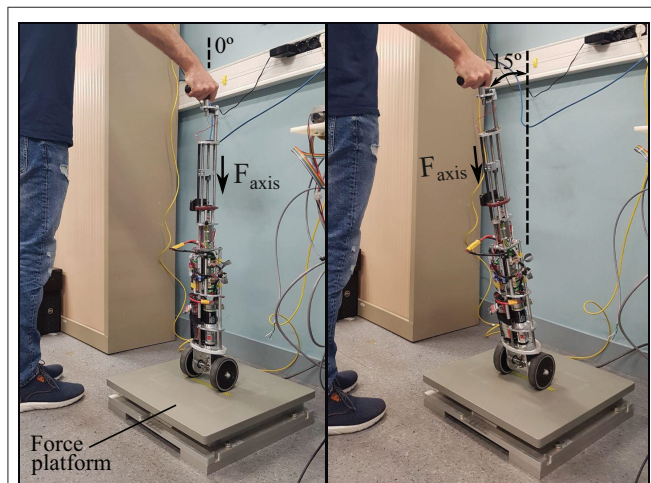


FIGURE 6 | Experimental testing of the forces that the robotic cane can withstand. The cane is placed on a force platform in a vertical position (**left**), and then inclined by 15° (**right**). Both motors' velocities were set to zero.

to zero while the user is exerting the highest vertical load. The participant applied forces on the cane which was put in two directions corresponding to the vertical 0° and one of 15° (see **Figure 7**). Note that these forces were artificially high since the purpose of this exercise was to test the cane support performance. One can see that the maximum vertical applied force to the cane was around 180 N, whereas the tangential force varied between 10 and 50 N for the vertical and 15° inclination, respectively. This is in accordance with the design objectives of section 2.1.

5.2. Cane Performance Assessment

5.2.1. Metrics for Tracking Performances

Here, the error parameters used to quantify the active cane performance are explained. On the one hand, the cane capacity to track the impaired leg motion is assessed by the Root Mean Square Error (RMSE). It provides insight into the control law tracking performance. On the other hand, the second parameter has been called Mean Distance-to-the-Foot Error (MDFE) and it is a measure of how successful the cane is fulfilling its assistive task, by stopping in the suitable area and providing proper support to the user.

- *Angle Root Mean Square Error*

The *Angle RMSE* provides a measurement of the difference between the angles of the active cane and the impaired leg during the assisted walk. It is computed for the swing phases of this leg since it is in these phases when the tracking is active.

$$\text{Angle RMSE} = \left[\sum_{i=1}^N (\theta_{ILi} - \theta_{ACi})^2 / N \right]^{1/2} \quad (12)$$

where θ_{IL} and θ_{AC} are the impaired leg and active cane angles, respectively, and N is the number of samples acquired in the impaired leg swing phases of the test for which the parameter is computed.

- *Mean Distance-to-the-Foot Error*

The *Mean Distance-to-the-Foot Error* (MDFE) aims to

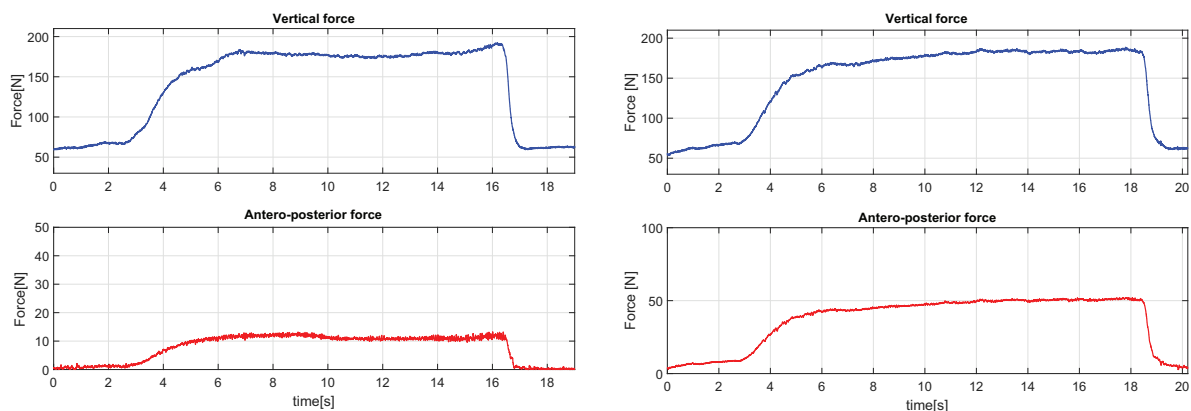


FIGURE 7 | Forces applied on the cane axis with a constant cane length of 0.88 m, an angle of 0° (**left**) and an angle of 15° (**right**).

quantify how good the support given by the cane is when users lean on it. Thus, from the assistance standpoint, this parameter tries to answer to the question: *is the cane well-placed during the impaired leg stance phases?* The MDFE is useful to check if the cane tip is properly located in the walking direction axis with respect to the position of the impaired leg foot.

Note that, as explained at the beginning of section 5, in the experiments the impaired leg is simulated with a hands free crutch (see **Figure 5**), so that this leg foot corresponds to the crutch distal base. The MDFE is computed as the mean

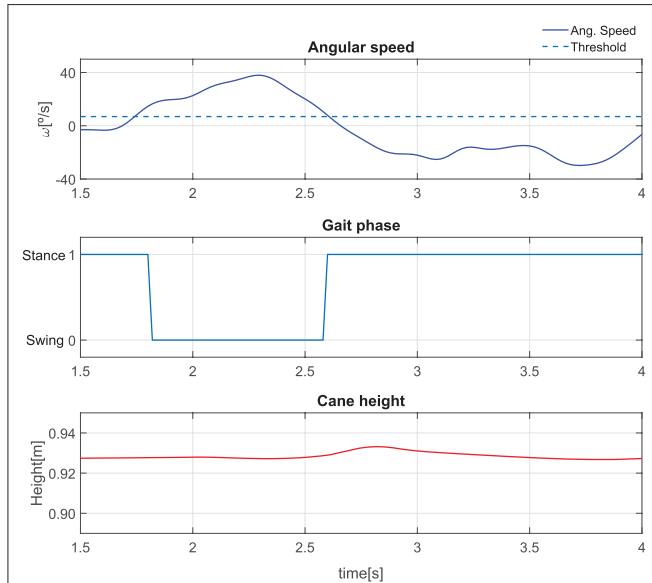


FIGURE 8 | Performance of a single step: angular speed captured by the IMU attached to the impaired leg (**top**). Gait phase detected using the angle acquired by the motion capture and the method in **Figure 3** (**center**). Cane height (**bottom**).

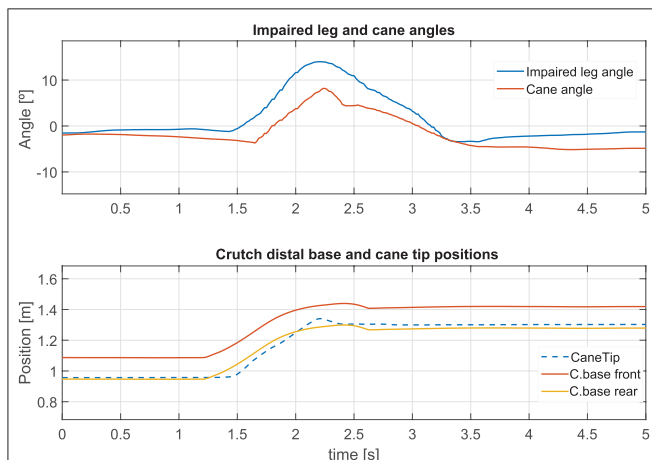


FIGURE 9 | Impaired leg and cane tip angles during a step (**top**). Position of the crutch base boundaries and the cane tip along the walking direction during a step (**bottom**).

Algorithm 1: Mean Distance-to-the-Foot Error computation.

Data: Arrays y_{Ctip} , $y_{CBfront}$, and y_{CBrear}

Result: MDFE

MDFE=0;

for ($i=1$; $i \leq N$; $i++$) **do**

if ($y_{Ctip}(i) > y_{CBfront}(i)$) **then**

 MDFE=MDFE+($y_{Ctip}(i)-y_{CBfront}(i)$);

else

if ($y_{CBrear}(i) > y_{Ctip}(i)$) **then**

 MDFE=MDFE+($y_{CBrear}(i)-y_{Ctip}(i)$);

MDFE=MDFE/N;

distance from the cane tip to the boundaries of this base. That is to say, for each test sample if the cane tip remains inside the crutch distal base boundaries, the error is zero. On the contrary, if the cane tip stops above or behind the coordinates of the base boundaries, the error is the distance between the cane tip and the base front or the base rear, respectively. Algorithm 1 helps clarify how this parameter is calculated. Let us consider y as the axis in the walking direction. y_{Ctip} , $y_{CBfront}$, and y_{CBrear} are the arrays with coordinates of the cane tip, the crutch base front, and the crutch base rear. N is the number of samples acquired in the impaired leg stance phases.

5.2.2. Cane Behavior During a Single Step

The results presented hereafter show the cane behavior during a step beginning the gait. The subject at rest, performed a 0.25 m step with its impaired leg. **Figure 8** compares the phase detection performed thanks to the angular speed provided by gyroscope of the impaired leg IMU with the detection obtained with the motion capture system (ground truth). The comparison indicates good performances of the proposed method. The stance to swing transition ($t = 1.77$ s) is obtained by monitoring the angular speed given by the gyroscope which is multiplied by 100 to

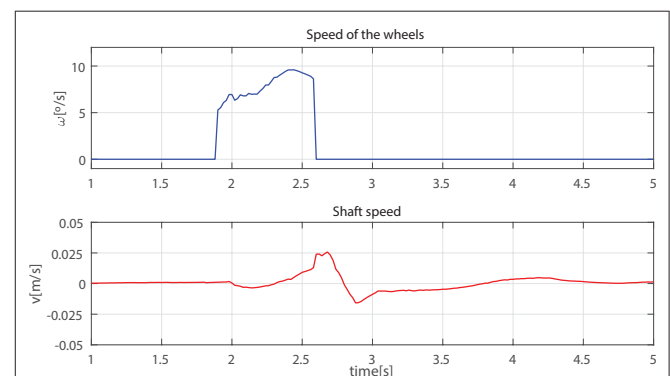
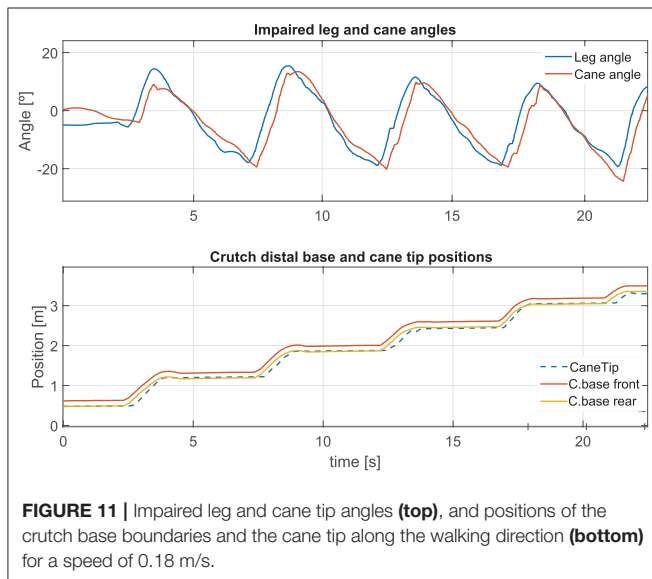


FIGURE 10 | Speed of the wheels (**top**) and the telescopic shaft (**bottom**) observed during a step.

make its observation easier. The swing is detected when the threshold indicated in dashed line is crossed as explained in **Figure 3**. During the swing phase (between $t = 1.77$ s and $t = 2.58$ s), the motion of the wheels is enabled. **Figure 9** represents the impaired leg following performed by the cane. The cane tip remains most of the time between the crutch base front and back boundaries. As the angular velocity given by the gyroscope becomes negative, the stance phase is detected as shown in **Figure 8**. During the whole stance phase, the shaft control maintains the cane handle height practically to its initial value of 0.93 m (**Figure 8** bottom) and the motion of the wheels is disabled so as to offer an immobile support point.



The evolution of the speeds of the wheels and the shaft is given in **Figure 10**.

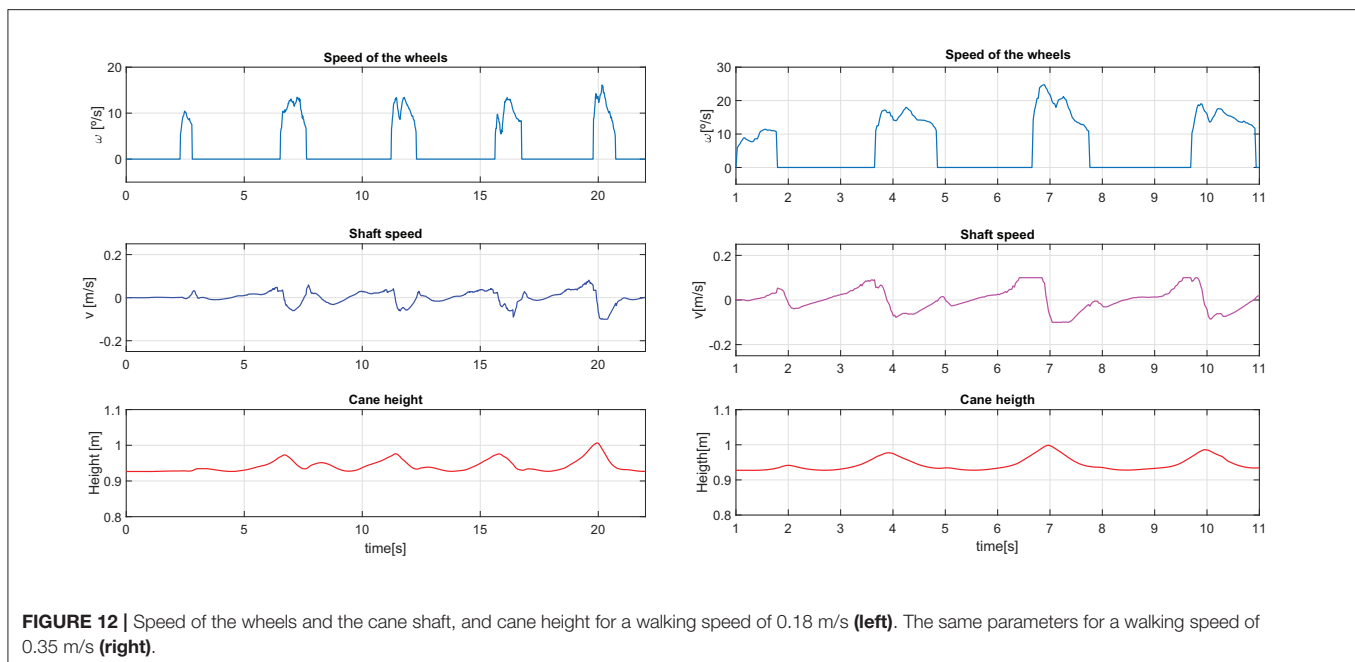
5.2.3. Robotic Cane-Assisted Gait for a Walking Speed of 0.18 m/s

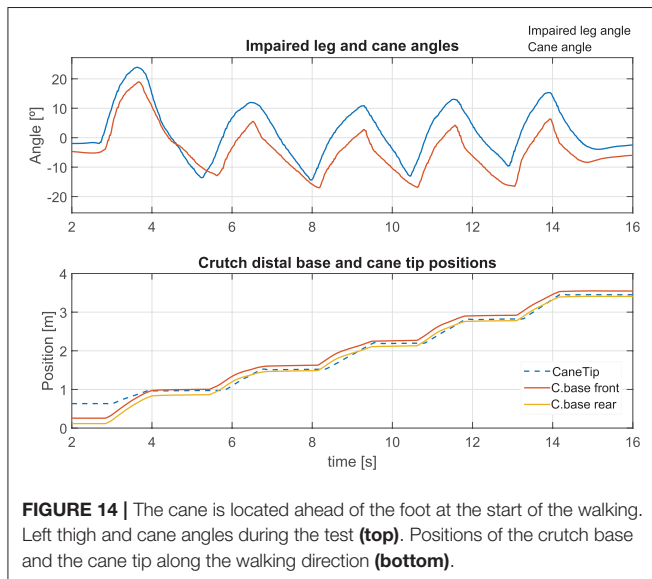
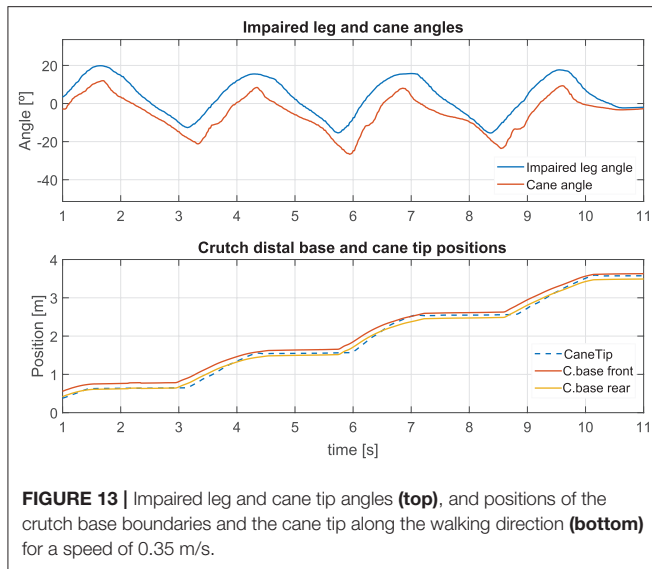
We observed the cane behavior for a slow walking speed of 0.18 m/s. The results of the left thigh following performed by the cane are presented in **Figure 11** top. As the wheels' motion occurs during the swing phase, this is the time span in which the error must be computed. The Angle RMSE is 7.81° . Note that the cane angle has a small lag. It is due to the fact that three consecutive samples have to exceed the swing phase detection threshold (see **Figure 3**) before the tracking starts. The latter accounts for the Angle RMSE increase. Despite the error during the cane following, we noticed that the cane tip remained near the front and back boundaries of the crutch distal base during the stance phases (see **Figure 11** bottom). It suggests that, despite starting moving later, the cane quickly shortens the angle difference with the weakest leg and stops at a point where proper support is given. The latter is backed by a little MDFE of 0.0061 m.

The cane handle height was almost maintained at a constant value (**Figure 12** left bottom). The wheel and shaft speeds provided in **Figure 12** left top and center remained between the speed boundaries implemented in the software. During the stance phase, the cane wheels remained still and the shaft speeds were reduced thanks to a lower gain.

5.2.4. Effect of an Increase of the Walking Pace on the Cane Performances

We compared the results presented above with an assisted gait performed with a higher walking speed of 0.35 m/s. During the latter, the impaired leg following performance (**Figure 13** top) was slightly lower than that obtained for a walking speed of





0.18 m/s, with an Angle RMSE of 8.57° . Nevertheless, the cane tip position remains inside the crutch distal base boundaries (**Figure 13** bottom) with a MDFE of 0.0001 m. Note that this value is lower than that computed for the 0.18 m/s test. It may seem contradictory but it may be due to the fact that the user has felt more comfortable at a higher speed. The accumulated experience in the use of the cane may also affect improving the performance.

In comparison with the walk at 0.18 m/s, a higher request of the shaft was observed in order to maintain the cane handle height near its initial value (**Figure 12** right center and bottom). Besides, a light increase of the maximum speed of the wheels was noticed (**Figure 12** right top).

5.2.5. How to Manage a Voluntary Hand Motion?

The synchronization strategy assumed the immobility of the hand holding the cane. This is hardly met since the user is not focused on his hand position while walking. Here we illustrate the issue by starting the walk with the cane placed 0.43 m ahead of its user. We show that, if the user brings back his hand toward his body, the synchronization works well. This is depicted in **Figure 14**. At the bottom, one can see the wrong positioning of the cane at the beginning of the walk, and how the normal functioning has been recovered afterwards.

5.3. Assessment of the Cane With Several Participants

The performance of the cane was also assessed through an experiment with six healthy participants, three males and three females (27.5 years old avg.), in conformity with the conditions already specified in the section 3.2 of this article. Although people with real mobility issues are the target population of the active cane, at this stage simulated walking impairment is enough to show the feasibility of the proposal. This way, the participants were equipped with a hands free crutch (see **Figure 5**) with the purpose of immobilizing their left leg and altering their gait (the crutch distal base is again considered as the impaired leg foot). They used the robotic cane in a contralateral way while equipping optical markers for motion capture. They were allowed to use the robotic cane for 5 min before starting the experiment. The experiment consisted of three tests of 3.5-m forward assisted-gait at their preferred speed. They did not receive any specific instruction on how the cane should be used. Once the tests were carried out, participants were asked informally about their impression after using the cane and none reported comfort issues.

The orientation angle of the robotic cane and the impaired leg were captured. The trajectories of the cane tip and the crutch base were as well-collected. The RMSE was computed for the impaired leg and cane angles during the swing phases, as explained in subsection 5.2.1. In the same way, the MDFE was also calculated. Both parameters, together with the test speed and the number of strides of each test, are listed in **Table 1**. As can be observed, there is some variability in the values of the Angle RSME, with a minimum of 6.42° and a maximum of 12.31° . The mean, considering all the subjects, is 8.93° , what is not far from that obtained for the tests of subsections 5.2.3 and 5.2.4. The MDFE shows a range that goes from zero (the cane tip remained inside the crutch distal base boundaries in the stance phases) to 0.028 m. The mean MDFE is 0.008 m, what would assure a good support for the user. The speeds are quite different from participant to participant. On the one hand, we find the case of Subject 1, that presents both the higher speeds and the slowest MDFE. On the other, we have the results of Subject 2, generally with much lower speeds and the highest MDFE. That supports the idea that, as with a conventional cane, users perform better with the active cane at their preferred pace so a higher speed does not mean necessarily

TABLE 1 | Results for the participants involved in the experiments.

Participant	Active cane–Imp. leg Angle RMSE (°) (swing phases)	Cane tip–Crutch base MDFE (m) (stance phases)	Speed (m/s)	N° of strides
1	10.06	0.000	0.21	5
	9.08	0.001	0.22	5
	9.95	0.001	0.21	5
2	7.28	0.015	0.13	7
	7.38	0.028	0.13	7
	6.98	0.023	0.17	6
3	6.44	0.005	0.13	9
	7.08	0.000	0.14	7
	6.42	0.022	0.12	8
4	10.75	0.000	0.19	8
	7.72	0.004	0.16	7
	9.58	0.013	0.16	8
5	12.31	0.000	0.21	7
	10.35	0.004	0.18	8
	8.79	0.012	0.16	8
6	11.03	0.008	0.12	9
	10.38	0.000	0.12	8
	9.17	0.009	0.10	8
All Subjects Mean	8.93	0.008		

The parameters in the columns, from left to right, are: subject identifier, Angle Root Mean Square Error (between the cane and the impaired leg), Mean Distance-to-the-Foot Error, test speed, and number of strides per test.

worse walking assistance. This is in line with that observed in subsection 5.2.4.

6. CONCLUSION

In this paper, a control scheme of a robotic cane, which relies on the synchronization of the device motion with the gait cycle, is presented. Its main advantage is its ability to adapt to its user gait parameters. If the step length or the pace change, the cane can automatically adapt its behavior.

The provided control scheme allows robotic canes to provide better assistance than conventional and non-actuated canes. Indeed, the working scheme is planned as follows: during the swing phase of the impaired leg, the robotic cane follows automatically this leg orientation; during the stance phase the cane tip is immobile and provides proper support to the user. Since the robotic cane is not supposed to be lifted during use, all the stumbling risks are eliminated. Besides, the cane handle height keeps as constant as possible to avoid pushing and pulling the user hand during

the cane motion. The control strategy feasibility has been shown experimentally.

A short term improvement is to make turning during walking feasible by just rotating the cane, held vertically, around its axis and continuing walking. Detecting a vertical rotation intention will make this improvement possible.

Future work will include the reduction of the robotic cane weight and the improvement of the control law, mainly by reducing the cane angle lag. Moreover, the cane usage time may be extended by using low consumption IMUs instead of the current ones. To improve ergonomics, smartphones can be used to provide the angular information instead of a wearable IMU. Note that smartphones already incorporate an IMU and, normally, people carry theirs with them. One can also think of integrating some new sensors in the cane that enable obstacle detection and other high order functionalities.

Although the proposed concept has been validated through this work, tests with the target population are necessary to confirm its efficacy. They will be planned in the next stage.

DATA AVAILABILITY STATEMENT

All datasets generated for this study are included in the article/supplementary material.

ETHICS STATEMENT

The studies involving human participants were reviewed and approved by Sorbonne University Ethics Committee. The patients/participants provided their written informed consent to participate in this study.

AUTHOR CONTRIBUTIONS

AT-L has been in charge of writing, designing and carrying out the experiments, analyzing the data and results, and drawing the conclusions. RA has contributed with the kinematic model and the original concept. DR has helped with the coding and electronics. WB has collaborated during the whole work providing ideas and supervising. All authors contributed to the article and approved the submitted version.

FUNDING

This work was funded by the ANR within the Investissements d'Avenir, programme under reference ANR-11-IDEX-0004-02 and within the project i-Gait, under reference ANR-16-CE33-0012.

ACKNOWLEDGMENTS

The authors would like to address their kind acknowledgment to Laurent Fabre for his valuable help during the design and the manufacturing of the robotic cane prototype.

REFERENCES

- Ady, R., Bachtá, W., and Bidaud, P. (2013). "Analysis of cane-assisted walking through nonlinear optimization," in *2013 IEEE International Conference on Robotics and Automation*, (Karlsruhe), 3866–3872. doi: 10.1109/ICRA.2013.6631121
- Ady, R., Bachtá, W., and Bidaud, P. (2014). "Development and control of a one-wheel telescopic active cane," in *5th IEEE RAS/EMBS International Conference on Biomedical Robotics and Biomechatronics*, (São Paulo), 461–466. doi: 10.1109/BIOROB.2014.6913820
- Au, L. K., Wu, W. H., Batalin, M. A., and Kaiser, W. J. (2008). "Active guidance towards proper cane usage," in *2008 5th International Summer School and Symposium on Medical Devices and Biosensors* (Hong Kong: IEEE), 205–208. doi: 10.1109/ISSMDBS.2008.4575054
- Chen, C. L., Chen, H. C., Wong, M. K., Tang, F. T., and Chen, R. S. (2001). Temporal stride and force analysis of cane-assisted gait in people with hemiplegic stroke. *Archiv. Phys. Med. Rehabil.* 82, 43–48. doi: 10.1053/apmr.2001.18060
- Dai, R., Stein, R. B., Andrews, B. J., James, K. B., and Wieler, M. (1996). Application of tilt sensors in functional electrical stimulation. *IEEE Trans. Rehabil. Eng.* 4, 63–72. doi: 10.1109/86.506403
- Di, P., Hasegawa, Y., Nakagawa, S., Sekiyama, K., Fukuda, T., Huang, J., et al. (2016). Fall detection and prevention control using walking-aid cane robot. *IEEE/ASME Trans. Mech.* 21, 625–637. doi: 10.1109/TMECH.2015.2477996
- European Public Health Association (2015). *Falls Among Older Adults in the EU-28*. Fact sheet. Amsterdam: European Public Health Association.
- Evans, A. L., Duncan, G., and Gilchrist, W. (1991). Recording accelerations in body movements. *Med. Biol. Eng. Comput.* 29, 102–104. doi: 10.1007/BF02446305
- Hassan, M., Kadone, H., Suzuki, K., and Sankai, Y. (2012). "Exoskeleton robot control based on cane and body joint synergies," in *2012 IEEE/RSJ International Conference on Intelligent Robots and Systems*, 1609–1614. doi: 10.1109/IROS.2012.6386248
- Hassan, M., Kadone, H., Ueno, T., Hada, Y., Sankai, Y., and Suzuki, K. (2018). Feasibility of synergy-based exoskeleton robot control in hemiplegia. *IEEE Trans. Neural Syst. Rehabil. Eng.* 26, 1233–1242. doi: 10.1109/TNSRE.2018.2832657
- Hwang, T., Reh, J., Effenberg, A. O., and Blume, H. (2018). Real-time gait analysis using a single head-worn inertial measurement unit. *IEEE Trans. Consumer Electron.* 64, 240–248. doi: 10.1109/TCE.2018.2843289
- Liu, H., Eaves, J., Wang, W., Womack, J., and Bullock, P. (2011). Assessment of canes used by older adults in senior living communities. *Archiv. Gerontol. Geriatr.* 52, 299–303. doi: 10.1016/j.archger.2010.04.003
- Maqbool, H. F., Husman, M. A. B., Awad, M. I., Abouhossein, A., Iqbal, N., and Dehghani-Sanij, A. A. (2017). A real-time gait event detection for lower limb prosthesis control and evaluation. *IEEE Trans. Neural Syst. Rehabil. Eng.* 25, 1500–1509. doi: 10.1109/TNSRE.2016.2636367
- Martínez-Hernández, U., Mahmood, I., and Dehghani-Sanij, A. A. (2018). Simultaneous bayesian recognition of locomotion and gait phases with wearable sensors. *IEEE Sens. J.* 18, 1282–1290. doi: 10.1109/JSEN.2017.2782181
- Mayagoitia, R. E., Nene, A. V., and Veltink, P. H. (2002). Accelerometer and rate gyroscope measurement of kinematics: an inexpensive alternative to optical motion analysis systems. *J. Biomech.* 35, 537–542. doi: 10.1016/S0021-9290(01)00231-7
- Mercado, J., Chu, G., Imperial, E. J., Monje, K. G., Pabustan, R. M., and Silverio, A. (2014). "Smart cane: instrumentation of a quad cane with audio-feedback monitoring system for partial weight-bearing support," in *International Symposium on Bioelectronics and Bioinformatics*. doi: 10.1109/ISBB.2014.6820893
- Murray, M. P., Seireg, A. H., and Scholz, R. C. (1969). A survey of the time, magnitude and orientation of forces applied to walking sticks by disabled men. *Am. J. Phys. Med. Rehabil.* 48, 1–13.
- Peel, N. M., Kuys, S. S., and Klein, K. (2012). Gait speed as a measure in geriatric assessment in clinical settings: a systematic review. *J. Gerontol. A Biol. Sci. Med. Sci.* 68, 39–46. doi: 10.1093/gerona/gls174
- Phi, L. V., and Fujimoto, Y. (2019). A robotic cane for balance maintenance assistance. *IEEE Trans. Ind. Inform.* 15, 3998–4009. doi: 10.1109/TII.2019.2903893
- Spenco, M., Yu, H., and Dubowsky, S. (2006). Robotic personal aids for mobility and monitoring for the elderly. *IEEE Trans. Neural Syst. Rehabil. Eng.* 14, 344–351. doi: 10.1109/TNSRE.2006.881534
- Sterling, D., O'Connor, J., and Bonadies (2001). Geriatric falls: injury severity is high and disproportionate to mechanism. *J. Trauma Injury Infect. Crit. Care* 50, 116–119. doi: 10.1097/00005373-200101000-00021
- Suzuki, S., Hirata, Y., and Kosuge, K. (2009). "Development of intelligent passive cane controlled by servo brakes," in *IEEE International Symposium on Robot and Human Interactive Communication*, (Toyama), 97–102. doi: 10.1109/ROMAN.2009.5326139
- Trujillo-León, A. R., Vidal-Verdú, F., and Bachtá, W. (2015). "A tactile handle for cane use monitoring," in *2015 37th Annual International Conference of the IEEE Engineering in Medicine and Biology Society (EMBC)*, (Milan), 3586–3589. doi: 10.1109/EMBC.2015.7319168
- Tyson, S. F., and Rogerson, L. (2009). Assistive walking devices in nonambulant patients undergoing rehabilitation after stroke: the effects on functional mobility, walking impairments, and patients' opinion. *Archiv. Phys. Med. Rehabil.* 90, 475–479. doi: 10.1016/j.apmr.2008.09.563
- Vallery, H., van Asseldonk, E., Buss, M., and van der Kooij, H. (2009). Reference trajectory generation for rehabilitation robots: complementary limb motion estimation. *IEEE Trans. Neural Syst. Rehabil. Eng.* 17, 23–30. doi: 10.1109/TNSRE.2008.2008278
- Wade, J. W., Boyles, R., Flemming, P., Sarkar, A., de Riesthal, M., Withrow, T. J., et al. (2018). Feasibility of automated mobility assessment of older adults via an instrumented cane. *IEEE J. Biomed. Health Inform.* 23, 1631–1638. doi: 10.1109/JBHI.2018.2873991
- Wakita, K., Huang, J., Di, P., Sekiyama, K., and Fukuda, T. (2013). Human-walking-intention-based motion control of an omnidirectional-type cane robot. *IEEE/ASME Trans. Mech.* 18, 285–296. doi: 10.1109/TMECH.2011.2169980
- Willemsen, A. T. M., Bloemhof, F., and Boom, H. B. K. (1990). Automatic stance-swing phase detection from accelerometer data for peroneal nerve stimulation. *IEEE Trans. Biomed. Eng.* 37, 1201–1208. doi: 10.1109/10.64463
- World Health Organization (2012). *Falls*. Fact sheet 344. Geneva: World Health Organization.

Conflict of Interest: The authors declare that the research was conducted in the absence of any commercial or financial relationships that could be construed as a potential conflict of interest.

Copyright © 2020 Trujillo-León, Ady, Reversat and Bachtá. This is an open-access article distributed under the terms of the Creative Commons Attribution License (CC BY). The use, distribution or reproduction in other forums is permitted, provided the original author(s) and the copyright owner(s) are credited and that the original publication in this journal is cited, in accordance with accepted academic practice. No use, distribution or reproduction is permitted which does not comply with these terms.



Compact Gearboxes for Modern Robotics: A Review

Pablo López García^{1,2*}, Stein Crispel^{1,2}, Elias Saerens^{1,2}, Tom Verstraten^{1,2} and Dirk Lefeber^{1,2}

¹ Robotics and Multibody Mechanics, Vrije Universiteit Brussel, Brussels, Belgium, ² Robotics and Multibody Mechanics, Flanders Make, Heverlee, Belgium

On the eve of Human-Robot-Interaction (HRI) becoming customary in our lives, the performance of HRI robotic devices remains strongly conditioned by their gearboxes. In most industrial robots, two relatively unconventional transmission technologies—Harmonic Drives[®] and Cycloid Drives—are usually found, which are not so broadly used in other industries. Understanding the origin of this singularity provides valuable insights in the search for suitable, future robotic transmission technologies. In this paper we propose an assessment framework strongly conditioned by HRI applications, and we use it to review the performance of conventional and emerging robotic gearbox technologies, for which the design criterion is strongly shifted toward aspects like weight and efficiency. The framework proposes to use virtual power as a suitable way to assess the inherent limitations of a gearbox technologies to achieve high efficiencies. This paper complements the existing research dealing with the complex interaction between gearbox technologies and the actuators, with a new gearbox-centered perspective particularly focused on HRI applications.

Keywords: transmissions, gearboxes, HRI, efficiency, virtual power, harmonic drive, cycloid drives

OPEN ACCESS

Edited by:

Jan Veneman,
Hocoma, Switzerland

Reviewed by:

Elliott J. Rouse,
University of Michigan, United States
Cor Meijneke,
Delft University of
Technology, Netherlands

*Correspondence:

Pablo López García
plopezga@vub.be

Specialty section:

This article was submitted to
Biomedical Robotics,
a section of the journal
Frontiers in Robotics and AI

Received: 14 May 2020

Accepted: 30 June 2020

Published: 14 August 2020

Citation:

García PL, Crispel S, Saerens E,
Verstraten T and Lefeber D (2020)
Compact Gearboxes for Modern
Robotics: A Review.
Front. Robot. AI 7:103.
doi: 10.3389/frobt.2020.00103

INTRODUCTION

Industrial robots represent the backbone of several large-scale, traditional manufacturing industries including automotive or electronics. Today, many regions in the world see a realistic opportunity to bring back manufacturing industry introducing robots in Small and Medium size Enterprises (SMEs) and in assistive services, typically in healthcare (SPARC, 2015).

For large-scale, highly automated industrial environments, the advantage of robotic solutions compared to human operators mainly lies in (i) larger availability and (ii) the ability to move—typically large—payloads with extreme positioning accuracy and at high speed. These aspects are of pivotal importance when designing and selecting suitable technologies for an industrial robot, particularly for the prime movers and transmissions providing movement to these devices.

Applications in SME manufacturing and personal assistance challenge this traditional robotics paradigm. The key to success in these new applications lies in a very high degree of flexibility, required to enable a safe and efficient, direct cooperation with humans in order to achieve shared goals. This objective requires robots to first develop the ability to interact safely with humans, in a discipline usually referred to as pHRI—physical Human-Robot Interaction.

pHRI has a wide-ranging impact on robotic actuation. The experience accumulated during the past decades, mainly in healthcare robotics, indicates that for safe and efficient interaction with humans, robots need basically to move like humans, hence sacrificing some of their traditional advantages in terms of payload, accuracy, and speed. This situation has led to profuse research in

the past years covering the optimal selection of prime movers and transmissions for HRI actuation (Zinn et al., 2004; Ham et al., 2009; Iqbal et al., 2011; Veale and Xie, 2016; Verstraten et al., 2016; Groothuis et al., 2018; Saerens et al., 2019).

Those works belong in a broader field of research studying the optimization of the coupling between prime mover and gearbox for a given task in automatic machines. A quick review of the main developments in this field provides useful insights to understand the impact of the gearbox on the overall system performance. Pasch and Seering (1983) identified the importance of inertia in actuation and proposed the use of a gear ratio to match the inertia of the motor and that of the reflected load as a means to minimize energy consumption for a purely inertial load. Chen and Tsai (1993) applied this idea to the field of robotics and identified the resulting acceleration capacity of the end-effector as a determining parameter. Van de Straete et al. (1998) separated motor and load characteristics to extend this approach to a general load and provided a method to identify suitable transmission ratios from a discrete set of motors and gearboxes. Roos et al. (2006) studied optimal actuator selection for electrical-vehicle powertrains adding the contribution of the gearbox efficiency. Giberti et al. (2010) confirm rotor inertia, transmission ratio, gearbox efficiency, and gearbox inertia as the most relevant parameters for actuation selection and propose a graphical method to optimize that selection for a dynamic task. Pettersson and Ölvander (2009) focused again on industrial robots and present a method which models the gearbox with a strong focus on mass, inertia, and friction. Rezazadeh and Hurst (2014) use a very accurate motor model and incorporate a fundamental bandwidth selection criterion, on addition to energy minimization. Dresscher et al. (2016) investigate the contribution of friction for a planetary gearbox in which Coulomb friction is the dominant friction mechanism and demonstrate how gearbox efficiency typically becomes dominant over motor efficiency at high transmission ratios.

From the initial gearbox models used in these works, where gearboxes are modeled as ideal transmission ratios, the complexity of the models increased progressively. Nevertheless, important—and unrealistic—simplifications need to be made to obtain good practicability in these methods. Important effects like those of torsional stiffness and lost motion are thus not incorporated, while gearbox inertia and efficiency models are strongly oversimplified. This is a justifiable approach for multiple applications, where simplified methods can help engineers select suitable transmissions. In HRI however, these properties are too pivotal for the suitability of the gearbox and they cannot be so strongly simplified.

A different approach is therefore required to provide useful guidance for gearbox selection in HRI, avoiding the excessive complexity of optimization tasks in this field. Providing detailed insight on the operational properties and performances of different gearbox technologies, to guide educated selection is another option, following the tradition of works like Schempf and Yoerger (1993) or Rosenbauer (1995). Following this approach, Siciliano et al. (2010), Li (2014), Scheinman et al. (2016), and Pham and Ahn (2018) provide interesting overviews on

high precision gearboxes for modern robotics. However, the technologies are not analyzed in sufficient detail to gain a good understanding of the complex mechanisms in which they affect the performance of the robotic task.

The main objective of this review is consequently to complement these works with a detailed analysis of the underlying principles, strengths, and limitations of available technologies. Apart from enabling a forecast of the future of gearbox technologies in robotics, this approach can help gearbox non-specialists identify suitable compact gearbox technologies for the highly multi-factorial requirements of new robotic applications (López-García et al., 2018). For gearbox specialists from other domains, this analysis can help them gain useful insight in the particular needs of HRI applications.

This study begins with a brief description of the main requirements for future robotic transmissions, to introduce then an assessment framework designed to assess the suitability and potential of a particular gearbox technology for this field. This framework incorporates a strong pHRI perspective and incorporates a new parameter—Latent Power Ratio—to evaluate the inherent efficiency of a certain gearbox topology. This new framework is used in first instance to review traditional gearbox technologies used in industrial robots and of emerging transmission technologies which are currently in the process of finding their way into the market. Finally, a summary of the findings resulting from this review, together with our conclusions and recommendations, is given at the end of the paper.

AN HRI-ENHANCED, ASSESSMENT FRAMEWORK FOR ROBOTIC TRANSMISSIONS

Control

The control of robotic devices is a very broad and complex topic, and the subject of extensive research literature. In this section we restrict ourselves to introducing the basic principles of Linearity and Reflected Inertia, which are basic to understand the gearbox influence on control.

Although in general speed and precision are conflicting requirements, conventional robotic devices excel in achieving high positioning accuracy at high speed thanks to the use of stiff actuators with very linear behaviors (Cetinkunt, 1991). The incorporation of a robotic transmission influences control complexity mainly in two ways: introducing additional non-linearities and strongly impacting the reflected inertias.

The non-linearities introduced by the incorporation of a transmission take basically the form of backlash and/or friction and reduce the system's bandwidth, creating important control challenges (Schempf, 1990). The statement *gears introduce backlash, friction, and (unwanted) compliance, which make accurate control difficult* (Hunter et al., 1991) is today just as valid as almost 30 years ago. For some technologies, large kinematic transmission errors and particularly non-linear friction behaviors can also induce considerable non-linearities.

Transmissions strongly impact a system's reflected inertias as well. In a robotic device, the inertia of the prime mover is typically several orders of magnitude smaller than that of the payload, a situation tending to make a system unstable and introducing strong control challenges. Adding a transmission strongly reduces the inertia of the payload seen by—reflected to—the prime mover by a factor equal to the squared reduction-ratio of the transmission. Thus, a careful selection of the transmission can result in more balanced inertias on both transmission's sides, contributing to minimize energy consumption and to more robust, stable, and precise system (Pasch and Seering, 1983).

Reflected inertias are particularly important when the end-effectors undergo rapid and frequent changes in speed and/or torque, a very common situation in automation and robotic tasks. In these cases, a bandwidth perspective is introduced to confirm the ability of the system to follow these changes (Sensing, 2010; Rezazadeh and Hurst, 2014). This underlies the principle of backdrivability, the ability of a system to show low mechanical impedance when it is driven from its natural output (back-driven). This is particularly important in the frequent bidirectional energy exchange happening between a robot and its user, typical for rehabilitation devices or exoskeletons. As Wang and Kim (2015) demonstrate, a gearbox's backdrivability includes the combined effect of reflected inertia, reflected damping and Coulomb friction, and it is therefore strongly linked with the efficiency of the gearbox.

This highlights the importance in order to assess the control impact of a certain gearbox technology of both its transmission ratio capabilities and the non-linearities (backlash, friction) that it introduces.

Safety

Industrial robots are traditionally placed behind fences, in highly structured environments where they can take advantage of their fast and accurate robotic movements without endangering the integrity of human operators.

A safe pHRI incorporating the ability to move safely in an unstructured/unknown environment is necessarily strongly linked to controllability. The current strategy used by roboticists to achieve this objective consists of *shaping the mechanical impedance* (Calanca et al., 2015), that is, letting a compliance-controller manage the complex dynamical relation between robot position/velocity and external forces (Hogan, 1984).

The principle is simple: to grant a good adaptation to an uncertain environment, as well as the integrity of the human operator/user during an interaction with a robotic device, the latter must move in a compliant, human-like manner (Karayiannidis et al., 2015). This underlines the importance of impedance and intrinsic compliance (De Santis et al., 2008) and explains the apparition of a new type of intrinsically flexible actuators for pHRI (Ham et al., 2009), where high compliance becomes desirable (Haddadin and Croft, 2016).

From a control perspective, the payload inertia reflected to the prime mover is reduced by a factor corresponding to the square of the gear ratio. In the same way, the typically small rotor inertia of the prime mover is amplified by this same factor when reflected to the payload side, which must be added to the inertia resulting

from the movement of the robotic device and the load for safety considerations, further restricting the operating speeds.

Although most pHRI actuators today use high-ratio gearboxes, some reputed roboticists Seok et al. (2014), Sensinger et al. (2011) see a high potential for robotics in the use of high-torque (out-runner) motors requiring very small transmission ratios. New manufacturers of robotic solutions like Genesis Robotics from Canada, or Halodi Robotics AS from Norway, propose actuators for robotics based on these principles. According to them, increasing the motor's inertia and reducing the gear ratio should result in lower motor inertias reflected to the end-effector, thus enabling higher operational speeds and/or payloads without compromising the operator's integrity. Low ratios also have an additional bandwidth advantage: they have lower friction and backlash, reducing the non-linearities contribution from the gearbox. On the other hand, a moderate gear-ratio cannot compensate the non-linear coupling terms—typically cogging torque (Siciliano et al., 2010).

A closer look at the specifications of these new motors raises some questions in terms of attainable efficiency, weight or compactness, and on the hardware implications resulting from an extreme thirst for high electrical currents (HALODI Robotics, 2018; GENESIS Robotics, 2020).

Summarizing, there is no full agreement on how to best approach safe actuation for robotics. Yet, the strong natural ties between safety and controllability are as certain as the pivotal importance of the transmission's ratio and its non-linearities.

Weight and Compactness

A lightweight design is of paramount importance to make safety and good performance compatible in the new robotics' applications (Albu-Schäffer et al., 2008). The latest Collaborative Robots (cobots) like KUKA's Lightweight-Robot, developed in collaboration with the Institute of Robotics and Mechatronics at the German Aerospace Center (DLR), live upon this principle and hence look very different to the heavy and bulky traditional industrial robots. Thanks to lower inertias, lightweight cobots enable higher productivities—higher speeds—without compromising user safety.

This advantageous aspect of a lightweight design has further advantages. For mobile robotic systems, lower weight means larger autonomies. In wearable, assistive robotic devices including prosthesis and exoskeletons, a lightweight design is also a key aspect to improve comfort (Toxiri et al., 2019).

High compactness is another characteristic shared by these new robotic devices: from cobots to assistive devices, being compact brings advantages in maneuverability and interaction comfort.

In robotic applications involving close cooperation with humans or the provision of mobile services, positions are inherently highly uncertain. Lightweight and compact designs are particularly advantageous (Loughlin et al., 2007) for these applications, with 2 fold consequences: prime movers and transmissions—typically the heaviest elements in a robotic device—need to be light and compact, but lightweight designs tend to demand lower torques.

In contrast to the weight of the gearbox, identifying a suitable criterion for assessing a gearbox's contribution to system compactness is more challenging. Physical volume definitely plays a role, but our experience demonstrates that the actual shape of the gearbox tends to have a larger impact. Another aspect worth mentioning here is the availability in some gearbox configurations of free space to allocate material or moving parts like electric motors or output bearings can also be of particular interest. We have therefore chosen to include in our evaluation framework the approximate shape (diameter \times length) of the selected gearbox, while the availability of extra space can be directly assessed with help of the provided figures of each of the configurations.

Efficiency and Virtual Power

Efficiency

In fields like automotive or wind turbines, gearbox efficiency has long been under strong focus. In robotics on the other hand, efficiency has not until very recently become a key decision parameter for the selection of a suitable gearbox (Arigoni et al., 2010; Dresscher et al., 2016).

Higher efficiencies—lower losses—enable lower energy consumptions and have a direct, positive contribution to both operation costs and to the environmental-footprint of a machine or device. For mobile and wearable robotic devices, better efficiencies help as well reduce the weight of the system—smaller batteries are required—and ultimately result in larger autonomies and better usability (Kashiri et al., 2018).

In gearboxes, there is one additional gain in going for lower losses: most mechanical transmissions used in robotics are form-closed and use some kind of teeth contact to transfer torque and movement between the prime mover and the end-effector. Owing to that, the kinematic ratio between input ω_{In} and output speeds ω_{Out} is locked by the number of teeth and defines its transmission ratio i_K . In a gearbox with no losses, the torque ratio i_τ between output and input torques τ corresponds precisely to the inverse of kinematic transmission ratio, with opposed sign. But in a real gearbox, the presence of losses alters this equality, and because the kinematic transmission ratio is locked by the number of teeth, that the absolute value of the torque ratio must decrease proportionally with the losses:

$$\frac{\omega_{In}}{\omega_{Out}} = i_K = -\eta i_\tau = -\eta \frac{\tau_{Out}}{\tau_{In}}; \text{ where } \eta \text{ represents} \\ \text{the system efficiency.}$$

Consequently, high gearbox losses mean that less torque is available for the end-effector and larger transmission ratios are required to achieve the same torque amplification.

Gearboxes are subject to several types of losses. To classify them, we adopt the criteria proposed by Talbot and Kahraman (2014) and separate them into load-dependent (mechanical) power losses—originated by sliding and rolling of contact surfaces, both in the gear contacts and in the bearings—and load-independent (spin) power losses—originated through the interaction of rotating components with air, oil or a mixture of the two.

Virtual Power

The term Virtual Power was—to the best knowledge of the authors—originally coined by Chen and Angeles (2006), but this phenomenon explaining the anomalous high losses present in some planetary topologies has been known for long time under different names including *Blindleistung* (Wolf, 1958; Mueller, 1998) and *latent or futile power* (Macmillan and Davies, 1965; Yu and Beachley, 1985; Pennestri and Freudenstein, 1993; Del Castillo, 2002).

Owing to its operating principle, a gearbox always includes a high-speed, low-torque side and a high-torque, low-speed side. Its internal gear meshings are hence typically subject to either high-torque and low-speed or to high-speed and low-torque conditions. In some gearboxes though, owing to their specific topology, some gear meshings may encounter simultaneously high-speed and high-torque. Gear meshings can easily reach efficiencies above 98%, but because the generated losses are approximately proportional to the product of the relative speed of the two geared elements and the torque being transferred through the meshing (Niemann et al., 1975), unexpectedly large losses appear on those highly-loaded meshings. Virtual Power provides a framework to evaluate the contribution of this phenomenon, which we will hereafter refer to as the *Topological Efficiency* of a gearbox.

Several of the aforementioned authors propose methods to assess the topological efficiency of a given configuration and to derive its impact on overall system efficiency. In Chen and Angeles (2006) framework, *virtual power* is defined as the power measured in a moving—non-inertial—frame of reference. The *latent power* as introduced by Yu and Beachley (1985) corresponds accordingly to the virtual power when reference frame is the carrier element of the gearbox, while virtual power ratio is the ratio between the virtual power and the power generated by an external torque applied at a link. Using these elements, we define the *Latent Power Ratio* of a gearbox topology as the ratio between the sum of the latent powers in on all meshings, to the power input to the gearbox. A large latent power ratio therefore corresponds to low topological efficiency and indicates a strong tendency to generate large meshing losses.

In order to facilitate the understanding of the practical impact on overall efficiency of the topological efficiency—characterized by its Latent Power Ratio—of a given gearbox configuration, we use at this stage the equations proposed by Macmillan and Davies (1965) to calculate a simplified example.

A complete robotics' gearbox typically involves several meshing contacts, each with different operating conditions and parameters therefore resulting in different individual meshing efficiencies. These efficiencies are very high in optimized geared meshings—frequently above 99%—and allow us to simplify our calculations considering a generic, unique meshing efficiency of $\eta_m = 99\%$ in all the meshing contacts in our gearbox.

First, a reference gearbox, ideal in terms of topological efficiency, would have just one single meshing and a latent power ratio $L = 1$. The power losses inside this reference gearbox can therefore be easily calculated as a function of the input power as:

$$P_{loss} = P_{IN} * (1 - \eta_m)$$

And the total meshing efficiency of the complete gearbox therefore corresponds to that of the single meshing contact:

$$\eta_{\text{sys},\text{ideal}} = \frac{P_{\text{IN}} - P_{\text{Loss}}}{P_{\text{IN}}} = \eta_m = 99\%;$$

A non-ideal gearbox with the same generic η_m in all its meshings, and with a Latent Power Ratio L characterizing its topological efficiency, indicates that the total losses in the gearbox can be approximated in first instance by:

$$P_{\text{loss},L} \approx P_{\text{IN}} * L * (1 - \eta_m)$$

And the total meshing efficiency of the complete gearbox becomes now:

$$\eta_{\text{sys},L} = \frac{P_{\text{IN}} - P_{\text{Loss},L}}{P_{\text{IN}}} \approx L * \eta_m + (1 - L)$$

Which for $\eta_m = 99\%$ and for a value of $L = 50$ results in:

$$\eta_{\text{sys},L} \approx 50\%$$

This result should be partially relativized because the accumulated losses in the first meshings engaged along the different internal power flows in a gearbox make that less virtual power as predicted by these equations will flow through the subsequent meshings. The effect of this is that the efficiencies will normally drop slightly less rapidly with Latent Power Ratio, and a more realistic value for the previous calculation would normally be between 55 and 60%.

To partially compensate this large impact of the topologic efficiency on the overall efficiency, configurations with large Latent Power Ratio therefore require extremely high meshing efficiencies: to achieve a system efficiency $>70\%$, a system with $L = 100$ needs average meshing efficiencies above 99.5%.

In our further analysis we will therefore focus only in assessing the contribution of topological efficiency to the efficiency of a gearbox. This allows us to use a simplified method to calculate the latent power ratio which neglects in first instance the effect on the losses caused by the torque reduction. The corresponding calculations used to determine the latent power ratio of the different gearbox configurations analyzed in this work are included in **Annex I**.

Summarizing, in order to characterize the important effect of gearbox efficiency we will assess the order of magnitude of three parameters: (i) load-dependent losses, (ii) no-load starting torque, and (iii) latent power ratio. Although it is additionally affected by static friction and not only by Coulomb and viscous friction, we have selected the no-load starting torque (relative to the nominal torque) as a practical way to characterize load-independent losses. Our exchanges with gearbox manufacturers indicate that this is a common practice, it does not depend on the input power, and it is readily available in manufacturer's datasheet.

Productivity

Compared to special-purpose and automatic-assembly machines, industrial robots cannot achieve the same standards of precision and speed. Both aspects had to be compromised to enable a larger degree of flexibility and mobility, and of the workspace (Rosenbauer, 1995). Seen from this perspective, HRI is just a further step in the same direction: in order to comply with further needs of flexibility and mobility in an unstructured environment, additional compromises are needed in terms of precision and speed. This transition is reflected in **Figure 1**.

Accuracy and Repeatability

Multiple aspects of a gearbox contribute to the resulting overall precision of a complete robotic device. These aspects have long been the focus of traditional robotics and are today well-understood, with works like those of Mayr (1989), Schempf and Yoerger (1993) or Rosenbauer (1995) providing very good references to understand these complex influences. Those studies identify the particularly important role played by lost motion and torsional rigidity.

Lost Motion is a further development of the principle of backlash which describes the total rotational displacement generated by the application of $\pm 3\%$ of the nominal input torque.

Torsional Rigidity characterizes the torsional compliance of all the elements in a gearbox involved along the complete force flow, under the influence of an external torque. It is established by means of blocking the gearbox input and progressively increasing the torque applied at the output, while changes in torsional stiffness—resulting in deviations from an ideally linear behavior—are registered.

Inherently precise—low lost motion and linear, high torsional rigidity—gearboxes simplify the control task and enable high precision ability, being ideally suited for position control, while less precise gearboxes put higher challenges to position control and can be used for more compliant actuation. In gearbox technologies where the speed has a strong influence on losses or with particularly non-linear friction behaviors, the contribution of this elements to accuracy must also be considered.

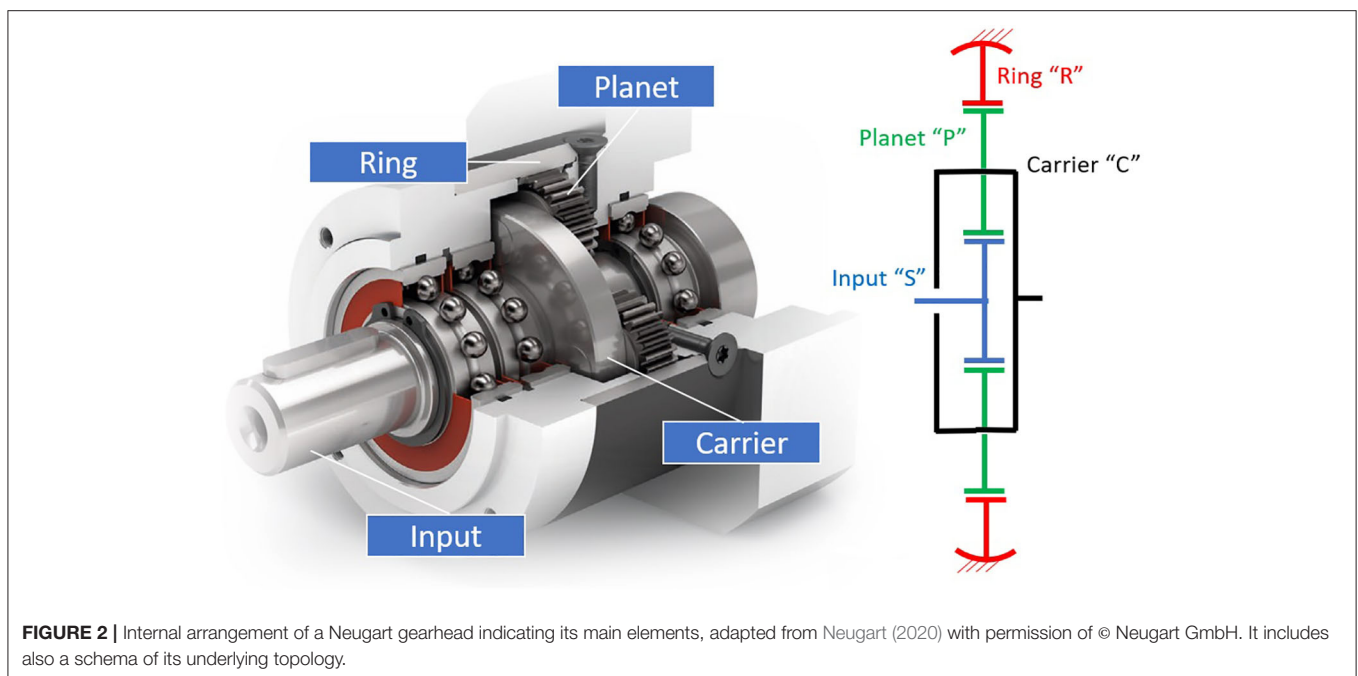
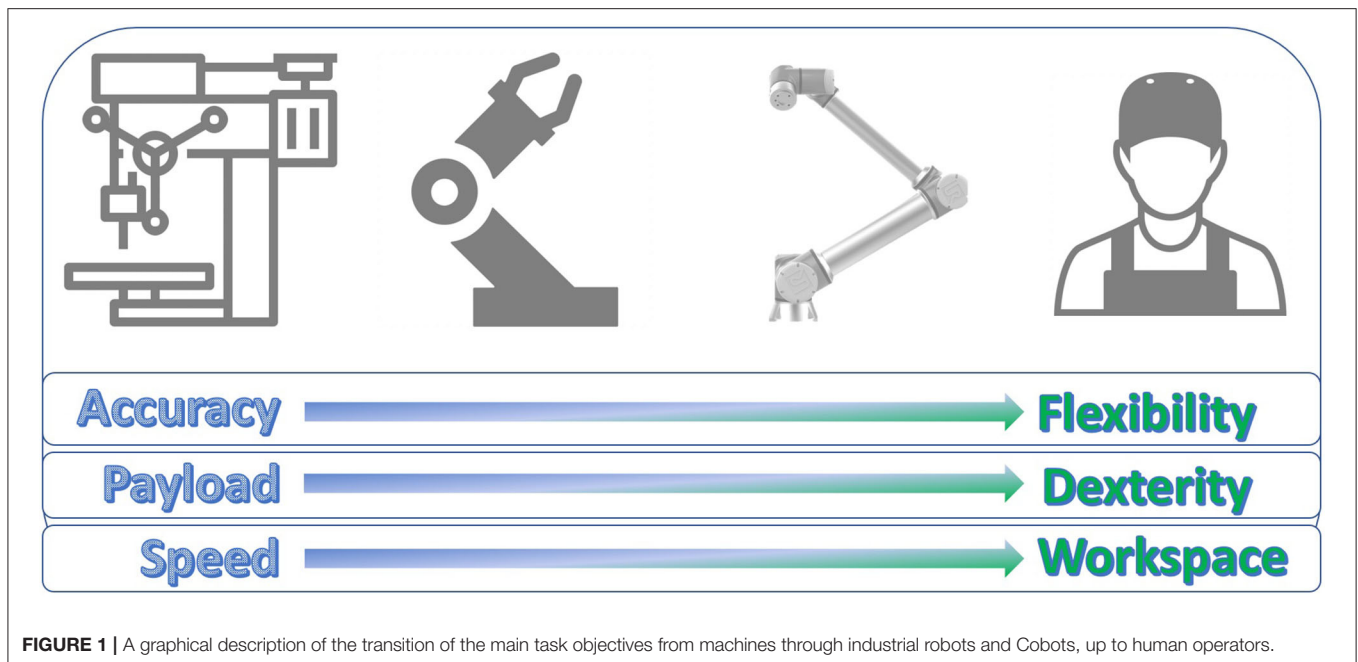
To characterize precision capabilities, our framework incorporates lost motion and torsional rigidity, together with a subjective assessment of the change in efficiency caused by speed/torque changes.

Speed and Payload

Industrial robots can handle large payloads at the cost of large inertias. For cobots on the other side, safety considerations imply that they are not expected to handle such large payloads, but thanks to lighter designs, they can actually achieve larger payload-to-weight ratios.

Safety considerations restrict also the extent to which this mass reduction can be exploited to increase the operational speeds (Haddadin et al., 2009). Yet, the lower torques promote the use of lighter and faster electrical motors, demanding in principle larger speed reduction ratios for these applications.

A criterion for characterizing a gearbox's contribution to speed and payload performance must reflect these aspects and motivates us to use in our framework (i) maximum



input speed, (ii) maximum repeatable output torque—termed acceleration torque—and nominal torque, (iii) transmission ratio, and (iv) torque-to-weight ratios for both the nominal- and the acceleration torques.

Summary

Characterizing robotic gearboxes is a challenging task: the high versatility of these devices, and their complex interactions with the prime movers and control systems, make a direct comparison of their performance particularly complex.

The transmission ratio has a demonstrated strong influence on the performance of a robotic system. This explains its preferent role in the literature dedicated to robotic actuation optimization, and the growing interest of roboticists in the possibilities to use variable transmissions (Kim et al., 2002; Carbone et al., 2004; Stramigioli et al., 2008; Girard and Asada, 2017). Although we are convinced that variable transmissions are very promising and will certainly contribute to shape the future robotics landscape, we have restricted our analysis here to constant-ratio compact gearboxes. At this point we believe that we are best served

with this limited scope, which can actually contribute also to identify potential areas of applications and suitable technologies for variable-ratio transmissions.

Based on this analysis, we propose an assessment framework of future robotic gearboxes based on the following parameters:

- Transmission Ratio
- Acceleration- and nominal output torques
- Weight
- Shape: Diameter \times Length
- Acceleration- and nominal torques-to-weight
- Efficiency: peak value and subjective dependency on speed and torque conditions
- Topological Efficiency: latent power ratio
- No-Load forward and backdriving starting torques in % of the nominal input torque
- Load-independent losses
- Lost Motion
- Maximal input speed
- Torsional rigidity

Our framework incorporates also a benchmark use case, representative for multiple pHRI tasks according to our own experience: acceleration torques above 100 Nm and gear ratios above 1:100, for which weight, compactness, and efficiency shall be optimized.

REVIEW OF TRANSMISSION TECHNOLOGIES CURRENTLY USED IN INDUSTRIAL ROBOTS

Electrical motors equipped with mechanical transmissions have typically been selected as actuators in robotics (Rosenbauer, 1995; Scheinman et al., 2016) also in industrial robots. These mechanical transmissions are almost inevitably based on some kind of gear technology (Sensinger, 2013).

Thanks to their larger ability to reduce the overall weight, and because electrical motors tend to have better efficiencies at high operating speeds, another characteristic of industrial robotic transmissions is the use of relatively large transmission gains (gear ratios), typically above 1:40 (Rosenbauer, 1995).

Planetary Gearheads: an Extremely Versatile Platform

Planetary Gear Trains (PGTs) are compact, highly versatile devices broadly used in power trains. Due to their characteristic coaxial configuration and good power density, they are particularly suited for rotative prime movers like electrical motors.

PGTs can use two differentiated strategies to achieve high gains: (i) adding several stages of conventional, highly-efficiency PGTs—here termed gearheads and presented in **Figure 2**—or (ii) using particularly compact PGT configurations with the ability to produce high gear ratios.

While using several stages of gearheads makes best usage of the high gear meshing efficiencies and leads to highly efficient gearboxes, it typically results in heavy and bulky solutions.

Compact PGT configurations on the other side can achieve high gear ratios in very compact shapes, but they suffer from surprisingly high losses derived from high virtual powers (Crispel et al., 2018).

A particularly compact PGT configuration for high ratios was first invented by Wolfrom (1912) and was used in the RE series gearboxes of the company ZF Friedrichshafen AG (ZF) aimed at industrial robotic applications (Looman, 1996). This configuration—shown on **Figure 3**—is strongly affected by Virtual Power and ZF's represents the only known commercial application of PGT configurations other than conventional gearheads. Although the manufacture of the RE series was discontinued in the 90's, Wolfrom PGT's are recently enjoying growing interest of the robotics research community, as we have summarized in a previous paper of the authors (López-García et al., 2019a).

Table 1 presents the PGT's assessment. Although over-dimensioned for our benchmark, we have used ZF's RG350 Wolfrom PGT to try to assess the potential of high-ratio PGT configurations, based on existing evidence of its suitability to achieve high-ratios (Arnaudov and Karaivanov, 2005; Mulzer, 2010; Kapelevich and AKGears LLC, 2013). For the gearheads we have selected—supported by the manufacturers—suitable solutions from the portfolios of Wittenstein and Neugart. Worth noting is the important role played by the maximum gear ratio per stage in a gearhead: while Wittenstein is closer to the feasibility maximum—given by contact avoidance between neighboring planets—Neugart selects in their PLE series (the PLFE series can reach 1:100 ratios in only two stages) a more restrictive approach and consequently needs three stages instead of two for Wittenstein, to achieve a total 1:100 gain. This leads to less compact solutions and lower efficiencies for a 1:100 application, but it allows Neugart to achieve higher gains—up to 1:512—without fundamental changes in weight, size, or efficiency.

Gearheads show weights around 4 kg, which cannot be directly compared to the over-dimensioned RG350. The RG350 shows a shape with larger diameters and shorter lengths than the gearheads. In terms of torque-to-weight ratios, the values of both solutions appear to be relatively close.

Gearheads have a strong advantage in their good efficiencies (above 90%), which are less sensitive as well to changes in operating conditions, and the no-load starting torques are very low. High-ratio configurations show how a strong limitation in topological efficiency, resulting in lower efficiencies. This probably explains the why gearheads are today the dominant PGT- technology in robotics.

PGTs show the highest input speeds (up to 8,500 rpm), but their lost motion are also the largest (4–6 Arcmin) in conventional gearboxes. In robotics, PGTs were broadly used in the first industrial robots, while in the last decades their use has declined strongly mainly as a consequence of their limitations to reduce backlash. Although mechanisms exist to limit the inherently larger backlash of PGTs, those are practically based on the introduction of a certain pre-loading, negatively affecting their efficiencies (Schempf, 1990).

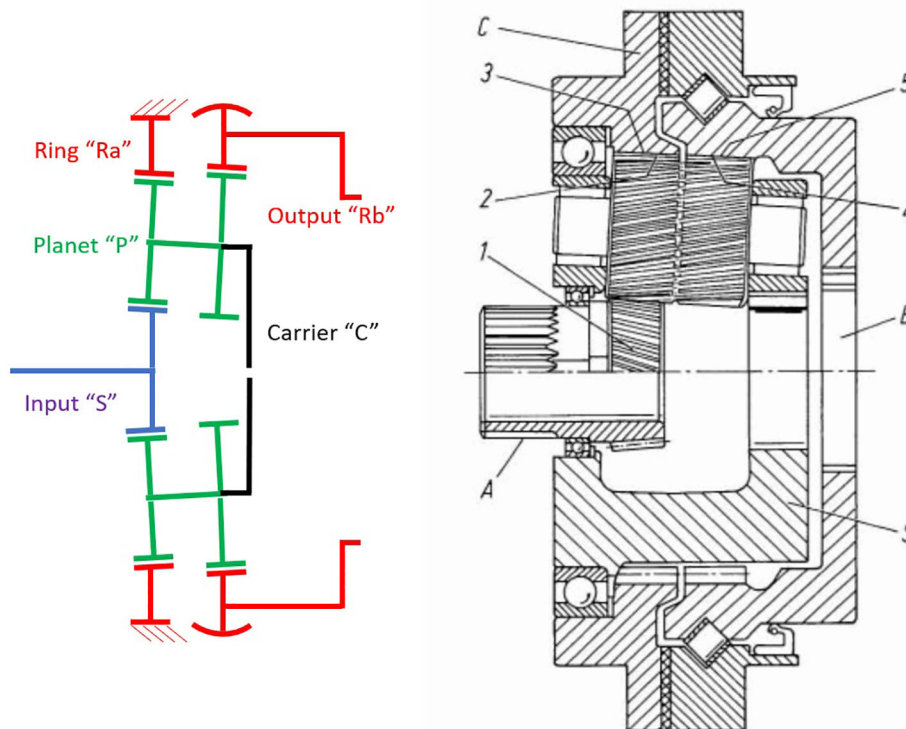


FIGURE 3 | Internal arrangement of a ZF's RG Series Wolf from PGT for robotic applications adapted from Looman (1996) with permission of © 1998 Springer-Verlag Berlin Heidelberg. It includes also a schema of its underlying topology.

Harmonic Drives: A Zero-Backlash, Lightweight Strain Wave Gearbox

The Strain Wave gearbox was invented by Musser (1955) and found broad application in the 70's, originally in aerospace. Its major space application was as the mechanical transmission element in the lunar rover vehicle on the Apollo 15, in 1971 (Schafer et al., 2005).

Its name results from the characteristic deformation of its *Flexspline*, a non-rigid, thin cylindrical cup with teeth that serves as output. The Flexspline engages with a fixed solid circular ring with internal gear teeth, the *Circular Spline*, while it is deformed by a rotating elliptical plug—the *Wave Generator*, as it can be observed in **Figure 4**. This type of gearbox is most commonly referred to as Harmonic Drive[®] (HD), owing to a very effective IP protection strategy.

For our benchmark analysis we have selected two suitable Harmonic Drive gearboxes, a CSD-25-2A meant for integration in a robotic joint to provide adequate structural boundary conditions, and an ultralight gear unit CSG-25-LW representing a structurally sufficient solution, which can be more directly compared to other technologies. Very recently SUMITOMO presented the new E-CYCLO gearbox, based as well of the strain wave principle of operation. SUMITOMO gave us access to its very recent catalog (SUMITOMO, 2020), enabling us to include it in our benchmark (**Table 2**). Another interesting Strain Wave, very similar to the Harmonic Drive, has recently been introduced

as well by GAM to its robotics gearbox series, which includes as well planetary gear trains and cycloid drives (GAM, 2020).

The selected CSG model has a substantially larger torque capacity than targeted in our benchmark. The shape is characterized by larger diameters than lengths, while the weights are substantially lower than for other technologies and result in the best torque-to-weight ratios of the analyzed technologies. Indeed, the characteristic multiple tooth-engagement allows for larger torque resistance than in PGTs, making this technology a very good suit for the joints closer to the end-effector, where they are frequently found in today's industrial robots.

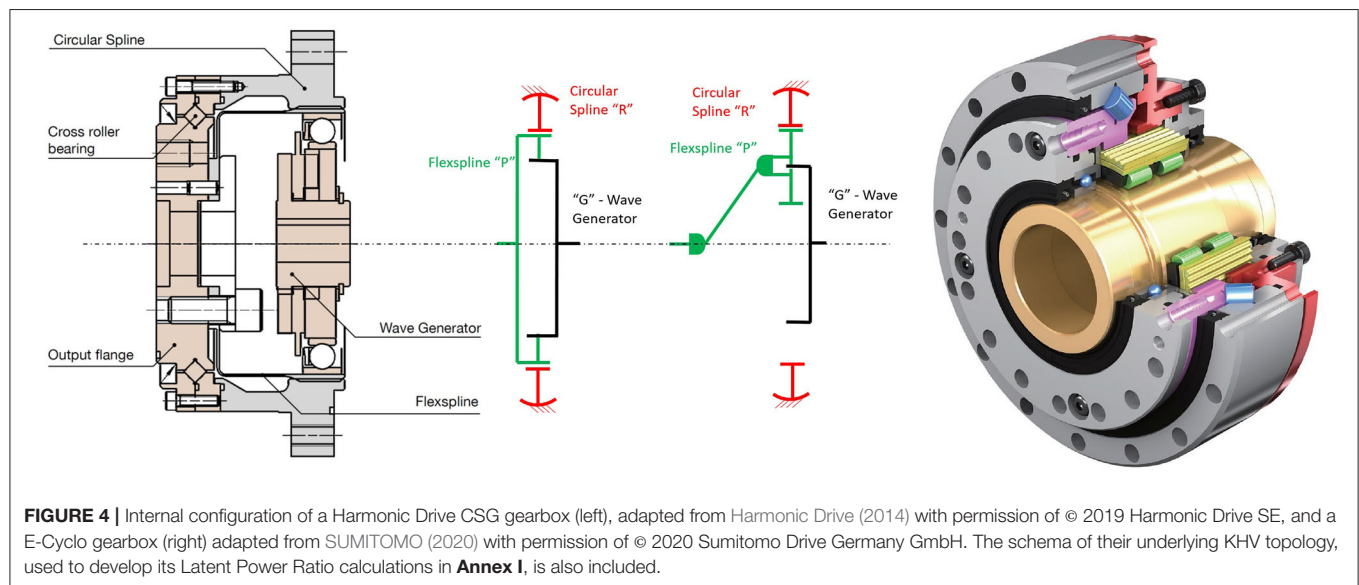
Peak efficiencies are lower than for gearheads and closer to the RG350, and efficiency is particularly sensitive to operating conditions. Strain Wave trains show large load-independent losses and no-load starting torques—particularly in back-driving conditions, which become particularly critical for high speeds and/or low torques (Harmonic Drive, 2014). For HRI robotic devices, subject to frequent speed and payload changes in combination with energy exchange between the robotic device and the user, this means that average efficiencies rapidly drop below 40–50% (López-García et al., 2019b). Worth noticing is also their large latent power ratio, indicating simultaneous presence of high torques and speeds in the teeth engagements, which helps also explain the relatively low efficiencies.

Thanks again to the multiple teeth engagement, lost motions below 1 arcmin can be reached and provide this gearbox

TABLE 1 | Assessment framework for planetary gear train solutions.

PGTs	WITTENSTEIN (2020)—Alpha SP+075MF	Neugart (2020)—PLE 080	Looman (1996) ZF—RG350
Transmission ratio	1:100 (2x stages)	1:100 (3x stages)	1:—76 (2x stages)
Acceleration/nominal torques	105/84 Nm	192/120 Nm	500*/350 Nm
Weight	3 kg	3.1 kg	6.4 kg
Shape	Φ95 × L120 mm	Φ80 × L168 mm	Φ160 × L90 mm
Torque-to-weight ratios	35/28 Nm/kg	62/39 Nm/kg	78/55 Nm/kg
Efficiency and subjective dependency on operating conditions	94%—low (speed and torque)	92%, low (speed and torque)	84%, low (speed and torque)
Latent power ratio (section/-s of Annex I including the calculations)	3.6 (GH, SGH)	4.7 (GH, SGH)	36.8 (WG)
No-load starting torque	0.5%*	0.7%*	1.5%*
Load-independent losses	5.5%	7.5%	14.5%
Lost motion	4–6 Arcmin	<11 Arcmin	()
Maximum input speed	8,500 rpm	7,000 rpm	5,000 rpm
Torsional rigidity	10 Nm/arcmin	8 Nm/arcmin	()

*Values extrapolated and/or approximated, see further detail on **Annex I**.



with a strong advantage which helping Harmonic Drives find broad applications in industrial robots. They were able to displace PGTs from many applications, particularly after a major improvement of the performance resulting from a new teeth geometry introduced by this company in the 90's—which also improved its stiffness linearity (Slatter, 2000).

Maximal input speed used to be a strong limitation for the use of HD gearboxes in the past (Schempf, 1990), but new advances and design improvements allow them now to reach up to 7,500 rpm.

Cycloid Drives: for High Robustness and Torsional Stiffness

Since their invention by Lorenz Braren in 1927 (Li, 2014), cycloid drives have found application mainly in boats, cranes, and some

large equipment as steel strip rolling trains or CNC machines. In cycloid drives, an eccentric input motion creates a wobbly cycloidal motion of a single, large planet wheel, which is then converted back in a rotation of the output shaft and results in a high reduction capacity (Gorla et al., 2008), see **Figure 5**.

Table 3 includes the market leader (NABTESCO RV) in this segment and the main challengers (SPINEA and SUMITOMO). The RV from NABTESCO and the Fine-Cyclo T-series of SUMITOMO include a pre-gearing, conventional PGT stage. The payload capability of these devices is larger than required for our benchmark and results in large weights. This provides already a valuable insight: more compact solutions are not available in the market and are—according to the information provided by some of the manufacturers—less interesting because they would need extreme manufacturing precision and ultimately result in high costs.

TABLE 2 | Assessment framework for strain wave solutions.

Strain wave	Harmonic Drive (2014)—CSD-25-160-2A	Harmonic Drive (2014)— CSG-25-160-2UJ-LW	SUMITOMO (2020) E—CYCLO
Transmission ratio	1:100	1:100	1:100
Acceleration/nominal torques	123/47 Nm	204/87 Nm	157/67 Nm
Weight	(0.24 kg) ^a	1.1 kg	1.6 kg
Shape	($\Phi 85 \times L20$ mm) ^a	$\Phi 107 \times L52$ mm	$\Phi 95 \times L58$ mm
Torque-to-weight ratios	(500/195 Nm/kg) ^a	208/79 Nm/kg	98/42 Nm/kg
Efficiency and subjective dependency on operating conditions	75%, high (speed and torque)	84%, high (speed and torque)	70%, high (speed and torque)
Latent power ratio	101 (SW)	101 (SW)	101 (PC)
No-load starting torque (forward and reverse direction)	17/20%	10/13%	45%/()
Load-independent losses	22% @ 500 rpm, nom. torque	18% @ 500 rpm, nom. torque	30% @ 500 rpm, nom. torque
Lost motion	<1 Arcmin	<1 Arcmin	<1 Arcmin
Maximum input speed	7,500 rpm	7,500 rpm	6,500 rpm
Torsional rigidity	9–17 Nm/arcmin	9–17 Nm/arcmin	11–16 Nm/arcmin

^aValues extrapolated and/or approximated, see further detail on **Annex I**.

(^a)—this values refer to a unit not suitable as a standalone gearbox which requires additional structural support—directly impacting the identified characteristics—to be provided by the robotic device in which it is incorporated.

Shapes are similar to those of strain wave gearboxes, while weights are larger and closer to those of the PGTs, for the aforementioned reasons. Torque-to-weight ratios are larger than those of PGTs but slightly lower than for strain wave gearboxes. The main advantage of cycloid drives lies precisely in their ability to withstand large loads and particularly impact loads, and in the little maintenance required.

Peak efficiencies are larger than for strain wave gearboxes and closer to those of PGTs, but efficiency is highly dependent on operating conditions (Mihailidis et al., 2014) and both the no-load start torques and the latent power ratio are high, both similar to strain wave gearboxes.

Although they tend to present some backlash, such if often compensated for in their design to reach levels comparable to those of the strain wave gearboxes, probably at the cost of slightly higher frictions. Their torsional rigidity is the largest of the analyzed gearbox technologies.

Cycloid drives have an inherent limitation to cope with high input speeds, caused by the presence of a large and relatively heavy planet (cam) wheel resulting in large inertias and imbalances. This motivates the use of typically two planet wheels, arranged in series and shifted 180 degrees to each other, to cancel out imbalance, reduce vibrations and enable larger input speeds. This explains how, by means of combining cycloid drives with pre-gearing stages consisting of conventional PGTs stages enabled cycloid drives to achieve their current broad acceptance in robotics. This arrangement improves efficiency, reduces sensitivity to high input speeds and provides for easy adaption of their gear ratios. In the 90's Harmonic Drives dominated the robotic gearbox market, but the improvements in cycloid technology enabled cycloid drives to start gaining terrain, first in Japan and then elsewhere (Rosenbauer, 1995). Nowadays manufacturers like NABTESCO, SUMITOMO or NIDEC propose cycloid hybrids integrating a PGT pre-gearing

cover over 60% of the robotic gearbox market, and have therefore become the new dominant technology, particularly for proximal joints subject to higher loads and lower weight restrictions (WinterGreen Research, 2018).

Finally, the presence of a relatively large torque-ripple which introducing non-linearities and complicating their control is also worth mentioning. This torque ripple is linked to the necessity of using cycloid tooth profiles to avoid teeth interference between the large planet wheel/-s and the ring gearwheel, making these devices extremely sensitive to the center-distance variations produced by even small manufacturing errors. Several attempts to improve this situation exist, using involute teeth—less sensitive to center-distance variations—with reduced pressure angles and/or contact ratios to minimize radial forces and improve efficiency (Morozumi, 1970), as well as using other forms of non-involute teeth (Koriakov-Savoysky et al., 1996; Hlebanja and Kulovec, 2015).

REVIEW OF EMERGING TRANSMISSION TECHNOLOGIES FOR ROBOTICS

The REFLEX Torque Amplifier

Genesis Robotics has drawn a lot of attention in the robotics community with the arrival of their direct-drive motor, the *LiveDrive*®. According to Genesis, the *LiveDrive* in the two available topologies—radial and axial fluxes—provides benchmarking performance in Torque-to-Weight ratio. The axial flux motor can achieve up to 15 Nm/kg, while the radial flux up is limited to maximum 10 Nm/kg.

To enlarge its application spectrum, Genesis Robotics introduced a compatible gearbox termed *Reflex*, which is shown in **Figure 6**. This injection-molded, ultralight plastic gearbox is targeted at lightweight robots and although it was initially designed to work together with the *LiveDrive* and is therefore

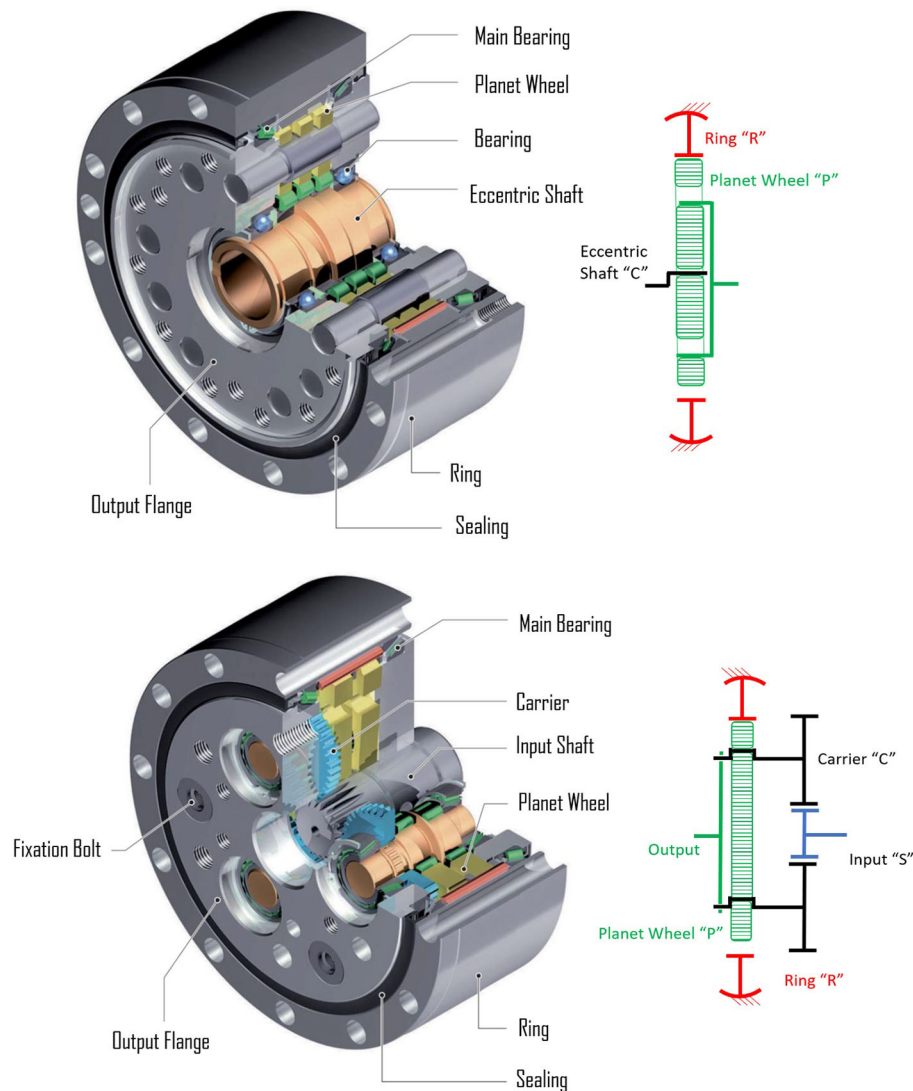


FIGURE 5 | Internal configuration of a SUMITOMO Fine Cyclo F2C-A15 and a Fine Cyclo F2C-T155 cycloid drives identifying its main elements, adapted from SUMITOMO (2017) with permission of © 2017 Sumitomo Cyclo Drive Germany GmbH. It includes also a schema of its underlying topologies.

targeted at gear ratios below 1:30, it is also capable of providing larger gear ratios up to 1:400 (GENESIS, 2018).

The underlying topology is that of Wolfrom PGT with multiple, smaller planets (Klassen, 2019), in which the reaction (stationary) ring gearwheel is split into two for balancing purposes, following a design originally proposed by Rossman (1934) and used as well in the Hi-Red gear of Tomcyk (2000).

In the Reflex gearbox, the output ring is also split to facilitate the assembly with helical teeth. Another interesting aspect of this design is the taped shape of the planets, which the authors suspect to be linked to the possibility of preloading the system in order to achieve the zero-backlash that Genesis claims is possible with this gearbox. The flexibility of the plastic planet wheels also provides

an advantage for the reduction of the backlash, according to the company.

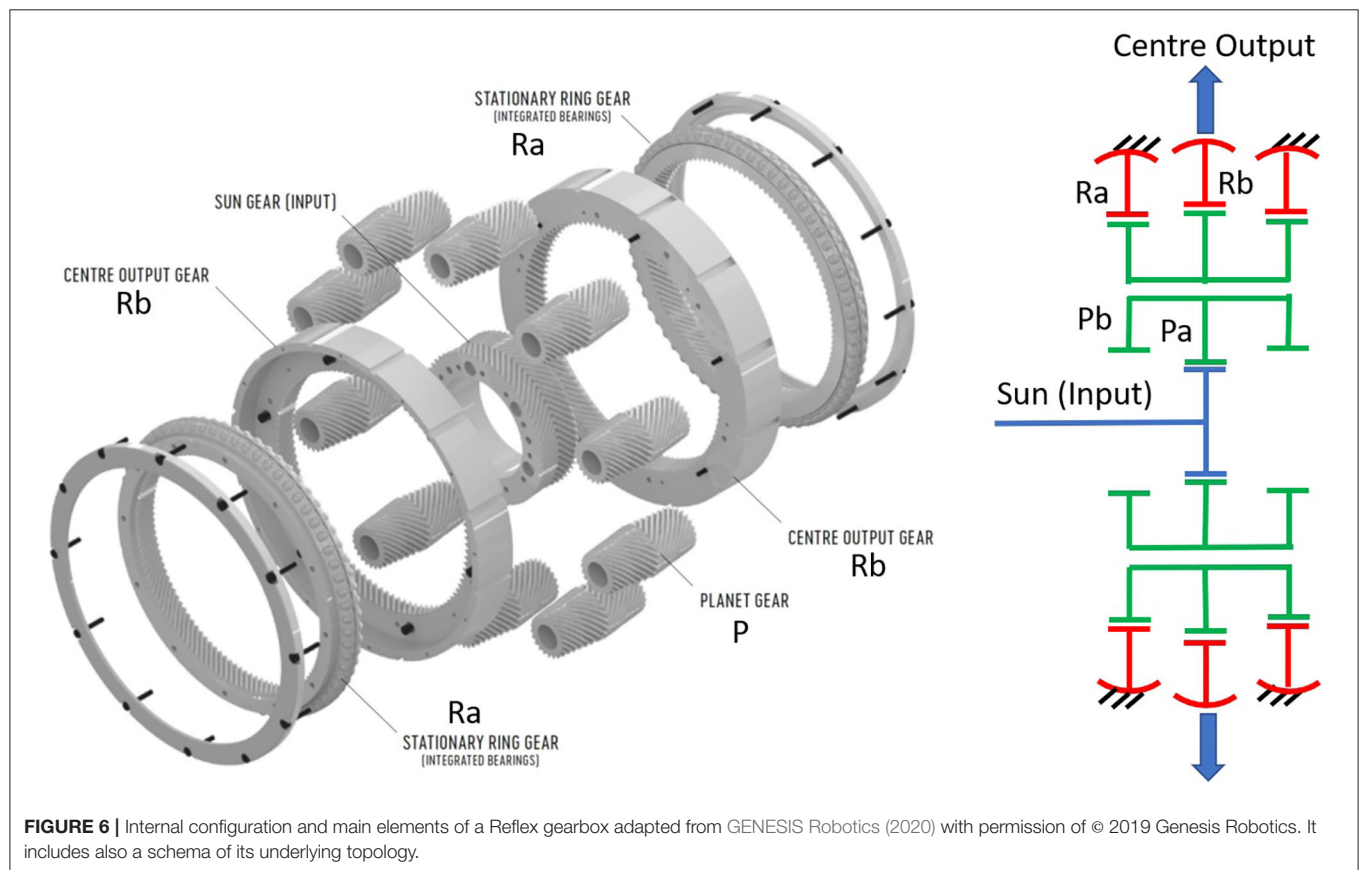
Unfortunately, independent tests are not available yet to confirm the given performances and no official data particularly on efficiency is for now available from Genesis, which is why **Table 4** includes only the Latent Power Ratio value resulting from its topology.

In summary, although the underlying Wolfrom topology indicates that efficiency will certainly be a complex challenge to solve, this innovative gearbox illustrates the large potential available for rethinking existing technologies and adapting those to the future needs in robotics. Genesis Robotics has recently entered an interesting partnership with established industrial companies as Koch Industries Inc. and Demarex AG.

TABLE 3 | Assessment framework for cycloid drive solutions.

CYCLOID drives	NABTESCO (2018)—RV-25N	SPINEA (2017)—TwinSpin TS110	SUMITOMO (2017)—Fine CYCLO F2C-T155	SUMITOMO (2017) Fine CYCLO F2C-A15
Transmission ratio	1:108	1:119	1:118	1:89
Acceleration/nominal torques	612/245 Nm	244/122 Nm	417/167 Nm	335/111 Nm
Weight	3.8 kg	3.8 kg	4.8 kg	2.7 kg
Shape	$\Phi 133 \times L62$ mm	$\Phi 110 \times L62$ mm	$\Phi 126 \times L68$ mm	$\Phi 126 \times L60$ mm
Torque-to-weight ratios	161/64 Nm/kg	64/32 Nm/kg	87/29 Nm/kg	124/41 Nm/kg
Efficiency and subjective dependency on operating conditions	87%, high (speed and torque)	74%, high (speed and torque)	87%, high (speed), medium (torque)	87%, high (speed and torque)
Latent power ratio	33.8* (CG)	120 (PC)	29.2* (CG)	90 (PG)
No-load starting torque	16% (@ 500 rpm)	19/27%	23% (@ 500 rpm)	64/67%
Load-independent losses	13%	25%	13%	13%
Lost motion	1 Arcmin	<1 Arcmin	<0.75 Arcmin	<1 Arcmin
Maximum input speed	0	4,500 rpm	8,500 rpm	5,600 rpm
Torsional rigidity	61 Nm/arcmin	>22 Nm/arcmin	25–41 Nm/arcmin	15–28 Nm/arcmin

*Values extrapolated and/or approximated, see further detail on **Annex I**.



The Archimedes Drive

IMSystems from the Netherlands is a spin-off of the Delft University of Technology, created in 2016 to exploit the invention of the *Archimedes Drive* (Schorsch, 2014).

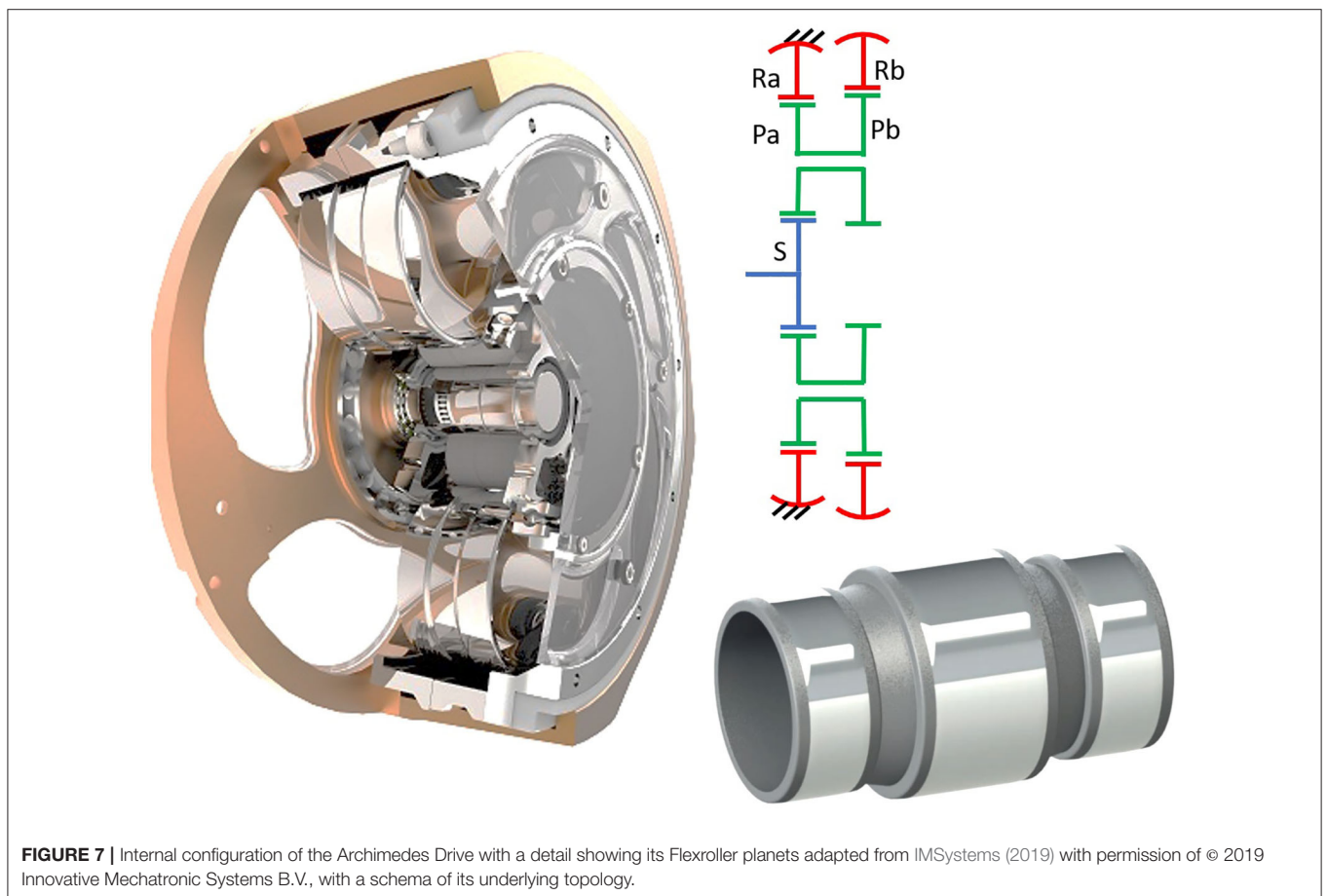
The Archimedes Drive follows again the topology of a Wolfrom gearbox (also with a split reaction ring gear in some

of its designs) but incorporates a breakthrough innovation in the use of rollers instead of gearwheels, to replace teeth contacts with rolling contacts, see **Figure 7**. The controlled deformation of the roller-planets enables the transmission of the torque between the planets, in a similar way as the wheels of a vehicle.

TABLE 4 | Assessment framework for emerging gearbox technologies.

Emerging technologies	GENESIS—reflex torque amplifier	IMSystems—archimedes drive	FUJILAB—bilateral drive
Achievable transmission ratios	1:30 (up to 1:400)	1:100 (up to 1:500)	1:96 ()
Acceleration/nominal torques	87/44 Nm	125/100 Nm	120/() Nm
Weight	0.76 kg	1.1 kg (embedded solution)	1.3 kg
Shape	Φ160 × L54 mm	Φ1500 × L80 mm	Φ94 × L62 mm
Torque-to-weight ratios	115/58 Nm/kg	113/91 Nm/kg	92/() Nm/kg
Efficiency and subjective dependency on operating conditions	()	()	90%, low (torque and speed)
Latent power ratio	22 (80 for 1:100) (WG)	80 (WG)	21 (WG)
No-load starting torque (forward and reverse direction)	()	()	<0.1%
Load-independent losses	()	()	1%*

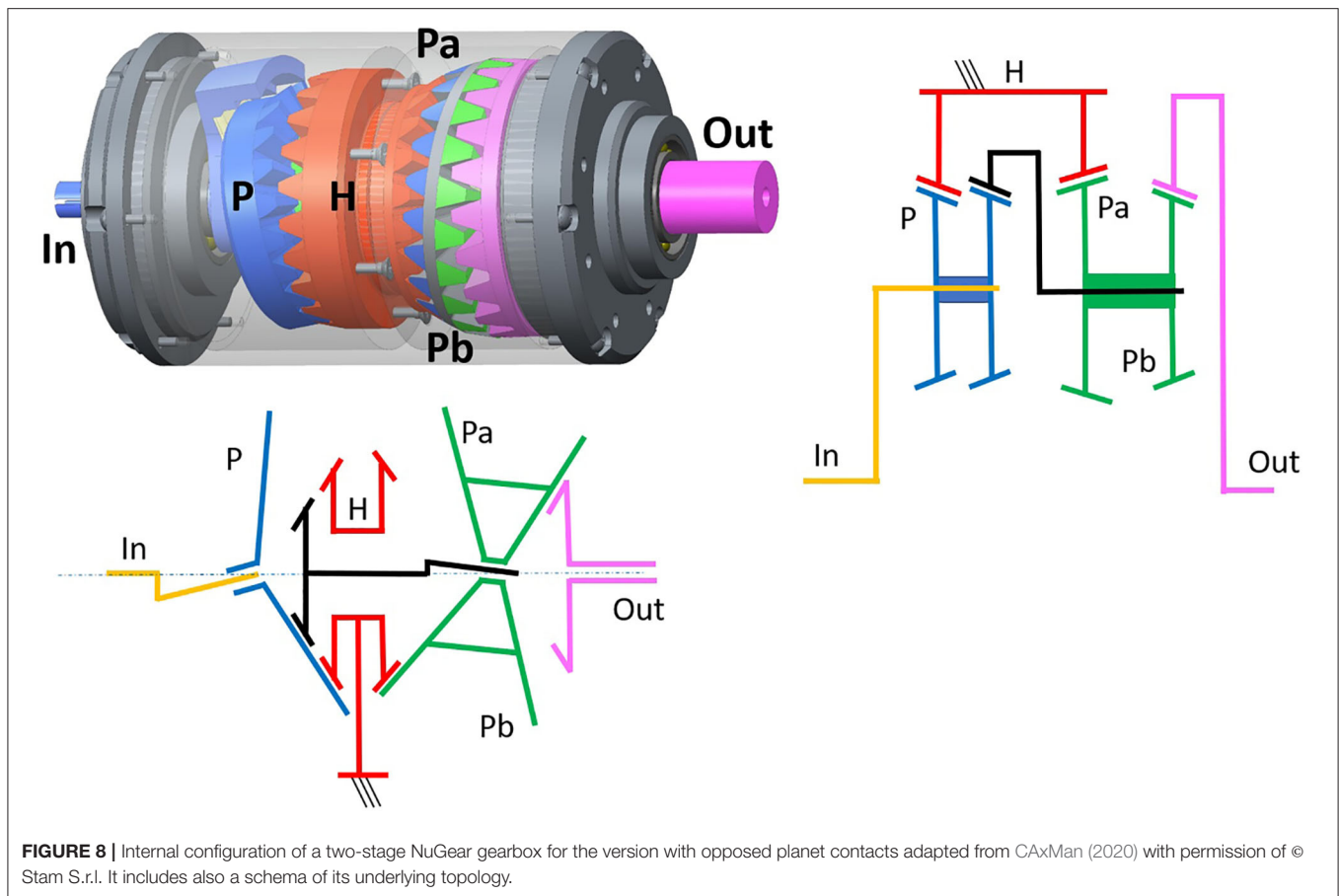
*Values extrapolated and/or approximated, see further detail on **Annex I**.



The performance shown in **Table 4**, extracted from the company's brochure (IMSystems, 2019) and available on demand, shows that the use of a Wolfrom topology provides this device with the ability to reach very high gear ratios in a compact shape, but it also results in low topological efficiency. According to IMSystems, the replacement of gear-teeth contact with rolling contact contributes to the minimization of the

contact losses, which particularly in the torque transfer between the planet and the ring rollers should compensate for the high Latent Power Ratio, and result in maximum efficiencies around 80% (IMSystems, 2019). No data is provided in terms of starting torques or load-independent losses.

To enable a high torque transfer without slip, the deformation of the planet rollers as well as the manufacturing tolerances of



the gearbox must be tightly controlled. This represents one of the main technological challenges, and it is the core of the innovation introduced by this technology (Schorsch, 2014).

The NuGear

STAM s.r.l. is a private engineering company based in Genova which helped develop a robotic joint for the I-Cub humanoid robot. Their NuGear is a nutating gearbox which was originally conceived (Barbagelata and Corsini, 2000) targeting space applications, but could develop its potential for robotics as well through the exploration of alternative manufacturing means.

No information is yet publicly available about the performance characteristics of this gearbox, which means that we can only provide here a preliminary analysis of its topology and the resulting performances which can be expected based upon the limited information available basically from the Caxman EU project (CAXMan, 2020) for which the NuGear was a use case, and from the available patents (Barbagelata et al., 2016).

In **Figure 8** the internal structure of the NuGear is presented using an equivalent PGT configuration—abstracting the nutating aspect to ease the understanding. By doing so it becomes clear that a NuGear resembles two Wolfrom PGTs for which the carrier is used as the input, connected in series and where each of them

corresponds to one of the two stages defined in Barbagelata et al. (2016). This indicates again that a relatively high Latent Power Ratios will be present in this gearbox. For a gear ratio of 1:100 and assuming a balanced gain of 1:10 on each of the two stages, as proposed in Barbagelata et al. (2016), we obtain using the equations derived in **Annex I** a latent power ratio of 32 indicating similar topological efficiency to that of a Wolfrom PGT.

It remains to be confirmed to which extent the use of Additive Manufacturing methods can help STAM s.r.l. reduce the large manufacturing cost of the bevel gears, and whether the nutating operation can achieve sufficient reliability and a more compact shape, which could open the door to its usage in the field of robotics (CAXMan, 2020).

The Bilateral Drive

The FUJILAB in Yokohama proposed in Fujimoto (2015) a highly backdrivable gearbox for robotics, which would be particularly suited for operation without need for a torque sensor (Kanai and Fujimoto, 2018).

As it can be observed in **Figure 9**, the configuration of this device is again that of a Wolfrom PGT. With this topology, Fujimoto et al. were able to reach, for a 1:102 gear ratio, forward efficiencies of 89.9% and backdriving efficiencies of 89.2%. The No-Load Starting torque in backdriving direction amounted to 0.016 Nm in a gearbox with an outer diameter of $\sim \Phi 50$ mm

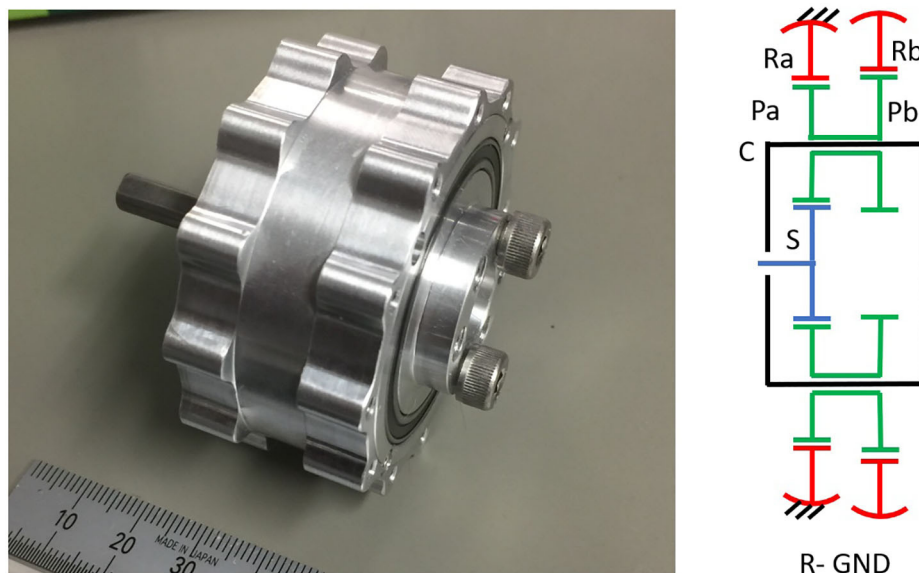


FIGURE 9 | Internal configuration of a Bilateral Drive, a highly efficient gearbox capable of achieving 1:102 gear ratios using a Wolfrom topology, courtesy of © Yasutaka Fujimoto.

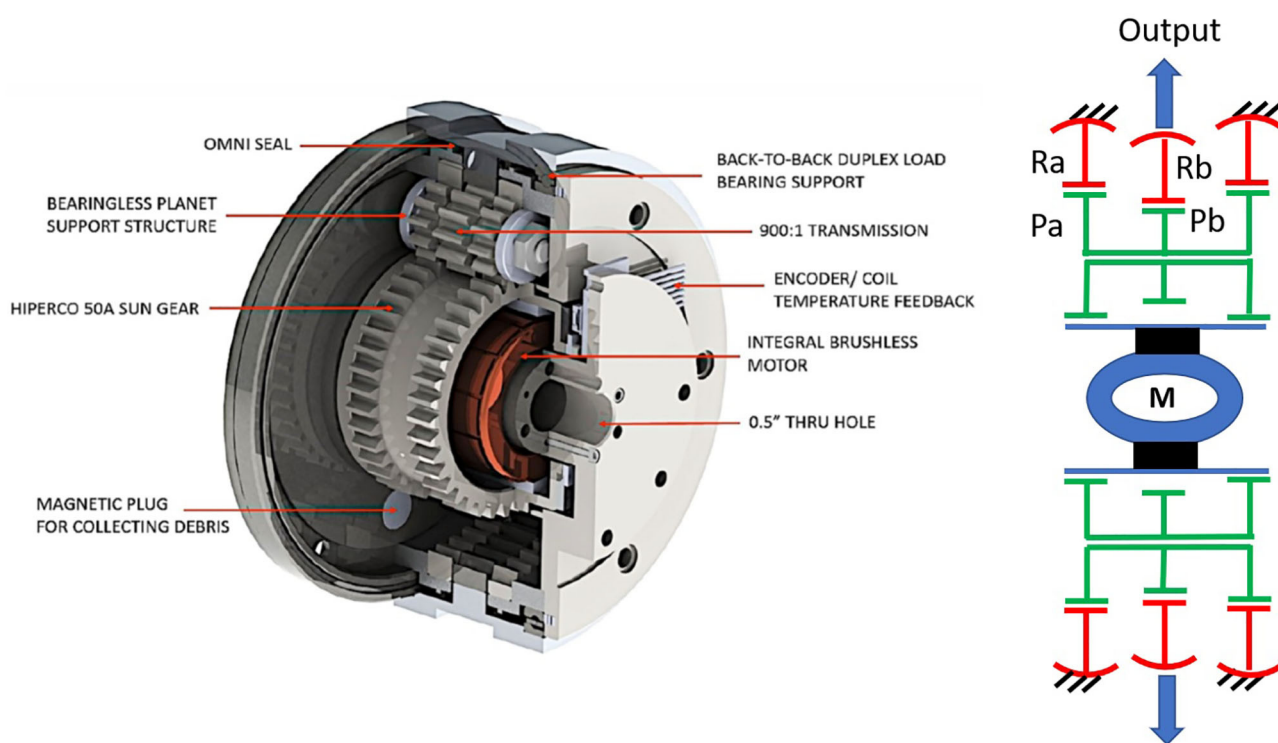


FIGURE 10 | Internal configuration of the Gear Bearing Drive, including the embedded brushless motor adapted from Brassitos and Jalili (2017) with permission of © 2017 American Society of Mechanical Engineers ASME. On the right the underlying Wolfrom topology with a split reaction ring is also shown.

(Kanai and Fujimoto, 2018). The strategy followed to reach such high efficiencies with a Wolfrom topology consists on the optimization of the profile-shift coefficients (Fujimoto and Kobuse, 2017).

These promising results—see **Table 4**—indicate that equalizing the approach and recess ratios through optimization of the profile-shift coefficients can lead to extremely high meshing efficiencies. To the best of the authors' knowledge, this

strategy was originally proposed by Hori and Hayashi (1994) and is particularly interesting in a Wolfrom topology, where it could ultimately enable efficiencies above 90% in combination with high-gear ratios and compact topologies.

The Gear Bearing Drive

Following the pioneering work in this field of John M. Vranish from NASA, which resulted in the invention of a carrier-less planetary gear in Vranish (1995) and of the partial tooth gear bearings (Vranish, 2006), the NASA Goddard Space Flight Center presented its concept of a new Gear Bearing Drive in Weinberg et al. (2008).

The Northeastern University in Boston continued the development of this new actuator for applications in robotic joints. As it can be observed in **Figure 10**, it incorporates a Wolfrom gearbox adapted to include Vranish's carrier-less design and gear bearings. The gear bearings are rolling contacts which are provided for each pair of meshings gears corresponding to their pitch diameter and reduce the load on the gearbox bearings (Brassitos et al., 2013). This topology enables a convenient integration of an electromotor, which is therefore embedded in the hollow area provided inside a large sun gearwheel in a configuration particularly aimed at space applications (Brassitos and Jalili, 2017).

In Brassitos and Jalili (2018) a metal prototype of a Gear Bearing Drive with a gear ratio of 1:40 is characterized in terms of stiffness, friction and kinematic error. The measurements are very in line with those of the FUJILAB and confirm the low no-load starting torque of this configuration (0.0165 Nm for an outer gearbox diameter of $\sim \Phi 100$ mm). After experimentally measuring the stiffness, friction and kinematic error of their drive, (Brassitos and Jalili, 2018) integrated those values into a dynamic model which was then simulated and compared to the open loop velocity response of the system under free sinusoidal motion, showing good correlation, and suggesting a very convenient high linearity in the transmission.

Preliminary measurements indicated good combined efficiencies for the motor and the Wolfrom gearbox with a gear ratio of 1:264 (Brassitos et al., 2013), which do not correlate very well with a calculated Latent Power Ratio of 196. Efficiency has not been again in the focus of the recent papers of the authors and we have unfortunately not been able at this point to confirm the final efficiency levels that the newer prototypes can reach.

In any case, the Gear Bearing drive brings in very interesting propositions to exploit the potential of the Wolfrom topology in robotics. The possibility to eliminate the carrier and embed an electric motor inside the gearbox, in a shared housing, results in impressively compact designs. The possibility of using gear bearing pitch-rollers to reduce radial loading on the bearings is as well a promising option for improving compactness, and to increase efficiency (Brassitos et al., 2019).

The Galaxie Drive

Schreiber and Schmidt (2015) protects the main innovations included in the Galaxie Drive, a gearbox which WITTENSTEIN is currently bringing into the precision gearbox market through its start-up Wittenstein Galaxie GmbH, created in April 2020.

Although datasheet and detailed information are not yet available, the principle of operation and expected gains have also been disclosed. The Galaxie Drive introduces a new kinematic approach based on a linear guidance of the singular tooth in a *Teeth Carrier*, but according to these authors its topology resembles that of a Strain Wave Gear, see **Figure 11**. The flexspline is replaced by a Teeth Carrier including two rows of individual teeth, arranged to move radially and engage with the circular spline as a rotating *Polygon Shaft* makes the role of a wave generator with polygonal perimeter (Schreiber and Röthlingshöfer, 2017). Multiple, individual teeth are consequently engaged simultaneously with the circular spline—just as in a Harmonic Drive. This, together with the highly torque-resistant two-point contact between each single tooth and the Teeth Carrier, provide this device with a characteristic zero-backlash, high torsional stiffness and a benchmark torque-to-weight ability, according to the manufacturer.

In a direct exchange, Wittenstein's representatives confirmed that the apparent issue of friction between the individual teeth and their guiding Circular Ring is solved and the Galaxie can reach peak efficiencies above 90%. Owed to its underlying KHV configuration, large Latent Power Ratios are expected, but it is not possible yet to gain further insights on the meshing efficiency that will result from the radial movement of the teeth, which incorporates a new logarithmic spiral tooth flank (Michel, 2015).

Originally the Galaxie Drive is targeted at precision machinery, where the high rigidity and torque resistance can help increase the speed and improve the productivity. In the future, we will certainly be able to assess the potential of this innovative technology as well for robotic applications.

DISCUSSION

A new generation of robotic devices is changing priorities in the selection of adequate gearboxes. Instead of extreme precision at high speeds, these devices impose stronger requirements in terms of lightweight and very efficient mechanical gain devices.

The ultralight strain wave drives (HD, E-cyclo) are certainly in a very good position to serve these needs, a fact confirmed by its current dominance in the field of cobots. When considering a strain wave drive for a pHRI robotic task, operation at low torques and speeds shall be reduced to a minimum if efficiency is to be maximized. Although their optimized teeth geometry contributes to a more linear torsional stiffness, friction remains highly non-linear and direction-dependent, inducing as well certain usage limitations. Ratcheting as a consequence of impact loading is a further limitation to consider for this type of gearbox, which the E-Cyclo should not present (SUMITOMO, 2020).

Cycloid Drives have come a long way to ultimately become the dominant technology in industrial robots. Through technological advances to improve their backlash and input speed limitations, they can now provide good accuracy with acceptable efficiency—despite of high Latent Power Ratios, resulting from an underlying

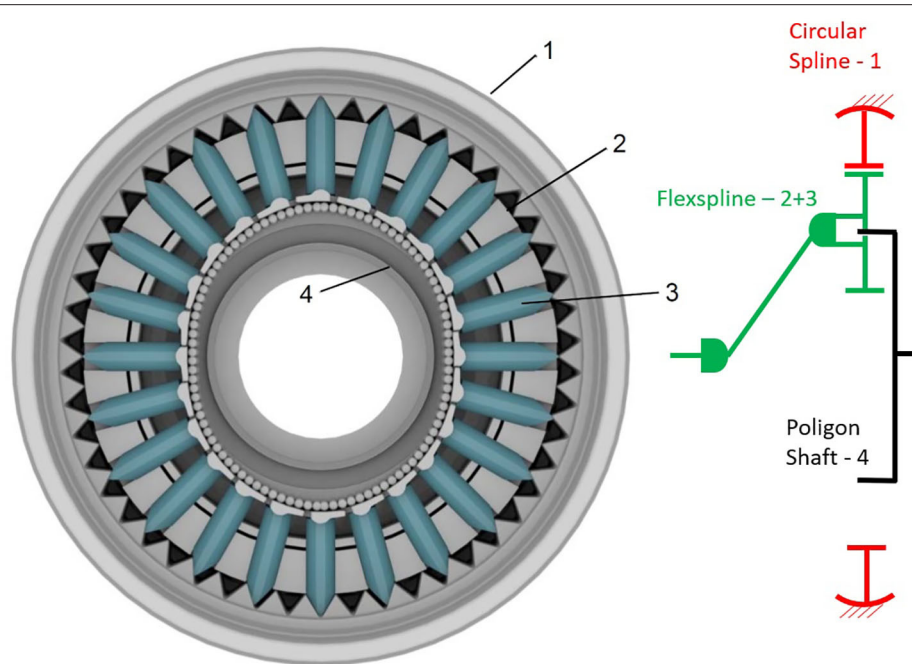


FIGURE 11 | Detail of the teeth engagement of a Galaxy (R) DF gearbox adapted from Schreiber (2015) with permission of © 2020 Wittenstein Galaxie GmbH. It includes a schema of the underlying KHV topology.

KHV topology equivalent to that of the strain wave drives. The use of a pre-gearing stage provides an important contribution as well to this objective by means of improving underlying topological efficiency. Ultralight designs like that of SPINEA show interesting potential, but eventually more disruptive approaches like plastic materials will be required to suit the needs of lighter gearboxes and larger gear ratios needed for HRI. Until this is possible, Cycloid Drives can only be considered for large payloads, where their larger weight and resulting inertias are not critical to function. When extreme accuracy is not needed, backlash compensation measures can be avoided in favor of better efficiencies and lower start-up torques. Care shall in any case be taken to adequately manage torque ripple, and the pre-gearing stage will probably need to stay in order to enable high input motor speeds.

The impossibility of Planetary Gearboxes to reduce backlash maintaining good performance and limitations in torsional stiffness has limited their use in industrial robotics. Yet, PGT's are extremely versatile, as their extensive usage in multiple modern industrial devices demonstrates. And they are inherently efficient, reliable, and relatively easy—cheap—to manufacture. This may explain the recent interest of roboticists in PGTs, and why five of the six highly innovative gearboxes studied here are based on a high-ratio, PGT configuration: the Wolfrom topology. A better topological efficiency combined with improvements on meshing efficiency with profile modifications or going even one step further to replace teeth with rolling contacts are promising features. In combination with the possibilities opened up by their hollow topology, these elements could potentially drive a PGT come-back in robotics.

Our research indicates that the large versatility of the gearbox technologies involved in robotics represent a major challenge

for a direct comparison of their performances. As the examples of backlash and maximum input speed show, adequate design modifications can suitably compensate most of the original weak points of a certain technology, at the cost of making compromises in other aspects typically including efficiency, size, weight, and cost. In the same way, large Latent Power Ratios indicate a significant topological disadvantage in terms of efficiency, but such can also be—at least partially—compensated for with adequate modifications. A learning effect of this is therefore that the selection of a suitable gearbox technology for a certain pHRI application is an extremely complex process demanding for a deep understanding of the fundamental weaknesses, improvement potentials, and derived compromises of each technology. Our initial research objective to contribute with a simple selection table capable of guiding unexperienced robotic engineers in the selection of suitable gearbox technologies for their robotic devices could consequently not be achieved. Instead, this paper collects and explains the main selection parameters and their related challenges in each of the available technologies, aiming at helping pHRI robotic engineers to develop the required skills necessary for an educated choice of a suitable, individually-optimized gearbox.

Two important aspects of robotic gearboxes for pHRI could unfortunately not be adequately assessed in our research at this stage: noise and cost. As robotic devices get closer to humans, noise is receiving more and more attention from roboticists. Gearboxes certainly represent an important source of noise (airborne and structure borne), but unfortunately two main limitations recommended to exclude noise from our analysis at this stage. First, most gearbox manufacturers do not provide yet quantitative noise performance evaluations and when they do, those tend to follow different testing methods which are also not

particularly suited for the operating conditions in pHRI. Second, current gearbox technologies still have to undergo a pending noise optimisation process.

Cost is as well an important parameter to make pHRI technologies more available and becomes therefore essential for the selection of suitable gearboxes for future robotic technologies. Unfortunately, here again insufficient background information is available to the scientific community in order to enable a systematic a fair assessment of the large-scale cost potential of a certain gearbox technology. Before a suitable framework to assess this potential can be defined, a large amount of research work is required which clearly exceeded the scope of our investigation.

These two limitations outline the main recommendations of the authors for interesting future lines of research. Defining standardized testing conditions for airborne and structure borne noise in gearboxes, particularly adapted to typical operating conditions and need in pHRI, could enable a direct comparison of different technologies and contribute to their noise optimization. Additionally, compiling available cost models for the manufacturing processes involved in the manufacture of gearboxes, and adapting those to the specificities of the particular technologies used in robotics, would enable putting together a framework to evaluate the large-scale cost potential (and barriers) of the different technologies.

AUTHOR CONTRIBUTIONS

All authors have been involved in the preliminary work related to this research topic and contributed to the conceptualization of the framework presented in the manuscript. PG worked on the derivation of a suitable assessment framework to perform

the gearbox analysis and took the lead in writing the manuscript and shaping it into its current form. PG and ES contributed equally to identify potentially suitable technologies, and on their analysis with the aid of the framework. All authors proof read and contributed to the final version of the paper.

FUNDING

SC, ES (SB Ph.D.) and TV (SB Postdoctoral) are Fellows at the Research Foundation Flanders—Fonds voor Wetenschappelijk Onderzoek (FWO). This work has been partially funded by the European Union's Horizon 2020 Research and Innovation Programme, under Grant Agreement No. 687662—SPEXOR project.

ACKNOWLEDGMENTS

The authors would like to thank Prof. Yasutaka Fujimoto, of the Yokohama National University, as well as the companies Neugart GmbH, Harmonic Drive SE, Sumitomo Drive Germany GmbH, Genesis Robotics, Innovative Mechatronic Systems B.V., Stam s.r.l. and Wittenstein Galaxy GmbH for the kind support and explanations received, and for giving us permission to use the included images of their devices.

SUPPLEMENTARY MATERIAL

The Supplementary Material for this article can be found online at: <https://www.frontiersin.org/articles/10.3389/frobt.2020.00103/full#supplementary-material>

REFERENCES

- Albu-Schäffer, A., Eiberger, O., Grebenstein, M., Haddadin, S., Ott, C., Wimbock, T., et al. (2008). Soft robotics. *IEEE Robot. Autom. Mag.* 15, 20–30. doi: 10.1109/MRA.2008.927979
- Arigoni, R., Cognigni, E., Musolesi, M., Gorla, C., and Concli, F. (2010). “Planetary speed reducers: efficiency, backlash, stiffness” in *VDI International Conference on Gears* (Munich).
- Arnaudov, K., and Karaivanov, D. (2005). “Higher compound planetary gear trains” in *VDI International Conference on Gears*, Vol. 1904 (Munich: VDI-Bericht), 327–344.
- Barbagelata, A., Corsini, R. (2000). *Riduttore Ingranaggi Conici Basculanti*. Italian Patent No. IT SV20000049A1. Rome: Ufficio Italiano Brevetti e Marchi.
- Barbagelata, A., Ellero, S., Lando, R. (2016). *Planetary Gearbox*. European Patent No. EP2975296A2. Munich: European Patent Office.
- Brassitos, E., and Jalili, N. (2017). Design and development of a compact high-torque robotic actuator for space mechanisms. *J. Mech. Robot.* 9, 061002–1–061002–11. doi: 10.1115/1.4037567
- Brassitos, E., and Jalili, N. (2018). “Identifying stiffness, friction, and kinematic error signature in gear bearing drive transmissions,” in *ASME 2018 International Design Engineering Technical Conferences and Computers and Information in Engineering Conference* (Quebec: American Society of Mechanical Engineers Digital Collection). doi: 10.1115/DETC2018-85647
- Brassitos, E., Mavroidis, C., and Weinberg, B. (2013). “The gear bearing drive: a novel compact actuator for robotic joints,” in *ASME 2013 International Design Engineering Technical Conferences and Computers and Information in Engineering Conference* (Portland, OR: American Society of Mechanical Engineers Digital Collection). doi: 10.1115/DETC2013-13461
- Brassitos, E., Weinberg, B., Qingchao, K., Mavroidis, C. (2019). *Curved Bearing Contact System*. U.S. Patent No. US10174810B2. Washington, DC: U.S. Patent and Trademark Office.
- Calanca, A., Muradore, R., and Fiorini, P. (2015). A review of algorithms for compliant control of stiff and fixed-compliance robots. *IEEE/ASME Trans. Mech.* 21, 613–624. doi: 10.1109/TMECH.2015.2465849
- Carbone, G., Mangialardi, L., and Mantriota, G. (2004). A comparison of the performances of full and half toroidal traction drives. *Mech. Mach. Theory* 39, 921–942. doi: 10.1016/j.mechmachtheory.2004.04.003
- CAXMan (2020). *H2020 project 680448 of the European Union. Presentation of the Use Case 1: NuGear*. Available online at: <https://www.caxman.eu/en/use-cases/nugear/> (accessed April 30, 2020).
- Cetinkunt, S. (1991). Optimal design issues in high-speed high-precision motion servo systems. *Mechatronics* 1, 187–201. doi: 10.1016/0957-4158(91)90043-A
- Chen, C., and Angeles, J. (2006). Virtual-power flow and mechanical gear-mesh power losses of epicyclic gear trains. *ASME J. Mech. Des.* 129, 107–113. doi: 10.1115/1.2359473
- Chen, D. Z., and Tsai, L. W. (1993). Kinematic and dynamic synthesis of geared robotic mechanisms. *J. Mech. Des.* 115, 241–246. doi: 10.1115/1.2919183
- Crispel, S., López-García, P., Verstraten, T., Convens, B., Saerens, E., Vanderborgh, B., and Lefebvre, D. (2018). “Introducing compound planetary gears (C-PGTs): a compact way to achieve high gear ratios for wearable robots” in *International Symposium on Wearable Robotics* (Pisa), 485–489. doi: 10.1007/978-3-030-01887-0_94

- De Santis, A., Siciliano, B., De Luca, A., and Bicchi, A. (2008). An atlas of physical human–robot interaction. *Mech. Mach. Theory* 43, 253–270. doi: 10.1016/j.mechmachtheory.2007.03.003
- Del Castillo, J. M. (2002). The analytical expression of the efficiency of planetary gear trains. *Mech. Mach. Theory* 37, 197–214. doi: 10.1016/S0094-114X(01)00077-5
- Dresscher, D., de Vries, T. J., and Stramigioli, S. (2016). “Motor-gearbox selection for energy efficiency,” in *2016 IEEE International Conference on Advanced Intelligent Mechatronics (AIM)* (Banff, AB: IEEE), 669–675. doi: 10.1109/AIM.2016.7576845
- Fujimoto, Y. (2015). *An Epicyclic Gear Drive and a Designing Method for the Same*. Japanese Patent No. JP2015164100. Tokyo: Japanese Patent Office.
- Fujimoto, Y., and Kobuse, D. (2017). “Highly backdrivable robotic actuators,” in *IEEE International Workshop on Sensing, Actuation, Motion Control, and Optimization (SAMCON)* (Nagaoka), IS2–1.
- GAM (2020). *GSL Strain Wave Gearbox*. Catalogue.
- GENESIS (2018). *Reflex Torque Amplifier—Powering the Future of Motion*. Tech Update Communicate.
- GENESIS Robotics (2020). *LiveDrive® Radial MOTOR* [Brochure]. Available online at: <https://genesishrobotics.com/products/livedrive-radial-motor/> (accessed April 30, 2020).
- Giberti, H., Cinquemani, S., and Legnani, G. (2010). Effects of transmission mechanical characteristics on the choice of a motor-reducer. *Mechatronics* 20, 604–610. doi: 10.1016/j.mechatronics.2010.06.006
- Girard, A., and Asada, H. H. (2017). Leveraging natural load dynamics with variable gear-ratio actuators. *IEEE Robot. Autom. Lett.* 2, 741–748. doi: 10.1109/LRA.2017.2651946
- Gorla, C., Davoli, P., Rosa, F., Longoni, C., Chiozzi, F., and Samarani, A. (2008). Theoretical and experimental analysis of a cycloid speed reducer. *J. Mech. Des.* 130:112604. doi: 10.1115/1.2978342
- Groothuis, S. S., Folkertsma, G. A., and Stramigioli, S. (2018). A general approach to achieving stability and safe behavior in distributed robotic architectures. *Front. Robot. AI* 5:108. doi: 10.3389/frobt.2018.00108
- Haddadin, S., Albu-Schäffer, A., and Hirzinger, G. (2009). Requirements for safe robots: measurements, analysis and new insights. *Int. J. Robot. Res.* 28, 1507–1527. doi: 10.1177/0278364909343970
- Haddadin, S., and Croft, E. (2016). “Physical human–robot interaction,” in *Springer Handbook of Robotics* (Cham: Springer), 1835–1874. doi: 10.1007/978-3-319-32552-1_69
- HALODI Robotics (2018). *Revo1™ Direct Drive MOTOR* [Brochure]. Moss. Available online at: <https://www.halodi.com/revo1> (accessed April 30, 2020).
- Ham, R. V., Sugar, T. G., Vanderborght, B., Hollander, K. W., and Lefeber, D. (2009). Compliant actuator designs. *IEEE Robot. Autom. Mag.* 16, 81–94. doi: 10.1109/MRA.2009.933629
- Harmonic Drive A. G. (2014). *Engineering Data CSD-2A Component Sets*. Catalogue.
- Hlebanja, G., and Kulovec, S. (2015). “Development of a planocentric gear box based on S-gear geometry,” in *11. Kolloquium Getriebetechnik* (Munich), 205–216.
- Hogan, N. (1984). “Impedance control: an approach to manipulation,” in *1984 American Control Conference* (San Diego, CA: IEEE), 304–313. doi: 10.23919/ACC.1984.4788393
- Hori, K., and Hayashi, I. (1994). Maximum efficiencies of conventional mechanical paradox planetary gears for reduction drive. *Trans. Jpn. Soc. Mech. Eng.* 60, 3940–3947. doi: 10.1299/kikaic.60.3940
- Hunter, I. W., Hollerbach, J. M., and Ballantyne, J. (1991). A comparative analysis of actuator technologies for robotics. *Robot. Rev.* 2, 299–342.
- IMSystems (2019). *Archimedes Drive. IMSystems—Drive Innovation* [Brochure], Delft.
- Iqbal, J., Tzagarakis, N. G., and Caldwell, D. G. (2011). “Design of a wearable direct-driven optimized hand exoskeleton device,” in *International Conference on Advances in Computer-Human Interactions (ACHI)* (Gosier).
- Kanai, Y., and Fujimoto, Y. (2018). “Torque-sensorless control for a powered exoskeleton using highly back-drivable actuators,” in *IECON 2018—44th Annual Conference of the IEEE Industrial Electronics Society* (Washington, DC: IEEE), 5116–5121. doi: 10.1109/IECON.2018.8591255
- Kapelevich, A., and AKGears LLC (2013). High gear ratio epicyclic drives analysis. *Ratio* 3, 10.
- Karayiannidis, Y., Droukas, L., Papageorgiou, D., and Doulgeri, Z. (2015). Robot control for task performance and enhanced safety under impact. *Front. Robot. AI* 2:34. doi: 10.3389/frobt.2015.00034
- Kashiri, N., Abate, A., Abram, S. J., Albu-Schäffer, A., Clary, P. J., Daley, M., et al. (2018). An overview on principles for energy efficient robot locomotion. *Front. Robot. AI* 5:129. doi: 10.3389/frobt.2018.00129
- Kim, J., Park, F. C., Park, Y., and Shizuo, M. (2002). Design and analysis of a spherical continuously variable transmission. *J. Mech. Des.* 124, 21–29. doi: 10.1115/1.1436487
- Klassen, J. B. (2019). *Differential Planetary Gearbox*. International Patent No. WO2019/051614A1. Geneva: World Intellectual Property Organization, International Bureau.
- Koriakov-Savoysky, B., Aleksahin, I., Vlasov, I. P. (1996). *Gear System*. U.S. Patent No. US5505668A. Washington, DC: U.S. Patent and Trademark Office.
- Li, S. (2014). “The latest design technologies for gear devices with great transmission ratios,” in *Proceedings of International Gear Conference* (Lyon), 427–436. doi: 10.1533/9781782421955.427
- Looman, J. (1996). *Zahnradgetriebe (Gear Mechanisms)*. Berlin: Springer-Verlag. doi: 10.1007/978-3-540-89460-5
- López-García, P., Crispel, S., Verstraten, T., Saerens, E., Convens, B., Vanderborght, B., and Lefeber, D. (2018). “Failure mode and effect analysis (FMEA)-driven design of a planetary gearbox for active wearable robotics,” in *International Symposium on Wearable Robotics* (Pisa), 460–464. doi: 10.1007/978-3-030-01887-0_89
- López-García, P., Crispel, S., Verstraten, T., Saerens, E., Vanderborght, B., Lefeber, D. (2019a). “Wolf from gearboxes for lightweight, human-centered robotics,” in *Proceedings of the International Conference on Gears 2019* (Munich: VDI), 753–764.
- López-García, P., Crispel, S., Verstraten, T., Saerens, E., Vanderborght, B., and Lefeber, D. (2019b). “Customizing planetary gear trains for human limb assistance and replication,” in *MATEC Web of Conferences* (Varna: EDP Sciences), 01014. doi: 10.1051/mateconf/201928701014
- Loughlin, C., Albu-Schäffer, A., Haddadin, S., Ott, C., Stemmer, A., Wimböck, T., and Hirzinger, G. (2007). The DLR lightweight robot: design and control concepts for robots in human environments. *Ind. Robot. Int. J.* 34, 376–385. doi: 10.1108/01439910710774386
- Macmillan, R. H., and Davies, P. B. (1965). Analytical study of systems for bifurcated power transmission. *J. Mech. Eng. Sci.* 7, 40–47. doi: 10.1243/JMES_JOUR_1965_007_009_02
- Mayr, C. (1989). *Präzisions-Getriebe für die Automation: Grundlagen und Anwendungsbeispiele*. Landsberg: Verlag Moderne Industrie.
- Michel, S. (2015). Logarithmische spirale statt evolvente. *Maschinenmarkt* Nr. 18, 40–42.
- Mihailidis, A., Athanasopoulos, E., and Okkas, E. (2014). “Efficiency of a cycloid reducer,” in *International Gear Conference* (Lyon Villeurbanne), 794–803. doi: 10.1533/9781782421955.794
- Morozumi, M. (1970). *Profile Shifted Involute Internal Gearing*. U.S. Patent No. US3546972A. Washington, DC: U.S. Patent and Trademark Office.
- Mueller, H. W. (1998). *Die Umlaufgetriebe: Auslegung und vielseitige Anwendungen*. Berlin; Heidelberg: Springer-Verlag. doi: 10.1007/978-3-642-58725-2
- Mulzer, F. (2010). *Systematik hoch übersetzender koaxialer getriebe* (Doctoral dissertation). Technische Universität München, Munich, Germany.
- Musser, C. W. (1955). *Strain Wave Gearing*. U.S. Patent No. US2906143A. Washington, DC: U.S. Patent and Trademark Office.
- NABTESCO (2018). *Precision Reduction Gear RV—N Series*. CAT.180410. Catalogue.
- Neugart, A. G. (2020). *PLE Economy Line*. Catalogue.
- Niemann, G., Winter, H., and Höhn, B. R. (1975). *Maschinenelemente, Vol. 1*. Berlin; Heidelberg; New York, NY: Springer.
- Pasch, K. A., and Seering, W. P. (1983). “On the drive systems for high-performance machines,” in *Mechanical Engineering* (New York, NY: ASME-AMER Society Mechanical Engineering), 107–107.
- Pennestri, E., and Freudenstein, F. (1993). The mechanical efficiency of epicyclic gear trains. *ASME J. Mech. Des.* 115, 645–651. doi: 10.1115/1.2919239
- Pettersson, M., and Ölvander, J. (2009). Drive train optimization for industrial robots. *IEEE Trans. Robot.* 25, 1419–1424. doi: 10.1109/TRO.2009.2028764

- Pham, A. D., and Ahn, H. J. (2018). High precision reducers for industrial robots driving 4th industrial revolution: state of arts, analysis, design, performance evaluation and perspective. *Int. J. Precis. Eng. Manuf. Green Technol.* 5, 519–533. doi: 10.1007/s40684-018-0058-x
- Rezazadeh, S., and Hurst, J. W. (2014). "On the optimal selection of motors and transmissions for electromechanical and robotic systems," in *2014 IEEE/RSJ International Conference on Intelligent Robots and Systems* (Chicago, IL: IEEE), 4605–4611. doi: 10.1109/IROS.2014.6943215
- Roos, F., Johansson, H., and Wikander, J. (2006). Optimal selection of motor and gearhead in mechatronic applications. *Mechatronics* 16, 63–72. doi: 10.1016/j.mechatronics.2005.08.001
- Rosenbauer, T. (1995). *Getriebe für Industrieroboter: Beurteilungskriterien. Kenndaten, Einsatzhinweise*: Shaker.
- Rossman, A. M. (1934). *Mechanical Movement*. U.S. Patent No. US1970251. Washington, DC: U.S. Patent and Trademark Office.
- Saerens, E., Crispel, S., García, P. L., Verstraten, T., Ducastel, V., Vanderborght, B., and Lefeber, D. (2019). Scaling laws for robotic transmissions. *Mech. Mach. Theory* 140, 601–621. doi: 10.1016/j.mechmachtheory.2019.06.027
- Schafer, I., Bourlier, P., Hantschack, F., Roberts, E. W., Lewis, S. D., Forster, D. J., and John, C. (2005). "Space lubrication and performance of harmonic drive gears," in *11th European Space Mechanisms and Tribology Symposium, ESMATS 2005* (Lucerne), 65–72.
- Scheinman, V., McCarthy, J. M., and Song, J. B. (2016). "Mechanism and actuation," in *Springer Handbook of Robotics* (Cham: Springer), 67–90. doi: 10.1007/978-3-319-32552-1_4
- Schempf, H. (1990). *Comparative design, modeling, and control analysis of robotic transmissions* (Ph.D. thesis). No. WHOI-90-43. Department of Mechanical Engineering, and Woods Hole Oceanographic Institute, Massachusetts Institute of Technology, Cambridge, MA, United States. doi: 10.1575/1912/5431
- Schempf, H., and Yoerger, D. R. (1993). Study of dominant performance characteristics in robot transmissions. *ASME J. Mech. Des.* 115, 472–482. doi: 10.1115/1.2919214
- Schorsch, J. F. (2014). *Compound Planetary Friction Drive*. Dutch Patent No. 2013496. De Haag: Octrooiencentrum Nederland.
- Schreiber, H. (2015). "Revolutionäres getriebeprinzip durch neuinterpretation von maschinenelementen—Die WITTENSTEIN Galaxie®-Kinematik," in *Dresdner Maschinenelemente Kolloquium, DMK* (Dresden), 2015.S.
- Schreiber, H., and Röthlingshöfer, T. (2017). "Kinematic classification of a gearbox comprising separate thrust teeth and its advantages regarding existing approaches," in *International Conference on Gears, ICG* (Munich).
- Schreiber, H., and Schmidt, M. (2015). *Getriebe*. Deutsche Patent No. DE 10 2015 105 525 A1. Munich: Deutsches Patent- und Markenamt.
- Sensinger, J. W. (2010). "Selecting motors for robots using biomimetic trajectories: optimum benchmarks, windings, and other considerations," in *2010 IEEE International Conference on Robotics and Automation* (Anchorage, AK: IEEE), 4175–4181. doi: 10.1109/ROBOT.2010.5509620
- Sensinger, J. W. (2013). Efficiency of high-sensitivity gear trains, such as cycloid drives. *ASME J. Mech. Des.* 135, 071006-1–071006-9. doi: 10.1115/1.4024370
- Sensinger, J. W., Clark, S. D., and Schorsch, J. F. (2011). "Exterior vs. interior rotors in robotic brushless motors," in *2011 IEEE International Conference on Robotics and Automation* (Montreal, QC: IEEE), 2764–2770. doi: 10.1109/ICRA.2011.5979940
- Seok, S., Wang, A., Chuah, M. Y. M., Hyun, D. J., Lee, J., Otten, D. M., et al. (2014). Design principles for energy-efficient legged locomotion and implementation on the MIT cheetah robot. *IEEE/ASME Trans. Mech.* 20, 1117–1129. doi: 10.1109/TMECH.2014.2339013
- Siciliano, B., Sciacivico, L., Villani, L., and Oriolo, G. (2010). *Robotics: Modelling, Planning and Control*. London: Springer Science and Business Media. doi: 10.1007/978-1-84628-642-1
- Slatter, R. (2000). *Weiterentwicklung eines Präzisionsgetriebes für die Robotik*. St. Leonard: Antriebstechnik.
- SPARC (2015). *Robotics 2020 Multi-Annual Roadmap for Robotics in Europe Horizon 2020 Call ICT-2017*. Available online at: <https://www.eu-robotics.net/sparc/about/roadmap/index.html> (accessed April 30, 2020).
- SPINEA (2017). *TwinSpin—High Precision Reduction Gears—Präzisionsgetriebe*. Katalog.
- Stramigioli, S., van Oort, G., and Dertien, E. (2008). "A concept for a new energy efficient actuator," in *2008 IEEE/ASME International Conference on Advanced Intelligent Mechatronics* (Xi'an: IEEE), 671–675. doi: 10.1109/AIM.2008.4601740
- SUMITOMO (2017). *Fine Cyclo® Spielfreie Präzisionsgetriebe*. Katalog 991311 DE 02/2017.
- SUMITOMO (2020). *E-Cyclo® Motion Control Drives*. Katalog F10001E-1.
- Talbot, D., and Kahraman, A. (2014). "A methodology to predict power losses of planetary gear sets," in *International Gear Conference* (Lyon-Villeurbanne), 26–28. doi: 10.1533/9781782421955.625
- Tomczyk, H. (2000). *Adjusting Device with Planetary Gears*. European Patent No. EP1244880B1. Munich: European Patent Office.
- Toxiri, S., Näf, M. B., Lazzaroni, M., Fernández, J., Sposito, M., Poliero, T., et al. (2019). "Back-support exoskeletons for occupational use: an overview of technological advances and trends," in *IJSE Trans. Occup. Ergon. Hum. Factors* 7, 3–4, 237–249. doi: 10.1080/24725838.2019.1626303
- Van de Straete, H. J., Degezelle, P., De Schutter, J., and Belmans, R. J. (1998). Servo motor selection criterion for mechatronic applications. *IEEE/ASME Trans. Mech.* 3, 43–50. doi: 10.1109/3516.662867
- Veale, A. J., and Xie, S. Q. (2016). Towards compliant and wearable robotic orthoses: a review of current and emerging actuator technologies. *Med. Eng. Phys.* 38, 317–325. doi: 10.1016/j.medengphy.2016.01.010
- Verstraten, T., Furnémont, R., Mathijssen, G., Vanderborght, B., and Lefeber, D. (2016). "Energy consumption of geared DC motors in dynamic applications: comparing modeling approaches," in *IEEE Robot. Autom. Lett.* 1, 524–530. doi: 10.1109/LRA.2016.2517820
- Vranish, J. M. (1995). *Carrier-Less, Anti-Backlash Planetary Drive System*. U.S. Patent No. US5409431. Washington, DC: U.S. Patent and Trademark Office.
- Vranish, J. M. (2006). *Partial Tooth Gear Bearings*. U.S. Patent No. US2006/0219039A1. Washington, DC: U.S. Patent and Trademark Office.
- Wang, A., and Kim, S. (2015). "Directional efficiency in geared transmissions: characterization of backdrivability towards improved proprioceptive control," in *2015 IEEE International Conference on Robotics and Automation (ICRA)* (Seattle, WA: IEEE), 1055–1062. doi: 10.1109/ICRA.2015.7139307
- Weinberg, B., Mavroidis, C., Vranish, J. M. (2008). *Gear Bearing Drive*. U.S. Patent No. US2008/0045374A1. Washington, DC: U.S. Patent and Trademark Office.
- WinterGreen Research (2018). *Precision Strain Wave Reducer Gearboxes and RV and RD Reducers: Market Shares, Strategy, and Forecasts, Worldwide, 2018 to 2024*. WIN0418002.
- WITTENSTEIN AG (2020). *Technische Broschüre SP+ und TP+ Getrieben*. Katalog.
- Wolf, A. (1958). *Die Grundgesetze der Umlaufgetriebe*. Braunschweig: Friedr. Vieweg und Sohn.
- Wolfrom, U. (1912). Der Wirkungsgrad von Planetenrädergetrieben. *Werkstattstechnik* 6, 615–617.
- Yu, D., and Beachley, N. (1985). On the mechanical efficiency of differential gearing. *ASME J. Mech. Trans. Autom.* 107, 61–67. doi: 10.1115/1.3258696
- Zinn, M., Roth, B., Khatib, O., and Salisbury, J. K. (2004). A new actuation approach for human friendly robot design. *Int. J. Robot. Res.* 23, 379–398. doi: 10.1177/0278364904042193

Conflict of Interest: The authors declare that the research was conducted in the absence of any commercial or financial relationships that could be construed as a potential conflict of interest.

Copyright © 2020 García, Crispel, Saerens, Verstraten and Lefeber. This is an open-access article distributed under the terms of the Creative Commons Attribution License (CC BY). The use, distribution or reproduction in other forums is permitted, provided the original author(s) and the copyright owner(s) are credited and that the original publication in this journal is cited, in accordance with accepted academic practice. No use, distribution or reproduction is permitted which does not comply with these terms.



A Novel User Control for Lower Extremity Rehabilitation Exoskeletons

Kiran K. Karunakaran^{1,2*}, Kevin Abbruzzese^{2,3}, Ghaith Androwis^{1,2} and Richard A. Foulds^{2,4}

¹ Kessler Foundation, West Orange, NJ, United States, ² Department of Biomedical Engineering, New Jersey Institute of Technology, Newark, NJ, United States, ³ Stryker Corporation, Mahwah, NJ, United States, ⁴ Really Useful Robots, LLC, Langhorne, PA, United States

OPEN ACCESS

Edited by:

Carlos A. Cifuentes,
Escuela Colombiana de Ingeniería
Julio Garavito, Colombia

Reviewed by:

Guillermo Asín-Prieto,
Consejo Superior de Investigaciones
Científicas (CSIC), Spain
Camilla Pierella,
École Polytechnique Fédérale de
Lausanne, Switzerland

*Correspondence:

Kiran K. Karunakaran
kkk7@njit.edu

Specialty section:

This article was submitted to
Biomedical Robotics,
a section of the journal
Frontiers in Robotics and AI

Received: 01 May 2020

Accepted: 13 July 2020

Published: 08 September 2020

Citation:

Karunakaran KK, Abbruzzese K,
Androwis G and Foulds RA (2020) A
Novel User Control for Lower
Extremity Rehabilitation Exoskeletons.
Front. Robot. AI 7:108.
doi: 10.3389/frobt.2020.00108

Lower extremity exoskeletons offer the potential to restore ambulation to individuals with paraplegia due to spinal cord injury. However, they often rely on preprogrammed gait, initiated by switches, sensors, and/or EEG triggers. Users can exercise only limited independent control over the trajectory of the feet, the speed of walking, and the placement of feet to avoid obstacles. In this paper, we introduce and evaluate a novel approach that naturally decodes a neuromuscular surrogate for a user's neutrally planned foot control, uses the exoskeleton's motors to move the user's legs in real-time, and provides sensory feedback to the user allowing real-time sensation and path correction resulting in gait similar to biological ambulation. Users express their desired gait by applying Cartesian forces via their hands to rigid trekking poles that are connected to the exoskeleton feet through multi-axis force sensors. Using admittance control, the forces applied by the hands are converted into desired foot positions, every 10 milliseconds (ms), to which the exoskeleton is moved by its motors. As the trekking poles reflect the resulting foot movement, users receive sensory feedback of foot kinematics and ground contact that allows on-the-fly force corrections to maintain the desired foot behavior. We present preliminary results showing that our novel control can allow users to produce biologically similar exoskeleton gait.

Keywords: lower extremity exoskeletons, gait, spinal cord injury, rehabilitation robotics, robot control systems

INTRODUCTION

Individuals with complete paraplegia due to spinal cord injury (SCI) have impaired motor control and sensory feedback that limits their ability to walk (Shepherd Center). While wheelchairs provide alternative mobility to individuals with paraplegia, they are not a complete substitute for natural ambulation. Current research has addressed this issue with wearable lower extremity exoskeletons (Dollar and Herr, 2008; Contreras-Vidal et al., 2016). The past decade has witnessed a dramatic growth in the study and implementation of such technology, not only for those with paraplegia due to SCI, but also for individuals with cerebral palsy, stroke, traumatic brain injury and multiple sclerosis (Canela et al., 2013; Murray et al., 2015; Kozłowski et al., 2017; Lerner et al., 2017; Patané et al., 2017; Androwis et al., 2019; Karunakaran et al., 2019). These exoskeletons are mechanically similar, consisting of a set of linkages that parallel the wearer's thighs, calves, and feet, and augmented with actuators to provide alternatives to muscle torque at the joints. Unlike devices developed for military and industrial tasks, most rehabilitation exoskeletons rely on the subject's use of crutches or canes to provide balance, as the devices lack sensory feedback and balance compensation (Contreras-Vidal et al., 2016).

Where current rehabilitation exoskeletons differ significantly is in their detection of user initiation of gait patterns (Dellon and Matsuoka, 2007; Strickland, 2012)^{1,2}. The Ekso (Ekso Bionics) has motors at the hip and knee, with passive springs at the ankles to provide gait only in the sagittal plane (Strickland, 2012)¹. The Ekso has two options to initiate the gait cycle. (1) The first allows a clinician to control gait by means of an external switch pad for training and therapy. (2) For independent control, sensors embedded in the device detect changes in the hip position¹. A step can be initiated by the user moving the hip forward and laterally or by changing tilt angle and making ground contact with sensors on the crutches¹. Goldfarb et al. developed what has been commercialized as the Indego (Parker Hannifin) (Farris, 2012; Farris et al., 2012; Quintero et al., 2012). It also has powered degrees of freedom (DOF) at the hip and knee, and passive ankle support in the sagittal plane. It uses Hall effect sensors, potentiometers, and accelerometers to detect the user's center of pressure (COP) (Farris, 2012; Quintero et al., 2012). When the user leans forward with both crutches touching the ground, the COP shifts in the direction of movement, and the exoskeleton initiates swing of the most rearward leg (Farris, 2012; Quintero et al., 2012). The Rewalk (Rewalk Robotics) also has two active DOFs with the ankle consisting of a simple orthotic joint with limited motion and spring assisted dorsiflexion (Esquenazi et al., 2012). The control system includes a tilt sensor to determine changes in trunk motion and center of gravity. Shifts in the center of gravity initiate the preprogrammed hip and knee displacement in the appropriate leg (Esquenazi et al., 2012). The HAL (Cyberdyne) employs a combination of EMG gait initiation detection with an accelerometer and gyroscope to sense body posture (Lee and Sankai, 2002, 2003; Hayashi et al., 2005). In contrast to the above exoskeletons that have two active degrees of freedom, the REX (REX Bionics) has 5 motors per leg and is the only available assistive exoskeleton to provide movement in the coronal as well as sagittal planes, and to be self-balancing (i.e., no crutches²). It is controlled by a joystick that signals one of 8 discrete directions of ambulation, and has button selection for sitting and rising².

Electrophysiological signals have also been employed to initiate exoskeleton gait (Kilicarslan et al., 2013; Kwak et al., 2015; Lebedev and Nicolelis, 2017). Contreras-Vidal et al. have demonstrated the use of EEG triggers to select various REX exoskeleton's discrete control commands (Farris et al., 2012). Similarly, other investigators have focused on detecting gait initiation and termination events using EEG, EOG, evoked potentials, and other bioelectric signals (Nicolelis, 2003; Kilicarslan et al., 2013; Kwak et al., 2015).

Beyond the triggering of preplanned gait patterns, extensive research has been pursued on control methods that allow users to plan and execute novel gait patterns similar to those of individuals with no disability. Gancet et al. have tried to interpret EEG signals from the motor cortex to calculate the kinematics of the gait cycle. A dynamic recurrent neural network was used to train the network to detect the gait patterns in the EEG

signal (Gancet et al., 2012). Lebedev and Nicolelis (2017) has also attempted to use BCI to communicate the user's desired gait cycle kinematics. Unfortunately, both groups have reported numerous challenges such as difficulty in identifying the user intention of each joint, removal of mechanical artifacts caused by relative movement of the EEG cap, and physiological artifacts due to muscle activity in the vicinity of the cap. Even with extensive signal processing, they were not able to completely isolate the relevant signals at all time periods. López-Larraz et al. (2016) have concluded that the current state of the art of non-invasive BCI knowledge is insufficient for precise decoding of neutrally intended leg kinematics.

Similar to our intention of redirecting controllable neuromuscular activities to define real-time novel gait patterns, Durandau et al. (2019) have explored the use of residual muscle force activity by using detecting EMG signals. These investigators explain that no other exoskeleton has the ability to amplify weak user muscle strength. Another group (Ferris and Lewis, 2009) have considered the use of proportional EMG signals to activate pneumatic muscles that power a lower extremity exoskeleton. Yet another group has recognized the contralateral synchronization of the arms and legs in unimpaired walking and has used the shoulder angles to define unique sets of hip, knee, and ankle angles that are provide to the exoskeleton (Fang et al., 2017).

Similar to those efforts, the long-term objective of our work is to allow users to intuitively express their desired gait kinematics and dynamics using their arms and hands as sensory and motor alternatives to their legs and feet. Our prior lower extremity research (Karunakaran et al., 2014, 2017) evaluated the feedback conditions required by the hand to produce gait kinematics. That study included 18 subjects controlling virtual feet using hand movements to produce gait trajectories in a virtual environment. Our results indicated that users, provided with haptic through a physical link, and visual feedback (both sensations felt by the hands and visual observation), produced hand and virtual foot trajectories similar to biological gait trajectories (Karunakaran et al., 2014, 2017). We showed that for this to be a viable exoskeleton control method, the hands must be haptically connected either contralaterally or ipsilaterally to the feet. This ensures that the hands and feet move in precise time synchrony, and that hands sense the movement of the feet in order to provide the central nervous system with both position and force feedback from the feet (Karunakaran et al., 2014, 2017). This study as well as our other prior work has shown that neural control of arm and finger walking-like movements generates kinematics very similar to biologically intact neurally determined leg movements and foot placement (DeMarco and Foulds, 2002; Birmingham et al., 2003; Karunakaran et al., 2014, 2017).

The goal of this work was to develop and user test an intuitive control mechanism that independently controls both legs, while producing symmetrical gait kinematics using trajectories generated by hand movements in real time. Balance and coordination are being addressed in the later phase of the work, and will be presented in a subsequent paper.

We have chosen to allow the user to control movement of each foot with movements of the ipsilateral hand and arm. This may appear counter intuitive since the arms swing contralaterally with

¹ Ekso Bionics. Available online at: <https://eksobionics.com/>

² RexBionics. Available online at: <https://www.rexbionics.com/>

respect to leg movements during normal walking. However, we believe that ipsilateral control presents little if any physiological impediment to a successful user/exoskeleton interface, while its advantages are significant.

Although contralateral arm swing is commonly observed, its function in human gait is not entirely understood. Recent studies (Meesen et al., 2006; Meyns et al., 2013) agree there may be an enhancement in balance and stability, however, they also note that walkers can carry objects and make purposeful arm movements without compromising balance.

Contralateral arm movement is the preferred pattern at walking speeds above 0.8 m/s, yet at speeds below 0.8 m/s, individuals will often adopt an ipsilateral pattern or not swing the arms at all (Ford et al., 2007). In studies of walking with constrained or impaired arm movements (Meesen et al., 2006; Ford et al., 2007) there were only minor reductions in walking speed, that could be voluntarily corrected by participants. Studies of ladder climbing (Armstrong et al., 2009) show a preference for ipsilateral hand and arm coordination. Most importantly, in Meesen et al. (2006) subjects were asked to make four types of simultaneous arm/leg movements: ipsilateral same direction movements (e.g., right arm and right leg raised up and down, or adducted/abducted), opposite direction ipsilateral movements (e.g., right arm up while right leg down, or right arm adducted and right leg abducted), contralateral same direction movements and contralateral opposite direction movements. When examining the quality to interlimb coordination, the investigators found that the ipsilateral, same direction movements were modestly more accurate in absolute position/angle and phase than both contralateral conditions (Meesen et al., 2006). Thus, we are confident that we could employ either ipsilateral or contralateral arm/hand control method.

For our purposes, ipsilateral control of foot movement has several significant advantages. Admittance control requires the user to apply forces to the foot of the exoskeleton. This is most easily accomplished via a rigid trekking pole on the same side as the foot. A pole on the same side of the body facilitates directing the foot to move vertically and horizontally in the sagittal plane as well as controlling ab/adduction in coronal plane. Also, the poles allow the user's to feel the impact of the ground reaction through the ipsilateral hands. This quality of sensory feedback is unavailable in any proposed exoskeleton control method, and has been shown in our earlier work (Karunakaran et al., 2017) to be of vital importance to controlling the movement of the feet.

MATERIALS AND METHODS

Apparatus

A 1/2 scale biped robot representing a lower extremity exoskeleton was built to test our control method. Each leg has 2 links, from hip to knee, and from knee to ankle, and a foot scaled to the anthropometry of the human leg.

Each robot leg has 5 DOF (**Figure 1**). The hip has 2 DOF for flexion/extension and abduction/adduction, the knee has 1 DOF for flexion/extension, and the ankle has 2 DOF for plantarflexion/dorsiflexion and inversion/eversion. Using previously published data (Hamill et al., 2013), maximum thigh angular velocities and angular accelerations were found to be 28 radians/second (rad/s) and 35 radians/second², respectively. Using this angular acceleration with an estimate of the robot leg moment of inertia relative to the hip, the motor torque required to achieve the maximum acceleration was computed to be 4.2 Newton-meter (N-m). The similarly computed maximum knee motor torque is smaller due to the smaller moment of inertia. We selected the Dynamixel MX-106 smart servomotor (Robotis,

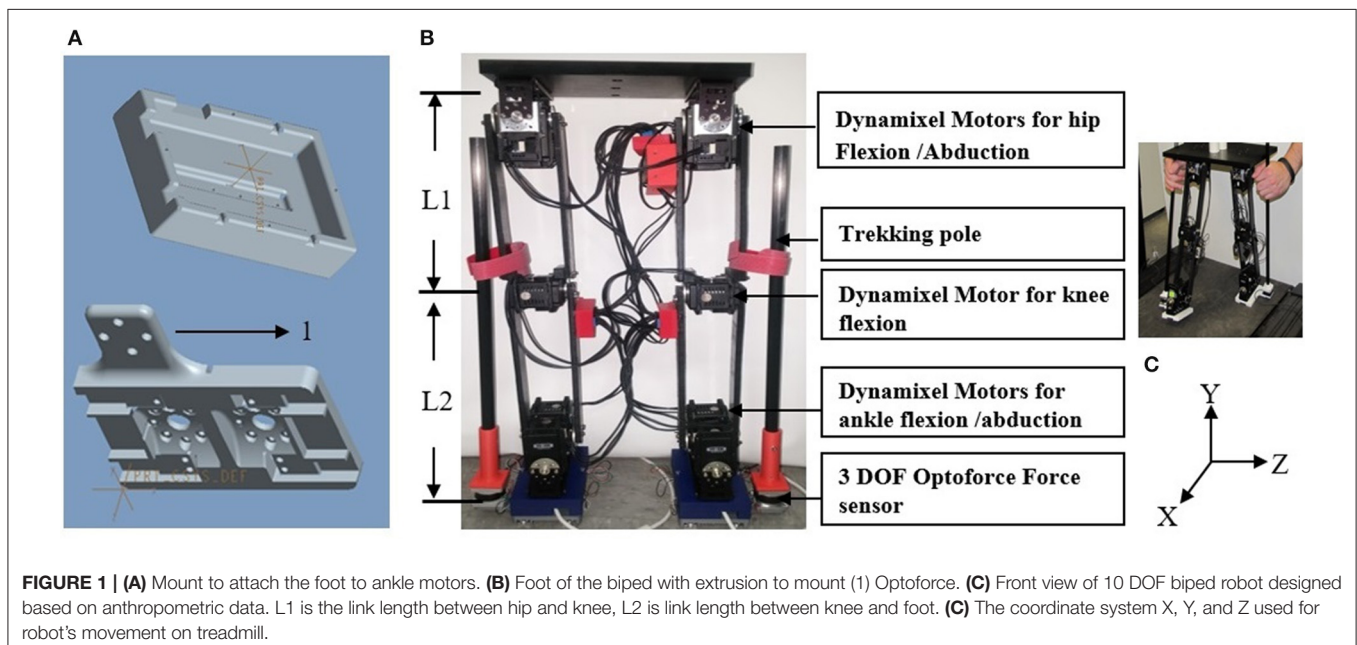
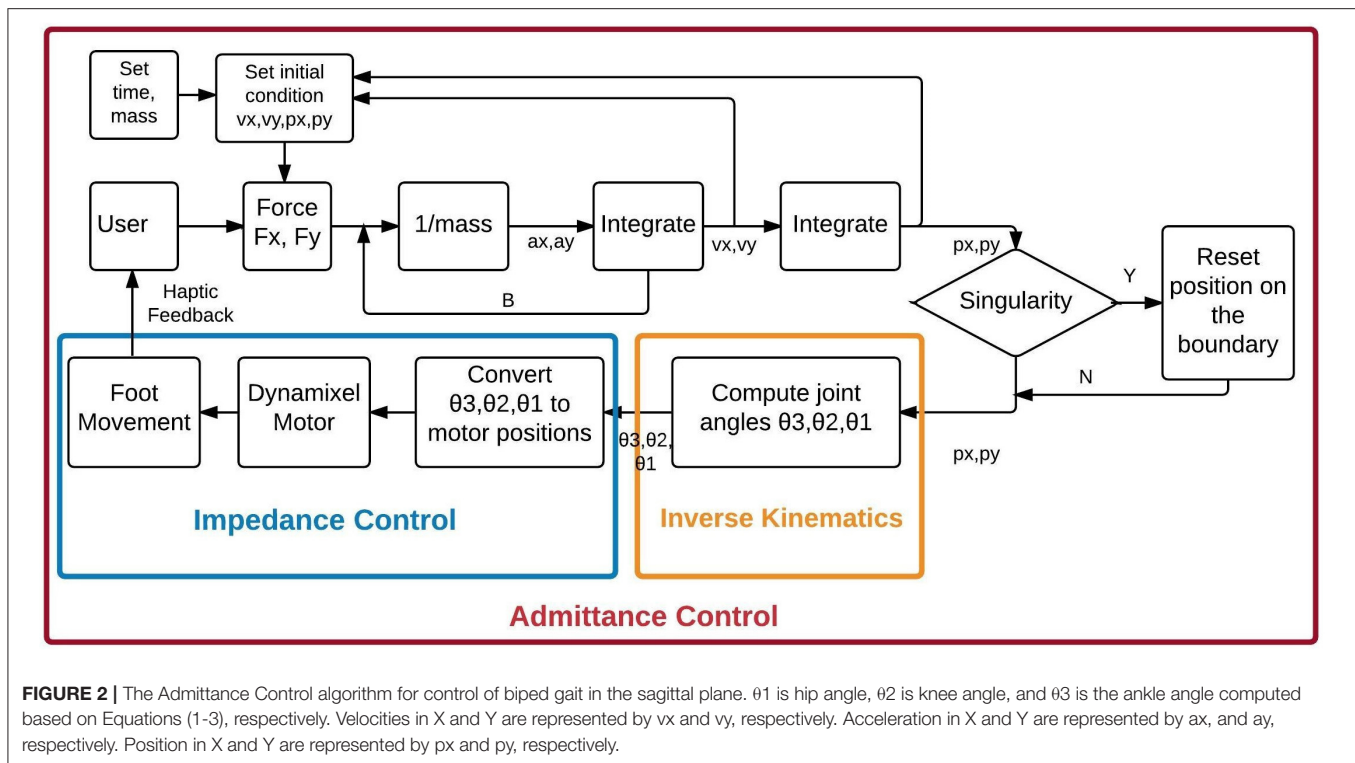


FIGURE 1 | (A) Mount to attach the foot to ankle motors. **(B)** Foot of the biped with extrusion to mount (1) Optoforce. **(C)** Front view of 10 DOF biped robot designed based on anthropometric data. L1 is the link length between hip and knee, L2 is link length between knee and foot. **(D)** The coordinate system X, Y, and Z used for robot's movement on treadmill.



USA)³ as the actuator for all joints, since both its angular velocity, 42 rad/s, resolution of 0.088 degrees and maximum torque, 8.5 N-m, allow the robot to match the physiological leg segment velocities and accelerations.

Dynamixel servos employ Maxon motors supported by 32-bit internal microcontrollers providing proportional/integrative/derivative (PID) control at 1,000 Hz. All motors are daisy chained by a 3-wire bus on which they are group addressed from MATLAB software at 1 Mbits/second so that the motors are activated simultaneously. A 3 DOF Optoforce sensor⁴ detects the forces exerted by the user on carbon-fiber trekking poles that are rigidly attached to the sensor.

User Control Algorithm

The control algorithm consists of an outer admittance loop running at 100 Hz and an inner impedance loop running at 1,000 Hz. The Dynamixel motor's internal PID controller serves as the inner loop. Our admittance loop receives the Cartesian forces applied to the trekking poles by the user's hands and generates desired Cartesian kinematics for the end-effectors of the robot every 10 milliseconds (ms). Admittance control offers a very intuitive control mechanism; where the robot end-effector will be directed to move in the Cartesian directions proportional to the force applied by the user (Van Der Linde et al., 2002). The force can be scaled to accommodate the user's needs. It is safe and

easy for human interaction (Van Der Linde et al., 2002; Haidegger et al., 2009).

Custom inverse kinematics algorithms transform the Cartesian positions generated by the admittance loop into joint angles used to command the motors. Algorithms are written in MATLAB, with time-dependent functions coded in C to maintain a 100 Hz update rate.

Sagittal Plane Control

Robot control in the sagittal plane is shown in **Figure 2**. User forces applied in the X and Y-direction are read at 1,000 Hz from two axes of the 3 DOF Optoforce force sensor, and averaged to provide 100 samples/second. For every cycle of the admittance loop these forces, virtual mass, virtual damping, as well as the foot's Cartesian position and velocity are passed to custom-written ordinary differential equation (ODE) that is implemented using the C source code Variable ordinary differential equation (Cvode) solver and compiled for use in MATLAB (Van Riel, 2012). The ODE is shown in **Figure 2** as a double integration that provides the desired positions and velocities in X and Y to be achieved in the next 10 ms. The value assigned to the mass allows scaling of the forces to meet the capabilities of the user's hands. The ODE also incorporates the admittance loop's damping that maintains stability of the system. No admittance stiffness is included in this version of the software, but can be added if required in future situations. The ODE function is coded to solve the second-order differential equation shown below:

$$X''(t) = \frac{F(X)}{M} - \frac{B * X'(t)}{M} \quad (1)$$

³Robotis. Available online at: http://www.robotis.com/xs/dynamixel_en

⁴<https://www.universal-robots.com/>

where, $F(X)$ = force (Newton), M = virtual mass (kilogram), B = virtual damping (Newton-second/meter), $X'(t)$ = velocity (meter/second), $X''(t)$ = acceleration (meter/second²).

Inverse Kinematics

Since the robot has revolute joints, inverse kinematics converts the X-Y position of the foot to angles of the hip and knee in the sagittal plane. For simplicity, the angle of the ankle is computed to keep the foot parallel to the floor. The angles are calculated using the law of cosines (Equations 2–4). The joint angles are in turn converted to hip, knee and ankle motor units in the sagittal plane. These values are in turn fed to the corresponding motors to generate the required torque to perform the movement intended by the user.

$$\theta_2 = -2 \tan^{-1} \sqrt{\frac{(L1 + L2)^2 - (X1 + Y1)^2}{(X1 + Y2)^2 - (L1 + L2)^2}} \quad (2)$$

$$\theta_1 = \tan\left(\frac{L2 \sin \theta_2}{L1 + L2 \cos \theta_2}\right) - \tan\left(\frac{Y1}{X1}\right) \quad (3)$$

$$\theta_3 = \theta_2 - \tan\left(\frac{Y1}{X1}\right) + \tan\left(\frac{L2 \sin \theta_2}{L1 + L2 \cos \theta_2}\right) \quad (4)$$

where, $X1$, $Y1$ is the desired end-effector position, $L1$ is the link length between hip and knee, $L2$ is link length between knee and ankle, θ_1 is hip angle, θ_2 is knee angle, and θ_3 is the ankle angle.

The Dynamixel motors have sufficiently fast mechanical and electrical response times (~ 4 ms) to relocate the robot end-effector to the desired location within the 10 ms loop period³. The new position is read at the beginning of the next admittance cycle and serves as the initial conditions for the ODE. As the user's hand is rigidly connected to the robot foot, the user receives real-time sensation of foot movement. The user can modulate his/her forces to alter the speed of foot movement independently in X

and Y, and also in response to external forces that may impede the foot.

Singularity Check

The algorithm verifies that the predicted X-Y position is within reach of the robot. If this check fails, the next position is set to a location on the boundary of the robot's range on a line between the former and predicted position. This maintains stability and smoothness at the singularity. The robot reaches singularity when the estimated position is outside the range of motion of the robot.

Coronal Plane Control

Force applied by the user to a trekking pole in the z-direction is similarly converted to rotation of the hip in the coronal plane as shown in **Figure 3**. The user input is treated as an applied torque, so the ODE implements the following rotational equation of motion:

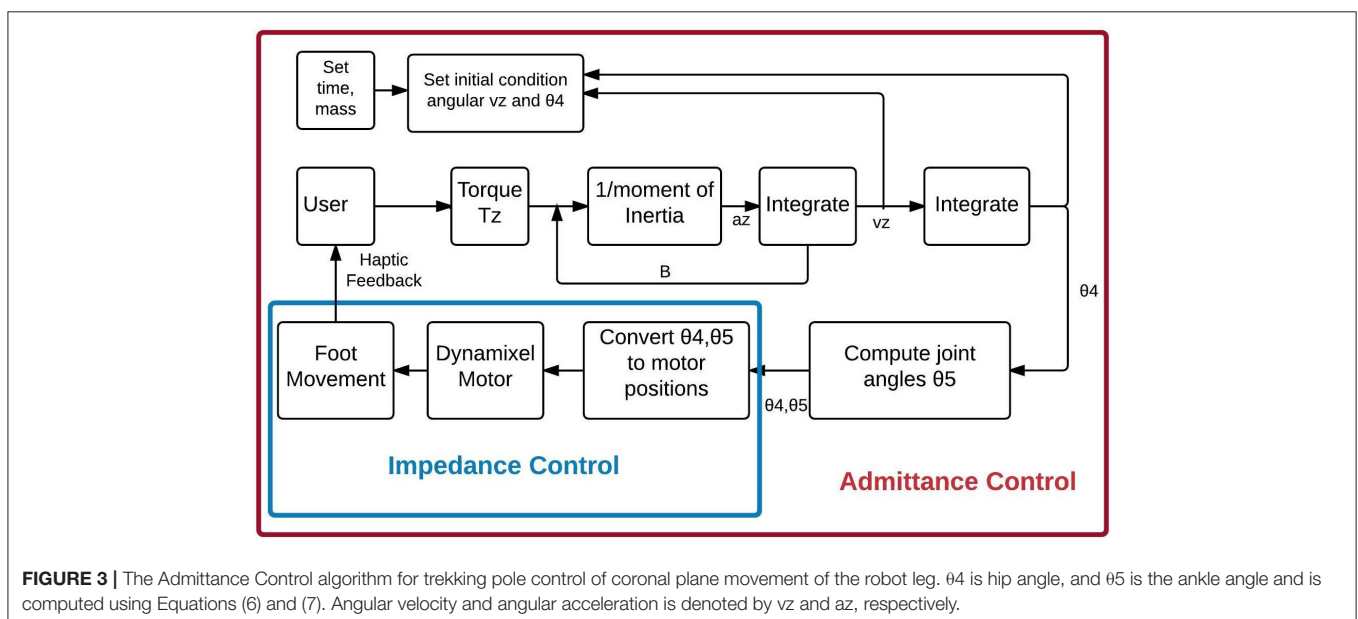
$$\theta''(t) = \frac{T(\theta)}{I} - \frac{B \cdot \theta'(t)}{I} \quad (5)$$

$$\theta_4 = \int \theta'(t) \quad (6)$$

$$\theta_5 = 180 - \theta_4 \quad (7)$$

where, $T(\theta)$ = user applied torque (Newton-meter), I = virtual moment of inertia (kilogram-meter²), B = rotational damping (Newton-second/meter), $\theta'(t)$ = angular velocity (meter/second), $\theta''(t)$ = angular acceleration (meter/second²). θ_4 is hip angle, and θ_5 is the ankle angle in the coronal plane.

The ab/adduction angle is executed by the second hip motor, with the new angle serving as the initial condition for the next admittance cycle, and the movement of the robot leg provides a haptic sensation to the user's hand. Similar to the sagittal plane, the inversion/eversion angle of the foot is computed to keep the foot parallel to the floor.



Biped Control Strategy for Users

Our biped control strategy allows the user to execute the swing and the stance phases of each robot leg independently by applying ipsilateral hand forces at the top of the trekking poles, as shown in **Figure 4**. The user forces are converted to desired foot positions by the admittance control software, with servomotor response occurring within 10 ms.

Forward progression in gait requires activation of both legs. The swing leg proceeds from ground contact (toe-off) to swing and ultimately to a subsequent heel contact in a new forward position on the ground. At the same time, the stance foot remains in the same position on the ground, with rotation of ankle and hip of the stance leg allowing forward progression of the torso (i.e., shifting the robot's center of gravity forward).

The swing foot movement is controlled by the user applying a time-varying upward hand force to define the Y-axis trajectory and a forward force to signify the desired X-axis foot trajectory. Simultaneously, the stance side hand applies a rearward force only in the negative X direction. As this foot remains in contact with the ground (while the swing foot is in the air), the admittance software controls the ankle, knee, and hip motors of the stance leg for forward progression.

Haptic feedback is provided through the physical link (trekking pole) between the hands and the feet. During the swing, as the user force is converted to foot movement, the trekking pole follows the foot, allowing the hand to move synchronously with the trekking poles to walk the biped. Near the end of swing, the user applies downward force to the trekking pole to bring the foot to heel strike. At heel strike, the ground precludes further downward movement, and the user's hand feels the ground reaction.

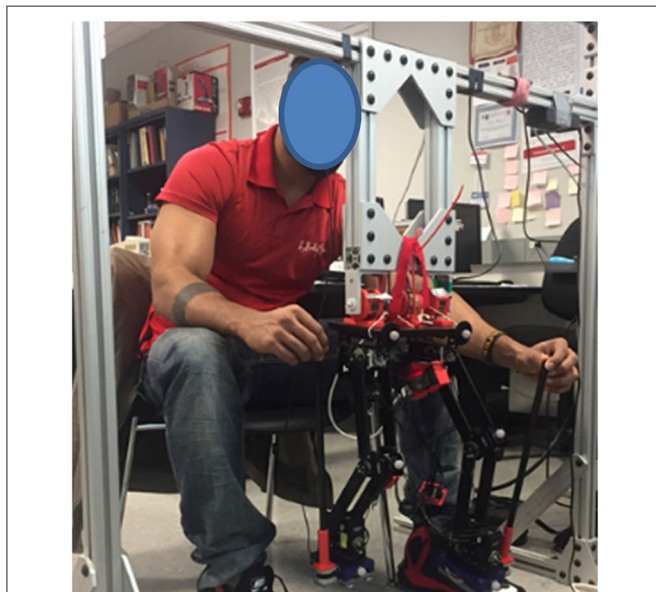


FIGURE 4 | User controlling the biped by holding the trekking poles on the ipsilateral side using hands. Constant force springs connect the robot to the overhead frame to maintain balance.

Evaluation of the Accuracy of the Control

A slow gait-like movement was performed by one healthy female participant (who was a member of the research team) for a period of 60 s in the air to evaluate the accuracy of the admittance control and inverse kinematics algorithms, and the time delay. This work was approved by the New Jersey Institute of Technology's (NJIT) institutional review board (IRB).

The accuracy of the control algorithm for the sagittal and coronal plane was assessed by comparing the desired and the actual Cartesian position of the feet in X, Y, and Z direction. The "desired position" is the position of the foot computed by the algorithm based on user input, and the "actual position" is the position reached by the foot of the biped. The accuracy of the Dymanixel's internal impedance control was evaluated by comparing the desired and actual joint angle. The accuracy of the hip and knee angles in the sagittal plane was evaluated while the participant performed the gait using the hand. The accuracy of the joint angle of the hip in the coronal plane was evaluated while the participant performed adduction/abduction. The "desired joint angles" are the angles computed by the algorithm, and the "actual angles" are the angles reached by each joint motor. The motor angles at the end of each iteration from each motor were converted to joint angles of the hip and knee. These joint angles were compared to the desired joint angles at every given time point. The accuracy in sagittal plane was evaluated using a forward kinematics algorithm developed to obtain the X and Y positions of the foot. This position was in turn compared with the desired X and Y positions (X and Y position computed using the admittance control) to evaluate the accuracy of the inverse kinematics algorithm.

A Pearson's r correlation was performed to quantify the similarity between the actual and desired joint angles (hip flexion/extension, knee flexion/extension, and hip adduction/abduction) and Cartesian positions (X, Y, and Z positions).

The average time delay was computed as the iteration time (time required to move all the joints by the motor from the time the forces were applied by the user).

Evaluation of Gait Using the Control Mechanism

After validating the accuracy of the experimental apparatus, data were collected for an extended study evaluating the control mechanism using seven naïve participants who controlled the gait of the biped on a treadmill using control mechanism.

Participants

The study included seven naïve participants (2 male and 5 female) for biped walking and one reference participant (control) from whom we collected data on human gait. All participants were between ages 18 and 35, with fully functional upper and lower extremities. Exclusion criteria included any disability to the upper or lower extremities or inability to perform normal gait. The study was approved by the NJIT IRB and the experiment was performed with the participants' consent.

Experimental Setup

The experimental setup included a Pro-form J6 treadmill around which a custom frame was built using 80–20 aluminum to support the biped. The frame allowed the users to have complete view of the treadmill and the robot. An Optitrack Trio motion capture system was used to record the biped gait as well as the reference participant gait. As the treadmill was designed for human use, its lowest speed would not accommodate the small-sized robot, thus its speed was reduced when used for biped walking by adding a power resistor in series with the motor. Optitrack markers were placed on the hip, knee, and ankle of both the legs to track the biped gait and the reference participant gait.

Biped Walking

The biped was placed on the treadmill and each participant was seated in a comfortable chair behind the treadmill. The participants were instructed to control the gait of the biped during each trial by applying small forces to the pole extending from the sensor on each leg in the direction of the intended movement. The study consisted of eight trials. Each trial lasted 1 min, followed by a 30 s rest. The speed of the treadmill during each trial was varied as shown in **Table 1**. The speed variations for the biped were 0.1 (low), 0.2 (medium), and 0.3 (high) mph.

The participants performed familiarization sessions before the start of the actual session and those data were not included in the analysis. The first familiarization session was performed without the treadmill for 1 min, where the participants controlled the leg of robot in the air to get accustomed to kinematics of the leg. The second familiarization session included eight trials, where each trail lasted 1 min and was performed on the treadmill with the lowest speed. The third familiarization session included controlling the biped at different speeds for a minute each, as shown in **Table 1**.

The participant from whom the reference gait data were collected for one trial used the same treadmill at a self-selected speed for comfortable walking.

Data Analysis

Horizontal and vertical trajectories collected at 120 Hz of the ankle, hip and knee were filtered using a 4th order, zero-lag Butterworth low-pass filter. The filtered data were used for further analysis. The data were further divided into gait cycles.

Spatial and temporal symmetry

The foot trajectories in the sagittal plane by 7 participants and 1 reference participant were evaluated for the effectiveness of the control using hand trajectories using temporal and spatial symmetry outcomes.

The swing and stance time of each foot during each gait cycle was computed, and equation 8 was used to compute the temporal

symmetry (Patterson et al., 2008). Similarly step length and step height of each foot were computed for each gait cycle, and equation 9 and 10 were used to compute spatial and step height symmetry (Patterson et al., 2008). The average temporal, spatial, and step height symmetries were computed for all participants in each trial.

Statistical analysis was performed on all trials across the seven participants. Shapiro-Wilk test ($p > 0.05$) of normality showed that data were normal for spatial and temporal symmetry. Repeated measures analysis of variance (ANOVA) was performed on the spatial and temporal symmetry, respectively to determine the effect of change in speed on the spatial and temporal symmetry, respectively. Further, a Greenhouse-Geisser test was performed, since the data showed significance with Mauchly's test for sphericity. Shapiro-Wilk test ($p < 0.05$) of normality showed that data were not normal for step height symmetry. Hence, Friedman Test was used to determine the difference between different trials.

$$\text{Temporal swing stance symmetry} = (\text{swing time})/(\text{stance time})$$

$$\text{Overall temporal symmetry} \quad (8a)$$

$$= \left(\frac{\text{Right temporal swing stance symmetry}}{\text{Left temporal swing stance symmetry}} \right) \quad (8b)$$

$$\text{Spatial symmetry} = \left(\frac{\text{Right step length}}{\text{Left step length}} \right) \quad (9)$$

$$\text{Step Height symmetry} = \left(\frac{\text{Right step height}}{\text{Left step height}} \right) \quad (10)$$

Duty cycle

The percentage of stance and swing phase for each gait cycle was calculated using equations 11, 12, and 13. The average duty cycle of all gait cycles was computed for all participants in each trial and for the reference participant.

Statistical Analysis was performed on all trials across the seven participants. Shapiro-Wilk test ($p > 0.05$) of normality showed that data were normal. Mixed design analysis of variance (ANOVA) was performed on the stance and swing duty cycle, respectively to determine the effect of change in speed as well difference between left and right leg on the stance and swing duty cycle, respectively. The Greenhouse-Geisser test was used, since the data showed significance with Mauchly's test for sphericity to determine the effect of change in speed.

$$\text{Duty cycle} = \text{Stance Phase} + \text{Swing Phase} \quad (11)$$

$$\text{Stance Phase\%} = 100 * \text{Stance phase/Duty Cycle} \quad (12)$$

$$\text{Swing Phase\%} = 100 * \text{Swing phase/Duty Cycle} \quad (13)$$

Joint angles

The joint angles of hip and knee of both the legs of the biped robot walking for all participants were computed from the filtered Cartesian position from the Optitrack data using inverse kinematics. The joint angles were also computed for the gait of the single reference participant.

We statistically compared the similarity of the hip and knee angles of all seven participants with those of the reference

TABLE 1 | Speed of treadmill for each trial.

Trial	1	2	3	4	5	6	7	8
Speed	Medium	Medium	High	Low	Medium	High	Low	Medium

participant by computing their Pearson's r correlation after the data had been time-warped to allow a direct comparison (Kianimajd et al., 2017). We followed the method described in La Scaleia et al. (2014).

User feedback

Subjective user feedback was obtained from all 7 participants after completing the study. The following questions elicited user experience of the control technique and the responses to each were averaged across all participants.

1. Was it easy, moderate or difficult to use hand movements as control? 0 being easy and 10 being difficult.
2. How tired were your hands after each session? 0 being not tired at all and 10 being very tired.
3. Was using hands to the control the leg intuitive? 0 being least intuitive and 10 being very intuitive.
4. How much force was required to move the leg in the direction intended? 0 being least force and 10 being great force.

5. Did you feel the haptic feedback every time foot made contact with the floor? Yes or No.

RESULTS

Accuracy of the Foot Positions and Joint Angles

Figures 5A–C show the actual and desired Cartesian positions of X, Y (sagittal plane), and Z (coronal plane), respectively, for a single evaluator of the control mechanism of the robot. The results exhibit minimal positional lag. This is quantitatively shown in Table 2, where the mean positional lag (difference between actual and desired position) is <1 cm in the X, Y, and Z-directions, with Pearson's r showing high correlation between the desired and the actual Cartesian positions in X (right $r = 0.9954$, $p < 0.05$, left $r = 0.9972$, $p < 0.05$), Y (left $r = 0.9995$, $p < 0.05$, right $r = 0.9986$, $p < 0.05$), and Z (left $r = 0.9979$, $p < 0.05$). This shows the accuracy of the control algorithm.

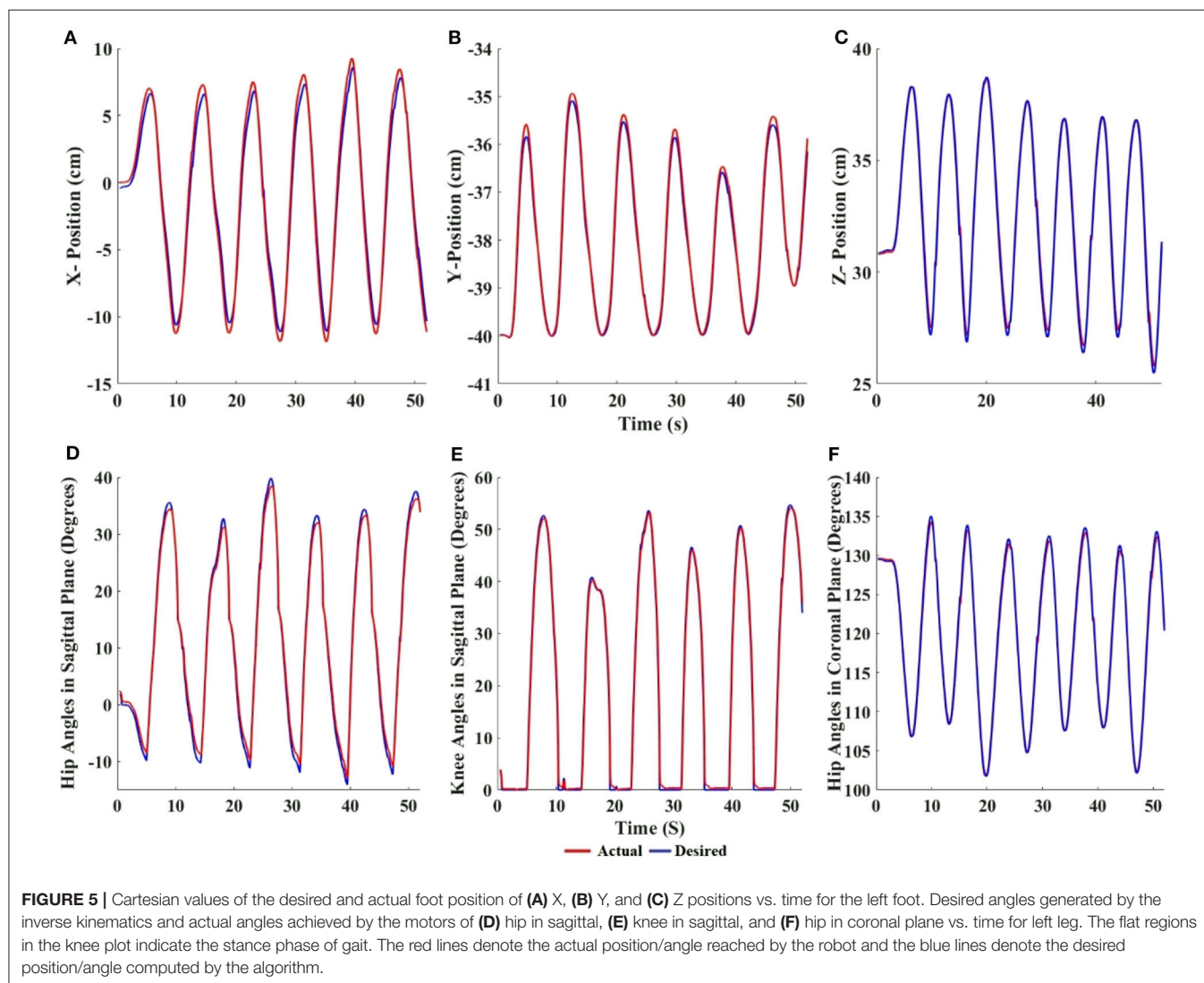


TABLE 2 | The table shows Mean \pm Std.

ERROR IN ANGLE	
Right—hip flexion/extension (degrees)	1.02 \pm 0.006
Left—hip flexion/extension (degrees)	0.81 \pm 0.006
Right—knee flexion/extension (degrees)	0.91 \pm 0.011
Left—knee flexion/extension (degrees)	1.021 \pm 0.011
Left—hip abduction/adduction (degrees)	0.55 \pm 0.003
ERROR IN POSITION	
Right—X position (cm)	0.68 \pm 0.005
Left—X position (cm)	0.54 \pm 0.004
Right—Y position (cm)	0.10 \pm 0.0008
Left—Y position (cm)	0.13 \pm 0.001
Left—Z position (cm)	0.23 \pm 0.002
Time delay (s)	0.008 \pm 0.0002

Error of the (a) difference between actual and desired position (error in position) in the left and right foot in X and Y direction and in the left foot in Z direction, (b) difference between actual and desired hip and knee angle in sagittal plane for right and left leg and hip angle in coronal plane for left leg (error in angle), and (c) time delay (time for each iteration of the loop) to reach the actual position based on user input force.

Figures 5D–F show the accuracy of the impedance control of the hip, knee (in the sagittal plane), and the hip (in the coronal plane), respectively. The actual joint angles follow the desired joint angles with minimal angular lag. This is quantitatively shown in **Table 2**, where the angular lag (difference between actual and desired angles) in the hip and knee (sagittal plane), and the hip (coronal plane) is $<1^\circ$, and Pearson's r showed that correlation was high between desired and actual joint angles in hip flexion/extension (right = 0.9985, $p < 0.05$, left = 0.9984, $p < 0.05$), knee flexion/extension (left = 0.9983, $p < 0.05$, right = 0.9978, $p < 0.05$), and hip abduction/adduction (left = 0.9982, $p < 0.05$). This shows the accuracy of the impedance control.

Taken together, the results show that the biped's foot position reaches the desired position of the user with minimal lag. The time delay or control loop time (time required to move all the joints by the motor from the time the forces were applied by the user) was <10 ms (**Table 2**). Studies have shown that a control loop frequency of 100 Hz is sufficient for human operators to feel smooth, nearly passive, movements of a robot (Van Der Linde et al., 2002). The maximum error in the Cartesian position is <1 cm, and the error in joint angles is $<1^\circ$ (**Table 2**). These results validate that our experimental control method and robot are appropriate for the multi-participant experiments.

Spatial and Temporal Symmetry

Figures 6A–C show the overall temporal, spatial and step height symmetry, respectively, for 7 participants and 1 reference participant. All symmetries are close to 1, irrespective of speed variations, indicating that the users were controlling the biped with a bilaterally symmetrical gait. Repeated measures ANOVA shows no significant difference between trials, indicating that speed did not affect the spatial ($p > 0.05$, $F = 0.796$) and temporal ($p > 0.05$, $F = 0.424$) symmetry. In addition, Cohen's d effect size shows a low effect for both spatial (effect size = 0.21) and temporal (effect size = 0.27) symmetry, again signifying that

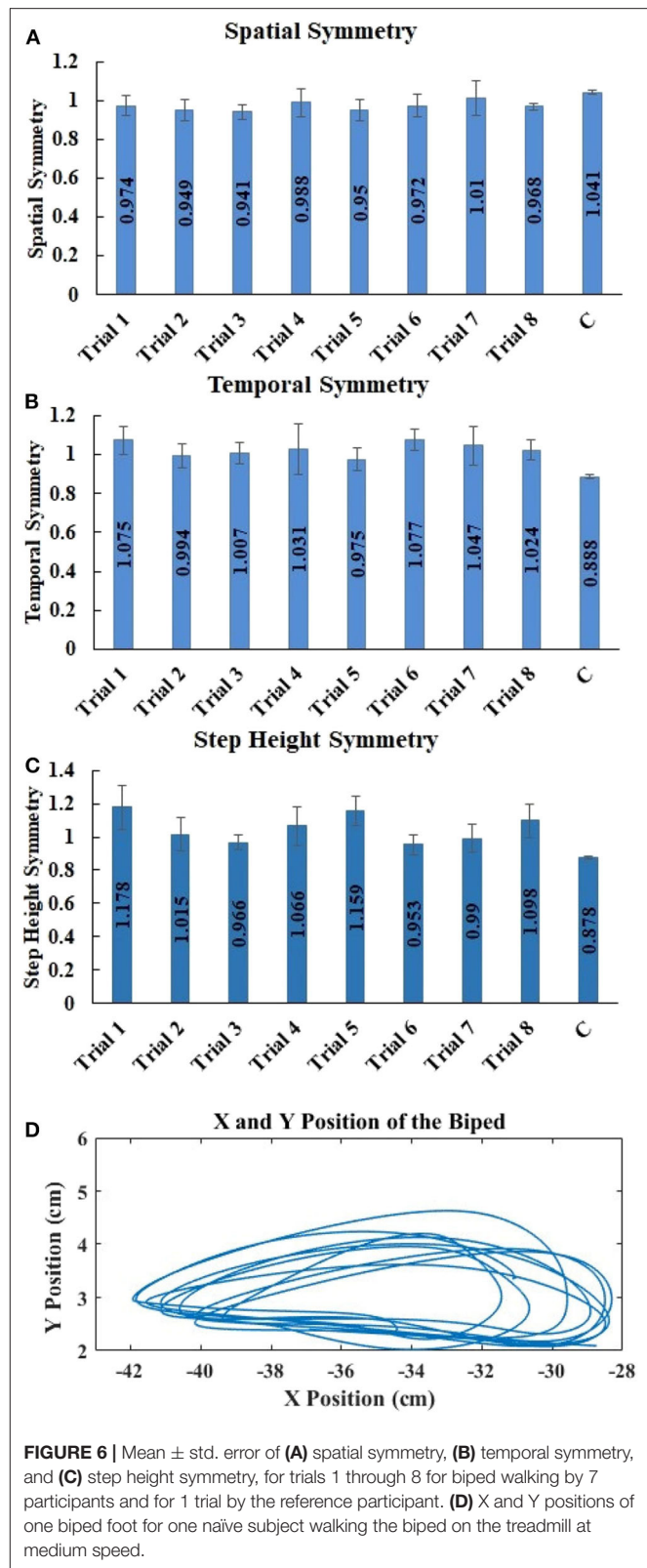


FIGURE 6 | Mean \pm std. error of (A) spatial symmetry, (B) temporal symmetry, and (C) step height symmetry, for trials 1 through 8 for biped walking by 7 participants and for 1 trial by the reference participant. (D) X and Y positions of one biped foot for one naïve subject walking the biped on the treadmill at medium speed.

difference between trials is very low. Friedman's test shows no significant difference between trials, indicating that speed did not affect the step height symmetry ($p > 0.05$, chi-square =

8.095). Kendall's W effect size shows a low effect for step height symmetry (effect size = 0.165), again signifying that difference between trials is very low.

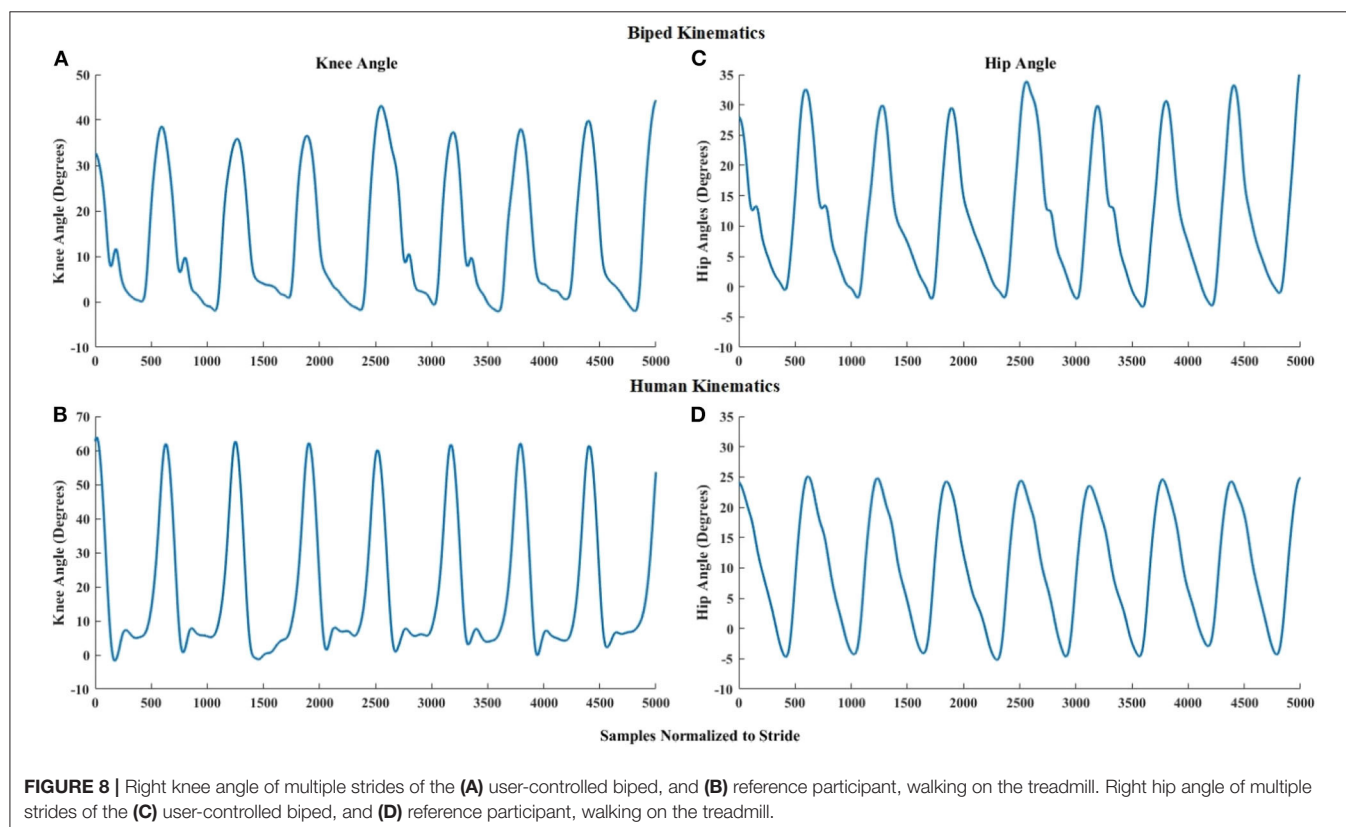
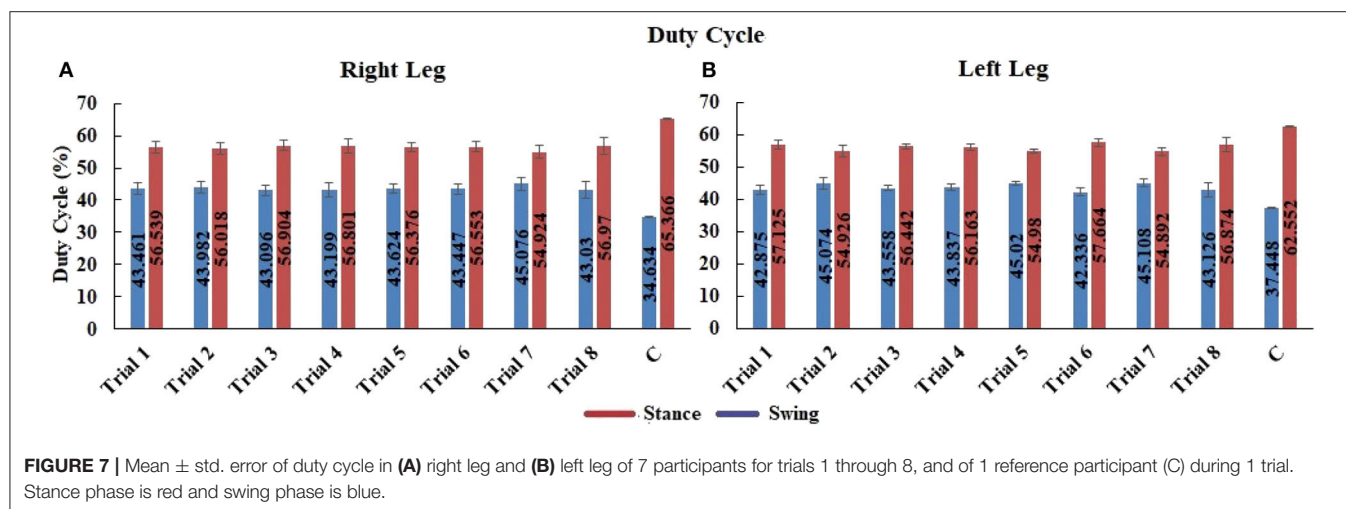
Duty Cycle

Figure 7 shows the average percentage of swing and stance phase in the gait cycle of all 7 participants for trials 1 through 8. In human gait, typical swing phase is ~40% and stance phase is 60% of the gait cycle (Winter, 2009). Our robot gait cycle across all trials was slightly over 40% swing and slightly below 60% stance. Mixed design ANOVA shows no significant difference between

either trials or legs. This indicates that speed did not affect swing ($p > 0.05$, between trials $F = 1.177$) or stance ($p > 0.05$, between trials $F = 1.177$), and that swing ($p > 0.05$, between legs $F = 0.022$) and stance ($p > 0.05$, between legs $F = 0.022$) were similar in both the legs.

Comparison of Biped and Human Gait Trajectories in the Sagittal Plane

Figure 8 shows a visual comparison of the hip and knee angles of a reference participant and the corresponding biped angles. The visual appearance of biped and reference participant hip



and knee angles in **Figure 8** is quite similar, with the human knee slightly flexing during stance. We attribute this to the knee accommodation of foot angle changes at toe-off by the human walker, while the biped maintained the foot parallel to the ground. We observe significant high positive correlations between the joint angles of the biped (for 7 participants) and the reference participant: For the knee, Pearson's mean $r = 0.7770$, $\text{std} \pm 0.0953$, with $p < 0.005$. For the hip, Pearson's mean $r = 0.9968$, $\text{std} \pm 0.0926$, with $p < 0.005$. This confirms that biped walking produces human-like knee and hip joint trajectories.

User Feedback

Participant responses show that hand control was quite easy and intuitive (**Table 3**). The participants required little force and did not get tired from using the control method (**Table 3**). Six out of the seven participants responded that they felt the ground impact with their hands.

DISCUSSION

Lower extremity exoskeletons show potential for restoring ambulation in individuals with paraplegia due to spinal cord injury. Currently, many lower extremity exoskeletons produce a preprogrammed gait that can be initiated by the user, but not completely controlled by the user. Thus, users have limited control over their gait (i.e., step length, width, and speed), and little feedback of foot placement and ground contact. In this paper, we proposed a novel control mechanism for lower extremity exoskeletons to address these shortcomings; allowing the users to control their gait in real-time, as well as receiving haptic feedback. The accuracy and efficacy of the control mechanism was evaluated using the following outcome measures: accuracy of the foot position and joint angles; time delay between user-desired and actual robot kinematics; temporal, spatial, and step height symmetry; duty cycle of stance and swing phases; and similarity of biped hip and knee angles to those of human gait.

Our results demonstrate the effectiveness of the control mechanism, which allows the user to interactively control both legs of a $\frac{1}{2}$ scale robot to produce a gait trajectory closely resembling human gait. As required for smooth real-time human-robot interaction (Van Der Linde et al., 2002), the time delay of the control mechanism is below 10 ms; ensuring smooth and stable movement. The difference between user-desired and actual robot Cartesian position and joint angles were <1 cm and 1° , respectively; showing that real-time accurate trajectories can be obtained over time by our system.

Admittance control provides the user with the following advantages: one-to-one correspondence between hand and foot

movement; force amplification; intuitive control (as the user applies desired force in the intended direction of movement); and accurate time-varying trajectory control (the leg moves in the direction of the force) (Glosser and Newman, 2002; Van Der Linde et al., 2002). Research has shown that admittance control is an effective strategy for human-robot interaction, and that it requires a minimum of 100 Hz for acceptable human interaction (Glosser and Newman, 2002; Van Der Linde et al., 2002); which we have achieved.

Human gait is a rhythmic movement that is symmetrical but out-of-phase between the two legs. Hence, an effective exoskeleton control strategy should be able to reproduce the same pattern of movement over a period of time, as well as coordinate inter-limb movement (Vaughan et al., 1999; Pearson, 2003). Inter-limb coordination or symmetry is the ability to maintain temporal and spatial symmetry, which results in healthy gait (Patterson et al., 2008). Temporal and spatial symmetry close to "1," signifies that both limbs are performing a symmetrical movement (Patterson et al., 2008). Our analysis shows that the participants controlling the biped were able to maintain inter-limb temporal, spatial, and step height symmetry close to 1 across all trials; irrespective of speed variations, and similar to that observed in human gait. Studies have shown that there is a correlation between large deviations in temporal & spatial symmetry away from 1 and falls & reduced walking speed (Balasubramanian et al., 2007; Patterson et al., 2008). Thus, we can conclude that our biped control mechanism will promote stable and safe human-exoskeleton walking. Our robot gait cycle has an average swing phase of just over 40% and a stance phase of just under 60%, as shown in **Figure 7**, across all trials. The deviation from the normal human gait cycle is small and likely due to the biped performing a flat-footed gait, as the foot is constrained to remain parallel to the ground, resulting in a shorter stance period. In addition, the percentage of time spent in stance and swing phase was the same between both legs, further indicating consistent temporal characteristics.

The results show that the joint angles produced by the biped (**Figures 5D–F**) are within the range of healthy biological gait in the sagittal plane (Winter, 2009), and that the joint angles of the reference participant and the biped are similar.

The relative horizontal and vertical excursions of biped walking were consistent with our earlier work on the benefits of haptic feedback to the hands for controlling the position of virtual feet (Karunakaran et al., 2017). More importantly, they have the same appearance as similar measures captured from unimpaired biological gait. **Figure 6D** shows that the right foot data from the biped (plotted as X and Y positions) bears a strong resemblance to unimpaired human foot data (Meesen et al., 2006). The user

TABLE 3 | The table shows the mean \pm std. error for user feedback questionnaire.

Question	Ease of using hand to control biped	Tiredness	Intuitiveness of hand control	Force required to move hands	Haptic feedback every time foot made contact to ground
Options	0—easy to 10—difficult	0—not tired to 10—very tired	0—least intuitive to 10—very intuitive	0—least force to 10—large force	Yes or no
Participant responses	3.29 \pm 0.52	1.14 \pm 0.59	7.43 \pm 1.19	1.86 \pm 0.59	6 participants answered yes and 1 participant answered no

feedback questionnaire indicated that biped control was easy, intuitive, and required only minimal force.

Current commercial exoskeletons are generally slow, with small step lengths and step heights (Kozłowski et al., 2015). They usually rely on control mechanisms that initiate each step separately, which results in a delay between steps (Dellon and Matsuoka, 2007; Strickland, 2012)^{1,2} and hence a prolonged stance phase (Esquenazi et al., 2012)¹. Our control method, on the other hand, provides continuous gait (smooth transition from swing to stance) with no delay between steps. It also provides the user with the ability to vary step length and height, based on the required speed. Thus, it produces a more natural gait in terms of temporal & spatial characteristics.

This preliminary work shows the feasibility of our algorithm to control exoskeleton kinematics and produce symmetrical gait patterns, using hands as a controller. However, there are several limitations that will need to be addressed in future work. This paper does not address balance, which will be addressed in a separate future publication. We also acknowledge that the benefits of our control mechanism must be thoroughly evaluated with participants walking independently in a full-scale exoskeleton. A wearable exoskeleton is under development for this purpose (Al Rashdan, 2016; Androwis et al., 2017).

While our work has focused on a specific SCI population of users, we are excited about expansion of the technique to individuals with other disabling conditions, such as people with diplegic cerebral palsy who have sufficient arm control to operate our trekking poles. We also see potential for the application of variations of our control mechanism in individuals with stroke and traumatic brain injury (both for assistance with ambulation, as well as for gait therapy), and multiple sclerosis.

CONCLUSIONS

We have developed and tested an admittance-control-based user-robot control strategy that allows the user to control foot trajectories with hand-generated forces and hand-sensed foot

kinematics, and thus gait in real-time. This new approach has the potential to be used with a wearable rehabilitation exoskeleton, as a control mechanism that provides users with lower leg disability complete control over gait. When implemented with wearable exoskeletons, our method has the potential to greatly improve community ambulation in individuals with lower extremity paralysis.

DATA AVAILABILITY STATEMENT

The datasets presented in this article are not available because New Jersey Institute of Technology Review Board approval does not include data sharing with external institutions.

ETHICS STATEMENT

The studies involving human participants were reviewed and approved by New Jersey Institute of Technology. The patients/participants provided their written informed consent to participate in this study.

AUTHOR CONTRIBUTIONS

KK designed the algorithm, evaluated the design, analyzed the data, and drafted and finalized the manuscript. KA assisted with the design. GA reviewed the manuscript. RF assisted with the design, revised, reviewed, and finalized the manuscript. All authors contributed to the article and approved the submitted version.

FUNDING

This work was supported by Gustavus and Louise Pfeiffer Research Foundation, and the Rehabilitation Engineering Research Center on Wearable Robots (NIDILRR grant 90RE5021).

REFERENCES

- Al Rashdan, A. (2016). *Hand Control of Bipedal Balance in Quiet Standing: Implementations for Lower Extremity Exoskeleton*. Newark, NJ: New Jersey Institute of Technology.
- Androwis, G. J., Karunakaran, K., Nunez, E., Michael, P., Yue, G., and Foulds, R. A. (2017). "Research and development of new generation robotic exoskeleton for over ground walking in individuals with mobility disorders (Novel design and control)," in *2017 International Symposium on Wearable Robotics and Rehabilitation* (Houston, TX: WeRob), 1–2. doi: 10.1109/WEROB.2017.8383864
- Androwis, G. J., Kwasnica, M. A., Niewrzol, P., Popok, P., Fakhoury, F. N., Sandroff, B. M., et al. (2019). Mobility and cognitive improvements resulted from overground robotic exoskeleton gait-training in persons with MS. *Conf. Proc. IEEE Eng. Med. Biol. Soc.* 2019, 4454–4457. doi: 10.1109/EMBC.2019.8857029
- Armstrong, T. J., Young, J., Woolley, C., Ashton-Miller, J., and Kim, H. (2009). Biomechanical aspects of fixed ladder climbing: style, ladder tilt and carrying. *Proc. Hum. Factors Ergon. Soc.* 53, 935–939. doi: 10.1177/154193120905301417
- Balasubramanian, C. K., Bowden, M. G., Neptune, R. R., and Kautz, S. A. (2007). Relationship between step length asymmetry and walking performance in subjects with chronic hemiparesis. *Arch. Phys. Med. Rehabil.* 88, 43–49. doi: 10.1016/j.apmr.2006.10.004
- Birmingham, C., Noesner, M., and Foulds, R. (2003). "Haptic controlled functional electrical stimulation of the lower extremities," in *Proceedings of the IEEE Annual Northeast Bioengineering Conference, NEBEC* (Newark, NJ), 287–288. doi: 10.1109/NEBC.2003.1216107
- Canela, M., del Ama, A. J., and Pons, J. L. (2013). "Design of a pediatric exoskeleton for the rehabilitation of the physical disabilities caused by cerebral palsy," in *Biosystems & Biorobotic*, Vol. 1, eds J. Pons, D. Torricelli, and M. Pajaro (Berlin; Heidelberg: Springer), 255–258. doi: 10.1007/978-3-642-34546-3_40
- Contreras-Vidal, J. L., Bhagat, N. A., Brantley, J., Cruz-Garza, J. G., He, Y., Manley, Q., et al. (2016). Powered exoskeletons for bipedal locomotion after spinal cord injury. *J. Neural Eng.* 13:031001. doi: 10.1088/1741-2560/13/3/031001
- Dellon, B., and Matsuoka, Y. (2007). Prosthetics, exoskeletons, and rehabilitation [grand challenges of robotics]. *IEEE Robot. Autom. Mag.* 14, 30–34. doi: 10.1109/MRA.2007.339622

- Dollar, A. M., and Herr, H. (2008). Lower extremity exoskeletons and active orthoses: challenges and state-of-the-art. *IEEE Trans. Robot.* 24, 144–158. doi: 10.1109/TRO.2008.915453
- Durandau, G., Farina, D., Asín-Prieto, G., Dimbwadyo-Terrer, I., Lerma-Lara, S., Pons, J. L., et al. (2019). Voluntary control of wearable robotic exoskeletons by patients with paresis via neuromechanical modeling. *J. Neuroeng. Rehabil.* 16:91. doi: 10.1186/s12984-019-0559-z
- Esquenazi, A., Talaty, M., Packel, A., and Saulino, M. (2012). The Rewalk powered exoskeleton to restore ambulatory function to individuals with thoracic-level motor-complete spinal cord injury. *Am. J. Phys. Med. Rehabil.* 9, 911–921. doi: 10.1097/PHM.0b013e318269d9a3
- Fang, J., Xie, Q., Yang, G. Y., and Xie, L. (2017). Development and feasibility assessment of a rotational orthosis for walking with arm swing. *Front. Neurosci.* 11:32. doi: 10.3389/fnins.2017.00032
- Farris, R. J. (2012). *Design of a Powered Lower-Limb Exoskeleton and Control for Gait Assistance in Paraplegics*. Nashville, TN: Vanderbilt University.
- Farris, R. J., Quintero, H. A., and Goldfarb, M. (2012). “Performance evaluation of a lower limb exoskeleton for stair ascent and descent with Paraplegia,” in *Proceedings of the Annual International Conference of the IEEE Engineering in Medicine and Biology Society, EMBS* (San Diego, CA), 1908–1911. doi: 10.1109/EMBC.2012.6346326
- Ferris, D. P., and Lewis, C. L. (2009). “Robotic lower limb exoskeletons using proportional myoelectric control,” in *Proceedings of the 31st Annual International Conference of the IEEE Engineering in Medicine and Biology Society: Engineering the Future of Biomedicine, EMBC 2009* (Minneapolis, MN), 2119–2124. doi: 10.1109/IEMBS.2009.5333984
- Ford, M. P., Wagenaar, R. C., and Newell, K. M. (2007). Arm constraint and walking in healthy adults. *Gait Posture* 26, 135–141. doi: 10.1016/j.gaitpost.2006.08.008
- Gancet, J., Ilzkovitz, M., Motard, E., Nevatia, Y., Letier, P., de Weerd, D., et al. (2012). “MINDWALKER: Going one step further with assistive lower limbs exoskeleton for SCI condition subjects,” in *Proceedings of the IEEE RAS and EMBS International Conference on Biomedical Robotics and Biomechatronics* (Rome), 1794–1800. doi: 10.1109/BioRob.2012.6290688
- Glosser, G. D., and Newman, W. S. (2002). “The implementation of a natural admittance controller on an industrial manipulator,” in *Proceedings of the 1994 IEEE International Conference on Robotics and Automation*, 1209–1215.
- Haidegger, T., Benyő, B., Kovács, L., and Benyő, Z. (2009). Force sensing and force control for surgical robots. *IFAC Proc. Vol.* 42, 401–406. doi: 10.3182/20090812-3-DK-2006.0035
- Hayashi, T., Kawamoto, H., and Sankai, Y. (2005). “Control method of robot suit HAL working as operator’s muscle using biological and dynamical information,” in *2005 IEEE/RSJ International Conference on Intelligent Robots and Systems, IROS* (Edmonton, Alta, AB), 3063–3068. doi: 10.1109/IROS.2005.1545505
- Hamill, J., Knudsen, K. M., Derrick, T. R. (2013). *Biological Basis of Human Movement, 4th Ed.* Baltimore, MD: Lippincott Williams & Wilkins.
- Karunakaran, K., Abbruzzese, K., Xu, H., Ehrenberg, N., and Foulds, R. (2014). “Haptic proprioception in a virtual locomotor task. *Conf. IEEE Eng. Med. Biol. Soc. IEEE Eng. Med. Biol. Soc.* 2014, 3594–3597. doi: 10.1109/EMBC.2014.6944400
- Karunakaran, K., Ehrenberg, N., Cheng, J., and Nolan, K. J. (2019). “Effects of robotic exoskeleton gait training on an adolescent with brain injury,” in *IEEE 41th Annual International Conference on Engineering in Medicine and Biology Society (EMBC)* (Berlin), 4445–4448. doi: 10.1109/EMBC.2019.8856787
- Karunakaran, K. K., Abbruzzese, K. M., Xu, H., and Foulds, R. A. (2017). The importance of haptics in generating exoskeleton gait trajectory using alternate motor inputs. *IEEE Trans. Neural Syst. Rehabil. Eng.* 25, 2328–2335. doi: 10.1109/TNSRE.2017.2726538
- Kianimajd, A., Ruano, M. G., Carvalho, P., Henriques, J., Rocha, T., Paredes, S., et al. (2017). Comparison of different methods of measuring similarity in physiologic time series. *IFAC-PapersOnLine* 50, 11005–11010. doi: 10.1016/j.ifacol.2017.08.2479
- Kilicarslan, A., Prasad, S., Grossman, R. G., and Contreras-Vidal, J. L. (2013). “High accuracy decoding of user intentions using EEG to control a lower-body exoskeleton,” in *Proceedings of the Annual International Conference of the IEEE Engineering in Medicine and Biology Society, EMBS* (Osaka), 5606–5609. doi: 10.1109/EMBC.2013.6610821
- Kozlowski, A. J., Bryce, T. N., and Dijkers, M. P. (2015). Time and effort required by persons with spinal cord injury to learn to use a powered exoskeleton for assisted walking. *Top. Spinal Cord Inj. Rehabil.* 21, 110–121. doi: 10.1310/sci2102-110
- Kozlowski, A. J., Fabian, M., Lad, D., and Delgado, A. D. (2017). Feasibility and safety of a powered exoskeleton for assisted walking for persons with multiple sclerosis: a single-group preliminary study. *Arch. Phys. Med. Rehabil.* 98, 1300–1307. doi: 10.1016/j.apmr.2017.02.010
- Kwak, N. S., Müller, K. R., and Lee, S. W. (2015). A lower limb exoskeleton control system based on steady state visual evoked potentials. *J. Neural Eng.* 12:056009. doi: 10.1088/1741-2560/12/5/056009
- La Scaleia, V., Sylos-Labini, F., Hoellinger, T., Wang, L., Cheron, G., Lacquaniti, F., et al. (2014). Control of leg movements driven by EMG activity of shoulder muscles. *Front. Hum. Neurosci.* 8:838. doi: 10.3389/fnhum.2014.00838
- Lebedev, M. A., and Nicolelis, M. A. L. (2017). Brain-machine interfaces: from basic science to neuroprostheses and neurorehabilitation. *Physiol. Rev.* 97, 767–837. doi: 10.1152/physrev.00027.2016
- Lee, S., and Sankai, Y. (2002). Power assist control for leg with HAL-3 based on virtual torque and impedance adjustment. *IEEE Int. Conf. Syst. Man Cybern.* 4:6. doi: 10.1109/ICSMC.2002.1173329
- Lee, S., and Sankai, Y. (2003). Power assist control for walking aid with HAL-3 based on EMG and impedance adjustment around knee joint. *IEEE/RSJ Int. Conf. Intell. Robot. Syst.* 2, 1499–1504. doi: 10.1109/IRDS.2002.1043967
- Lerner, Z. F., Damiano, D. L., Park, H. S., Gravunder, A. J., and Bulea, T. C. (2017). A robotic exoskeleton for treatment of crouch gait in children with cerebral palsy: design and initial application. *IEEE Trans. Neural Syst. Rehabil. Eng.* 25, 650–659. doi: 10.1109/TNSRE.2016.2595501
- López-Larraz, E., Trincado-Alonso, F., Rajasekaran, V., Pérez-Nombela, S., del-Ama, A. J., Aranda, J., et al. (2016). Control of an ambulatory exoskeleton with a brain-machine interface for spinal cord injury gait rehabilitation. *Front. Neurosci.* 10:359. doi: 10.3389/fnins.2016.00359
- Meesen, R. L. J., Wenderoth, N., Temprado, J. J., Summers, J. J., and Swinnen, S. P. (2006). The coalition of constraints during coordination of the ipsilateral and heterolateral limbs. *Exp. Brain Res.* 174, 367–375. doi: 10.1007/s00221-006-0471-1
- Meyns, P., Bruijn, S. M., and Duysens, J. (2013). The how and why of arm swing during human walking. *Gait Posture* 38, 555–562. doi: 10.1016/j.gaitpost.2013.02.006
- Murray, S. A., Ha, K. H., Hartigan, C., and Goldfarb, M. (2015). An assistive control approach for a lower-limb exoskeleton to facilitate recovery of walking following stroke. *IEEE Trans. Neural Syst. Rehabil. Eng.* 23, 441–449. doi: 10.1109/TNSRE.2014.2346193
- Nicolelis, M. A. L. (2003). Brain-machine interfaces to restore motor function and probe neural circuits. *Nat. Rev. Neurosci.* 4, 417–422. doi: 10.1038/nrn1105
- Patané, F., Rossi, S., Del Sette, F., Taborri, J., and Cappa, P. (2017). WAKE-up exoskeleton to assist children with cerebral palsy: design and preliminary evaluation in level walking. *IEEE Trans. Neural Syst. Rehabil. Eng.* 25, 906–916. doi: 10.1109/TNSRE.2017.2651404
- Patterson, K. K., Parafianowicz, I., Danells, C. J., Closson, V., Verrier, M. C., Richard Staines, W., et al. (2008). Gait asymmetry in community-ambulating stroke survivors. *Arch. Phys. Med. Rehabil.* 89, 304–310. doi: 10.1016/j.apmr.2007.08.142
- Pearson, K. G. (2003). Common principles of motor control in vertebrates and invertebrates. *Annu. Rev.*

- Neurosci.* 16, 265–297. doi: 10.1146/annurev.ne.16.030193.001405
- Quintero, H. A., Farris, R. J., and Goldfarb, M. (2012). A method for the autonomous control of lower limb exoskeletons for persons with Paraplegia. *J. Med. Device.* 6:041003. doi: 10.1115/1.4007181
- DeMarco, R., and Foulds, R. (2002). “Sensory-motor substitution for improved ambulation.” in *IEEE 28th Annual Northeast Bioengineering Conference* (Philadelphia, PA), 147–148.
- Shepherd Center (2020). *Understanding Spinal Cord Injury*. Available online at: <https://www.spinalinjury101.org/details> (accessed October 01, 2020).
- Strickland, E. (2012). Good-bye, wheelchair. *IEEE Spectr.* 49, 30–32. doi: 10.1109/MSPEC.2012.6117830
- Van Der Linde, R., Lammertse, P., and Frederiksen, E. B. (2002). “The HapticMaster, a new high-performance haptic interface,” in *Proceedings of EuroHaptic* (Edinburgh), 1–5.
- Van Riel, N. (2012). *Speeding Up Simulations of ODE Models in Matlab Using CVode and MEX Files*. Eindhoven, NL: Eindhoven University of Technology.
- Vaughan, C. L., Davis, B. L., O'Connor, J. C. (1999). “The three-dimensional and cyclic nature of gait.” in *Dynamics of Human Gait*, Vol. 168 (Cape Town: Kiboho Publishers), 16–17.
- Winter, D. A. (2009). *Biomechanics and Motor Control of Human Movement*. Hoboken, NJ: John Wiley & Sons. doi: 10.1002/9780470549148
- Conflict of Interest:** The research for this study was conducted when the authors were employed by NJIT. Currently, KA is now employed by the company Stryker Corporation, and RF consults at Really Useful Robots, LLC, in addition to being Professor Emeritus at NJIT. The companies had no role in the design of the study; in the collection, analyses, or interpretation of data; in the writing of the manuscript; or in the decision to publish the results.
- The remaining authors declare that the research was conducted in the absence of any commercial or financial relationships that could be construed as a potential conflict of interest.
- Copyright © 2020 Karunakaran, Abbruzzese, Androwis and Foulds. This is an open-access article distributed under the terms of the Creative Commons Attribution License (CC BY). The use, distribution or reproduction in other forums is permitted, provided the original author(s) and the copyright owner(s) are credited and that the original publication in this journal is cited, in accordance with accepted academic practice. No use, distribution or reproduction is permitted which does not comply with these terms.



Portable Take-Home System Enables Proportional Control and High-Resolution Data Logging With a Multi-Degree-of-Freedom Bionic Arm

Mark R. Brinton^{1†*}, Elliott Barcikowski², Tyler Davis³, Michael Paskett¹, Jacob A. George¹ and Gregory A. Clark¹

¹ Biomedical Engineering, University of Utah, Salt Lake City, UT, United States, ² Ripple Neuro, Salt Lake City, UT, United States, ³ Neurosurgery, University of Utah, Salt Lake City, UT, United States

OPEN ACCESS

Edited by:

Jan Veneman,
Hocoma, Switzerland

Reviewed by:

Strahinja Dosen,
Aalborg University, Denmark
Silvia Muceli,
Chalmers University of
Technology, Sweden

*Correspondence:

Mark R. Brinton
brintonm@etown.edu

†Present address:

Mark R. Brinton,
Engineering and Physics,
Elizabethtown College, Elizabethtown,
PA, United States

Specialty section:

This article was submitted to
Biomedical Robotics,
a section of the journal
Frontiers in Robotics and AI

Received: 04 May 2020

Accepted: 21 August 2020

Published: 25 September 2020

Citation:

Brinton MR, Barcikowski E, Davis T,
Paskett M, George JA and Clark GA
(2020) Portable Take-Home System
Enables Proportional Control and
High-Resolution Data Logging With a
Multi-Degree-of-Freedom Bionic Arm.
Front. Robot. AI 7:559034.
doi: 10.3389/frobt.2020.559034

This paper describes a portable, prosthetic control system and the first at-home use of a multi-degree-of-freedom, proportionally controlled bionic arm. The system uses a modified Kalman filter to provide 6 degree-of-freedom, real-time, proportional control. We describe (a) how the system trains motor control algorithms for use with an advanced bionic arm, and (b) the system's ability to record an unprecedented and comprehensive dataset of EMG, hand positions and force sensor values. Intact participants and a transradial amputee used the system to perform activities-of-daily-living, including bi-manual tasks, in the lab and at home. This technology enables at-home dexterous bionic arm use, and provides a high-temporal resolution description of daily use—essential information to determine clinical relevance and improve future research for advanced bionic arms.

Keywords: bionic arm, myoelectric prostheses, proportional control, Kalman filter, take-home

INTRODUCTION

Electromyography (EMG) from the residual forearm has been used to control commercially available and research-grade prosthetic arms (Kuiken et al., 2016; Hargrove et al., 2017; Ottobock, 2017; Touch Bionics Inc, 2017; Wendelken et al., 2017; George et al., 2018; Page et al., 2018; Perry et al., 2018; Mobius Bionics, 2020). Although research has demonstrated proportional control of multiple, independent degrees of freedom (DOFs) (Davis et al., 2016; George et al., 2018; Page et al., 2018), commercially available prostheses still suffer from a variety of limitations (Biddiss and Chau, 2007), including limited number of pre-determined grips (Touch Bionics Inc, 2017), temporal delay due to sequential inputs used to select grips (Ottobock, 2017; Mobius Bionics, 2020), fixed output force (e.g., from traditional classifier algorithms) (Resnik et al., 2018a), extensive training that lasts days to weeks (Resnik et al., 2017, 2018a, 2019), and non-intuitive methods of control [e.g., inertial measurement units (IMUs) on residual limb or feet] (Resnik et al., 2018b; Mobius Bionics, 2020).

Dexterous control of multiple DOFs, and the training associated with them, are not always amenable to deployment on portable systems with limited computational power, and as a result only a few pattern-recognition (i.e., classifiers) (Kuiken et al., 2016; Resnik et al., 2017; Mastinu et al., 2018; Simon et al., 2019) or direct control algorithms have been studied at home (Pasquina et al., 2015; Simon et al., 2019). A Kalman filter (Wu et al., 2006), modified with non-linear, *ad-hoc* adjustments (George et al., 2019a; Nieveen et al., in review) can provide a computationally efficient

approach (George et al., 2020c) to study proportionally and independently controlled multi-DOF prostheses at home. Proportional control algorithms enable realistic and life-like prosthetic control and can induce device embodiment in transradial amputees (Page et al., 2018).

High temporal resolution of the position and forces applied to the prosthesis is necessary to describe the interactive and refined movements made possible with proportionally controlled prostheses. These data are also necessary to describe key aspects of actual prosthesis use: revealing when objects were manipulated; whether movements were performed unilaterally or bilaterally (for bilateral amputees); which grasps were preferred; how often each DOF was used; and when new inter-digit collaborative movements were employed.

Preliminary at-home use of this portable, prosthetic control system, capable of providing six-DOF, real-time, proportional control was published previously (George et al., 2019a). Here we describe the portable system and the tasks completed at home in greater detail, including how the modified Kalman filter is trained and implemented on the portable system, as well as the system's ability to record an unprecedented dataset of EMG, hand positions, and force sensor values. This technology constitutes an important step toward the commercialization of dexterous bionic arms by demonstrating at-home use and the ability to record prosthesis use with high temporal resolution.

MATERIALS AND METHODS

Design Considerations

A portable take-home system designed to research advanced bionic arms should meet several criteria for optimal performance and data collection: (a) the system must accurately and efficiently control the prosthesis; (b) training of the control algorithm must not be too long or burdensome to prevent its daily use—and thus should include the ability to quickly load a previously trained control algorithm; (c) high-temporal-resolution data should be stored automatically so that researchers can study at-home use without influencing the users with in-person observation; and (d) the system must be easy to use and allow the user to adjust control preferences.

Accurate and Efficient Control

For accurate and efficient control, the system must be able to record EMG from the residual forearm, predict new kinematic positions, and send those positions to the prosthesis quickly with minimal or no perceived delay between the intention to move and the movement itself. Previous work in our lab has demonstrated responsive control of prostheses at update cycles of 33 ms (30 Hz) using a modified Kalman filter (Wendelken et al., 2017; George et al., 2018; Page et al., 2018; Kluger et al., 2019). The goal of this work was to implement these algorithms on a portable computer and provide position updates with minimal delay between the user intent (muscle activation) and the prosthesis movement. We have shown that updates at 33 ms provide responsive control and lead to embodiment of the physical prosthesis (Page et al., 2018). Updates at this speed are also within the optimal controller delay for prosthesis control (Farrell and Weir, 2007).

Fast Training for Daily Use

For daily use, training of the control algorithm should be intuitive and fast. The time required to train a control algorithm includes data collection while the participant mimics preprogrammed movements of the prosthesis (George et al., 2020d), and training of the control algorithm itself (e.g., training the modified Kalman filter matrices). When training, or retraining, is required, it should be as fast as possible to minimize the setup time prior to use. Lengthy setup and training could make advanced prostheses burdensome to incorporate into daily life and prevent their acceptance among amputees. The system should also allow reloading of a previously trained control algorithm on demand.

Comprehensive Record of Unsupervised Arm Use

A common approach to measure prosthesis use is to place IMUs on the prosthesis and record movement acceleration and angular velocity (Hargrove et al., 2017; Resnik et al., 2017, 2018b; Graczyk et al., 2018). However, this approach fails to discriminate between gross movements from the residual limb and actual movement of the prosthesis's hand and wrist. Video collection via body cameras can be used to record actual prosthesis use and other metrics (such as compensation strategies), but require storage of large video files and time-intensive *post-hoc* analyses (Spiers et al., 2017). Furthermore, the presence of a video camera reminds study participants they are being watched even though lab personnel are not physically present. However, with a portable system, prosthesis use at home can be studied by recording every movement for each DOF. By also recording the force applied to DOFs, interactive prosthesis use can be discerned from passive arm movements, such as those that might occur during walking or exploratory hand movements that are not functionally directed. Beyond describing total prosthesis use, this rich dataset can reveal detailed, refined movements and collaborative interactions between DOFs—including the force applied with each movement.

User-Friendly Control Adjustments

Finally, a prosthetic control system should be easy to use and allow adjustments to fit unique preferences. This includes a quick and simple approach to turn the system on, train the control algorithm and load a previously trained control algorithm. Control adjustments could also include flexibility to lock a DOF during dexterous tasks to prevent unwanted movements—for example locking the thumb and solely using the index finger could provide a more stable pinch. In addition, feedback from participants in our lab suggest the system should also provide users flexibility to operate specific DOFs (e.g., wrist) in a velocity-control mode (Kluger, 2019).

Hardware and Signal Acquisition

The components of the portable system are shown in **Figure 1**. The DEKA LUKE Arm (DEKA; Manchester NH, USA) has 6 DOFs including thumb (D1) adduction/abduction; D1 flexion/extension; index (D2) flexion/extension; coupled middle, ring, and pinky (D3–D5) flexion/extension; wrist flexion/extension, which also includes a slight radial and ulnar deviation, respectively; and wrist pronation/supination. It also

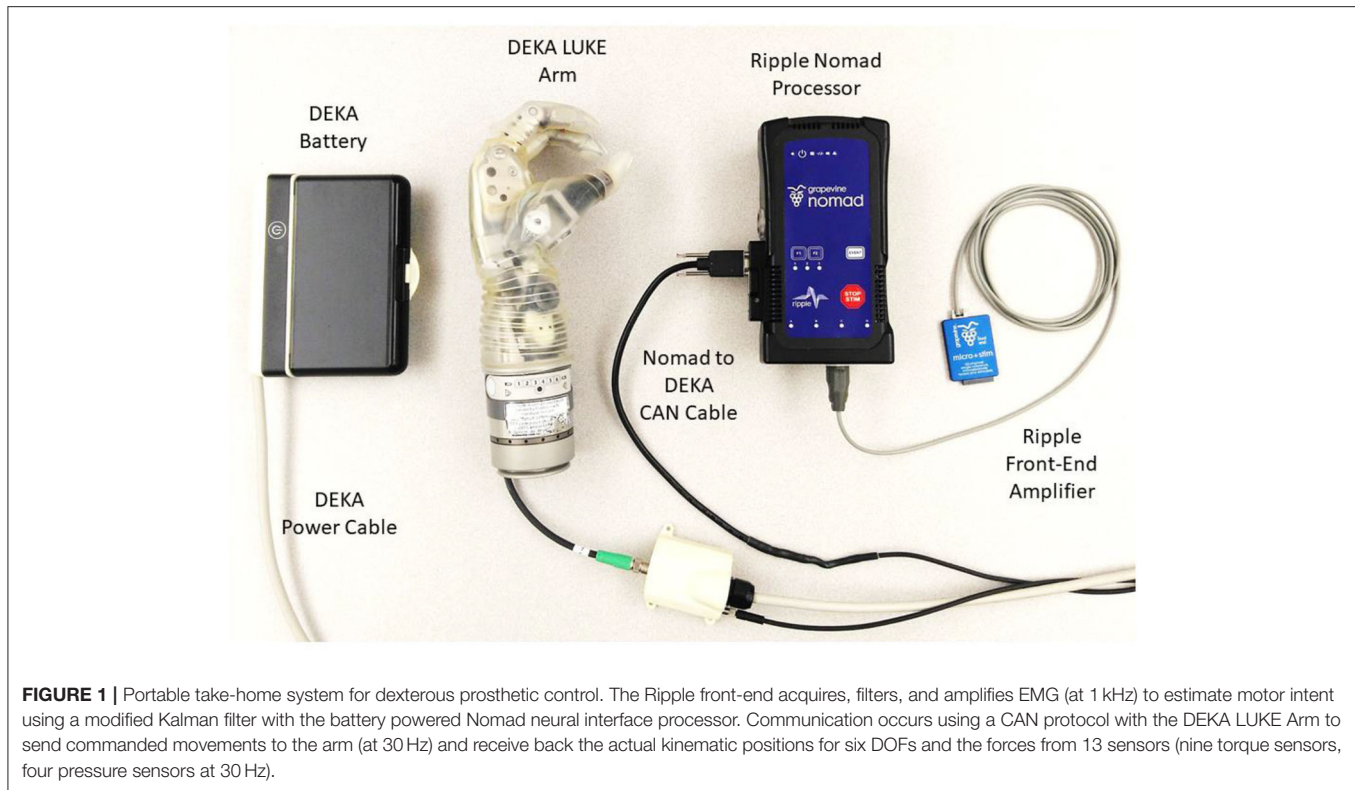


FIGURE 1 | Portable take-home system for dexterous prosthetic control. The Ripple front-end acquires, filters, and amplifies EMG (at 1 kHz) to estimate motor intent using a modified Kalman filter with the battery powered Nomad neural interface processor. Communication occurs using a CAN protocol with the DEKA LUKE Arm to send commanded movements to the arm (at 30 Hz) and receive back the actual kinematic positions for six DOFs and the forces from 13 sensors (nine torque sensors, four pressure sensors at 30 Hz).

has 19 sensors: six that report the position of each DOF and 13 that report the forces on each digit—including four directions on D1, two on the D2, and one on each of D3, D4, and D5—and on the lateral, dorsal, and palmar (distal and proximal) aspects of the hand. The prosthesis itself records the aggregated use (i.e., time) within bins of movement velocity and electrical current draw for each DOF. It also records the total time each sensor experienced various forces (ten bins from zero to a max of 25.5 N) and the total time each DOF spent in various positions (ten bins across range of motion, which varies by DOF). We designed a custom python socket so that our compiled algorithms could communicate with and store data from the DEKA LUKE Arm's CAN-BUS interface (at 30 Hz).

For the prosthetic control algorithm and data storage we used the Nomad neural interface processor (Ripple Neuro; Salt Lake City, UT, USA) for several reasons: an external, exchangeable battery provides up to 4 h of power; wireless communication to external devices; 500 GB of hard disk storage; and up to 512 channels for data acquisition and stimulation. We modified the Ripple firmware provided with the Nomad so that our compiled control algorithms could directly: acquire, filter and store EMG (1 kHz); start and stop via external buttons; and communicate over WiFi with external devices (TCP socket). Using a front-end amplifier (**Figure 1**; Ripple Neuro, Salt Lake City, UT, USA) we filtered (15 to 375 Hz bandpass; 60/120/180 Hz notch) the implanted EMG (iEMG) or surface EMG (sEMG, both were sampled at 1 kHz). sEMG in intact participants was recorded with a Micro + Stim front-end (Ripple Neuro, Salt Lake City, UT, USA), and iEMG in the amputee participant was recorded

with an active gator front end (Ripple Neuro, Salt Lake City, UT, USA). The Nomad runs Linux 8 (jessie) environment with an Intel® Celeron™ processor (CPU N2930) at 1.83 GHz with 2-GB RAM. Control algorithms were converted to C using MATLAB® Coder and compiled for stand-alone use on the portable Nomad.

EMG Feature Calculation and Decoding of Motor Intent

Training the prosthetic control algorithm [i.e., modified Kalman filter (George et al., 2019a)] first requires the user to mimic preprogrammed movements of the prosthesis as it cycles through several movement trials for each DOF (**Figure 2C**; George et al., 2020d). Features were then calculated for each differential EMG pair (496 total pairs from 32 single-ended electrodes, **Figure 2D**) by taking the mean-absolute value of a moving 300-ms window (**Figure 2E**). Using the kinematic positions and the EMG features, the portable computer chose 48 optimal features using the Gram-Schmidt forward-selection algorithm (Efron et al., 2004; Hwang et al., 2014; Nieveen et al., 2017) and computed the Kalman filter matrices (Wu et al., 2006). Forty-eight channels were used because, anecdotally, that number had consistently provided good control for in-lab experiments using our desktop system. Nieveen et al. suggests that a small improvement in performance could be achieved with a few more channels (e.g., 55), although this number will vary by participant and training session (Nieveen et al., 2017). Increasing the number

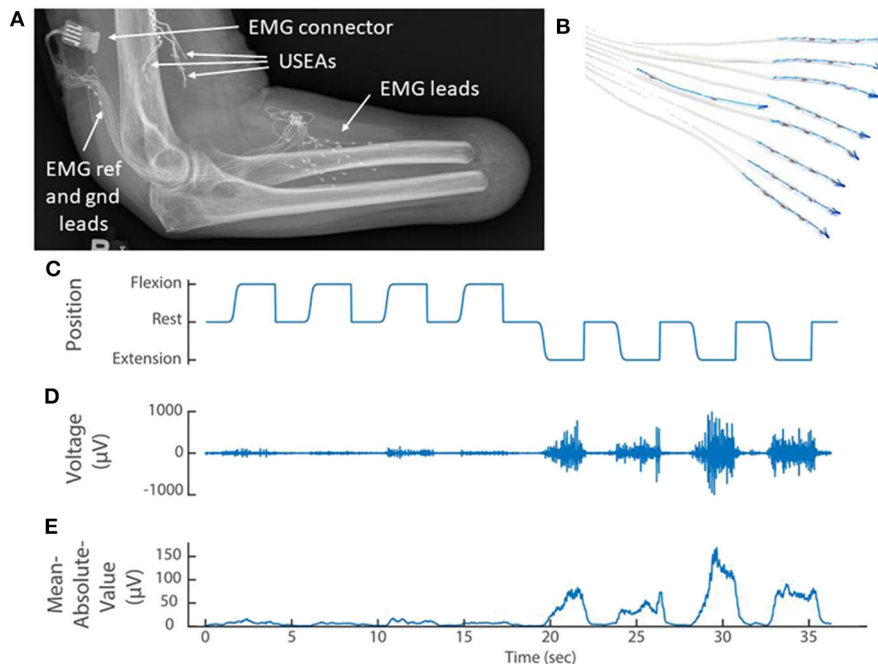


FIGURE 2 | (A) X-ray of the elbow and residual forearm of a transradial amputee implanted with implanted three Utah Slanted Electrode Arrays (USEAs) and **(B)** 32 single-ended EMG leads (iEMG) and reference and ground. **(C)** The amputee mimics preprogrammed movements of the prosthesis (kinematics) while the portable Nomad system records iEMG voltage signals. **(D)** A representative iEMG channel that is active primarily during extension of the index finger. **(E)** A representative feature [mean absolute value of the iEMG channel in **(D)**] that is used to train the prosthetic control algorithm. Implanted Utah Slanted Electrode Arrays (USEAs) were not used with the portable system, but could be incorporated in future versions.

of channels will also increase the control algorithm training and prediction times.

The Kalman filter presented by Wu et al. (2006) was modified to improve stability and reduce the effort required to sustain grasping movements by using an *ad-hoc* latching filter (Nieveen et al., in review). External, *ad-hoc* thresholds were also then applied as follows and as previously described in George et al. (2020a):

$$\hat{x}_{mod} = \begin{cases} \frac{\hat{x}_{new} \cdot G - T}{1 - T} & \text{when } \hat{x}_{new} \geq T \\ 0 & \text{when } \hat{x}_{new} < T \end{cases} \quad (1)$$

where \hat{x}_{new} is the output from the Kalman filter (defined to exist between -1 and $+1$), \hat{x}_{mod} is the output with the modifications applied, G is the gain (set to 1), and T is the threshold (set to 0.2 for all DOFs). This equation is for the positive direction of each DOF (e.g., flexion, abduction, pronation); a similar equation that preserves the sign and directionality for the negative direction was applied accordingly. Note that the non-modified output (\hat{x}_{new}) is fed recursively back to the Kalman filter to preserve stability while the modified output is only used to control prosthetic arm. In equation (1), \hat{x}_{mod} is normalized to 0 to $+1$ (or -1 , if in the negative direction) using the ' $1 - T$ ' divisor.

Human Subjects

In this manuscript, one amputee and two intact participants used the portable system. All participants used the system in the lab,

but only the amputee and one of the intact participants used the system, under supervision, at home.

Transradial Amputee

For the amputee, eight iEMG leads (Ripple Neuro; Salt Lake City, Utah, USA) with four electrodes each, and a ninth lead with an electrical reference and ground, were implanted in lower-arm extensor and flexor muscles as described previously (George et al., 2019a; **Figures 2A,B**). The electrode connector exited through a percutaneous incision and mated with an active gator connector (**Figure 2A**; Ripple Neuro; Salt Lake City, Utah, USA). This participant also had Utah Slanted Electrode Arrays implanted in the median and ulnar nerves but these devices were not used with the portable system. Surgical details have been previously described (Wendelken et al., 2017; George et al., 2018, 2019a; Page et al., 2018).

Intact Participants

Intact individuals were able to use the portable system with a 3D printed, custom-made bypass socket (Paskett et al., 2019) and a custom-made neoprene sleeve with 32 sEMG electrodes, plus one reference and one ground (George et al., 2020b). Inexpensive, stainless steel-coated, marine grade, brass snaps were crimped into the neoprene to serve as dry electrodes and soldered to flexible wire for easy connection via a SAMTEC connector. The electrodes were roughly evenly spaced over flexor and extensor forearm muscles, about half on the flexors, and half on the

extensors (covering about 8 inches distal to the elbow). Precise placement was not a concern as we relied on the Gram–Schmidt forward selection algorithm to choose the 48 most informative bipolar pairs for the motor decode algorithm (see section EMG feature calculation and decoding of motor intent).

As described previously (Paskett et al., 2019), the bypass socket is an open source device which suspends a prosthetic arm beneath the intact arm of the healthy volunteer and provides adequate range-of-motion so that the healthy volunteer can perform activities of daily living with an upper-limb prosthesis. The bypass socket was designed so that the electrode sleeve could be pulled up onto the forearm, locating the 32 recording electrodes over the extrinsic flexor and extensor hand muscles and the reference and ground electrodes over the ulna, about 2 cm distal to the elbow.

All experiments and procedures were performed with approval from the University of Utah Institutional Review Board.

RESULTS

EMG Recordings Are Consistent Across Desktop and Portable Systems

To ensure that the EMG was stored correctly on the Nomad, we concurrently recorded EMG with the portable system and a laboratory desktop system in one intact participant while the participant completed a training session (394 s in length). The correlation coefficient was calculated after concatenating the sEMG data from all 32 recorded channels. As expected, concurrent recordings of sEMG on the portable and desktop systems were highly correlated ($\rho = 0.95$; $p < 0.001$) and the sEMG features (mean-absolute value sEMG data with a 300-ms window) were nearly identical between the two systems ($\rho = 0.99$; $p < 0.001$). Due to slight variation in clock speeds,

a temporal delay was observed (about 100 ps/sample) which reduced the correlation coefficient. However, the correlation of the sEMG features suggests functional equivalency between the two recording systems.

Portable System Offers a Simple User Interface and Customizable Control Options

Three external buttons were employed to create a simple user-friendly interface. Pressing the first button initiated a new training session, which automatically granted control of the prosthesis to the user once training was complete (**Figure 3A**, see also **Supplementary Video 1**). The second button initiated a previously trained and compiled control algorithm (if available), so that the user could have on-demand control of the prosthesis. Finally, sequential inputs on a third button was used to toggle between position or velocity control modes or to freeze a DOF at a desired position.

Portable System Can Be Trained Rapidly Using Steady-State Modified Kalman Filter

The system was trained in 7.5 min—including the time needed to collect the training data (4.2 min) and the subsequent channel selection and computation of the modified Kalman filter matrices (about 3.3 min) (**Table 1**). Timing data for **Table 1** were recorded during training and testing with one intact participant in the lab. Because training data and the corresponding Kalman filter matrices have the same dimensions regardless of the user, the times listed in **Table 1** are universal. Loop speeds were calculated as the average over a 16.5 second window (500 samples) while the user actively controlled the prosthesis. Training data included four trials of flexion and extension for D1, D2, D3/D4/D5, and the wrist; D1 adduction and abduction; wrist pronation

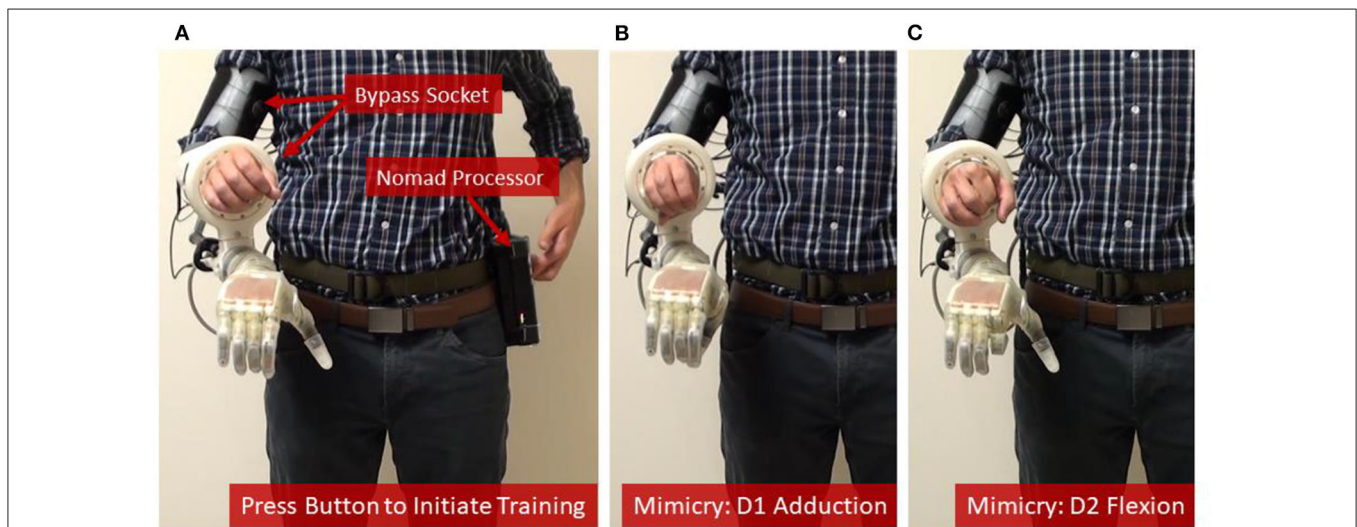


FIGURE 3 | Training the prosthetic control algorithm with the portable system. **(A)** The user [shown here as an intact subject using a bypass socket (Paskett et al., 2019) to support the LUKE Arm] presses a button on the Nomad to start the training sequence, and then mimics the prosthesis while the Nomad cycles through each of six DOFs—**(B,C)** show D1 adduction and D2 flexion, respectively.

TABLE 1 | Computational times required for training and testing (running) the steady-state, modified Kalman filter on the portable system.

Process	Computation time
Training	
Data collection	252 s
Channel selection	198 s
Train steady state Kalman filter	0.7 s
Total Time	7.5 min
Testing	
Update positions	0.7 ms

and supination; and grasping and extending all digits together (Figures 3B,C, see also **Supplementary Video 1**). The trained modified Kalman filter was automatically saved to a log file and could be recompiled onto the Nomad as a stand-alone application for on-demand use (e.g., the second external button). This was accomplished over the Nomad's wireless network using a laptop and required <30 s.

Prior to use, the steady-state modified Kalman gain matrix (K) was calculated by iteratively running the filter until the fluctuations in each value of the gain matrix were $<1 \times 10^{-6}$, reaching steady state after about 25 ms. With the gain (K), the observation (H) and the state-transition (A) matrices, a steady state matrix (Γ) was then calculated:

$$\Gamma = A - K^*H^*A \quad (2)$$

Thus, new position predictions (\hat{x}_{new}) were calculated with only two matrix multiplications involving the previous positions ($\hat{x}_{previous}$) and 48 EMG features (z):

$$\hat{x}_{new} = \Gamma^* \hat{x}_{previous} + K^*z \quad (3)$$

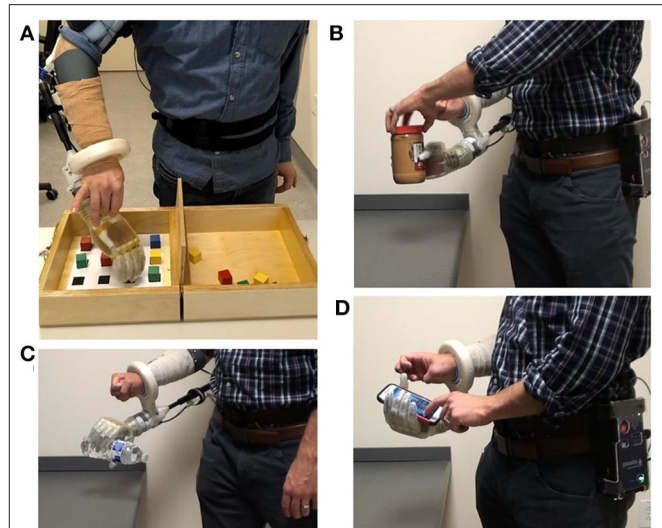
This simplification avoided a computationally expensive matrix inversion required by the recursive algorithm. Consequently, the time required to predict new positions and update the prosthesis was on average <1 ms, far below the update loop speed of 33 ms (Table 1). If the user desires, a velocity control mode for any DOF can also be provided using the position output from the Kalman filter (\hat{x}_{new}):

$$\hat{x}_{velocity} = \hat{x}_{velocity} + \hat{x}_{new}^* \Delta t^* \gamma \quad (4)$$

where Δt is the loop speed (33 ms) and γ a dampening factor (set to 0.95). In our previous experiments, some amputee subjects have preferred specific DOFs, such as wrist rotation or wrist flexion, to operate in velocity mode (Kluger, 2019).

Portable System Can Be Used at Home to Complete Various Activities of Daily Living

The portable system was used by both intact participants to perform arm dexterity tests and activities of daily living in the

**FIGURE 4** | After the motor control algorithm was trained, intact participants used the portable system with a bypass socket in the lab to perform (A) an arm dexterity test and activities of daily living: (B) opening a jar; (C) pouring motion; and (D) using a smart phone.

lab (Figure 4), as well as by one intact participant to perform two-handed tasks at home (Figure 5). One transradial amputee used the system at home, under staff supervision, to perform tasks of his choosing, some of which were not possible with his commercial prosthesis (Table 2 and Figure 6). Table 2 shows that the most common movements used were grasp (D1–D5 flexion) and pinch (D1 and D2 flexion) in combination with the wrist movements. Several successfully completed tasks were not listed in Table 2 because of similarity to other tasks (e.g., picking up another dog toy, pill bottle, TV remote, or a potato from the pantry; or turning on exterior faucet).

Rich Dataset From Portable System Reveals Novel Information About Prosthesis Use

EMG (sampled at 1 kHz), kinematic positions and forces applied to the prosthesis (both sampled at 30 Hz) were stored on the Nomad while a transradial amputee grasped, held and released an orange (Figure 7; see also **Supplementary Video 4**). Three phases of movement were clearly identified: preparing to grasp (when the index finger is near full extension); grasping (where the algorithm predicted the finger to be near full flexion but the orange restricted the actual position to about the rest position, which resulted in a dramatic increase in force); and releasing the orange (where the finger extended toward near full extension).

Data are saved at a rate of 250 MB/h in an '.hd5' format. As a result, the 500 GB capacity of the Nomad can record nearly 2,000 h of arm use.

DISCUSSION

We have described a portable, prosthetic control system and the first at-home use of a multi-degree-of-freedom,

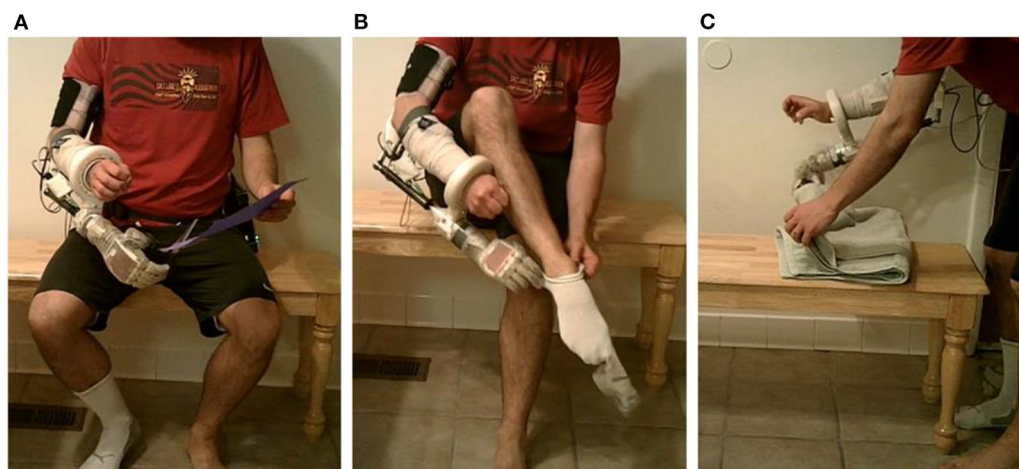


FIGURE 5 | Two-handed activities of daily living at home using a bypass socket and the portable system: **(A)** using scissors; **(B)** donning a sock; and **(C)** folding a towel.

TABLE 2 | List of tasks chosen by the amputee to attempt at home using the portable system.

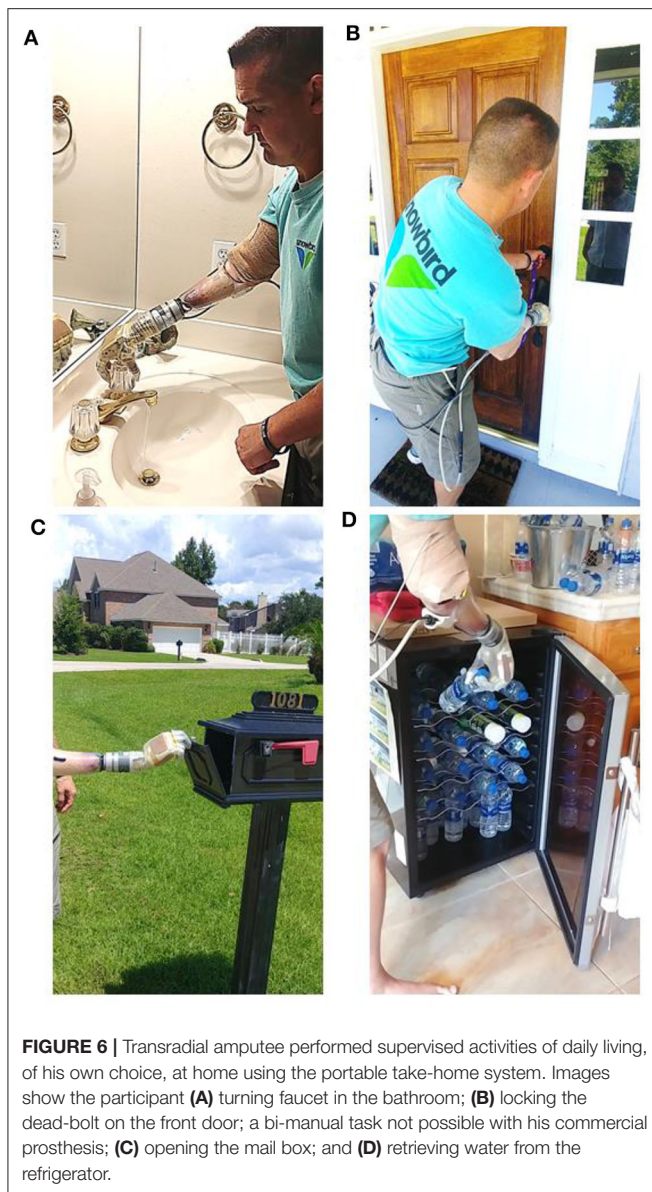
Task	Completion time	Detailed description
Successful		
Lock front door (dead-bolt) [†]	13 s	Used grasp (D1–D5 flexion) to grab and pull the door toward him so the bolt lined up and could be locked using intact arm
Open front door	7 s	Used grasp to pull down on the handle and to pull door open
Open refrigerator and retrieve water bottle	25 s	Used grasp and wrist flexion/extension to open refrigerator, grasp water bottle, and transfer to intact arm
Open oven door	16 s	Used grasp and wrist flexion/extension to grab the handle, open, and then shut the door
Turn on bathroom faucet	29 s	Used both grasp and pinch (D1 and D2 flexion) while turning faucet with gross arm movement
Open cabinet doors	22 s	Used precise pinch and wrist flexion/extension to grab small handles and pull doors open (2 doors)
Pick up dog toy	8 s	Used grasp and wrist flexion/extension to pick up a dog toy, and hold it for dog to bite
Put on shoe [†]	22 s	Used grasp and wrist flexion to hold shoe tongue while donning shoe held with the intact arm. Included a release and readjustment of the grip on the shoe tongue
Move garbage can	9 s	Used grasp and wrist flexion/extension to grasp the garbage can handle and move it about 10 feet
Check for mail at box	8 s	Used pinch and wrist extend to open mail box (as if he were to put/take mail) and then close with intact arm
Failed		
Input garage code on key pad	NA	This task required a pointed finger position (D2 extended; D1, D3, D4, and D5 flexed) which, was not included in the training. The amputee could make the motion; however, it was not stable enough to successfully complete task
Turn on push button oven light	NA	This task required a pointed finger position (D2 extended; D1, D3, D4, and D5 flexed) which was not included in the training. Amputee could make the motion; however, it was not stable enough to successfully complete task

[†]Denotes a task where amputee used the prosthesis and their intact hand simultaneously.

proportionally controlled bionic arm. The system uses a modified Kalman filter to provide real-time, proportional control—including independent, and simultaneous movement—across 6 DOFs. We have shown that the modified Kalman filter can be trained in 7.5 min using the Nomad, a portable electrophysiological recording system equipped with an ordinary processor. In addition, the time needed to acquire EMG and compute and update the prosthetic arm positions was <1 ms on average—far below the 33 ms update cycle—and provided real-time movement updates for the users.

The portable system also stores EMG, position and force data with unprecedented temporal resolution. This comprehensive dataset will be crucial for fully understanding how proportional control algorithms are used during unsupervised at-home use. Because of the Nomad's large storage capacity and USB and Bluetooth connections it could also be configured to collect and store other types of data (e.g., video, bilateral arm use with IMUs).

To study at-home prosthetic use, previous take-home systems have stored limited usage data, including the time the device was turned on (Graczyk et al., 2018; Simon et al., 2019), aggregated hand movement (Simon et al., 2019), how often



specific predefined grasps were used (Kuiken et al., 2016; Hargrove et al., 2017; Simon et al., 2019) or force applied to a limited number of sensors on the hand (Graczyk et al., 2018). Although these approaches may be sufficient for less refined control algorithms, to fully understand how proportional control is used, both high-temporal-resolution kinematic and force data for each DOF are necessary.

The example in **Figure 7** highlights how the comprehensive data recorded reveals complex interactions between the various DOFs with proportional control. The stable D2 kinematics implies that the amputee held the orange with a fixed grasp from pick up to release; however, the force data revealed a dip in force during this same period. Close inspection of the kinematics from the opposing D1 also shows that a subtle readjustment occurred to improve the grasp stability (this can be seen in

Supplementary Video 4). These refined movements are possible because of proportional control algorithms. Because DOFs are coupled together during object manipulation, the connection between each DOF must be considered.

Rich datasets like this will help researchers and clinicians study at-home, unsupervised use; improve prosthetic control algorithms, and training paradigms (George et al., 2018) by understanding the types of grasps and DOFs commonly used; understand when mastery of prosthesis control occurs and when interventions might be applied or lifted; better describe noise encountered in real-world environments and design features and algorithms that reduce its influence on motor performance; and address many other unanswered questions about at-home use of advanced upper-limb prostheses. These rich datasets will also enable future at-home trials to study the benefits and use of high-resolution sensory feedback from intraneural electrical stimulation—a feature soon to be added to the portable system.

In contrast, previous data collection during at-home prosthetic use has relied on subjective surveys, usage logs, IMUs, and the amount of time the device is turned on to describe prosthetic use (Hargrove et al., 2017; Resnik et al., 2017, 2018b; Graczyk et al., 2018). However, these approaches only approximate actual prosthesis use and could be misinterpreted. Some pattern recognition studies have recorded kinematic output and use of predefined grasps (Kuiken et al., 2016; Simon et al., 2019).

Two of the tasks successfully completed by the amputee at home required use of the intact arm along with the prosthesis—donning a shoe and locking the front door (**Table 2**). However, other tasks on the list could also be two-handed, such as using the intact hand to remove mail from the box or food from the refrigerator or oven while holding the door open with the prosthesis. The two tasks where the amputee was unsuccessful required a pointed finger position (D2 extended while D1, D3, D4, and D5 were flexed). Even though this combination was not included in the training sequence the amputee was able to position the digits appropriately; however, the positions were not stable enough to complete the task. Both of these tasks also required the amputee to lift and hold the heavy prosthesis vertically, which could have also added instability to the control.

The most common arm movements used in the at-home setting where opening and closing the hand, or pinching the thumb and index finger, in combination with wrist movements. Combination movements can be performed simultaneously because the Kalman filter algorithm assumes independent DOFs. To simplify control, the participant controlled the wrist with a velocity mode (while the digits were in position control)—allowing the user to first set a wrist position prior to completing the grasp or pinch, if desired.

Because combination movements involving wrist were so prevalent during at-home use, we recently studied the benefits of training the modified Kalman filter with combination movements involving the wrist, in addition to single DOF movements (Paskett et al., in review). We found that combination training sequences provide the user with improved, intuitive wrist position control during simultaneous

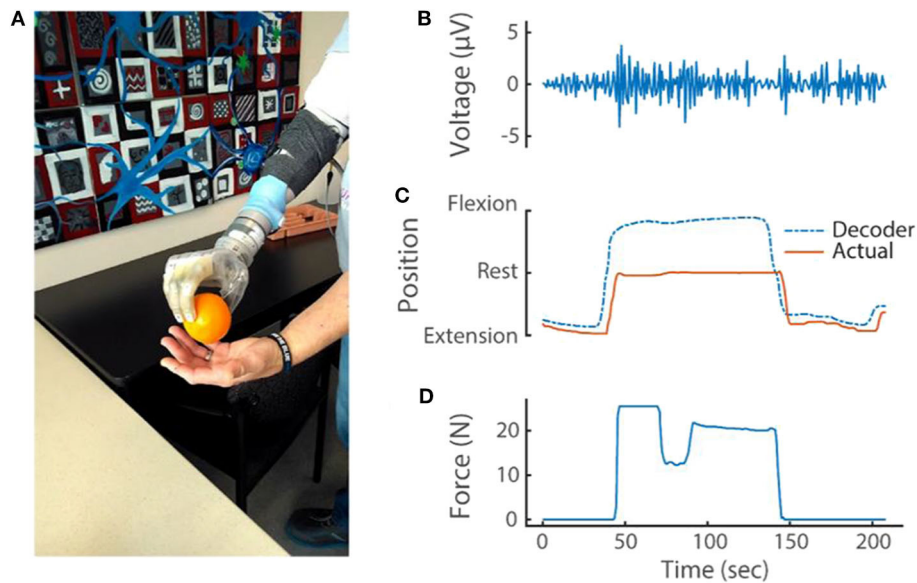


FIGURE 7 | (A) Transradial amputee picking up an orange using implanted EMG electrodes and the portable system. During this task, the portable system recorded and stored **(B)** differential EMG (at 1 kHz), **(C)** kinematic output of the modified Kalman filter and actual kinematics of the prosthesis (at 30 Hz) and **(D)** prosthesis sensor values (at 30 Hz). For simplicity, only one differential EMG channel (of 48 total) and only one sensor (D1 pressure sensor; out of 13 total pressure and torque sensors and six DOFs) are shown.

movements. As a result, our future studies will also include wrist combination movements.

An important aspect of the portable system is the fast computation of position updates using a steady-state Kalman filter. We initially implemented the full recursive Kalman filter within each update cycle. However, the time required to complete the update was near and often exceeded our 33-ms update loop speed. Updating movement positions with the steady-state Kalman filter was quick (less than our loop time) and straightforward to implement. Malik et al. performed a rigorous comparison of the steady-state and full recursive Kalman filter using neural spike data and concluded that after steady-state convergence the two predictions are essentially identical (Malik et al., 2011). Our fast position update speeds will allow additional features to be added, including high-resolution, biomimetic, sensory feedback from intraneural (Wendelken et al., 2017; George et al., 2019b) or electrocutaneous (George et al., 2020a) stimulation.

The most computationally demanding aspect of training was performing Gram-Schmidt forward selection to choose the 48 most useful features out of the 496 differential pairs. Despite taking considerable time up front, this down-selection method has several advantages (Nieveen et al., 2017). First, choosing the features up-front enables fast loop speeds (below 33 ms) by eliminating the need to calculate complex features (e.g., principal components) or even all 496 differential EMG features during each update cycle. Second, forward selection recursively selects features that are maximally correlated with the training kinematics and minimally correlated with each other by orthogonalizing the remaining channels after each channel

is selected. This ensures that each selected feature describes kinematics and not uncorrelated noise. Refined movements, the hallmark of proportional control algorithms, account for little variance and could be inadvertently discarded using techniques agnostic to the training kinematics. Finally, orthogonalization in the forward selection algorithm avoids redundant features and singularities.

It was possible to avoid the need for down-selection and only use the original 32 single-ended features. However, by calculating all possible differential pairs, signal from a specific muscle might be better isolated from unwanted signal or noise and identified by the forward selection algorithm. Indeed, when we allow the forward selection algorithm to choose from among both the 32 monopolar and 496 bipolar pairs—which is the case in our lab desktop system but not the portable system—the monopolar channels are rarely selected.

Importantly, within 8 min of powering the system on, the user can have real-time proportional control of six DOFs. The amount of time required to both collect training data by mimicking preprogrammed movements and to train the prosthetic control algorithm are related to the number of trials for each mimicked movement. In this work, and published elsewhere (George et al., 2019a), an amputee familiar with the training process trained with only four trials on each DOF and a grasp and extension of all digits. With this training, he was able to control the prosthesis in the lab and perform tasks not possible with his commercial prosthesis at home (George et al., 2019a). A less experienced user may require training with more trials; however, even if a naïve user requires twice as many trials, the total training time is still under 15 min.

An important question we have yet to fully explore is how often will retraining be required? The amputee in this study successfully used a trained algorithm the following day, suggesting daily training may not be necessary. It is also reasonable to believe that training with data collected across multiple days could provide better control (George et al., 2020b), especially considering that iEMG leads are relatively stationary when implanted into residual musculature. However, training daily provides new users with the best control algorithm given the EMG features collected on that day and our experience suggests that over time they will become more stereotyped and thus have improved control. From the start, our training requires less time than pattern recognition algorithms which can require 14–40 h of upfront, in-lab training with experienced professionals (Resnik et al., 2017, 2018a).

Currently, to use a previously trained control algorithm, the modified Kalman filter's parameters must be recompiled into a stand-alone application on the Nomad. Although this process is very fast (<30 sec) and wireless, it currently requires an external computer running MATLAB®. Planned future work includes the ability to directly load trained parameters from a local file stored on the Nomad for on-demand use.

Ultimately, the ability to communicate with an application running on the Nomad was limited to one button (the other two could only start and stop a compiled application). Thus, we implemented sequential button pressing to selectively lock an individual DOF. The amputee used this feature to lock wrist rotation when using the system at home. For this amputee, poor wrist control was not uncommon and was likely due to dystonic muscle activity, common among those afflicted with complex regional pain syndrome and multi-year arm disuse prior to amputation (George et al., 2018). However, despite the amputee's having low-amplitude EMG signals (e.g., **Figure 7B**), the modified Kalman filter algorithm provided control for five degrees of freedoms. Intact users did not lock any DOFs and had all six, independent, proportionally controlled DOFs.

Near the end of **Supplementary Video 4**, the amputee displays difficulty releasing the orange. Release is normally an easy task, requiring only muscle relaxation for the position control algorithm to move the digits into an open resting position. However, delayed object release in this case was due to the participant's dystonia—he could not relax muscle easily for the hand to open. This did not occur often, but dystonia was more prevalent during some lab visits than others.

Future improvements will include wireless communication to a tablet or phone app where control selections can be easily made, communicated and saved locally on the Nomad. This will enable real-time adjustments including setting specific DOFs to velocity mode; adjusting the *ad-hoc* gains and thresholds of the modified Kalman filter on a DOF-by-DOF basis; and reloading a previous training or retraining the prosthesis with a modified training protocol if the first training was not satisfactory.

In its current form, the portable system is programmed to communicate only with the DEKA LUKE Arm. However, other custom communication sockets could be designed to communicate through the micro D-sub, USB or Bluetooth connections available to Nomad for proportional control of and data logging from other prosthetic limbs.

The current system also has significant cabling that connect the DEKA LUKE Arm to its battery and the Nomad to the DEKA LUKE Arm and the Ripple front-end amplifier. Upcoming, at-home, unsupervised studies will likely require a supportive partner/care-taker to assist the amputee when donning the equipment and to aid in securing the cables. The take-home study will begin with an acclimation phase where the amputee (and partner/care-taker) receive in-lab and at-home supervised training prior to unsupervised use. We also envision a hip or back-pack where the Nomad, batteries and excess cable length can be organized and housed. In the future, wireless communication between the Nomad, implanted electrodes and prosthesis could eliminate cables and provide amputees with greater independence.

The importance of reliability in a take-home system cannot be understated—software and hardware must function as intended in the everyday environment. To fully test reliability, the system must be used at home, over many days and for many uses. To date, the system has been used on numerous occasions on campus and in the lab, but only at home by our laboratory staff and by one transradial amputee under staff observation (George et al., 2019a). Ultimately, this system will be used in upcoming take-home clinical trials to record high-resolution data and study advanced, proportional control algorithms for upper-limb prosthesis use.

DATA AVAILABILITY STATEMENT

All datasets presented in this study are included in the article/**Supplementary Material**.

ETHICS STATEMENT

The studies involving human participants were reviewed and approved by University of Utah Institutional Review Board. The patients/participants provided their written informed consent to participate in this study. Written informed consent was obtained from the individual(s) for the publication of any potentially identifiable images or data included in this article.

AUTHOR CONTRIBUTIONS

MB, EB, and TD designed the software running on the portable system. MB, TD, MP, and JG tested the system with the human participants. MB wrote the manuscript. All authors revised the manuscript. GC oversaw all aspects of this research.

FUNDING

This work was sponsored by the Hand Proprioception and Touch Interfaces (HAPTIX) program (Grant No. N66001-15-C-4017; BTO, DARPA).

ACKNOWLEDGMENTS

We thank Ripple Neuro, for their generous support with custom firmware that enabled many features including

REFERENCES

- Biddiss, E., and Chau, T. (2007). Upper-limb prosthetics: critical factors in device abandonment. *Am. J. Phys. Med. Rehabil.* 86, 977–987. doi: 10.1097/PHM.0b013e3181587f6c
- Davis, T. S., Wark, H. A., Hutchinson, D. T., Warren, D. J., O'Neill, K., Scheinblum, T., et al. (2016). Restoring motor control and sensory feedback in people with upper extremity amputations using arrays of 96 microelectrodes implanted in the median and ulnar nerves. *J. Neural Eng.* 13:036001. doi: 10.1088/1741-2560/13/3/036001
- Efron, B., Hastie, T., Johnstone, I., Tibshirani, R., Ishwaran, H., Knight, K., et al. (2004). Least angle regression. *Ann. Stat.* 32, 407–499. doi: 10.1214/009053604000000067
- Farrell, T. R., and Weir, R. F. (2007). The optimal controller delay for myoelectric prostheses. *IEEE Trans. Neural Syst. Rehabil. Eng.* 15, 111–118. doi: 10.1109/TNSRE.2007.891391
- George, J. A., Brinton, M. R., Colgan, P. C., Colvin, G. K., Bensmaia, S. J., and Clark, G. A. (2020a). “Intensity discriminability of electrocutaneous and intraneural stimulation pulse frequency in intact individuals and amputees.” in *42nd Annual International Conference of the IEEE Engineering in Medicine and Biology Society (EMBC)* (Montreal, CA). doi: 10.1109/EMBC44109.2020.9176720
- George, J. A., Brinton, M. R., Duncan, C. C., Hutchinson, D. T., and Clark, G. A. (2018). “Improved training paradigms and motor-decode algorithms: results from intact individuals and a recent transradial amputee with prior complex regional pain syndrome,” in *Proceedings of the Annual International Conference of the IEEE Engineering in Medicine and Biology Society (EMBS)* (Honolulu, HI), 3782–3787. doi: 10.1109/EMBC.2018.8513342
- George, J. A., Davis, T. S., Brinton, M. R., and Clark, G. A. (2019a). Intuitive neuromyoelectric control of a dexterous bionic arm using a modified Kalman filter. *J. Neurosci. Methods* 330:108462. doi: 10.1016/j.jneumeth.2019.108462
- George, J. A., Kluger, D. T., Davis, T. S., Wendelken, S. M., Okorokova, E. V., He, Q., et al. (2019b). Biomimetic sensory feedback through peripheral nerve stimulation improves dexterous use of a bionic hand. *Sci. Robot.* 4:eaax2352. doi: 10.1126/scirobotics.aax2352
- George, J. A., Neibling, A., Paskett, M. D., and Clark, G. A. (2020b). “Inexpensive surface electromyography sleeve with consistent electrode placement enables dexterous and stable prosthetic control through deep learning,” in *Myoelectric Controls and Upper Limb Prosthetics Symposium* (Fredericton, CA).
- George, J. A., Radhakrishnan, S., Brinton, M. R., and Clark, G. A. (2020c). “Inexpensive and portable system for dexterous high-density myoelectric control of multiarticulate prostheses,” in *2020 IEEE International Conference on Systems, Man and Cybernetics (SMC)* (Toronto, CA).
- George, J. A., Tully, T. N., Colgan, P. C., and Clark, G. A. (2020d). “Bilaterally mirrored movements improve the accuracy and precision of training data for supervised learning of neural or myoelectric prosthetic control,” in *42nd Annual International Conference of the IEEE Engineering in Medicine and Biology Society (EMBC)* (Montreal, CA). doi: 10.1109/EMBC44109.2020.9175388
- Graczyk, E. L., Resnik, L., Schiefer, M. A., Schmitt, M. S., and Tyler, D. J. (2018). Home use of a neural-connected sensory prosthesis provides the functional and psychosocial experience of having a hand again. *Sci. Rep.* 8:9866. doi: 10.1038/s41598-018-26952-x
- Hargrove, L. J., Miller, L. A., Turner, K., and Kuiken, T. A. (2017). Myoelectric pattern recognition outperforms direct control for transhumeral amputees with targeted muscle reinnervation: a randomized clinical trial. *Sci. Rep.* 7:13840. doi: 10.1038/s41598-017-14386-w
- Hwang, H.-J., Mathias Hahne, J., and Müller, K.-R. (2014). Channel selection for simultaneous and proportional myoelectric prosthesis control of multiple degrees-of-freedom. *J. Neural Eng.* 11:056008. doi: 10.1088/1741-2560/11/5/056008
- Kluger, D. T., (2019). *Using Utah Slanted Electrode Arrays For Treatment of Peripheral Nerve Neuropathy and for Closed-Loop Control of Prosthetic Limbs*. Salt Lake City, UT: University of Utah.
- Kluger, D. T., Joyner, J. S., Wendelken, S. M., Davis, T. S., George, J. A., Page, D. M., et al. (2019). Virtual reality provides an effective platform for functional evaluations of closed-loop neuromyoelectric control. *IEEE Trans. Neural Syst. Rehabil. Eng.* 27, 876–886. doi: 10.1109/TNSRE.2019.2908817
- Kuiken, T. A., Miller, L. A., Turner, K., and Hargrove, L. J. (2016). A comparison of pattern recognition control and direct control of a multiple degree-of-freedom transradial prosthesis. *IEEE J. Transl. Eng. Health Med.* 4:2100508. doi: 10.1109/JTEHM.2016.2616123
- Malik, W. Q., Truccolo, W., Brown, E. N., and Hochberg, L. R. (2011). Efficient decoding with steady-state Kalman filter in neural interface systems. *IEEE Trans. Neural Syst. Rehabil. Eng.* 19, 25–34. doi: 10.1109/TNSRE.2010.2092443
- Mastinu, E., Ahlberg, J., Lendaro, E., Hermansson, L., Hakansson, B., and Ortiz-Catalan, M. (2018). An alternative myoelectric pattern recognition approach for the control of hand prostheses: a case study of use in daily life by a dysmelia subject. *IEEE J. Transl. Eng. Health Med.* 6:2600112. doi: 10.1109/JTEHM.2018.2811458
- Mobius Bionics (2020). LUKE Arm Details. Available online at: <http://www.mobiusbionics.com/luke-arm/> (accessed September 09, 2020).
- Nieveen, J., Warren, D., Wendelken, S., Davis, T., Kluger, D., and Page, D. (2017). “Channel selection of neural and electromyographic signals for decoding of motor intent,” in *Myoelectric Controls Conference* (Fredericton, CA), 720.
- Ottobock (2017). *Bebionic Technical Manual*. RSLIT317. Duderstadt, DE: Ottobock.
- Page, D. M., George, J. A., Kluger, D. T., Duncan, C., Wendelken, S., Davis, T., et al. (2018). Motor control and sensory feedback enhance prosthesis embodiment and reduce phantom pain after long-term hand amputation. *Front. Hum. Neurosci.* 12:352. doi: 10.3389/fnhum.2018.00352
- Paskett, M. D., Olsen, N. R., George, J. A., Kluger, D. T., Brinton, M. R., Davis, T. S., et al. (2019). A modular transradial bypass socket for surface myoelectric prosthetic control in non-amputees. *IEEE Trans. Neural Syst. Rehabil. Eng.* 27, 2070–2076. doi: 10.1109/TNSRE.2019.2941109
- Pasquina, P. F., Evangelista, M., Carvalho, A. J., Lockhart, J., Griffin, S., Nanos, G., et al. (2015). First-in-man demonstration of fully implanted myoelectric sensors for control of an advanced electromechanical arm by transradial amputees. *J. Neurosci. Methods* 244, 85–93. doi: 10.1016/j.jneumeth.2014.07.016
- Perry, B. N., Moran, C. W., Armiger, R. S., Pasquina, P. F., Vandersee, J. W., and Tsao, J. W. (2018). Initial clinical evaluation of the modular prosthetic limb. *Front. Neurol.* 9:153. doi: 10.3389/fneur.2018.00153
- Resnik, L., Acluche, F., Borgia, M., Latief, G., and Phillips, S. (2019). EMG pattern recognition control of the DEKA arm : impact on user ratings of satisfaction and usability. *IEEE J. Transl. Eng. Health Med.* 7:2100113. doi: 10.1109/JTEHM.2018.2883943

SUPPLEMENTARY MATERIAL

The Supplementary Material for this article can be found online at: <https://www.frontiersin.org/articles/10.3389/frobt.2020.559034/full#supplementary-material>

- Resnik, L., Cancio, J., Fantini, C., Ikeda, A., and Sasson, N. (2017). "Pattern recognition control of the DEKA arm in two transhumeral amputees with targeted muscle reinnervation," *MEC 17 - A Sense of What's to Come*, 3–6. Available online at: https://www.unb.ca/research/institutes/biomedical/mec/_resources/docs/MEC17-papers/resnik-pattern-recognition-control.pdf (accessed September 09, 2020).
- Resnik, L. J., Acluche, F., Borgia, M., Cancio, J., Latief, G., Phillips, S., et al. (2018b). EMG pattern recognition compared to foot control of the DEKA arm. *PLoS ONE* 13:e0204854. doi: 10.1371/journal.pone.0204854
- Resnik, L. J., Acluche, F., and Lieberman Klinger, S. (2018a). User experience of controlling the DEKA Arm with EMG pattern recognition. *PLoS ONE* 13:e0203987. doi: 10.1371/journal.pone.0203987
- Simon, A. M., Turner, K. L., Miller, L. A., Hargrove, L. J., and Kuiken, T. A. (2019). "Pattern recognition and direct control home use of a multi-articulating hand prosthesis," in *2019 IEEE 16th International Conference on Rehabilitation Robotics (ICORR)* (Toronto, CA), 386–391.
- Spiers, A. J., Resnik, L., and Dollar, A. M. (2017). "Analyzing at-home prosthesis use in unilateral upper-limb amputees to inform treatment and device design," in *IEEE International Conference on Rehabilitation Robotics* (London), 1273–1280.
- Touch Bionics Inc. (2017). *I-Limb Quantum*. MA01374US(2). Livingston: Touch Bionics Inc.
- Wendelken, S., Page, D. M., Davis, T., Wark, H. A. C., Kluger, D. T., Duncan, C., et al. (2017). Restoration of motor control and proprioceptive and cutaneous sensation in humans with prior upper-limb amputation via multiple Utah slanted electrode arrays (USEAs) implanted in residual peripheral arm nerves. *J Neuroeng. Rehabil.* 14:121. doi: 10.1186/s12984-017-0320-4
- Wu, W., Gao, Y., Bienenstock, E., Donoghue, J. P., and Black, M. J. (2006). Bayesian population decoding of motor cortical activity using a Kalman filter. *Neural Comput.* 18, 80–118. doi: 10.1162/089976606774841585

Conflict of Interest: EB was an employee of Ripple Neuro, during the development of the portable system.

The remaining authors declare that the research was conducted in the absence of any commercial or financial relationships that could be construed as a potential conflict of interest.

Copyright © 2020 Brinton, Barcikowski, Davis, Paskett, George and Clark. This is an open-access article distributed under the terms of the Creative Commons Attribution License (CC BY). The use, distribution or reproduction in other forums is permitted, provided the original author(s) and the copyright owner(s) are credited and that the original publication in this journal is cited, in accordance with accepted academic practice. No use, distribution or reproduction is permitted which does not comply with these terms.



Benchmarking Wearable Robots: Challenges and Recommendations From Functional, User Experience, and Methodological Perspectives

Diego Torricelli¹, Carlos Rodriguez-Guerrero², Jan F. Veneman³, Simona Crea^{4,5}, Kristin Briem⁶, Bigna Lenggenhager⁷ and Philipp Beckerle^{8,9*}

¹ Cajal institute, Spanish National Research Council (CSIC), Madrid, Spain, ² Robotics and Multibody Mechanics Research Group, Department of Mechanical Engineering, Vrije Universiteit Brussel and Flanders Make, Brussels, Belgium, ³ Hocoma AG, Volketswil, Switzerland, ⁴ The BioRobotics Institute, Scuola Superiore Sant'Anna, Pontedera, Italy, ⁵ IRCCS Fondazione Don Carlo Gnocchi, Florence, Italy, ⁶ Department of Physical Therapy, Faculty of Medicine, Research Centre of Movement Science, University of Iceland, Reykjavik, Iceland, ⁷ Department of Psychology, University of Zurich, Zurich, Switzerland, ⁸ Elastic Lightweight Robotics Group, Department of Electrical Engineering and Information Technology, Robotics Research Institute, Technische Universität Dortmund, Dortmund, Germany, ⁹ Institute for Mechatronic Systems, Department of Mechanical Engineering, Technical University of Darmstadt, Darmstadt, Germany

OPEN ACCESS

Edited by:

Elena De Momi,
Politecnico di Milano, Italy

Reviewed by:

Marianna Semprini,
Italian Institute of Technology (IIT), Italy
Joo-Ho Lee,
Ritsumeikan University, Japan

*Correspondence:

Philipp Beckerle
philipp.beckerle@tu-dortmund.de

Specialty section:

This article was submitted to
Biomedical Robotics,
a section of the journal
Frontiers in Robotics and AI

Received: 13 May 2020

Accepted: 12 October 2020

Published: 13 November 2020

Citation:

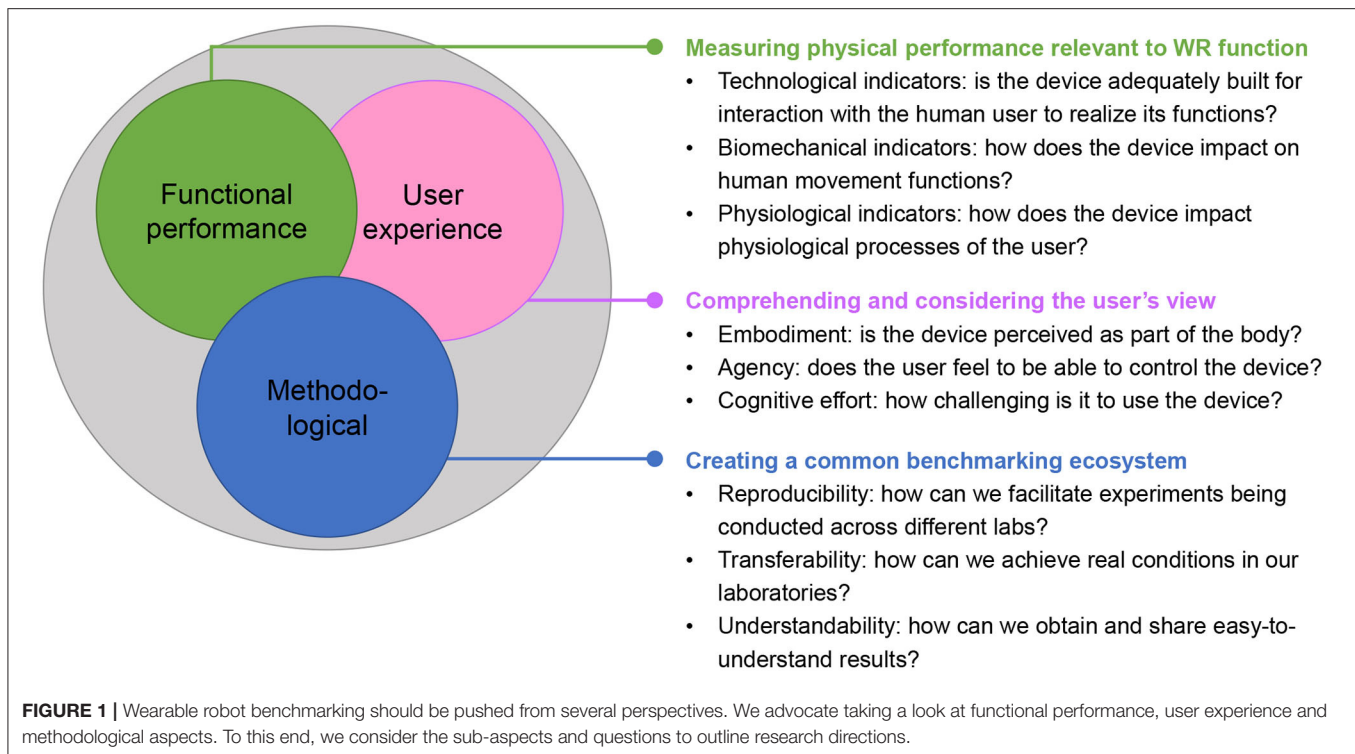
Torricelli D, Rodriguez-Guerrero C, Veneman JF, Crea S, Briem K, Lenggenhager B and Beckerle P (2020) Benchmarking Wearable Robots: Challenges and Recommendations From Functional, User Experience, and Methodological Perspectives.
Front. Robot. AI 7:561774.
doi: 10.3389/frobt.2020.561774

Wearable robots (WRs) are increasingly moving out of the labs toward real-world applications. In order for WRs to be effectively and widely adopted by end-users, a common benchmarking framework needs to be established. In this article, we outline the perspectives that in our opinion are the main determinants of this endeavor, and exemplify the complex landscape into three areas. The first perspective is related to quantifying the technical performance of the device and the physical impact of the device on the user. The second one refers to the understanding of the user's perceptual, emotional, and cognitive experience of (and with) the technology. The third one proposes a strategic path for a global benchmarking methodology, composed by reproducible experimental procedures representing real-life conditions. We hope that this paper can enable developers, researchers, clinicians and end-users to efficiently identify the most promising directions for validating their technology and drive future research efforts in the short and medium term.

Keywords: benchmarking, wearable robots, function, user experience, methodology

1. INTRODUCTION

Performance evaluation is becoming an urgent issue in wearable robotics. The community strongly needs reliable and replicable testing methods to verify and compare the performance of the numerous and diverse exoskeletal and prosthetic solutions available (Windrich et al., 2016; Price et al., 2019; Torricelli and Pons, 2019). Without clear and quantitative benchmarks, this rapidly expanding market runs the risk of spreading chaotically, losing sight of real users' needs. This situation is aggravated by the fact that the application domains are now rapidly expanding from the healthcare scenario toward industrial and logistic settings, characterized by a multitude of new functional goals and safety constraints (Gopura et al., 2016; Bogue, 2018). This multifaceted picture calls for a multidimensional approach that can guide not only developers in identifying the most efficient path to market introduction and survival, but also users in identifying the



best solution according to their unique abilities, desires, expectations, and needs. Fortunately, the scientific community has already addressed some of these issues in the past two decades: hundreds of studies have explored the biomechanical, physiological, and psychological implications of the interaction between humans and wearable robots (WRs) (Beckerle et al., 2017b, 2019; Pinto-Fernandez and Torricelli, 2020). This has been a multidisciplinary endeavor, which has resulted not only in scientific evidence and better robotic prototypes, but also in a plethora of potentially useful evaluation methods and protocols (Ghillebert et al., 2019; Ármannsdóttir et al., 2020; Davis et al., 2020). If well-organized and appropriately conveyed to the relevant users, a careful selection of these methods can become the foundation of a unified and standardized benchmarking ecosystem for WRs. Different international consortia are now targeting this ambitious goal, such as the COST Action for Wearable Robots¹, the EUROBENCH project (Torricelli and Pons, 2019), the COVR project (Bessler et al., 2018), and the Exskallerate project², as well as the ASTM-driven Exo Technology Center of Excellence³, to mention a few.

With the support of some of these projects, we gathered several experts into a workshop titled “Benchmarking Wearable Robots: from key enabling technologies, experimental methods to final applications,” held during the 2019 edition of the

ExoBerlin conference⁴. The main goal was to promote the discussion across researchers and stakeholders from different perspectives, to identify the key aspects that should be addressed in the near future in the field of performance evaluation. We identified three areas in which intensive research and scientific discourse appears necessary (see **Figure 1**). The first one addresses the functional performance, i.e., how the WR interacts with and affects the user's physical functions. Depending on the specific application, performance may be related to different desired outcomes, such as promoting a more physiological and efficient movement pattern, reducing the user's physical fatigue or improving balance. The second one focuses on considering and assessing the user's experience, i.e., the perceptual, emotional, and cognitive processes involved in the use of a WR. The third area highlights the importance of standardizing the experimental procedures, data collection and processing algorithms, in order to ensure a wide adoption of the same testing methods worldwide, fostering discussion and comparison among the different stakeholders in the field.

This perspective paper aims to provide a concise description of each of these three areas and thereby promote a common understanding of the meaning and relevance of WRs benchmarking. Such an effort may enable developers, researchers, clinicians, end-users, and any other relevant stakeholder to focus their efforts toward the most promising directions that should be addressed in the short and medium term.

¹<https://www.researchgate.net/project/COST-Action-CA16116-Wearable-Robots-for-Augmentation-Assistance-or-Substitution-of-Human-Motor-Functions>

²<https://northsearegion.eu/exskallerate/>

³<https://www.etcoe.org/>

⁴<https://www.exo-berlin.de/>

2. FUNCTIONAL PERFORMANCE PERSPECTIVE

WRs have an intrinsic, circular causal relationship with the human user, in which the actions of the robot are determinant for the behavior of the human and vice versa. Therefore, performance should be characterized on technological, biomechanical and physiological levels, within the context of specific functional tasks.

Technological indicators describe the physical capabilities of a WR. These indicators are obtained independently from a specific user, but are essential to evaluate the applicability of a WR for a specific target application with human users. One important aspect is the kinematic compatibility, which describes the ability of the robotic structure to follow the 3D kinematic trajectories of the human limbs. Kinematic compatibility is one of the main determinants of relative motion between the human limbs and the device (Näf et al., 2018a), which has direct effects on functionality, comfort and safety. On the kinetic side, the evaluation of torque/force control behavior and the mechanical impedance/admittance characteristics of the actuators is crucial. Unfortunately, most of the existing benchmarking techniques are realized under static assumptions, which result in unrealistic reported actuation characteristics. Recent works are pointing toward dynamic characterization procedures (Molledo et al., 2019), which in our opinion are essential to measure the potential of a WR to interact safely and efficiently with the human in daily activity tasks.

Biomechanical and physiological indicators relate to the assessment of the physical human-robot interaction. Given the complex nature of the systems under evaluation, i.e., the WR, the user and their physical coupling—the choice of the set of metrics and experimental methods is not trivial. Several biomechanical and physiological metrics have been used in human-in-the-loop studies to assess the effects of a WR on the user's physical capabilities. Among all, kinematics-related metrics have been extensively reported in several works (Pinto-Fernandez and Torricelli, 2020). Comparing joint kinematic profiles in WR-assisted conditions with normative data is a widely used method to assess whether a WR influences the movement pattern of a user (Näf et al., 2018b). In the majority of state-of-the-art papers on lower-limb WRs and gait rehabilitation, gait speed, joint range of motion and spatiotemporal parameters, such as cadence, step width, and stride length, are the most recurring kinematics metrics (Lee et al., 2019). However, given the high diversity of subject conditions, other indicators could be highly relevant to assess the effects of a WR. For instance, assessing the joint torque profiles can provide useful information about the quality of the movement pattern and may guide the interpretation of other outcomes, such as those related to electromyographic (EMG) measurements or metabolic efficiency. EMG measurements have become extremely popular as a way to measure the internal joint dynamics, thus to assess the physiological effects of the human-machine interaction. The technological maturity of commercial systems have made EMG one of the key metrics to evaluate a WR's efficacy in several application scenarios, from rehabilitation, assistance (Collins et al., 2015), and industrial

(Pacífico et al., 2020) scenarios, particularly in out-of-the-lab contexts, given that most of the EMG system are wireless and portable. Energy expenditure is currently one of the most adopted metrics to assess the effectiveness of a WR. Reduced metabolic cost has been widely considered as valuable evidence of effective human-robot interaction, with several recent studies proving that such results can be achieved in several contexts, ranging from walking and running (Kim et al., 2019), elderly gait training (Martini et al., 2019), and to repetitive upper-limb assistance of workers (Maurice et al., 2019; Baltrusch et al., 2020; Koopman et al., 2020). Currently, to the author's knowledge, no studies have provided evidence that metabolic cost reductions could be reliably assessed in out-the-lab conditions, but worldwide many research teams are investigating this issue.

Lastly, estimating the interaction forces between the user and the robot is particularly relevant for two main reasons. From a design perspective the assessment of shear and compressive components of the interaction forces can provide useful data to design more comfortable and ergonomic physical interfaces (Langlois et al., 2018), with reduced undesired parasitic forces on the user's musculoskeletal system, wide areas to distribute pressure and tailored coupling with the user's soft tissues. From a functional perspective, the assessment of interaction forces could provide information about the effectiveness and quality of the WR assistance. Despite their great importance, assessing interaction forces may be limited by technological constraints, as either the WR needs to integrate *ad-hoc* force/torque sensors or the experimental set-up should be designed to include sensory systems at the human-robot interface (Donati et al., 2013). Currently, techniques, both accurate and practical, for dynamic in-the-loop pressure measurements are still lacking. Human-machine interaction is one area in which kinetics are of utmost importance. Nevertheless, interaction forces between the user and the machine are likely underestimated and rarely reported in the literature (del Carmen Sanchez-Villamañan et al., 2019).

Considering the complexity and intrinsic variability of measuring human/robot performance indicators for WRs, it is important to further explore the use of models, both software simulations of human robot interaction as well as advanced testing dummies that simulate the human on all relevant aspects. Once such models can be validated for their ability to represent a certain population, and are approved by the community, important gains in efficiency may be reached. Thereby, the wide range of WR application scenarios needs to be taken into account, e.g., medical WRs call for specific biomechanical and/or physiological metrics and exhibit very strict requirements.

3. USER EXPERIENCE PERSPECTIVE

Due to their tight connection with human users, the adequacy of WRs strongly depends on the experience of and the interaction with their users. When assessing the user outcomes of a WR application, experiences will likely reflect the benefits perceived in terms of physical function, but perceptual, emotional, and cognitive aspects also need to be considered. Recent research has explored how to measure, understand, and consider the users' views. For systematic consideration, existing human-oriented design approaches evaluate user experience and integrate it into

design processes, e.g., ISO 9241 (Jokela et al., 2003) or human-machine-centered design (Beckerle et al., 2017a). ISO 9241 defines user experience as perception and reactions of a person resulting from the use of a system, i.e., including aesthetic aspects (Hassenzahl and Tractinsky, 2006) or effects of neural plasticity through co-adaptation (Beckerle et al., 2019). Considering user experience early on could help to improve designs already during their development and experience measures could be meshed in the process of co-adaptation. In design, for instance, experience might directly be assessed for particular components, e.g., the intuitivity of a control algorithm, and serve as a predictor of device acceptance and efficacy (Beckerle et al., 2017b), which also relates the users' attitudes and predispositions (Gauthier-Gagnon et al., 1999; Gallagher, 2005; Kammers et al., 2006).

To quantitatively assess and understand users' views and needs in the first place, studies of human factors influencing the experience of the technical system and, in the long term, validated assessment methods are required. To this end, theoretical models of human factors are helpful (Karwowski, 2006; Wilson and Sharples, 2015), but might require customization regarding the specific application: Gauthier-Gagnon et al. (1999), for example, have proposed a model of human factors regarding lower limb prostheses. The model distinguishes between enabling factors, which might be altered by design, as well as predisposing and psychosocial factors. From an engineering point of view, the latter two might appear less important, but on the contrary, the model explains how technical design might not be able to meet a user's needs since unforeseen psychological effects might alter the resulting cybernetic performance, e.g., when the user's perceived security is compromised by the device (Legro et al., 1998; Gallagher and MacLachlan, 2000; Beckerle et al., 2017a). The literature provides extensive information about potentially relevant psychological concepts that influence acceptance and performance of WRs. For some devices, for example, the subjective sense of embodiment (Rognini and Blanke, 2016; Beckerle et al., 2019), the sense of agency over the device (Caspar et al., 2015; Endo et al., 2020), or the subjective cognitive effort (Beckerle et al., 2017a) have been suggested to be crucial.

Human-in-the-loop experiments that get users in touch with prototypal components or system implementations appear promising and may provide useful information about how variations of the technical system modulate the users' experiences (Beckerle et al., 2017b, 2019). Assuming device embodiment, agency, and cognitive effort are promising measures in WR benchmarking: nevertheless, accepted standardized testing procedures are still missing. These might include psychometric tools to evaluate subjective experience (Hart and Staveland, 1988; Longo et al., 2008; Caspar et al., 2015) as well as more objective behavioral measures, e.g., proprioceptive drift for embodiment (Christ and Reiner, 2014), intentional binding techniques for agency (Caspar et al., 2015; Endo et al., 2020), or physiological measures, such as heart rate (Ikehara and Crosby, 2005), electrodermal activity, or neurophysiological measures (Christ and Reiner, 2014). Such systematic measures might not only be used to consider user experience in WR design, but could also be a means to implement adaptive control schemes that

coordinate control behavior to improve user experience, e.g., predicting embodiment outcome to foster it by appropriately adjusted control (Schürmann et al., 2019). While physiological measurements and electrical stimulation might support this by exploiting neuroplastic effects, deeper investigation of brain plasticity is subject to ongoing research (McGie et al., 2015; Makin et al., 2017). Future human-machine interfaces might be able to mediate affective signals, and thereby, also forward emotional and social information to the users (Beckerle et al., 2018).

4. METHODOLOGICAL PERSPECTIVE

Turning the existing metrics, protocols, and algorithms into one harmonized benchmarking ecosystem is an important challenge that needs to be addressed for benchmarking to be converted into common practice. This process has to consider several perspectives (see **Figure 1**) and faces the challenge of finding new and common terminology.

First, benchmarking should allow reproducibility of results, defined as "the obtention of comparable results by different teams, measuring systems, and locations" (Plesser, 2018). The development of a reproducible experiment should clearly consider at least the following four aspects: the physical testbed and environment, the experimental procedure, the data format, and the performance metrics (Torricelli et al., 2015). The concept of reproducibility claims that a range of variations in these elements may not affect the comparability of results, while it greatly improves the chance to be adopted by many users. The main question in this respect is "how different can two testbeds, protocols, measurement systems be to still allow for a truthful comparison?" Currently, there are no guidelines available to help researchers answer this question and to provide a clear description of these components in a standardized way. Fortunately, some editorial initiatives are currently encouraging this direction, e.g., the "R-articles" initiative proposed by (Bonsignorio, 2017). Reproducibility in WRs experiments can be particularly complicated, because the results may be influenced by variables related to human-related aspects that can be hardly controlled or classified, such as the neurological and physical conditions of the user, the amount and type of familiarization with the device, the tuning procedure of the control system, as well as several environmental, i.e., non-technical, factors.

The second aspect is the transferability of results, i.e., the ability of predicting how a system would behave in the real world, by means of experiments conducted in a controlled (typical laboratory) environment. This problem is now becoming more and more relevant due to the increasing number of applications of exoskeletons in diverse contexts. Performing the experiments in a real setting may be either not possible (e.g., in industrial settings) or too complex, due to the multiple variations in the environment, which would imply the execution of an excessive number of experiments. Two promising approaches are the use of complex mechatronic simulators, e.g., the CAREN system from MOTEK, or the

decomposition of the complex tasks into basic environmental conditions and motor skills (Torricelli and Pons, 2019). The problem of transferability is particularly complex when it refers to user experience, due to the difficulty to generalize across multiple potential users with variable needs. This may explain why these methods appear to be scarcely applied in the field of WRs up to now (Beckerle et al., 2017b). Moreover, qualitative data can provide very rich information for development processes, but still not very easy to be considered as a hard benchmark.

The third aspect is related to understandability. Benchmarks should not only serve developers and researchers to perform deep technical analysis on their systems, but also to the end-users, to help them compare the different (but apparently similar) solutions available in the market and make the right choice. This can be done only if the user can grasp the main features of the system clearly and quickly. Thus, conveying the benchmarking results using non-technical terminology is of utmost importance. Language should also consider that a single term may have different meanings depending on the user, e.g., medical doctor, industrial stakeholder, generic user, etc., and the related application domain. Last but not least: shareability. Let's consider the hypothetical case in which benchmarking is adopted massively by the WR community worldwide. Where will all those data generated by the different laboratories be stored? Benchmarking, by definition, should allow the comparison with a point of reference. How can such a reference be calculated? How can we derive comparisons? Standards may help in this process by establishing fixed reference values to categorize performance into discrete levels but, in this evolving field, it is more than likely that the performance references will also evolve over time. This calls for a centralized software platform that can gather both data and algorithms, and allow comparisons between the scores obtained by one system with all those already tested. However, there are currently two main barriers that can be identified. First, the availability of researchers and developers to provide access to data obtained on their WRs. In this respect, some questions emerge: at what level of detail need data be shared? To what extent can benchmarking and confidentiality matters coexist? The second potential roadblock is the compliance with privacy regulation, e.g., GDPR, which applies to any experiment generating human sensible data. Overcoming these barriers would considerably increase the probability of benchmarking to be used worldwide, and being converted into the de-facto methodology for evaluation of performance.

5. CONCLUSIONS

Benchmarking is more than measuring or assessing. It is a methodology that allows the entire innovation chain to be monitored and potentially predicted. Without benchmarks, development efforts risk to reach only a small portion of the market, instead of favoring a global shift of the society toward the inclusion of wearable robotic technologies in daily

life. The close interaction between a human and a WR poses special challenges to researchers willing to quantify the different aspects of the symbiotic performance. Several international initiatives are paving the way for a standardized benchmarking ecosystem, which has the ambitious goal of facilitating the matching between user demands and product capabilities.

In this article, we outline the research directions that in our opinion are the main determinants of this endeavor and exemplify the complex landscape into the three main areas here described. In the following, we highlight a number of research questions that, in our opinion, will be key to drive future efforts in the field.

Since functional performance and user experience are in reality highly intertwined to each other, we should ask ourselves: would it be possible to predict the user's view from objective physiological, psychophysiological or biomechanical measurements? If we could do so, this would significantly contribute to speed up testing-development iterations and improve individualizing WRs.

The human and the machine are two intelligent counterparts that should learn to interact with each other to achieve a given goal (Beckerle et al., 2017b, 2019). The particular contributions of both agents to the joint task are not fully understood. Establishing the cause-effect relationship between the internal processes and the achievement of the goals is one of the main challenges in benchmarking research, with tremendous potential benefits. Due to the unavoidable presence of the human in the loop, technology providers may encounter difficulties in demonstrating a certain level of performance for their device. In other words: how can the contribution of the human be excluded when comparing different systems' performances? This problem, clearly evident, e.g., in Cybathlon competition—where the performance strongly relies on the pilot's skills, is an open issue that should be urgently considered (Makin et al., 2017).

Finally, a good measured variable does not mean a useful measure of performance. A typical example is kinematics: having a joint profile closer to human healthy reference, e.g., Winter's data, may not tell anything about stability, efficiency, or safety of the device. Additionally, time profiles are usually difficult to grasp for non-technical users. How can we convert these variables into useful indicators of performance? We advocate that WR research and development should strive for finding the optimal balance between measurable, well-defined, and relatively easy-to-administer benchmarks to improve users' outcomes.

AUTHOR CONTRIBUTIONS

DT and PB conceptualized the article and coordinated its development as well as the integration of individual contributions. All authors contributed the content, perspectives, and references as well as discussed and revised the manuscript.

FUNDING

This work has been supported by the H2020 Project EUROBENCH (grant no. 779963), and was partly based on

REFERENCES

- Ármannsdóttir, A. L., Beckerle, P., Moreno, J. C., van Asseldonk, E. H. F., Manrique-Sancho, M.-T., del Ama, A., et al. (2020). Assessing the involvement of users during development of lower limb wearable robotic exoskeletons: a survey study. *Hum. Factors* 62, 351–364. doi: 10.1177/0018720819883500
- Baltrusch, S. J., van Dieën, J. H., Koopman, A. S., Näf, M. B., Rodriguez-Guerrero, C., Babič, J., et al. (2020). Spexor passive spinal exoskeleton decreases metabolic cost during symmetric repetitive lifting. *Eur. J. Appl. Physiol.* 120, 401–412. doi: 10.1007/s00421-019-04284-6
- Beckerle, P., Castellini, C., and Lengenbacher, B. (2019). Robotic interfaces for cognitive psychology and embodiment research: a research roadmap. *Wiley Interdiscipl. Rev. Cogn. Sci.* 10:e1486. doi: 10.1002/wcs.1486
- Beckerle, P., Christ, O., Schürmann, T., Vogt, J., von Stryk, O., and Rinderknecht, S. (2017a). A human-machine-centered design method for (powered) lower limb prosthetics. *Robot. Auton. Syst.* 95, 1–12. doi: 10.1016/j.robot.2017.05.004
- Beckerle, P., Kõiva, R., Kirchner, E. A., Bekrater-Bodmann, R., Dosen, S., Christ, O., et al. (2018). Feel-good robotics: requirements on touch for embodiment in assistive robotics. *Front. Neurobot.* 12:84. doi: 10.3389/fnbot.2018.00084
- Beckerle, P., Salvietti, G., Unal, R., Prattichizzo, D., Rossi, S., Castellini, C., et al. (2017b). A human-robot interaction perspective on assistive and rehabilitation robotics. *Front. Neurobot.* 11:24. doi: 10.3389/fnbot.2017.00024
- Bessler, J., Schaake, L., Bidard, C., Buurke, J. H., Lassen, A. E. B., Nielsen, K., et al. (2018). “COVR-towards simplified evaluation and validation of collaborative robotics applications across a wide range of domains based on robot safety skills,” in *International Symposium on Wearable Robotics* (Pisa; Cham: Springer), 123–126. doi: 10.1007/978-3-030-01887-0_24
- Bogue, R. (2018). Exoskeletons-a review of industrial applications. *Ind. Robot Int. J.* 45, 585–590. doi: 10.1108/IR-05-2018-0109
- Bonsignorio, F. (2017). A new kind of article for reproducible research in intelligent robotics [from the field]. *IEEE Robot. Autom. Mag.* 24, 178–182. doi: 10.1109/MRA.2017.2722918
- Caspar, E. A., Cleeremans, A., and Haggard, P. (2015). The relationship between human agency and embodiment. *Conscious. Cogn.* 33, 226–236. doi: 10.1016/j.concog.2015.01.007
- Christ, O., and Reiner, M. (2014). Perspectives and possible applications of the rubber hand and virtual hand illusion in non-invasive rehabilitation: technological improvements and their consequences. *Neurosci. Biobehav. Rev.* 44, 33–44. doi: 10.1016/j.neubiorev.2014.02.013
- Collins, S. H., Wiggan, M. B., and Sawicki, G. S. (2015). Reducing the energy cost of human walking using an unpowered exoskeleton. *Nature* 522, 212–215. doi: 10.1038/nature14288
- Davis, K. G., Reid, C. R., Rempel, D. D., and Treaster, D. (2020). Introduction to the human factors special issue on user-centered design for exoskeleton. *Hum. Factors* 62, 333–336. doi: 10.1177/0018720820914312
- del Carmen Sanchez-Villamañan, M., Gonzalez-Vargas, J., Torricelli, D., Moreno, J. C., and Pons, J. L. (2019). Compliant lower limb exoskeletons: a comprehensive review on mechanical design principles. *J. Neuroeng. Rehabil.* 16:55. doi: 10.1186/s12984-019-0517-9
- Donati, M., Vitiello, N., De Rossi, S. M. M., Lenzi, T., Crea, S., Persichetti, A., et al. (2013). A flexible sensor technology for the distributed measurement of interaction pressure. *Sensors* 13, 1021–1045. doi: 10.3390/s130101021
- Endo, S., Fröhner, J., Music, S., Hirche, S., and Beckerle, P. (2020). Effect of external force on agency in physical human-machine interaction. *Front. Hum. Neurosci.* 14:114. doi: 10.3389/fnhum.2020.00114
- Gallagher, P., and MacLachlan, M. (2000). Development and psychometric evaluation of the trinity amputation and prosthesis experience scales (TAPES). *Rehabil. Psychol.* 45, 130–154. doi: 10.1037/0090-5550.45.2.130
- Gallagher, S. (2005). Dynamic models of body schematic processes. *Adv. Conscious. Res.* 62:233. doi: 10.1075/aicr.62.15gal
- Gauthier-Gagnon, C., Grisé, M. C., and Potvin, D. (1999). Enabling factors related to prosthetic use by people with transtibial and transfemoral amputation. *Archiv. Phys. Med. Rehabil.* 80, 706–713. doi: 10.1016/S0003-9993(99)90177-6
- Ghillebert, J., De Bock, S., Flynn, F., Geeroms, J., Tassignon, B., Roelands, B., et al. (2019). Guidelines and recommendations to investigate the efficacy of a lower-limb prosthetic device: a systematic review. *IEEE Trans. Med. Robot. Bionics* 1, 279–296. doi: 10.1109/TMRB.2019.2949855
- Gopura, R. A. R. C., Bandara, D. S. V., Kiguchi, K., and Mann, G. K. I. (2016). Developments in hardware systems of active upper-limb exoskeleton robots: a review. *Robot. Auton. Syst.* 75, 203–220. doi: 10.1016/j.robot.2015.10.001
- Hart, S. G., and Staveland, L. E. (1988). Development of NASA-TLX (task load index): results of empirical and theoretical research. *Adv. Psychol.* 52, 139–183. doi: 10.1016/S0166-4115(08)62386-9
- Hassenzahl, M., and Tractinsky, N. (2006). User experience-a research agenda. *Behav. Inform. Technol.* 25, 91–97. doi: 10.1080/01449290500330331
- Ikehara, C. S., and Crosby, M. E. (2005). “Assessing cognitive load with physiological sensors,” in *Proceedings of the 38th Annual Hawaii International Conference on System Sciences* (Big Island, HI: IEEE). doi: 10.1109/HICSS.2005.103
- Jokela, T., Iivari, N., Matero, J., and Karukka, M. (2003). “The standard of user-centered design and the standard definition of usability: analyzing ISO 13407 against ISO 9241-11,” in *Proceedings of the Latin American Conference on Human-Computer Interaction* (Rio de Janeiro), 53–60. doi: 10.1145/944519.944525
- Kammers, M. P. M., van der Ham, I. J. M., and Dijkerman, H. C. (2006). Dissociating body representations in healthy individuals: differential effects of a kinaesthetic illusion on perception and action. *Neuropsychologia* 44, 2430–2436. doi: 10.1016/j.neuropsychologia.2006.04.009
- Karwowski, W. (2006). *The Discipline of Human Factors and Ergonomics*. Hoboken, NJ: John Wiley & Sons, Inc.
- Kim, J., Lee, G., Heimgartner, R., Revi, D. A., Karavas, N., Nathanson, D., et al. (2019). Reducing the metabolic rate of walking and running with a versatile, portable exosuit. *Science* 365, 668–672. doi: 10.1126/science.aav7536
- Koopman, A. S., Näf, M., Baltrusch, S. J., Kingma, I., Rodriguez-Guerrero, C., Babič, J., et al. (2020). Biomechanical evaluation of a new passive back support exoskeleton. *J. Biomech.* 102:109795. doi: 10.1016/j.jbiomech.2020.109795
- Langlois, K., Moltedo, M., Bacek, T., Rodriguez-Guerrero, C., Vanderborcht, B., and Lefebvre, D. (2018). “Design and development of customized physical interfaces to reduce relative motion between the user and a powered ankle foot exoskeleton,” in *IEEE International Conference on Biomedical Robotics and Biomechanics* (Enschede: IEEE). doi: 10.1109/BIOROB.2018.8487706
- Lee, H.-J., Lee, S.-H., Seo, K., Lee, M., Chang, W. H., Choi, B.-O., et al. (2019). Training for walking efficiency with a wearable hip-assist robot in patients with stroke: A pilot randomized controlled trial. *Stroke* 50, 3545–3552. doi: 10.1161/STROKEAHA.119.025950
- Legro, M. W., Reiber, G. D., Smith, D. G., del Aguila, M., Larsen, J., and Boone, D. (1998). Prosthesis evaluation questionnaire for persons with lower limb amputations: assessing prosthesis-related quality of life. *Archiv. Phys. Med. Rehabil.* 79, 931–938. doi: 10.1016/S0003-9993(98)90090-9
- Longo, M. R., Schüür, F., Kammers, M. P. M., Tsakiris, M., and Haggard, P. (2008). What is embodiment? A psychometric approach. *Cognition* 107, 978–998. doi: 10.1016/j.cognition.2007.12.004
- Makin, T. R., de Vignemont, F., and Faisal, A. A. (2017). Neurocognitive barriers to the embodiment of technology. *Nat. Biomed. Eng.* 1, 1–3. doi: 10.1038/s41551-016-0014
- Martini, E., Crea, S., Parri, A., Bastiani, L., Faraguna, U., McKinney, Z., et al. (2019). Gait training using a robotic hip exoskeleton improves metabolic gait efficiency in the elderly. *Sci. Rep.* 9, 1–12. doi: 10.1038/s41598-019-43628-2
- Maurice, P., Čamernik, J., Gorjan, D., Schirrmaster, B., Bornmann, J., Tagliapietra, L., et al. (2019). Objective and subjective effects of a passive exoskeleton

- on overhead work. *IEEE Trans. Neural Syst. Rehabil. Eng.* 28, 152–164. doi: 10.1109/TNSRE.2019.2945368
- McGie, S. C., Zariffa, J., Popovic, M. R., and Nagai, M. K. (2015). Short-term neuroplastic effects of brain-controlled and muscle-controlled electrical stimulation. *Neuromod. Technol. Neural Interface* 18, 233–240. doi: 10.1111/ner.12185
- Molledo, M., Cavallo, G., Baček, T., Lataire, J., Vanderborght, B., Lefeber, D., et al. (2019). Variable stiffness ankle actuator for use in robotic-assisted walking: control strategy and experimental characterization. *Mech. Mach. Theory* 134, 604–624. doi: 10.1016/j.mechmachtheory.2019.01.017
- Näf, M. B., Junius, K., Rossini, M., Rodriguez-Guerrero, C., Vanderborght, B., and Lefeber, D. (2018a). Misalignment compensation for full human-exoskeleton kinematic compatibility: state of the art and evaluation. *Appl. Mech. Rev.* 70:050802. doi: 10.1115/1.4042523
- Näf, M. B., Koopman, A. S., Baltrusch, S., Rodriguez-Guerrero, C., Vanderborght, B., and Lefeber, D. (2018b). Passive back support exoskeleton improves range of motion using flexible beams. *Front. Robot. AI* 5:72. doi: 10.3389/frobt.2018.00072
- Pacifico, I., Scano, A., Guanzoli, E., Moise, M., Morelli, L., Chiavenna, A., et al. (2020). An experimental evaluation of the proto-mate: a novel ergonomic upper-limb exoskeleton to reduce workers' physical strain. *IEEE Robot. Autom. Mag.* 27, 54–65. doi: 10.1109/MRA.2019.2954105
- Pinto-Fernandez, D., and Torricelli, E. A. (2020). Performance evaluation of lower limb exoskeletons: a systematic review. *IEEE Trans. Neural Syst. Rehabil. Eng.* 28, 1573–1583. doi: 10.1109/TNSRE.2020.2989481
- Plesser, H. E. (2018). Reproducibility vs. replicability: a brief history of a confused terminology. *Front. Neuroinform.* 11:76. doi: 10.3389/fninf.2017.00076
- Price, M. A., Beckerle, P., and Sup, F. C. (2019). Design optimization in lower limb prostheses: a review. *IEEE Trans. Neural Syst. Rehabil. Eng.* 27, 1574–1588. doi: 10.1109/TNSRE.2019.2927094
- Rognini, G., and Blanke, O. (2016). Cognetics: robotic interfaces for the conscious mind. *Trends Cogn. Sci.* 20, 162–164. doi: 10.1016/j.tics.2015.12.002
- Schürmann, T., Mohler, B. J., Peters, J., and Beckerle, P. (2019). How cognitive models of human body experience might push robotics. *Front. Neurobot.* 13:14. doi: 10.3389/fnbot.2019.00014
- Torricelli, D., Gonzalez-Vargas, J., Veneman, J. F., Mombaur, K., Tsagarakis, N., Del-Ama, A. J., et al. (2015). Benchmarking bipedal locomotion: a unified scheme for humanoids, wearable robots, and humans. *IEEE Robot. Autom. Mag.* 22, 103–115. doi: 10.1109/MRA.2015.2448278
- Torricelli, D., and Pons, J. L. (2019). “Eurobench: preparing robots for the real world,” in *International Symposium on Wearable Robotics* (Houston, TX: Springer), 375–378. doi: 10.1007/978-3-030-01887-0_72
- Wilson, J. R., and Sharples, S. (2015). *Evaluation of Human Work*. Boca Raton, FL: CRC Press.
- Windrich, M., Grimmer, M., Christ, O., Rinderknecht, S., and Beckerle, P. (2016). Active lower limb prosthetics: a systematic review of design issues and solutions. *Biomed. Eng. Online* 15, 5–19. doi: 10.1186/s12938-016-0284-9
- Conflict of Interest:** JV works at Hocoma AG, a company that develops and markets robots for functional movement therapy. SC is a shareholder and scientific advisor of IUVO S.r.l., a spin-off company of Scuola Superiore Sant'Anna, which develops wearable robots.
- The remaining authors declare that the research was conducted in the absence of any commercial or financial relationships that could be construed as a potential conflict of interest.

Copyright © 2020 Torricelli, Rodriguez-Guerrero, Veneman, Crea, Briem, Lengenbacher and Beckerle. This is an open-access article distributed under the terms of the Creative Commons Attribution License (CC BY). The use, distribution or reproduction in other forums is permitted, provided the original author(s) and the copyright owner(s) are credited and that the original publication in this journal is cited, in accordance with accepted academic practice. No use, distribution or reproduction is permitted which does not comply with these terms.



Occurrence and Type of Adverse Events During the Use of Stationary Gait Robots—A Systematic Literature Review

Jule Bessler^{1,2*}, Gerdienke B. Prange-Lasonder^{1,3}, Robert V. Schulte^{1,2},
Leendert Schaake¹, Erik C. Prinsen^{1,3} and Jaap H. Buurke^{1,2}

¹ Roessingh Research and Development, Enschede, Netherlands, ² Department of Biomedical Signals and Systems, University of Twente, Enschede, Netherlands, ³ Department of Biomechanical Engineering, University of Twente, Enschede, Netherlands

OPEN ACCESS

Edited by:

Eduardo Rocon,
Consejo Superior de Investigaciones
Científicas (CSIC), Spain

Reviewed by:

Giorgia Chini,
Sapienza University of Rome, Italy
Guillermo Asín-Prieto,
Independent Researcher,
Abadiño, Spain

*Correspondence:

Jule Bessler
j.bessler@rrd.nl

Specialty section:

This article was submitted to
Biomedical Robotics,
a section of the journal
Frontiers in Robotics and AI

Received: 30 April 2020

Accepted: 05 October 2020

Published: 16 November 2020

Citation:

Bessler J, Prange-Lasonder GB,
Schulte RV, Schaake L, Prinsen EC
and Buurke JH (2020) Occurrence
and Type of Adverse Events During
the Use of Stationary Gait Robots—A
Systematic Literature Review.
Front. Robot. AI 7:557606.
doi: 10.3389/frobt.2020.557606

Robot-assisted gait training (RAGT) devices are used in rehabilitation to improve patients' walking function. While there are some reports on the adverse events (AEs) and associated risks in overground exoskeletons, the risks of stationary gait trainers cannot be accurately assessed. We therefore aimed to collect information on AEs occurring during the use of stationary gait robots and identify associated risks, as well as gaps and needs, for safe use of these devices. We searched both bibliographic and full-text literature databases for peer-reviewed articles describing the outcomes of stationary RAGT and specifically mentioning AEs. We then compiled information on the occurrence and types of AEs and on the quality of AE reporting. Based on this, we analyzed the risks of RAGT in stationary gait robots. We included 50 studies involving 985 subjects and found reports of AEs in 18 of those studies. Many of the AE reports were incomplete or did not include sufficient detail on different aspects, such as severity or patient characteristics, which hinders the precise counts of AE-related information. Over 169 device-related AEs experienced by between 79 and 124 patients were reported. Soft tissue-related AEs occurred most frequently and were mostly reported in end-effector-type devices. Musculoskeletal AEs had the second highest prevalence and occurred mainly in exoskeleton-type devices. We further identified physiological AEs including blood pressure changes that occurred in both exoskeleton-type and end-effector-type devices. Training in stationary gait robots can cause injuries or discomfort to the skin, underlying tissue, and musculoskeletal system, as well as unwanted blood pressure changes. The underlying risks for the most prevalent injury types include excessive pressure and shear at the interface between robot and human (cuffs/harness), as well as increased moments and forces applied to the musculoskeletal system likely caused by misalignments (between joint axes of robot and human). There is a need for more structured and complete recording and dissemination of AEs related to robotic gait training to increase knowledge on risks. With this information, appropriate mitigation strategies can and should be developed and implemented in RAGT devices to increase their safety.

Keywords: robot-assisted gait training, adverse event (AE), safety, physical human-robot interaction (pHRI), injuries (MeSH), stationary gait robots, rehabilitation robotics

INTRODUCTION

Robot-assisted gait training (RAGT) is frequently used in rehabilitation to promote walking function in individuals with various disabilities, such as stroke, spinal cord injury (SCI), or cerebral palsy. The rates of disability, e.g., as a result of chronic stroke, are rising due to population aging. According to the World Health Organization, the proportion of the world's population aged over 60 years will increase drastically from 12% in 2015 to 22% in 2050 (World Health Organization, 2018). This leads to an increasing amount of persons with chronic walking disabilities that will in turn lead to a lack of skilled physical therapists.

Robotic gait trainers can be used for various patient groups to provide them with high-intensity gait training. While traditional gait training on a treadmill is associated with high physical strain on the therapists and a need for two to three therapists per patient, robotic gait trainers have the advantage of reducing the time and effort required from the therapist. As a result, they potentially allow for longer or more frequent sessions of high-intensity gait training for the patient (Hesse et al., 2003).

There are different types of robotic gait trainers. Overground gait trainers include ambulatory exoskeletons, such as the ReWalk (Argo Medical Technologies Ltd., Israel), Ekso GT (Ekso Bionics, USA), HAL (Cyberdyne, Japan), REX (Rex Bionics, New Zealand), and Indego (Parker Hannifin Corp., USA). Stationary gait trainers can be divided into two subcategories: exoskeleton-type devices and end-effector-type devices. Exoskeleton-type devices usually consist of a treadmill, an overhead harness for body-weight support (BWS), and a lower limb exoskeleton fixed to a frame. Examples of exoskeleton-type devices are the Lokomat (Hocoma, Switzerland), AutoAmbulator (Motorika, USA), RoboGait (Bama Technology, Turkey), Walkbot (P&S Mechanics, South Korea), and NX-A3 (Guangzhou YiKing Medical Equipment Industrial, China). End-effector-type devices, such as the G-EO system (Reha-Technology, Switzerland), LokoHelp (Woodway, Germany), Gait Trainer GT II (Reha Stim Medtec, Germany), and THERA-Trainer Lyra (medica Medizintechnik, Germany), consist of an overhead BWS and robotic end-effectors that are attached to the patient's feet and are moved along reference trajectories of normal walking.

The advantages of RAGT with regard to time and physical effort required by the therapist are obvious (Mehrholtz et al., 2017). However, the mechanical power of the robots in combination with the close physical connection with the patient inevitably introduces safety issues. The robot is attached to the patient's limbs, which can lead to dangerous interaction forces. Safe ranges of normal and shear forces that can be applied to a patient during training with a robot are yet to be defined. While recent research has focused on safe limit values in collision situations of physical human-robot interaction (pHRI) (Haddadin et al., 2007; Behrens and Elkmann, 2014), situations of continuous contact are challenging to assess. This is mostly due to a lack of reliable measurement methods, especially concerning shear forces. Much effort has recently been put into the development of those measurement methods (Lenzi et al., 2011; Sugiura et al., 2012; Makino et al., 2013; Castellini

and Ravindra, 2014; Ito et al., 2014; Tamez-Duque et al., 2015; Wilkening et al., 2016; Alavi et al., 2017; Sadarangani et al., 2017). A method that can be considered as the gold standard for measuring normal and tangential forces is the load cell. However, these sensors are rather bulky and expensive, which are possible reasons why many studies implement force sensitive resistors to assess the interaction between a human and a robotic, orthotic or load-carrying device (Castellini and Ravindra, 2014; Tamez-Duque et al., 2015; Sadarangani et al., 2017). Drawbacks of force sensitive resistors include a typically non-linear transfer function, as well as sensitivity to changes of humidity and surface curvature (Castellini and Ravindra, 2014; Wettenschwiler et al., 2015), which are highly relevant during the measurement of prolonged human-robot interaction (HRI) between skin and cuff. A number of studies have focused on developing and implementing alternative sensing devices, such as optical sensors (Lenzi et al., 2011; Sugiura et al., 2012; Makino et al., 2013), vision-based tactile sensors (Ito et al., 2014), and pneumatic padding (Wilkening et al., 2016; Alavi et al., 2017); however, these methods are still in the research state.

Besides the much needed safe limit values for continuous HRI, simplifying the safety evaluation process is another contributor to improving safety in collaborative and rehabilitation robotics. This is, for example, done in the COVR project (www.safearoundrobots.com) by providing various structured tools for robot developers, including establishing the best practices for safety-related measurements and promoting the development and application of unified safety testing procedures. As a first step in this, specifically regarding rehabilitation robots, risks, and needs covering all aspects of continuous patient-robot interaction should be assessed in a structured way, which in turn should inform the development of relevant measurement methods. Therefore, adverse events (AEs) of existing rehabilitation robots need to be taken into account and associated risks need to be identified. A recent review assessed the aspects of risk management and the occurrence of AEs in overground exoskeletons (He et al., 2017). Both the FDA (Food and Drug Administration of the United States) database MAUDE (Manufacturer and User Facility Device Experience) and peer-reviewed publications including any of the overground exoskeleton device names mentioned above were searched for AEs during the usage of exoskeletons. The review found, among other AEs, a number of device malfunctions, skin and tissue damages, and two incidences of bone fractures. Both incidences of bone fractures were attributed to misalignment of the device causing a discrepancy between human joint axis and robot joint axis. This is an indication for the need for extensive post-market surveillance and appropriate testing methods for safety of robotic gait rehabilitation devices.

A recent Cochrane review assessing the clinical effects of electromechanical-assisted training for walking after stroke (Mehrholtz et al., 2017) also collected information on any AEs reported in those studies. The most frequently documented adverse effects and reasons for dropout were pain and skin breakdown. In light of obvious differences between stationary RAGT and overground exoskeletons, such as the use of BWS in stationary RAGT compared with crutches in overground

exoskeletons to decrease the risk of falls, and professional supervision compared with oversight by a trained family member, it seems straightforward to assume that AEs in stationary RAGT are less frequent and less severe than those in overground exoskeletons due to its controlled environment. However, there is insufficient structured information available on the occurrence of AEs in stationary RAGT. Moreover, there currently is no European equivalent to the US MAUDE database in operation, and other parts of the world have in turn different processes (Mishra, 2017), which makes it difficult to find reliable worldwide information on the frequency and severity of AEs.

Therefore, this paper presents a systematic literature review of AEs that occurred during training with stationary robotic gait trainers. We hypothesized that there are incidences of skin breakdown and bone fractures in RAGT and further expected that the reporting of these events is lacking detail. We searched both bibliographic and full-text literature databases for peer-reviewed articles describing the outcomes of RAGT and specifically mentioning AEs. From this, we extracted information about AEs and their reporting, with the objective to get an overview of the occurrence and type of AEs in stationary robotic gait trainers and identify particular risks involved.

METHODS

Search Strategy and Data Sources

We conducted an electronic database search in relevant bibliographic (PubMed, Scopus, Web of Science) and full-text databases (IEEE Xplore Digital Library, SpringerLink, ScienceDirect, SAGE Publications, AHA Journals) from inception to mid-June 2019. We used the following search terms for all databases:

- Electro-mechanical, electromechanical, robotics, robot-assisted, robotics-assisted
- Exercise therapy, rehabilitation, training
- Gait, walk, walking, step, stepping, locomotor, locomotion
- Bodyweight-supported treadmill training, locomotor training, Lokomat, Gangtrainer (GT), G-EO, WALKBOT, LokoHelp
- Adverse, skin breakdown, skin lesion, skin sore, pressure sore, discomfort, abrasion.

The complete search strategy used in PubMed can be found in the Appendix (Supplementary Material). This search was adapted to suit the other databases, and we searched full text (where available), title, abstract, and keywords. Reference lists of included articles were scanned for potentially relevant additions.

Study Selection

The criteria that were applied for study selection can be found in **Table 1**. We did not apply criteria in terms of study design, population, or comparators as we aimed to find all available information on AEs in stationary robotic gait training with humans. After exclusion of duplicate entries, the titles were screened by two reviewers independently (GP and JB). Following that, the abstracts of the remaining studies were screened by EP and JB, and in the third step, the full texts were screened

by RS and JB. A third reviewer could be consulted in case of a disagreement between the two respective reviewers (EP for title screening and GP for abstract and full-text screening). Title and abstract screening were performed using a web-based tool (Ouzzani et al., 2016).

Data Extraction and Analysis

As this systematic review's main aim was to collect and analyze AEs in RAGT, we did not perform a methodological quality judgment. We employed the PRISMA reporting guidelines (Moher et al., 2009) as far as they were applicable to this review. Restrictions of their applicability were due to the fact that this review does not focus on the clinical effects of an intervention. For collecting relevant data from all included studies, we developed a structured table. The data categories that the studies were screened for are:

1. Subject characteristics
2. Training device
3. Study design
4. Description of AEs and dropouts.

We collected information on the number of subjects performing gait training, age, diagnoses, time since onset, and severity. Since the diagnoses varied strongly, no overarching measure for disease severity or disease stage could be defined to describe the functional level or chronicity. The study design type as well as the number and duration of sessions were noted. Device types (exoskeleton-type, end-effector-type, soft exosuit) and names were collected. Moreover, we screened for information on the amount of BWS and the type of HRI. Types of HRI, such as active, passive, and assistive, were based on the review by Basteris et al. (2014).

Regarding AEs, we collected the number of studies reporting the presence of AEs, number of affected study participants, methods used to detect AEs, as well as numbers and types of AEs. Where it became apparent that several studies reported on the same trial (same intervention and same patients), we excluded any double reports to avoid bias. The description of AEs was assessed for completeness. An AE description was considered as complete whenever it included (1) a description of the AE itself including the number of occurrence, (2) the number of subjects affected, and (3) the intervention during which the AE occurred. A statement that no AE occurred was rated as incomplete if it contained contradictory information or was lacking information [e.g., only part of the intervention considered, only referring to serious adverse events (SAEs)]. We only collected AEs that were related to RAGT. When an event was described by the authors as unrelated to the intervention, it was not included in the data for this review. We did, however, include events with unspecified causes.

For better comparison between studies, AE type and severity were categorized as follows. For the type of AEs, we used the categories soft tissue-related (e.g., skin reddening, lesions, bruises, discomfort from harness), musculoskeletal (e.g., joint pain, muscle pain, bone fractures), and physiological (e.g., blood pressure changes). Events that matched neither of these categories (e.g., headache, fear) were classified as other. Severity

TABLE 1 | Inclusion and exclusion criteria.

Criteria	Inclusion criteria	Exclusion criteria
1	Articles must be peer-reviewed (full) papers	Conference abstracts and other non-peer-reviewed articles were excluded
2	Articles must be trials with human subjects	All articles that were not trials including human subjects (e.g., literature reviews, study protocols, animal studies) were excluded
3	Articles must address robotic-assisted stationary gait training <ul style="list-style-type: none"> • Either exoskeleton-type or end-effector-type • Person standing upright, doing stepping movements • Being attached to the lower extremity • Stationary 	Articles addressing other technologies (e.g., surgical robots, overground exoskeletons, upper-limb robots) were excluded
4	Articles must include a specific statement about AE (this can also be a statement saying that no AE occurred)	Articles not including any statement about AE related to the robotic gait training were excluded
5	Articles must be available in the English language	Articles written in other languages were excluded

of AEs was classified as mild, moderate, or severe (adapted from Borggraefe et al., 2010; U.S. Department of Health Human Services, 2017):

- Mild: event is noticeable but easily tolerable. No medical intervention is needed, and treatment does not have to be interrupted or only for a short rest (e.g., minor discomfort, reddening)
- Moderate: event interferes with activities or treatment but can be managed by simple measures. No long-term effects (e.g., skin lesions without complications)
- Severe: event is incapacitating and requires medical attention/treatment, and normal treatment cannot be continued (e.g., bone fractures, skin lesions with complications)

If there was no description of an interruption of training or any other indication of a more severe event, the AE was assumed to be mild. Where there was no description of the AE that allowed us to conclude the severity, it was counted as unknown. Note that a severe AE as classified in this study does not automatically constitute an SAE according to the definition of the Medical Device Regulation (Regulation (EU) 2017/745 of the European Parliament of the Council of 5 April 2017 on medical devices, amending Directive 2001/83/EC, Regulation (EC) No 178/2002 and Regulation (EC) No 1223/2009 and repealing Council Directives 90/385/EEC and 93/42/EE, 2017). However, any SAE would be counted as severe in this review. To compare the severity of different AE types and between different devices or device types, we rated mild AEs with a severity of 1, moderate AEs with a severity of 4, and severe AEs with a severity of 10 and calculated the overall severity per device and per AE type as follows:

$$severity_{overall} = \frac{1 \cdot n_{mild} + 4 \cdot n_{moderate} + 10 \cdot n_{severe}}{n_{total} - n_{unknown}},$$

where n_{mild} is the number of mild AEs, $n_{moderate}$ is the number of moderate AEs, n_{severe} is the number of severe AEs, n_{total} is the

total number of reported AEs, and $n_{unknown}$ is the number of AEs with unknown severity level.

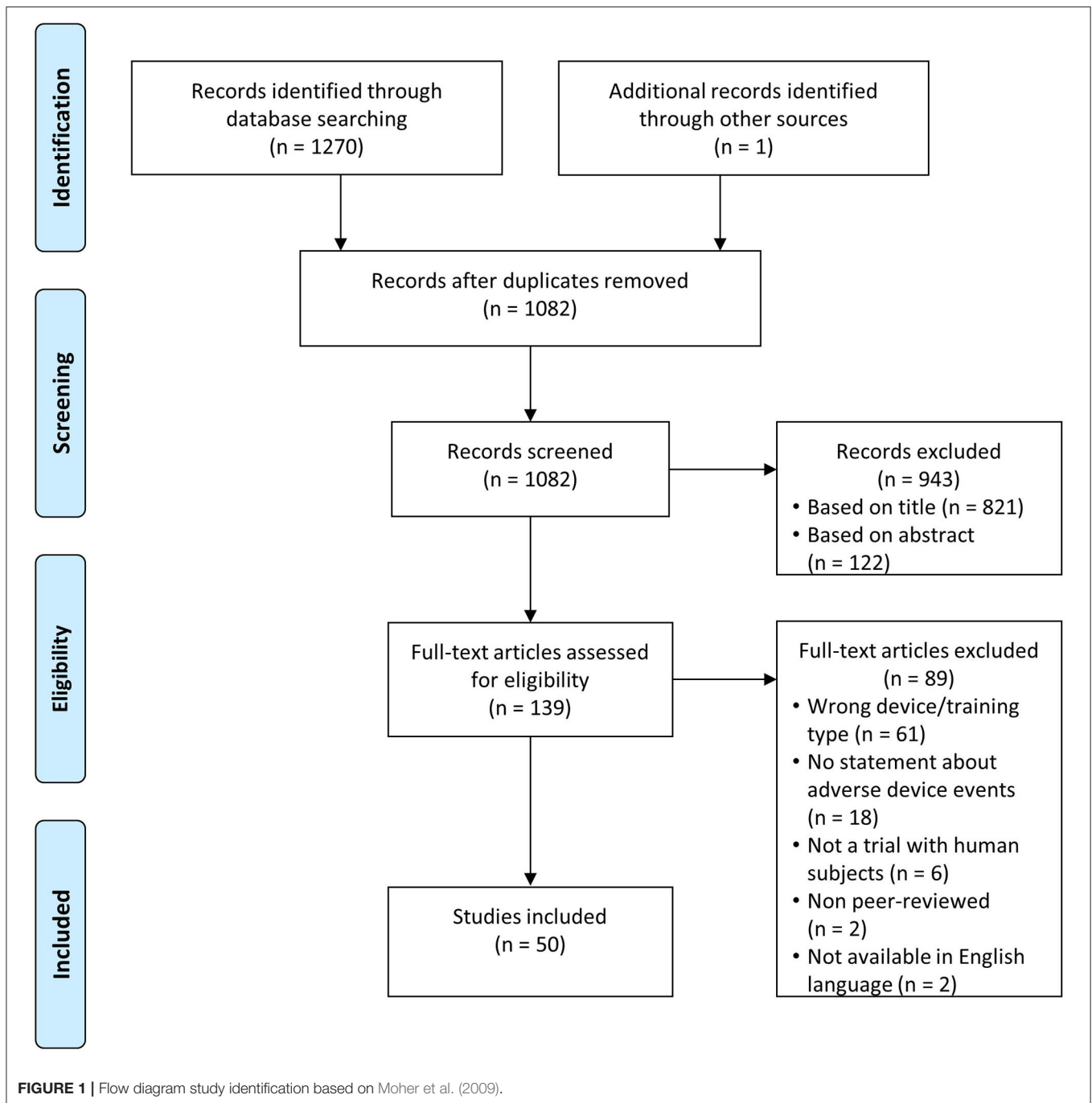
The classes of AE severity and their ratings (1 for mild, 4 for moderate, and 10 for severe) are chosen arbitrarily based on the authors' experience and judgment. They are not validated and are used solely to get a rough estimate of severities for comparisons between device types or AE types.

We performed Pearson's chi-squared tests of independence (MATLAB®, version 2019b, MathWorks, Natick, Massachusetts, USA) to investigate whether (1) devices (e.g., Lokomat, GT) are associated with AE types (e.g., soft tissue-related AEs, musculoskeletal AE), (2) device types (e.g., exoskeleton-type, end-effector-type) are associated with AE types, (3) AE types are associated with severity level (i.e., mild, moderate, severe), (4) devices are associated with severity level, and (5) device types are associated with severity level. We employed a significance level of 5%.

RESULTS

Study Selection

We identified 1,081 unique records through database searching and one addition through reference searching (Figure 1). Of those, 139 records remained after title and abstract screening, of which 50 met the inclusion criteria and were analyzed (Husemann et al., 2007; Mayr et al., 2007; Freivogel et al., 2008, 2009; Lo and Triche, 2008; Ng et al., 2008; Hesse and Werner, 2009; Borggraefe et al., 2010; Chin et al., 2010; Lo et al., 2010; Geroi et al., 2011; Morone et al., 2011; Turiel et al., 2011; Benito-Penalva et al., 2012; Carda et al., 2012; Gizzi et al., 2012; Picelli et al., 2012, 2015; Vaney et al., 2012; Geigle et al., 2013; Kelley et al., 2013a,b; Aach et al., 2014; Labruière and van Hedel, 2014; Nilsson et al., 2014; Stoller et al., 2014, 2015; Asbeck et al., 2015; Filippo et al., 2015; Ochi et al., 2015; Schoenrath et al., 2015a,b; Sczesny-Kaiser et al., 2015, 2017; Wu et al., 2015; Chua et al., 2016; Forrester et al., 2016; Ikumi et al., 2016; Kumru et al., 2016a,b; Aurich-Schuler et al., 2017; Bae et al., 2017; Chisholm et al., 2017; Esquenazi et al., 2017; Grasmücke et al., 2017; Jansen et al., 2017, 2018; Kim et al., 2019; Straudi et al., 2019; Tanaka



et al., 2019). We identified some studies with overlap in patients (Kelley et al., 2013a,b; Aach et al., 2014; Stoller et al., 2014, 2015; Sczesny-Kaiser et al., 2015; Jansen et al., 2017, 2018) and excluded double reports in the analysis of subject numbers and AE numbers.

Patients and Devices

The included studies described RAGT in 985 subjects of which 14 were healthy individuals, 341 SCI patients, 326 stroke patients, 42 traumatic brain injury patients, 67 cerebral palsy patients,

74 Parkinson's disease patients, 76 multiple sclerosis patients, 15 cardiac patients, and 30 patients with other diagnoses. Two of the included studies focused on children and adolescents (Borggraefe et al., 2010; Aurich-Schuler et al., 2017). The identified studies reported on gait training in 10 different devices: Lokomat (489 subjects in 27 studies), Gait Trainer GT (301 subjects in 8 studies; 244 subjects trained in GT II, 24 in GT I, and for 33 subjects the model was not specified), HAL (108 subjects in 9 studies), MorningWalk (25 subjects in 1 study), LokoHelp (22 subjects in 2 studies), Anklebot (14 subjects in 1 study), Gait-Assistance

TABLE 2 | Overview of studies with adverse events vs. studies without adverse events.

	Studies that reported adverse events	Studies that reported no adverse events
Number of studies	18	32
Completeness of AE description (complete/incomplete)	14/4	28/4
Number of subjects performing RAGT	291	694
Dropouts	19 dropouts in 6 studies, 0 lost to follow-up, 1 not stated	47 dropouts in 8 studies, 6 lost to follow-up in 4 studies, 3 not stated
Diagnosis	SCI, TBI, CP, stroke, PD, MS, other	SCI, TBI, CP, stroke, PD, MS, cardiac, other, healthy
Age (mean [SD of means])	42 (19)	53 (12)
Months since onset (range)	[0;276]	[1;420]
Level of severity	Mild to severe (FAC 0–4, ASIA A–D)	Mild to severe (FAC 0–5, ASIA A–D)
Study design type	7 RCT (2 pilot), 3 longitudinal uncontrolled, 2 longitudinal repeated measure (1 randomized, 1 controlled), 1 retrospective review of data, 4 case reports, 1 case series	16 RCT (2 pilot, 3 repeated measures), 9 longitudinal uncontrolled (2 pilot), 4 cross-sectional repeated measure (1 pilot), 2 longitudinal controlled, 1 longitudinal repeated measure
Number of studies per device	12 Lokomat ^a , 3 HAL ^b , 2 LokoHelp ^c , 1 GT ^d , 1 G-EO ^e	15 Lokomat ^f , 6 HAL ^g , 7 GT ^h , 1 soft exosuit ⁱ , 1 Anklebot ^j , 1 Morning Walk ^k , 1 GAR ^l , 1 PH-EXOS ^m
Number of sessions per participant (range)	[4;60]	[1;179]
Training duration per session (range) [min]	[6;60]	[0.5;45]
Total duration of training period (range) (days)	[8;84]	[1;365]
BWS (range)	(0% body weight; 100% body weight)	[0% body weight; 50% body weight]
Device types	15 exoskeleton, 4 end-effector	24 exoskeleton, 8 end-effector, 1 exosuit
Types of HRI	Assistive, active, passive	Assistive, active, passive, path guidance, resistive

SCI, spinal cord injury; TBI, traumatic brain injury; CP, cerebral palsy; PD, Parkinson's disease; MS, multiple sclerosis; SD, standard deviation; FAC, functional ambulation category; ASIA, American Spinal Injury Association; RCT, randomized controlled trial.

^aHusemann et al. (2007), Borggraefe et al. (2010), Chin et al. (2010), Carda et al. (2012), Vaney et al. (2012), Geigle et al. (2013), Kelley et al. (2013a,b), Stoller et al. (2014, 2015), Filippo et al. (2015), and Esquenazi et al. (2017).

^bNilsson et al. (2014), Ikumi et al. (2016), and Jansen et al. (2018).

^cFreivogel et al. (2008, 2009).

^dMorone et al. (2011).

^eEsquenazi et al. (2017).

^fMayr et al. (2007), Lo and Triche (2008), Lo et al. (2010), Turiel et al. (2011), Benito-Penalva et al. (2012), Gizzi et al. (2012), Labruyère and van Hedel (2014), Schoenrath et al. (2015a,b), Kumru et al. (2016a,b), Aurich-Schuler et al. (2017), Bae et al. (2017), Chisholm et al. (2017), and Straudi et al. (2019).

^gAach et al. (2014), Sczesny-Kaiser et al. (2015, 2017), Grasmücke et al. (2017), Jansen et al. (2017), and Tanaka et al. (2019).

^hNg et al. (2008), Hesse and Werner (2009), Geroin et al. (2011), Benito-Penalva et al. (2012), Picelli et al. (2012, 2015), and Chua et al. (2016).

ⁱAsbeck et al. (2015).

^jForrester et al. (2016).

^kKim et al. (2019).

^lOchi et al. (2015).

^mWu et al. (2015).

Robot GAR (13 subjects in 1 study), G-EO (7 subjects in 1 study), a soft exosuit (5 subjects in 1 study), and PH-EXOS (1 subject in 1 study). One study reported the use of both Lokomat and G-EO, and one study reported the use of both Lokomat and GT.

Adverse Events

Of the 50 included studies, 18 reported AEs, and 32 reported that there were no AEs (Table 2). The information on AEs was rated as incomplete in 8 (16%) of the 50 studies. In the studies with reported AEs, 78% of the AE descriptions were complete, whereas in the studies without reported AEs, 88% of the descriptions were complete. The dropout rate was 7% of the participants in both groups. Studies with AEs had 16 participants on average, and studies without AEs had 22 participants on average. Apart from the fact that none of the studies with healthy participants reported AEs, there were no striking differences in

subject characteristics. Both age and diagnoses were comparable. Studies with AEs were less frequently randomized controlled trials (39 compared with 50% of studies without AEs) and were more likely to be case reports or case series, some of which were focused on reporting AEs (Geigle et al., 2013; Kelley et al., 2013b; Filippo et al., 2015). Concerning devices involved, 44% of the Lokomat studies, 33% of the HAL studies, and 13% of the GT studies reported AEs. There were no AEs reported for MorningWalk, Anklebot, Gait-Assistance Robot GAR, the soft exosuit, or PH-EXOS. The range of BWS in studies reporting AEs was between 0 and 100% of body weight, whereas it was between 0 and 50% of body weight in the studies reporting no AEs.

The AE descriptions from the 18 studies that did report AEs are collected in Table 3. The most frequently reported AEs were changes to the skin or soft tissue (more than 47 occurrences in 40 subjects) including skin reddening, skin

TABLE 3 | Adverse events detailed.

References	Device	Adverse event description	AE occurrence	Severity	Category AE	Caused by	Caused dropouts
Borggraefe et al. (2010)	Lokomat	Muscle pain	16	Mild	Musculoskeletal	Not stated	No
		Joint pain	14	Mild (12), moderate (2)	Musculoskeletal	Not stated	Yes (2)
		Skin erythema	12	Mild	Soft tissue-related	Cuffs	No
		Open skin lesions	4	Mild (2), moderate (1), severe (1)	Soft tissue-related	Cuffs	Yes (2)
		Tendinopathy	1	Severe	Musculoskeletal	Not stated	Yes
Carda et al. (2012)	Lokomat	Mild discomfort	3	Mild	Soft tissue-related	Harness	No
Chin et al. (2010)	Lokomat	Discomfort and redness in groin area	A few	Mild	Soft tissue-related	Harness	No
		Skin abrasions	3	Moderate	Soft tissue-related	Cuffs	No
		Giddiness	1	Mild	Physiological	Not stated	No
		Lower limb bruises	1	Moderate	Soft tissue-related	Cuffs	Yes
		Fear of gait trainer	1	Moderate	Other	Not stated	Yes
Esquenazi et al. (2017)	Not stated (Lokomat or G-EO)	Skin irritation and pain	4	Unknown	Soft tissue-related/other	Not stated	No
Filippo et al. (2015)	Lokomat	Proximal tibia fracture	1	Severe	Musculoskeletal	Not stated	Not applicable
Freivogel et al. (2008)	LokoHelp	Discomfort in groin or armpit	11	Mild	Soft tissue-related	Harness	No
		Discomfort in right hip	1	Mild	Musculoskeletal	Not stated	No
		Lower back pain	1	Mild	Musculoskeletal	Not stated	No
		Headache	3 (1) ^a	Mild	Other	Not stated	No
		Menstrual cramps	1	Mild	Other	Not stated	No
		Knee pain	1	Moderate	Musculoskeletal	Not stated	No
		Not described	5	Unknown	Unknown	Not stated	No
Freivogel et al. (2009)	LokoHelp	Discomfort	33	Unknown	Soft tissue-related	Mostly harness	No
		Knee pain	1	Unknown	Musculoskeletal	Not stated	No
Geigle et al. (2013)	Lokomat	Atypical autonomic dysreflexia	4 (1) ^a	Moderate	Physiological	Exercise (did not occur during pure suspension)	Yes (dropped out due to elevated BP)
		Knee pain	1	Minor	Musculoskeletal	Not stated	
		Discomfort	1	Minor	Soft tissue-related	Harness	
Husemann et al. (2007)	Lokomat	Skin lesions	2	Moderate	Soft tissue-related	Not stated	Yes
Ikumi et al. (2016)	HAL	Transient blood pressure change	6 (1) ^a	Moderate	Physiological	Not stated	No
Jansen et al. (2018)	HAL	Skin reddening	4	Mild	Soft tissue-related	EMG electrodes, leg cuffs, shoes	No
Kelley et al. (2013a,b)	Lokomat	Skin changes (redness or broken skin)	12 (5) ^a	Moderate	Soft tissue-related	Straps/cuffs	No
Morone et al. (2011)	GT	Severe symptomatic hypotension	8 (3) ^a	Moderate	Physiological	Not stated	Not stated
		Knee pain	1	Moderate	Musculoskeletal	Not stated	Not stated
Nilsson et al. (2014)	HAL	Knee/malleolus pain	2	Moderate	Musculoskeletal	Cuff pressure	No
		Discomfort (feeling of being trapped)	1	Moderate	Other	Straps	No
		Discomfort (shoulders)	2	Mild	Soft tissue-related	Straps	No
		Sense of suit being heavy over lower back	1	Mild	Other	Weight of suit	No
		Skin irritation	1	Mild	Soft tissue-related	EMG electrodes	No
		Groin pain, chafing	1	Moderate	Soft tissue-related	Harness	No
Stoller et al. (2014, 2015)	Lokomat	Tibia skin lesion	1	Moderate	Soft tissue-related	Cuffs (padding)	Yes
		Groin pain	1	Moderate	Soft tissue-related	Harness	Yes
		High blood pressure	2 (1) ^a	Moderate	Physiological	Not stated	No
Vaney et al. (2012)	Lokomat	Minor bruising	Some	Mild	Soft tissue-related	Straps	No

^aWhen AE occurrence is presented as X (Y), X is the number of events, and Y is the number of subjects.

lesions, skin abrasions, a blood blister, chafing, skin irritation due to electromyography (EMG) electrodes, and bruises (Husemann et al., 2007; Borggraefe et al., 2010; Vaney et al., 2012; Kelley et al., 2013a,b; Nilsson et al., 2014; Stoller et al., 2014; Esquenazi et al., 2017; Jansen et al., 2018). The most severe AE reported was one bone fracture in the context of Lokomat training (Filippo et al., 2015). The fracture to the proximal anterior and medial part of the tibia occurred in a patient with T12 incomplete paraplegia. The authors did not report any unusual event causing the injury. The patient had trained 18 sessions in the Lokomat (30 min per session, 5 times per week, 50% BWS, guiding force between 75 and 100%) and complained of pain in the anterior region of the knee at the beginning of session 19 (Filippo et al., 2015). Bone densitometry performed after the event revealed low bone mineral density. The result of this did not classify as severe osteoporosis, which would have constituted a contraindication for Lokomat training. The two other severe AEs were an open skin lesion and a tendinopathy during Lokomat training (Borggraefe et al., 2010). Mild or moderate joint pain was reported 21 times and occurred mostly in the knee (Freivogel et al., 2008, 2009; Borggraefe et al., 2010; Morone et al., 2011; Geigle et al., 2013; Nilsson et al., 2014). Other musculoskeletal AEs included muscle pain, tendinopathy, and low back pain (Freivogel et al., 2008; Borggraefe et al., 2010), totaling 40 occurrences. There were 21 physiological AEs in 7 subjects including giddiness (mild) (Chin et al., 2010), and blood pressure changes (both hypotension and hypertension) (Morone et al., 2011; Geigle et al., 2013; Stoller et al., 2014; Ikumi et al., 2016) that were all classified as moderate (**Figure 2**). Another frequent AE (more than 17 occurrences) was discomfort related to the harness (e.g., to the groin, armpit, or shoulders) that was mostly classified as mild (Freivogel et al., 2008, 2009; Chin et al., 2010; Carda et al., 2012; Geigle et al., 2013; Nilsson et al., 2014; Stoller et al., 2014). Other AEs identified in this review with seven occurrences were pain (not specified) (Esquenazi et al., 2017), fear of the gait robot (Chin et al., 2010), headache, menstrual cramps (Freivogel et al., 2008), the feeling of being trapped, and the sense of the gait robot being heavy over the lower back (Nilsson et al., 2014).

There was limited information available on the duration of gait training before an AE occurred. Chin et al. (2010) stated that the dropouts due to bruises and fear of the Lokomat system occurred after 2–5 training sessions of 15–45 min each, and the tibia fracture (Filippo et al., 2015) occurred after 18 sessions of 30 min each. Knee pain in LokoHelp (Freivogel et al., 2008) occurred after 4 sessions of 30 min. Autonomic dysreflexia during Lokomat training (Geigle et al., 2013) occurred 20 min into the 10th training session after having completed 9 40-min sessions, and transient blood pressure change in HAL training (Ikumi et al., 2016) was observed 6 times in 10 sessions of 60 min including preparation time. In a case report on the management of skin injuries during Lokomat training (Kelley et al., 2013b), it is reported that the subject walked a total of 2 h in 5 sessions in the Lokomat before the first injury was observed. Borggraefe et al. (2010) found no correlation between AE incidence and age, duration of RAGT, number of sessions, or total distance walked. They did, however, report that both obese children included in

the study developed soft tissue-related AEs (skin erythema, open skin lesion) and that in two cases, skin lesions developed next to skin areas covered by diapers.

Methods used to detect AEs included documentation of patient feedback or complaints (Freivogel et al., 2008, 2009; Borggraefe et al., 2010; Geigle et al., 2013; Nilsson et al., 2014; Stoller et al., 2014, 2015; Filippo et al., 2015), patient questionnaires (Borggraefe et al., 2010), MRI for the detection of a fracture (Filippo et al., 2015), blood pressure monitoring (Geigle et al., 2013; Stoller et al., 2014, 2015; Ikumi et al., 2016), and medical screening before, after, and when needed during each training session (Kelley et al., 2013a,b).

Table 4 summarizes the frequencies of injury types, severities, and causes in the different devices. More than 169 AEs were reported in more than 79 subjects. Exact numbers cannot be stated as the description of AEs was incomplete in four studies (Freivogel et al., 2009; Chin et al., 2010; Vaney et al., 2012; Esquenazi et al., 2017). Therefore, the occurrences are displayed as ranges in this table. In graphical representations and further analysis of this data, the minimum numbers will be used and presented. In total, between 8 and 13% of the participants experienced AEs. For the Lokomat users, this was between 12 and 18%, for the LokoHelp users between 18 and 90%, for the HAL users 9%, for the GT users 1%, and for the G-EO users between 0 and 57%.

The chi-squared tests indicated that there is no independence of variables in all tested combinations: devices and reported AE types ($\chi^2 = 88.05$, $p < 0.01$), device types and reported AE types ($\chi^2 = 15.88$, $p < 0.01$), AE types and severity level ($\chi^2 = 75.70$, $p < 0.01$), devices and severity level ($\chi^2 = 115.05$, $p < 0.01$), and device types and severity level ($\chi^2 = 70.80$, $p < 0.01$). We can therefore conclude that there are relationships between devices, device types, AE types, and severity levels of AEs. In other words, the occurrence of AE types differs between device types and between devices, as does the severity between devices, device types, and AE types. Articles that did not state absolute numbers (Chin et al., 2010; Vaney et al., 2012; Esquenazi et al., 2017) were excluded from this analysis.

Relations of AE severity and AE types with device types and devices are detailed in **Figure 3**. Relative to the total number of subjects that trained in each of the devices, on average, 16.6 AE occurrences per 100 subjects were reported for Lokomat training, 259 occurrences per 100 subjects for LokoHelp training, 16.7 occurrences per 100 subjects for HAL training, and 3 occurrences in 100 subjects for GT training. While there were no physiological AEs reported in LokoHelp and only physiological AEs in GT, subjects training in the two exoskeleton-type devices Lokomat and HAL were reported to have experienced soft tissue-related, musculoskeletal, and physiological AEs (**Figure 3A**). The overall severity of AEs in GT was the highest (4.00) with all AEs being moderate, followed by HAL (2.67), Lokomat (2.44), and LokoHelp (1.17) with the majority of AEs being mild (**Figure 3B**). Regarding AE types, physiological AEs had the highest overall severity (3.86), followed by soft tissue-related AEs (2.27) and other AEs (1.86). Musculoskeletal AEs had the lowest overall severity of 1.92.

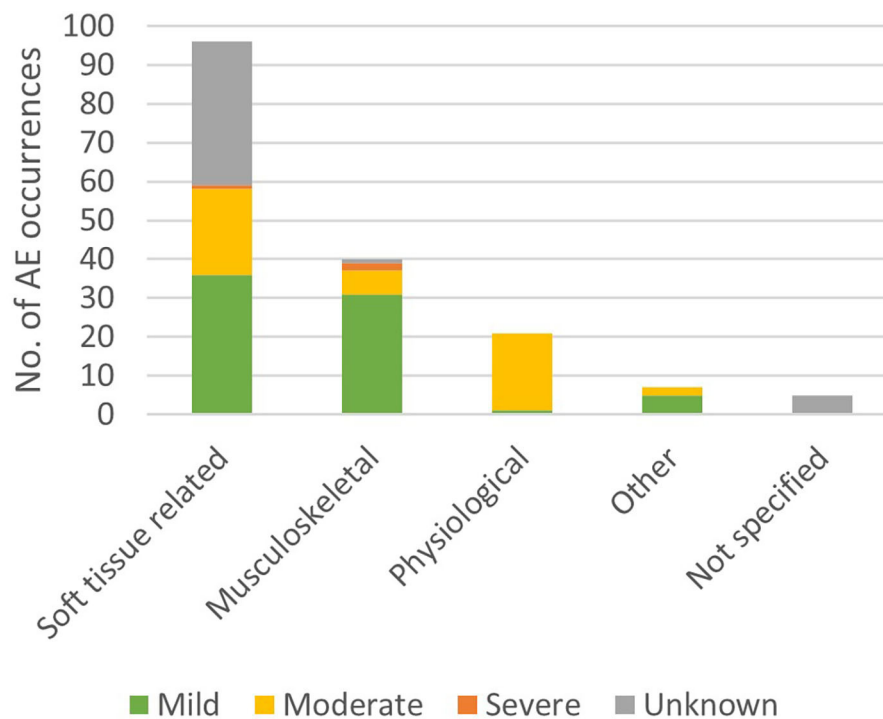


FIGURE 2 | Occurrences of adverse event severities per adverse event types.

DISCUSSION

In this systematic literature review, we extracted and analyzed information on AEs in RAGT from 50 included studies, involving 985 subjects in total. AEs occurred in 36% of the included studies and in 8–13% of the subjects. The findings show that skin injuries and a bone fracture occurred in RAGT, supporting our hypothesis. Moreover, a substantial amount of reports of joint pain, blood pressure change, and discomfort caused by the harness indicates that injuries associated with RAGT are broader than skin damage and bone fractures.

The most frequently reported AEs (>96 occurrences, constituting more than half of all AEs) were injuries or discomfort to the skin or underlying tissue (Husemann et al., 2007; Borggraefe et al., 2010; Vaney et al., 2012; Kelley et al., 2013a,b; Nilsson et al., 2014; Stoller et al., 2014, 2015; Esquenazi et al., 2017; Jansen et al., 2018), joint pain (21 occurrences) (Freivogel et al., 2008, 2009; Borggraefe et al., 2010; Morone et al., 2011; Geigle et al., 2013; Nilsson et al., 2014), blood pressure change (20 occurrences) (Morone et al., 2011; Geigle et al., 2013; Stoller et al., 2014, 2015; Ikumi et al., 2016), and discomfort related to the harness (more than 20 occurrences) (Freivogel et al., 2008, 2009; Chin et al., 2010; Carda et al., 2012; Geigle et al., 2013; Nilsson et al., 2014; Stoller et al., 2014, 2015). Next to a tendinopathy and an open skin lesion (Borggraefe et al., 2010) classified as severe AEs, the most severe AE (and only SAE) was a tibia fracture (Filippo et al., 2015).

Occurrence and Severity of AEs

The overall severity of physiological AEs was the highest (3.86), which is related to the fact that training is usually interrupted when a sudden blood pressure change occurs. While one might expect that musculoskeletal AEs are generally more severe than soft tissue-related AEs, the overall severity of musculoskeletal AEs (1.92) was slightly lower than that of soft tissue-related AEs (2.27). Mild musculoskeletal AEs were minor pain or discomfort to the joints or muscles. There were 22 moderate and 1 severe soft tissue-related AEs that included open skin lesions (one of which was severe), bruises, and groin pain. For 37 soft tissue-related events, no severity could be inferred from the reported information that might have an influence on the overall severity. It can, however, be concluded that not only physiological and musculoskeletal but also soft tissue-related AEs can require interrupting the RAGT or even medical attention. Specifically in subjects with restricted blood flow or reduced sensation, complications can arise from smaller skin or soft tissue injuries, and healing can be impaired (Bader et al., 2019), which can explain the relatively high overall severity of soft tissue-related AEs. Remarkably, in studies that included healthy subjects, no AEs were experienced, which supports the notion that disturbed physiological and/or sensory function in patients could be a relevant factor. This implies that risks for soft tissue-related AEs should be taken just as seriously as risks for musculoskeletal AEs.

Regarding the devices, the largest absolute number of AEs was reported for training in Lokomat (more than 81 events in 57–90 subjects). However, one has to keep in mind that the 50

TABLE 4 | Adverse events classified per device.

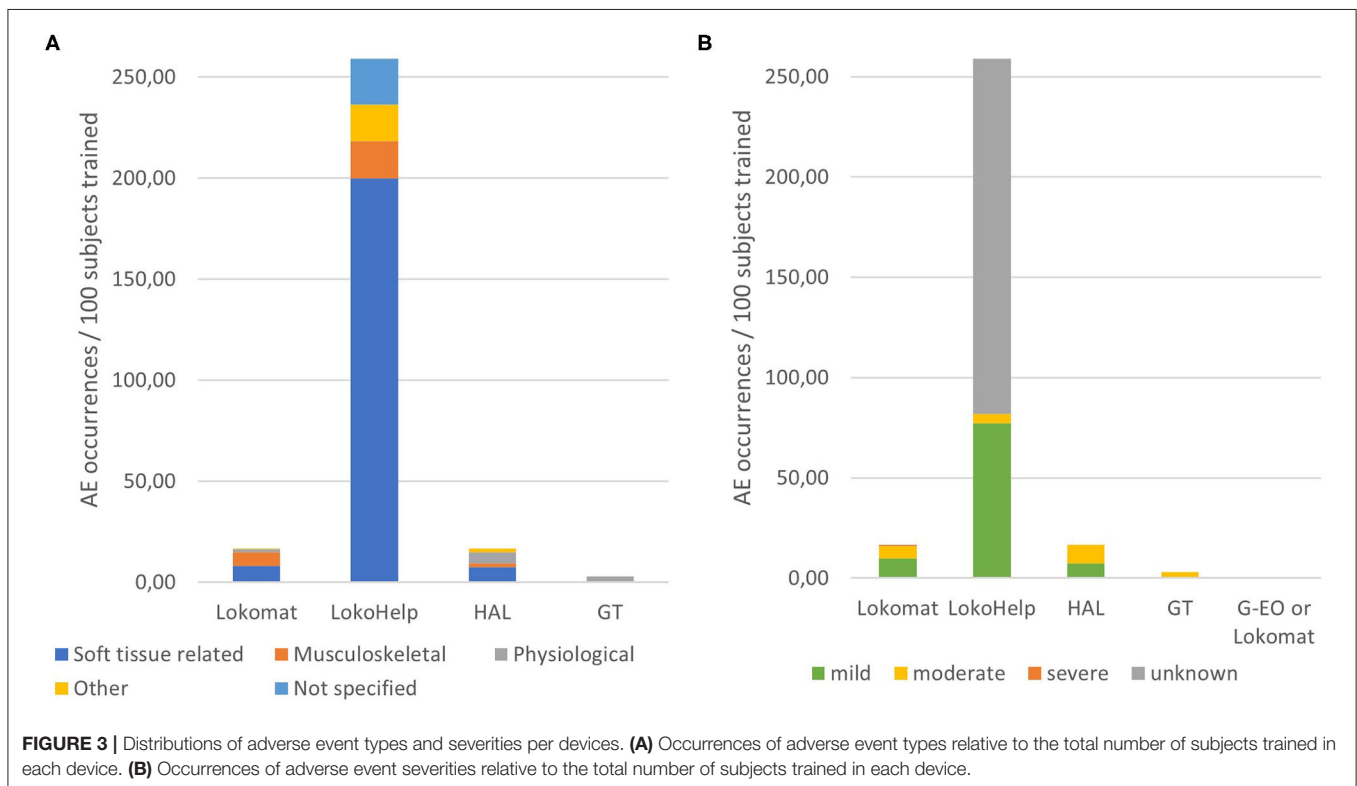
	Total	Lokomat	LokoHelp	HAL	GT	G-EO
Event types						
Soft tissue-related	>96 ^{a,b,c,d}	>40 ^{a,b,d}	44 ^c	8	–	≤4 ^b
Musculoskeletal	40	33	4	2	1	–
Physiological	21	7	–	6	8	–
Other	7	1	4	2	–	–
Not specified	5	–	5	–	–	–
Event severity						
Mild	>73 ^{a,d}	>48 ^{a,b,d}	17	8	–	–
Moderate	50	30	1	10	9	–
Severe	3	3	–	–	–	–
Unknown	43 ^c	≤4 ^b	39 ^c	–	–	≤4 ^b
Part of device causing AE						
Cuffs/straps	>42 ^d	>33 ^d	–	9	–	–
Harness	>50 ^a	>5 ^a	≤44 ^c	1	–	–
Total no. of events	>169 ^{a,d}	>81 ^{a,b,d}	57	18	9	≤4 ^b
Total no. of subjects	79 < n ≤ 124 ^{a,b,d}	57 < n ≤ 90 ^{a,b,d}	4 < n ≤ 20 ^d	10	4	≤4 ^b

^a"A few patients experienced discomfort and developed redness in their groin area"; unknown how many patients/events (Chin et al., 2010).

^b"4 reported adverse events that were study related due to skin irritation and pain"; unknown whether adverse events occurred in Lokomat or G-EO training, and how many subjects were affected (Esquenazi et al., 2017).

^c34 complaints, unclear by how many of the 16 subjects; "mostly" related to the harness (soft tissue) (Freivogel et al., 2009).

^d"Some minor bruising from the straps"; number of affected subjects/events not stated (Vaney et al., 2012).



included articles included 27 Lokomat studies with 489 subjects. So, per 100 subjects, an average of 16.6 AEs was reported in Lokomat training. This is comparable with 18 AEs in 108 subjects performing RAGT with HAL resulting in an average of 16.7 AEs

per 100 subjects. For GT, an average of 3.0 AEs per 100 subjects was reported (9 AEs in 301 subjects) and for G-EO between 0 and 57.1 events per 100 subjects. By far, the highest relative AE occurrence was reported for LokoHelp training, where the

reports (57 AEs in 22 subjects) result in an average of 259 AEs per 100 subjects. Interestingly, while LokoHelp training resulted in the highest relative number of AEs, it also resulted in the lowest overall severity (1.17). Lokomat and HAL are comparable not only in occurrence but also in overall severity of AEs (2.44 and 2.67, respectively). All AEs reported in relation with GT training were moderate (overall severity 4).

Risk Factors

The results of the analyses suggest that AEs do occur in RAGT, independent of the subjects' age and diagnosis. There were no striking differences in the level of severity or time since onset of the disease. We did, however, observe that there were no reports of AEs in healthy participants. This could be due to a number of reasons. Firstly, only 14 out of 985 subjects (1.4%) were healthy individuals. Secondly, RAGT with healthy individuals was only performed during 1 day in each of the studies (Gizzi et al., 2012; Asbeck et al., 2015; Wu et al., 2015), as they are not the targeted population for a training program to improve walking. Both of these aspects decrease the chance of suffering an injury. Thirdly, the characteristics of certain patient groups, such as restricted blood flow, reduced sensation, uncontrolled muscle activities, or reduced bone mineral density, might increase the risk of sustaining injuries in RAGT, in contrast to healthy individuals. The current findings allow us to identify which risk factors are most likely involved in the various AEs reported during stationary RAGT in patients.

Soft Tissue-Related Adverse Events

According to the results, skin, and other soft tissue injuries are the most frequent AEs related to RAGT. They are mostly caused by either the cuffs/straps (Borggraeve et al., 2010; Chin et al., 2010; Vaney et al., 2012; Kelley et al., 2013a,b; Nilsson et al., 2014; Stoller et al., 2014, 2015; Jansen et al., 2018) or the harness (Freivogel et al., 2008, 2009; Chin et al., 2010; Carda et al., 2012; Geigle et al., 2013; Nilsson et al., 2014; Stoller et al., 2014, 2015) and occurred in both device types, although slightly more frequently in end-effector-type devices (13.5 occurrences per 100 subjects) than in exoskeleton-type devices (7.7 occurrences per 100 subjects on average). Both the cuffs/straps and the harness are mentioned as causes for soft tissue injuries in seven unique studies, respectively. In addition to that, one article mentions diapers as well as obesity as possible risk factors for skin injuries (Borggraeve et al., 2010). Remarkably, issues related specifically to cuffs or straps have only been reported in exoskeleton-type devices (Lokomat and HAL). End-effector-type devices are only attached to the foot and sometimes to the shank, which decreases the number of contact interfaces between human (skin) and robot, reducing the chances for skin irritation at the cuffs and straps in end-effector-type devices. In contrast, exoskeletons have a risk of misalignment between joint axes, which can lead to displacements of the cuff relative to the human limb, resulting in increased shear and pressure in the interface between cuff or strap and skin, which can contribute to soft tissue injuries (Rocon et al., 2008; Akiyama et al., 2015; Mao et al., 2015).

The harness has been stated to be the cause of AEs in Lokomat (>5 AEs) (Chin et al., 2010; Carda et al., 2012), HAL (1 AE)

(Nilsson et al., 2014), and LokoHelp (44 AEs) (Freivogel et al., 2008, 2009) with 88% of the events related to the end-effector-type device LokoHelp. The affected body regions included the groin area (Freivogel et al., 2008; Chin et al., 2010; Nilsson et al., 2014; Stoller et al., 2014) and armpits (Freivogel et al., 2008). One might assume that higher percentages of BWS lead to a higher risk of discomfort or injuries related to the harness because the pressure in the interface harness-skin is increased. The range of documented BWS in end-effector-type devices was between 0 and 50% and in exoskeleton-type devices between 0 and 100%. It is striking that all studies with BWS above 50% of body weight reported AEs. In the studies reporting discomfort due to the harness, the maximum BWS ranged between 30 and 100% of body weight. All studies reporting BWS above 55% also reported discomfort related to the harness, with the exception of one case report (Kelley et al., 2013b) where only the first session was started at 100% BWS but as of the end of session 1, BWS was always <50%. Nevertheless, the large number of harness-related AEs in LokoHelp training was reported in two studies with BWS under 30% (Freivogel et al., 2008, 2009). Therefore, lower BWS might decrease but not completely avoid the risk of discomfort related to the harness. Other possible factors might be the design, fitting, or material of the harness as well as the clothes worn by the subjects (Rocon et al., 2008; Kelley et al., 2013b).

Overall, the susceptibility to soft tissue-related AEs could be influenced by harness or cuff design and fit, subject characteristics, and materials involved in the cuff-skin interface. One study analyzed this aspect and reported that there was no correlation between the incidence of AEs and age (Borggraeve et al., 2010), but that both obese children included in the study developed a soft tissue-related AEs. Moreover, they observed two open skin lesions adjacent to the area where diapers were worn. Another study reported that wrapping the legs of a subject presenting with thin and flaky skin with viscoelastic polymer sheets and elastic bandages helped manage soft tissue-related AEs (Kelley et al., 2013b). Therefore, in addition to the fit of cuffs and harness, both the subjects' weight and/or body composition and materials present in the interface between skin and robot cuffs or the harness might alter the risk for soft tissue-related AEs.

Musculoskeletal Adverse Events

The findings of this review show that RAGT can lead to musculoskeletal injuries, such as a bone fracture and joint pain. Musculoskeletal AEs were reported in relation to training in Lokomat, LokoHelp, GT, and HAL and therefore in both exoskeleton-type devices and end-effector-type devices. However, 88% of the reported musculoskeletal AEs occurred in an exoskeleton-type device (on average 5.6 musculoskeletal AEs per 100 subjects in exoskeleton-type devices compared with 1.4 musculoskeletal AEs per 100 subjects in end-effector-type devices). This leads to the assumption that the risk of sustaining a musculoskeletal injury is higher during exoskeleton-type RAGT. However, it is possible that this is influenced by a single study reporting many occurrences of musculoskeletal AEs (31) in one exoskeleton-type device (Borggraeve et al., 2010). The only SAE (bone fracture) reported in the included articles occurred in an exoskeleton-type device. To the best of our knowledge, there are

no reports of bone fractures in end-effector-type devices. While this was the only occurrence of a bone fracture in RAGT found through this review, there are several reports of bone fractures in overground exoskeletons (He et al., 2017; van Herpen et al., 2019). Misalignment is frequently mentioned as the assumed cause for bone fractures in overground exoskeleton devices (He et al., 2017; van Herpen et al., 2019), but this has not been discussed as a possible cause in the case report of the tibia fracture sustained during Lokomat training (Filippo et al., 2015). The authors of this case report discussed low bone mineral density as a possible influencing factor but did not report any details of the relevant training session or discussed other possible reasons. Due to the oversimplification of exoskeleton joints compared with anatomical joints, misalignments are unavoidable (Rocon et al., 2008; Akiyama et al., 2012). This might lead to the assumption that end-effector-type devices are inherently safer than exoskeleton-type devices. However, end-effector-type devices provide less guidance of the movements and could therefore create movements in arbitrary directions and excessive moments that can cause considerable harm (Rocon et al., 2008). In end-effector-type gait trainers, this risk could be mitigated by providing appropriate BWS. However, in all end-effector-type gait trainer studies included in this review, BWS was reported to be 50% or lower, whereas exoskeleton-type studies reported BWS up to 100%. This is not related to less severely affected subjects being involved in end-effector-type RAGT studies. The subjects in studies with both types of gait trainers varied strongly in disease severity and walking ability.

Physiological Adverse Events

Giddiness and changes in blood pressure were reported in relation to Lokomat, HAL, and GT training (Chin et al., 2010; Morone et al., 2011; Geigle et al., 2013; Stoller et al., 2014, 2015; Ikumi et al., 2016). There were 13 occurrences in 4 subjects reported in exoskeleton-type devices and 8 occurrences in 3 subjects reported in end-effector-type devices. It is striking that all reported blood pressure changes occurred in more severely affected subjects with SCI [American Spinal Injury Association (ASIA) A and C] or subacute stroke [functional ambulation category (FAC) <3]. This indicated that the risk for blood pressure changes in RAGT might be increased in subjects who do not ambulate independently. It is also worth noting that hypertension in SCI as a result of autonomic dysreflexia seems to be linked to the stepping movements in combination with the upright position and did not occur during pure suspension in the harness (Geigle et al., 2013). A close blood pressure monitoring of patients with a history of blood pressure changes or high risks of orthostatic hypotension or autonomic dysreflexia could help mitigate the risk of physiological AEs.

Documentation of Adverse Events

The documentation of AEs lacks detail in most studies. A significant amount of included articles (36%) did not provide a complete description of AEs, even though the requirements for regarding AE documentation as complete were relatively low: description of events, the number of affected subjects, and the associated device. The assumed cause of the event was only

stated in about half of the reports. Moreover, there is a need for documentation on how different types of AEs can be managed or avoided (Kelley et al., 2013b).

Although we did not consider this as critical for documenting AEs, it is striking that most reports did not include any information on the duration of training before the AEs occurred or the characteristics of the affected subjects. Training time before the occurrence of an AE was often not stated. Based on the literature, one could assume that skin-related AEs are more likely to occur in the first training sessions as the skin can habituate to the stress (Sanders et al., 1995; Yandell et al., 2020). In the two studies stating the durations of training before the soft tissue-related AEs, they occurred between session 2 and 5 (Chin et al., 2010; Kelley et al., 2013b). A more detailed analysis of this aspect is not possible as there is not enough information available on whether the complaints occurred in the beginning or end of the sessions and due to the fact that most studies did not report on training time before AE onset. Subject characteristics related to AEs were only analyzed in detail in one of the included studies (Borggraefe et al., 2010). In order to establish more generalizable relations between subject or training characteristics and risk factors, more detailed reports of those aspects in relation to AEs are needed.

Structural documentation of AEs related to RAGT (or any medical device for that matter) is currently not optimally supported or facilitated by regulatory bodies. In other words, AE reporting is not sufficiently obligatory and public. Although some information on safety is shared through the reporting system of the FDA in the US, reporting is only mandatory if it is an SAE and only for manufacturers and healthcare institutions, but not for individual healthcare professionals and consumers (Maak and Wylie, 2016). In the EU, there is currently no central reporting system. There are obligations for the manufacturers to report AEs to the competent authorities on a national level, but this information is currently not shared with the public. In relation to the current transition from the EU Medical Device Directive to Medical Device Regulation, the reporting system EUDAMED is expected to be (re-)launched in May 2022, with more firm rules for reporting. Information on SAEs, device deficiencies, vigilance, and post-market surveillance is intended to be submitted through this platform, which will be partly open to the public. Dissemination will include information on device safety and issued certificates, vigilance, and post-market surveillance (European Commission, 2019), although the exact extent to which information will be accessible to whom is currently unknown. Based on the outcomes of the current review, such facilities are needed to allow and stimulate a more structural reporting of and access to AEs (and not only SAEs). This cannot only inform the end user of risks associated with a certain device but also encourage new, safety-related developments, and ultimately improve safety of RAGT.

Limitations

The findings of this systematic literature review need to be interpreted with care for several reasons. The primary outcome of the study is AEs reported in RAGT, which is why terms related to AEs and injuries were included in the search query. However,

most bibliographic databases search for the entered search terms in titles, keywords, and abstracts of articles. During this process, we found that information on AEs is frequently not contained in those elements but in the body of the text, complicating the search for relevant articles. Therefore, we also searched full-text databases, but we cannot be sure that we identified all relevant articles with that method.

Another limitation of this review is a potential overlap of studies. We excluded double reports as much as possible, but we cannot rule out that some articles contained information on the same participants in the same experiment without stating this (e.g., data from a case report on a specific AE might be part of a clinical trial too). Furthermore, some of the relationships between AE occurrence and device type could be biased by few studies stating many AEs for one specific device (Freivogel et al., 2008, 2009; Borggraefe et al., 2010) or including vague statements, such as only reporting on (the absence of) SAE or not specifying AE occurrence for each of the interventions involved (Chin et al., 2010; Wu et al., 2015; Esquenazi et al., 2017).

Other limitations are related to an expected underrepresentation and incomplete documentation of AEs. It is possible that many other studies where no AEs occurred were published but not included in this article, if they did not contain a statement about AE occurrence. Moreover, we noticed strong variations in the level of detail in which AEs are recorded during a study and reported in articles: while some articles only include more obvious or severe AEs, others may mention all cases of slight discomfort and have asked participants specifically about their experience. The high relative occurrence of AEs in LokoHelp, but with the lowest overall severity, is a likely example of this. This hampered a reliable comparison of AE occurrence and severities between device types or devices. More detailed descriptions of AEs and their effects with regard to the interruption of training or the needed medical attention would allow for a more accurate and detailed severity rating, thereby enabling more valid comparisons. We therefore suggest that editors focus on a correct and complete statement on AEs in scientific reports on medical devices. A statement saying that there were no AEs is just as important as a detailed description on occurred AEs to learn about the risks associated with a device. The extension to the CONSORT statement (Schulz et al., 2010) for reporting of harms in randomized controlled trials (Ioannidis et al., 2004) could serve as a guideline for this. While the CONSORT statement is specifically designed for improving reporting in randomized controlled trials, we suggest that the checklist for reporting of harms is also relevant for other study types. Based on the experiences collected in the process of this systematic literature review, we would like to encourage a focus on the following aspects when reporting on AEs in medical device trials:

- Collection of AE information: how were numbers of AEs obtained? Who reported them and were any questionnaires or procedures involved?
- Documentation of AE information: are all AEs reported or only a specific subset? Report both number of affected subjects

and number of occurrences per subject. If no AE occurred, this should be stated clearly.

- AE descriptions: describe the observed AE concisely including the location. Describe unusual events or subject characteristics that might be related to the AE and discuss possible reasons.
- AE consequences: did the intervention have to be interrupted? For how long? Was medical attention required? Did the AE cause a dropout and who made that decision? Preferably use standardized definitions of severity levels.

Implications for the Use of Rehabilitation Robots

The aim of this review is to raise awareness of the safety of rehabilitation robots, and while it focuses on the risks and needs of rehabilitation robots, it is not intended to discourage their use. Although AEs do occur in RAGT, it has positive effects on gait and has potential to decrease the burden on healthcare professionals (Freivogel et al., 2009; Hesse and Werner, 2009; Mehrholz et al., 2017). Therefore, a proper balancing of risks and benefits is needed, but in order to do this, proper information about AEs is needed as part of ethical and regulatory decisions to allow the use of rehabilitation robots in clinical practice. In order to do this well, correct and sufficient information about AEs is needed. Moreover, AEs should not only be documented but also be disseminated to raise awareness of risks. The need for information flow goes both ways: manufacturers should make their risk/benefit weighting more transparent to allow for healthcare professionals ideally to make an informed decision on the use of robotic devices in therapy, in-/exclusion criteria, associated risks, and possible measures. In return, healthcare professionals and researchers should report on AEs and their management, where applicable, in a structured and systematic way to inform developers of rehabilitation robots about ways to improve safety of their devices.

Conclusions

In the present systematic literature review on AEs during the use of stationary robotic gait trainers, including 50 studies and 985 subjects, we found that a total of 169 AEs occurred in 36% of the studies, affecting between 8 and 13% of the subjects. The most frequent types of AEs were soft tissue-related AEs and musculoskeletal AEs, whereas physiological AEs had the highest overall severity, followed by soft tissue-related AEs. Soft tissue-related AEs occurred slightly more frequently in end-effector-type devices than in exoskeleton-type devices and were often associated with the cuffs or straps (only mentioned in relation to exoskeleton-type devices) or with the harness (mostly mentioned in relation to end-effector-type devices). Musculoskeletal AEs were reported more frequently in exoskeleton-type devices than in end-effector-type devices. We have identified two main risk factors: forces in the skin-robot interface causing skin injuries and forces on the musculoskeletal level causing pain or injuries to the musculoskeletal system. On a more detailed level, hazards are most likely related to an incorrect model fit, insufficient compliance at the points of force transmission from robot to human, materials present at the human-robot interface, misalignments of rotation axes, or

subject characteristics, such as uncontrolled muscle activities or susceptibility to injuries due to overall health status. We additionally identified a lack of completeness of AE reporting in RAGT studies and would like to stress the need for accurate and complete documentation and dissemination of AEs for the identification of hazards and possible mitigation measures. Therefore, AE documentation should receive more attention, and researchers, relevant authorities, as well as journal editors should ensure the appropriate documentation and dissemination of RAGT-related AEs.

The present findings suggest that future developments in RAGT should focus on the subjects' safety, especially mitigating risks associated with pressure and shear applied to the subject's skin, as well as forces applied to the musculoskeletal system that can be harmful due to misalignments. To further investigate the effects of these hazards, appropriate measurement methods and experiments are needed. Further, the investigation of forces present in the human-robot interface as well as investigations on acceptable limit values for comfort and safety could help to establish best practices for safe use of rehabilitation robots.

REFERENCES

- Aach, M., Cruciger, O., Sczesny-Kaiser, M., Höfken, O., Meindl, R. C., Tegenthoff, M., et al. (2014). Voluntary driven exoskeleton as a new tool for rehabilitation in chronic spinal cord injury: a pilot study. *Spine J.* 14, 2847–2853. doi: 10.1016/j.spinee.2014.03.042
- Akiyama, Y., Yamada, Y., Ito, K., Oda, S., Okamoto, S., and Hara, S. (2012). "Test method for contact safety assessment of a wearable robot -analysis of load caused by a misalignment of the knee joint," in *2012 IEEE RO-MAN: The 21st IEEE International Symposium on Robot and Human Interactive Communication* (Paris: IEEE) 539–544. doi: 10.1109/ROMAN.2012.6343807
- Akiyama, Y., Yamada, Y., and Okamoto, S. (2015). Interaction forces beneath cuffs of physical assistant robots and their motion-based estimation. *Adv. Robot.* 29, 1315–1329. doi: 10.1080/01691864.2015.1055799
- Alavi, N., Zampierin, S., Komeili, M., Cocuzza, S., Debei, S., and Menon, C. (2017). A preliminary investigation into the design of pressure cushions and their potential applications for forearm robotic orthoses. *Biomed. Eng. Online* 16, 1–20. doi: 10.1186/s12938-017-0345-8
- Asbeck, A. T., De Rossi, S. M. M., Holt, K. G., and Walsh, C. J. (2015). A biologically inspired soft exosuit for walking assistance. *Int. J. Rob. Res.* 34, 744–762. doi: 10.1177/0278364914562476
- Aurich-Schuler, T., Grob, F., van Hedel, H. J. A., and Labruyère, R. (2017). Can Lokomat therapy with children and adolescents be improved? *An adaptive clinical pilot trial comparing guidance force, path control, and freeD.* *J. Neuroeng. Rehabil.* 14:76. doi: 10.1186/s12984-017-0287-1
- Bader, D. L., Worsley, P. R., and Gefen, A. (2019). Bioengineering considerations in the prevention of medical device-related pressure ulcers. *Clin. Biomech.* 67, 70–77. doi: 10.1016/j.clinbiomech.2019.04.018
- Bae, Y.-H., Lee, S. M., and Ko, M. (2017). Comparison of the effects on dynamic balance and aerobic capacity between objective and subjective methods of high-intensity robot-assisted gait training in chronic stroke patients: a randomized controlled trial. *Top. Stroke Rehabil.* 24, 309–313. doi: 10.1080/10749357.2016.1275304
- Basteris, A., Nijenhuis, S. M., Stienen, A. H. A., Buurke, J. H., Prange, G. B., and Amirabdollahian, F. (2014). Training modalities in robot-mediated upper limb rehabilitation in stroke: a framework for classification based on a systematic review. *J. Neuroeng. Rehabil.* 11, 1–15. doi: 10.1186/1743-0003-11-111
- Behrens, R., and Elkmann, N. (2014). "Study on meaningful and verified thresholds for minimizing the consequences of human-robot collisions," in *2014 IEEE International Conference on Robotics and Automation (ICRA)* (Hong Kong: IEEE) 3378–3383. doi: 10.1109/ICRA.2014.6907345
- Benito-Penalva, J., Edwards, D. J., Opisso, E., Cortes, M., Lopez-Blazquez, R., Murillo, N., et al. (2012). Gait training in human spinal cord injury using electromechanical systems: effect of device type and patient characteristics. *Arch. Phys. Med. Rehabil.* 93, 404–412. doi: 10.1016/j.apmr.2011.08.028
- Borggraeve, I., Klaiber, M., Schuler, T., Warken, B., Schroeder, S. A., Heinen, F., et al. (2010). Safety of robotic-assisted treadmill therapy in children and adolescents with gait impairment: a bi-centre survey. *Dev. Neurorehabil.* 13, 114–119. doi: 10.3109/17518420903321767
- Carda, S., Invernizzi, M., Baricich, A., Comi, C., Croquelois, A., and Cisari, C. (2012). Robotic gait training is not superior to conventional treadmill training in parkinson disease: a single-blind randomized controlled trial. *Neurorehabil. Neural Repair.* 26, 1027–1034. doi: 10.1177/1545968312446753
- Castellini, C., and Ravindra, V. (2014). "A wearable low-cost device based upon force-sensing resistors to detect single-finger forces," in *Proceedings of 2014 5th IEEE RAS EMBS Int. Conf. Biomed. Robot. Biomechatronics* (São Paulo: IEEE), 199–203. doi: 10.1109/BIOROB.2014.6913776
- Chin, L. F., Lim, W. S., and Kong, K. H. (2010). Evaluation of robotic-assisted locomotor training outcomes at a rehabilitation centre in Singapore. *Singapore Med. J.* 51, 709–15.
- Chisholm, A. E., Alamro, R. A., Williams, A. M. M., and Lam, T. (2017). Overground vs. treadmill-based robotic gait training to improve seated balance in people with motor-complete spinal cord injury: a case report. *J. Neuroeng. Rehabil.* 14:27. doi: 10.1186/s12984-017-0236-z
- Chua, J., Culpán, J., and Menon, E. (2016). Efficacy of an electromechanical gait trainer poststroke in Singapore: a randomized controlled trial. *Arch. Phys. Med. Rehabil.* 97, 683–690. doi: 10.1016/j.apmr.2015.12.025
- Esquenazi, A., Lee, S., Wikoff, A., Packel, A., Toczyłowski, T., and Feeley, J. (2017). A comparison of locomotor therapy interventions: partial-body weight-supported treadmill, lokomat, and G-EO training in people with traumatic brain injury. *PM&R* 9, 839–846. doi: 10.1016/j.pmrj.2016.12.010
- European Commission (2019). *Draft Functional Specifications for the European Database on Medical Devices (Eudamed) - First Release to be Audited*, 1–91. Available online at: <https://ec.europa.eu/docsroom/documents/34304> (accessed April 27, 2020).
- Filippo, T. R. M., De Carvalho, M. C. L., Carvalho, L. B., de Souza, D. R., Imamura, M., and Battistella, L. R. (2015). Proximal tibia fracture in a patient with incomplete spinal cord injury associated with robotic treadmill training. *Spinal Cord* 53, 875–876. doi: 10.1038/sc.2015.27
- Forrester, L. W., Roy, A., Hafer-Macko, C., Krebs, H. I., and Macko, R. F. (2016). Task-specific ankle robotics gait training after stroke: a

DATA AVAILABILITY STATEMENT

The original contributions presented in the study are included in the article/supplementary material, further inquiries can be directed to the corresponding author/s.

AUTHOR CONTRIBUTIONS

JBu, GP-L, LS, and JBe contributed to conception and design of the study. EP, GP-L, RS, and JBe contributed to the literature screening process. JBe performed the data analysis and wrote the first draft of the manuscript. GP-L wrote sections of the manuscript. All authors contributed to manuscript revision, read, and approved the submitted version.

FUNDING

This work as part of the COVR project has received funding from the European Union's Horizon 2020 research and innovation program under Grant Agreement No. 779966.

- randomized pilot study. *J. Neuroeng. Rehabil.* 13:51. doi: 10.1186/s12984-016-0158-1
- Freivogel, S., Mehrholz, J., Husak-Sotomayor, T., and Schmalohr, D. (2008). Gait training with the newly developed 'LokoHelp'-system is feasible for non-ambulatory patients after stroke, spinal cord and brain injury. *A feasibility study. Brain Inj.* 22, 625–632. doi: 10.1080/02699050801941771
- Freivogel, S., Schmalohr, D., and Mehrholz, J. (2009). Improved walking ability and reduced therapeutic stress with an electromechanical gait device. *J. Rehabil. Med.* 41, 734–739. doi: 10.2340/16501977-0422
- Geigle, P. R., Frye, S. K., Perreault, J., Scott, W. H., and Gorman, P. H. (2013). Atypical autonomic dysreflexia during robotic-assisted body weight supported treadmill training in an individual with motor incomplete spinal cord injury. *J. Spinal Cord Med.* 36, 153–156. doi: 10.1179/2045772312Y.0000000033
- Geroni, C., Picelli, A., Munari, D., Waldner, A., Tomelleri, C., and Smania, N. (2011). Combined transcranial direct current stimulation and robot-assisted gait training in patients with chronic stroke: a preliminary comparison. *Clin. Rehabil.* 25, 537–548. doi: 10.1177/0269215510389497
- Gizzi, L., Nielsen, J., Felici, F., Moreno, J. C., Pons, J. L., and Farina, D. (2012). Motor modules in robot-aided walking. *J. Neuroeng. Rehabil.* 9:76. doi: 10.1186/1743-0003-9-76
- Grasmücke, D., Cruciger, O., Meindl, R. C., Schildhauer, T. A., and Aach, M. (2017). "Experiences in four years of HAL exoskeleton SCI rehabilitation," in *Converging Clinical and Engineering Research on Neurorehabilitation II Biosystems & Biorobotics*, eds J. Ibáñez, J. González-Vargas, J. M. Azorín, M. Akay, and J. L. Pons (Cham: Springer International Publishing), 1235–1238. doi: 10.1007/978-3-319-46669-9_201
- Haddadin, S., Albu-Schaeffer, A., and Hirzinger, G. (2007). "Safety evaluation of physical human-robot interaction via crash-testing," in *Proceedings of Robotics: Science and Systems*, eds W. Burgard, O. Brock, and C. Stachniss (Atlanta, GA: MIT Press), 217–224. doi: 10.15607/RSS.2007.III.028
- He, Y., Eguren, D., Luu, T. P., and Contreras-Vidal, J. L. (2017). Risk management and regulations for lower limb medical exoskeletons: a review. *Med. Devices Evid. Res.* 10, 89–107. doi: 10.2147/MDER.S107134
- Hesse, S., Schmidt, H., Werner, C., and Bardeleben, A. (2003). Upper and lower extremity robotic devices for rehabilitation and for studying motor control. *Curr. Opin. Neurol.* 16, 705–10. doi: 10.1097/00019052-200312000-00010
- Hesse, S., and Werner, C. (2009). Connecting research to the needs of patients and clinicians. *Brain Res. Bull.* 78, 26–34. doi: 10.1016/j.brainresbull.2008.06.004
- Husemann, B., Müller, F., Krewer, C., Heller, S., and Koenig, E. (2007). Effects of locomotion training with assistance of a robot-driven gait orthosis in hemiparetic patients after stroke. *Stroke* 38, 349–354. doi: 10.1161/01.STR.0000254607.48765.cb
- Ikumi, A., Kubota, S., Shimizu, Y., Kadone, H., Marushima, A., Ueno, T., et al. (2016). Decrease of spasticity after hybrid assistive limb® training for a patient with C4 quadriplegia due to chronic SCI. *J. Spinal Cord Med.* 40, 573–578. doi: 10.1080/10790268.2016.1225913
- Ioannidis, J. P. A., Evans, S. J. W., Gøtzsche, P. C., O'Neill, R. T., Altman, D. G., Schulz, K., et al. (2004). Better reporting of harms in randomized trials: an extension of the CONSORT statement. *Ann. Intern. Med.* 141, 781–788. doi: 10.7326/0003-4819-141-10-200411160-00009
- Ito, Y., Kim, Y., and Obinata, G. (2014). Acquisition of contact force and slippage using a vision-based tactile sensor with a fluid-type touchpad for the dexterous handling of robots. *Adv. Robot. Autom.* 3, 1–9. doi: 10.4172/2168-9695.1000116
- Jansen, O., Grasmücke, D., Meindl, R. C., Tegenthoff, M., Schwenkreis, P., Szesny-Kaiser, M., et al. (2018). Hybrid assistive limb exoskeleton HAL in the rehabilitation of chronic spinal cord injury: proof of concept; the results in 21 patients. *World Neurosurg.* 110, e73–e78. doi: 10.1016/j.wneu.2017.10.080
- Jansen, O., Schildhauer, T. A., Meindl, R. C., Tegenthoff, M., Schwenkreis, P., Szesny-Kaiser, M., et al. (2017). Functional outcome of neurologic-controlled HAL-exoskeletal neurorehabilitation in chronic spinal cord injury: a pilot with one year treatment and variable treatment frequency. *Glob. Spine J.* 7, 735–743. doi: 10.1177/2192568217713754
- Kelley, C. P., Childress, J., Boake, C., and Noser, E. A. (2013a). Over-ground and robotic-assisted locomotor training in adults with chronic stroke: a blinded randomized clinical trial. *Disabil. Rehabil. Assist. Technol.* 8, 161–168. doi: 10.3109/17483107.2012.714052
- Kelley, C. P., Childress, J., and Noser, E. A. (2013b). Management of skin-related adverse events during locomotor training with robotic-assisted body weight supported treadmill: a case report. *Physiother. Theory Pract.* 29, 309–318. doi: 10.3109/09593985.2012.731139
- Kim, J., Kim, D. Y., Chun, M. H., Kim, S. W., Jeon, H. R., Hwang, C. H., et al. (2019). Effects of robot-(morning walk®) assisted gait training for patients after stroke: a randomized controlled trial. *Clin. Rehabil.* 33, 516–523. doi: 10.1177/0269215518806563
- Kumru, H., Benito-Penalva, J., Valls-Sole, J., Murillo, N., Tormos, J. M., Flores, C., et al. (2016a). Placebo-controlled study of rTMS combined with lokomat® gait training for treatment in subjects with motor incomplete spinal cord injury. *Exp. Brain Res.* 234, 3447–3455. doi: 10.1007/s00221-016-4739-9
- Kumru, H., Murillo, N., Benito-Penalva, J., Tormos, J. M., and Vidal, J. (2016b). Transcranial direct current stimulation is not effective in the motor strength and gait recovery following motor incomplete spinal cord injury during lokomat® gait training. *Neurosci. Lett.* 620, 143–147. doi: 10.1016/j.neulet.2016.03.056
- Labruyère, R., and van Hedel, H. J. A. (2014). Strength training versus robot-assisted gait training after incomplete spinal cord injury: a randomized pilot study in patients depending on walking assistance. *J. Neuroeng. Rehabil.* 11:4. doi: 10.1186/1743-0003-11-4
- Lenzi, T., Vitiello, N., Rossi, S. M. M., De Persichetti, A., Giovacchini, F., Roccella, S., et al. (2011). Mechatronics measuring human – robot interaction on wearable robots: a distributed approach. *Mechatronics* 21, 1123–1131. doi: 10.1016/j.mechatronics.2011.04.003
- Lo, A. C., Chang, V. C., Gianfrancesco, M. A., Friedman, J. H., Patterson, T. S., and Benedicto, D. F. (2010). Reduction of freezing of gait in Parkinson's disease by repetitive robot-assisted treadmill training: a pilot study. *J. Neuroeng. Rehabil.* 7:51. doi: 10.1186/1743-0003-7-51
- Lo, A. C., and Triche, E. W. (2008). Improving gait in multiple sclerosis using robot-assisted, body weight supported treadmill training. *Neurorehabil. Neural Repair.* 22, 661–671. doi: 10.1177/1545968308318473
- Maak, T. G., and Wylie, J. D. (2016). Medical device regulation. *J. Am. Acad. Orthop. Surg.* 24, 537–543. doi: 10.5435/JAAOS-D-15-00403
- Makino, Y., Sugiyama, Y., Ogata, M., and Inami, M. (2013). "Tangential force sensing system on forearm," in *Proceedings of the 4th Augmented Human International Conference* (Stuttgart), 29–34. doi: 10.1145/2459236.2459242
- Mao, X., Yamada, Y., Akiyama, Y., Okamoto, S., and Yoshida, K. (2015). "Development of a novel test method for skin safety verification of physical assistant robots," in 2015 IEEE International Conference on Rehabilitation Robotics (ICORR) (Singapore: IEEE), 319–324. doi: 10.1109/ICORR.2015.7281219
- Mayr, A., Kofler, M., Quirbach, E., Matzak, H., Fröhlich, K., and Saltuari, L. (2007). Prospective, blinded, randomized crossover study of gait rehabilitation in stroke patients using the lokomat gait orthosis. *Neurorehabil. Neural Repair.* 21, 307–314. doi: 10.1177/1545968307300697
- Mehrholz, J., Thomas, S., Werner, C., Kugler, J., Pohl, M., and Elsner, B. (2017). Electromechanical-assisted training for walking after stroke. *Cochrane Database Syst. Rev.* 5:CD006185. doi: 10.1002/14651858.CD006185.pub4
- Mishra, S. (2017). FDA, CE mark or something else?—thinking fast and slow. *Indian Heart J.* 69, 1–5. doi: 10.1016/j.ihj.2016.11.327
- Moher, D., Liberati, A., Tetzlaff, J., and Altman, D. G. (2009). Preferred reporting items for systematic reviews and meta-analyses: the PRISMA statement. *PLoS Med.* 6:e1000097. doi: 10.1371/journal.pmed.1000097
- Morone, G., Bragoni, M., Iosa, M., De Angelis, D., Venturiero, V., Coiro, P., et al. (2011). Who may benefit from robotic-assisted gait training? *A randomized clinical trial in patients with subacute stroke. Neurorehabil. Neural Repair.* 25, 636–644. doi: 10.1177/1545968311401034
- Ng, M. F. W., Tong, R. K. Y., and Li, L. S. W. (2008). A pilot study of randomized clinical controlled trial of gait training in subacute stroke patients with partial body-weight support electromechanical gait trainer and functional electrical stimulation. *Stroke* 39, 154–160. doi: 10.1161/STROKEAHA.107.495705
- Nilsson, A., Vreede, K., Häglund, V., Kawamoto, H., Sankai, Y., and Borg, J. (2014). Gait training early after stroke with a new exoskeleton – the hybrid assistive limb: a study of safety and feasibility. *J. Neuroeng. Rehabil.* 11:92. doi: 10.1186/1743-0003-11-92
- Ochi, M., Wada, F., Saeki, S., and Hachisuka, K. (2015). Gait training in subacute non-ambulatory stroke patients using a full weight-bearing gait-assistance robot: a prospective, randomized, open, blinded-endpoint trial. *J. Neurol. Sci.* 353, 130–136. doi: 10.1016/j.jns.2015.04.033

- Ouzzani, M., Hammady, H., Fedorowicz, Z., and Elmagarmid, A. (2016). Rayyan—a web and mobile app for systematic reviews. *Syst. Rev.* 5:210. doi: 10.1186/s13643-016-0384-4
- Picelli, A., Melotti, C., Origano, F., Neri, R., Verzè, E., Gandolfi, M., et al. (2015). Robot-assisted gait training is not superior to balance training for improving postural instability in patients with mild to moderate Parkinson's disease: a single-blind randomized controlled trial. *Clin. Rehabil.* 29, 339–347. doi: 10.1177/0269215514544041
- Picelli, A., Melotti, C., Origano, F., Waldner, A., Fiaschi, A., Santilli, V., et al. (2012). Robot-assisted gait training in patients with parkinson disease: a randomized controlled trial. *Neurorehabil. Neural Repair.* 26, 353–361. doi: 10.1177/1545968311424417
- Regulation (EU) 2017/745 of the European Parliament and of the Council of 5 April 2017 on medical devices, amending Directive 2001/83/EC, Regulation (EC) No 178/2002 and Regulation (EC) No 1223/2009 and repealing Council Directives 90/385/EEC and 93/42/EE (2017). *Official Journal of the European Union* 60, 2–175. Available online at: <http://eur-lex.europa.eu/legal-content/EN/TXT/PDF/?uri=OJ:L:2017:117:FULL&from=EN> (accessed April 27, 2020).
- Rocon, E., Ruiz, A. F., Raya, R., Schiele, A., Pons, J. L., Belda-Lois, J. M., et al. (2008). "Human-robot physical interaction," in *Wearable Robots: Biomechatronic Exoskeletons*, ed J. L. Pons (Chichester: John Wiley and Sons), 127–163. doi: 10.1002/9780470987667.ch5
- Sadarangani, G. P., Jiang, X., Simpson, L. S., Eng, J. J., and Menon, C. (2017). Force myography for Monitoring grasping in individuals with stroke with Mild to moderate upper-extremity impairments : a Preliminary investigation in a controlled environment. *Front. Bioeng. Biotechnol.* 5:42. doi: 10.3389/fbioe.2017.00042
- Sanders, J. E., Goldstein, B. S., and Leotta, D. F. (1995). Skin response to mechanical stress: adaptation rather than breakdown - a review of the literature. *J. Rehabil. Res. Dev.* 32, 214–26.
- Schoenrath, F., Markendorf, S., Brauchlin, A. E., Frank, M., Wilhelm, M. J., Saleh, L., et al. (2015a). Robot-assisted training for heart failure patients - a small pilot study. *Acta Cardiol.* 70, 665–671. doi: 10.1080/AC.70.6.3120178
- Schoenrath, F., Markendorf, S., Brauchlin, A. E., Seifert, B., Wilhelm, M. J., Czerny, M., et al. (2015b). Robot-assisted training early after cardiac surgery. *J. Card. Surg.* 30, 574–580. doi: 10.1111/jocs.12576
- Schulz, K. F., Altman, D. G., and Moher, D. (2010). CONSORT 2010 statement: updated guidelines for reporting parallel group randomised trials. *BMJ* 340, c332. doi: 10.1136/bmj.c332
- Szczesny-Kaiser, M., Höffken, O., Aach, M., Cruciger, O., Grasmücke, D., Meindl, R., et al. (2015). HAL® exoskeleton training improves walking parameters and normalizes cortical excitability in primary somatosensory cortex in spinal cord injury patients. *J. Neuroeng. Rehabil.* 12:68. doi: 10.1186/s12984-015-0058-9
- Szczesny-Kaiser, M., Kowalewski, R., Schildhauer, T. A., Aach, M., Jansen, O., Grasmücke, D., et al. (2017). Treadmill training with HAL exoskeleton—a novel approach for symptomatic therapy in patients with limb-girdle muscular dystrophy—preliminary study. *Front. Neurosci.* 11:449. doi: 10.3389/fnins.2017.00449
- Stoller, O., de Bruin, E. D., Schindelholz, M., Schuster-Amft, C., de Bie, R. A., and Hunt, K. J. (2014). Cardiopulmonary exercise testing early after stroke using feedback-controlled robotics-assisted treadmill exercise: test-retest reliability and repeatability. *J. Neuroeng. Rehabil.* 11:145. doi: 10.1186/1743-0003-11-145
- Stoller, O., de Bruin, E. D., Schindelholz, M., Schuster-Amft, C., de Bie, R. A., and Hunt, K. J. (2015). Efficacy of feedback-controlled robotics-assisted treadmill exercise to improve cardiovascular fitness early after stroke: a randomized controlled pilot trial. *J. Neurol. Phys. Ther.* 39, 156–165. doi: 10.1097/NPT.0000000000000095
- Straudi, S., Manfredini, F., Lamberti, N., Martinuzzi, C., Maietti, E., and Basaglia, N. (2019). Robot-assisted gait training is not superior to intensive overground walking in multiple sclerosis with severe disability (the RAGTIME study): a randomized controlled trial. *Mult. Scler. J.* 26, 716–24. doi: 10.1177/1352458519833901
- Sugiura, Y., Inami, M., and Igarashi, T. (2012). "A thin stretchable interface for tangential force measurement," in *Proceedings of the 25th Annual ACM Symposium on User Interface Software and Technology* (Cambridge, MA), 529–535. doi: 10.1145/2380116.2380182
- Tamez-Duque, J., Cobian-Ugalde, R., Kilicarslan, A., Venkatakrishnan, A., Soto, R., and Contreras-Vidal, J. L. (2015). Real-time strap pressure sensor system for powered exoskeletons. *Sensors* 15, 4550–4563. doi: 10.3390/s150204550
- Tanaka, H., Nankaku, M., Nishikawa, T., Hosoe, T., Yonezawa, H., Mori, H., et al. (2019). Spatiotemporal gait characteristic changes with gait training using the hybrid assistive limb for chronic stroke patients. *Gait Posture* 71, 205–210. doi: 10.1016/j.gaitpost.2019.05.003
- Turiel, M., Sitia, S., Cicala, S., Magagnin, V., Bo, I., Porta, A., et al. (2011). Robotic treadmill training improves cardiovascular function in spinal cord injury patients. *Int. J. Cardiol.* 149, 323–329. doi: 10.1016/j.ijcard.2010.02.010
- U.S. Department of Health and Human Services (2017). *Common Terminology Criteria for Adverse Events (CTCAE) Version 5.0*. Available online at: https://ctep.cancer.gov/protocolDevelopment/electronic_applications/docs/CTCAE_v5_Quick_Reference_8.5x11.pdf (accessed April 29, 2020).
- van Herpen, F. H. M., van Dijksseldonk, R. B., Rijken, H., Keijsers, N. L. W., Louwerens, J. W. K., and van Nes, I. J. W. (2019). Case report: description of two fractures during the use of a powered exoskeleton. *Spinal Cord Ser. Cases* 5:99. doi: 10.1038/s41394-019-0244-2
- Vaney, C., Gattlen, B., Lugon-Moulin, V., Meichtry, A., Hausammann, R., Foinant, D., et al. (2012). Robotic-assisted step training (Lokomat) not superior to equal intensity of over-ground rehabilitation in patients with multiple sclerosis. *Neurorehabil. Neural Repair.* 26, 212–221. doi: 10.1177/1545968311425923
- Wettenschwiler, P. D., Stämpfli, R., Lorenzetti, S., Ferguson, S. J., Rossi, R. M., and Annaheim, S. (2015). How reliable are pressure measurements with tekscan sensors on the body surface of human subjects wearing load carriage systems? *Int. J. Ind. Ergon.* 49, 60–67. doi: 10.1016/j.ergon.2015.06.003
- Wilkening, A., Puleva, N., and Ivlev, O. (2016). Estimation of physical human-robot interaction. *Robotics* 5:17. doi: 10.3390/robotics5030017
- World Health Organization (2018). *Ageing and Health*. Available online at: <https://www.who.int/news-room/fact-sheets/detail/ageing-and-health> (accessed May 7, 2019).
- Wu, Q., Wang, X., Du, F., and Zhang, X. (2015). Design and control of a powered hip exoskeleton for walking assistance. *Int. J. Adv. Robot. Syst.* 12:18. doi: 10.5772/59757
- Yandell, M. B., Ziemnicki, D. M., McDonald, K. A., and Zelik, K. E. (2020). Characterizing the comfort limits of forces applied to the shoulders, thigh and shank to inform exosuit design. *PLoS ONE* 15:e0228536. doi: 10.1371/journal.pone.0228536

Conflict of Interest: The authors declare that the research was conducted in the absence of any commercial or financial relationships that could be construed as a potential conflict of interest.

Copyright © 2020 Bessler, Prange-Lasonder, Schulte, Schaaake, Prinsen and Buurke. This is an open-access article distributed under the terms of the Creative Commons Attribution License (CC BY). The use, distribution or reproduction in other forums is permitted, provided the original author(s) and the copyright owner(s) are credited and that the original publication in this journal is cited, in accordance with accepted academic practice. No use, distribution or reproduction is permitted which does not comply with these terms.

APPENDIX

Search Strategy PubMed

- #1 robotics [MeSH] OR robot-assisted OR robotics-assisted OR electromechanical OR electro-mechanical
- #2 exercise therapy [MeSH] OR rehabilitation OR training
- #3 gait OR walk OR walking OR step OR stepping OR locomotor OR locomotion
- #4 #1 AND #2 AND #3
- #5 “body weight support” OR “body weight supported”
- #6 #5 AND “treadmill training”
- #7 #4 OR #6 OR “locomotor training” OR Lokomat OR Gangtrainer OR G-EO OR WALKBOT OR LokoHelp
- #8 adverse OR “skin breakdown” OR “skin lesion” OR “skin sore” OR “pressure sore” or discomfort OR abrasion
- #9 #7 AND #8



Bioinspired Postural Controllers for a Locked-Ankle Exoskeleton Targeting Complete SCI Users

Jemina Fasola^{1*†}, Romain Baud^{2†}, Tristan Vouga², Auke Ijspeert² and Mohamed Bouri^{2,3}

¹ Laboratory of Cognitive Neuroscience (LNCO), School of Life Sciences, Ecole Polytechnique Fédérale de Lausanne (EPFL), Geneva, Switzerland, ² Biorobotics Laboratory (BIOROB), School of Engineering, Ecole Polytechnique Fédérale de Lausanne (EPFL), Lausanne, Switzerland, ³ Translational Neural Engineering (TNE), School of Engineering, Ecole Polytechnique Fédérale de Lausanne (EPFL), Geneva, Switzerland

OPEN ACCESS

Edited by:

Jan Veneman,
Hocoma, Switzerland

Reviewed by:

Antonio J. del-Ama,
Rey Juan Carlos University, Spain
Noel Keijsers,
Sint Maartens Clinic, Netherlands

*Correspondence:

Jemina Fasola
jemina.fasola@epfl.ch

[†]These authors have contributed
equally to this work

Specialty section:

This article was submitted to
Biomedical Robotics,
a section of the journal
Frontiers in Robotics and AI

Received: 20 April 2020

Accepted: 05 October 2020

Published: 16 November 2020

Citation:

Fasola J, Baud R, Vouga T, Ijspeert A
and Bouri M (2020) Bioinspired
Postural Controllers for a
Locked-Ankle Exoskeleton Targeting
Complete SCI Users.
Front. Robot. AI 7:553828.
doi: 10.3389/frobt.2020.553828

Several lower-limb exoskeletons enable overcoming obstacles that would impair daily activities of wheelchair users, such as going upstairs. Still, as most of the currently commercialized exoskeletons require the use of crutches, they prevent the user from interacting efficiently with the environment. In a previous study, a bio-inspired controller was developed to allow dynamic standing balance for such exoskeletons. It was however only tested on the device without any user. This work describes and evaluates a new controller that extends this previous one with an online model compensation, and the contribution of the hip joint against strong perturbations. In addition, both controllers are tested with the exoskeleton TWICE One, worn by a complete spinal cord injury pilot. Their performances are compared by the mean of three tasks: standing quietly, resisting external perturbations, and lifting barbells of increasing weight. The new controller exhibits a similar performance for quiet standing, longer recovery time for dynamic perturbations but better ability to sustain prolonged perturbations, and higher weightlifting capability.

Keywords: balance, posture, controller, exoskeleton, position-control, standing, paraplegic

INTRODUCTION

Lower-limb exoskeletons have gained much interest in the last decade. This growing interest is mainly driven by the aim of enhancing human performance and improving neuromotor rehabilitation. Therefore, developing novel features to improve user safety, mobility and autonomy is a constant research challenge. In the field of wearable robotic systems for complete spinal cord injured (SCI) patients, walking is the main function targeted by the majority of lower-limb exoskeletons. Balance management while walking and standing is generally performed by the user with the help of crutches, and thus impairing the use of their hands for other activities. Very few full-mobilization exoskeletons are able to self-stabilize (Donati et al., 2016; Gurriet et al., 2018; Rex Bionics, 2020), and thus, allow to free the user's hands. This comes at the cost of low walking speed and an important overall weight. In addition, none of them can climb stairs for example. Standing and walking balance are essential functions to promote exoskeleton usage during daily activities, that however should not come to the detriment of other features. In daily-life activities, manual tasks and environmental interactions happen mainly while standing (e.g., shaking hands, grabbing an object, drinking) rather than walking. Therefore, a valuable trade-off would be to enable the usage of the hands during standing for exoskeletons actuated only in the sagittal plane. While the

fore-aft balance could be actively regulated, the lateral stability can be maintained passively if the space between the feet is large enough, thanks to the wider base of support (BoS).

Humans are constantly adjusting their posture to act against gravity and are capable to resist to moderate internally generated or environmental perturbations using body coordination only (i.e., without stepping). To counteract these perturbations, proactive and reactive forms of postural movements are generated by the sensorimotor system to keep the center of mass (CoM) within the BoS (Rogers and Mille, 2018). Thus, coping with unexpected and self-generated perturbations requires a robust postural controller. As of today, there is no full-mobilization exoskeleton, position-controlled, actuated only in the sagittal plane capable of maintaining a standing posture with users that do not have any control of their lower limbs. Therefore, our goal is to develop a postural controller for TWIICE One, a lower-limb exoskeleton for complete SCI users.

Several research groups work on partial assistance during stance in the goal to improve the balance of people with incomplete SCI. Most of these control strategies are using torque control (Rajasekaran et al., 2015; Emmens et al., 2018; Farkhatdinov et al., 2019; van Asseldonk et al., 2019). These studies mimic the most common postural strategies highlighted by Winter (1995): the ankle, the hip, and their combined strategies. However, the limited number of degrees of freedom of TWIICE One, especially its locked ankles, does not allow to directly adopt these control strategies. For that reason, a bioinspired approach was adopted to identify and then implement the elicited postural strategies on TWIICE One. From this approach, two postural controllers have been developed. This case study aims to present and characterize the performance of these two postural controllers enabling a complete SCI user to stand without crutches.

These controllers are potentially useful for the current generation of full-mobilization exoskeletons, because they do not need torque control in the joints, or load cells in the feet. The hardware can then be kept minimal, so the device can be simpler, less expensive and more robust.

BIOINSPIRED APPROACH: LEARN FROM A PASSIVE EXOSKELETON

In a previous study, we observed how young healthy participants adapted their postural control strategies when wearing a passive exoskeleton (Fasola et al., 2019). This device, called INSPIRE (see **Figure 1A**), has the same kinematic constraints as TWIICE One, and fully curved foot soles, see **Figure 1F**. It has been found that healthy adults mainly manage their postural balance by flexing and extending their knees to move the contact point along the anteroposterior axis while standing quietly inside a passive locked-ankle exoskeleton (**Figure 1B**). Based on segmental analysis, this strategy is referred to as a vertical strategy, meaning that the trunk and the shank orientations move in phase and thus the whole body moves along the vertical axis (Nashner and McCollum, 1985). In case of more consequent perturbations, the hip strategy was used to maintain balance.

During the hip strategy, the shank rotation is not sufficient to keep the CoM over the base of support; therefore, the trunk rotates in the opposite direction to compensate and reposition the CoM.

Drawing inspiration from this human sensorimotor adaptation, a novel postural position controller has been implemented and tested on TWIICE with no user (Baud et al., 2019). This controller regulated the balance with a proportional-derivative (PD) controller, acting on the angle of the knee, and fed with the estimated CoM position (**Figure 1C**). This “knee controller” was able to manage the balance of TWIICE autonomously and resist to short perturbations.

In this article, the controller developed by Baud in 2019 is tested with a complete SCI user. In addition, an extended version of this knee controller is described and compared to the baseline knee controller. It is designed to resist stronger long-term perturbations.

POSTURAL CONTROL FRAMEWORK

Lower Limb Exoskeleton “TWIICE ONE”

The two postural controllers have been implemented on the lower limb exoskeleton TWIICE One 2018, **Figure 1D**. This exoskeleton is similar to the version of 2016 introduced in (Vouga et al., 2017). The mechanical design and the control framework are the same, while the actuators are more compact and more powerful (Billet et al., 2019). TWIICE One provides two active DoFs per leg for the flexion/extension of the hip and knee joints in the sagittal plane. The ankle joints are locked at 90°. To match the experimental conditions of the passive exoskeleton (Fasola et al., 2019), the foot soles profile has been modified. It is then fully curved (no flat part in the middle) to prevent passive postural stability (**Figure 1E**). Its 0.65 m radius is the same as the previous study, which is smaller than the height of the CoM of the test-pilot, so passive equilibrium is not possible. The sole is 227 mm long, which corresponds to a maximum range of movement of 242 mm for the contact point, when the sole is rolling on the floor. The top part of the exoskeleton foot is tilted forward by 5°, so when the middle of the foot is in contact with the floor, the shank axis has a 5° angle with respect to the vertical axis (Baud et al., 2019). The soles are covered with a rubber layer, to prevent slippage when standing.

The width of the BoS is 244 mm, measured between the two outer faces of the sole skates.

The elevation angle on the sagittal plane (also called “pitch angle”) of the exoskeleton’s foot is estimated from the inertial measurement unit (IMU) data with a simple complementary filter algorithm similar to Gui et al. (2015). Since the IMU is aligned with the exoskeleton, only a single gyroscope axis, and two accelerometer axes are required. The elevation angle of the thigh and trunk segments are computed from the estimated foot elevation angle and the joints encoders angles. Instead of using the trunk IMU as in Baud et al. (2019), the IMU located in the left foot is used instead. It is expected to increase the performance for two reasons. First, when swinging fore-aft the whole body, the foot is the location with the lowest linear acceleration, which makes the state estimation more accurate.

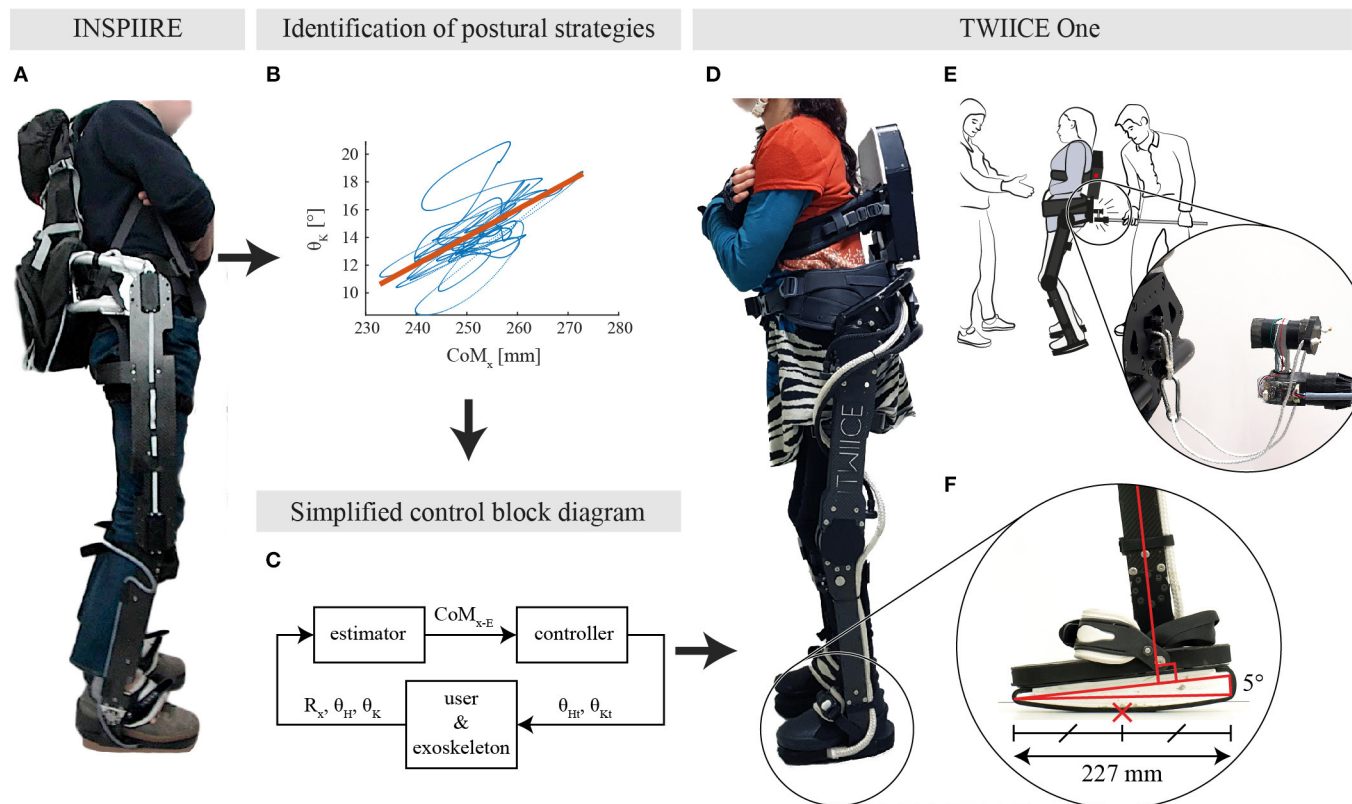


FIGURE 1 | (A) Healthy participant standing while being constrained by INSPIRE, a passive exoskeleton. **(B)** Identified relation between the knee angle and the CoM_x for a typical young healthy participant in the eyes closed condition from Fasola et al. (2019). **(C)** Overview of the controller block diagram. CoM_{x-E} is the estimated projection of the center of mass, R_x represents the foot angle with respect to the ground line, while θ_H and θ_K are the hip and knee angles, respectively. **(D)** TWIICE running with the knee controller (BKC) and a complete SCI user. **(E)** Overview of the experimental setup, with the experimenter in the back, and the spotter in front. The experimenter interacts with the exoskeleton through the instrumented stick. **(F)** Close-up view on the TWIICE foot, with the rounded sole and the 5° wedge. The red cross is the position of the CoP, at the middle of the foot in this case. This is considered as the "horizontal" position of the foot.

Second, there is more vibration in the trunk, that is less rigid and in a cantilever configuration, which can generate closed-loop self-sustained uncontrolled oscillations.

The embedded computer of TWIICE collects at 1 kHz the data from the inertial measurement unit (IMU) and the joints encoders.

TWIICE is not a certified commercial device, but it is deemed safe, so it is very unlikely that the pilot could be harmed in this experiment. Its hardware and operation are fully documented, and a failure mode and effects analysis (FMEA) was performed. It was also inspected and approved by the organizers of the CYBATHLON (Riener, 2016), as a prerequisite to participate in this event.

Proposed Postural Controllers

Baseline Knee Controller

The “Baseline Knee Controller” (BKC) regulates the balance with a proportional-derivative (PD) controller, setting the angle of the knee, and fed with the CoM position (**Figure 2**). This “Baseline Knee Controller” was described, simulated and experimentally tested (Baud et al., 2019). The knees are flexed proportionally to the estimated position of the CoM. This makes the foot sole rotate forward and backward, and move the point of contact with the floor. Since the sole is only in contact with the ground at one point, this point corresponds also to the center of pressure, x_{CoP} , on the anteroposterior axis. CoM_x is the position of the projection on the ground of the CoM, on the anteroposterior axis. Its origin is defined at the middle of the foot when it is in contact with the ground. In this BKC controller, the CoM_x estimation is computed using a simple 2D model consisting of 3 segments (foot to knee, knee to hip, trunk including the head). The trunk length was measured on the user, while the shank and thigh lengths were obtained from the 3D model of the exoskeleton. The masses were obtained by summing the pilot's and exoskeleton's segments. The masses of the user segments were estimated from the full bodyweight using the mass repartition from Fang et al. (2017), considering the data corresponding to “chronic SCI ≥ 3 years” and “BMI < 25.” Finally, an offset, CoM_{x-off} , is added to the estimation of CoM_x to obtain CoM_{x-E} , which is called CoM_{x-E1} in the BKC case. This offset is necessary because the model is not accurate.

CoM_{x-E} is first filtered by a low-pass filter with a cut-off frequency fc_1 , then fed into a proportional-derivative controller (PD) with the parameters Kp_K (proportional part gain) and Kd_K (derivative part gain). Before differentiation, the signal is filtered by a stronger low-pass filter with a cut-off frequency fc_2 . This gives a knee flexion angle, which is offset by θ_{K-off} to increase the flexion, and thus avoids hyperextension of the knee when the output of the BKC controller is negative. For safety, the value is finally clamped to the range $[2 \text{ to } 40^\circ]$. The hip joint is fixed at the angle θ_{H-off} .

A pilot study with the BKC controller has demonstrated its ability to make a complete SCI user stand dynamically with TWIICE. However, it was performing poorly for the task of grabbing heavy objects (several kilograms), unless they were close to the body. The first reason is that the CoM_{x-E1} computation is not accurate since it does not consider the added mass. The other

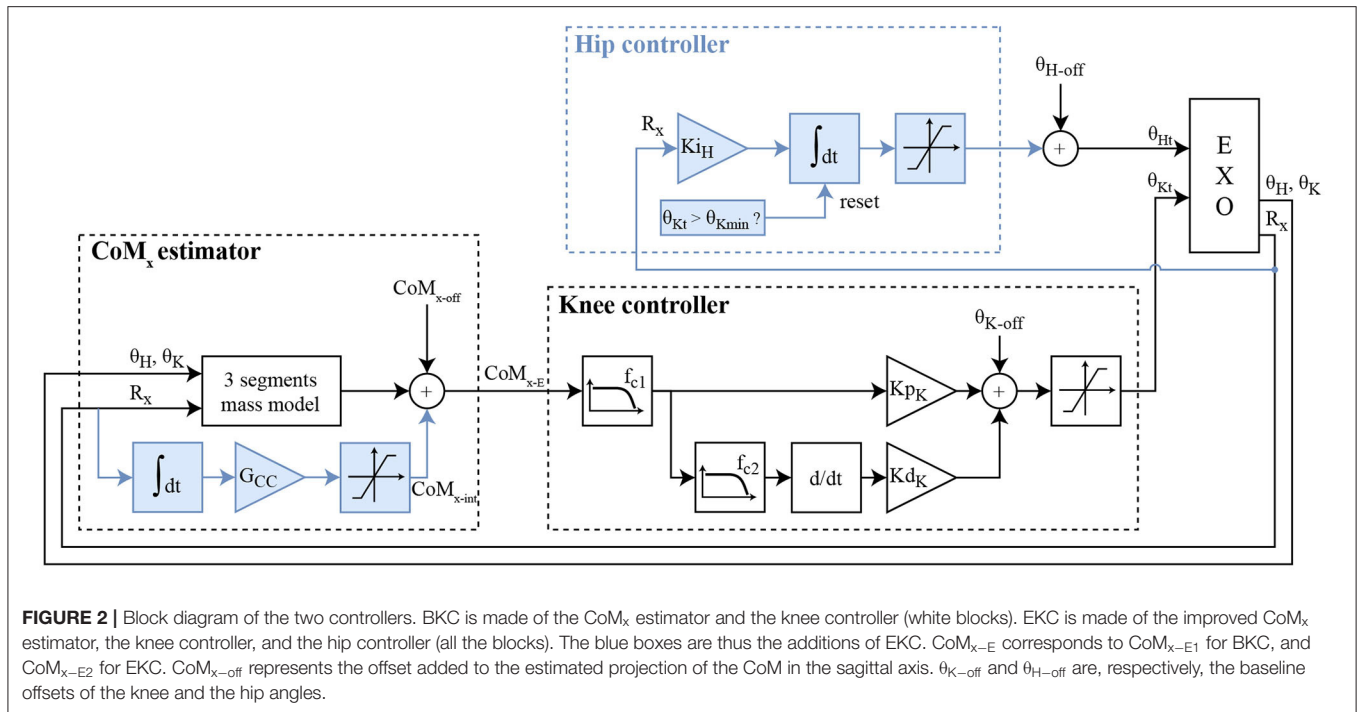
reason is that the controller is managing the balance by moving the position of the CoP along the foot length, but this does not work in the case the added weight shifts the CoM beyond the span of the feet.

Extended Knee Controller

The extended knee controller (EKC) is based on the BKC, but with two additions to overcome the two aforementioned issues (**Figure 2**, blue boxes). The first change is the extension of the CoM_x estimator, to adapt the model online when a constant perturbation (added mass or horizontal force) arises. This is done with a gain (G_{CC}) and an integrator of the R_x value, R_x being the foot angle with respect to the ground line (or the elevation angle of the foot, minus 90°). The output of this integrator is added as a variable offset to the CoM_{x-E} calculation, called CoM_{x-E2} for this controller (**Figure 2**, CoM_x , blue boxes). The idea is that in case of a permanent perturbation, the CoP will move durably, closer to an end of the foot, which decreases the robustness against perturbations in this direction. Continuously increasing the CoM_{x-E} offset will increase the correction of the PD controller, until the sole starts to roll in the other direction. This means that if a steady-state exists, the center part of the foot will be in contact with the floor. Adding an integrator to the regulator to make a PID controller instead would not have the same results. This will not be proved analytically here, but intuitively, in case of constant perturbation with BKC and a PID, the steady-state will be reached when the CoM_{x-E1} reaches zero, but the CoP will probably not be in the middle of the foot, so the robustness would be lower in one direction.

The second change is the addition of the hip contribution when the knee reached the full extension. In case the knee reaches the full extension, an integrator with a gain Ki_H will gradually increase the hip flexion angle, to bring the trunk forward, and thus shift the CoM toward the front (**Figure 2**, Hip controller, blue boxes). This flexion angle is limited to 60° for safety. If the knee angle is not saturating, the integrator value is reset to zero smoothly at a $2^\circ/s$ rate. This conservative low value was selected to make sure it does not interfere with the knee control and avoid oscillations.

Simulations have been performed with the same Simulink simulation environment described in Baud et al. (2019). The goal of this model is to check the proper operation of the controller, i.e., keeping the body standing without falling. The stability is assessed from the values of CoM_{x-E} and the foot elevation angle, which should remain close to 90° . This model contains a three weighted segments model, lumping together the user body and the exoskeleton, the feet rolling on the floor with no slippage. It is subject to a horizontal perturbation force, applied at the hip joint axis, with a square profile: 0 N, then 20 N forward for 8 s, then 0 N again. The parameters have been set as follows: $Kp_K = 340^\circ/m$, $Kd_K = 170^\circ/(m/s)$, no filtering. For BKC, $Ki_K = 340^\circ/(m.s)$ and $G_{cc} = 0 \text{ m}/(^{\circ}.s)$. Ki_K is the integral coefficient if the knee PD controller is replaced by a PID. It is not required and will not be used on the actual device, but it allows a clearer comparison between the results obtained with BKC and EKC, thanks to the eventual cancellation of the CoM_{x-E} steady-state error (it will show that the effect of the integral component of EKC is not



equivalent as using a PID with BKC). For EKC, $K_{iK} = 0^\circ/(\text{m.s})$ and $G_{cc} = 0.000002 \text{ m}/(^\circ.\text{s})$.

The results are exposed in **Figure 3**. It can be noticed that both BKC and EKC both maintained the standing balance despite the perturbation. Both the foot elevation angle and CoM_{x-E} exhibit minimal oscillations. With BKC, the system is stable during the

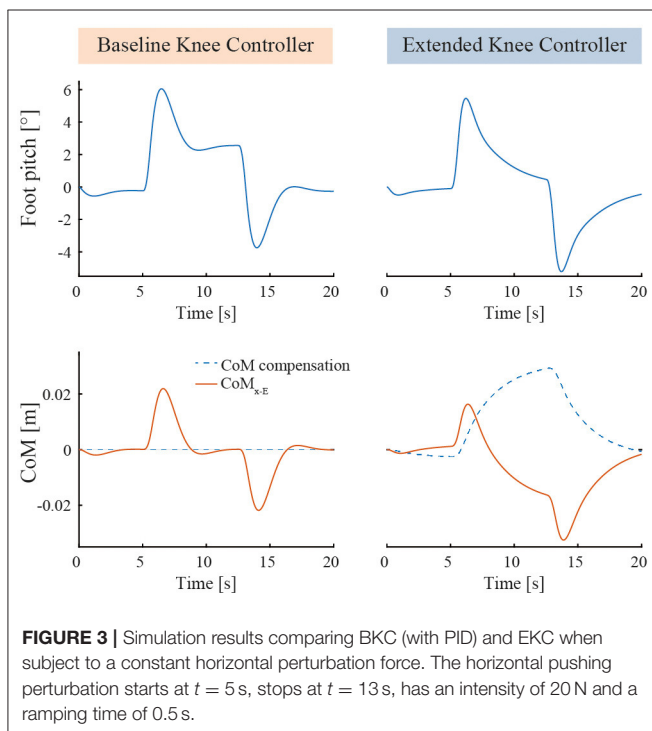
perturbation, but the foot is not horizontal at steady-state (2.6°), which leaves less control leeway for further pushes. In fact, the CoP reaches the end of the foot when $|R_x| > 10^\circ$. With EKC, R_x also reaches approximately 6° when the perturbation is applied but then returns slowly to 0° (CoP at the middle of the foot), which results in having the same room for maneuver in both directions again. While returning to the horizontal position, R_x follows an exponential function with a time constant of 2.4 s ($R^2 = 0.997$). This means that a stronger long-term perturbation should rise slowly, not quicker than a few seconds, otherwise the integral action of EKC will not compensate fast enough to avoid the fall.

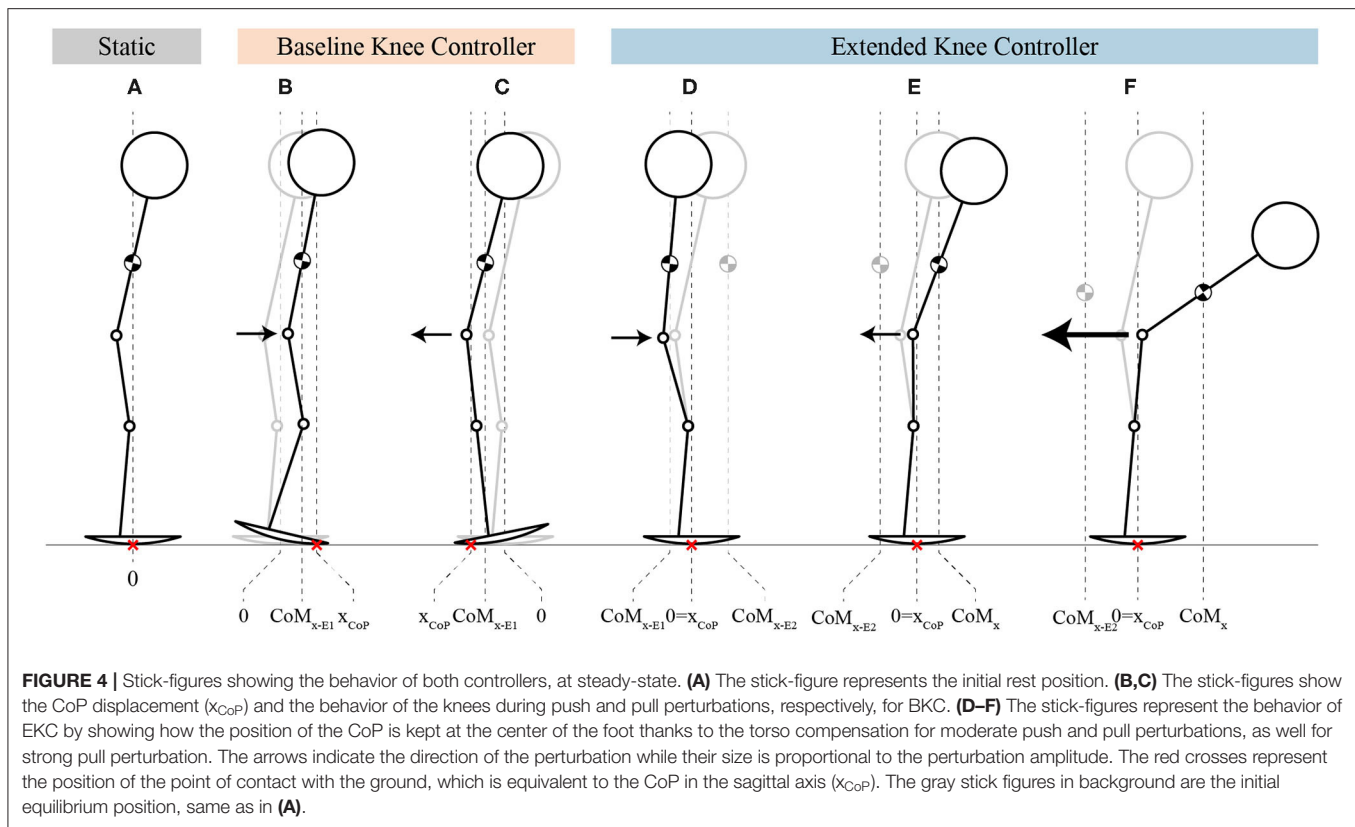
The general behavior of the two controllers at steady-state can be seen in **Figure 4**. In the BKC case, the system statically resists the perturbation by keeping the CoP more in the front (**Figure 4B**) or in the rear of the foot (**Figure 4C**). In the EKC case, the system resists statically by keeping the CoM toward the back (**Figure 4D**) or toward the front (**Figure 4E**), such that the CoP is at the middle of the foot. In the last case (**Figure 4F**), the pulling force is stronger, and the knee reached the full extension and cannot extend more. The hip then flexes to move the CoM even more in front.

METHODS

Test-Pilot

Both postural controllers were tested with one chronic (10 years post-injury) and functionally complete SCI participants (ASIA A) with a lesion at the T10 level. She is 158 cm tall and weighs 45 kg. She has no contraindications for the use of an exoskeleton (strong spasms, contractures, low bone density, or cognitive deficiency) and uses regularly a passive verticalization device.





She will be called “test-pilot” of the lower limb exoskeleton. She had a previous experience with the standing balance with two preliminary sessions, the exoskeleton running a provisional controller, similar to the current implementation of BKC. She gave informed consent to participate in the test sessions.

Only one participant was involved because this experiment aims assessing the performance of the device, not the user. The guidelines on assistive devices by the Swiss Ethics Committees on research involving humans (Swissethics, 2018) specify that exploratory works (evaluating “beta prototypes,” their overall operation, the function or robustness of the sensors and actuators, etc.) are not subject to the swiss law about research on humans.

Protocol

The tuning of the controller parameters occurred during a dedicated session, 10 days before the actual experiment.

The experiment was composed of four tasks: quiet standing, pulse and static perturbations, and object lifting perturbation. The test-pilot was instructed to keep her arms crossed and look straight at a cross on the wall in front of her during the whole experiment. The floor is made of hard linoleum floor, with virtually no rolling resistance.

At all times, there were one spotter in front and one behind the pilot to catch her in case of loss of balance, since the controllers will not trigger a step when the stability margin is exceeded. The spotters’ hands were very close to the exoskeleton handles or the pilot’s body to ensure quick grabbing in case of loss of

balance. Contact only occurs in case of loss of balance. The usual harness, cable and support frame could not be used because the cable would disturb the balance, probably positively and biasing the results.

Tuning Session

The regulator gains were first set to zero to disable the closed-loop control. θ_{K-off} was fixed arbitrarily, then CoM_{x-off} , θ_{H-off} and were obtained by hand-tuning such that CoM_{x-E1} is zero when the exoskeleton stands still in the unstable equilibrium position, while the middle of the sole in contact with the ground. This procedure was repeated several times, to maximize θ_{K-off} under the condition that the posture is comfortable for the test-pilot.

Then, the low-pass filters and the PD parameters were tuned to maximize the disturbance rejection performance while no self-sustained oscillations or vibrations can be observed. Finally, K_{IH} and G_{CC} were tuned to the highest value that does not generate self-sustained oscillations.

Quiet Standing

For both controllers, 1 min of quiet standing was performed in order to compare the sway amplitude without any perturbation.

Pulse Perturbations

The goal of the second task of the experiment consists in evaluating the responsiveness and stability of both controllers, when the exoskeleton is subject to short and high-intensity horizontal perturbations. The back part of the exoskeleton

was pushed and pulled horizontally at the pelvic height (960 mm above the ground level) with a stick operated by an experimenter behind the pilot, so that she cannot expect the pulses (**Figure 1E**).

As in Emmens et al. (2018), the perturbation amplitude is defined by the push/pull force multiplied by the perturbation duration. The experimenter keeps the duration of the pulses short and as constant as possible. As long as the user is swinging, the LED on the backpack is red, and the experimenter will not interfere with the movement. When the sway velocity of the trunk (computed by time-derivation of the trunk elevation angle, obtained with the foot IMU and the joints encoders) remains below 0.015 rad/s (0.86°/s) for more than 2 s, the LED on the backpack turns green again, and a new perturbation can be applied. The perturbations are applied randomly by the experimenter. The supervision laptop counts the perturbations and sorts them into the weak/medium/strong categories for both directions, to help the experimenter applying all types of perturbations.

The stick is instrumented with a load cell, mounted with a stiff string such that it can push (posterior perturbation) and pull (anterior perturbation) the exoskeleton, or apply virtually no force when the pusher is not in contact and the string is loose. A custom amplifier and sampling board is also mounted on the stick, based on the ADS1146 chip (Texas Instruments, United States). It is wired to the exoskeleton embedded computer with four loose thin wires (0.129 mm² copper section) to apply only minimal parasitic force on the exoskeleton. This allows the exoskeleton to log the load cell signal with the same time base as the exoskeleton data, to avoid the manual synchronization step after the experiment.

Static Pull and Push Forces

To assess the performance of both controllers during prolonged perturbations, the maximum horizontal force that is sustainable before losing balance was measured in both directions. The experimenter pushes with the instrumented stick, increasing slowly, and monotonically the force, until static equilibrium is lost. This procedure was repeated 3 times, and then was reiterated also 3 times by pulling the test-pilot backward. The user is caught and brought back to the vertical position by the experimenter at the end of each trial, so the recovery cannot be evaluated.

Object Lifting Perturbation

Finally, to define the anterior static margin of stability in a situation close to an actual use case, the test-pilot was asked to lift a barbell in front of her, and raise it gently at the shoulder height with the arms straight forward, then lower it down. Raising starts with the barbell at the lowest possible height, in contact with the legs. The mass of the barbell was changed from 0 kg (i.e., weight of the arms only) to 6 kg with increments of 2 kg. Each mass was lifted once. The task was failed if the spotters had to catch the test-pilot to prevent the fall, or if the test-pilot is unable to complete the task in <1 min. Unlike the previous test, the recovery back to the vertical position with no load is part of the task. The pilot then has no assistance at all from the experimenters while

TABLE 1 | Controller parameters values.

Parameter	BKC-value	EKC-value
CoM _{x-off}		0.04 m
f _{c1}		20 Hz
f _{c2}		5 Hz
θ _{K-off}		8°
θ _{H-off}		0°
K _{pK}		420°/m
K _{dK}		110°/(m/s)
K _{iH}	0°/(°·s)	0.3°/(°·s)
G _{cc}	0 m/(°·s)	0.000002 m/(°·s)

lifting, hovering and lowering. As opposed to the previous tasks, the participant has to use her arms for a simulated activity. This is the main reason why a manikin could not replace an actual participant in this protocol.

Data Analysis

The analysis of the stability is performed using the CoM_{x-E1} metric, because there was no extra instrumentation that could measure the actual CoM_x, and CoM_{x-E2} would be irrelevant when considering the static pull and push perturbations.

For quiet standing, a high-pass filter was applied to CoM_{x-E1} to discard potential position shift due to the slow head movement of the test-pilot. Then, the root mean square (RMS) of the CoM_{x-E1} was used to evaluate the amplitude of body sway for both controllers. For the pull and push task, perturbations with a duration deviating more than 0.1 s from the median duration were excluded. Thus, for each controller, only responses with similar perturbation duration were analyzed. Then, the pull and push perturbations were sorted each in three categories based on the distribution of the perturbation magnitude. These categories were the same for the two controllers.

The main assessment metrics were the recovery time and the maximal perturbation magnitude that the controllers can handle in both directions. The recovery time was defined as the time needed after a perturbation for the CoM_{x-E1} velocity to fall below a threshold set to 0.005 m/s. This threshold value was selected because it was the highest that still considered the oscillations due to the perturbations of the first category. A moving average filter with a span of 10% of the total number of data points was applied to the CoM_{x-E1} derivative. The maximal sustainable pulse perturbation amplitude in both directions was defined by the maximum perturbation amplitude that does not result in a loss of balance.

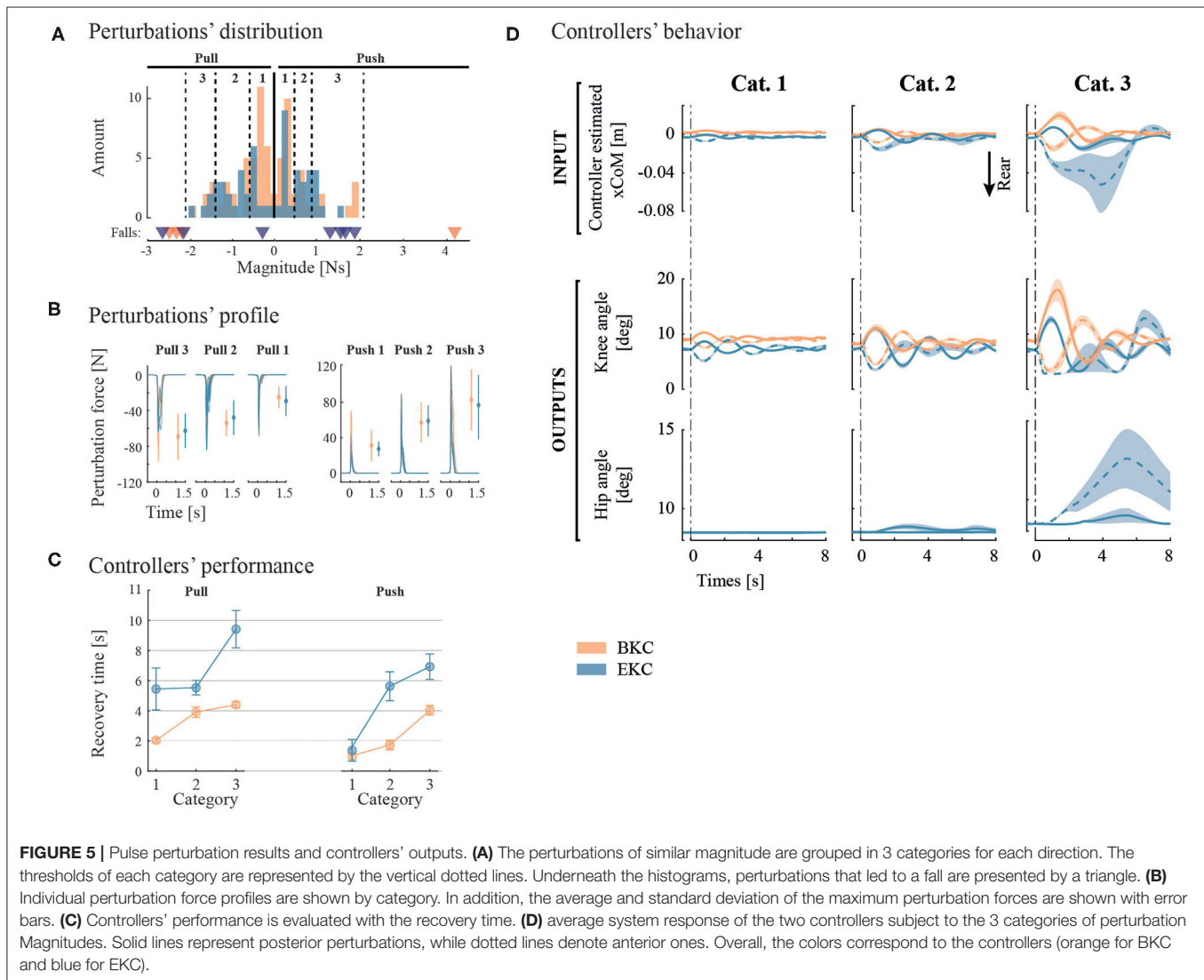
For the maximum sustainable pull and push force, the average of the 3 peak forces in each direction was computed.

RESULTS

The results of the parameters tuning session are shown in **Table 1**.

Quiet Standing

The oscillation frequency is similar in both cases: 0.60 Hz for BKC and 0.63 Hz for EKC. It was computed by finding the frequency of



the highest peak in the Fourier transform of the CoM_{x-E1} signal. The RMS of the body sway is also similar (0.31 mm for BKC and 0.38 mm for EKC).

Pulse Perturbations

For BKC, 74 perturbations were applied, resulting in 4 fall initiations and 1 exclusion. For EKC, the test-pilot underwent 63 perturbations, including 7 fall initiations and 1 exclusion. The distribution of the perturbations' magnitudes and perturbations' forces by category are shown in **Figures 5A,B**. The average perturbation duration was 0.18 ± 0.006 s and 0.19 ± 0.006 s for BKC and EKC, respectively.

To characterize the robustness of the controllers, we determined the maximum anterior (pull) and posterior (push) perturbation amplitude the controllers can bear before a fall starts. For BKC, the maximal anterior perturbation magnitude that can be sustained is about 2 N.s. Beyond that threshold, 3 backward falls were recorded (see **Figure 5A**, orange triangles). The threshold for posterior perturbations is between 2 and

4 N.s, as a push with a magnitude of 4 N.s triggered a frontal fall. For EKC, the maximal anterior perturbation magnitude is also around 2 N.s. Two perturbations above this threshold triggered a backward fall. The maximal threshold for posterior perturbations is between 1.2 and 1.6 N.s. Indeed, 4 falls were observed when the perturbation magnitude was above this threshold (see **Figure 5A**, blue triangles). It is important to note that the falls were in the backward direction although the perturbations were posterior (pushes). In summary, BKC is more robust than EKC for posterior perturbations, while they perform similarly for anterior perturbations.

To assess the performance of the controllers, the average recovery time has been extracted and plotted on **Figure 5C**. BKC recovered faster in all conditions [mean 2.95 s, 95% CIs (2.55, 3.34)] than EKC [mean 5.49 s, 95% CIs (4.65, 6.34)].

The average system response is shown on **Figure 5D**. For the first and second perturbation categories, the response is similar, although the oscillations last longer with EKC. There are more

differences for the third category. The pulling perturbations for EKC are producing a larger deviation of the CoM (~ 4 cm instead of ~ 2 cm for the other conditions), because the full extension of the knee was reached, and lowered the control capability. This is only the case for EKC, because initially, the knee was less flexed (the steady-state was not exactly the same), so there is less margin before the full extension is reached. It is also noticeable that even for the pushing perturbation, the hip contribution is used. This is because the oscillations have a high amplitude and low damping, this is why the system also reaches the backward position and result in saturating the knee angle in full extension and starts using the hip contribution.

Maximum Static Push and Pull Forces

The maximum pushing force that can be sustained is higher for EKC [mean 75.07 N, 95% CIs (66.25, 83.90)] than for BKC [mean 13.69 N, 95% CIs (5.29, 22.09)]. The maximum pulling force is also higher for EKC [mean 27.92 N, 95% CIs (11.86, 43.97)] than for BKC [mean 13.26 N, 95% CIs (10.39, 16.13)]. EKC can endure higher static forces when the test-pilot is pushed forward than pulled backward (unpaired t -test $p < 0.001$), while there is no effect of perturbation direction for BKC (unpaired t -test $p = 0.84$).

Object Lifting Perturbations

The results of this test are visible in **Figure 6**. With BKC, the test-pilot could lift her arms but failed to lift the 2 kg barbells

because she started falling forward before reaching the shoulder height, even though the ascent was slow. With EKC, the test-pilot could successfully lift the 2, 4, and 6 kg barbells. The time for the pilot to perform each movement (lifting and lowering) is shown in **Table 2**.

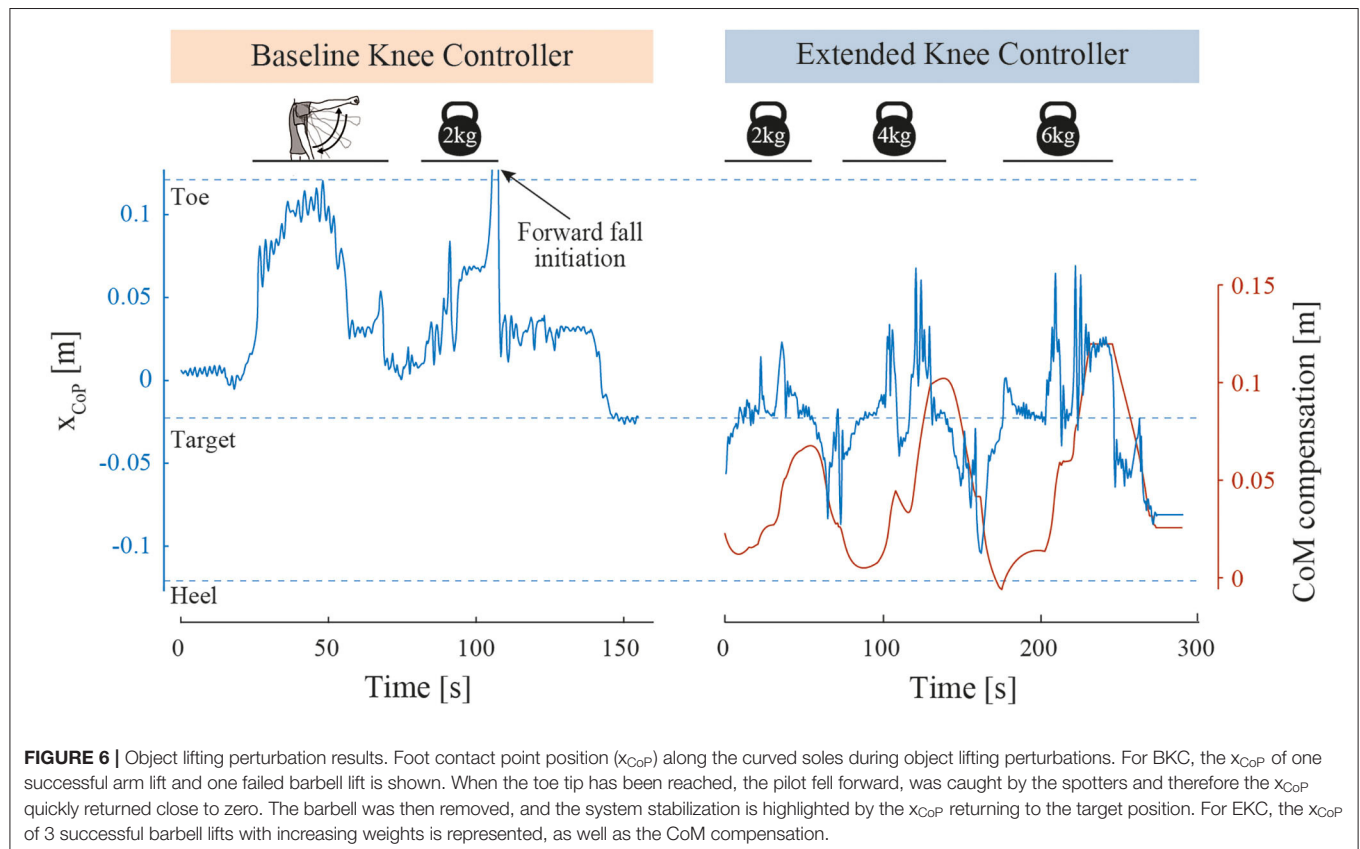
DISCUSSION

The goal of this study was to test and compare two postural controllers with a low-actuator count exoskeleton and a complete SCI pilot. Both controllers were able to manage quiet standing with almost no body sway and to cope with anterior-posterior perturbations. In that respect, postural adaptation strategies observed in healthy participants with a passive exoskeleton have been successfully transferred onto an active full-mobilization

TABLE 2 | Time required to perform raising and lowering, for the barbell test.

Condition	Raising time [s]	Lowering time [s]
BKC, 0 kg	18	19
BKC, 2 kg	4*	N/A
EKC, 2 kg	15	17
EKC, 4 kg	17	21
EKC, 6 kg	16	21

*The starred value denotes failure (fall initiation) before completion.



exoskeleton. This results in the first exoskeleton with only two degrees of freedom per leg able to balance during standing with a complete SCI user. Overall, the EKC controller was more performant, although the recovery time is slightly slower.

For pulse perturbations, EKC damps the oscillations more slowly due to its integrative behavior, and thus has higher recovery times. Moreover, the falling direction was not always the same as the perturbation direction. Since the knees can flex more than they can extend in the actual configuration, it would be possible to increase the posterior margin of stability by increasing the knee offset angle (θ_{K-off}). However, this would imply that the hip flexion angle should also be increased to remain balanced, which results in an unnatural crouch standing. This also causes more load on the interfaces and in particular the trunk belt, which was reported to be an uncomfortable posture by the test-pilot during the tuning session. Overall, since the arms do not help to support the trunk through the crutches, the upper belt of the exoskeleton maintaining the torso should be sufficient and comfortable.

For static perturbations, EKC sustained higher pushing forces thanks to the torso adjustment and repositioning of the CoM, while there was no significant difference when pulling. It is important to note that EKC could resist even higher pulling forces, just by increasing the value of the maximum flexion of the hip, and if these forces change slowly. This would however be even more difficult to recover from.

The main motivation for the curved sole is to walk by rolling the foot on the floor, to compensate for the lack of a mobile ankle joint. However, it also enables the use of these balance controllers, which could give more stability than passive balance with a flat sole of the same length. In practice, this ability was limited by the clamping on the knee and hip angles. The theoretical maximum force that the system could resist without falling in the same conditions with flat feet can be computed by the simple static equilibrium model depicted in **Figure 7**. At equilibrium:

$$\begin{aligned}\sum \tau_A &= 0 \\ \Rightarrow \frac{l_{foot}}{2} mg &= F_{eq} h_p \\ \Leftrightarrow F_{eq} &= \frac{\frac{l_{foot}}{2} mg}{h_p} = 70.2 \text{ N}\end{aligned}$$

where, τ_A is the torque at the pivot point A, l_{foot} is the length of the foot, m is the mass, g is the gravity, F_{eq} is the equivalent force applied and h_p is the height of the perturbation application. So, the EKC can resist a higher pushing force (75.07 N) than the passive balance with a flat foot (70.2 N, see equation), but this is not the case with the pulling force (27.91 N). This limitation comes from the fact the knee cannot overextend, and that the hip joint was limited to 60° of flexion.

The static perturbations assessment gives us some functional insights on how much the pilot, while standing in the exoskeleton, could pull and push an object during daily activities such as opening a door, reaching for a pack of water on a supermarket shelf or closing a car trunk. The current EKC controllers could make this kind of activities possible without the need for crutches.

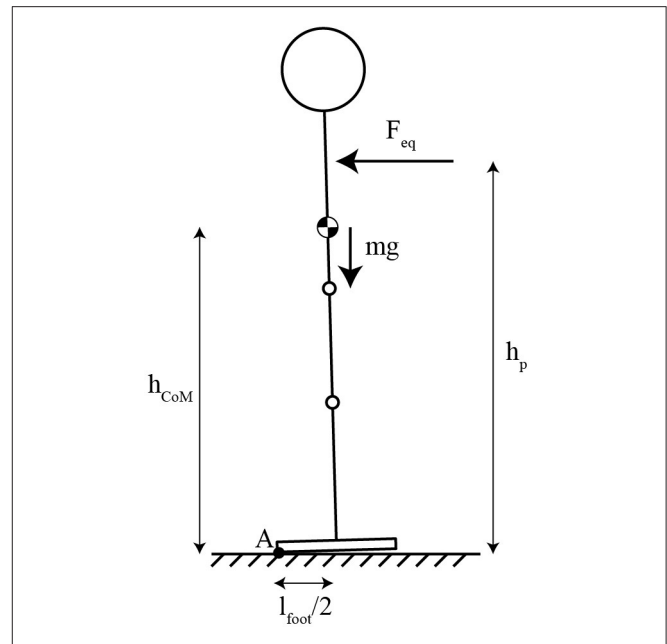


FIGURE 7 | Equivalent system for the static balance calculation with flat feet.

Another functional assessment was the object lifting task. With the EKC controller, the user is able to manipulate a heavy object far from his body, but again, this is only possible if the movements are slow, otherwise the point of contact with the ground may reach one end of the foot, and the user will start falling. Nevertheless, the EKC controller would for example enable to drink from a 1L bottle without worrying about balance management. To facilitate the user to apprehend the ability of the exoskeleton to manage balance, acoustic or haptic feedback could be given when the CoP is close to the limits, so the user could, for example, decelerate the movement. Sensory feedback, in addition to being warning signals could also promote embodiment, and thus facilitate acceptance of the device (Pazzaglia and Molinari, 2016; Beckerle et al., 2018). More extensive training with the device and the controller is necessary to further improve the performance and to apprehend the behavior the exoskeleton should follow in case of risk of fall. The main limitations of this study are that these controllers have been tested with only one test-pilot and in a controlled environment. It would be interesting to observe how the performance varies as function of the ground texture and inclination, as well as with different users.

The main limitation of EKC is that the compensator adapts slowly to a permanent disturbance. Increasing the gain G_{cc} is not possible since it leads to an oscillatory behavior. An alternative would be to reuse the three segments model and associate it to a Kalman filter. This would allow to estimate the CoM_x offset quicker without inducing increasingly large oscillations.

For an actual use with the ADLs, the safety is of the utmost importance. The major concern is that there is no stable position, so in case of failure, the user would fall and cannot use the crutches to recover. Two safety approaches could be implemented. First, following special design rules and manufacturing processes, it is possible to ensure the system keeps

operating despite a failure, which is also called fault-tolerant approach (IEC, 2011). An example of similar device using this approach is the Segway Personal Transporter (Segway Inc, United States), which has redundant sensors, control electronics, and motor windings (Segway Switzerland, 2020). Another solution is to deploy an airbag to protect the user in case a fall is detected, as suggested by a ReWalk patent (Goffer and Tivon, 2014).

CONCLUSION

A major result of this study was that postural adaptation strategies observed in healthy participants and elicited by standing in a passive exoskeleton could be ported onto an active exoskeleton with equivalent mobility. This conducted to the first full-mobilization exoskeleton able to balance during standing with only two degrees of freedom per leg. This could have important implications for the independence of individuals with paraplegia, their inclusion in social activities and their potential inclination to use an exoskeleton on a daily basis for the associated health benefits.

DATA AVAILABILITY STATEMENT

The original contributions presented in the study are included in the article, further inquiries can be directed to the corresponding author.

REFERENCES

- Baud, R., Fasola, J., Vouga, T., Ijspeert, A., and Bouri, M. (2019). "Bio-inspired standing balance controller for a full-mobilization exoskeleton." in *2019 IEEE 16th International Conference on Rehabilitation Robotics (ICORR)* (Toronto, ON), 849–854.
- Beckerle, P., Kõiva, R., Kirchner, E. A., Bekrater-Bodmann, R., Dosen, S., Christ, O., et al. (2018). Feel-good robotics: requirements on touch for embodiment in assistive robotics. *Front. Neurobot.* 12:84. doi: 10.3389/fnbot.2018.00084
- Billet, L., Delbaere, M., and Pinel, T. (2019). Compact mechatronic drive for robotic applications. *Robot. Tom.* 28. Available online at: <https://www.roboticstomorrow.com/article/2019/05/compact-mechatronic-drive-for-robotic-applications/13676>
- Donati, A. R., Shokur, S., Morya, E., Campos, D. S., Moiola, R. C., Augusto, P. B., et al. (2016). Long-term training with a brain-machine interface-based gait protocol induces partial neurological recovery in paraplegic patients. *Sci. Rep.* 6:30383. doi: 10.1038/srep30383
- Emmens, A., van Asseldonk, E., Masciullo, M., Arquilla, M., Pisotta, I., Tagliamonte, N. L., et al. (2018). "Improving the standing balance of paraplegics through the use of a wearable exoskeleton," in *2018 7th IEEE International Conference on Biomedical Robotics and Biomechatronics (Biorob)* (Enschede), 707–712.
- Fang, Y., Morse, L. R., Nguyen, N., Tsantes, N. G., and Troy, K. L. (2017). Anthropometric and biomechanical characteristics of body segments in persons with spinal cord injury. *J. Biomech.* 55, 11–17. doi: 10.1016/j.jbiomech.2017.01.036
- Farkhatdinov, I., Ebert, J., van Oort, G., Vlutters, M., van Asseldonk, E., and Burdet, E. (2019). Assisting human balance in standing with a robotic exoskeleton. *IEEE Robot. Automat. Lett.* 4, 414–21. doi: 10.1109/LRA.2018.2890671
- Fasola, J., Vouga, T., Baud, R., Bleuler, H., and Bouri, M. (2019). "Balance control strategies during standing in a locked-ankle passive exoskeleton," *2019 IEEE 16th International Conference on Rehabilitation Robotics (ICORR)* (Toronto, ON), 593–98. doi: 10.1109/ICORR.2019.8779500

ETHICS STATEMENT

Ethical review and approval was not required for the study on human participants in accordance with the local legislation and institutional requirements. The patients/participants provided their written informed consent to participate in this study.

AUTHOR CONTRIBUTIONS

JF conceived the idea and concept, designed the experiment, collected, analyzed and interpreted the data, and drafted the manuscript. RB and TV helped in conceiving the idea and concept. RB implemented the experiment, designed the controllers, participated in data acquisition, analysis and interpretation, and took part to the redaction. TV predominantly developed the two exoskeletons used in this study. AI and MB helped in drafting the manuscript and critically revising it. All authors contributed to the article and approved the submitted version.

ACKNOWLEDGMENTS

The authors wish to thank the test-pilot who volunteered to part in the experiment, as well as the company Sonceboz SA that partially funded this study.

- Goffer, A., and Tivon, K. (2014). *Airbag For Exoskeleton Device*. US20140005577A1. Available online at: <https://patents.google.com/patent/US20140005577A1/en> (accessed January 30, 2020).
- Gui, P., Tang, L., and Mukhopadhyay, S. (2015). "MEMS based IMU for tilting measurement: comparison of complementary and kalman filter based data fusion." in *2015 IEEE 10th Conference on Industrial Electronics and Applications (ICIEA)*, (Auckland: IEEE), 2004–9.
- Guiriet, T., Finet, S., Boeris, G., Duburcq, A., Hereid, A., Harib, O., et al. (2018). "Towards restoring locomotion for paraplegics: realizing dynamically stable walking on exoskeletons." in *2018 IEEE International Conference on Robotics and Automation (ICRA)*, (Brisbane, QLD: IEEE), 2804–2811.
- IEC (2011). *Functional Safety of Electrical/Electronic/Programmable Electronic Safety-Related Systems*. CEI/IEC 61508. Geneva: International Electrotechnical Commission (IEC).
- Nashner, L. M., and McCollum, G. (1985). The organization of human postural movements: a formal basis and experimental synthesis. *Behav. Brain Sci.* 8, 135–150. doi: 10.1017/S0140525X00020008
- Pazzaglia, M., and Molinari, M. (2016). The embodiment of assistive devices-from wheelchair to exoskeleton. *Phys. Life Rev.* 16, 163–75. doi: 10.1016/j.plrev.2015.11.006
- Rajasekaran, V. A. J., Casals, A., and Pons, J. L. (2015). An adaptive control strategy for postural stability using a wearable robot. *Robot. Auton. Syst.* 73, 16–23. doi: 10.1016/j.robot.2014.11.014
- Rex Bionics. (2020). *Rex Bionics - Reimagining Rehabilitation*. Rex Bionics. Available online at: <https://www.rexbionics.com/> (accessed September 26, 2019).
- Riener, R. (2016). The cybathlon promotes the development of assistive technology for people with physical disabilities. *J. NeuroEng. Rehabil.* 13:49. doi: 10.1186/s12984-016-0157-2
- Rogers, M. W., and Mille, M. L. (2018). *Balance perturbations*. *Handb. Clin. Neurol.* 159, 85–105. doi: 10.1016/B978-0-444-63916-5.00005-7
- Segway Switzerland. (2020). *Technology – SEGWAY*. Available online at: <http://www.segway.ch/en/infos/technologie.php> (accessed February 4, 2020).

- Swissethics (2018). *Lignes Directrices Dispositifs d'assistance Technique – Dispositifs Médicaux. Commissions D'éthique Suisses Relative à la Recherche sur l'être Humain (Swissethics)*. Available online at: https://swissethics.ch/assets/pos_papier_leitfaden/leitfaden_technische_assistenzsysteme_final_f.pdf (accessed June 01, 2020).
- van Asseldonk, E. H. F., Emmens, A., Brug, T. J. H., Pisotta, I., Arquilla, M., Tamburella, F., et al. (2019). "Training balance recovery in people with incomplete SCI wearing a wearable exoskeleton." in *Wearable Robotics: Challenges and Trends, Biosystems & Biorobotics*, eds M. C. Carrozza, S. Micera, and L. José Pons (Cham: Springer International Publishing), 334–338.
- Vouga, T., Baud, R., Fasola, J., Bouri, M., and Bleuler, H. (2017). "TWIICE—A lightweight lower-limb exoskeleton for complete paraplegics," in *Rehabilitation Robotics (ICORR), 2017 International Conference On*, (London: IEEE), 1639–1645.
- Winter, D. A. (1995). Human balance and posture control during standing and walking. *Gait Posture* 3, 193–214. doi: 10.1016/0966-6362(96)82849-9
- Conflict of Interest:** The authors declare that this study received funding from Sonceboz SA. The funder was not involved in the study design, collection, analysis, interpretation of data, the writing of this article or the decision to submit it for publication.

Copyright © 2020 Fasola, Baud, Vouga, Ijspeert and Bouri. This is an open-access article distributed under the terms of the Creative Commons Attribution License (CC BY). The use, distribution or reproduction in other forums is permitted, provided the original author(s) and the copyright owner(s) are credited and that the original publication in this journal is cited, in accordance with accepted academic practice. No use, distribution or reproduction is permitted which does not comply with these terms.



Effective Multi-Mode Grasping Assistance Control of a Soft Hand Exoskeleton Using Force Myography

Muhammad Raza UI Islam and Shaoping Bai*

Department of Materials and Production, Aalborg University, Aalborg, Denmark

OPEN ACCESS

Edited by:

Carlos A. Cifuentes,
Escuela Colombiana de Ingeniería
Julio Garavito, Colombia

Reviewed by:

Dongming Gan,
Purdue University, United States
Chaoyang Song,
Southern University of Science and
Technology, China

*Correspondence:

Shaoping Bai
shb@mp.aau.dk

Specialty section:

This article was submitted to
Biomedical Robotics,
a section of the journal
Frontiers in Robotics and AI

Received: 02 June 2020

Accepted: 04 September 2020

Published: 16 November 2020

Citation:

Islam MRU and Bai S (2020) Effective
Multi-Mode Grasping Assistance
Control of a Soft Hand Exoskeleton
Using Force Myography.
Front. Robot. AI 7:567491.
doi: 10.3389/frobt.2020.567491

Human intention detection is fundamental to the control of robotic devices in order to assist humans according to their needs. This paper presents a novel approach for detecting hand motion intention, i.e., rest, open, close, and grasp, and grasping force estimation using force myography (FMG). The output is further used to control a soft hand exoskeleton called an SEM Glove. In this method, two sensor bands constructed using force sensing resistor (FSR) sensors are utilized to detect hand motion states and muscle activities. Upon placing both bands on an arm, the sensors can measure normal forces caused by muscle contraction/relaxation. Afterwards, the sensor data is processed, and hand motions are identified through a threshold-based classification method. The developed method has been tested on human subjects for object-grasping tasks. The results show that the developed method can detect hand motions accurately and to provide assistance w.r.t to the task requirement.

Keywords: human intention detection, FSR sensor band, exoskeleton control, grasping assistance, soft hand exoskeletons

1. INTRODUCTION

Grasping tasks are performed repeatedly in both the home and in workplaces. Studies have shown that a human in a work/home environment performs grasp and transition between different grasps approximately 4,700 times within a 7.45 h window (Zheng et al., 2011; Bullock et al., 2013). Performing these tasks repeatedly over a longer period of time can cause fatigue and injuries. Hand exoskeletons (Gull et al., 2020) have the capability to assist in these tasks, which can reduce human effort and the risk of getting injured/fatigued.

Proper control of the exoskeleton depends mainly on accurate human intention detection. Several methods to determine human intention that are based on electromyography (EMG) (Anam et al., 2017; Meng et al., 2017; Pinzón-Arenas et al., 2019; Qi et al., 2019; Zhang et al., 2019; Asif et al., 2020) and force myography (FMG) (Islam and Bai, 2019; Xiao and Menon, 2019, 2020) have been proposed. Leonardis et al. (2015) used EMG to control a hand exoskeleton for bilateral rehabilitation. Here, a paretic hand was provided with grasping assistance by estimating the grasping force of the non-paretic hand. In another work (Lu et al., 2019), pattern-recognition-based hand exoskeleton control was proposed for spinal cord injury patients. An FMG-based hand gesture classification method was proposed to control a hand prosthetic device in Cho et al. (2016). In total, 10 hand grips were classified using a linear discriminant analysis technique. A high-density force myography-based hand and wrist gesture classification approach was proposed by Radmand et al. (2016). It was shown that for static hand postures 0.33% RMSE is achieved. While variation in upper limb position reduces the accuracy, better performance can be achieved by introducing

limb position variation in training protocol. Several other works on force estimation and pattern-recognition-based hand exoskeleton control have also been reported (Wege and Zimmermann, 2007; Rasouli et al., 2016; Ferigo et al., 2017; Secciani et al., 2019; Arteaga et al., 2020).

In all of the reported works, methods to control a hand exoskeleton are limited to either pattern recognition or force estimation. Furthermore, in these methods machine learning and deep learning techniques are used that requires large training datasets to achieve good classification/estimation accuracy.

In this work we develop a new sensing method for both pattern recognition and force estimation using FMG. A multi-mode task detection approach, i.e., motion classification and grasp force estimation, is proposed for controlling a hand exoskeleton. In this method, four hand motion states are classified i.e., rest, open, close, and grasp. The classification algorithm is based on threshold approach and requires a small training dataset. Once the grasp is detected, the control mode is switched to grasp assistance. This is achieved by virtue of two sensor bands built with FSRs, which can detect muscle activities conveniently and effectively. In terms of its sensing method, FMG has exhibited a better performance than EMG in classification and estimation tasks considering accuracy, repeatability, and cost (Ravindra and Castellini, 2014; Jiang et al., 2017). Moreover, unlike EMG, FMG is not affected by skin conditions and has a simple electronics interface.

This paper is organized as follows. The design and implementation of the sensor band and exoskeleton control strategy are described in section 2. Section 3 presents the data processing and algorithm design for grasp detection and assistance. Experimental setup and testing results are described in section 4. Discussion on the developed method is presented in section 5. The work is concluded in section 6.

2. MATERIALS AND METHODS

In this section, a methodology to detect hand motions i.e., rest, open, close, and grasp is described. Sensor bands, a hand exoskeleton, and control methods are also presented.

2.1. Methodology

In this work, four hand motion states are classified, i.e., rest, open, close, and grasp. The last three motion states are classified as dynamic states, whereas rest is identified as a static hand state in any posture, e.g., keeping the hand fully opened/closed or holding an object in a fixed posture.

In object grasping, fingers have to be flexed. During flexion, the muscle belly shortens in length and contracts toward the side of the elbow joint, which is referred as isotonic muscle contraction. As the object comes into contact with the hand, muscle shortening stops, and an isometric contraction state is initiated. In this state the muscle belly along the forearm contracts as long as the force applied to hold an object reaches the steady state.

In this work contraction states and the transition between them, i.e., isotonic and isometric, are measured through FMG, using sensor bands built with FSR sensors. In this method,

normal forces caused by muscle contraction and applied to the sensor band, hereafter called muscle contraction-induced (MCI) force, are measured. Flexor digitorum profundus and flexor digitorum superficialis are the prime muscles that govern fingers flexion to close the hand. During hand closing movement, the length of these muscle shortens and they contract toward elbow joint. MCI force near the elbow will therefore increase, while it will decrease near the wrist joint. As soon as the object is grasped, muscles stop shortening and isometric contraction takes over. In this case, MCI forces over the muscle belly will increase. This principle can be expanded further to explain hand opening task. In hand opening the object is ungrasped, MCI force on both ends of the forearm will decrease. On the other hand, as the object is released and the fingers are further extended, MCI force measured near the elbow will decrease, while the force measured near wrist will increase. From these changes of MCI force, hand motion states can be determined with certain algorithms.

2.2. Sensor Band

The aforementioned hand motion detection relies on an effective and convenient method to detect MCI forces. To this end, two sensor bands are constructed at Aalborg University exoskeleton lab, as shown in **Figure 1A**.

The sensor bands are designed to be placed on the forearm, as shown in **Figure 1B**. One is placed near the elbow joint. This band, referred to as SB_e , is comprised of eight FSR sensors. The other band is placed near wrist joint, referred to as SB_w , which has an array of four FSR sensors embedded. The placements of FSR sensors inside the sensor bands are shown in **Figure 1A**. All FSR sensors are FSR-402, developed by Interlink electronics, and have the capability of measuring 0.1–10 N. More information on the construction of sensor bands can be found in Islam and Bai (2019).

2.3. SEM Glove

In this work a soft hand exoskeleton SEM Glove (Nilsson et al., 2012; Hashida et al., 2019) is used to provide physical grasping assistance, as shown in **Figure 1B**. The SEM Glove is equipped with FSR sensors placed at the middle and index fingertips and at the thumb. The assistance provided by the exoskeleton can be measured by these sensors. Moreover, in the SEM Glove's own control unit, the assistance level is also controlled using the same sensor data. The tighter the object is grasped the higher the assistance level will be. In this work, the assistance level provided by SEM Glove is controlled through MCI force measured by the sensor band placed near elbow joint instead of using the SEM Glove's own sensors.

2.4. Sensing Data

The sensor bands allow us to collect hand motion data effectively. An example of a dataset of rest, open, close, and grasp, labeled as "R," "O," "C," and "G," respectively, is shown in **Figure 2**. Isotonic contraction during opening and closing of hand can be seen in **Figure 2A**. **Figure 2B** shows the data of an object being grasped

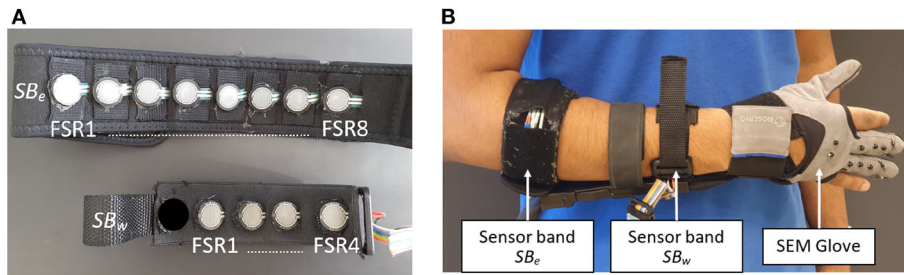


FIGURE 1 | (A) FSR sensors placement inside sensor bands SB_w and SB_e and **(B)** SEM Glove and sensor bands placement on forearm.

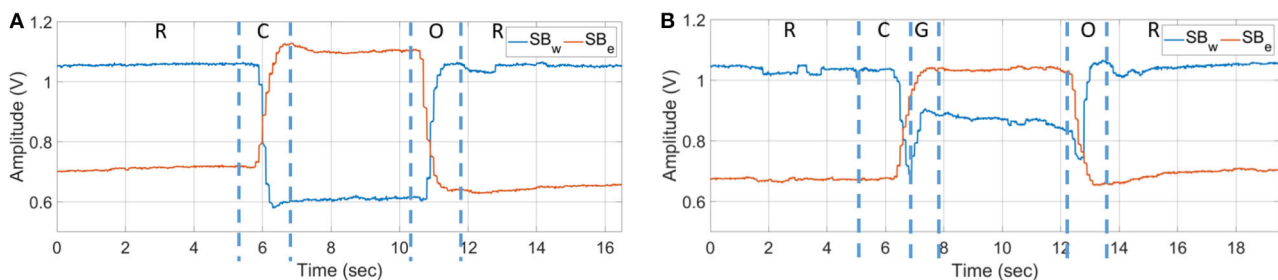


FIGURE 2 | Net output voltage measured from sensor bands for opening and closing of hand **(A)** without grasping and **(B)** grasping an object.

when isometric contraction occurs. The state when the object is grasped is labeled as “G.”

In the hand opening task, shown in **Figure 2B**, it can be seen the sensor amplitude first goes down. This muscle activity represents loosening of grip on the object. Afterwards, increase in muscle activity at SB_w and decrease in muscle activity at SB_e are observed, which represents fingers extension to open the hand. In the implementation phase, loosening of grip is treated as a steady state.

2.5. Multi-Mode Control

In this work, a multi-mode control approach is used to assist in grasping, which is shown in **Figure 3**.

The control strategy is divided into two stages i.e., motion classification and grasp force assistance. Motion classification is based on a threshold approach. Out of four actions, i.e., rest, open, close, and grasp, once the algorithm identifies grasp action, the control mode is shifted to grasp force assistance. In this mode a proportional control is implemented, where the assistance force is determined using MCI force measured through SB_e .

3. DATA PROCESSING

3.1. Sensor Calibration

The FSR sensors in the two sensor bands are interfaced with a non-inverting amplifier. The output voltage of the amplifier is thus given by the following equation:

$$V_{out} = \left(1 + \frac{R_{ref}}{R_{fsr}}\right) V_{in} \quad (1)$$

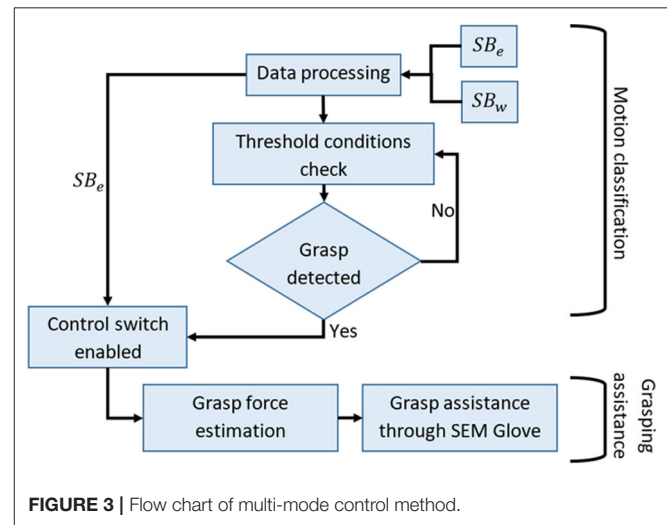


FIGURE 3 | Flow chart of multi-mode control method.

Here, V_{out} is the output voltage of the amplifier, V_{in} is the input voltage applied to positive terminal of the amplifier, R_{ref} is the reference resistance, and R_{fsr} represents the FSR resistance, which varies with force applied on it.

With the amplifier designed, it is possible to change the range of force measured by FSR. This is done either by changing the reference resistance R_{ref} or input voltage V_{in} . In our design, the reference resistance is fixed to 100 kohm. We therefore adjust the input voltage V_{in} through a DAC port from micro-controller for this purpose, which is a task of sensor calibration.



FIGURE 4 | Gestures used in calibration and training stage. (A) open hand gesture to calibrate SB_w , (B) close hand gesture to calibrate SB_e , and (C) rest state gesture to collect data for threshold determination.

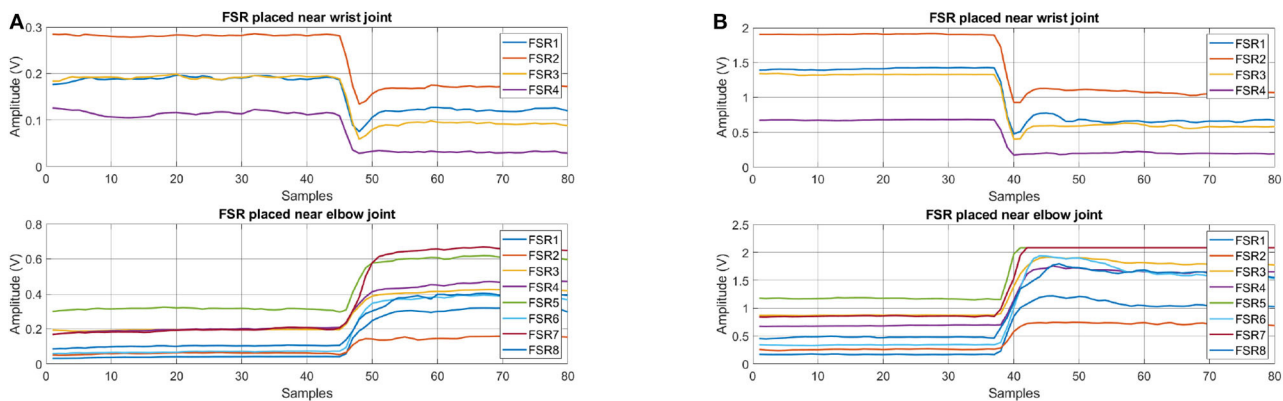


FIGURE 5 | FSR data for hand closing gesture (A) before and (B) after calibration.

In the calibration stage, input voltage V_{in} is adjusted so that at least three of the FSR sensors from both SB_e and SB_w have reached the maximum voltage limit. In this way, the sensor bands can have high resolution in all detections.

During calibration of SB_w , the subject is asked to keep the hand open, as shown in **Figure 4A**. This posture initiates the calibration procedure. An automated program checks the sensors outputs above threshold level. If the number is less than three, input voltage V_{in} is increased gradually until the condition is fulfilled, i.e., at least three sensors are above threshold limit. Similar procedure is followed for the calibration of SB_e but for the close hand gesture, as shown in **Figure 4B**, to complete the calibration. In the current setup it is set to 1.5 V.

An example dataset of the calibration stage is shown in **Figure 5**. This dataset represents the task of hand closing from fully opened state. **Figure 5A** is the dataset collected before calibration and **Figure 5B** is the dataset collected after calibration.

The improvement in signal resolution, ν , is computed by taking the ratio of change in signal amplitude, from open to close hand gesture, to the standard deviation of signal value during the steady state condition. Mathematically it is given as,

$$\nu = \frac{|\mu(V_O) - \mu(V_C)|}{\max(\sigma(V_O), \sigma(V_C))} \quad (2)$$

Here, V_O and V_C represent the net voltage measured from the sensor bands for open hand and close hand gestures respectively,

TABLE 1 | Resolution measured before and after calibration.

Sensor band	Resolution ν		% increase
	Without calibration	With calibration	
SB_w	27.88	60.13	221
SB_e	27.94	61.74	222

and μ and σ are the mean and standard deviation respectively. The results obtained through aforementioned equation are provided in **Table 1**. The results clearly show that the resolution of both sensor bands is increased significantly, more than two times, after calibration.

3.2. Features Selection

While grasping an object, sensor readings highly depend on the shape and weight of the object. Moreover, donning and doffing of the sensor band also affects the sensor response. Developing a threshold- or machine-learning-based task-detection algorithm will require a large amount of data if the signal amplitude or its RMS value is used as the input feature. It is noted that when a user takes off the sensor band and puts it back on, it is desirable that the sensor band has to be placed exactly at the same place and with the same tightness, but this is very challenging. All these factors will affect the classification performance.

With experiments, it is observed that the feature that gives consistent results with less deviation is slope. This feature

represents the change in signal amplitude w.r.t time. An example dataset of grasping different shape and weight objects is shown in **Figure 6**. A grasping dataset for each object is represented in 3s windows. From time 0 to 3, 3 to 6, and 6 to 9 s objects A, B, and C are grasped sequentially, as shown in **Figure 8**. From 9 to 18 s a dumbbell bar is grasped three times with different weight hanged on the sides of it. The weights of the dumbbells, applied from $t = 9$ to 12, 12 to 15, and 15 to 18 s were 1.2, 2.3, and 3.4 kg, respectively. Data sessions from 0 to 9 and from 9 to 18 s were recorded separately. It can be seen from **Figure 6A** that there is big variation in FSR reading, as it depends on the shape and weight of the object. However, if we look at the slope feature in **Figure 6B**, a similar pattern but with different peaks can be observed. Initially, fingers are flexed therefore we see opposite slopes for the FSR sensors placed near elbow and wrist joint. As soon as an object is grasped, positive slopes for both sensor bands are observed. By carefully selecting the threshold value, grasp action can be detected very effectively. In this work we therefore selected slope feature for detection of hand motion.

3.3. Features Extraction

Two features are extracted from raw sensor data, i.e., root mean square (RMS) and slopes. RMS from raw sensor data is obtained using a 150 ms window in which 100 ms is non-overlapping and 50 ms is overlapping from previous window. After calculating RMS values for each FSR sensor, slopes are obtained using the following equation:

$$\kappa = \frac{R^i - R^{i-1}}{t_{ws}} \quad (3)$$

Here, κ represents the slope feature, R^i represents the newest sample of RMS data, and t_{ws} is the window time to extract features.

3.4. Threshold Determination

In this method each state, i.e., rest, open, close, and grasp, is identified using a threshold-based classification approach. To determine the threshold limits, subject is asked to hold rest state, as shown in **Figure 4C**, for 5 s. Raw data obtained in this task is post processed to obtain slopes, which are further used to determine threshold limits.

After the computation of slope feature, the minimum and maximum slope value for each FSR was computed:

$$\xi_w^{max} = \max(\Delta_w), \quad \xi_w^{min} = \min(\Delta_w) \quad (4)$$

$$\xi_e^{max} = \max(\Delta_e), \quad \xi_e^{min} = \min(\Delta_e) \quad (5)$$

with

$$\Delta_w = [\kappa_w^1 \dots \kappa_w^N], \quad \Delta_e = [\kappa_e^1 \dots \kappa_e^M] \quad (6)$$

Here, N and M are the numbers of FSR sensors embedded inside the sensor bands SB_w and SB_e , respectively. ξ_w^{min} and ξ_w^{max} are row matrices of order $1 \times N$ and contain minimum and maximum slope values of SB_w sensor band data computed for rest state. ξ_e^{min} and ξ_e^{max} are also row matrices of order $1 \times M$ and contain

minimum and maximum slope values of SB_e sensor band data. Δ_w is a $1 \times N$ matrix, where 1 is the number of slope feature samples computed from rest gesture data, and Δ_e is also a matrix but of $1 \times M$ dimension.

Using (4) and (5), threshold conditions to detect each task are given as

$$H_R = \Delta_w^r \leq \kappa_w^{max} \& \Delta_e^r \leq \kappa_e^{max} \quad (7)$$

$$H_O = \Delta_w^r > \kappa_w^{max} \& \Delta_e^r < \kappa_e^{min} \quad (8)$$

$$H_C = \Delta_w^r < \kappa_w^{min} \& \Delta_e^r > \kappa_e^{max} \quad (9)$$

$$H_G = \Delta_w^r > \kappa_w^{max} \& \Delta_e^r > \kappa_e^{max} \quad (10)$$

Here, H_R , H_O , H_C , and H_G are the thresholds for rest, open, close, and grasp task detection. Δ_w^r and Δ_e^r are row matrices that are computed during real-time testing. The information in these matrices is in same order as in Δ_w and Δ_e .

3.5. Grasp Force Estimation

During the motion classification stage, if grasp action is detected, the control method is switched to grasp assistance. In this mode, we need to determine and control the grasp assistance provided by the SEM Glove. In this work, it is determined using the following equation:

$$u = (SB_e^{rms} - LB_e)K \quad (11)$$

Here, u is the control input relayed to the SEM Glove, K is the proportional gain and SB_e^{rms} is the net FSR output measured from the sensor band SB_e . LB_e is the net FSR output measured at the time of grasp detection and is given by following equation:

$$LB_e = \text{mean}(R_e^i, R_e^{i-1}) \quad (12)$$

Here, i is the sample when grasp action was detected, and $i - 1$ represents the sample before.

3.6. Performance Analysis

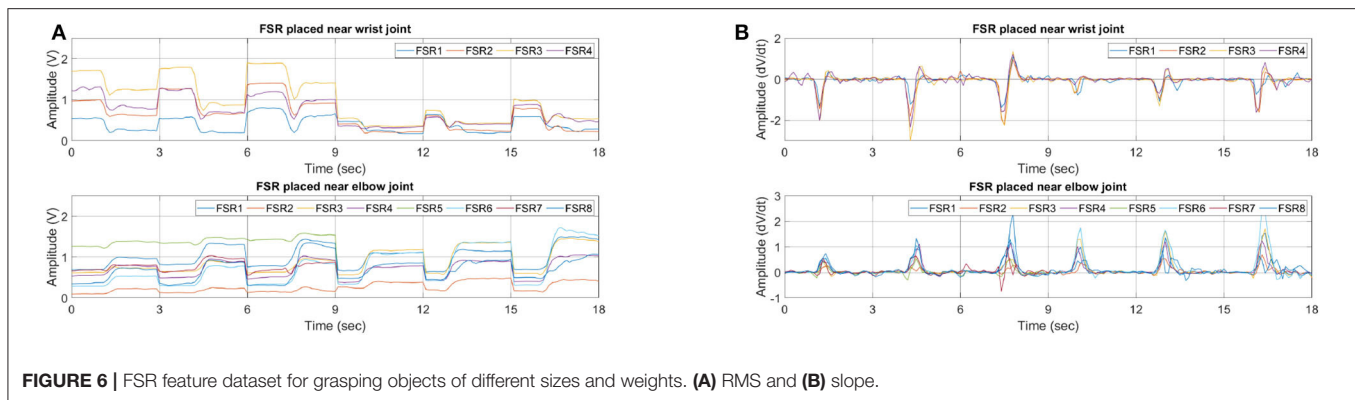
The performance of the task detection technique is analyzed with a group of four parameters, namely, precision, recall, F1-score, and accuracy (Powers, 2011). Mathematically, these parameters are calculated by

$$P_{pre} = \frac{N_{TP}}{N_{TP} + N_{FP}} \quad (13)$$

$$P_{rec} = \frac{N_{TP}}{N_{TP} + N_{FN}} \quad (14)$$

$$P_{F1} = 2 \cdot \frac{P_{pre} \cdot P_{rec}}{P_{pre} + P_{rec}} \quad (15)$$

$$P_{acc} = \frac{N_{TP} + N_{TN}}{N_{TP} + N_{TN} + N_{FP} + N_{FN}} \quad (16)$$



Predicted \ Actual	Class A	Other
	Class A	Other
Class A	TP	FP
Other	FN	TN

FIGURE 7 | Classification of TP, TN, FP, and FN samples.

Here, N_{TP} , N_{TN} , N_{FP} , and N_{FN} represent number of samples that are true positive, true negative, false positive, and false negative, respectively, as illustrated in **Figure 7**. P_{pre} , P_{rec} , P_{F1} , and P_{acc} are the performance measures that represents precision, recall, F1-score, and accuracy, respectively. Of these measures, precision, recall, and F1-score are defined in the range of 0–1, whereas, accuracy is expressed in percentage.

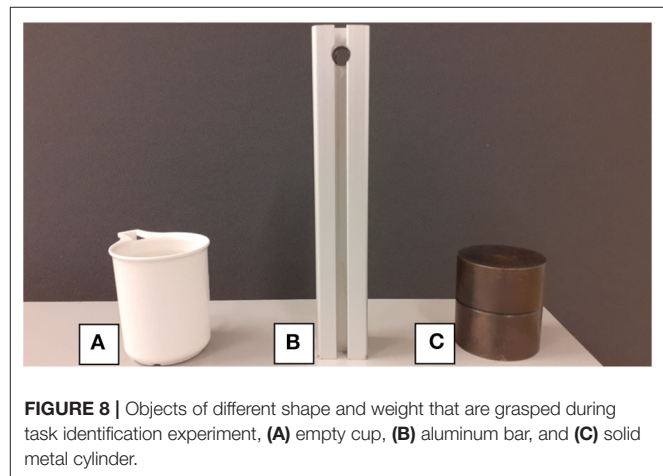
Using these four parameters we can evaluate the classification performance comprehensively and in an unbiased manner. From mathematical representations, we can see that the fundamental difference between accuracy and other parameters is TN samples. In our designed experiment the number of samples in each class is not consistent. In such cases precision and recall can also provide very useful insight into classification performance. Taking the example of rest task, precision calculates from the total number of samples that are classified as rest how many were actually rest. Meanwhile, recall calculates, from the number of times a user was instructed to keep rest state, how many samples were correctly identified as rest state. Finally, the F1-score tells the balance between precision and recall.

4. EXPERIMENTS AND RESULTS

With the developed method, three experiments are performed, i.e., task identification, influence of sensor placement, and grasping assistance. Details and results of each task are provided in forthcoming sections.

4.1. Task Identification

Six subjects participated in this experiment. All of them were healthy, right-handed, and aged between 25 and 35 years. Ethical



approval for these experiments was obtained from an ethical committee, Region Nordjylland, Denmark.

In this experiment, performance measures, i.e., precision, recall, F1-score, and accuracy, are computed to evaluate the classification performance. For this purpose, an experiment was designed where a subject performs hand opening and closing, first without any object and afterwards with three objects, as shown in **Figure 8**, of different attributes.

The protocol of the experiment is as follows: the subject is instructed to sit in a chair with their hands resting on the table beside the objects. The first task the subject performs is calibration, as explained in section 3.1, which is followed by a rest state gesture, as shown in **Figure 4C**, which is held for 5 s to determine the threshold limits. Afterwards, real-time testing tasks are performed in which, for open and close tasks, the subject lifts his/her hand from the table and keeps it in open state, as shown in **Figure 4A**. The subject closes his/her hand when the instruction is shown on the screen and opens it up when the instruction to open is shown on the screen again. The subject is instructed that an open hand posture should be maintained throughout the experiment. For the grasp task, hand is lifted from the table and kept open, as shown in **Figure 4A**. When the grasp instruction is shown on the screen, subject grasps the

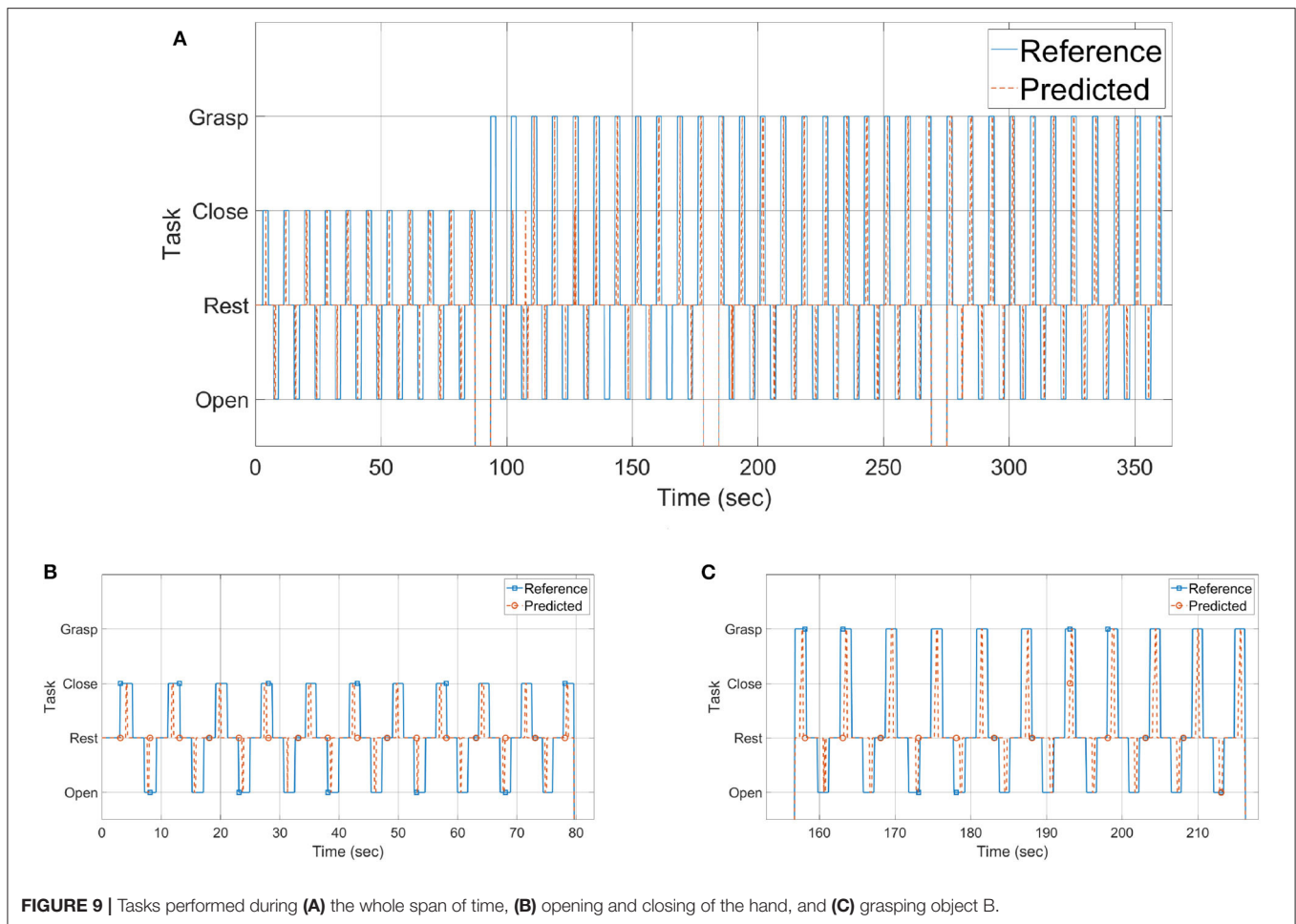


FIGURE 9 | Tasks performed during (A) the whole span of time, (B) opening and closing of the hand, and (C) grasping object B.

object and slightly lifts it from the table with a small clearance of approximately 1.0 cm.

The results of the experiment are shown in **Figures 9–12** and summarized in **Table 2**. **Figure 9** shows the experimental results for one of the subjects. **Figure 9A** shows the reference and predicted tasks. In the first 80 s of the experiment, the subject is instructed to perform the rest, open, and close tasks. From $t = 80$ to 155, $t = 155$ to 220, and $t = 220$ to 285 s, the subject is instructed to grasp objects A, B, and C sequentially. In this figure, the solid blue line shows the task to be performed and the dotted red line the result predicted by a classifier when a subject performs that particular task. A zoomed-in view of open and close tasks is shown in **Figure 9B** and of grasping task for object B is shown in **Figure 9C**.

Single instances of abovementioned tasks are shown in **Figure 10**. **Figure 10A** is the result of an open and close task. The results show that, initially, the hand was in the close state; as the subject opens the hand, a drop in signal amplitude near the elbow and an increase in signal amplitude near the wrist joint is observed. The classifier is able to detect that the hand is opened as the movement is performed. Afterwards, when the hand is closed, the inverse muscle activity pattern can be seen, and, as

the movement is performed, the classifier is again able to detect that the hand is closed.

The instances of grasping object A, B, and C are shown in **Figures 10B–D**, respectively. Data is presented in the same order as represented for **Figure 10A**. Initially, the subject is holding the object. As the hand is opened, it is seen from the FSR readings that their associated muscle contraction near the wrist increases, and contraction near elbow is decreased. From the opened hand state when the subject is instructed to grasp the object, it can be seen that classifier first detects that the hand is closing. It can also be seen from the FSR readings that it is increasing near the elbow and decreasing near the wrist, indicating hand closing. As the object is grasped, an increase in readings on both sensor bands is seen, and the classifier correctly detects that an object is being grasped. These results show that the threshold-based classifier is able to distinguish between all four motion states, i.e., rest/steady, open, close, and grasp, accurately.

Results in terms of precision, recall, F1-score, and accuracy are shown in **Figures 11, 12** and **Table 2**. In the figures, the error bar represents the performance deviation within the tasks, i.e., rest, open, close, and grasp.

The average performance values w.r.t each task are shown in **Figure 12**. Considering the rest state, it can be seen that

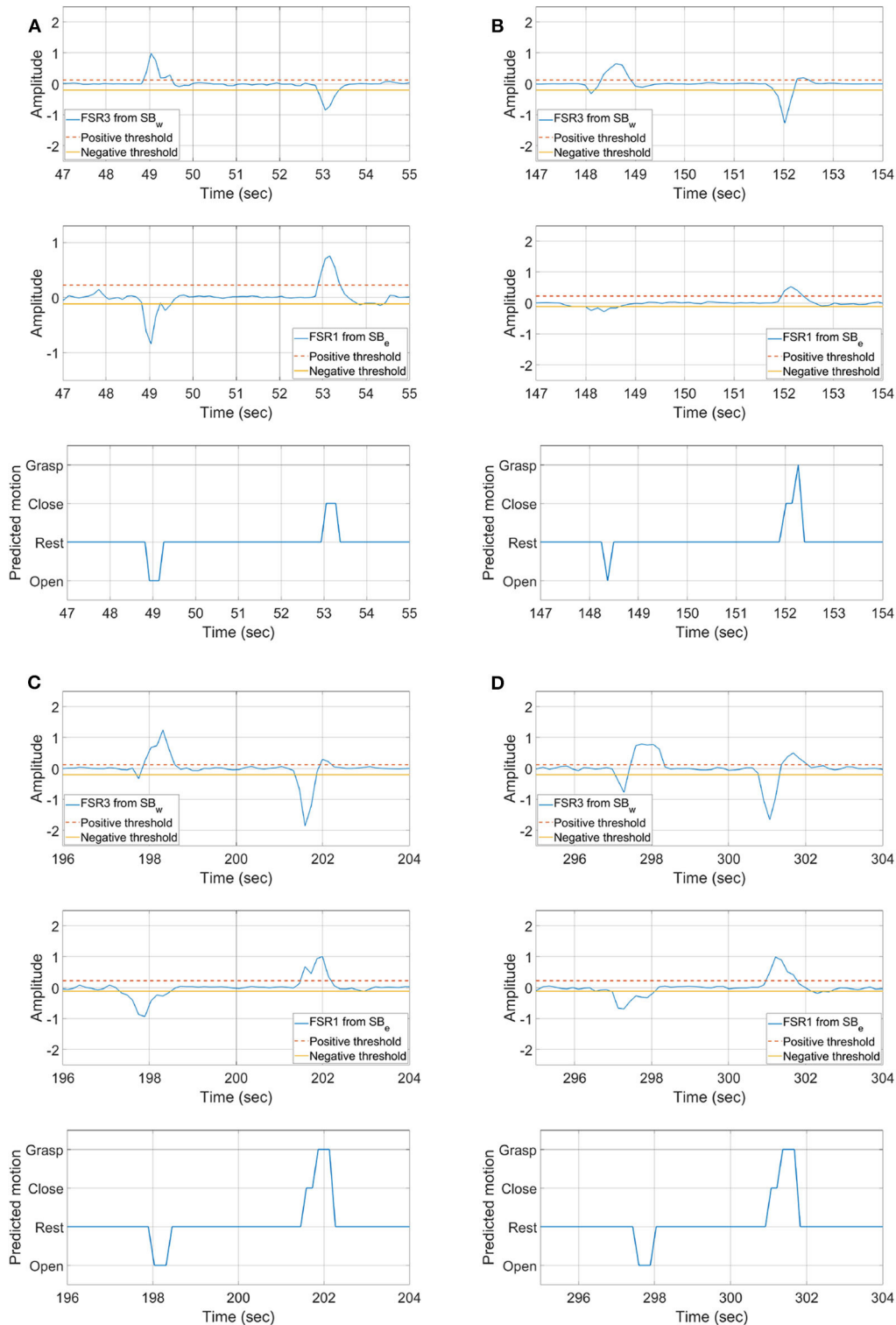
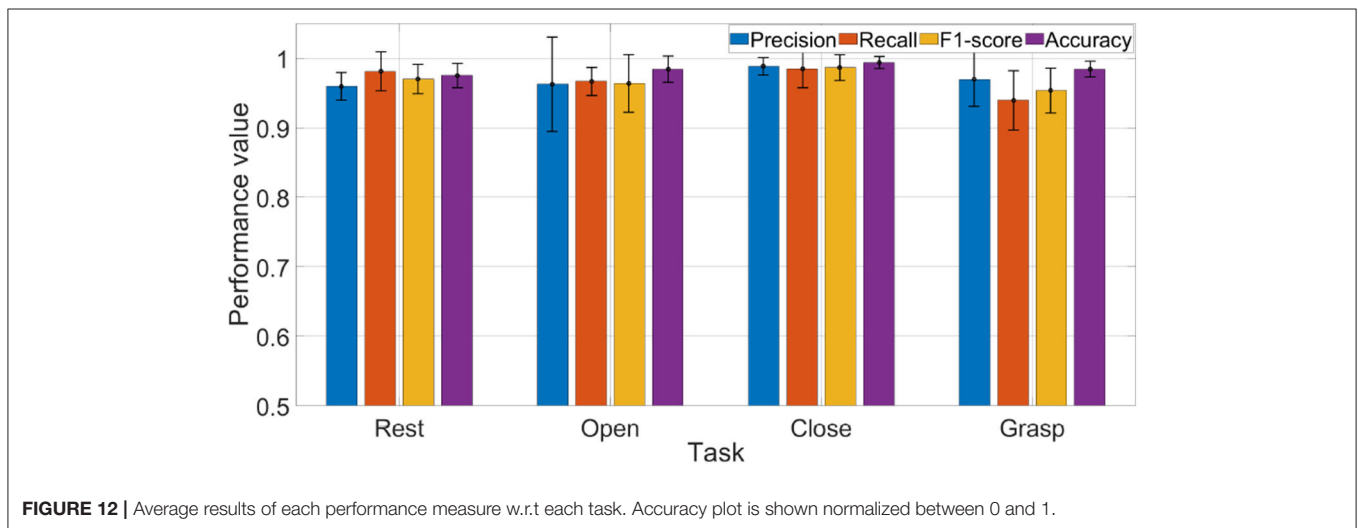
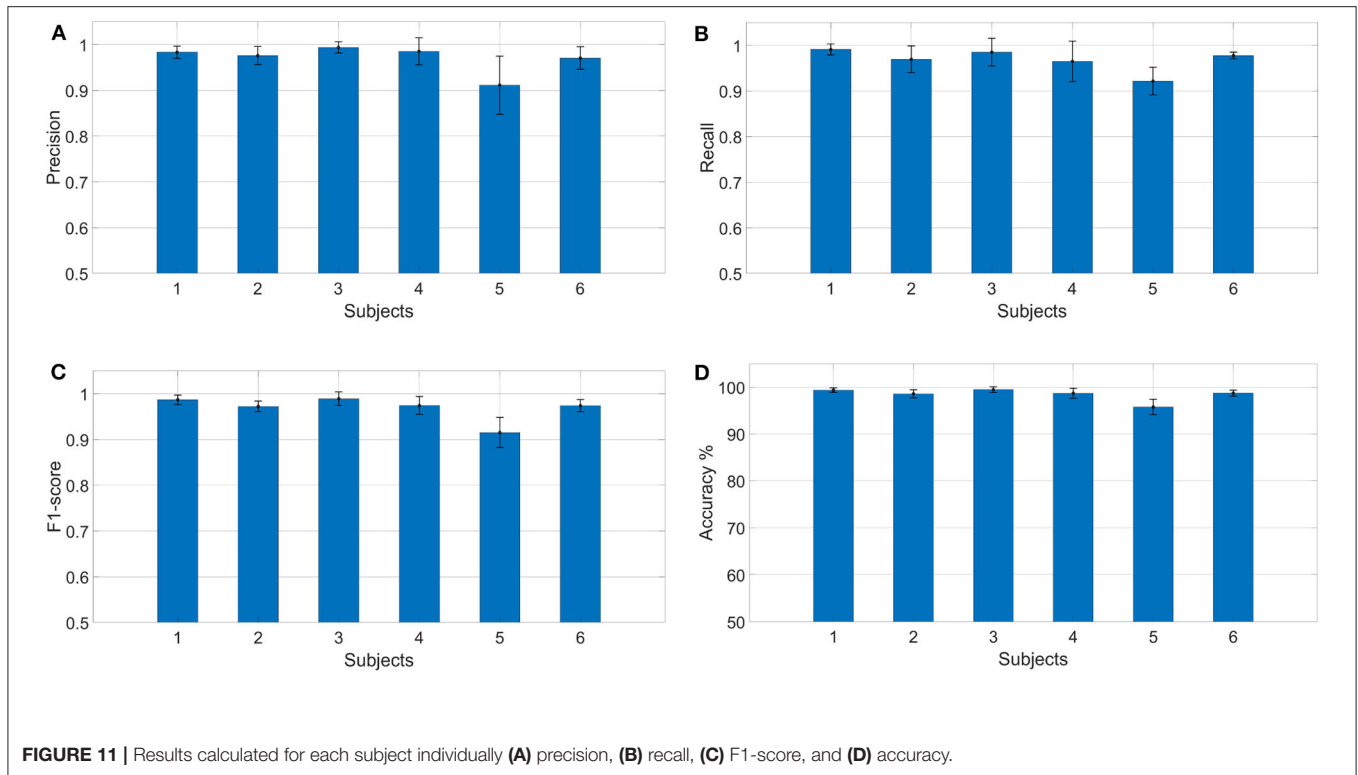


FIGURE 10 | Results of single instances (A) open/close, grasping objects (B) A, (C) B, and (D) C, shown in Figure 8.

average recall value is 0.98, which reveals that only 2% of the rest states were not detected. It is to be noted that rest state was held in all postures, i.e., open hand, close hand, and grasp.

In the context of real-time operation, this result is very critical. Any miss-classification can cause undesirable movement/action, especially if subject is holding an object. The results show that the



algorithm is highly accurate in detecting the rest state. Precision for detecting rest state is equal to 0.96, which shows that in only few cases where subject was performing another task (open, close, or grasp), classifier detected it as rest state.

For open and close tasks, it can be seen that recall and precision scores are very similar. For grasp, we can see that precision (0.97) is higher than recall (0.94). From precision, we can deduce that, of all the tasks that were classified as grasp, only 3% of them were miss-classifications. Meanwhile, the recall result tells us that 6% of the times when a subject grasped an object, the classifier did not detect it as grasp. To improve precision, the threshold level should be raised, but this

will affect the performance of recall. Raising the threshold will have the opposite impact on other performances. It will improve the recall but might reduce the precision. With the current setup, classification performance of the algorithm depends on the trade-off between recall and precision. Depending on the applications, threshold levels can be tuned to get better results. The performance can be improved by incorporating more FSR sensors or by using more features for threshold determination.

4.2. Influence of Sensor Placement

In this experiment, the effect of sensor placement on motion detection is studied. To achieve this objective

sensor bands are placed over the forearm in three different orientations/placements, as shown in **Figure 13**. In placement A, FSR1 from sensor bands SB_e and SB_w is aligned with brachioradialis and near insertion of brachioradialis. In placement B, it is aligned with brachioradialis and flexor carpi ulnaris muscles. Finally, in placement C, it is aligned with palmaris longus and near the insertion of brachioradialis.

Tasks performed for each placement of sensor bands are as follows:

- Open and close of hand without grasping any object
- Grasping object C as shown in **Figure 8**.

Each task is performed 10 times under same conditions as explained in section 4.1. The results of each experiment are shown in **Figure 14**, where **Figures 14A–C** are the results of placement A, B, and C, respectively, by sensor band orientation. In each sub-figure of **Figure 14**, the first figure is the FSR sensors data from the sensor band placed near the wrist, and the second is the data of FSR sensors placed near the elbow, and the third figure displays the reference and predicted tasks.

Even though the raw data is not similar for each sensor placement, the developed method is able to detect all four hand gestures accurately. The performance of task detection is less affected. As seen from predicted results, rest state, hand opening, closing, and grasping achieved the average accuracies of 98.15, 99.24, 100, and 98.16% for all three placements.

4.3. Grasping Assistance

In this work, grasping assistance is provided using SEM Glove where the desired assistance level is regulated by implementing a proportional control scheme. The block

diagram of the control scheme is shown in **Figure 15**. Referring to Equation (11), the input of the proportional control is the average MCI force measured by the sensor band placed near the elbow, and the output u is then relayed to the exoskeleton. Moreover, grasping assistance provided by SEM Glove is further validated by measuring the grasping force through force sensors embedded inside SEM Glove exoskeleton.

In this experiment the sensor bands are worn on right forearm and exoskeleton is worn on the left hand. Furthermore, three different payloads, i.e., 1.2, 2.3, and 3.4 kg, applied from $t = 0$ to 20, $t = 20$ to 40, and $t = 40$ to 60 s, respectively, are being grasped for three times each. The results of the experiment are shown in **Figure 16**.

Figure 16A shows the task predicted by the classifier. Net MCI force measured by the SB_e sensor band is shown in **Figure 16B**. The resulting grasping force measured from SEM Glove sensors is shown in **Figure 16C**. Whereas, the single instance of grasp task is shown in **Figure 17**. With the detection of a grasping task and MCI force, assistance is provided by the exoskeleton, which is evident from the sensor reading of the SEM Glove.

If we look closely at **Figures 16B,C**, we can see that the MCI forces are increasing with the payload grasped by the subject. It is also seen that the forces read by the sensors placed at the middle finger and thumb are increasing with the payload. These are the grasping forces that are caused by the physical interaction between fingertips and the object. When assistance provided by the exoskeleton is increased, the exoskeleton will help to grasp the object tightly and in turn grasping force measured the sensors, placed in finger tips, will increase. This validates that with the increase in MCI force, shown in **Figure 16B**, exoskeleton is able to provide the grasping assistance accordingly.

TABLE 2 | Average results of performance measures calculated for each subject.

Performance measures	Precision	Recall	F1-score	Accuracy %
Subject 1	0.98 ± 0.013	0.99 ± 0.012	0.99 ± 0.010	99 ± 0.5
Subject 2	0.98 ± 0.019	0.97 ± 0.029	0.97 ± 0.011	99 ± 0.9
Subject 3	0.99 ± 0.012	0.98 ± 0.030	0.99 ± 0.014	99 ± 0.6
Subject 4	0.99 ± 0.029	0.96 ± 0.044	0.97 ± 0.019	99 ± 1.0
Subject 5	0.91 ± 0.063	0.92 ± 0.030	0.92 ± 0.032	96 ± 1.6
Subject 6	0.97 ± 0.024	0.98 ± 0.007	0.97 ± 0.013	99 ± 0.7
Average	0.97 ± 0.029	0.97 ± 0.024	0.97 ± 0.027	98 ± 1.3

5. DISCUSSION

In this work a novel method is developed for hand motion detection and for the provision of assistance in carrying out an object grasping task. We also addressed the challenge of data collection for training and proposed an alternative solution for it.

The new method is advantageous in reducing the complexity and increasing the usability of the system for a longer period. In an AI-based pattern recognition method, obtaining a correct



FIGURE 13 | Three placements of sensor bands, **(A)** two FSR1 from SB_e and SB_w are aligned with brachioradialis and near insertion of brachioradialis, **(B)** aligned with brachioradialis and flexor carpi ulnaris, **(C)** aligned with palmaris longus and near insertion of brachioradialis.

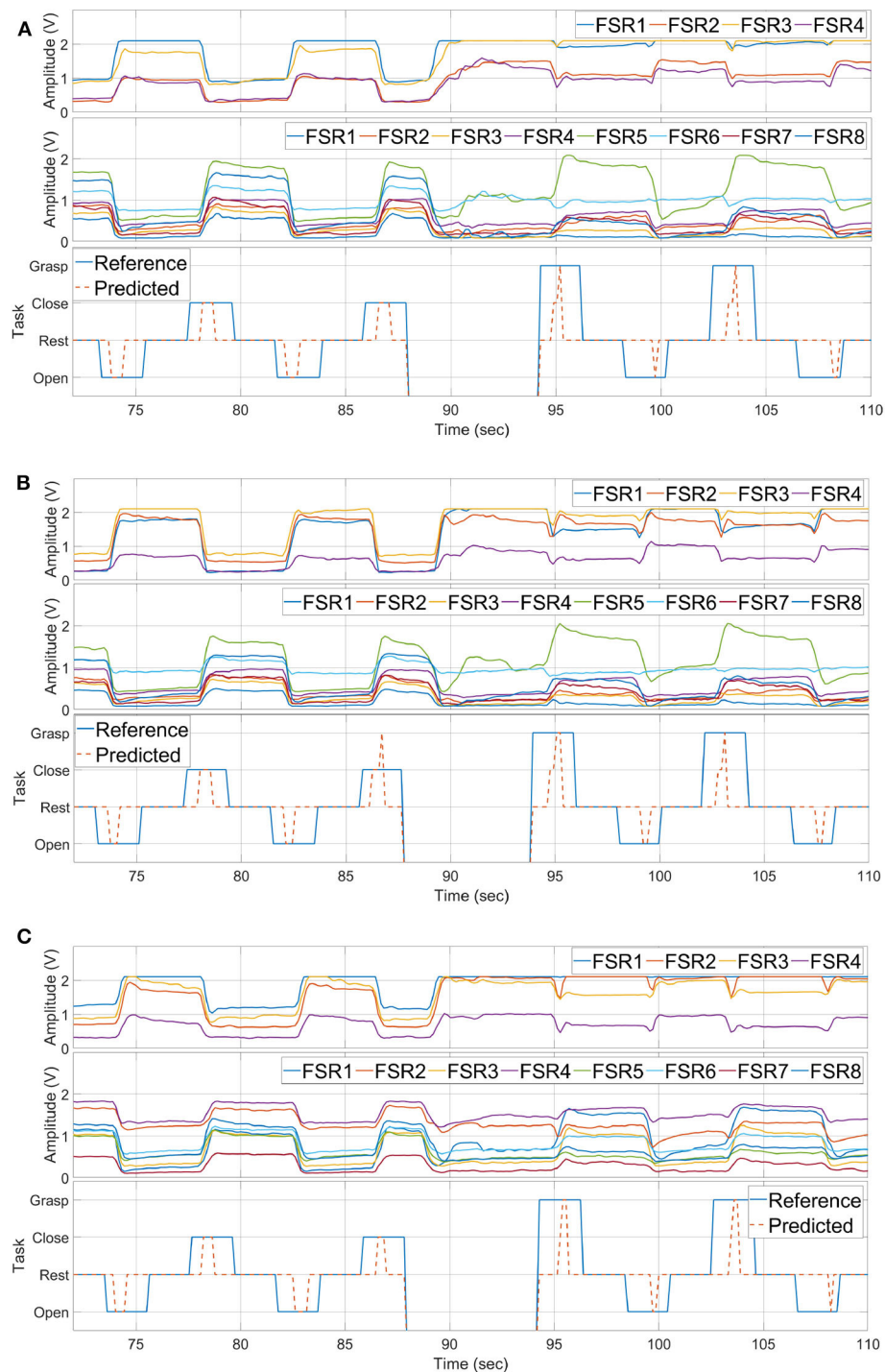


FIGURE 14 | Hand motion detection with three placements of the sensor bands, **(A)** with placement A, **(B)** with placement B, **(C)** with placement C.

and sufficient training dataset is one of the major challenges. Moreover, even if the training data is obtained correctly there still exists another challenge of reusing it from time to time. The reason is due to the placement of sensor at the exact location and change in muscle activity levels. The method proposed in this

work effectively addresses these challenges. The method requires sensor calibration and rest state data of the hand. Afterwards, the system can detect the hand motions based on change in activity level. Additionally, the requirement on placing sensor band at exact location is mitigated. Moreover, the calibration procedure

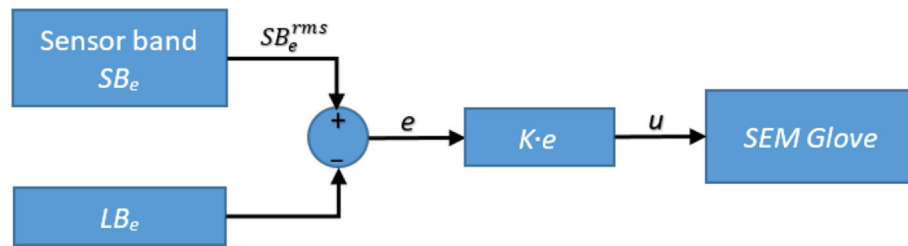


FIGURE 15 | Block diagram of the exoskeleton control.

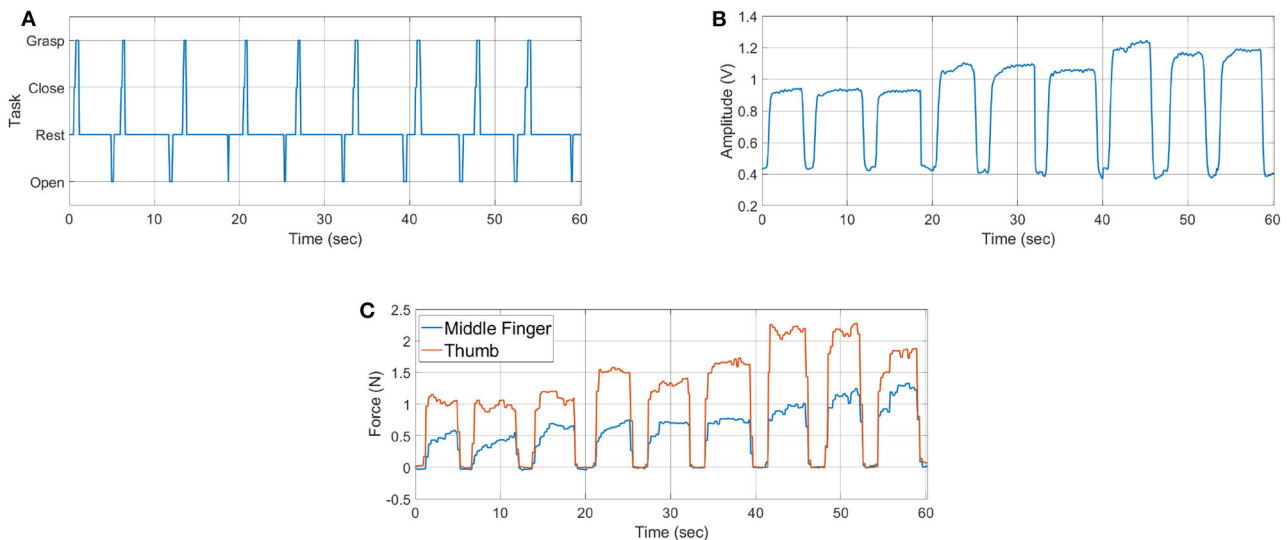


FIGURE 16 | Hand exoskeleton control results: (A) task identified, (B) MCI force measured from sensor band placed near elbow joint, and (C) assistance force provided by SEM Glove.

increases the sensor's sensitivity and solves the problem of sensor resolution if the band tightness is changed from one day to the next.

Another advantage of this method is the dual working modes of the sensor band. Besides motion recognition, the sensor band is also used to control assistance level in grasping an object, which is proportional to the MCI force measured.

The results in this work are significant for physical assistance in workplaces. For a workplace environment, it is critical for any solution that it be accurate, robust, involving less training, and is not sensitive to environmental conditions. With these requirements in mind, comparing our method to other detection methods like sEMG, which is highly prone to noise that is caused by sensor placement, orientation, and skin conditions, our method is less affected by skin condition and can be worn without very exact orientation and placement. Moreover, our developed method has the advantage of using small training datasets. In Arteaga et al. (2020) and Pinzón-Arenas et al. (2019), each gesture was repeated for more than 10 times. Whereas, in our method beside calibration, rest data is recorded for only one time. By this advantage the user can take off the device and put it back on conveniently without worrying about its performance.

This novel method using FSR sensor bands offers a robust and accurate alternative for human-robot interaction. The works presented in this paper and in previous studies (Islam et al., 2018; Islam and Bai, 2019) have shown that FSR-based sensor bands can be applied for control of upper-body assistive exoskeletons in different ways. Beside these, sensor bands can be applied for other types of applications of upper-limb and lower-limb exoskeletons. Moreover, this method can be used to assess the muscle activities for medical purposes and design of control strategies.

Besides these advantages, some limitations of the method are noted. External contact with the sensor band can change the sensor readings, which can result in incorrect motion detection. Hand motion speed is also a factor that can lead to misclassification. If the motion is performed at slow speed, the algorithm might not be able to detect the task. These challenges can be addressed by either placing the FSR array outside of the sensor band or by implementing robust AI techniques for fault detection. Movement speed challenge can be addressed by increasing the window size during features extraction stage. However, increasing the window size can introduce delay in exoskeleton response.

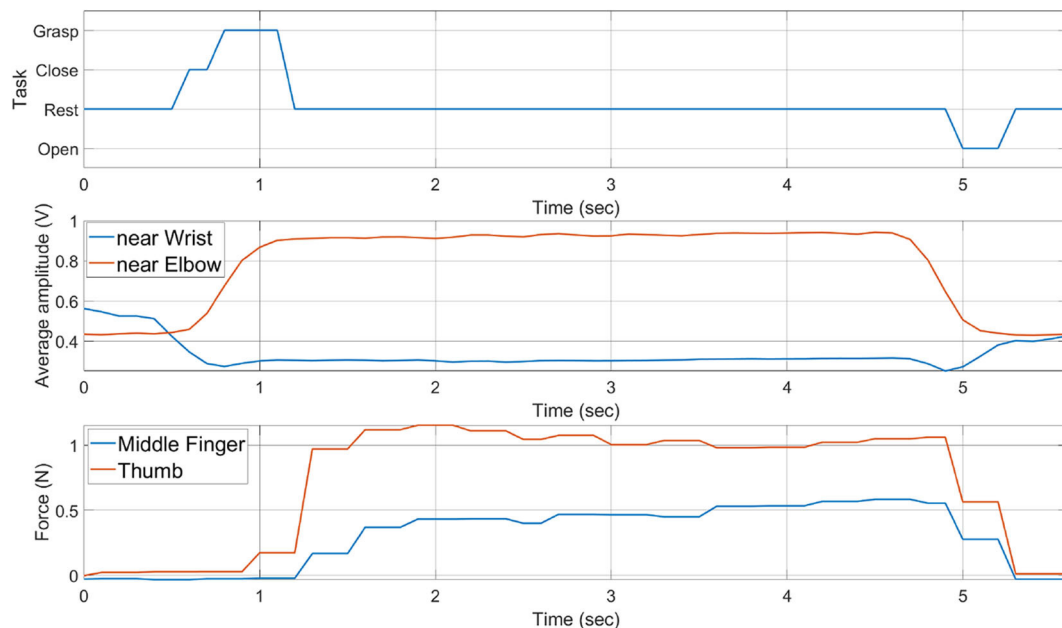


FIGURE 17 | History of task performed, average MCI forces, and grasping forces measured by SEM Glove.

6. CONCLUSIONS

This work is aimed at developing an effective and convenient method to detect hand motions, i.e., rest, open, close, and grasp, using FSR-based sensor bands, which is further used to control hand exoskeleton and provide assistance in grasping task. The objectives are achieved by developing a threshold-based task detection algorithm to determine the hand motion, which is based on the change in MCI forces. Moreover, with the detection of grasping task a proportional force control is also implemented to provide assistance through a soft hand exoskeleton.

The contribution of this work is to experimentally validate whether the sensor bands can be used to detect hand motion and to implement proportional assistance control. Detection of hand motion with the requirement of minimal training data and its validation with testing on multiple subjects are other contributions of this work. The results showed that the developed method can detect each task with high precision, recall, and accuracy. Furthermore, experimental verification of proportional assistance control with SEM Glove in a grasping task is another contribution of this work. The results have shown that the developed method can be used with soft exoskeleton to assist workers in grasping tasks.

In this work, experiments were performed in a controlled environment. In order to test the method for daily routine activities, our future work will focus on sensor fusion techniques to improve robustness against disturbances, which can be caused by other limb movements. Furthermore, the method can be extended to detect other hand gestures and elbow and lower extremity motions.

DATA AVAILABILITY STATEMENT

The raw data supporting the conclusions will be made available by the lead author on reasonable request.

ETHICS STATEMENT

The studies involving human participants were reviewed and approved by ethical committee, Region Nordjylland, Denmark. The participants provided their written informed consent to participate in this study.

AUTHOR CONTRIBUTIONS

MI and SB defined and developed this research work. MI developed the initial protocol draft, collected data, performed the analysis, and wrote the first draft of the manuscript. SB finalized the protocol, reviewed the manuscript, and approved the final version. Both authors contributed to the article and approved the submitted version.

FUNDING

This work was supported by Innovation Fund Denmark for project EXO-AIDER (<https://www.exo-aider.dk>).

ACKNOWLEDGMENTS

The authors would like to thank participants for their time contributed to this study.

REFERENCES

- Anam, K., Rosyadi, A. A., Sujankar, B., and Al-Jumaily, A. (2017). "Myoelectric control systems for hand rehabilitation device: a review," in *2017 4th International Conference on Electrical Engineering, Computer Science and Informatics (EECSI)*, 1–6. doi: 10.1109/EECSI.2017.8239091
- Arteaga, M. V., Castiblanco, J. C., Mondragon, I. F., Colorado, J. D., and Alvarado-Rojas, C. (2020). EMG-driven hand model based on the classification of individual finger movements. *Biomed. Signal Process. Control* 58:101834. doi: 10.1016/j.bspc.2019.101834
- Asif, A. R., Waris, A., Gilani, S. O., Jamil, M., Ashraf, H., Shafique, M., et al. (2020). Performance evaluation of convolutional neural network for hand gesture recognition using EMG. *Sensors* 20:1642. doi: 10.3390/s20061642
- Bullock, I. M., Zheng, J. Z., De La Rosa, S., Guertler, C., and Dollar, A. M. (2013). Grasp frequency and usage in daily household and machine shop tasks. *IEEE Trans. Hapt.* 6, 296–308. doi: 10.1109/TOH.2013.6
- Cho, E., Chen, R., Merhi, L.-K., Xiao, Z., Pousett, B., and Menon, C. (2016). Force myography to control robotic upper extremity prostheses: a feasibility study. *Front. Bioeng. Biotechnol.* 4:18. doi: 10.3389/fbioe.2016.00018
- Ferigo, D., Merhi, L.-K., Pousett, B., Xiao, Z. G., and Menon, C. (2017). A case study of a force-myography controlled bionic hand mitigating limb position effect. *J. Bion. Eng.* 14, 692–705. doi: 10.1016/S1672-6529(16)60435-3
- Gull, M. A., Bai, S., and Bak, T. (2020). A review on design of upper limb exoskeletons. *Robotics* 9:16. doi: 10.3390/robotics9010016
- Hashida, R., Matsuse, H., Bekki, M., Omoto, M., Morimoto, S., Hino, T., et al. (2019). Evaluation of motor-assisted gloves (SEM Glove) for patients with functional finger disorders: a clinical pilot study. *Kurume Med. J.* 64, 1–18. doi: 10.2739/kurumemedj.MS652007
- Islam, M. R., Xu, K., and Bai, S. (2018). "Position sensing and control with FMG sensors for exoskeleton physical assistance," in *International Symposium on Wearable Robotics* (Pisa: Springer), 3–7. doi: 10.1007/978-3-030-01887-0_1
- Islam, M. R. U., and Bai, S. (2019). Payload estimation using force myography sensors for control of upper-body exoskeleton in load carrying assistance. *Model. Identif. Control* 40, 189–198. doi: 10.4173/mic.2019.4.1
- Jiang, X., Merhi, L.-K., Xiao, Z. G., and Menon, C. (2017). Exploration of force myography and surface electromyography in hand gesture classification. *Med. Eng. Phys.* 41, 63–73. doi: 10.1016/j.medengphy.2017.01.015
- Leonardis, D., Barsotti, M., Loconsole, C., Solazzi, M., Troncosi, M., Mazzotti, C., et al. (2015). An EMG-controlled robotic hand exoskeleton for bilateral rehabilitation. *IEEE Trans. Hapt.* 8, 140–151. doi: 10.1109/TOH.2015.2417570
- Lu, Z., Stampas, A., Francisco, G. E., and Zhou, P. (2019). Offline and online myoelectric pattern recognition analysis and real-time control of a robotic hand after spinal cord injury. *J. Neural Eng.* 16:036018. doi: 10.1088/1741-2552/ab0cf0
- Meng, Q., Meng, Q., Yu, H., and Wei, X. (2017). "A survey on sEMG control strategies of wearable hand exoskeleton for rehabilitation," in *2017 2nd Asia-Pacific Conference on Intelligent Robot Systems (ACIRS)* (Wuhan), 165–169. doi: 10.1109/ACIRS.2017.7986086
- Nilsson, M., Ingvast, J., Wikander, J., and von Holst, H. (2012). "The soft extra muscle system for improving the grasping capability in neurological rehabilitation," in *2012 IEEE-EMBS Conference on Biomedical Engineering and Sciences* (Langkawi), 412–417. doi: 10.1109/IECBES.2012.6498090
- Pinzón-Arenas, J. O., Jiménez-Moreno, R., and Herrera-Benavides, J. E. (2019). "Convolutional neural network for hand gesture recognition using 8 different EMG signals," in *2019 XXII Symposium on Image, Signal Processing and Artificial Vision (STSIVA)* (Bucaramanga), 1–5. doi: 10.1109/STSIVA.2019.8730272
- Powers, D. M. (2011). Evaluation: from precision, recall and F-measure to ROC, informedness, markedness and correlation. *J. Mach. Learn.* 2, 37–63.
- Qi, J., Jiang, G., Li, G., Sun, Y., and Tao, B. (2019). Intelligent human-computer interaction based on surface EMG gesture recognition. *IEEE Access* 7, 61378–61387. doi: 10.1109/ACCESS.2019.2914728
- Radmand, A., Scheme, E., and Englehart, K. (2016). High-density force myography: a possible alternative for upper-limb prosthetic control. *J. Rehabil. Res. Dev.* 53, 443–456. doi: 10.1682/JRRD.2015.03.0041
- Rasouli, M., Chellamuthu, K., Cabibihan, J.-J., and Kukreja, S. L. (2016). "Towards enhanced control of upper prosthetic limbs: a force-myographic approach," in *2016 6th IEEE International Conference on Biomedical Robotics and Biomechanics (BioRob)* (University Town), 232–236. doi: 10.1109/BIOROB.2016.7523629
- Ravindra, V., and Castellini, C. (2014). A comparative analysis of three non-invasive human-machine interfaces for the disabled. *Front. Neurobot.* 8:24. doi: 10.3389/fnbot.2014.00024
- Secciani, N., Bianchi, M., Meli, E., Volpe, Y., and Ridolfi, A. (2019). A novel application of a surface electromyography-based control strategy for a hand exoskeleton system: a single-case study. *Int. J. Adv. Robot. Syst.* 16, 1–13. doi: 10.1177/1729881419828197
- Wege, A., and Zimmermann, A. (2007). "Electromyography sensor based control for a hand exoskeleton," in *2007 IEEE International Conference on Robotics and Biomimetics (ROBIO)* (Sanya), 1470–1475. doi: 10.1109/ROBIO.2007.4522381
- Xiao, Z. G., and Menon, C. (2019). A review of force myography research and development. *Sensors* 19:4557. doi: 10.3390/s19204557
- Xiao, Z. G., and Menon, C. (2020). Towards the investigation on the effect of the forearm rotation on the wrist FMG signal pattern using a high-density FMG sensing matrix. *Cogent Eng.* 7:1795051. doi: 10.1080/23311916.2020.1795051
- Zhang, Z., Yang, K., Qian, J., and Zhang, L. (2019). Real-time surface EMG pattern recognition for hand gestures based on an artificial neural network. *Sensors* 19:3170. doi: 10.3390/s19143170
- Zheng, J. Z., De La Rosa, S., and Dollar, A. M. (2011). "An investigation of grasp type and frequency in daily household and machine shop tasks," in *2011 IEEE International Conference on Robotics and Automation* (Shanghai), 4169–4175. doi: 10.1109/ICRA.2011.5980366

Conflict of Interest: The authors declare that the research was conducted in the absence of any commercial or financial relationships that could be construed as a potential conflict of interest.

Copyright © 2020 Islam and Bai. This is an open-access article distributed under the terms of the Creative Commons Attribution License (CC BY). The use, distribution or reproduction in other forums is permitted, provided the original author(s) and the copyright owner(s) are credited and that the original publication in this journal is cited, in accordance with accepted academic practice. No use, distribution or reproduction is permitted which does not comply with these terms.



Inertial-Robotic Motion Tracking in End-Effector-Based Rehabilitation Robots

Arne Passon*, Thomas Schauer and Thomas Seel

Control Systems Group, Technische Universität Berlin, Berlin, Germany

OPEN ACCESS

Edited by:

Jan Veneman,
Hocoma, Switzerland

Reviewed by:

Joan Lobo Prat,
ABLE Human Motion, Spain
Alejandro Melendez-Calderon,
The University of Queensland,
Australia

*Correspondence:

Arne Passon
passon@control.tu-berlin.de

Specialty section:

This article was submitted to
Biomedical Robotics,
a section of the journal
Frontiers in Robotics and AI

Received: 22 April 2020

Accepted: 12 October 2020

Published: 27 November 2020

Citation:

Passon A, Schauer T and Seel T
(2020) Inertial-Robotic Motion Tracking
in End-Effector-Based Rehabilitation
Robots. *Front. Robot. AI* 7:554639.
doi: 10.3389/frobt.2020.554639

End-effector-based robotic systems provide easy-to-set-up motion support in rehabilitation of stroke and spinal-cord-injured patients. However, measurement information is obtained only about the motion of the limb segments to which the systems are attached and not about the adjacent limb segments. We demonstrate in one particular experimental setup that this limitation can be overcome by augmenting an end-effector-based robot with a wearable inertial sensor. Most existing inertial motion tracking approaches rely on a homogeneous magnetic field and thus fail in indoor environments and near ferromagnetic materials and electronic devices. In contrast, we propose a magnetometer-free sensor fusion method. It uses a quaternion-based algorithm to track the heading of a limb segment in real time by combining the gyroscope and accelerometer readings with position measurements of one point along that segment. We apply this method to an upper-limb rehabilitation robotics use case in which the orientation and position of the forearm and elbow are known, and the orientation and position of the upper arm and shoulder are estimated by the proposed method using an inertial sensor worn on the upper arm. Experimental data from five healthy subjects who performed 282 proper executions of a typical rehabilitation motion and 163 executions with compensation motion are evaluated. Using a camera-based system as a ground truth, we demonstrate that the shoulder position and the elbow angle are tracked with median errors around 4 cm and 4°, respectively; and that undesirable compensatory shoulder movements, which were defined as shoulder displacements greater ± 10 cm for more than 20% of a motion cycle, are detected and classified 100% correctly across all 445 performed motions. The results indicate that wearable inertial sensors and end-effector-based robots can be combined to provide means for effective rehabilitation therapy with likewise detailed and accurate motion tracking for performance assessment, real-time biofeedback and feedback control of robotic and neuroprosthetic motion support.

Keywords: end-effector-based robots, inertial measurement units, sensor fusion, posture biofeedback, real-time tracking, rehabilitation robots, compensation motion detection, upper-limb rehabilitation

1. INTRODUCTION

1.1. Motivation and Background

Spinal cord injury or stroke can lead to movement disorders like a paresis of the upper limb (Gowland et al., 1992; Popovic and Sinkjaer, 2000). As a result, patients are often gravely impaired in activities of daily living for the rest of their lives. Primary objectives during rehabilitation training are the enhancement of patients' health situation and self-sufficiency. Stroke patients can often additionally benefit from regained motor functions due to the therapy. Robot-assisted rehabilitation and Functional Electrical Stimulation (FES) are well-known technologies and popular means for enhancement of the physical therapy in modern rehabilitation settings (Oujamaa et al., 2009; McCabe et al., 2015). These systems actively support patients during motions that they cannot perform sufficiently well or not often enough without support.

The role of sensor systems in such rehabilitation systems is 3-fold:

1. Feedback control is commonly used to adjust the motion support to the individual patient in real time and thereby enable the execution of accurate movements (Marchal-Crespo and Reinkensmeyer, 2009; Schauer, 2017). This requires sufficiently precise sensor systems that yield real-time measurements of the currently conducted motion.
2. At the same time, such sensor systems facilitate objective recording and assessment of the patients' motor performance, such as speed of execution, completion of tasks and reaction times (Oña et al., 2018).
3. A third major advantage of motion tracking in rehabilitation systems is that it enables biofeedback that informs the patients about their own motion and positive or negative aspects of that motion and their performance (Zhi et al., 2018), for example in a virtual reality environment. While such a biofeedback facilitates gamification of the rehabilitation tasks (Novak et al., 2014), it is also of crucial importance when the patients perform undesired compensatory motions, which means they compensate weakness of the to-be-trained joint or muscle by exaggerated or unphysiological motions of other joints or muscles (Ma et al., 2019).

In upper limb motion, for example, a decreased range of motion of the shoulder and/or elbow joint is often compensated by movement (flexion, inclination, translation) of the upper body or, with the upper body fixed, by movement of the shoulder girdle (Liu et al., 2013; Grimm et al., 2016; Levin et al., 2016). Both movements are possible, both facilitate the desired movement in an undesirable way. The trunk is, for example, moved forward to reach an object instead of extending the arm (Robertson and Roby-Brami, 2011). Preventing compensation during rehabilitation training improves the therapy outcome and decreases long-term problems, such as pain, orthopedic illnesses and learned non-use (Levin et al., 2009). In reaching tasks, moderately to severely impaired patients exhibit mean shoulder displacements of 14 cm, while these displacements are only around 4 cm in healthy subjects (Cirstea and Levin, 2000). An automatic biofeedback that prevents compensatory motion

requires a real-time motion tracking solution that is sufficiently precise to distinguish these levels of shoulder displacement due to upper-body or shoulder girdle movements.

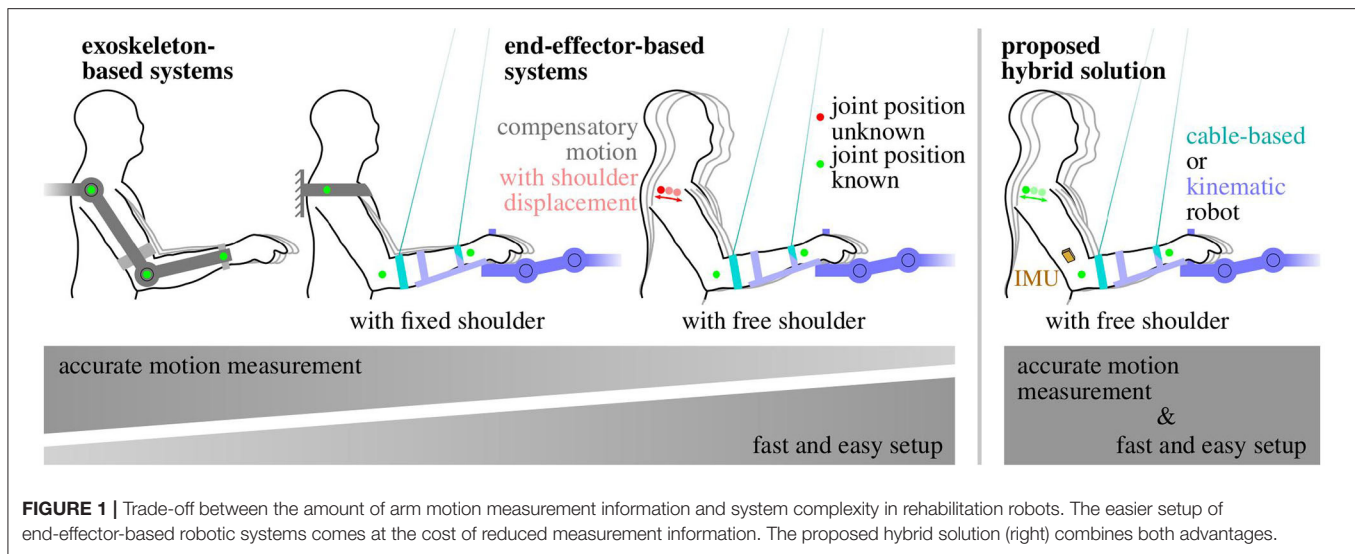
1.2. Motion Tracking in Exoskeletons vs. End-Effector-Based Robots

In robot-assisted rehabilitation training of the upper limb, a range of different rehabilitation systems with different motion tracking solutions are available or have been proposed (Vito et al., 2014). They can be subdivided into two main groups: (1) exoskeleton-based systems and (2) end-effector-based systems (Maciejasz et al., 2014). The amount of inherently available measurement information decreases from exoskeletons to end-effectors, as illustrated in **Figure 1** and detailed in the following.

Exoskeletons reproduce the kinematic structure of the limb they are attached to. The joints of the human limb are assisted and moved by the corresponding joints of the exoskeleton, which also provide measurement information by means of built-in sensors. Major drawbacks of exoskeletons are that they are quite obtrusive and must be adjusted precisely to the individual segment lengths and joint axes, which can be time-consuming (Maciejasz et al., 2014). A misalignment can even cause unwanted pain and in the worst case long-term damage (Sicuri et al., 2014; Bertomeu-Motos et al., 2018). Besides that, the estimation of the human arm joint angles from the exoskeleton ones is often non-trivial if their kinematic structures differ (Nordin et al., 2014). Therefore, rather complex solutions have been proposed, such as extended inverse kinematics posture estimation (EIKPE) models (Wu et al., 2015; Cortés et al., 2016). Some exoskeletons even self-align the robot's active rotational axes to the user's joint axes by means of passive rotational joints, which further increases kinematic complexity (Trigili et al., 2019). If the exoskeleton is well-adjusted to the subject and a transformation of its kinematics to the anatomical frames is available, good measurements of the subject's arm pose and joint angles can be obtained (Nordin et al., 2014).

End-effector-based systems are robotic systems that are only attached to the distal segments of the limbs, which is typically realized by a handle for the hand, a forearm brace, or a footplate. A subgroup of end-effector-based systems are cable-driven motion support robots, which use ropes to provide gravitation-compensating and motion-promoting forces to a distal limb segment. Compared to exoskeletons, end-effector-based systems require far less adjustment to individual patients (Burgar et al., 2000; Lum et al., 2002). However, as a direct consequence of the reduced contact between human and robotic system, only the motion of one body segment is measured by the robot, and the motion of all adjacent segments must be inferred using mechanical models (Nordin et al., 2014) or additional sensors. For end-effector-based upper limb rehabilitation systems, which yield direct measurement of a distal segment, the motion of the upper arm is commonly inferred using the simple assumption of a fixed shoulder position (Dipietro et al., 2007; Rosati et al., 2007).

Figure 1 summarizes the general observation that an easier setup and positioning of the patient comes at the cost of reduced measurement information and accuracy. This drawback can be compensated if end-effector-based systems are combined



with wearable sensor technology that ideally requires only little setup effort.

The conventional gold standard for human motion assessment are multi-camera systems that track a set of reflective or active markers that are worn on anatomical landmarks. However, these systems are expensive, and they require a complex marker and camera setup as well as a clear line-of-sight between each marker and at least two cameras at all times (Kirk et al., 2005; Zhou and Hu, 2008). Other optical systems, such as depth cameras (e.g., Microsoft Kinect) or single cameras have not reached comparable accuracy due to occlusion, jitter, low and varying sampling frequency or viewing-angle-dependent performance deterioration (Yahya et al., 2019).

Body-worn goniometers overcome the line-of-sight restrictions and can yield root-mean-squared error values (RMSE) around 2° (Tognetti et al., 2015). However, they are obtrusive in the sense that they span across joints, and they only measure joint angles but neither orientations nor velocities nor positions (Tognetti et al., 2015).

Inertial measurement units (IMUs) are wearable sensors that provide all this information without requiring cables or clear lines of sight between the sensors (Held et al., 2018). However, IMUs require, in general, more complex sensor fusion algorithms to address magnetic disturbances, integration drift, and sensor-to-segment misalignment. Each IMU is composed of three types of sensors (gyroscopes, accelerometers, and magnetometers) and measures the three-dimensional angular rate, acceleration, and magnetic field vector in its intrinsic coordinate system. IMUs are small and lightweight enough to be considered completely unobtrusive and assure zero influence on the motion performance. Recent advances in inertial motion tracking have helped to overcome long-standing challenges, such as sensor-to-segment calibration (Taetz et al., 2016; Nowka et al., 2019; Olsson et al., 2019) or the requirement of a homogeneous magnetic field (Laidig et al., 2017b; Laidig et al., 2019; Seel and Ruppert, 2017) and to provide a similar accuracy as optical systems (Seel et al., 2015; Filippeschi et al., 2017; Salchow-Hömmen et al., 2019).

1.3. State of the Art in Sensor Systems for End-Effector-Based Upper Limb Therapy

Since the application-related focus of the present work lies on upper-limb rehabilitation robots, we also briefly review existing systems and solutions for this specific application domain. A comprehensive survey of upper-limb rehabilitation systems is given in Maciejasz et al. (2014) and Mekki et al. (2018). We focus more specifically on systems and methods that combine end-effector-based motion support systems with wearable or optical motion tracking solutions to compensate the lack of measurement information of the former by means of the latter. Below we provide an overview of existing combinations and of their solutions for compensatory motion detection.

For end-effector-based rehabilitation robots, two main sensor setups have been proposed: on the one hand the combination with a depth camera and on the other hand combinations with inertial sensors or solely accelerometers.

Regarding camera-based solutions, Brokaw et al. (2013) combined a wrist brace robot with a Kinect (Microsoft, USA) sensor to calculate the trunk and arm joint angles during reaching motions and demonstrated that these angles can be used to prevent compensatory movements. However, they reported large tracking errors of the Kinect due to occlusion and problems to distinguish between the subject's arm and the robot. In a similar work, Zhi et al. (2018) recently published results on compensatory motion classification based on Kinect's skeletal tracking information. Occlusion occurred, and a solution for posture biofeedback was not presented. Another approach using a Kinect and two end-effectors for each arm was evaluated by Valdés and der Loos (2017). They detected trunk compensation by measuring motions of the shoulder-spine joint using the Kinect. Two biofeedback strategies were compared, both of which were shown to reduce compensatory movements. However, yet again a continuous clear line-of-sight is required, which is especially a problem if the therapist has for any reason to act on the patient.

Mihelj (2006) presented the combination of a hand-attached robot with two accelerometers at the upper arm. This approach yields accurate upper-limb joint angles. However, the inverse-kinematics algorithm requires shoulder joint fixation, for example by binding the trunk to a chair with belts, which leads to additional setup effort. Bertomeu-Motos et al. (2015b) further improved the method by Mihelji proposing only the use of one accelerometer at the upper arm, but also for this method the shoulder position must be known and fixed during the therapy. A similar yet even more restrictive approach, which uses a forearm cuff that prevented forearm pronation-supination and wrist movements, is found in Papaleo et al. (2015) and is also used by Scotto di Luzio et al. (2018).

To our best knowledge, the only combination of an end-effector-based robot with inertial sensors that does not require shoulder fixation was proposed by Bertomeu-Motos et al. (2015a) and validated in stroke patients (Bertomeu-Motos et al., 2018). The elbow angle and shoulder position are estimated using inertial sensors on the upper arm (only accelerometer) and on the outer edge of the shoulder, with accuracies below 6° and 5 cm, respectively. However, the proposed algorithms require two sensor units, and they rely on magnetometer readings, which implies that they are unreliable if the earth-magnetic field is disturbed, such as in indoor environments, near ferromagnetic material or electronic devices, i.e., practically in all realistic clinical settings (de Vries et al., 2009; Le Grand and Thrun, 2012; Subbu et al., 2013; Shu et al., 2015; Salchow-Hömmen et al., 2019). Furthermore, compensatory motion detection or biofeedback has not been considered in that article.

In a previous work, we combined a cable-driven end-effector-based robot with magnetometer-free inertial sensors worn on the forearm and upper arm (Passon et al., 2018). We demonstrated that fusing cuff position measurements of the robotic system with inertial sensor readings is advantageous and enables magnetometer-free tracking of the complete forearm orientation and position. For temporary compensatory displacements of the trunk or shoulder (less than a half minute), we were able to estimate the upper arm heading and the true shoulder position accurately. However, the approach failed to provide long-time stable estimates under longer lasting compensation movements or static compensatory postures.

In summary, depth-camera-based solutions can lead to reliable compensation motion detection but only under continuous line-of-sight restrictions. These restrictions can be overcome by means of wearable inertial sensors, but there is a lack of practical solutions that provide long-time stable motion tracking of the entire upper limb in realistic environments with inhomogeneous magnetic fields. To date there is no inertial sensor-based solution that yields all of the following desirable features:

- (1) Accurate measurement information of the complete orientation of the upper arm independent of the local magnetic field;
- (2) Reliable long-time stable real-time detection of shoulder displacements and associated compensatory motion.

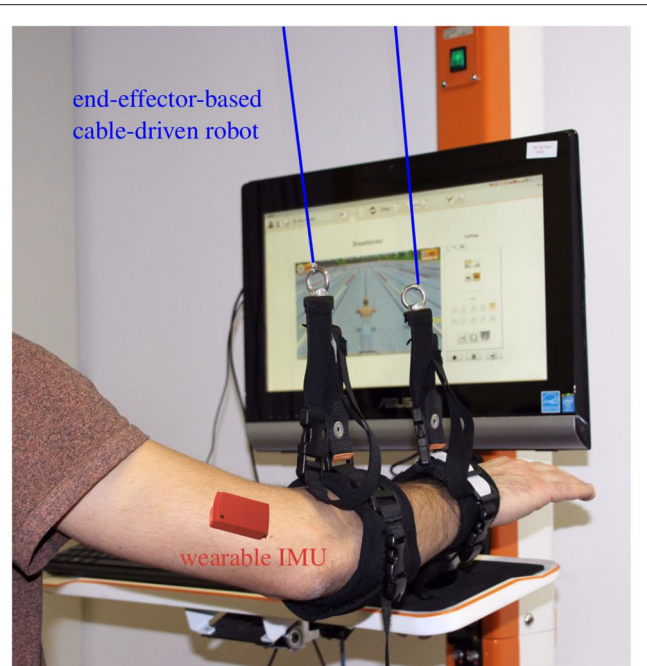


FIGURE 2 | Example setup: the cable-based rehabilitation robot Diego (Tyromotion GmbH, Austria) is augmented by one wearable inertial sensor at the upper arm to enable tracking of the upper arm and shoulder motion.

1.4. Contributions of the Paper

In order to address the aforementioned challenges, we propose new methods that leverage the full potential of combining end-effector-based rehabilitation robots with wearable inertial sensors. We will demonstrate in one particular experimental setup that the measurement limitations of an end-effector-based robot can be overcome by exploiting inertial measurements. Simultaneously, fundamental limitations of inertial motion tracking are overcome by a novel magnetometer-free sensor fusion method that exploits the end-effector-based measurements. In brief, the main contributions of this paper are:

1. We introduce sensor fusion methods that combine robotic measurements from one segment and inertial measurements of an adjacent segment to determine long-time stable measurements of the full orientation and the endpoint of that adjacent segment in the robotic measurement frame while
 - using *no* magnetometer readings at all,
 - allowing the adjacent segment to move freely,
 - and requiring no initial heading alignment or position calibration.
2. We apply the proposed methods to augment the cable-based forearm-attached robot shown in **Figure 2** with a wearable IMU and determine long-time stable measurements of the upper arm orientation and shoulder position in real time.
3. We perform an experimental validation with five subjects and a camera-based ground truth measurement, and we

demonstrate that the achieved measurement accuracy is around 4° and 4 cm, respectively.

4. We propose a method that detects compensatory motions with shoulder displacements greater ± 10 cm that last for more than 20% of a motion cycle, and we demonstrate that typical rehabilitation motions conducted by healthy subjects with and without compensatory motion are 100% correctly classified by this method.

The remaining paper is structured as follows. The general hardware setup and problem statement are presented in **Section 2**. The developed methods for sensor fusion, shoulder position estimation and detection of compensation movements are introduced in **Section 3**. The experimental procedure including a description of the rehabilitation robot that is considered for validation and the analysis of conducted experiments with five healthy subjects is given in **Section 4**. Finally, a discussion of the results is presented in **Section 5**, and conclusions follow in **Section 6**.

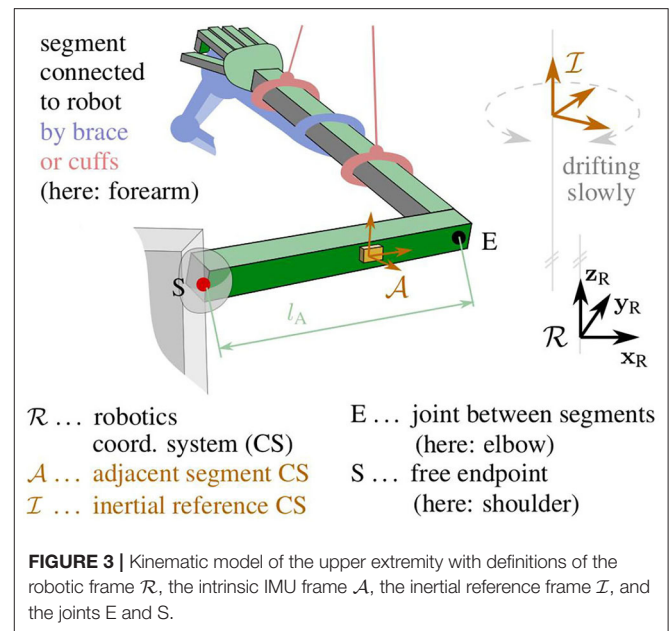
2. KINEMATIC MODEL AND SENSOR FUSION TASK

Before defining the sensor fusion task, we describe the general properties and assumptions of the kinematic system and possible example realizations. Consider a kinematic chain consisting of two rigid segments, and let both be connected by a joint with up to three rotational degrees of freedom.

- (i) Assume that one of both segments is in contact with a robotic system, and call this segment the *connected* segment and the other one the *adjacent* segment.
- (ii) The robot is assumed to yield real-time information of the position of the joint between both segments in a fixed robotic coordinate system.
- (iii) The robot, however, yields no information on the orientation of the adjacent segment, and we also *refrain* from assuming that any point along that segment remains fixed in space.

Two examples are given to illustrate the relevance of this general kinematic system and the meaning of the assumptions. In the first example, the connected and adjacent segments are the shank and thigh, respectively. A cable-based robotic system with above-ankle and below-knee cuffs measures the cuff positions and determines the knee position by extrapolating the line between both cuffs. The orientation of the thigh, however, cannot be determined if we refrain from assuming a fixed hip position. In the second example, a robotic system connects to the upper extremity via a forearm brace, which enables measurements of the orientation and position of the forearm and elbow but not the motion of upper arm and the unconstrained shoulder. In both examples, the adjacent segment is the proximal one of both segments, which makes sense in the context of end-effector-based robots. However, it should be noted that neither the kinematic model nor the methods we will propose are limited to that case.

To obtain complete measurement information of the motion of both segments, a wireless wearable IMU is attached to the



adjacent segment. **Figure 3** shows one specific example of such a hybrid inertial-robotic measurement system for the upper extremity. We assume that the distance of the sensor to the joint is approximately known. We further assume that the relative orientation between the inertial sensor and the segment is known either by careful sensor-to-segment attachment or by employing methods that automatically determine this information from almost arbitrary movements of the kinematic system (Müller et al., 2016; Laidig et al., 2017a; Olsson et al., 2019).

The IMU yields three-dimensional measurements of the acceleration, the angular rate and the magnetic field vector in its own intrinsic coordinate system. Since these measurements are obtained from micro-electro-mechanical systems (MEMS), they are prone to considerable bias and noise errors. Nevertheless, the orientation of the sensor can be determined with respect to an inertial frame of reference with a vertical axis and a horizontally northbound axis. This is a standard problem in inertial sensor fusion, and several suitable orientation estimation algorithms exist.

However, two issues arise: Firstly, the inertial reference is not aligned with the robotic coordinate system—only the vertical axes of both frames coincide. Secondly, IMU-based orientation estimation requires a homogeneous magnetic field and therefore fails in indoor environments and in the proximity of ferromagnetic material and electronic devices. In the realistic case of a disturbed and inhomogeneous magnetic field, only the inclination but not the heading of the sensor can be determined reliably.

We conclude that neither the robotic system nor the inertial sensor yields the desired orientation and position information of the adjacent segment. Only the inclination of the segment and the position of one of its ends can be determined. The task that should be addressed in the following is to determine the full

orientation and position of the segment by fusing the robotic and inertial measurements.

For the specific example application of a forearm-connected robotic system, we deduce accuracy requirements for the hybrid system to detect the shoulder displacements that are characteristic for compensatory motions in upper-limb rehabilitation of neurological patients: to reliably distinguish between the aforementioned physiological and compensatory shoulder displacement amplitudes [4 vs. 14 cm (Cirstea and Levin, 2000)] during one motion, a method should ideally be able to track the shoulder position with a tracking error of at most 5 cm in average over the course of that motion.

3. PROPOSED METHODS

The novel methods are presented in three steps: First we will propose methods that solve the given sensor fusion task for the general kinematic system and determine the orientation of the adjacent segment. We will then demonstrate how the joint angle and the adjacent segment's endpoint position can be calculated from the estimated segment orientation. Finally, we will consider the specific application of upper-limb rehabilitation and propose methods for distinguishing proper motions from motion with undesirable shoulder displacements.

3.1. Coordinate Systems and Notation

Let the right-handed robotic workspace coordinate system $\{\mathbf{x}_R, \mathbf{y}_R, \mathbf{z}_R\}$ be defined by the y-axis \mathbf{y}_R pointing horizontally forward and the z-axis \mathbf{z}_R straight up, as illustrated in **Figure 3**. The adjacent segment's coordinate system $\{\mathbf{x}_A, \mathbf{y}_A, \mathbf{z}_A\}$, in which the inertial measurements are taken, is defined with the x-axis \mathbf{x}_A being parallel to the longitudinal axis of the segment and pointing toward the joint with the connected segment. The inertial reference coordinate system of the orientation estimates is denoted $\{\mathbf{x}_I, \mathbf{y}_I, \mathbf{z}_I\}$. The reference frame \mathcal{I} has a vertical z-axis but horizontal x- and y-axes with an arbitrary, slowly drifting heading, as will be explained later on.

While the lower right index is used to denote to which coordinate system a vector is attached, the lower left index is used to describe in which coordinate systems it is expressed. For example, \mathbf{x}_A denotes the x-axis of the coordinate system \mathcal{A} ; ${}_A\mathbf{x}_A$ denotes the coordinates of that x-axis in the very same frame, which trivially and constantly is $[1, 0, 0]^T$; finally, ${}_R\mathbf{x}_A$ denotes the coordinates of that x-axis in the robotic workspace frame \mathcal{R} . For quaternions, the upper and lower left indices are defined such that ${}_R\mathbf{q}$ is the quaternion that fulfills $[0, {}_R\mathbf{v}^T]^T = {}_R\mathbf{q} \otimes [0, {}_A\mathbf{v}^T]^T \otimes {}_A\mathbf{q}$ for any vector $\mathbf{v} \in \mathbb{R}^3$. Note that the abbreviated notation ${}_R\mathbf{v} = {}_R\mathbf{q} \otimes {}_A\mathbf{v} \otimes {}_A\mathbf{q}$ is used in the further course of this work, i.e., we assume that the quaternion multiplication operator \otimes regards three-dimensional vectors automatically as their pure quaternion counterpart. Finally, we define the operator $[\cdot]_{\text{normalize}}$ that maps any vector to a vector with the same direction but Euclidean norm one.

3.2. Estimation of the Adjacent Segment's Orientation

We estimate the orientation of the adjacent segment with respect to an inertial reference frame by employing a quaternion-based sensor fusion algorithm that uses strapdown integration of the angular rates and geodetic accelerometer-based corrections (Seel and Ruppel, 2017). Note that, while the algorithm is capable of also performing magnetometer-based corrections, we refrain from using the magnetometer readings and only fuse gyroscope and accelerometer measurements.

Denote the raw accelerometer readings of the IMU by ${}_A\tilde{\mathbf{a}}_A$ and the raw gyroscope readings by ${}_A\tilde{\boldsymbol{\omega}}_A$ in the coordinate system of the adjacent segment. Here, $\tilde{\mathbf{a}}$ is the specific force (Titterton et al., 2004), which is the sum of the linear acceleration \mathbf{a} due to velocity changes and gravitational acceleration. At each sampling instant t , the sensor fusion algorithm takes ${}_A\tilde{\mathbf{a}}_A(t)$, ${}_A\tilde{\boldsymbol{\omega}}_A(t)$ and provides the quaternion ${}_I^A\mathbf{q}$ that describes the orientation of the segment frame \mathcal{A} with respect to the reference frame \mathcal{I} .

This orientation estimate has reliable and accurate inclination components, but the heading is unknown in the following sense: The reference frame has a vertical z-axis but an arbitrary heading that depends on the initial orientation of the IMU and the initial values of the orientation estimation filter. Moreover, that heading of the reference frame is drifting slowly due to gyroscope bias and integration drift, which implies that there is an unknown and slowly drifting heading offset δ between the frames \mathcal{I} and \mathcal{R} .

In the present contribution, we demonstrate that this missing heading information can be inferred if the position ${}_R\mathbf{p}_E$ of the joint in the robotic frame is known. We will estimate the heading of the adjacent segment by exploiting the kinematic relation between the acceleration measured by the inertial sensor and the numerically determined second time derivative of ${}_R\mathbf{p}_E$.

3.2.1. Joint Acceleration Disagreement

We use the approximately known distance ${}_A\mathbf{p}_E$ between the IMU and the joint to determine an IMU-based estimate of the joint acceleration \mathbf{a}_E in the inertial reference frame. For this purpose, we first determine the specific force $\tilde{\mathbf{a}}_E$ in the \mathcal{A} -frame by accounting for the radial and tangential acceleration due to rotation around the joint:

$${}_A\tilde{\mathbf{a}}_E = {}_A\tilde{\mathbf{a}}_A + ([{}_A\boldsymbol{\omega}_A]_{\times})^2 {}_A\mathbf{p}_E + [{}_A\dot{\boldsymbol{\omega}}_A]_{\times} {}_A\mathbf{p}_E, \quad (1)$$

where $[\cdot]_{\times}$ denotes the cross product matrix, and the time derivative ${}_A\dot{\boldsymbol{\omega}}_A$ is determined by numerical differentiation of the low-pass filtered angular rate (5th-order Butterworth filter with a cutoff frequency of 2.5 Hz). We then use the orientation quaternion ${}_I^A\mathbf{q}$ to transform the specific force into the inertial reference frame and to remove the gravitational acceleration to obtain the acceleration of the joint:

$${}_I\mathbf{a}_E = {}_I^A\mathbf{q} \otimes {}_A\tilde{\mathbf{a}}_E \otimes {}_I^A\mathbf{q} - [0, 0, 9.81]^T. \quad (2)$$

Ideally, ${}_I\mathbf{a}_E$ and the second time derivative ${}_R\ddot{\mathbf{p}}_E$ are the same quantity expressed in different frames (\mathcal{I} and \mathcal{R}), which only

differ in their heading. In practice, however, when transforming both signals into the same frame, we find high frequency deviations caused by noise and soft-tissue motion. Thus, the best we can ask for is that they are similar in the sense of a small sum of squared differences of the low-pass filtered signals (5th-order Butterworth filter with a cutoff frequency of 0.5 Hz).

Denote the unknown heading offset between the frames \mathcal{R} and \mathcal{I} by $\delta(t) \in [0, 2\pi)$ and recall that it is an unknown but only slowly drifting angle. For any given value of δ and any moment in time, we can determine the disagreement $d(\delta): [0, 2\pi) \rightarrow \mathbb{R}$ between a given value of ${}_{\mathcal{I}}\mathbf{a}_E$ and a given value of ${}_{\mathcal{R}}\ddot{\mathbf{p}}_E$ by

$$d(\delta, {}_{\mathcal{I}}\mathbf{a}_E, {}_{\mathcal{R}}\ddot{\mathbf{p}}_E) := \begin{bmatrix} \cos(\frac{\delta}{2}) \\ 0 \\ 0 \\ \sin(\frac{\delta}{2}) \end{bmatrix} \otimes {}_{\mathcal{I}}\mathbf{a}_E \otimes \begin{bmatrix} \cos(\frac{\delta}{2}) \\ 0 \\ 0 \\ -\sin(\frac{\delta}{2}) \end{bmatrix} - {}_{\mathcal{R}}\ddot{\mathbf{p}}_E. \quad (3)$$

Let the cost function $c(\delta, t): [0, 2\pi) \times \mathbb{R}^+ \rightarrow \mathbb{R}$ be the sum of the squares of this disagreement over a moving window:

$$c(\delta, t) := \sum_{k=1}^m d(\delta, {}_{\mathcal{I}}\mathbf{a}_E(t - kT_s), {}_{\mathcal{R}}\ddot{\mathbf{p}}_E(t - kT_s))^2, \quad (4)$$

where m is the width of the moving window. Finally, define a grid-based optimization function $\text{optdelta}(\Delta, t)$ that takes a given moment $t > mT_s$ and a given set Δ of heading offset values and returns the value from the grid-set that minimizes the disagreement over the time window $[t - mT_s, t]$:

$$\text{optdelta}(\Delta, t) = \arg \min_{\delta \in \Delta} (c(\delta, t)). \quad (5)$$

3.2.2. Relative-Heading Estimation

The slowly drifting relative heading δ , and thus the heading of the adjacent segment in the robotic workspace frame \mathcal{R} , is determined by the following algorithm.

Every 5 s, a time window containing the last 20 s of data is considered, and that time window is split into five sub-windows (see **Figure 4**). For each sub-window, we say that there is no

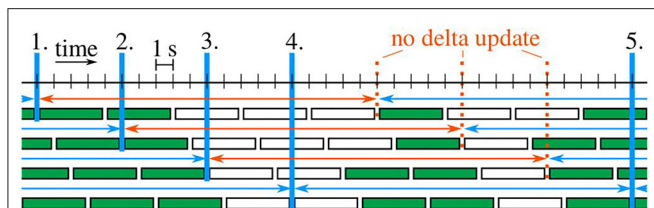


FIGURE 4 | Example case with five delta updates (blue verticals).

Sub-windows are filled green if enough considerable motion is contained.

Each time window with at least three green sub-windows is marked by a blue (otherwise red) arrow.

considerable motion if the elbow position ${}_{\mathcal{R}}\mathbf{p}_E$ remains within a sphere of ten-centimeters diameter throughout the 4 s. If at least three sub-windows of the considered time window contain considerable motion, then the entire window is said to contain enough considerable motion.

Initially, the estimated heading offset $\hat{\delta}$ is undefined. At each of the first five time windows that contain enough considerable motion, the estimate is updated by the following two-steps:

$$\tilde{\delta} = \text{optdelta}(\{0^\circ, 5^\circ, \dots, 355^\circ\}, t), \quad (6)$$

$$\hat{\delta} = \text{optdelta}(\{\tilde{\delta} - 5^\circ, \tilde{\delta} - 4^\circ, \dots, \tilde{\delta} + 5^\circ\}, t). \quad (7)$$

At all subsequent time windows that contain enough considerable motion, the algorithm checks whether the last five estimates each change by at most 5° from one estimate to the next. As soon as this condition is fulfilled, the algorithm is said to have converged, and all following estimates are determined in a one-step update on a reduced grid that is centered around the estimate $\hat{\delta}^-$ of the previous time window:

$$\hat{\delta} = \text{optdelta}(\{\hat{\delta}^- - 5^\circ, \hat{\delta}^- - 4^\circ, \dots, \hat{\delta}^- + 4^\circ, \hat{\delta}^- + 5^\circ\}, t). \quad (8)$$

Obviously, we could likewise use the two-step update for all time windows with enough considerable motion or we could switch back to that two-step update whenever consecutive results of the one-step update are five degrees apart. However, the experimental results in **Section 4.3** will demonstrate that such extensions would be useless in the sense that they are never triggered.

The proposed periodic updates provide new estimates of the heading offset $\hat{\delta}$ every 5 s as long as the adjacent segment moves. When there is almost no motion, the estimate remains constant. Note that the method's accuracy level is directly determined by the user. With the proposed parametrization, the highest accuracy that the algorithm can achieve is 1° , which is more than sufficient for the present application.

3.3. Estimation of the Joint Angle and Segment Endpoint Position

We use the estimated heading offset $\hat{\delta}$ between the frames \mathcal{R} and \mathcal{I} to determine the orientation ${}_{\mathcal{R}}^A\mathbf{q}$ of the adjacent segment in the robotic workspace frame \mathcal{R} :

$${}_{\mathcal{R}}^{\mathcal{I}}\mathbf{q} = \begin{bmatrix} \cos(\frac{\hat{\delta}}{2}) \\ 0 \\ 0 \\ \sin(\frac{\hat{\delta}}{2}) \end{bmatrix}, \quad (9)$$

$${}_{\mathcal{R}}^A\mathbf{q} = {}_{\mathcal{R}}^{\mathcal{I}}\mathbf{q} \otimes {}_{\mathcal{I}}^A\mathbf{q}. \quad (10)$$

By assumption, the longitudinal axis \mathbf{x}_C of the connected segment is known in the robotic workspace frame \mathcal{R} . The joint angle can

thus be determined as the angle between the longitudinal axes of both segments:

$$\vartheta_{E,hyb} = \angle(\mathcal{R}\mathbf{x}_C, \mathcal{A}\mathbf{q} \otimes \mathcal{A}\mathbf{x}_A \otimes \mathcal{R}\mathbf{q}). \quad (11)$$

The orientation $\mathcal{A}\mathbf{q}$ is further used to calculate the position $\mathcal{R}\mathbf{p}_S$ of the endpoint of the adjacent segment from the joint position $\mathcal{R}\mathbf{p}_E$ and the segment length l_A :

$$\mathcal{R}\mathbf{p}_S = \mathcal{R}\mathbf{p}_E - \mathcal{R}\mathbf{q} \otimes \mathcal{A}\mathbf{x}_A l_A \otimes \mathcal{R}\mathbf{q}. \quad (12)$$

For segment lengths of up to half a meter, orientation errors of 1° cause endpoint position errors below 1 cm. Therefore, if position errors in the range of 1 cm are negligible, then a heading estimation accuracy level of 1° is sufficient.

3.4. Detection of Compensatory Motions for Biofeedback

In upper-limb rehabilitation, compensatory shoulder motions lead to an inefficient rehabilitation training and can even have a harmful effect for the user. The methods proposed above enable upper arm and shoulder motion tracking by combining end-effector-based robots that connect to the forearm and a wearable IMU on the upper arm.

We propose a method that detects whether the user compensates weakness of affected muscles or joints by trunk or shoulder girdle motions. Without loss of generality, we consider a scenario with periodic arm rehabilitation motions, and we aim at distinguishing the following two cases:

- The *proper movement* (*prop.mov.*) in which most of the motion is realized by shoulder joint and elbow joint motions and only minor shoulder displacements around a mean of 4 cm occur (cf. Cirstea and Levin, 2000),
- The *compensatory movement* (*comp.mov.*) in which the shoulder and elbow joint remain rather stiff and large portions of the motion are realized by shoulder girdle or trunk motions, which leads to shoulder displacements around a mean of 14 cm (cf. Cirstea and Levin, 2000).

The estimated shoulder position $\mathcal{R}\mathbf{p}_S$ is monitored in real-time whether it leaves a tolerated range. An acceptable region of ± 10 cm around the therapeutically desired shoulder position covers typical variations during proper arm motions (see Section 4.3). Even healthy subjects sometimes temporarily exceed this limit. In order to tolerate for such short-time deviations, we allowed shoulder displacements of more than ± 10 cm for up to 20% of an iteration during repetitive movement training. In applications where such a violation is unacceptable or undesired, these values could of course be lowered. Each iteration is examined when it is completed and detected shoulder displacements are then directly signaled. Whenever such compensatory motions are detected, the user is instructed to move back to the nominal shoulder position and to redo or resume the therapy task. Figure 5 shows one potential implementation of a visual biofeedback. The indicator in the lower right corner of the rehabilitation game

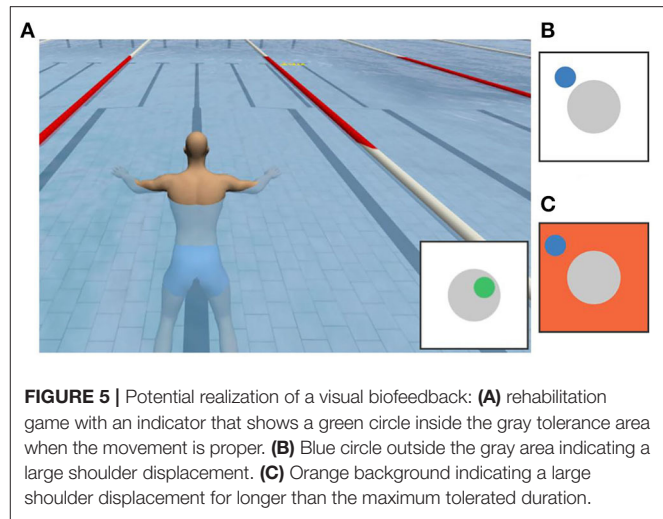


FIGURE 5 | Potential realization of a visual biofeedback: (A) rehabilitation game with an indicator that shows a green circle inside the gray tolerance area when the movement is proper. (B) Blue circle outside the gray area indicating a large shoulder displacement. (C) Orange background indicating a large shoulder displacement for longer than the maximum tolerated duration.

shows the tolerated shoulder position region as a gray circle in the center. The estimated current shoulder position is indicated by a smaller circle, which is green during proper movements and turns blue when it is outside the gray tolerance area, i.e., when the shoulder displacement is larger than the preset threshold. If that condition is fulfilled for longer than a short user-defined duration, which might be chosen as a percentage of the current cycle duration, the indicator's background is highlighted in orange to provide a strong warning feedback.

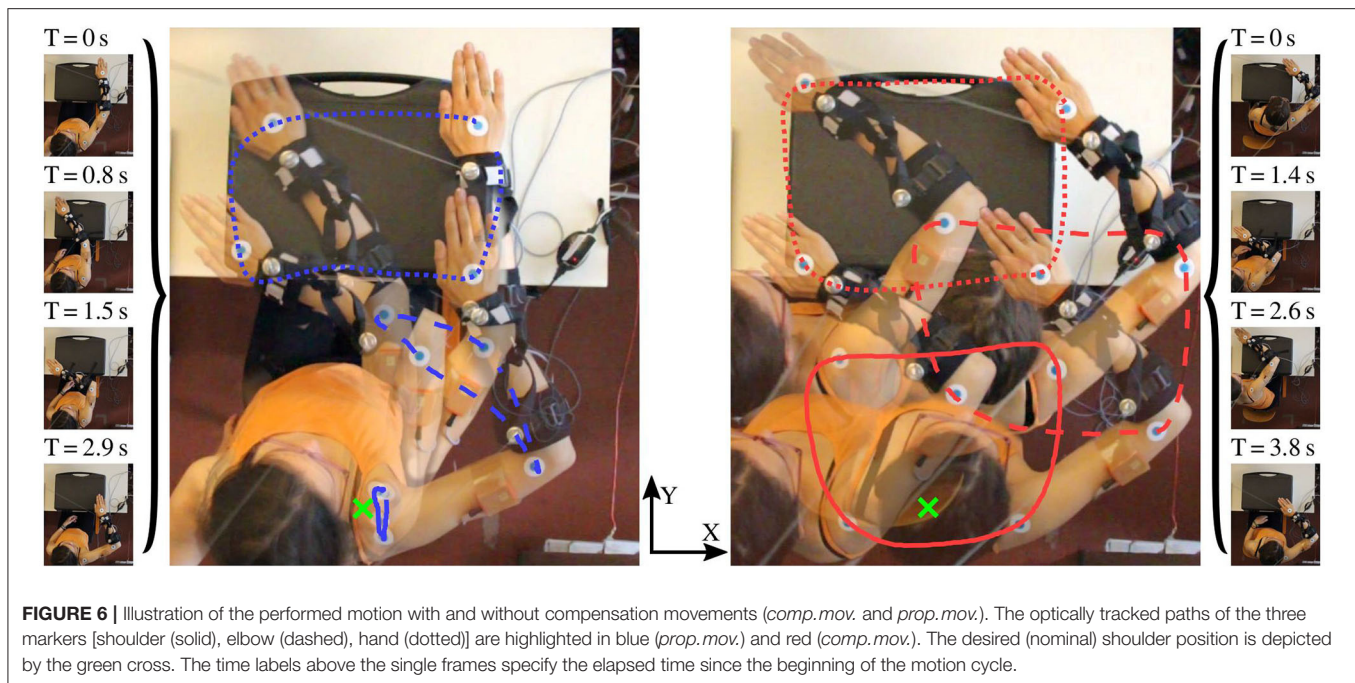
4. EXPERIMENTAL VALIDATION

The proposed methods are validated experimentally in a specific application example of robot-assisted upper-limb rehabilitation. We first describe the robotic system, then the experimental procedure, and finally the results.

4.1. The Cable-Based Rehabilitation Robot

We consider the cable-based rehabilitation robot Diego (Tyromotion GmbH, Austria), which is an active arm weight compensation and motion support system (Jakob et al., 2018). It facilitates three-dimensional arm therapies that would otherwise be impossible for patients with paretic upper limbs or would require continuous manual support by a therapist. Such motion support can reduce physical fatigue of the patient and therapist and can thereby enable longer therapy sessions. The therapy focus can be on different movements like reaching or lifting or even on the motion of specific joints. The robot is equipped with a virtual game environment to further motivate the patient, even during frequent repetitions of the same movement.

Two retractable ropes are connected to the forearm using one cuff around the wrist and another cuff close to the elbow, as depicted in Figure 2. The rope forces are controlled by independent drives, which also provide measurements of the length of the ropes. Near the outlet of each rope, a low-friction spherical shell moves along with the rope and provides



two-dimensional measurement of the rope deflection angle. Combining the length and angle measurements yields estimates of the rope end points, i.e., the forearm cuff positions $\mathcal{R}\mathbf{P}_W$ at the wrist and $\mathcal{R}\mathbf{P}_P$ of the proximal cuff, in a robot-fixed coordinate system. The elbow position in the robotic workspace frame is calculated by extrapolating the line between both cuff positions into the elbow joint:

$$\mathcal{R}\mathbf{P}_E = l_p [\mathcal{R}\mathbf{P}_P - \mathcal{R}\mathbf{P}_W]_{\text{normalize}} + \mathcal{R}\mathbf{P}_P, \quad (13)$$

where l_p is the known approximate distance between the proximal cuff attachment point and the elbow.

It is important to note that these robotic position measurements are drift-free but provided at a sampling rate of only 25 Hz and susceptible to disturbances by rope oscillations. These disturbances are significant, since the ropes are not always taut—especially when the direction of motion changes suddenly—and small changes of the aforementioned deflection angles have large effects on the estimated endpoint position. In previous research, we have demonstrated that these shortcomings can be overcome by augmenting the robot with a wearable IMU on the forearm, and highly accurate measurements of the forearm position and orientation can be achieved (Passon et al., 2018). In the present work, we build on this previous result and use the improved forearm measurements. However, the methods proposed in **Section 3** can likewise be applied when direct measurements of the Diego system or another robotic system are used.

While the Diego system can measure the wrist and elbow position, it has no means for determining the shoulder position. Instead the system requires that the nominal shoulder position

$\mathcal{R}\mathbf{P}_S^{\text{nom}}$ is defined at the beginning of each trial. For this purpose, the therapist positions the patient into the desired upper-body posture and briefly holds the end of one of the ropes onto the shoulder joint. Throughout the trial, the robotic system estimates the upper arm motion using the assumption that the shoulder remains fixed at the nominal position, as proposed in previous literature (Dipietro et al., 2007; Rosati et al., 2007). This implies that the elbow angle is determined according to (11) but with $\mathcal{R}\mathbf{x}_A$ being the normalized vector between the elbow position and the nominal shoulder position. It is assumed that the therapist restraints the trunk or shoulder such that the shoulder position remains constant throughout the session or that the patient follows the instruction to perform the exercise without compensatory motion. In the following, we will compare the results of the *conventional* literature method of the non-augmented system with the results of the proposed *hybrid* method of the inertial-robotic augmented system. We will generally consider the case of a *proper movement* in which the aforementioned assumptions are fulfilled and the case of a *compensatory movement* in which either the fixation is not accomplished correctly or the patient does not follow the instruction, i.e., in both cases the shoulder deviates from its nominal position.

4.2. Experimental Setting and Procedure

The proposed methods for hybrid motion tracking and posture biofeedback are evaluated in experiments with five healthy subjects (age of 25–35 years, two female and three male), hereinafter also termed S1–S5. The performed trials involving human participants were reviewed and approved by the ethics committee of the Berlin Chamber of Physicians (Eth-40/15). The chosen subjects cover a large range of body height (160–192 cm)

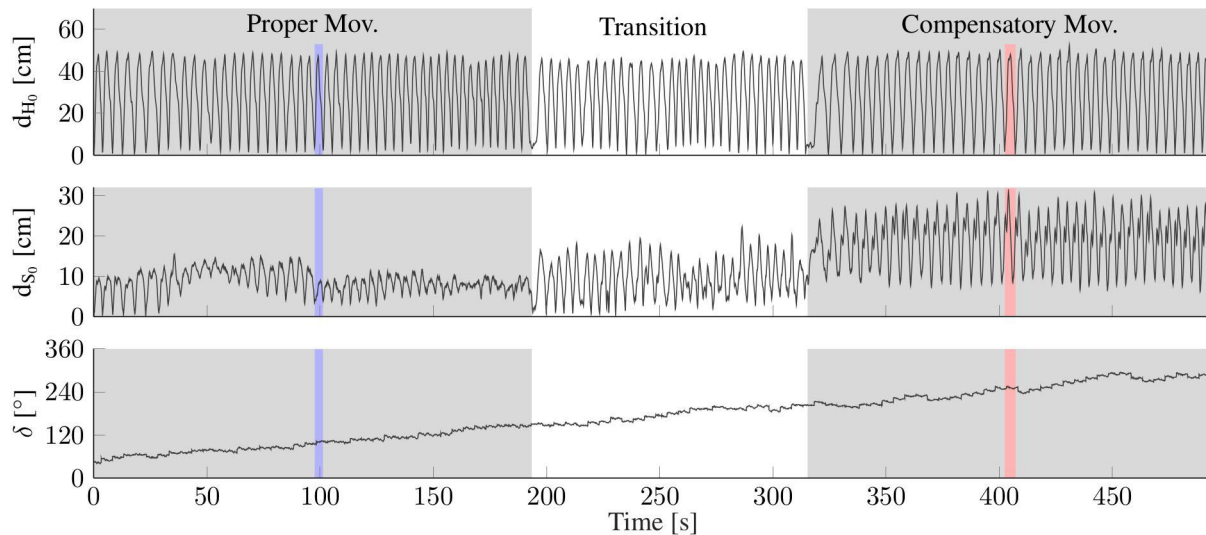


FIGURE 7 | Exemplary data from one complete trial of one subject with colored vertical bands highlighting the time periods of exemplary trials (cf. **Figures 8, 9**). **(Top/Middle)** Distance of the hand (d_{H_0}) and shoulder (d_{S_0}) from their respective initial positions at $t = 0$, as measured by the optical reference (*opt.ref.*). While hand motion is similar, the proper and compensatory movements exhibit clearly different amounts of shoulder motion. **(Bottom)** The upper arm heading offset (δ) drifts by more than 180° within the 8-min trial.

and upper arm length (28–33 cm). During the trials, each subject sits on a chair with the right arm connected to the Diego system as shown in **Figure 2**. Both ropes of the robotic system Diego are attached at the forearm and the IMU (MTxTM, Xsens, Netherlands) is fixed on the lateral aspect of the upper arm (approximately midway along the longitudinal axis). The weight relief of both ropes is adjusted to 6 N to assure tightly stretched ropes, which minimizes position measurement errors. A standard PC (Intel®, CoreTM i5 with four cores) running Linux (Ubuntu 18.04) was utilized to run the software and connect to the devices. The control algorithms and device interfaces were implemented in Matlab/Simulink (MATLAB R2017b; MathWorks, USA) and C/C++ using a modified Linux real-time target to generate an executable (Sojka and Piša, 2014). Using this setup, the methods are found to be highly real-time-capable. The real-time-critical magnetometer-free orientation estimation algorithm part is definitely able to run at the sampling rate of the sensor (here 100 Hz), even on-board the sensor. The most time-consuming part of the methods is the heading estimation including the joint acceleration disagreement. This non-real-time-critical procedure requires about half a second of computation time and must be executed every 5 s in parallel to the real-time-critical part.

A box-shaped object (suitcase) is placed on a table in front of the subject at such height that its top surface is slightly lower than the shoulder. The outer edge of that surface marks a rectangular path that the right hand should follow in counterclockwise cyclic motions, as illustrated in **Figure 6**. Note that the path is dimensioned and positioned such that the subject can comfortably perform the motion by shoulder joint and elbow joint motions, i.e., without bending the trunk and without considerable displacements of the shoulder. This ensures that each subject can conduct

both the proper and the compensatory movements as defined in **Section 3.4**.

The subjects are asked to perform each of both movements for time periods of at least two and up to 5 min. In the transition phase between both time periods, the subjects are instructed to slowly increase the level of compensatory movements and to accustom themselves to the unnatural motion performance. Both time periods and the transition phase are indicated in **Figure 7**, while the difference between proper and compensatory motion is illustrated in **Figure 6**.

A camera (Canon EOS 600D) is positioned above the subject to obtain reference measurements of positions and angles in the horizontal plane of the motion. The trials are recorded with a frame rate of 50 frames per second and a resolution of $1,280 \times 720$ pixels. Three adhesive labels (blue filled circle on a bigger white circle, cf. **Figure 6**) are affixed on the subject's arm—one on the center of the back of the hand, another one on the skin above the center of the shoulder joint, and a third one close to the elbow joint but with sufficient distance to the proximal forearm cuff to assure visibility of the marker from above.

After each trial, the trajectories of the markers are reconstructed from the recorded video by means of the open source software Kinovea (<https://www.kinovea.org>), and the elbow angle as well as the heading of the upper arm are calculated using standard vector algebra. This yields an approximate ground truth, which is hereafter termed *optical reference* (*opt.ref.*).

The robotic workspace coordinate system and the one of the *opt.ref.* were initially calibrated and aligned with each other. For this purpose, the length and width of the suitcase were measured. The robot's coordinate system was calibrated by measurements of each cable while they were subsequently pulled to all four edges of

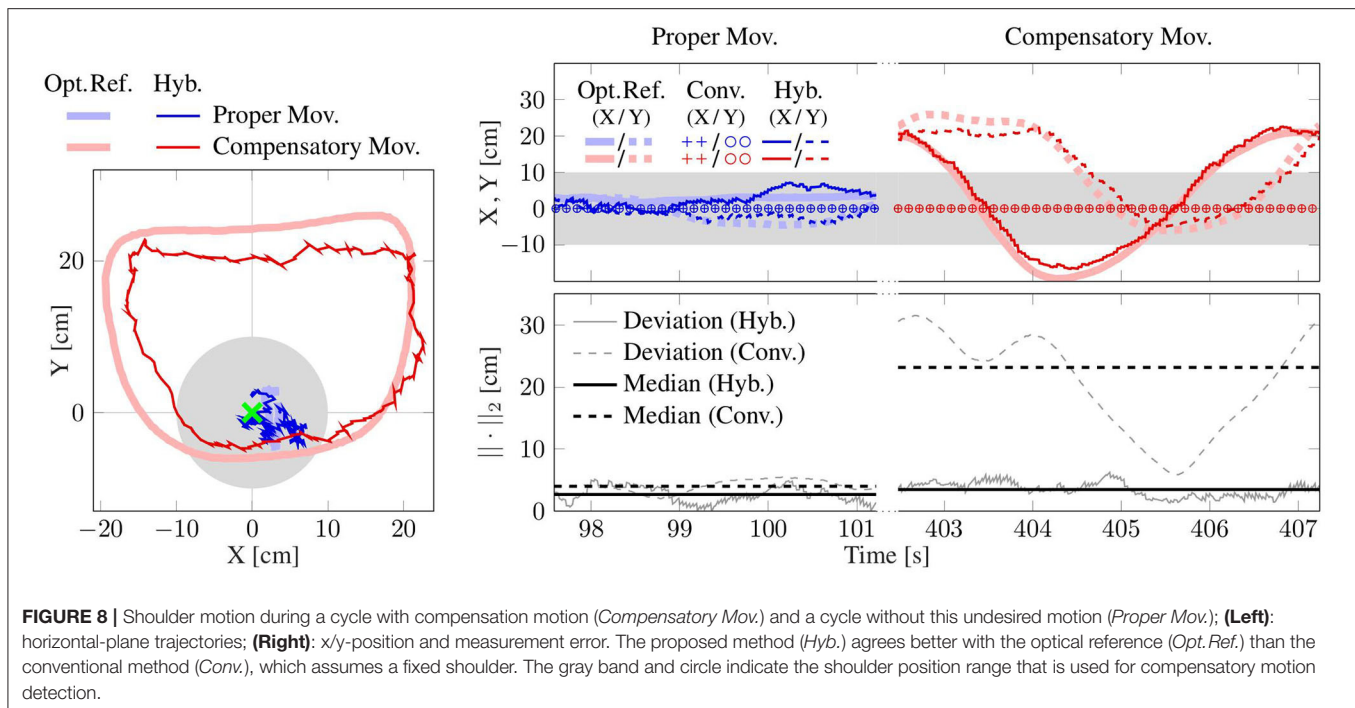


TABLE 1 | Estimated shoulder position deviations (Euclidean distance) from *opt.ref.*, medians over all subjects in centimeter.

Type	Method	Median	Probability/Correlation
Proper mov.	Conv.	3.9	$p = 0.106, r = 0.003$
	Hyb.	3.7	
Compensatory mov.	Conv.	20.1	$p < 0.001, r = 0.845$
	Hyb.	4.1	

A Welch's T-test (probability p and Pearson correlation coefficient r) between *Conv.* and *Hyb.* yields no significant effect for *prop.mov.*, but a large effect for *comp.mov.*

the suitcase. For the *opt.ref.*, the length and width of the suitcase were adjusted in the software Kinovea. The nominal shoulder position $\mathcal{R}\mathbf{p}_s^{\text{nom}}$ of the robot alone, as explained in Section 4.1, was initially determined by one rope pulled to the shoulder joint just before each trial. This nominal shoulder position was set as the origin of both the *rob.* and *opt.ref.* coordinate systems.

4.3. Experimental Results

The proposed method for hybrid motion tracking is validated on recorded data of experimental trials with five subjects as outlined above. On average they performed *prop.mov.* for around 4:15 min [3:13 (S2)–5:00 (S4) min] and *comp.mov.* for around 2:47 min [2:04 (S4)–4:09 (S1) min]. This resulted in an average of 57 [45 (S2)–69 (S1)] *prop.mov.* cycles and in an average of 33 [16 (S4)–48 (S1)] *comp.mov.* cycles. The average cycle time of all five subjects is 4.6 s for the *prop.mov.* and 5.4 s for the *comp.mov.*

The validation results of all five subjects are given in Figures 10–12 as well as in Tables 1–3. Detailed insights are

provided by plots of exemplary data from S2 shown in Figures 7–9 as well as in Figure 6.

Figure 7 presents the motion of the hand and shoulder with respect to the initial position that is defined at time 0. The figure also depicts the heading offset δ for the entire duration of the experiment for S2. The hand moved along the same path throughout the experiment. However, while the shoulder displacements are mostly below 10 cm for *prop.mov.*, the shoulder deviates between 10 and 30 cm during the *comp.mov.* from the nominal shoulder position. The colored vertical bands in Figure 7 highlight the time periods of exemplary trials, for which detailed data is presented in Figures 8, 9. In Figure 6, for both highlighted time periods, four still images of the camera system are superimposed, and trajectories of the hand, elbow and shoulder markers are indicated.

The plot at the bottom of Figure 7 shows that the heading offset of the magnetometer-free inertial orientation estimation is drifting at $\sim 0.5 \text{ deg/s}$ during the entire experiment due to integration of gyroscope bias. This observation is in good agreement with *a-posteriori* analysis of the gyroscope readings during rest, which revealed bias magnitudes of 0.1–0.76 deg/s (average of 0.34 deg/s) for the utilized IMU. Note that the proposed method does *not* require initial rest phases or static gyroscope calibration and that the aforementioned bias values were only determined for validation purposes but *not* removed from the gyroscope readings at any point.

4.3.1. Shoulder Position Results

The shoulder position is estimated using the upper arm orientation and the elbow position (see Section 3.4). For one exemplary trial of both movement types, Figure 8 depicts the

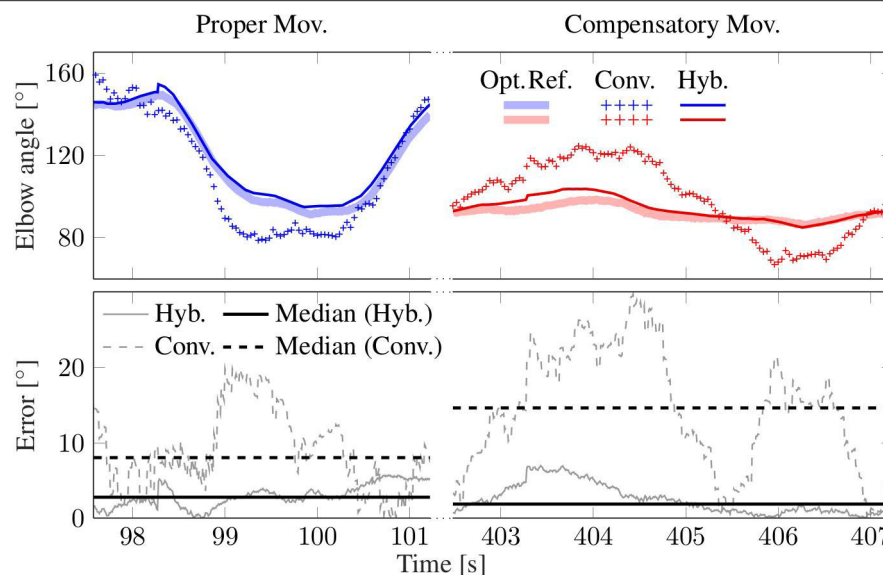


FIGURE 9 | Elbow angle from a trial with compensatory movement (*Compensatory Mov.*, red) and another without (*Proper Mov.*, blue). The result of the hybrid method (*Hyb.*) agrees well with the optical reference (*Opt.Ref.*), while the conventional method (*Conv.*) that assumes a constant shoulder position yields clearly larger errors, especially in the case of *comp.mov.*

TABLE 2 | Estimated elbow angle errors with respect to *opt.ref.*, median values over all subjects in degree.

Type	Method	Median	Probability/Correlation
Proper mov.	Conv.	9.3	$p < 0.001, r = 0.706$
	Hyb.	2.3	
Compensatory mov.	Conv.	16.3	$p < 0.001, r = 0.724$
	Hyb.	3.6	

A Welch's T-test (probability p and Pearson correlation coefficient r) between *Conv.* and *Hyb.* yields large effects for both, *prop.* and *comp.mov.*

motion in the horizontal plane. The deviation from the *opt.ref.* is calculated using the Euclidean norm. The *hyb.* estimates shown in **Figure 8** agree well with the *opt.ref.*, with median values below 4 cm. The *conv.method* assumes a fixed shoulder position, which works adequately for *prop.mov.* but yields errors above 20 cm during the depicted *comp.mov.* cycle. Here, the robot does not measure any shoulder motion and the resulting *conv.* errors reproduce the actually conducted shoulder motion as measured by the *opt.ref.* The presented exemplary results are consistent with the medians over all subjects (see **Table 1**), which are all close to 4 cm except for the median of 20.1 cm of the *conv.method* during *comp.mov.*

Figure 10 shows the distributions of the deviations from the *opt.ref.* for conventional (*conv.*) measurements and for the results of the proposed hybrid (*hyb.*) methods. The upper whisker represent the 95th percentile and the lower one the 5th percentile of all values over time. The inner boxes themselves depict the quartiles, i.e., the 25th percentile, the median and the 75th percentile. All time-based medians of the proposed *hyb.method* are near or below 5 cm, and all corresponding upper whiskers

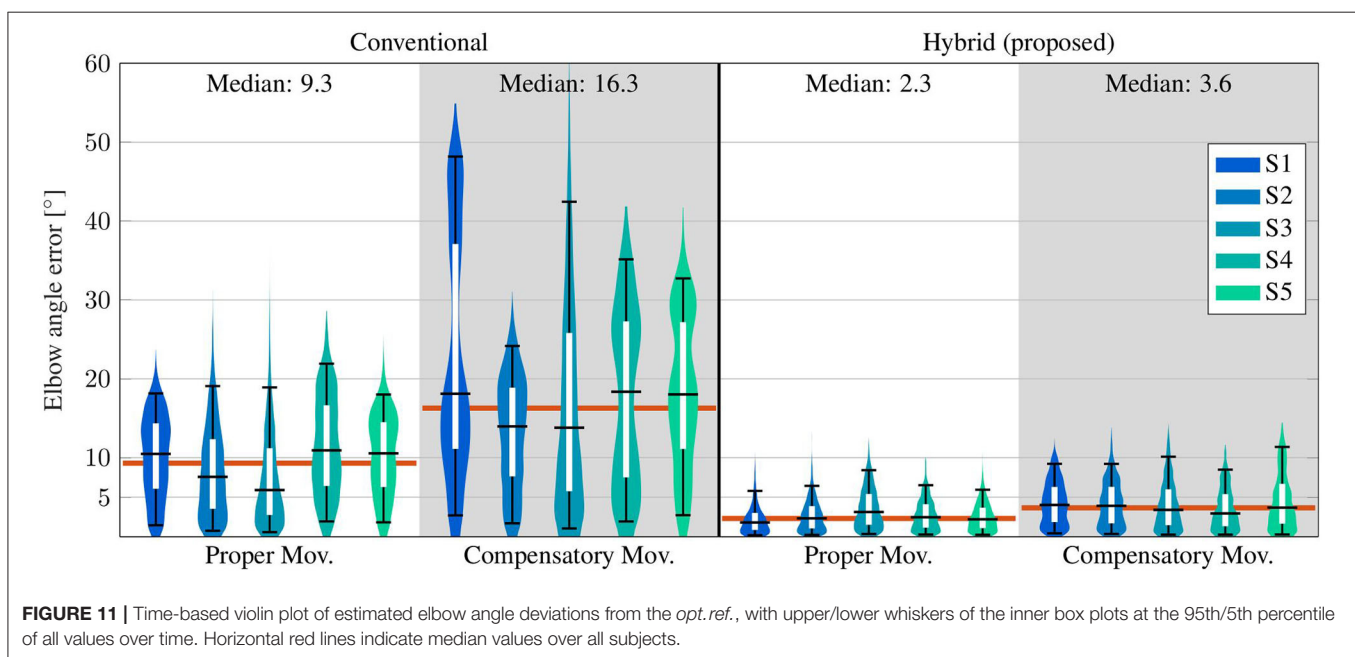
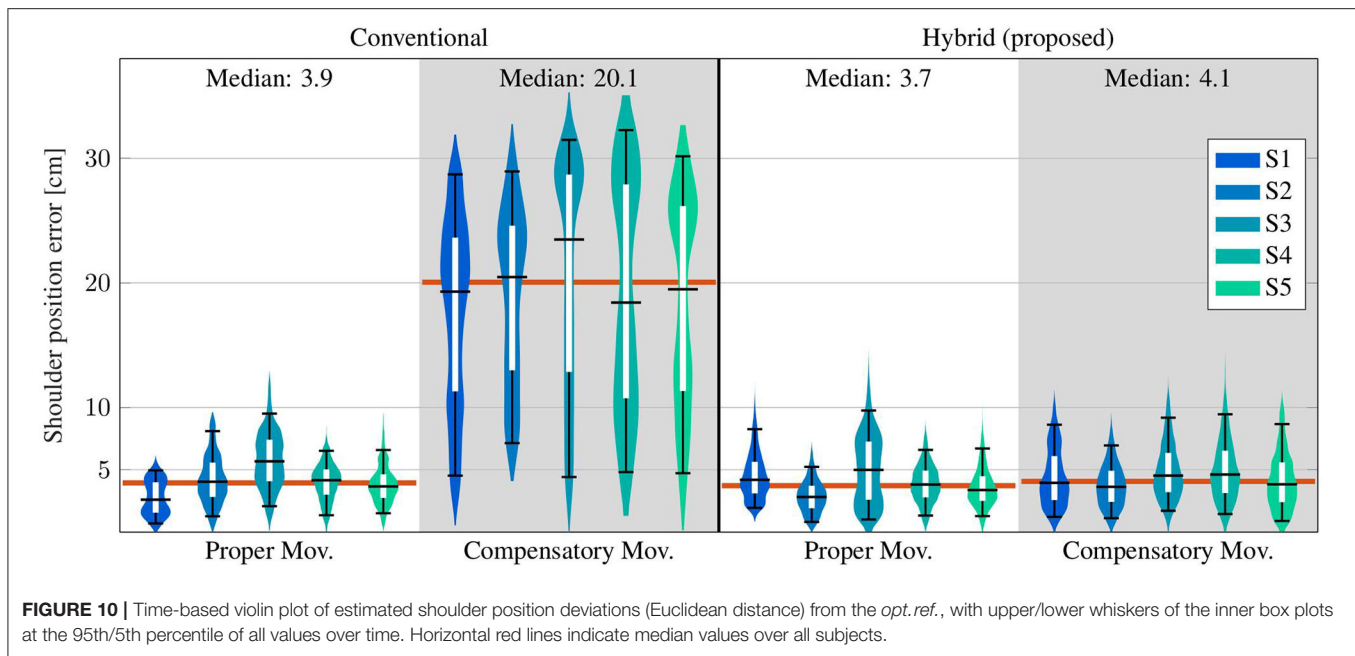
stay below 10 cm. The results of the conventional (*conv.*) method are comparable for the *prop.mov.*, but reach significantly higher time-based medians of up to 23.5 cm (S3) and upper-whisker values up to 32.3 cm (S4) for the *comp.mov.* Welch's *T*-test states a large effect for *comp.mov.* (probability $p < 0.001$ and Pearson correlation coefficient $r = 0.845$). No significant effect is stated for *prop.mov.* with $p = 0.106$ and $r = 0.003$.

4.3.2. Elbow Angle Results

The elbow angles of exemplary motion cycles are shown in **Figure 9**. The results, as presented in that figure, of the proposed *hyb.method* resemble the *opt.ref.* signals even during *comp.mov.*, and medians below 3° are achieved. In contrast, deviations of up to 20° occur with the *conv.method* even in the *prop.mov.* cycle, and the median during the *comp.mov.* cycle reaches almost 15°. These results are consistent with the results over all subjects, as presented in **Table 2** and **Figure 11**. All time-based median deviations between the *hyb.* measurement and the *opt.ref.* are near or below 4°, and the 95th percentiles mostly stay below 10°. The *conv.* measurements yield significantly larger time-based medians in the range of 5.9–18.4° and upper whiskers with up to 48.2°. Welch's *T*-test states large effects for both, *prop.* and *comp.mov.*, with $p < 0.001$ and $r > 0.7$.

4.3.3. Parameter Sensitivity Analysis

The distance $_{AP}E$ of the IMU to the elbow joint, the length l_A of the adjacent segment (here upper arm) and the cutoff frequency for the determination of the time derivative $_{A}\dot{\omega}_A$ have to be manually determined or chosen. We perform a parameter sensitivity analysis to investigate their impact on the estimated

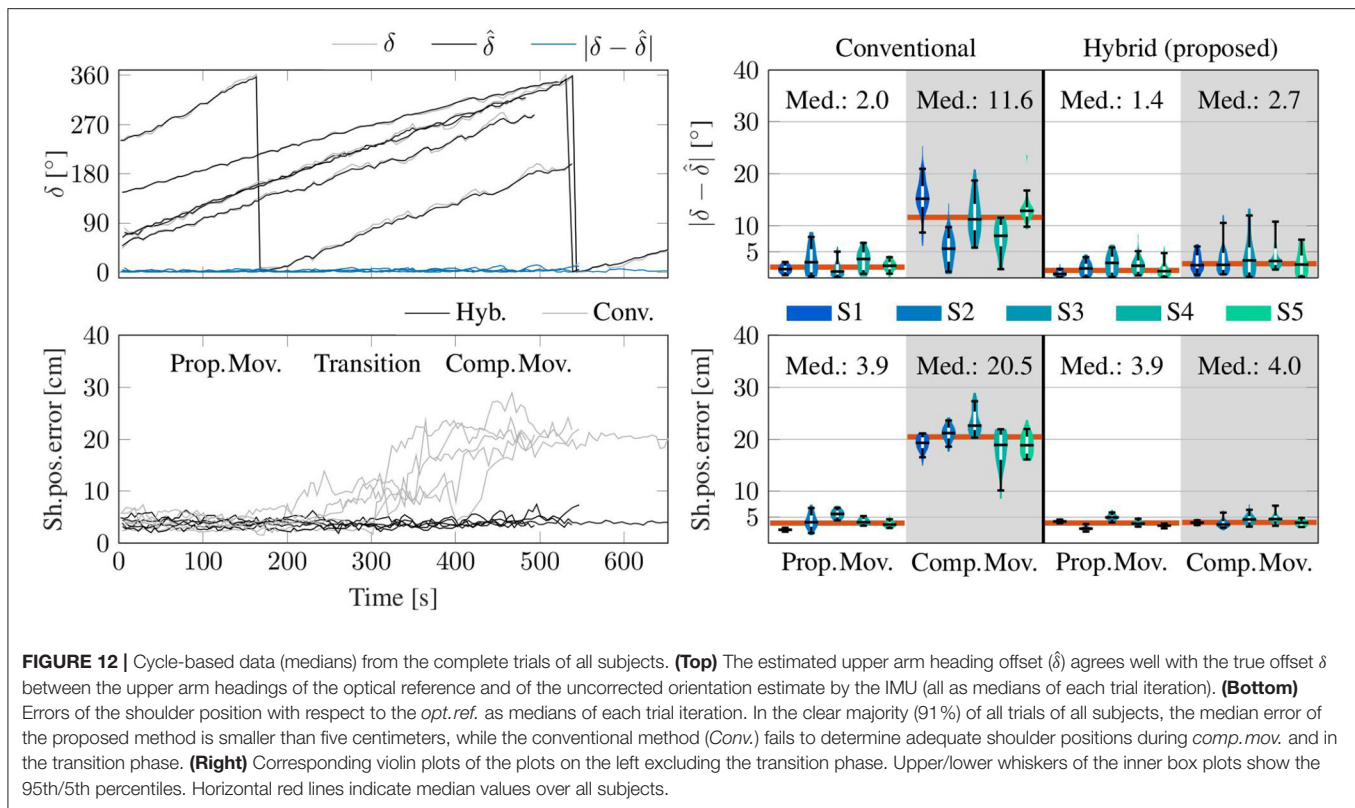


shoulder position and elbow angle. None of these parameters is particularly sensitive.

The distance l_{PE} was chosen as 15 cm, which is approximately half the average upper arm length of humans; e.g., Chaffin et al. (2006) recommend 28.1 and 29.8 cm for the upper arm length of female and male humans, respectively. We now consider the case in which the assumed and the actual IMU-to-elbow distance differ by 7.5 cm, and we investigate how the measurement errors reported in Sections 4.3.1 and 4.3.2 are affected by this parameter change. The median measurement deviations increase by 0.06 cm (shoulder position) and 0.21°

(elbow angle) on average over all subjects. This corresponds to relative changes of <2% in the median shoulder position error and <8% in the median elbow angle error. The 95th percentile errors increase by 0.17 cm and 0.41° on average over all subjects, respectively. This corresponds to relative changes of <3% in the 95th percentile shoulder position error and <6% in the 95th percentile elbow angle error. The corresponding intra-subject changes are reported in detail in Supplementary Tables 1, 2.

The length l_A of the upper arm was measured manually. We now consider the case in which the measured upper length



differ by ± 2.5 cm, and we investigate how the measurement errors are affected by these parameter variations. They have no impact on the accuracy of the elbow angle results but on the shoulder position error. We call that this error is defined as the difference between the *hybrid* and the *opt.ref.* displacements of the shoulder with respect to the nominal position. Since the considered parameter change also affects the nominal shoulder position of the *hybrid* measurement, it does not lead to a direct offset in the shoulder displacement but has a more indirect effect. The median measurement errors of the shoulder position change by 0.05 cm ($I_A + 2.5$ cm) and 0.07 cm ($I_A - 2.5$ cm) on average over all subjects. This corresponds to relative changes of $<2\%$ in the median shoulder position error. The 95th percentile errors change by 0.58 and -0.36 cm on average over all subjects, respectively. This corresponds to relative changes of $<8\%$ in the 95th percentile shoulder position errors. The corresponding intra-subject changes are reported in detail in **Supplementary Table 3**.

The cutoff frequency for the determination of the time derivative $\dot{\omega}_A$ was chosen as 2.5 Hz. We now consider variations of ± 1 Hz, and we investigate how the measurement errors are affected by these parameter changes. The median measurement deviations change by <0.005 cm (cutoff frequency + 1 Hz) and by -0.01 cm (cutoff frequency -1 Hz) for the shoulder position, and by $<0.005^\circ$ (cutoff frequency ± 1 Hz) for the elbow angle on average over all subjects. This corresponds to relative changes of $<1\%$ in the median shoulder position error and $<1\%$ in the median elbow angle error. The 95th percentile errors change by <0.005 cm and $<0.005^\circ$ (cutoff frequency ± 1 Hz)

on average over all subjects, respectively. This corresponds to relative changes of $<1\%$ in the 95th percentile shoulder position errors and $<1\%$ in the 95th percentile elbow angle errors. The corresponding intra-subject changes are reported in detail in **Supplementary Tables 4, 5**.

4.3.4. Long-Time Stability Analysis

The cycle-based medians of the shoulder position errors of the hybrid method and the conventional method with respect to the *opt.ref.* are shown in **Figure 12**. It is evident that the results of the proposed *hyb.method* constantly remain around 3–5 cm and no linear long-time trend is present. This is in line with the results presented in the violin plot on the bottom right of **Figure 12**: the median cycle-based errors between the *hyb.* measurement and the *opt.ref.* stay below 5 cm for all subjects (95th percentiles between 3.7 and 7.4 cm) and around 4 cm over all subjects. The *conv.* measurements yield significantly larger medians up to 22.6 cm (20.5 cm over all subjects) and upper whiskers with up to 27.3 cm in the case of *comp.mov.*. The estimated upper arm heading offset $\hat{\delta}$ is also depicted as cycle-based medians over all trials of all subjects and reveals long-time stable estimates of the heading offset with absolute errors remaining under 5° for 90% of the measurements. This is in line with the results shown in the violin plot on the top right of **Figure 12**: the median absolute errors of the estimated upper arm heading offset stay below 4° for all subjects (95th percentiles between 1.7 and 12.0°) and the median absolute errors over all subjects are 1.4 and 2.7° for *prop.mov.* and *comp.mov.*, respectively.

TABLE 3 | Table of confusion for real-time detection of compensatory motion from data of a single motion cycle.

Subject	Actual type	Predicted type	
		Prop.	Comp.
S1	Prop.	69	0
	Comp.	0	48
S2	Prop.	45	0
	Comp.	0	40
S3	Prop.	61	0
	Comp.	0	31
S4	Prop.	47	0
	Comp.	0	16
S5	Prop.	62	0
	Comp.	0	28

4.3.5. Compensatory Motion Detection Results

The estimated shoulder position is utilized to detect compensatory movements, for which biofeedback can be provided as described in **Section 3.4**. A tolerated compensatory shoulder motion range of ± 10 cm is shown in the exemplary plots of **Figure 8**. The detection algorithm identifies *comp.mov.*, i.e., displacements of the shoulder which might be due to a not correctly fixated patient's shoulder or that the patient does not follow the instruction to move with a fixed shoulder position, when the tolerated shoulder range of ± 10 cm is exceeded for more than 20% of the duration of a trial. **Table 3** demonstrates that all 284 *prop.mov.* cycles are correctly recognized as proper and that all 163 *comp.mov.* cycles are likewise correctly classified, i.e., all 447 cycles out of 447 cycles are correctly classified.

5. DISCUSSION

The proposed augmentation of end-effector-based robotic systems leads to considerable improvements in the considered application scenario of the cable-based upper-limb rehabilitation robot. It provides accurate shoulder motion measurements in real time with time-based median measurement errors around 4 cm (all 95th percentiles below 10 cm) as well as real-time elbow angle measurements with time-based median errors below 4° (95th percentiles mostly below 10°). This is, particularly during compensatory movements, a significant improvement compared to the conventional approach of assuming a fixed shoulder position during end-effector-based therapy (Dipietro et al., 2007; Rosati et al., 2007). In **Section 4.3.4**, it is shown that the cycle-based medians of the shoulder position errors of the proposed method constantly remain around 3–5 cm (91% are smaller than 5 cm). Thus, the accuracy over one course of the conducted motion is within the range, which meets the requirements we defined toward the end of **Section 2**.

This accuracy is comparable to the results presented by Bertomeu-Motos et al. (2015a), which uses a magnetometer-based approach that was shown to depend on unrealistic or restrictive homogeneity properties of the magnetic field

(Madgwick et al., 2011; Seel and Ruppel, 2017; Salchow-Hömmen et al., 2019). Such an assumption is known to be violated if robot components, nearby furniture or objects that are handled by the subjects contain iron or other ferromagnetic materials or electronic components. In fact, magnetic fields inside buildings are so inhomogeneous that their patterns can be analyzed for indoor localization and mapping (Le Grand and Thrun, 2012; Subbu et al., 2013; Shu et al., 2015). For this reason magnetometers do *not* provide reliable heading information for robust motion tracking in indoor environments. The fact that the methods proposed in **Section 3** are magnetometer-free makes them highly suitable for indoor applications and realistic robotic environments. Long-time stability of the estimated positions and orientations is achieved, and the proposed methods are highly real-time-capable as described above. The combination of these properties defines the novelty of the current approach with respect to previous methods. One previous method (Wittmann et al., 2019) exploits the patterns of the magnetic field in indoor environments and only relies on IMUs. It provides accurate estimates of the arm motion, however it requires the user to rest in-between the therapy session to re-correct the magnetometer-based drift. In contrast, the proposed method is magnetometer-free and does not need that the user rests at any time. Additionally, applied rehabilitation robots modify the magnetic field due to their ferromagnetic materials, which will influence the accuracy of the method by Wittmann et al. (2019). Furthermore, the proposed approach provides the shoulder joint position in the robotic coordinate system, which cannot be provided by algorithms that do not include measurements of the robot. This is also the case for other methods providing accurate estimates of the arm orientation solely based on IMUs (Kok et al., 2014). The latter approach by Kok et al. (2014) is even magnetometer-free, however it cannot directly be implemented in real-time. The proposed method of the current article is novel in the sense that it provides long-time stable, magnetometer-free, and real-time estimates of the orientation of the adjacent segment and the endpoint of that segment, e.g., shoulder position, in the robotic coordinate frame.

Although all motions are performed in a horizontal plane, the two-dimensional optical motion tracking yields only an approximate ground truth. In preliminary trials, we investigated the variance of the distance between the elbow and shoulder marker. This distance, which should ideally be constant, has been found to have standard deviations between at least 0.7 cm (S2) and at most 1.2 cm (S3) around their mean value. We conclude that this approximate ground truth is sufficiently precise for the desired proof of concept.

Limitations of the validation are that healthy subjects performed the motions and that the accuracy of the approximate optical ground truth does not achieve the same level as the golden standard of marker-based stereophotogrammetric tracking systems, which is mainly due to the horizontal projection, distortions by the camera lens symmetry, and marker displacement caused by skin and muscle motion. As mentioned above, the resulting inaccuracies of the camera-based reference measurements are below 5 cm, which is small enough for the present proof-of-concept study but not small

enough to decide whether the proposed method yields accuracies below state-of-the-art results. Furthermore, a limitation of the proposed methods is the number of parameters and that their ideal choice is not yet clear. However, first investigations, as described in **Section 4.3.3**, revealed that their sensitivity against changes is not severe. Variations of the cutoff frequency of ± 1 Hz cause only negligible changes in the range of 1% in the measurement accuracy. The sensitivity of the measurement errors to displacements of the IMU seems acceptable in practice if the user places the sensor within a 15 cm (± 7.5 cm) wide area around the middle of the upper arm; even a distance of 7.5 cm between assumed and actual position causes error increases below 8% of the original error. To interpret the sensitivity of the proposed methods against inexact upper-arm lengths, consider a 1.50 and a 1.90 m tall subject with average upper-arm lengths of 27.9 and 35.3 cm, respectively Winter (2005). Even if one simply uses the proposed 30 cm for both subjects, the measurement error increase can be expected to stay below 5% in both cases. In sum, the proposed methods are not very sensitive against these parameters and they can be used with the proposed values in practice without jeopardizing the measurement accuracy.

It is worth noting that the proposed methods can be extended to cases in which the motion of more segments than only the directly adjacent body segment is of interest. For example, if the foot is connected to an end-effector-based robotic system, then we might want to track the motion of the shin and the thigh. In such a case, the proposed method can be used with an IMU on the shin to track the knee position. This knee position estimate might then be used to apply the method again with an IMU on the thigh and determine the hip joint position. While the feasibility of such a cascaded approach follows directly from the properties of the proposed methods, further research is needed to investigate which levels of accuracy can be achieved in practice and also which performance is achieved by the proposed methods in other application scenarios.

As mentioned in **Section 1**, preventing compensation during rehabilitation training improves the therapy outcome and decreases long-term problems, such as pain, orthopedic illnesses and learned non-use (Levin et al., 2009). One possibility to avoid compensation are trunk and shoulder girdle restraints. Their effects are discussed diversely in the literature. For example, 5 of 8 studies named by Greisberger et al. (2016) showed improvements of arm motion recovery, whereas one of the included studies states auditory feedback as more effective on movement patterns directly after training, and the other two studies did not reveal any effect. In conclusion, Greisberger et al. (2016) considered the magnitude of change of the observed improvements as not consistently clinically relevant. Indisputably there is an additional donning and doffing effort, as well as a restriction of natural trunk and shoulder girdle motion, which can also be seen in healthy people performing arm movements. These disadvantages can be avoided by using real-time biofeedback. In contrast to trunk and shoulder restraint, biofeedback can be adapted to the needs of the individual, e.g., in the case of progress (Valdés and der Loos, 2017). Furthermore, indications suggest that improvements are rather maintained after feedback that is only provided when it is needed than after training

with concurrent physical guidance (Schmidt and Lee, 2014). One possibility to detect compensation motion would be the additional use of more IMUs as, e.g., on the torso. However, the tracking of the trunk or shoulder position is severely limited due to the occurring position drift. It is, of course, possible to detect inclination changes, but translational motion of the trunk without bending the torso would not be detectable nor drift-free estimable. To detect motions of the shoulder girdle, even more IMUs and thus more donning and doffing would be required. Using only one IMU and the already available measurements of the robot, as proposed here, reduces the hardware effort and provides a drift-free and accurate tracking of the shoulder position, that can be utilized to detect compensation motion of the trunk and shoulder. In sum, the natural trunk and shoulder motion is not restricted with the proposed solution, while still the full monitoring of compensatory movements is possible facilitating biofeedback when needed. Cirstea and Levin (2000) found mean shoulder displacements of 14 cm for moderate to severe impaired stroke subjects and around 4 cm for healthy participants. Valdés and der Loos (2017) stated 3 cm of shoulder-spine motion as physiological movements. The experimental results in **Section 4.3** show that the proposed method can reliably distinguish between small shoulder displacements and shoulder displacements of more than 10 cm that are performed to compensate reduced motion in other joints. The proposed and applied toleration of range violations for up to 20% of the trial duration can of course be replaced by a tolerated time period in case of non-repetitive motions. In our case, the 20% of the trial duration equated to a time period of one second, which would have led to the same perfect classification results. It is, of course, necessary to determine the appropriate degree of compensatory motion detection in clinical use, individually for the desired therapy application and setting, i.e., when is a biofeedback helpful and not useless or annoying.

6. CONCLUSIONS

End-effector-based rehabilitation robots offer motion support with fast and easy robot-to-patient setup and adjustment. This advantage is, however, achieved at the cost of a reduced amount and accuracy of motion measurement information. A conventional solution is to rely on a fixed shoulder position assumption (Dipietro et al., 2007; Rosati et al., 2007). We demonstrated that these limitations can be overcome by a hybrid system design that uses wearable inertial sensors and real-time sensor fusion methods without requiring a clear line-of-sight and thus overcomes a major restriction in depth-camera-based designs. The proposed approach accurately tracks the motion of a body segment that is adjacent to the robot-connected body segment. It assures long-time stability and complete immunity to magnetic disturbances, which are common in indoor applications and robotic environments. The generalizability and the transfer of the proposed method's benefits to other kinematic chains and application scenarios are expected but cannot be guaranteed from the investigated particular setup. Consequently, this has to be investigated and demonstrated in future work.

We demonstrated that the method can be used to infer real-time estimates of the complete orientation of the upper

arm and the shoulder position in the robotic frame. This enables the detection of undesirable compensatory trunk and shoulder motions in upper-limb rehabilitation training and thus facilitates real-time biofeedback, which is expected to improve active involvement and therapy outcome (Levin et al., 2009). Clinical validation in neurological patients will be subject of future research. Simultaneously, it will be investigated if the hybrid system can be utilized for feedback-controlled Functional Electrical Stimulation (FES) and what its impact on such solutions is.

Beyond the proposed methods, we believe that the general approach of augmenting easy to setup end-effector-based robotic systems with wearable sensors is promising and might provide additional advantages over existing solutions in a range of application scenarios, in which accurate real-time motion tracking is required to realize feedback control, objective motion assessment or biofeedback.

DATA AVAILABILITY STATEMENT

The raw data supporting the conclusions of this article will be made available by the authors, without undue reservation.

ETHICS STATEMENT

The studies involving human participants were reviewed and approved by Berlin Chamber of Physicians. The patients/participants provided their written informed consent to participate in this study. Written informed consent

was obtained from the individual(s) for the publication of any potentially identifiable images or data included in this article.

AUTHOR CONTRIBUTIONS

AP, TSc, and TSe: conceptualization, investigation, and writing—review and editing. AP and TSe: formal analysis, methodology, software, visualization, and writing—original draft. TSc and TSe: funding acquisition and supervision. All authors contributed to the article and approved the submitted version.

FUNDING

The work was partially funded by a research scholarship for young researchers of the Verein zur Förderung des Fachgebietes Regelungssysteme an der Technischen Universität Berlin e.V. It was also partially conducted within the research project BeMobil, which is supported by the German Federal Ministry of Education and Research (BMBF) (FKZ16SV7069K). We acknowledge support by the German Research Foundation and the Open Access Publication Fund of TU Berlin.

SUPPLEMENTARY MATERIAL

The Supplementary Material for this article can be found online at: <https://www.frontiersin.org/articles/10.3389/frobt.2020.554639/full#supplementary-material>

REFERENCES

- Bertomeu-Motos, A., Blanco, A., Badesa, F. J., Barios, J. A., Zollo, L., and Garcia-Aracil, N. (2018). Human arm joints reconstruction algorithm in rehabilitation therapies assisted by end-effector robotic devices. *J. Neuroeng. Rehabil.* 15:10. doi: 10.1186/s12984-018-0348-0
- Bertomeu-Motos, A., Lledó, L. D., Díez, J. A., Catalan, J. M., Ezquerro, S., Badesa, F. J., et al. (2015a). Estimation of human arm joints using two wireless sensors in robotic rehabilitation tasks. *Sensors* 15, 30571–30583. doi: 10.3390/s151229818
- Bertomeu-Motos, A., Morales, R., Lledó, L. D., Díez, J. A., Catalan, J. M., and Garcia-Aracil, N. (2015b). “Kinematic reconstruction of the human arm joints in robot-aided therapies with Hermes robot,” in *2015 37th Annual International Conference of the IEEE Engineering in Medicine and Biology Society (EMBC)* (Milan), 1190–1193. doi: 10.1109/EMBC.2015.7318579
- Brokaw, E. B., Lum, P. S., Cooper, R. A., and Brewer, B. R. (2013). “Using the kinect to limit abnormal kinematics and compensation strategies during therapy with end effector robots,” in *2013 IEEE 13th International Conference on Rehabilitation Robotics (ICORR)*, (Seattle, WA) 1–6. doi: 10.1109/ICORR.2013.6650384
- Burgar, C. G., Lum, P. S., Shor, P. C., and Van der Loos, H. M. (2000). Development of robots for rehabilitation therapy: The Palo Alto VA/Stanford experience. *J. Rehabil. Res. Dev.* 37, 663–674.
- Chaffin, D. B., Andersson, G. B. J., and Martin, B. J. (2006). *Occupational Biomechanics*. New Jersey, NJ: John Wiley & Sons.
- Cirstea, M. C., and Levin, M. F. (2000). Compensatory strategies for reaching in stroke. *Brain* 123, 940–953. doi: 10.1093/brain/123.5.940
- Cortés, C., de los Reyes-Guzmán, A., Scorza, D., Bertelsen, Á., Carrasco, E., Gil-Agudo, Á., et al. (2016). Inverse kinematics for upper limb compound movement estimation in exoskeleton-assisted rehabilitation. *Biomed. Res. Int.* 2016:2581924. doi: 10.1155/2016/2581924
- de Vries, W. H. K., Veeger, H. E. J., Baten, C. T. M., and van der Helm, F. C. T. (2009). Magnetic distortion in motion labs, implications for validating inertial magnetic sensors. *Gait Posture* 29, 535–541. doi: 10.1016/j.gaitpost.2008.12.004
- Dipietro, L., Krebs, H. I., Fasoli, S. E., Volpe, B. T., Stein, J., Bever, C., et al. (2007). Changing motor synergies in chronic stroke. *J. Neurophysiol.* 98, 757–768. doi: 10.1152/jn.01295.2006
- Filippeschi, A., Schmitz, N., Miezal, M., Bleser, G., Ruffaldi, E., and Stricker, D. (2017). Survey of motion tracking methods based on inertial sensors: a focus on upper limb human motion. *Sensors* 17:1257. doi: 10.3390/s17061257
- Gowland, C., DeBruin, H., Basmajian, J. V., Plews, N., and Burcea, I. (1992). Agonist and antagonist activity during voluntary upper-limb movement in patients with stroke. *Phys. Ther.* 72, 624–633. doi: 10.1093/ptj/72.9.624
- Greisberger, A., Aviv, H., Garbade, S. F., and Diermayr, G. (2016). Clinical relevance of the effects of reach-to-grasp training using trunk restraint in individuals with hemiparesis poststroke: a systematic review. *J. Rehabil. Med.* 48, 405–416. doi: 10.2340/16501977-2077
- Grimm, F., Naros, G., and Gharabaghi, A. (2016). Compensation or restoration: closed-loop feedback of movement quality for assisted reach-to-grasp exercises with a multi-joint arm exoskeleton. *Front. Neurosci.* 10:280. doi: 10.3389/fnins.2016.00280
- Held, J. P. O., Klaassen, B., Eenhoorn, A., van Beijnum, B. -J. F., Buurke, J. H., Veltink, P. H., et al. (2018). Inertial sensor measurements of upper-limb kinematics in stroke patients in clinic and home environment. *Front. Bioeng. Biotechnol.* 6:27. doi: 10.3389/fbioe.2018.00027
- Jakob, I., Kollreider, A., Germanotta, M., Benetti, F., Cruciani, A., Padua, L., et al. (2018). Robotic and sensor technology for upper limb rehabilitation. *PM&R* 10, 189–197. doi: 10.1016/j.pmrj.2018.07.011

- Kirk, A., O'Brien, J., and Forsyth, D. (2005). "Skeletal parameter estimation from optical motion capture data," in *2005 IEEE Computer Society Conference on Computer Vision and Pattern Recognition (CVPR'05)*, Vol. 2 (San Diego, CA), 782–788. doi: 10.1109/CVPR.2005.326
- Kok, M., Hol, J. D., and Schön, T. B. (2014). An optimization-based approach to human body motion capture using inertial sensors. *IFAC Proc. Vol.* 47, 79–85. doi: 10.3182/20140824-6-ZA-1003.02252
- Laidig, D., Lehmann, D., Bégin, M., and Seel, T. (2019). "Magnetometer-free realtime inertial motion tracking by exploitation of kinematic constraints in 2-DOF joints," in *2019 41st Annual International Conference of the IEEE Engineering in Medicine and Biology Society (EMBC)* (Berlin), 1233–1238. doi: 10.1109/EMBC.2019.8857535
- Laidig, D., Müller, P., and Seel, T. (2017a). Automatic anatomical calibration for IMU-based elbow angle measurement in disturbed magnetic fields. *Curr. Direct. Biomed. Eng.* 3, 167–170. doi: 10.1515/cdbme-2017-0035
- Laidig, D., Schauer, T., and Seel, T. (2017b). "Exploiting kinematic constraints to compensate magnetic disturbances when calculating joint angles of approximate hinge joints from orientation estimates of inertial sensors," in *Proceedings of 15th IEEE Conference on Rehabilitation Robotics (ICORR)* (London), 971–976. doi: 10.1109/ICORR.2017.8009375
- Le Grand, E., and Thrun, S. (2012). "3-Axis magnetic field mapping and fusion for indoor localization," in *2012 IEEE International Conference on Multisensor Fusion and Integration for Intelligent Systems (MFI)* (Hamburg), 358–364. doi: 10.1109/MFI.2012.6343024
- Levin, M. F., Kleim, J. A., and Wolf, S. L. (2009). What do motor "recovery" and "compensation" mean in patients following stroke? *Neurorehabil. Neural Repair* 23, 313–319. doi: 10.1177/1545968308328272
- Levin, M. F., Liebermann, D. G., Parmet, Y., and Berman, S. (2016). Compensatory versus noncompensatory shoulder movements used for reaching in stroke. *Neurorehabil. Neural Repair* 30, 635–646. doi: 10.1177/1545968315613863
- Liu, W., Waller, S. M., Kepple, T., and Whitall, J. (2013). Compensatory arm reaching strategies after stroke: induced position analysis. *J. Rehabil. Res. Dev.* 50, 71–84. doi: 10.1682/JRRD.2011.04.0074
- Lum, P. S., Burgar, C. G., Shor, P. C., Majmundar, M., and Van der Loos, M. (2002). Robot-assisted movement training compared with conventional therapy techniques for the rehabilitation of upper-limb motor function after stroke. *Archiv. Phys. Med. Rehabil.* 83, 952–959. doi: 10.1053/apmr.2001.33101
- Ma, K., Chen, Y., Zhang, X., Zheng, H., Yu, S., Cai, S., et al. (2019). sEMG-based trunk compensation detection in rehabilitation training. *Front. Neurosci.* 13:1250. doi: 10.3389/fnins.2019.01250
- Maciejasz, P., Eschweiler, J., Gerlach-Hahn, K., Jansen-Troy, A., and Leonhardt, S. (2014). A survey on robotic devices for upper limb rehabilitation. *J. Neuroeng. Rehabil.* 11:3. doi: 10.1186/1743-0003-11-3
- Madgwick, S. O. H., Harrison, A. J. L., and Vaidyanathan, R. (2011). "Estimation of IMU and MARG orientation using a gradient descent algorithm," in *2011 IEEE International Conference on Rehabilitation Robotics (Zurich)*, 1–7. doi: 10.1109/ICORR.2011.5975346
- Marchal-Crespo, L., and Reinkensmeyer, D. J. (2009). Review of control strategies for robotic movement training after neurologic injury. *J. Neuroeng. Rehabil.* 6:20. doi: 10.1186/1743-0003-6-20
- McCabe, J., Monkiewicz, M., Holcomb, J., Pundik, S., and Daly, J. J. (2015). Comparison of robotics, functional electrical stimulation, and motor learning methods for treatment of persistent upper extremity dysfunction after stroke: a randomized controlled trial. *Archiv. Phys. Med. Rehabil.* 96, 981–990. doi: 10.1016/j.apmr.2014.10.022
- Mekki, M., Delgado, A. D., Fry, A., Putrino, D., and Huang, V. (2018). Robotic rehabilitation and spinal cord injury: a narrative review. *Neurotherapeutics* 15, 604–617. doi: 10.1007/s13311-018-0642-3
- Mihelj, M. (2006). Human arm kinematics for robot based rehabilitation. *Robotica* 24, 377–383. doi: 10.1017/S0263574705002304
- Müller, P., Bégin, M. A., Schauer, T., and Seel, T. (2016). Alignment-free, self-calibrating elbow angles measurement using inertial sensors. *IEEE J. Biomed. Health Inform.* 21, 312–319. doi: 10.1109/BHI.2016.7455965
- Nordin, N., Xie, S. Q., and Wünsche, B. (2014). Assessment of movement quality in robot-assisted upper limb rehabilitation after stroke: a review. *J. Neuroeng. Rehabil.* 11:137. doi: 10.1186/1743-0003-11-137
- Novak, D., Nagle, A., Keller, U., and Riener, R. (2014). Increasing motivation in robot-aided arm rehabilitation with competitive and cooperative gameplay. *J. Neuroeng. Rehabil.* 11:64. doi: 10.1186/1743-0003-11-64
- Nowka, D., Kok, M., and Seel, T. (2019). "On motions that allow for identification of hinge joint axes from kinematic constraints and 6D IMU data," in *2019 18th European Control Conference (ECC)* (Naples), 4325–4331. doi: 10.23919/ECC.2019.8795846
- Olsson, F., Seel, T., Lehmann, D., and Halvorsen, K. (2019). "Joint axis estimation for fast and slow movements using weighted gyroscope and acceleration constraints," in *22nd International Conference on Information Fusion (FUSION)* (Ottawa, ON), 1–8.
- Oña, E., Cano-de la Cuerda, R., Sánchez-Herrera, P., Balaguer, C., and Jardón, A. (2018). A review of robotics in neurorehabilitation: towards an automated process for upper limb. *J. Healthc. Eng.* 2018:9758939. doi: 10.1155/2018/9758939
- Oujamaa, L., Relave, I., Froger, J., Mottet, D., and Pelissier, J.-Y. (2009). Rehabilitation of arm function after stroke. Literature review. *Ann. Phys. Rehabil. Med.* 52, 269–293. doi: 10.1016/j.rehab.2008.10.003
- Papaleo, E., Zollo, L., Garcia-Aracil, N., Badesa, F. J., Morales, R., Mazzoleni, S., et al. (2015). Upper-limb kinematic reconstruction during stroke robot-aided therapy. *Med. Biol. Eng. Comput.* 53, 815–828. doi: 10.1007/s11517-015-1276-9
- Passon, A., Schauer, T., and Seel, T. (2018). "Hybrid inertial-robotic motion tracking for posture biofeedback in upper limb rehabilitation," in *2018 7th IEEE International Conference on Biomedical Robotics and Biomechatronics (BioRob)* (Enschede), 1163–1168. doi: 10.1109/BIOROB.2018.8487203
- Popovic, D., and Sinkjaer, T. (2000). *Control of Movement for the Physically Disabled*. 1st Edn. Berlin: Springer.
- Robertson, J. V. G., and Roby-Brami, A. (2011). The trunk as a part of the kinematic chain for reaching movements in healthy subjects and hemiparetic patients. *Brain Res.* 1382, 137–146. doi: 10.1016/j.brainres.2011.01.043
- Rosati, G., Gallina, P., and Masiero, S. (2007). Design, implementation and clinical tests of a wire-based robot for neurorehabilitation. *IEEE Trans. Neural Syst. Rehabil. Eng.* 15, 560–569. doi: 10.1109/TNSRE.2007.908560
- Salchow-Hömmen, C., Callies, L., Laidig, D., Valtin, M., Schauer, T., and Seel, T. (2019). A tangible solution for hand motion tracking in clinical applications. *Sensors* 19:208. doi: 10.3390/s19010208
- Schauer, T. (2017). Sensing motion and muscle activity for feedback control of functional electrical stimulation: ten years of experience in Berlin. *Annu. Rev. Control* 44, 355–374. doi: 10.1016/j.arcontrol.2017.09.014
- Schmidt, R. A., and Lee, T. D. (2014). *Motor Learning and Performance: From Principles to Application*. Champaign: Human Kinetics.
- Scotto di Luzio, F., Simonetti, D., Cordella, F., Miccinilli, S., Sterzi, S., Draicchio, F., et al. (2018). Bio-cooperative approach for the human-in-the-loop control of an end-effector rehabilitation robot. *Front. Neurobot.* 12:67. doi: 10.3389/fnbot.2018.00067
- Seel, T., Graurock, D., and Schauer, T. (2015). Realtime assessment of foot orientation by accelerometers and gyroscopes. *Curr. Direct. Biomed. Eng.* 1, 466–469. doi: 10.1515/cdbme-2015-0112
- Seel, T., and Ruppig, S. (2017). Eliminating the effect of magnetic disturbances on the inclination estimates of inertial sensors. *IFAC-Papers Online* 50, 8798–8803. doi: 10.1016/j.ifacol.2017.08.1534
- Shu, Y., Bo, C., Shen, G., Zhao, C., Li, L., and Zhao, F. (2015). Magicol: indoor localization using pervasive magnetic field and opportunistic WiFi sensing. *IEEE J. Select. Areas Commun.* 33, 1443–1457. doi: 10.1109/JSAC.2015.2430274
- Sicuri, C., Porcellini, G., and Merolla, G. (2014). Robotics in shoulder rehabilitation. *Muscles Ligaments Tendons J.* 4:207. doi: 10.11138/mltj/2014.4.2.207
- Sojka, M., and Piša, P. (2014). "Usable Simulink embedded coder target for Linux," in *Proceedings 16th Real Time Linux Workshop* (Düsseldorf), 1–6.
- Subbu, K. P., Gozick, B., and Dantu, R. (2013). LocateMe: magnetic-fields-based indoor localization using smartphones. *ACM Trans. Intell. Syst. Technol.* 4:73. doi: 10.1145/2508037.2508054
- Taetz, B., Bleser, G., and Miezal, M. (2016). "Towards self-calibrating inertial body motion capture," in *2016 19th International Conference on Information Fusion (FUSION)* (Heidelberg), 1751–1759.
- Titterton, D., Weston, J. L., and Weston, J. (2004). *Strapdown Inertial Navigation Technology*. London: IET.
- Tognetti, A., Lorusi, F., Carbonaro, N., and De Rossi, D. (2015). Wearable goniometer and accelerometer sensory fusion for knee joint angle

- measurement in daily life. *Sensors* 15, 28435–28455. doi: 10.3390/s151128435
- Trigili, E., Crea, S., Moisé, M., Baldoni, A., Cempini, M., Ercolini, G., et al. (2019). Design and experimental characterization of a shoulder-elbow exoskeleton with compliant joints for post-stroke rehabilitation. *IEEE/ASME Trans. Mechatron.* 24, 1485–1496. doi: 10.1109/TMECH.2019.2907465
- Valdés, B. A., and der Loos, H. F. M. V. (2017). Biofeedback vs. game scores for reducing trunk compensation after stroke: a randomized crossover trial. *Top. Stroke Rehabil.* 25, 96–113. doi: 10.1080/10749357.2017.1394633
- Vito, L. D., Postolache, O., and Rapuano, S. (2014). Measurements and sensors for motion tracking in motor rehabilitation. *IEEE Instrum. Meas. Mag.* 17, 30–38. doi: 10.1109/MIM.2014.6825386
- Winter, D. A. (2005). *Biomechanics and Motor Control of Human Movement*. New Jersey, NJ: John Wiley & Sons.
- Wittmann, F., Lambercy, O., and Gassert, R. (2019). Magnetometer-based drift correction during rest in IMU arm motion tracking. *Sensors* 19:1312. doi: 10.3390/s19061312
- Wu, Q.-C., Wang, X.-S., and Du, F.-P. (2015). Analytical inverse kinematic resolution of a redundant exoskeleton for upper-limb rehabilitation. *Int. J. Hum. Robot.* 13:1550042. doi: 10.1142/S0219843615500425
- Yahya, M., Shah, J. A., Kadir, K. A., Yusof, Z. M., Khan, S., and Warsi, A. (2019). Motion capture sensing techniques used in human upper limb motion: a review. *Sensor Rev.* 39, 504–511. doi: 10.1108/SR-10-2018-0270
- Zhi, Y. X., Lukasik, M., Li, M. H., Dolatabadi, E., Wang, R. H., and Taati, B. (2018). Automatic detection of compensation during robotic stroke rehabilitation therapy. *IEEE J. Transl. Eng. Health Med.* 6, 1–7. doi: 10.1109/JTEHM.2017.2780836
- Zhou, H., and Hu, H. (2008). Human motion tracking for rehabilitation—a survey. *Biomed. Signal Process. Control* 3, 1–18. doi: 10.1016/j.bspc.2007.09.001

Conflict of Interest: The authors declare that the research was conducted in the absence of any commercial or financial relationships that could be construed as a potential conflict of interest.

Copyright © 2020 Passon, Schauer and Seel. This is an open-access article distributed under the terms of the Creative Commons Attribution License (CC BY). The use, distribution or reproduction in other forums is permitted, provided the original author(s) and the copyright owner(s) are credited and that the original publication in this journal is cited, in accordance with accepted academic practice. No use, distribution or reproduction is permitted which does not comply with these terms.



ExoNet Database: Wearable Camera Images of Human Locomotion Environments

Brock Laschowski^{1,2*}, William McNally^{1,2}, Alexander Wong^{1,2} and John McPhee^{1,2}

¹ Department of Systems Design Engineering, University of Waterloo, Waterloo, ON, Canada, ² Waterloo Artificial Intelligence Institute, University of Waterloo, Waterloo, ON, Canada

Keywords: artificial intelligence, environment recognition, exoskeletons, rehabilitation robotics, prosthetics, biomechatronics, computer vision, wearable technology

INTRODUCTION

Hundreds of millions of individuals worldwide have mobility impairments resulting from degenerative aging and/or neuro-musculoskeletal disorders (Grimmer et al., 2019). Fortunately, robotic lower-limb exoskeletons and prostheses can allow otherwise wheelchair-bound seniors and rehabilitation patients to perform movements that involve net positive mechanical work (e.g., climbing stairs and standing from a seated position) using onboard actuators and intelligent control systems (Tucker et al., 2015; Young and Ferris, 2017; Laschowski and Andrysek, 2018; Krausz and Hargrove, 2019; Zhang et al., 2019a). Generally speaking, the high-level controller recognizes the patient's locomotion mode (intention) by analyzing real-time measurements from wearable sensors using machine learning algorithms. The mid-level controller then translates the locomotion intentions into mode-specific reference trajectories. This control level typically comprises a finite state machine, which implements a discrete parametrized control law (e.g., joint position or mechanical impedance control) for each locomotion mode. Finally, the low-level controller tracks the reference trajectories and minimizes the signal error by modulating the device actuators using feedforward and feedback control loops (Tucker et al., 2015; Young and Ferris, 2017; Laschowski and Andrysek, 2018; Krausz and Hargrove, 2019; Zhang et al., 2019a).

Accurate transitions between different locomotion modes is important since even rare misclassifications can cause loss-of-balance and injury. In many commercial devices like the ReWalk and Indego lower-limb exoskeletons, the patient acts as the high-level controller by performing volitional movements to manually switch between locomotion modes (Tucker et al., 2015; Young and Ferris, 2017). These human-controlled methods can be time-consuming, inconvenient, and cognitively demanding. Researchers have recently developed automated locomotion mode recognition systems using wearable sensors like inertial measurement units (IMUs) and surface electromyography (EMG) to automatically switch between different locomotion modes (Tucker et al., 2015; Young and Ferris, 2017; Laschowski and Andrysek, 2018; Krausz and Hargrove, 2019; Zhang et al., 2019a). Whereas mechanical and inertial sensors respond to the patient's movements, the electrical potentials of biological muscles, as recorded using surface EMG, precede movement initiation and thus could (marginally) predict locomotion mode transitions. Several researchers have combined mechanical sensors with surface EMG for automated locomotion mode recognition. Such neuromuscular-mechanical data fusion has improved the locomotion mode recognition accuracies and decision times compared to implementing either system individually (Huang et al., 2011; Du et al., 2012; Wang et al., 2013; Liu et al., 2016). However, these measurements are still patient-dependent, and surface EMG are susceptible to fatigue, changes in electrode-skin conductivity, and crosstalk from adjacent muscles (Tucker et al., 2015).

OPEN ACCESS

Edited by:

Carlos Rodriguez-Guerrero,
Vrije University Brussel, Belgium

Reviewed by:

Luigi Manfredi,
University of Dundee School of
Medicine, United Kingdom
Michel Paindavoine,
Université de Bourgogne, France

*Correspondence:

Brock Laschowski
blaschow@uwaterloo.ca

Specialty section:

This article was submitted to
Biomedical Robotics,
a section of the journal
Frontiers in Robotics and AI

Received: 14 May 2020

Accepted: 06 November 2020

Published: 03 December 2020

Citation:

Laschowski B, McNally W, Wong A
and McPhee J (2020) ExoNet
Database: Wearable Camera Images
of Human Locomotion Environments.
Front. Robot. AI 7:562061.
doi: 10.3389/frobt.2020.562061

Supplementing neuromuscular-mechanical data with information about the upcoming walking environment could improve the high-level control performance. Similar to the human visual system, environment sensing would precede modulation of the patient's muscle activations and/or walking biomechanics, therein enabling more accurate and real-time locomotion mode transitions. Environment sensing could also be used to adapt low-level reference trajectories (e.g., changing toe clearance corresponding to an obstacle height) (Zhang et al., 2020) and optimal path planning (e.g., identifying opportunities for energy regeneration) (Laschowski et al., 2019a, 2020a). Preliminary research has shown that supplementing an automated locomotion mode recognition system with environment information can improve the classification accuracies and decision times compared to excluding terrain information (Huang et al., 2011; Wang et al., 2013; Liu et al., 2016). Several researchers have explored using radar detectors (Kleiner et al., 2018) and laser rangefinders (Zhang et al., 2011; Wang et al., 2013; Liu et al., 2016) for environment sensing. However, vision-based systems can provide more detailed information about the field-of-view and detect physical obstacles in peripheral locations. Most environment recognition systems have included either RGB cameras (Krausz and Hargrove, 2015; Diaz et al., 2018; Khademi and Simon, 2019; Laschowski et al., 2019b; Novo-Torres et al., 2019; Da Silva et al., 2020; Zhong et al., 2020) or 3D depth cameras (Krausz et al., 2015, 2019; Varol and Massalin, 2016; Hu et al., 2018; Massalin et al., 2018; Zhang et al., 2019b,c,d).

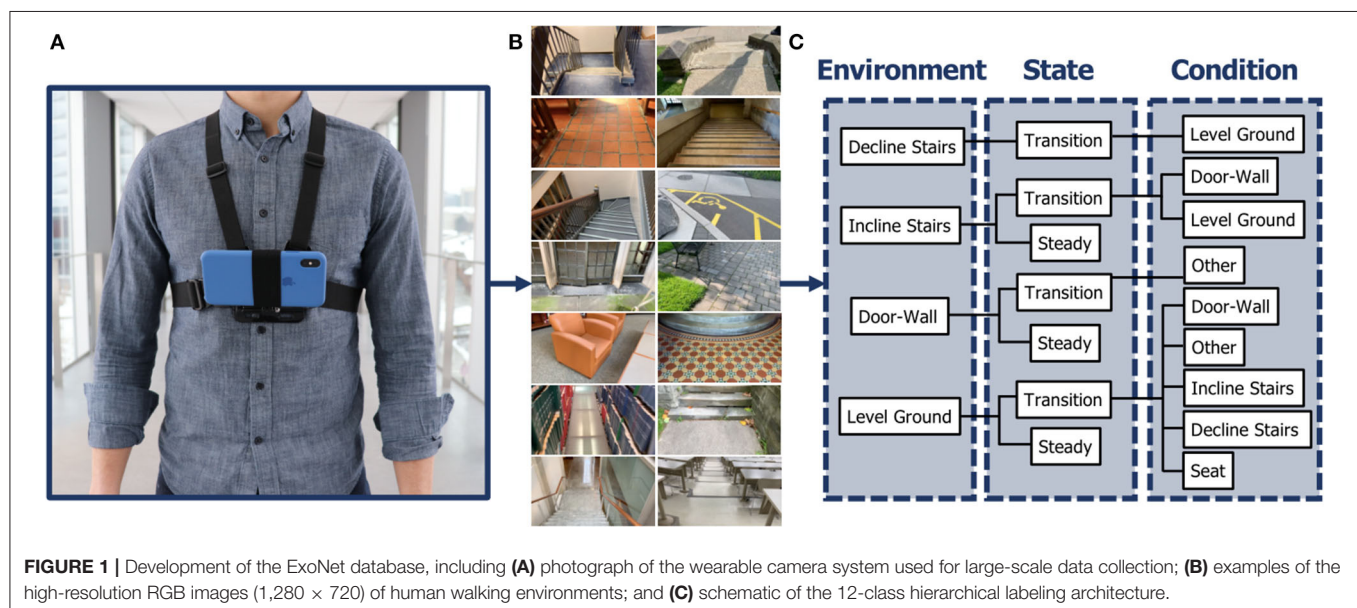
For image classification, researchers have used learning-based algorithms like support vector machines (Varol and Massalin, 2016; Massalin et al., 2018) and deep convolutional neural networks (Rai and Rombokas, 2018; Khademi and Simon, 2019; Laschowski et al., 2019b; Novo-Torres et al., 2019; Zhang et al., 2019b,c,d; Zhong et al., 2020). Although convolutional neural networks typically outperform support vector machines for

image classification (LeCun et al., 2015), deep learning requires significant and diverse training images to prevent overfitting and promote generalization. Deep learning has become pervasive ever since AlexNet (Krizhevsky et al., 2012) popularized convolutional neural networks by winning the 2012 ImageNet challenge. ImageNet is an open-source dataset containing ~15 million labeled images and 22,000 different classes (Deng et al., 2009). The lack of an open-source, large-scale dataset of human locomotion environment images has impeded the development of environment-aware control systems for robotic lower-limb exoskeletons and prostheses. Until now, researchers have been required to individually collect training images to develop their classification algorithms. These repetitive measurements are time-consuming and inefficient, and individual private datasets have prevented comparisons between classification algorithms from different researchers (Laschowski et al., 2020b). Drawing inspiration from ImageNet, we developed ExoNet—the first open-source, large-scale hierarchical database of high-resolution wearable camera images of human walking environments. In accordance with the Frontiers submission guidelines, this article provides a detailed description of the research dataset. Benchmark performance and analyses of the ExoNet database for human locomotion environment classification will be presented in future work.

MATERIALS AND METHODS

Large-Scale Data Collection

One subject was instrumented with a lightweight wearable smartphone camera system (iPhone XS Max); photograph shown in **Figure 1A**. Unlike limb-mounted systems (Zhang et al., 2011, 2019b,c; Varol and Massalin, 2016; Diaz et al., 2018; Hu et al., 2018; Kleiner et al., 2018; Massalin et al., 2018; Rai and Rombokas, 2018; Da Silva et al., 2020), chest-mounting can provide more stable video recording and allow users to wear



pants and long dresses without obstructing the sampled field-of-view. The chest-mount height was ~ 1.3 m from the ground when the participant stood upright. The smartphone contains two 12-megapixel RGB rear-facing cameras and one 7-megapixel front-facing camera. The front and rear cameras provide $1,920 \times 1,080$ and $1,280 \times 720$ video recording at 30 frames/s, respectively. The smartphone weighs ~ 0.21 kg, and features an onboard rechargeable lithium-ion battery, 512-GB of memory storage, and a 64-bit ARM-based integrated circuit (Apple A12 Bionic) with six-core CPU and four-core GPU. These hardware specifications can support onboard machine learning for real-time environment classification. The relatively lightweight and unobtrusive nature of the wearable camera system allowed for unimpeded human walking biomechanics. Ethical review and approval were not required for this research in accordance with the University of Waterloo Office of Research Ethics.

While most environment recognition systems have been limited to controlled indoor environments and/or prearranged walking circuits (Zhang et al., 2011, 2019b,c,d; Du et al., 2012; Wang et al., 2013; Krausz et al., 2015, 2019; Liu et al., 2016; Hu et al., 2018; Kleiner et al., 2018; Khademi and Simon, 2019), our subject walked around unknown outdoor and indoor real-world environments while collecting images with occlusions, signal noise, and intraclass variations. Data were collected at various times throughout the day to incorporate different lighting conditions. Similar to human gaze fixation during walking (Li et al., 2019), the sampled field-of-view was ~ 1 –5 meters ahead of the participant, thereby showing upcoming walking environments rather than the ground underneath the subject's feet. The camera's pitch angle slightly differed between data collection sessions. Images were sampled at 30 Hz with $1,280 \times 720$ resolution. More than 52 h of video were recorded, amounting to ~ 5.6 million images (examples shown in **Figure 1B**). The same environment was never sampled twice to maximize diversity among the ExoNet images. Data were collected throughout the summer, fall, and winter seasons to incorporate different weathered surfaces like snow, grass, and multicolored leaves. In accordance with the Frontiers submission guidelines, the ExoNet database was deposited in a public repository (IEEE DataPort) and is available for download at <https://iee-dataport.org/open-access/exonet-database-wearable-camera-images-human-locomotion-environments>. The file size of the uncompressed videos is ~ 140 GB.

Hierarchical Image Labeling

Given the subject's preferred walking speed, there were minimal differences between consecutive images sampled at 30 Hz. The labeled images were therefore downsampled to 5 frames/s to minimize the demands of manual annotation and increase the diversity in image appearances. However, for real-time environment classification and control of robotic lower-limb exoskeletons and prostheses, higher sampling rates would be more advantageous for accurate locomotion mode recognition and transitioning. Similar to ImageNet (Deng et al., 2009), the ExoNet database was human-annotated using a hierarchical labeling architecture (see **Figure 1C**). Images were labeled according to exoskeleton

and prosthesis control functionality, rather than a purely computer vision perspective. For instance, images of level-ground environments showing either pavement or grass were not differentiated since both surfaces would use the same level-ground walking state controller. In contrast, computer vision researchers might label these different surface textures as separate classes.

Approximately 923,000 images in ExoNet were manually labeled and organized into 12 classes using the following descriptions, which also include the number of labeled images/class: {IS-T-DW = 31,628} shows incline stairs with a door and/or wall; {IS-T-LG = 11,040} shows incline stairs with level-ground thereafter; {IS-S = 17,358} shows only incline stairs; {DS-T-LG = 28,677} shows decline stairs with level-ground thereafter; {DW-T-O = 19,150} shows a door and/or wall with *other* (e.g., hand or window); {DW-S = 36,710} shows only a door and/or wall; {LG-T-DW = 379,199} shows level-ground with a door and/or wall; {LG-T-O = 153,263} shows level-ground with *other* (e.g., humans, cars, bicycles, or garbage cans); {LG-T-IS = 26,067} shows level-ground with incline stairs thereafter; {LG-T-DS = 22,607} shows level-ground with decline stairs thereafter; {LG-T-SE = 119,515} shows level-ground with seats (e.g., couches, chairs, or benches); and {LG-S = 77,576} shows only level-ground. These classes were selected to encompass the different walking environments encountered during the data collection sessions. We included the *other* class to improve image classification performance when confronted with non-terrain related features like humans or bicycles.

Inspired by previous work (Huang et al., 2011; Du et al., 2012; Wang et al., 2013; Liu et al., 2016; Khademi and Simon, 2019), the hierarchical labeling architecture included both *steady* (S) and *transition* (T) states. A steady state describes an environment where an exoskeleton or prosthesis user would continuously perform the same locomotion mode (e.g., only level-ground terrain). In contrast, a transition state describes an environment where the exoskeleton or prosthesis high-level controller might switch between different locomotion modes (e.g., level-ground and incline stairs). Manually labeling the transition states was relatively subjective. For example, an image showing level-ground terrain was labeled *level-ground-transition-incline stairs* (LG-T-IS) when an incline staircase was approximately within the sampled field-of-view and forward-facing. Similar labeling principles were applied to transitions to other conditions. The Python code used for labeling the ExoNet database was uploaded to GitHub and is publicly available for download at <https://github.com/BrockLaschowski2/ExoNet>.

DISCUSSION

Environment recognition systems can improve the control of robotic lower-limb exoskeletons and prostheses during human locomotion. However, small-scale and private training datasets have impeded the widespread development and dissemination of image classification algorithms for human

TABLE 1 | Comparison of the ExoNet database with previous environment recognition systems for robotic lower-limb prostheses and exoskeletons.

Reference	Sensor	Position	Dataset	Resolution	Classes
Da Silva et al. (2020)	RGB camera	Lower-limb	3,992 Images	512 × 512	6
Diaz et al. (2018)	RGB camera	Lower-limb	3,992 Images	1,080 × 1,920	6
Khademi and Simon (2019)	RGB camera	Waist	7,284 Images	224 × 224	3
Krausz and Hargrove (2015)	RGB camera	Head	5 Images	928 × 620	2
Krausz et al. (2015)	Depth camera	Chest	170 Images	80 × 60	2
Krausz et al. (2019)	Depth camera	Waist	4,000 Images	171 × 224	5
Laschowski et al. (2019b)	RGB camera	Chest	34,254 Images	224 × 224	3
Massalin et al. (2018)	Depth camera	Lower-limb	402,403 Images	320 × 240	5
Novo-Torres et al. (2019)	RGB camera	Head	40,743 Images	128 × 128	2
Varol and Massalin (2016)	Depth camera	Lower-limb	22,932 Images	320 × 240	5
Zhang et al. (2019b,c)	Depth camera	Lower-limb	7,500 Images	224 × 171	5
Zhang et al. (2019d)	Depth camera	Waist	4,016 Images	2,048 Point Cloud	3
Zhang et al. (2020)	Depth camera	Lower-limb	7,500 Images	100 × 100	5
Zhong et al. (2020)	RGB camera	Head and lower-limb	327,000 Images	1,240 × 1,080	6
ExoNet database	RGB camera	Chest	922,790 Images	1,280 × 720	12

locomotion environment recognition. Motivated by these limitations, we developed ExoNet—the first open-source, large-scale hierarchical database of high-resolution wearable camera images of human walking environments. Using a lightweight wearable camera system, we collected over 5.6 million RGB images of different indoor and outdoor real-world walking environments, of which ~923,000 images were human-annotated using a 12-class hierarchical labeling architecture. Available publicly through IEEE DataPort, ExoNet provides researchers an unprecedented communal platform to develop and compare next-generation image classification algorithms for human locomotion environment recognition. Although ExoNet was originally designed for environment-aware control systems for lower-limb exoskeletons and prostheses, applications could extend to humanoids and autonomous legged robots (Park et al., 2015; Villarreal et al., 2020). Users of the ExoNet database are requested to reference this dataset report.

Aside from being the only open-source image database of human locomotion environments, the large scale and diversity of ExoNet significantly distinguishes itself from previous environment recognition systems, as illustrated in **Table 1**. ExoNet contains ~923,000 individually labeled images. In comparison, the previous largest dataset contained ~402,000 images (Massalin et al., 2018). While most environment recognition systems have included fewer than six classes (Krausz and Hargrove, 2015; Krausz et al., 2015, 2019; Varol and Massalin, 2016; Massalin et al., 2018; Khademi and Simon, 2019; Laschowski et al., 2019b; Novo-Torres et al., 2019; Zhang et al., 2019b,c,d; Zhang et al., 2020), the ExoNet database features a 12-class hierarchical labeling architecture. These differences have real-world implications given that learning-based algorithms like convolutional neural networks require significant and diverse training images (LeCun et al., 2015). The spatial resolution of the ExoNet images

(1,280 × 720) is considerably higher than previous efforts (e.g., 224 × 224 and 320 × 240). Poor image resolution has been attributed to decreased classification accuracy of human walking environments (Novo-Torres et al., 2019). Although higher resolution images can increase the computational and memory storage requirements, that being unfavorable for real-time mobile computing, researchers have been moving toward the development of efficient convolutional neural networks that require fewer operations (Tan and Le, 2020), therein enabling the processing of larger images for relatively similar computational power. Here we assume mobile computing for the exoskeleton and prosthesis control (i.e., untethered and no wireless communication to cloud computing). Nevertheless, an exoskeleton or prosthesis controller may not always benefit from additional information provided by higher resolution images, particularly when interacting with single surface textures (i.e., only pavement or grass). With ongoing research and development in computer vision and artificial intelligence, larger and more challenging training datasets are needed to develop better image classification algorithms for environment-aware locomotor control systems.

A potential limitation of the ExoNet database is the two-dimensional nature of the environment information. Whereas RGB cameras measure light intensity information, depth cameras also provide distance measurements (Krausz et al., 2015, 2019; Varol and Massalin, 2016; Hu et al., 2018; Massalin et al., 2018; Zhang et al., 2019b,c,d). Depth cameras work by emitting infrared light and calculate distances by measuring the light time-of-flight between the camera and physical environment (Varol and Massalin, 2016). Depth measurement accuracies typically degrade in outdoor lighting conditions (e.g., sunlight) and with increasing measurement distance. Consequently, most environment recognition systems using depth cameras have been tested in indoor environments (Krausz et al., 2015, 2019; Varol and Massalin, 2016; Hu et al., 2018; Massalin

et al., 2018) and have had limited capture volumes (i.e., between 1 and 2 m of maximum range imaging) (Krausz et al., 2015; Varol and Massalin, 2016; Massalin et al., 2018). Assuming mobile computing, the application of depth cameras for environment sensing would also require robotic lower-limb exoskeletons and prostheses to have embedded microcontrollers with significant computing power and minimal power consumption, the specifications of which are not supported by existing untethered systems (Massalin et al., 2018). These practical limitations motivated our decision to use RGB images.

Our camera images could be fused with the smartphone IMU measurements to improve high-level control performance. For example, if an exoskeleton or prosthesis user unexpectedly stops while walking toward an incline staircase, the acceleration measurements would indicate static standing rather than stair ascent, despite the staircase being accurately detected in the field-of-view. Since environment information does not explicitly represent the locomotor intent, environment recognition systems should supplement, rather than replace, the automated locomotion mode recognition systems based on patient-dependant measurements like mechanical and inertial sensors. The smartphone IMU measurements could also be used for sampling rate control (Zhang et al., 2011; Diaz et al., 2018; Khademi and Simon, 2019; Da Silva et al., 2020). Faster walking speeds would likely benefit from higher sampling rates for continuous classification. In contrast, static standing does not necessarily require environment information and therefore the smartphone camera could be powered down, or the sampling rate decreased, to minimize the computational and memory storage requirements. However, the optimal method for fusing the smartphone camera images with the onboard IMU measurements remains to be determined.

REFERENCES

- Da Silva, R. L., Starliper, N., Zhong, B., Huang, H. H., and Lobaton, E. (2020). Evaluation of embedded platforms for lower limb prosthesis with visual sensing capabilities. *arXiv [Preprint]*. arXiv:2006.15224.
- Deng, J., Dong, W., Socher, R., Li, L. J., Li, K., and Fei-Fei, L. (2009). "ImageNet: a large-scale hierarchical image database," in *IEEE Conference on Computer Vision and Pattern Recognition (CVPR)* (Miami, FL: IEEE), 248–255. doi: 10.1109/CVPR.2009.5206848
- Diaz, J. P., Da Silva, R. L., Zhong, B., Huang, H. H., and Lobaton, E. (2018). "Visual terrain identification and surface inclination estimation for improving human locomotion with a lower-limb prosthetic," in *Annual International Conference of the IEEE Engineering in Medicine and Biology Society (EMBC)* (Honolulu, HI: IEEE), 1817–1820. doi: 10.1109/EMBC.2018.8512614
- Du, L., Zhang, F., Liu, M., and Huang, H. (2012). Toward design of an environment-aware adaptive locomotion-mode-recognition system. *IEEE Trans. Biomed. Eng.* 59, 2716–2725. doi: 10.1109/TBME.2012.2208641
- Grimmer, M., Riener, R., Walsh, C. J., and Seyfarth, A. (2019). Mobility related physical and functional losses due to aging and disease - a motivation for lower limb exoskeletons. *J. Neuroeng. Rehabil.* 16:2. doi: 10.1186/s12984-018-0458-8
- Hu, B. H., Krausz, N. E., and Hargrove, L. J. (2018). "A novel method for bilateral gait segmentation using a single thigh-mounted depth sensor and IMU," in *IEEE International Conference on Biomedical Robotics and Biomechanics (BIOROB)* (Enschede: IEEE), 807–812. doi: 10.1109/BIOROB.2018.8487806
- Huang, H., Dou, Z., Zheng, F., and Nunnery, M. J. (2011). "Improving the performance of a neural-machine interface for artificial legs using prior knowledge of walking environment," in *Annual International Conference of the IEEE Engineering in Medicine and Biology Society (EMBC)* (Boston, MA: IEEE), 4255–4258. doi: 10.1109/IEMBS.2011.6091056
- Khademi, G., and Simon, D. (2019). "Convolutional neural networks for environmentally aware locomotion mode recognition of lower-limb amputees," in *ASME Dynamic Systems and Control Conference (DSCC)* (Park City, UT: ASME), 11. doi: 10.1115/DSCC2019-9180
- Kleiner, B., Ziegenspeck, N., Stolyarov, R., Herr, H., Schneider, U., and Verl, A. (2018). "A radar-based terrain mapping approach for stair detection towards enhanced prosthetic foot control," in *IEEE International Conference on Biomedical Robotics and Biomechanics (BIOROB)* (Enschede: IEEE), 105–110. doi: 10.1109/BIOROB.2018.8487722
- Krausz, N. E., and Hargrove, L. J. (2015). "Recognition of ascending stairs from 2D images for control of powered lower limb prostheses," in *International IEEE/EMBS Conference on Neural Engineering (NER)* (Montpellier: IEEE), 615–618. doi: 10.1109/NER.2015.7146698
- Krausz, N. E., and Hargrove, L. J. (2019). A survey of teleceptive sensing for wearable assistive robotic devices. *Sensors* 19:5238. doi: 10.3390/s19235238

DATA AVAILABILITY STATEMENT

The datasets presented in this study can be found in online repositories. The names of the repository/repositories and accession number(s) can be found below: <https://iee-dataport.org/open-access/exonet-database-wearable-camera-images-human-locomotion-environments>. The name of the online repository is "IEEE DataPort" and the name of the image database is "ExoNet".

ETHICS STATEMENT

Ethical review and approval was not required for the study on human participants in accordance with the local legislation and institutional requirements. Written informed consent for participation was not required for this study in accordance with the national legislation and the institutional requirements.

AUTHOR CONTRIBUTIONS

BL was responsible for the study design, literature review, data collection, image labeling, data interpretation, and manuscript writing. WM assisted with the study design, image labeling, data interpretation, and manuscript writing. AW and JM assisted with the study design, data interpretation, and manuscript writing. All authors read and approved the final manuscript.

FUNDING

This research was funded by the Natural Sciences and Engineering Research Council of Canada (NSERC), the Waterloo Engineering Excellence Ph.D. Fellowship, JM's Tier I Canada Research Chair in Biomechatronic System Dynamics, and AW's Tier II Canada Research Chair in Artificial Intelligence and Medical Imaging.

- Krausz, N. E., Hu, B. H., and Hargrove, L. J. (2019). Subject- and environment-based sensor variability for wearable lower-limb assistive devices. *Sensors* 19:4887. doi: 10.3390/s19224887
- Krausz, N. E., Lenzi, T., and Hargrove, L. J. (2015). Depth sensing for improved control of lower limb prostheses. *IEEE Trans. Biomed. Eng.* 62, 2576–2587. doi: 10.1109/TBME.2015.2448457
- Krizhevsky, A., Sutskever, I., and Hinton, G. E. (2012). “ImageNet classification with deep convolutional neural networks,” in *Advances in Neural Information Processing Systems Conference (NIPS)* (Lake Tahoe, NV), 1097–1105. doi: 10.1145/3065386
- Laschowski, B., and Andrysek, J. (2018). “Electromechanical design of robotic transfemoral prostheses,” in *ASME International Design Engineering Technical Conferences and Computers and Information in Engineering Conference (IDETC-CIE)* (Quebec City: ASME), V05AT07A054. doi: 10.1115/DETC2018-85234
- Laschowski, B., McNally, W., Wong, A., and McPhee, J. (2019b). “Preliminary design of an environment recognition system for controlling robotic lower-limb prostheses and exoskeletons,” in *IEEE International Conference on Rehabilitation Robotics (ICORR)* (Toronto: IEEE), 868–873. doi: 10.1109/ICORR.2019.8779540
- Laschowski, B., McNally, W., Wong, A., and McPhee, J. (2020b). “Comparative analysis of environment recognition systems for control of lower-limb exoskeletons and prostheses,” in *IEEE International Conference on Biomedical Robotics and Biomechanics (BIOROB)* (New York City, NY: IEEE). doi: 10.1109/BioRob49111.2020.9224364
- Laschowski, B., McPhee, J., and Andrysek, J. (2019a). Lower-limb prostheses and exoskeletons with energy regeneration: mechatronic design and optimization review. *ASME J. Mech. Robot.* 11:040801. doi: 10.1115/1.4043460
- Laschowski, B., Razavian, R. S., and McPhee, J. (2020a). Simulation of stand-to-sit biomechanics for design of lower-limb exoskeletons and prostheses with energy regeneration. *bioRxiv*. doi: 10.1101/801258
- LeCun, Y., Bengio, Y., and Hinton, G. (2015). Deep learning. *Nature* 521, 436–444. doi: 10.1038/nature14539
- Li, M., Zhong, B., Liu, Z., Lee, I. C., Fylstra, B. L., Lobaton, E., et al. (2019). “Gaze fixation comparisons between amputees and able-bodied individuals in approaching stairs and level-ground transitions: a pilot study,” in *Annual International Conference of the IEEE Engineering in Medicine and Biology Society (EMBC)* (Berlin: IEEE). doi: 10.1109/EMBC.2019.8857388
- Liu, M., Wang, D., and Huang, H. (2016). Development of an environment-aware locomotion mode recognition system for powered lower limb prostheses. *IEEE Trans. Neural Syst. Rehabilitation Eng.* 24, 434–443. doi: 10.1109/TNSRE.2015.2420539
- Massalin, Y., Abdrakhmanova, M., and Varol, H. A. (2018). User-independent intent recognition for lower limb prostheses using depth sensing. *IEEE Trans. Biomed. Eng.* 65, 1759–1770. doi: 10.1109/TBME.2017.2776157
- Novo-Torres, L., Ramirez-Paredes, J. P., and Villarreal, D. J. (2019). “Obstacle recognition using computer vision and convolutional neural networks for powered prosthetic leg applications,” in *Annual International Conference of the IEEE Engineering in Medicine and Biology Society (EMBC)* (Berlin: IEEE), 3360–3363. doi: 10.1109/EMBC.2019.8857420
- Park, H. W., Wensing, P., and Kim, S. (2015). “Online planning for autonomous running jumps over obstacles in high-speed quadrupeds,” in *Robotics: Science and Systems Conference (RSS)* (Rome). doi: 10.15607/RSS.2015.XI.047
- Rai, V., and Rombokas, E. (2018). “Evaluation of a visual localization system for environment awareness in assistive devices,” in *Annual International Conference of the IEEE Engineering in Medicine and Biology Society (EMBC)* (Honolulu, HI: IEEE), 5135–5141. doi: 10.1109/EMBC.2018.8513442
- Tan, M., and Le, Q. V. (2020). EfficientNet: rethinking model scaling for convolutional neural networks. *arXiv [Preprint]*. arXiv:1905.11946v115.
- Tucker, M. R., Olivier, J., Pagel, A., Bleuler, H., Bouri, M., Lambercy, O., et al. (2015). Control strategies for active lower extremity prosthetics and orthotics: a review. *J. Neuroeng. Rehabil.* 12:1. doi: 10.1186/1743-0003-12-1
- Varol, H. A., and Massalin, Y. (2016). “A feasibility study of depth image based intent recognition for lower limb prostheses,” in *Annual International Conference of the IEEE Engineering in Medicine and Biology Society (EMBC)* (Orlando, FL: IEEE), 5055–5058. doi: 10.1109/EMBC.2016.7591863
- Villarreal, O., Barasuol, V., Wensing, P., and Semini, C. (2020). “MPC-based controller with terrain insight for dynamic legged locomotion,” in *IEEE International Conference on Robotics and Automation (ICRA)* (Paris: IEEE), arXiv:1909.13842. doi: 10.1109/ICRA40945.2020.9197312
- Wang, D., Du, L., and Huang, H. (2013). “Terrain recognition improves the performance of neural-machine interface for locomotion mode recognition,” in *IEEE International Conference on Computing, Networking and Communications (ICNC)* (San Diego, CA: IEEE), 87–91. doi: 10.1109/ICCNC.2013.6504059
- Young, A. J., and Ferris, D. P. (2017). State of the art and future directions for lower limb robotic exoskeletons. *IEEE Trans. Neural Syst. Rehabilitation Eng.* 25, 171–182. doi: 10.1109/TNSRE.2016.2521160
- Zhang, F., Fang, Z., Liu, M., and Huang, H. (2011). “Preliminary design of a terrain recognition system,” in *Annual International Conference of the IEEE Engineering in Medicine and Biology Society (EMBC)* (Boston, MA: IEEE), 5452–5455. doi: 10.1109/IEMBS.2011.6091391
- Zhang, K., De Silva, C. W., and Fu, C. (2019a). Sensor fusion for predictive control of human-prosthesis-environment dynamics in assistive walking: a survey. *arXiv [Preprint]*. arXiv:1903.07674.
- Zhang, K., Luo, J., Xiao, W., Zhang, W., Liu, H., Zhu, J., et al. (2020). A subvision system for enhancing the environmental adaptability of the powered transfemoral prosthesis. *IEEE Trans. Cybern.* doi: 10.1109/TCYB.2020.2978216
- Zhang, K., Wang, J., and Fu, C. (2019d). Directional PointNet: 3D Environmental Classification for Wearable Robotics. *arXiv [Preprint]*. arXiv:1903.06846.
- Zhang, K., Xiong, C., Zhang, W., Liu, H., Lai, D., Rong, Y., et al. (2019c). Environmental features recognition for lower limb prostheses toward predictive walking. *IEEE Trans. Neural Syst. Rehabilitation Eng.* 27, 465–476. doi: 10.1109/TNSRE.2019.2895221
- Zhang, K., Zhang, W., Xiao, W., Liu, H., De Silva, C. W., and Fu, C. (2019b). Sequential decision fusion for environmental classification in assistive walking. *IEEE Trans. Neural Syst. Rehabilitation Eng.* 27, 1780–1790. doi: 10.1109/TNSRE.2019.2935765
- Zhong, B., Da Silva, R. L., Li, M., Huang, H., and Lobaton, E. (2020). Environmental context prediction for lower limb prostheses with uncertainty quantification. *IEEE Trans. Autom. Sci. Eng.* doi: 10.1109/TASE.2020.2993399

Conflict of Interest: The authors declare that the research was conducted in the absence of any commercial or financial relationships that could be construed as a potential conflict of interest.

Copyright © 2020 Laschowski, McNally, Wong and McPhee. This is an open-access article distributed under the terms of the Creative Commons Attribution License (CC BY). The use, distribution or reproduction in other forums is permitted, provided the original author(s) and the copyright owner(s) are credited and that the original publication in this journal is cited, in accordance with accepted academic practice. No use, distribution or reproduction is permitted which does not comply with these terms.



Dynamic Margins of Stability During Robot-Assisted Walking in Able-Bodied Individuals: A Preliminary Study

Arvind Ramanujam^{1,2}, Kamyar Momeni^{1,3}, Manikandan Ravi¹, Jonathan Augustine¹, Erica Garbarini¹, Peter Barrance^{1,3}, Ann M. Spungen⁴, Pierre Asselin⁴, Steven Knezevic⁴ and Gail F. Forrest^{1,3*}

¹ Kessler Foundation, West Orange, NJ, United States, ² Koneksa Health, New York, NY, United States, ³ Rutgers, New Jersey Medical School, Newark, NJ, United States, ⁴ James J. Peters Veterans Affairs Medical Center, Bronx, NY, United States

OPEN ACCESS

Edited by:

Jan Veneman,
Hocoma, Switzerland

Reviewed by:

Guillermo Asín-Prieto,
Independent Researcher,
Abadío, Spain
Hassène Gritli,
University of Tunis, Tunisia

*Correspondence:

Gail F. Forrest
gforrest@kesslerfoundation.org

Specialty section:

This article was submitted to
Biomedical Robotics,
a section of the journal
Frontiers in Robotics and AI

Received: 19 June 2020

Accepted: 21 October 2020

Published: 09 December 2020

Citation:

Ramanujam A, Momeni K, Ravi M, Augustine J, Garbarini E, Barrance P, Spungen AM, Asselin P, Knezevic S and Forrest GF (2020) Dynamic Margins of Stability During Robot-Assisted Walking in Able-Bodied Individuals: A Preliminary Study. *Front. Robot. AI* 7:574365. doi: 10.3389/frobt.2020.574365

Background: Gait analysis studies during robot-assisted walking have been predominantly focused on lower limb biomechanics. During robot-assisted walking, the users' interaction with the robot and their adaptations translate into altered gait mechanics. Hence, robust and objective metrics for quantifying walking performance during robot-assisted gait are especially relevant as it relates to dynamic stability. In this study, we assessed bi-planar dynamic stability margins for healthy adults during robot-assisted walking using EksoGTTM, ReWalkTM, and Indego[®] compared to independent overground walking at slow, self-selected, and fast speeds. Further, we examined the use of forearm crutches and its influence on dynamic gait stability margins.

Methods: Kinematic data were collected at 60 Hz under several walking conditions with and without the robotic exoskeleton for six healthy controls. Outcome measures included (i) whole-body center of mass (CoM) and extrapolated CoM (X_{CoM}), (ii) base of support (BoS), (iii) margin of stability (MoS) with respect to both feet and bilateral crutches.

Results: Stability outcomes during exoskeleton-assisted walking at self-selected, comfortable walking speeds were significantly ($p < 0.05$) different compared to overground walking at self-selected speeds. Unlike overground walking, the control mechanisms for stability using these exoskeletons were not related to walking speed. MoSs were lower during the single support phase of gait, especially in the medial-lateral direction for all devices. MoSs relative to feet were significantly ($p < 0.05$) lower than those relative to crutches. The spatial location of crutches during exoskeleton-assisted walking pushed the whole-body CoM, during single support, beyond the lateral boundary of the lead foot, increasing the risk for falls if crutch slippage were to occur.

Conclusion: Careful consideration of crutch placement is critical to ensuring that the margins of stability are always within the limits of the BoS to control stability and decrease fall risk.

Keywords: robotic exoskeleton, stability, kinematics, gait, center of mass

INTRODUCTION

Commercially available exoskeletons, such as the EksoGT™ (Ekso Bionics, Richmond, CA), ReWalk™ (ReWalk Robotics, Inc., Marlborough, MA), and Indego® (Parker Hannifin Corp, Cleveland, OH), are suggested rehabilitative modalities for overground (OG) walking among individuals with movement limitations (U.S. Food Drug Administration, 2014, 2016a,b, 2017). Walking using these exoskeletons requires assistive devices like bilateral canes, forearm crutches, or a walker; however, these assistive devices can inhibit dynamic stability (Bateni and Maki, 2005; Saunders et al., 2013). Additionally, slipping or sliding of bilateral cane and crutch tips due to the material used or different walking surfaces (e.g., wet pavements, snow, ice) can lead to further injuries (Kennaway, 1970; Bennett and Murphy, 1977). Therefore, understanding the posture and balance control strategies during robotic exoskeleton (RE) gait compared to independent OG walking is crucial in ensuring the safety of these individuals and preventing falls. Although researchers have studied the kinematic, spatiotemporal, cardio-pulmonary, cognitive, neuromuscular, and safety outcomes associated with RE training (Nozaki et al., 2005; Sayenko et al., 2015; Miller et al., 2016; Ramanujam et al., 2017, 2018, 2019a; Saleh et al., 2017; Gordon et al., 2018; Tefertiller et al., 2018; Forrest et al., 2019; Guanzioli et al., 2019; Khan et al., 2019; Luger et al., 2019; Momeni et al., 2019; Wang et al., 2019; Yildirim et al., 2019; McIntosh et al., 2020), a thorough assessment of dynamic stability during RE walking is important to understanding the mechanics of human-machine interactions during exoskeleton-assisted gait and the potential to lower fall risk.

Research studies involving gait analysis during RE-assisted gait have been predominantly focused on lower limb biomechanics (Sylos-Labini et al., 2014; Louie et al., 2015; Ramanujam et al., 2017, 2018, 2019a,b; Husain et al., 2018; Forrest et al., 2019). With the advances in research and development of powered lower limb exoskeletons (Jiménez-Fabian and Verlinden, 2012; Molteni et al., 2018), optimal exoskeleton choice depends on a variety of factors including the design and control of the device, user's ability, task, and environment. During RE-assisted walking, the users' interaction with the RE and their adaptation to the subtle differences between the devices translate into altered gait mechanics (Ramanujam et al., 2018, 2019a). As a result, robust and objective metrics for quantifying walking performance during RE-assisted gait are especially relevant as it relates to dynamic stability.

Whole-body center of mass (CoM) is a key determinant for balance control mechanisms in the quantification of dynamic gait stability (Kaya et al., 1998; Lee and Chou, 2006). Several authors have used CoM to describe postural sway, symmetry, and stability (Kaya et al., 1998; Lee and Chou, 2006; McAndrew Young et al., 2012; Ramanujam et al., 2019a,b). The instantaneous position and velocity of the whole-body CoM in relation to the base of support (BoS) has been used previously to calculate margins of stability (MoSs) (Hof et al., 2005) and evaluate the step-to-step changes in MoS during walking.

Our group has recently published articles to assess the posture and balance of individuals with spinal cord injury (SCI) and able-bodied (AB) controls during RE-assisted gait with forearm crutches in the EksoGT™ and ReWalk™ by examining their instantaneous three-dimensional CoM excursions (whole body, trunk, and lower extremity) with respect to the BoS (Ramanujam et al., 2019a,b). As an extension to our already-published work, in this study, we used the instantaneous CoM measures to further compute the dynamic stability margins for healthy adults during RE walking using EksoGT™, ReWalk™, and Indego® at self-selected, comfortable, and safe walking speeds to test our hypothesis that the MoS measures during RE-assisted walking will differ based on the device and assist mode, compared to independent OG walking at a self-selected speed. Additionally, we assessed fast and slow walking speeds during OG walking to evaluate the effect of speed on stability outcomes. Further, we examined the control of stability during the different phases of a gait cycle and the influence of forearm crutches in conjunction with RE walking on dynamic gait stability margins.

METHODS

Participant Demographics

Six male AB individuals (age: 29.50 ± 4.97 years, weight: 82.57 ± 13.23 kg, height: 1.80 ± 0.07 m) completed an informed consent form, approved by the Kessler Foundation and James J. Peters Veterans Affairs Medical Center Institutional Review Boards, to participate in the study. The inclusion and exclusion criteria have been previously reported (Ramanujam et al., 2019a).

Data Collection

AB individuals were first trained, under the guidance of a physical therapist, to walk independently with each RE under minimal supervision using bilateral forearm crutches before the scheduled data collection session. Individuals were asked to walk across a 10 m walkway multiple times under several walking conditions (**Table 1**) with and without the RE as previously reported (Ramanujam et al., 2019a). Kinematic data (Motion Analysis Corporation, Santa Rosa, CA) were collected at 60 Hz, and data from at least 10 gait cycles per condition were used for further analysis.

Exoskeleton Settings and Training Modes

Individuals were fitted with the RE devices per anthropometric measurements and by adjusting segments of the exoskeleton. The settings and operating principle for all RE devices tested are listed in **Table 2** (EksoGT™ Operating Manual Copyright © 2013 Ekso GT Bionics, Inc Part Number 103299 REV B1). OG walking conditions, without the RE, included walking at FAST, self-selected (SS), and SLOW speeds. Individuals were given a few practice walks at these three speeds (SLOW, SS, and FAST) and instructed to walk at their own safe and comfortable pace before kinematic data were collected. All walking trials with the REs were collected with the use of forearm crutches at their self-selected, comfortable, and safe walking speeds. The RE training modes (**Table 2**), with the addition of Indego® as

TABLE 1A | Demographics and testing conditions.

	AB 1	AB 2	AB 3	AB 4	AB 5	AB 6
Age (years)	38	30	26	26	25	32
Weight (Kg)	86.4	104.5	81.8	84.1	65.9	72.7
Height (m)	1.83	1.78	1.90	1.80	1.70	1.80

TABLE 1B | Walking conditions.

1	Walking with Indego [®] exoskeleton
2	Walking with ReWalk [™] exoskeleton
3	Walking with EksoGT [™] exoskeleton in 2Free mode
4	Walking with EksoGT [™] exoskeleton in Fixed-Assist mode
5	Walking with EksoGT [™] exoskeleton in Max-Assist mode
6	Overground walking at FAST speed
7	Overground walking at self-selected (SS) speed
8	Overground walking at SLOW speed

TABLE 1C | List of abbreviations.

SCI	-	Spinal Cord Injury
RE	-	Robotic Exoskeleton
CoM	-	Center of Mass
X_{CoM}	-	Extrapolated CoM
BoS	-	Base of Support
MoS	-	Margin of Stability
OG	-	Overground
AP	-	Anterior-posterior
ML	-	Medial-lateral
AB	-	Able-Bodied
SS	-	Self-Selected
F	-	Foot
C	-	Crutch
RMSD	-	Root Mean Squared Difference
IDS	-	Initial Double Support
SLS	-	Single Limb Support
TDS	-	Terminal Double Support
SW	-	Swing

an additional device, were selected based on our previous work (Ramanujam et al., 2019b) on individuals with SCI and AB controls and on the individual's ability to walk independently with minimal supervision.

Training and testing with the EksoGT[™] was performed under multiple conditions and swing assist modes, which provide adaptive assistance during the swing phase of the gait. These modes include “Max-Assist,” “Fixed-Assist,” and “2Free.” The Max-Assist mode provides a constant, maximum amount of motor power (100%) to move a user's leg through the trajectory-controlled swing phase. The Fixed-Assist mode provides assistance throughout the trajectory-controlled swing phase up to a predetermined value that is set as a percentage of the maximum amount of motor power (100–0%). In other words, if

users complete the swing phase with their own strength, without using the power of the motors, the value set on the Fixed-Assist mode would make no difference in the process. For instance, at 35% Fixed-Assist, the individual may use up to, or less than, 35% of the maximum motor power to complete the swing phase with a predetermined trajectory. Similarly, 0% Fixed-Assist requires individuals to utilize their own effort to finish the swing phase without using any amount of motor power; if they fail to do so, a safety feature will initiate to complete the swing phase. The 2Free mode allows users to freely move their leg with their own strength without being constrained to a predetermined swing trajectory.

In this study, to cover the entire range of available Fixed-Assist levels (100–0%) and also match the assist levels used while training individuals with SCI (depending on their ability and the therapist's recommendations) (Ramanujam et al., 2019b), we chose 0, 35, and 60% as the levels at which the device was tested for every individual. In Fixed-Assist mode, the goal is to encourage the participant to provide maximal effort in order to complete the swing phase while receiving up to a ceiling amount of motor power in assistance. We collected three to five trials (at least 10 complete gait cycles) at 0, 35, and 60% fixed assistance levels as a low, moderate, and high level of assistance, respectively, and calculated average profiles across these conditions for the Fixed-Assist mode.

Data Analysis

Kinematic data were filtered, time-normalized, and averaged across multiple gait cycles to create mean kinematic profiles (Ramanujam et al., 2019a). The outcome measures calculated from kinematics using custom written programs in MATLAB (MathWorks[®], Natick, MA) include: (i) whole-body CoM and the velocity-adjusted extrapolated CoM (X_{CoM}), (ii) margin of stability (MoS) in the anterior–posterior (AP) and medial–lateral (ML) directions with respect to both feet (MoS^F) and bilateral crutches (MoS^C), and (iii) walking speed; see **Figure 1**.

MoS parameters (**Figure 1**) were computed using the instantaneous CoM and X_{CoM} values (Hof, 2008). The coefficient of correlation (*R*) was calculated to examine relationships between MoS outcomes and walking speed and categorized into weak ($|R| \leq 0.40$), moderate ($0.40 < |R| \leq 0.60$), strong ($0.60 < |R| \leq 0.80$), and very strong ($0.80 < |R| \leq 1$) correlations (Evans, 1996). First-return plots (McAndrew Young et al., 2012) to assess stride-to-stride variability in MoS outcomes were generated (MoS_{*i*} vs. MoS_{*i-1*}), and root mean squared differences (RMSD) were computed to compare the variance from the 45° line of symmetry. MoS outcomes were computed at the point of heel-strike (bilaterally). Also, the least stable point (lowest MoS value and its associated T) during each phase of a gait cycle (i.e., initial double support, IDS: ipsilateral foot strike to contralateral foot off; single limb support, SLS: contralateral foot off to contralateral foot strike; terminal double support, TDS: contralateral foot strike to ipsilateral foot off; and swing, SW: ipsilateral foot off to subsequent ipsilateral foot strike) was identified and represented as a stability matrix.

TABLE 2 | Robotic exoskeleton operating principle and settings.

	Device operating principle	Device settings
EksoGT™	Lateral weight shift onto one foot to complete the stepping on the contralateral foot combined with moving the contralateral crutch forward	<i>Max-Assist</i> (100%): <i>Max-Assist</i> provides the maximum amount of motor assistance to the user at all times where the leg moves consistently through swing and is less susceptible to the user's interaction. <i>Fixed-Assist</i> (100–0%): <i>Fixed-Assist</i> is when the forward motor assistance is set to a fixed maximum value provided throughout the swing phase. In this study, the <i>Fixed-Assist</i> modes chosen were 0, 35, and 60%. <i>2Free</i> : <i>2Free</i> mode signals that the leg is not being controlled by motors and programming and is free to move under the user's control.
ReWalk™	Initiates a step by tilting the trunk anteriorly and moving both crutches forward simultaneously	Hip angle = 25°, knee angle = 37°, velocity/swing time = 600 ms, tilt = 7°
Indego®	Postural cues with predefined step trajectory to trigger all transitions (e.g., to walk forward, the user just leans forward)	Motion+ mode (assist = 20%, speed = medium, length = long, step height = medium)

Margins of Stability

As shown in **Figure 1**, the instantaneous location of the whole-body CoM and the X_{CoM} were calculated from kinematics.

$$X_{CoM} = c + \dot{c}/\omega_0 \quad (1)$$

$$\omega_0 = \sqrt{g/l} \quad (2)$$

The CoM position and velocity components are denoted as c and \dot{c} respectively, “ g ” = 9.81 m/s² (gravitational constant) with an oscillation frequency of “0,” and “1” (equivalent pendulum length) was the mean distance from the heel marker to the CoM at heel-strike. The X_{CoM} was then projected onto the floor (transverse plane) to establish its relationship with respect to the boundaries of BoS, bilaterally. BoS was defined as the linear distance between the boundaries (AP and ML) of the farthest support points in contact with the ground. In this study, BoS was calculated with respect to bilateral feet as well as crutches. The lateral boundary of BoS (left or right, foot or crutch) for MoS calculations was chosen so as to match the directionality of CoM velocity.

Different combinations of dynamic MoS were then calculated in the AP and ML directions with respect to (i) BoS between the feet (MoS^F) and (ii) BoS defined by the bilateral crutches (MoS^C) as follows:

$$MoS_j^i = X_{CoM_j} - BoS_j^i \quad (3)$$

where

$$i = F \text{ or } C \quad (4)$$

$$j = AP \text{ or } ML \quad (5)$$

A higher positive value for MoS is associated with greater stability. Negative MoS values are considered unstable. Further, the MoS values were normalized to CoM velocity to calculate a temporal index (T) indicative of stability as defined below.

$$T_j^i = MoS_j^i / \dot{c}_j \quad (6)$$

T values represent the temporal deviation (in seconds) from the limits of BoS. Similar to the sign convention for MoS, a positive T value indicates the time available until the point of instability,

while $T < 0$ is indicative of the time elapsed beyond the point of instability. Hence, higher positive or negative T values represent greater stability or instability, respectively.

Statistical Analysis

A multivariate analysis of variance (ANOVA), to compare RE and OG walking conditions, was performed for all outcome variables using Bonferroni correction. Tukey *post hoc* tested for all possible two-way comparisons. Paired-sample *t*-tests were used to compare the means across devices and modes, as well as OG walking conditions ($p < 0.05$).

RESULTS

MoS Outcomes During OG vs. RE Walking

At heel-strike during RE walking across all tested devices and conditions, the overall mean MoSs calculated using the BoS defined by the bilateral crutches (MoS_{ML} = 0.56 ± 0.09 m; MoS_{AP} = 0.31 ± 0.08 m) were significantly ($p < 0.05$) greater than OG walking (MoS_{ML} = 0.11 ± 0.03 m; MoS_{AP} = 0.06 ± 0.17 m) across all speeds in both directions (**Figure 2A**).

For RE walking, a weak negative correlation was observed for MoS_{ML} ($R = -0.39$) vs. walking speed ($R = -0.07$ for MoS_{AP}). During OG walking, the correlation between MoS_{ML} and walking speed was weak ($R = -0.27$); however, the correlation for MoS_{AP} was significantly ($p < 0.05$) strong and negative ($R = -0.98$, **Figures 2B,C**).

First-return plots (**Figures 2D,E**) showed that overall RMSD values were significantly ($p < 0.05$) greater for RE walking compared to OG walking in both AP (RMSD_{RE-AP} = 0.03 ± 0.02 m; RMSD_{OG-AP} = 0.02 ± 0.02 m) and ML (RMSD_{RE-ML} = 0.04 ± 0.03 m; RMSD_{OG-ML} = 0.01 ± 0.01 m) directions.

Effect of Device Settings and Speed on MoS

A significant moderate negative correlation ($R = -0.48$, $p < 0.05$) was observed for MoS_{ML} with walking speed for the Indego®. For EksoGT™ in the *Max-Assist* mode, the correlation was weak ($R = -0.37$) for MoS_{ML} with speed, while it was moderate ($R = -0.42$, $p < 0.05$) for MoS_{AP} (**Figures 3A,B** and **Table 3**). In the *Fixed-Assist* mode, the correlations were relatively weaker ($|R|$

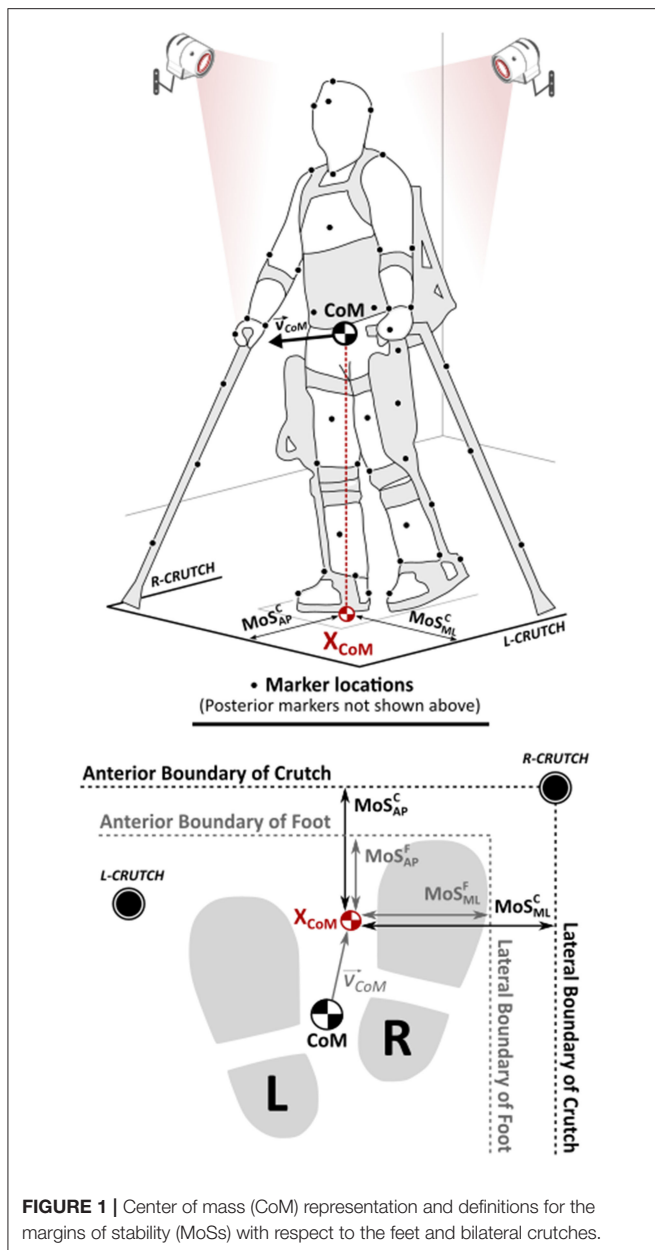


FIGURE 1 | Center of mass (CoM) representation and definitions for the margins of stability (MoSs) with respect to the feet and bilateral crutches.

< 0.36) and significantly negative ($p < 0.05$) in both directions during EksoGTTM walking. For OG walking, the correlations for MoS_{ML} and walking speeds were moderately negative ($-0.51 < R < -0.42$, $p < 0.05$); however, they were significantly very strong for MoS_{AP} ($-0.98 < R < -0.89$, $p < 0.05$).

First-return plots (Figures 3C,D) showed that RMSD values across AP and ML directions were the lowest for OG walking across all speeds compared to all RE walking and settings (Table 3). For OG walking, faster speeds produced greater $RMSD_{AP}$ values. Walking in the EksoGTTM under the *Max-Assist* and *Fixed-Assist* modes was associated with greater RMSD values in the ML direction, while walking in the EksoGTTM (2Free mode), Indego[®], and ReWalkTM produced greater RMSD

values in the AP direction (Figures 3C,D and Table 3). In both directions, RMSD values for the RE devices were significantly ($p < 0.05$) greater than OG walking, except for EksoGTTM (2Free mode). Correlations between MoS_{ML} and MoS_{AP} (Figure 3E) were moderate ($0.40 < R < 0.59$) and significantly positive ($p < 0.05$) for OG walking across all speeds. For RE walking, only ReWalkTM produced positive correlations for these measures ($R = 0.52$, $p < 0.05$).

MoS Representation Referenced to Feet vs. Crutches

MoS outcomes calculated relative to bilateral foot were significantly lower ($MoS^F < 0.13$ m, $p < 0.05$) compared to those relative to bilateral crutches ($MoS^C > 0.48$ m). MoS^F values for Indego[®] (0.11 m) and EksoGTTM (2Free mode, 0.12 m) were not significantly different from OG walking in the ML direction, while it was the highest for ReWalkTM (0.18 m, $p < 0.05$). In the AP direction, although less than MoS^C (> 0.29 m), MoS^F values (< 0.26 m) were still significantly ($p < 0.05$) greater than OG walking at all speeds. For Indego[®], MoS_{AP} outcomes when referenced to bilateral crutches (MoS^C) were the highest amongst all RE devices; however, it was the lowest when referenced to the feet (MoS^F).

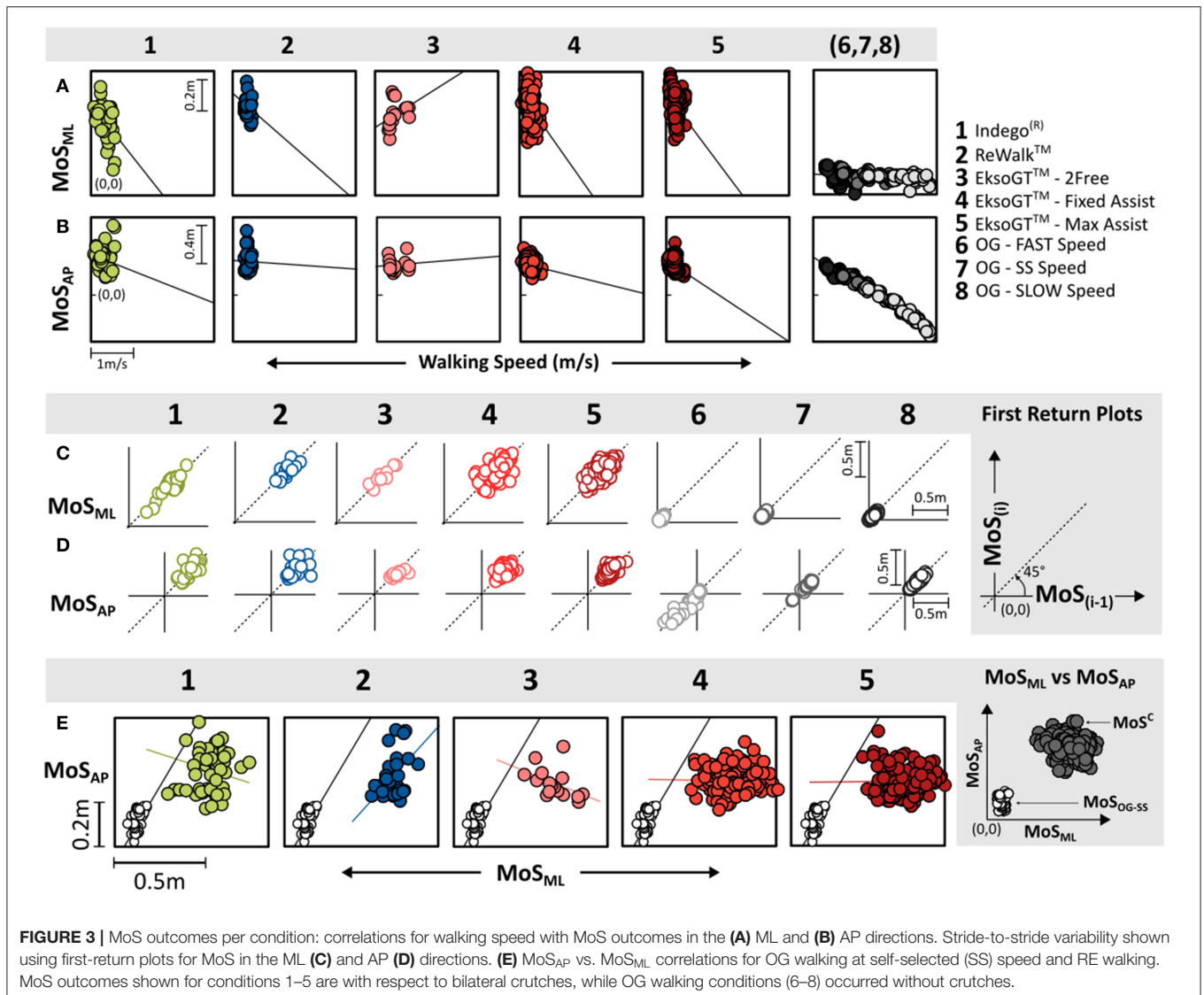
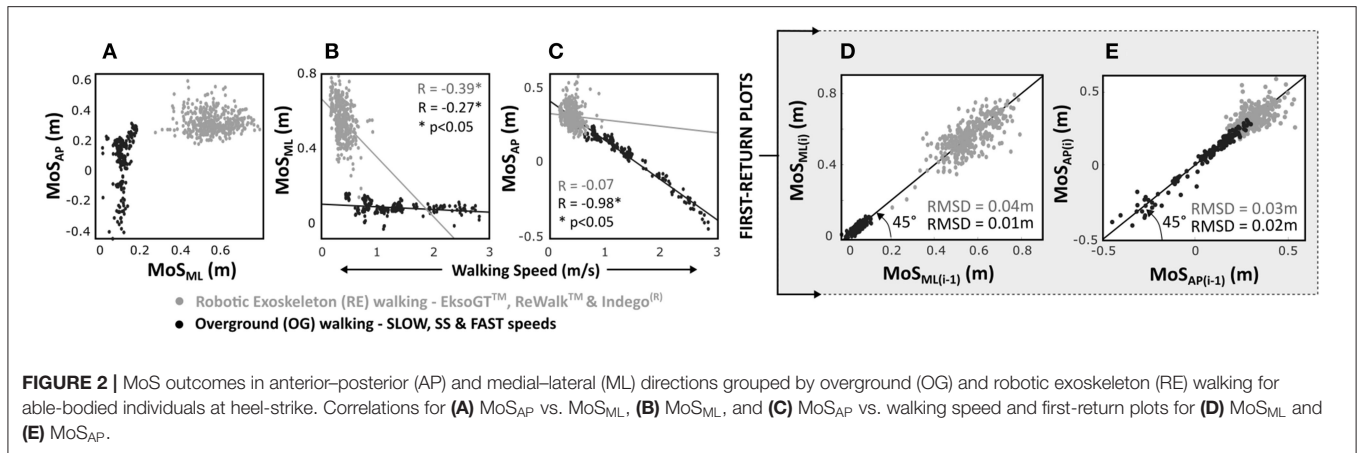
Stability Matrix

In addition to MoS outcomes computed at the point of heel-strike, the least stable point (MoS_{min}) during each phase of a gait cycle (IDS, SLS, TDS, and SW) was also determined (Figure 4). Medial-laterally, MoS^C and MoS^F stayed positive (0.05 m $< MoS_{ML} < 0.11$ m) during IDS and TDS. With RE walking, MoS_{ML} was highest with the ReWalkTM during IDS and TDS (> 0.10 m). Conversely, MoS values were negative during SS and SW. In the AP direction, during RE walking, MoS^C was positive during the entire gait cycle except for EksoGTTM in the 2Free mode that experienced negative values (< -0.16 m) during SS and SW, while MoS^F was found to be negative (< -0.11 m) during the SS and SW. Between OG and RE walking, MoS_{AP} values were consistently lower during OG walking across all speeds (especially faster speeds) and gait phases (especially SS).

Figure 4B shows the velocity-normalized representation of MoS (referred to as “T,” temporal stability), which was calculated by dividing the MoS values in Figure 4A by the mean directional CoM velocity during the corresponding phase of the gait cycle (see Equation 4). During OG and RE walking, bidirectional T^F was negative (-3.11 s $< T^F < -0.39$ s) during SS and SW, while it was close to or greater than zero (0.02 s $< T^F < 0.94$ s) during IDS and TDS, except for T_{AP} during OG walking at FAST and SS speeds. Between OG and RE walking, unlike MoS_{AP} outcomes, T_{AP} values were relatively similar.

DISCUSSION

Previously, walking performance involving RE-assisted gait has included clinical measures, functional measures, and gait analysis studies focused primarily on spatiotemporal and lower limb kinematic outcomes during quadrupedal gait using inverse dynamic techniques (Sylos-Labini et al., 2014; Ramanujam et al.,



2017, 2018, 2019a,b; Husain et al., 2018; Forrest et al., 2019; Wang et al., 2019). Moreover, our group has not only published articles on upper and lower extremity kinematics but also studied the

posture and balance of individuals (both SCI and AB controls) during RE-assisted gait with forearm crutches by examining their instantaneous CoM excursions (whole body, trunk, and

TABLE 3 | Margin of stability (MoS) outcomes across robotic exoskeleton (RE) devices and overground (OG) walk conditions at heel-strike.

				RE walking conditions					OG walking conditions**		
				1	2	3	4	5	6	7	8
MoS _{ML} ^F		(m)		0.11 ± 0.02	0.18 ± 0.01	0.12 ± 0.02	0.13 ± 0.02	0.13 ± 0.03	0.11 ± 0.02	0.11 ± 0.02	0.11 ± 0.04
MoS _{ML} ^C		(m)		0.48 ± 0.09	0.57 ± 0.06	0.52 ± 0.09	0.58 ± 0.09	0.58 ± 0.09	- Walking without crutch -		
MoS _{AP} ^F		(m)		0.22 ± 0.03	0.24 ± 0.02	0.23 ± 0.03	0.26 ± 0.04	0.26 ± 0.03	-0.16 ± 0.15	0.09 ± 0.08	0.18 ± 0.06
MoS _{AP} ^C		(m)		0.36 ± 0.12	0.33 ± 0.11	0.29 ± 0.07	0.30 ± 0.05	0.30 ± 0.06	- Walking without crutch -		
MoS _{ML} ^C	vs.	Walking speed	R	-0.48*	-0.23	0.36	-0.36*	-0.37*	-0.51*	-0.42*	-0.49*
MoS _{AP} ^C	vs.	Walking speed	R	-0.20	-0.02	0.09	-0.18*	-0.42*	-0.98*	-0.96*	-0.89*
MoS _{AP} ^C	vs.	MoS _{ML} ^C	R	-0.24	0.52*	-0.45	-0.03	0.01	0.48*	0.40*	0.59*
MoS _{ML(i)} ^C	vs.	MoS _{ML(i-1)} ^C	RMSD (m)	0.03 ± 0.02	0.03 ± 0.02	0.02 ± 0.02	0.04 ± 0.03	0.04 ± 0.03	0.01 ± 0.01	0.01 ± 0.01	0.01 ± 0.01
MoS _{AP(i)} ^C	vs.	MoS _{AP(i-1)} ^C	RMSD (m)	0.04 ± 0.05	0.06 ± 0.06	0.04 ± 0.04	0.03 ± 0.03	0.02 ± 0.02	0.03 ± 0.03	0.01 ± 0.01	0.01 ± 0.01
Walking Speed		(m/s)		0.47 ± 0.13	0.48 ± 0.06	0.61 ± 0.17	0.37 ± 0.08	0.31 ± 0.09	2.10 ± 0.49	1.24 ± 0.32	0.84 ± 0.26

Walking conditions 1 to 8 are as described previously; **OG walking occurred without the use of crutches; values are presented as mean ± SD or number; * $p < 0.05$.

lower extremity) in relation to the BoS (Ramanujam et al., 2019a,b). For this manuscript, we have combined all of these parameters to determine the instantaneous MoS for investigating stability control using different RE devices. To date, there is limited research to evaluate balance control using different powered RE devices. In this study, human-machine interaction for computed dynamic margins of stability were quantified for walking performance during RE-assisted walking compared to independent OG walking for healthy adults.

MoS Outcomes vs. Speed During OG and RE Walking

MoS outcomes were negatively correlated ($p < 0.05$, Table 3) to walking speed during OG walking. Therefore, with an increase in walking speed, instability increased in both AP and ML directions. By comparison, 80% (8/10 correlations) of RE conditions showed weak ($|R| < 0.37$) correlations for either direction. Therefore, control mechanisms for stability using REs were not related to changes in walking speed. The exceptions were the Indego[®] ($p < 0.05$) medial-laterally and EksoGT[™] (Max-Assist mode; $p < 0.05$) in the AP direction.

For many REs, device parameters such as the assist modes or motor assistance levels determined the human-machine interactions affecting walking speed. The greater stance time required to meet the forward and lateral targets for step initiation translated to slower walking speeds (Sylos-Labini et al., 2014; Ramanujam et al., 2017), whereas faster speed required rapid and spatially extensive weight shifts (predominantly by the trunk and pelvis) onto the lead limb for a quicker step initiation with the trail limb during stance to increase CoM velocity and negatively affect the margins of stability. This is especially true while walking with the EksoGT[™] (assist modes) and ReWalk[™] since they operate on the principle of lateral and anterior weight

shifts, respectively, on to the lead limb, to initiate the next step. This delay in weight acceptance can affect overall walking speed. By comparison, for OG walking, dynamic stability can be controlled by lower extremity foot placement, especially lateral foot placement (Hof, 2008). These progressive step changes in foot placement are essential to walking stability in the prevention of disturbances such as slips and falls (Kennaway, 1970; Bennett and Murphy, 1977; Bateni and Maki, 2005; Saunders et al., 2013).

Crutches for quadrupedal gait increase the BoS to improve balance (Bateni and Maki, 2005; Saunders et al., 2013). However, assistive devices have been associated with an increased risk of falling and injuries during the expected or unexpected transition (crutch lift or slippage) from quadrupedal to bipedal gait during non-exoskeleton gait (Bateni and Maki, 2005). Lifting or slippage of the assistive device is similar to lifting the foot, causing the CoM to fall toward the unsupported side during unassisted gait, creating a state of imbalance where the CoM lies outside the limits of BoS (Bateni and Maki, 2005). During RE walking (especially, EksoGT[™]), the devices' limitation toward choosing the desired lateral foot placement puts more emphasis on crutch location outside the leading limb to provide a stable BoS, resulting in reduced ML control of stability. The location of this crutch may also be influenced by the different surfaces (e.g., carpet, pavement) (Wang et al., 2019).

Device Operation and its Effect on Stability

In addition to moderate-to-strong relationships between MoS outcomes and walking speed, for OG gait, MoS_{AP} was significantly positive and moderately correlated ($p < 0.05$) to MoS_{ML}. Therefore, during OG gait, the mechanisms for controlling dynamic stability were multi-planar and changed based on gait speed. For RE devices, there were very weak and non-significant relationships between MoS_{AP} and MoS_{ML} except

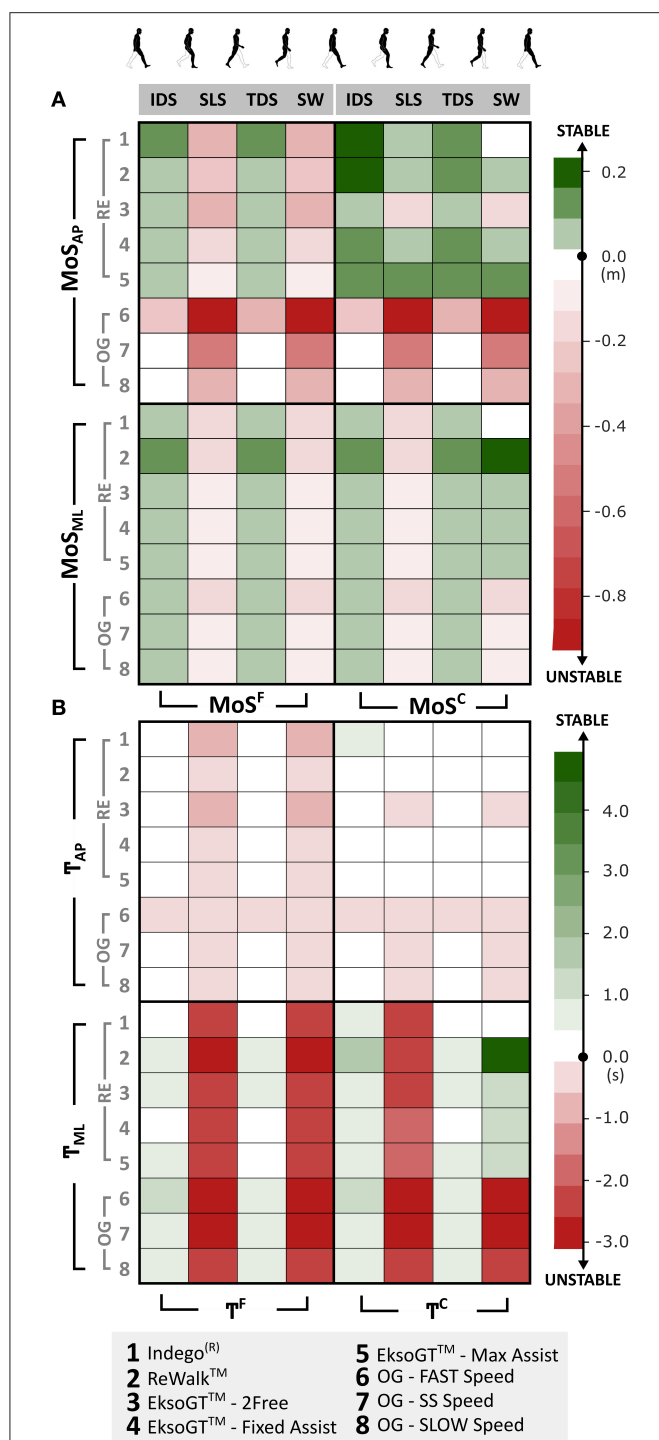


FIGURE 4 | (A) Stability matrix showing the lowest stability values (MoS_{min}) in both AP and ML directions during each phase of gait cycle [initial double support (IDS), single support (SS), terminal double support (TDS), and SWING] across RE and OG walking. **(B)** MoS normalized to CoM velocity (referred to as “temporal stability”—?) within each phase of the gait cycle.

for ReWalkTM and EksoGTTM (2Free), which exhibited positive and negative relationships for MoS_{AP} and MoS_{ML} , respectively. Therefore, gains in stability were bi-planar only in the ReWalkTM.

The inherent differences in the design and control mechanisms of these devices altered the way users maintain balance and control their dynamic stability. As found earlier, the control of MoS was not necessarily related to speed during RE walking. The changes in MoS during RE walking were governed more by the positional aspect of the CoM due to the necessary ML and/or AP weight shifts for step initiation rather than its velocity component. For instance, the EksoGTTM operates on the principle of lateral weight shift onto one foot to complete the stepping on the contralateral foot combined with moving the contralateral crutch forward, while the ReWalkTM uses a “tilt” action that initiates a step by tilting the trunk anteriorly and moving both crutches forward simultaneously. This increase in trunk lean angle at heel-strike and greater AP excursion of CoM while walking with the ReWalkTM, as previously reported in our earlier study (Ramanujam et al., 2019a), translated into a more anterior location of the CoM, resulting in lower stability values (for MoS^F) in the AP direction compared to EksoGTTM (Max-Assist and Fixed-Assist). Similar is the case with AP stability in the Indego[®] that uses postural cues to trigger all transitions (e.g., to walk forward, the user just leans forward) and EksoGTTM (2Free mode) where the user is free to move in any direction while stepping and not restricted to ML weight shifts.

It should also be noted that each standard deviation associated with the mean MoS (ML or AP) for Fixed-Assist modes (Table 3) is low, indicating that the difference in levels of assistance in the Fixed-Assist mode (60, 35, 0%) had a minimal effect on MoS values.

Effect of Crutch Placement on Stride-to-Stride Control

Stride-to-stride variability in MoS outcomes is indicative of the control of stability during consecutive steps. The dispersion of points on the first-return plots determines step-to-step adaptations during gait. For OG walking, as expected, the stride-to-stride variability was significantly low except for FAST speeds in the AP direction compared to RE devices. One of the major determinants of faster walking speed is increased step and stride lengths. The variability in terms of anterior foot placements across strides and individuals, to increase step lengths and achieve faster speeds, translated into higher $RMSD_{AP}$ values. During RE walking, the foot placements are, for the most part, governed and limited by the device settings and hence quite similar from one step to another. However, the placement of bilateral crutches varies stride to stride, across individuals and devices/modes. The precise location of crutch placement is based on individual preferences. Therefore, variability in crutch placement translates into higher dispersion of stride-to-stride stability measures and, hence, reduced control of stability especially during the transition to a bipedal gait.

For RE walking, $RMSD_{ML}$ values were found to be significantly greater ($p < 0.05$) with EksoGTTM for the Max-Assist and Fixed-Assist modes, while $RMSD_{AP}$ values were significantly greater with the Indego[®] and ReWalkTM. During Max-Assist (EksoGTTM), individuals tend to load onto their leading limb to achieve the required lateral weight shift for step

initiation with the trailing limb. Hof (2008) found in their study that stability might be maintained or controlled by the lateral foot placement during walking. However, during RE walking (especially EksoGT™), the extent of lateral foot placement is restricted by the device design and setting. Consequently, the crutch is more lateral to the leading limb to provide a stable BoS, resulting in higher $RMSD_{ML}$ values and reduced ML control of stability. This is especially relevant to the *Fixed-Assist* mode. Conversely, with the ReWalk™ and Indego®, the emphasis is on forward trunk lean for step initiation and hence a more anterior location of crutches. This results in greater AP stride-to-stride variability in MoS and a reduced AP control of stability.

Control of Stability During a Gait Cycle

As noted earlier, for quadrupedal RE gait, the majority of postural adaptations and weight transfer within each device occur during the phases of SS just prior to step initiation. As a result, all stability outcome measures are lower during these phases.

Dynamic margins of stability in the ML direction were found to be stable during the double support phases of OG walking at all speeds as well as RE walking across the tested devices. Anterior–posteriorly, all three devices were most stable for both the crutch (MoS^C) and foot (MoS^F) margins of stability during double support. However, instability was observed during SS (MoS^F only). In the EksoGT™, although the *Max-Assist* and *Fixed-Assist* modes necessitate users to shift their weight laterally to complete the stepping motion, the *2Free* mode provides more freedom to translate or step anteriorly. This is supported by lower values of MoS_{AP} in the *2Free* mode of EksoGT™ walking during SS. Similar observations were seen while walking in the ReWalk™ and Indego®, which requires users to lean forward with their trunk for step initiation.

Since the analyses for MoS outcomes for RE were not related to speed and there were large device differences for walking speeds compared to OG walking, MoS outcomes were normalized relative to speed for each phase of a gait cycle, defined as the temporal stability margin (T). T^F in the AP direction during RE walking was similar to OG walking at SLOW and SS speeds. Therefore, the RE gait stability based on MoS parameters normalized to speed was like OG gait. Therefore, despite the assistance and postural support offered by the RE, it did not necessarily alter the AP stability measures compared to OG walking. Of note, while walking with EksoGT™ in the *2Free* mode, the temporal AP stability with respect to feet (T^F) as well as crutches (T^C) was much lower compared to other RE devices and modes during SS.

Significance of MoS Referenced to Feet

Since RE walking occurred exclusively with the use of bilateral forearm crutches and at relatively low speeds (<0.6 m/s), the mean MoS outcomes (MoS^C) were significantly greater than those experienced during independent OG walking across all speeds (>0.8 m/s). The wider BoS provided by the crutches compared to just the feet (OG walking) increased the overall dynamic stability for a quadrupedal gait for all RE devices tested. However, although the margins of stability were high with crutch usage, it is still important to examine and evaluate the postural

orientation of the whole-body CoM relative to feet (bipedal gait). In the event of crutch slippage caused by a variety of reasons, the feet will act as a bipedal BoS for individuals during RE walking. To further examine this, MoS outcomes were also computed relative to feet as the BoS (MoS^F), which were found to be considerably lower compared to those calculated relative to crutches (MoS^C).

Bilateral stability outcomes relative to feet, both MoS^F and T^F (Figure 4), are considerably lower throughout the gait cycle compared to those calculated relative to crutches (MoS^C and T^C). During the SS phases of RE walking, majority of postural adjustments and ML weight transfers occur to initiate stepping with the trail limb. Using the crutch during RE walking is not only precautionary to provide support, but individuals tend to lean on the crutches during these phases, especially medial–laterally (for EksoGT™) and anterior–posteriorly (for, ReWalk™ and Indego®), in order to propel themselves forward. As a result, all the stability outcome measures are lower during these phases.

Assistive devices can inhibit balance during gait to increase fall risk (Kennaway, 1970; Phonthee et al., 2013). Crutch slippage due to the material used or different walking surfaces (e.g., wet pavements, snow, ice, etc.) can lead to injuries (Kennaway, 1970; Bennett and Murphy, 1977). MoS data and analyses indicate that the reliance on crutches during RE walking moves the CoM laterally and in some cases beyond the BoS defined by the feet, thereby increasing postural instability and fall risk if the crutch were to slip.

Limitations

While the results provided significant insight into human–robotic interaction for stability during RE gait and directly addressed the hypothesis to show significant differences in the MoS measures during RE-assisted walking based on device, compared to independent OG walking for all speeds, these results are preliminary. A greater number of trials for all conditions and number of training sessions per individual are needed to further analyze stability. The mechanical measures determined the dynamic MoS without consideration given to the difference in neuromuscular strategies, for recovery of gait and balance. Research in these areas is required for community and rehabilitation devices.

Conclusion and Future Works

For healthy adults, stability outcomes alone and their relationship to walking speed during RE walking compared to independent OG walking were significantly different. Due to exoskeleton design, margins of stability or control mechanisms for stability during RE walking were not related to walking speed. Despite the dissimilarities in the design and operation of these RE devices, the dynamic margins of stability for these individuals were found to be lower during SS, especially in the ML direction across all devices. Further, the reliance on crutches and their spatial location during RE walking pushed the CoM, during SS, beyond the lateral boundary of the lead foot, thereby placing the individuals at risk for falls if crutch slippage was to occur, especially relevant when individuals

cannot recover from an unbalanced posture. Consideration of crutch placement is therefore relevant to stride-to-stride postural control and margins of stability within the limits of bipedal BoS for dynamic stability. Understanding the interactions between humans, RE devices, and assistive devices (if used) combined with training adaptations is relevant to the advancements in the field of exoskeleton technology, both in research and in the clinic. Future research will include a more comprehensive analysis of the different assist modes within each exoskeleton and the possible use of the Monte Carlo statistical technique to further evaluate the associated outcome measures.

DATA AVAILABILITY STATEMENT

The raw data supporting the conclusions of this article will be made available by the authors, without undue reservation.

REFERENCES

- Bateni, H., and Maki, B. E. (2005). Assistive devices for balance and mobility: benefits, demands, and adverse consequences. *Arch. Phys. Med. Rehabil.* 86, 134–145. doi: 10.1016/j.apmr.2004.04.023
- Bennett, L., and Murphy, E. F. (1977). Slipping cane and crutch tips. Part I—static performance of current devices. *Bull. Prosthet. Res.* 71–90.
- Evans, J. D. (1996). *Straightforward Statistics for the Behavioral Sciences*. Brooks/Cole Pub. Co. Available online at: https://books.google.com/books/about/Straightforward_Statistics_for_the_Behav.html?id=8Ca2AAAAIAAJ (accessed June 15, 2020).
- Forrest, G. F., Ramanujam, A., Spungen, A. M., Cirnigliaro, C., Momeni, K., Husain, S. R., et al. (2019). “Exoskeleton controller and design considerations: Effect on training response for persons with SCI,” in *Biosystems and Biorobotics* eds Carrozza, M., Micera, S., and Pons, J. (Cham: Springer), 22, 314–318. doi: 10.1007/978-3-030-01887-0_60
- Gordon, D. F. N., Henderson, G., and Vijayakumar, S. (2018). Effectively quantifying the performance of lower-limb exoskeletons over a range of walking conditions. *Front. Robot. AI* 5:27. doi: 10.3389/frobt.2018.00061
- Guanziroli, E., Cazzaniga, M., Colombo, L., Basilico, S., Legnani, G., and Molteni, F. (2019). Assistive powered exoskeleton for complete spinal cord injury: correlations between walking ability and exoskeleton control. *Eur. J. Phys. Rehabil. Med.* 55, 209–216. doi: 10.23736/S1973-9087.18.05308-X
- Hof, A. L. (2008). The “extrapolated center of mass” concept suggests a simple control of balance in walking. *Hum. Mov. Sci.* 27, 112–125. doi: 10.1016/j.humov.2007.08.003
- Hof, A. L., Gazendam, M. G. J., and Sinke, W. E. (2005). The condition for dynamic stability. *J. Biomech.* 38, 1–8. doi: 10.1016/j.jbiomech.2004.03.025
- Husain, S. R., Ramanujam, A., Momeni, K., and Forrest, G. F. (2018). “Effects of exoskeleton training intervention on net loading force in chronic spinal cord injury,” in *Proceedings of the Annual International Conference of the IEEE Engineering in Medicine and Biology Society, EMBS* (Institute of Electrical and Electronics Engineers Inc.), 2793–2796.
- Jiménez-Fabián, R., and Verlinden, O. (2012). Review of control algorithms for robotic ankle systems in lower-limb orthoses, prostheses, and exoskeletons. *Med. Eng. Phys.* 34, 397–408. doi: 10.1016/j.medengphys.2011.11.018
- Kaya, B. K., Krebs, D. E., and Riley, P. O. (1998). Dynamic stability in elders: momentum control in locomotor ADL. *J. Gerontol. A. Biol. Sci. Med. Sci.* 53, M126–M134. doi: 10.1093/gerona/53A.2.M126
- Kennaway, A. (1970). On the reduction of slip of rubber crutch-tips on wet pavement, snow, and ice. *Bull. Prosthet. Res.* 10, 130–144.
- Khan, A. S., Livingstone, D. C., Hurd, C. L., Duchcherer, J., Misiaszek, J. E., Gorassini, M. A., et al. (2019). Retraining walking over ground in a powered exoskeleton after spinal cord injury: a prospective cohort study to

ETHICS STATEMENT

The studies involving human participants were reviewed and approved by Kessler Foundation and James J. Peters VA Medical Center’s Institutional Review Boards. The patients/participants provided their written informed consent to participate in this study.

AUTHOR CONTRIBUTIONS

All authors listed have made a substantial, direct and intellectual contribution to the work, and approved it for publication.

FUNDING

Research supported by the New Jersey Commission on Spinal Cord Research (Grant# CSCR131RG013).

- examine functional gains and neuroplasticity. *J. Neuroeng. Rehabil.* 16:145. doi: 10.1186/s12984-019-0585-x
- Lee, H.-J., and Chou, L.-S. (2006). Detection of gait instability using the center of mass and center of pressure inclination angles. *Arch. Phys. Med. Rehabil.* 87, 569–575. doi: 10.1016/j.apmr.2005.11.033
- Louie, D. R., Eng, J. J., and Lam, T. (2015). Gait speed using powered robotic exoskeletons after spinal cord injury: A systematic review and correlational study. *J. Neuroeng. Rehabil.* 12, 1–10. doi: 10.1186/s12984-015-0074-9
- Luger, T., Seibt, R., Cobb, T. J., Rieger, M. A., and Steinhilber, B. (2019). Influence of a passive lower-limb exoskeleton during simulated industrial work tasks on physical load, upper body posture, postural control and discomfort. *Appl. Ergon.* 80, 152–160. doi: 10.1016/j.apergo.2019.05.018
- McAndrew Young, P. M., Wilken, J. M., and Dingwell, J. B. (2012). Dynamic margins of stability during human walking in destabilizing environments. *J. Biomech.* 45, 1053–1059. doi: 10.1016/j.jbiomech.2011.12.027
- McIntosh, K., Charbonneau, R., Bensaada, Y., Bhatiya, U., and Ho, C. (2020). The safety and feasibility of exoskeletal-assisted walking in acute rehabilitation after spinal cord injury. *Arch. Phys. Med. Rehabil.* 101, 113–120. doi: 10.1016/j.apmr.2019.09.005
- Miller, L. E., Zimmermann, A. K., and Herbert, W. G. (2016). Clinical effectiveness and safety of powered exoskeleton-assisted walking in patients with spinal cord injury: systematic review with meta-analysis. *Med. Devices* 9, 455–466. doi: 10.2147/MDER.S103102
- Molteni, F., Gasperini, G., Cannaviello, G., and Guanziroli, E. (2018). Exoskeleton and end-effector robots for upper and lower limbs rehabilitation: narrative review. *PMR* 10, S174–S188. doi: 10.1016/j.pmrj.2018.06.005
- Momeni, K., Ramanujam, A., Garbarini, E. L., and Forrest, G. F. (2019). Multi-muscle electrical stimulation and stand training: Effects on standing. *J. Spinal Cord Med.* 42, 378–386. doi: 10.1080/10790268.2018.1432311
- Nozaki, D., Nakazawa, K., and Akai, M. (2005). Uncertainty of knee joint muscle activity during knee joint torque exertion: the significance of controlling adjacent joint torque. *J. Appl. Physiol.* 99, 1093–1103. doi: 10.1152/japplphysiol.00365.2005
- Phonthee, S., Saengsuwan, J., and Amatachaya, S. (2013). Falls in independent ambulatory patients with spinal cord injury: incidence, associated factors and levels of ability. *Spinal Cord* 51, 365–368. doi: 10.1038/sc.2012.147
- Ramanujam, A., Cirnigliaro, C. M., Garbarini, E., Asselin, P., Pilkar, R., and Forrest, G. F. (2018). Neuromechanical adaptations during a robotic powered exoskeleton assisted walking session. *J. Spinal Cord Med.* 41, 518–528. doi: 10.1080/10790268.2017.1314900
- Ramanujam, A., Momeni, K., Husain, S. R., Augustine, J., Garbarini, E., Barrance, P., et al. (2019a). “Center of mass and postural adaptations during robotic exoskeleton-assisted walking for individuals with spinal cord injury,” in

- Biosystems and Biorobotics* eds Carrozza, M., Micera, S., and Pons, J. (Cham: Springer), 22, 309–313. doi: 10.1007/978-3-030-01887-0_59
- Ramanujam, A., Momeni, K., Ravi, M., Augustine, J., Garbarini, E., Barrance, P., et al. (2019b). “Center of mass adaptations and its interaction between the trunk and lower-extremity during exoskeleton walking,” in *2019 Wearable Robotics Association Conference, WearACon 2019* (Institute of Electrical and Electronics Engineers Inc.), 57–62.
- Ramanujam, A., Spungen, A., Asselin, P., Garbarini, E., Augustine, J., Canton, S., et al. (2017). “Training response to longitudinal powered exoskeleton training for SCI,” in *Biosystems and Biorobotics* González-Vargas, J., Ibáñez, J., Contreras-Vidal, J., van der Kooij, H., and Pons J. (Cham: Springer), 16, 361–366. doi: 10.1007/978-3-319-46532-6_59
- Saleh, S., Ramanujam, A., Momeni, K., Hoxha, A., Husain, S. R., Allexandre, D., et al. (2017). “Cortical control of walking with and without powered exoskeleton assistance: an EEG pilot study,” in *2017 International Symposium on Wearable Robotics and Rehabilitation (WeRob)* (IEEE), 1–2.
- Saunders, L. L., Krause, J. S., DiPiro, N. D., Kraft, S., and Brotherton, S. (2013). Ambulation and complications related to assistive devices after spinal cord injury. *J. Spinal Cord Med.* 36, 652–659. doi: 10.1179/2045772312Y.0000000082
- Sayenko, D. G., Atkinson, D. A., Dy, C. J., Gurley, K. M., Smith, V. L., Angeli, C., et al. (2015). Spinal segment-specific transcutaneous stimulation differentially shapes activation pattern among motor pools in humans. *J. Appl. Physiol.* 118, 1364–1374. doi: 10.1152/japplphysiol.01128.2014
- Sylos-Labini, F., La Scaleia, V., D’Avella, A., Pisotta, I., Tamburella, F., Scivoletto, G., et al. (2014). EMG patterns during assisted walking in the exoskeleton. *Front. Hum. Neurosci.* 8:423. doi: 10.3389/fnhum.2014.00423
- Tefertiller, C., Hays, K., Jones, J., Jayaraman, A., Hartigan, C., Bushnik, T., et al. (2018). Initial outcomes from a multicenter study utilizing the indigo powered exoskeleton in spinal cord injury. *Top. Spinal Cord Inj. Rehabil.* 24, 78–85. doi: 10.1310/sci17-00014
- U.S. Food and Drug Administration (2014). *Device Classification under Section 513(f)(2)(de novo)*. ReWalk, Argo Med. Technol. Inc. Available online at: <https://www.accessdata.fda.gov/scripts/cdrh/cfdocs/cfpmn/denovo.cfm?ID=DEN130034> (accessed June 15, 2020).
- U.S. Food and Drug Administration (2016a). *510(k) Premarket Notification*. Indego: Park. Hannifin Corp. Available online at: <https://www.accessdata.fda.gov/scripts/cdrh/cfdocs/cfpmn/pmn.cfm?ID=K171334> (accessed June 15, 2020).
- U.S. Food and Drug Administration (2016b). *510(k) Premarket Notification*. EksoGT, Ekso Bionics, Inc. Available online at: <https://www.accessdata.fda.gov/scripts/cdrh/cfdocs/cfpmn/pmn.cfm?ID=K161443> (accessed June 15, 2020).
- U.S. Food and Drug Administration (2017). *510(k) Premarket Notification*. HAL, Cyberdyne Inc. Available online at: <https://www.accessdata.fda.gov/scripts/cdrh/cfdocs/cfpmn/pmn.cfm?ID=K171909> (accessed June 15, 2020).
- Wang, J., Qiu, J., Hou, L., Zheng, X., and Yu, S. (2019). Effect of common pavements on interjoint coordination of walking with and without robotic exoskeleton. *Appl. Bionics Biomech.* 2019, 1–8. doi: 10.1155/2019/2161038
- Yildirim, M. A., Öneş, K., and Gökşenoglu, G. (2019). Early term effects of robotic assisted gait training on ambulation and functional capacity in patients with spinal cord injury. *Turkish J. Med. Sci.* 49, 838–843. doi: 10.3906/sag-1809-7

Conflict of Interest: The authors declare that the research was conducted in the absence of any commercial or financial relationships that could be construed as a potential conflict of interest.

Copyright © 2020 Ramanujam, Momeni, Ravi, Augustine, Garbarini, Barrance, Spungen, Asselin, Knezevic and Forrest. This is an open-access article distributed under the terms of the Creative Commons Attribution License (CC BY). The use, distribution or reproduction in other forums is permitted, provided the original author(s) and the copyright owner(s) are credited and that the original publication in this journal is cited, in accordance with accepted academic practice. No use, distribution or reproduction is permitted which does not comply with these terms.



Applicability of an Active Back-Support Exoskeleton to Carrying Activities

Tommaso Poliero^{1,2*}, Maria Lazzaroni^{1,3}, Stefano Toxiri¹, Christian Di Natali¹, Darwin G. Caldwell¹ and Jesús Ortiz¹

¹ Department of Advanced Robotics, Istituto Italiano di Tecnologia, Genoa, Italy, ² Department of Informatics Bioengineering Robotics and Systems Engineering, University of Genoa, Genoa, Italy, ³ Department of Electronics, Information and Bioengineering, Politecnico di Milano, Milan, Italy

OPEN ACCESS

Edited by:

Jan Veneman,
Hocoma, Switzerland

Reviewed by:

Lorenzo Grazi,
Sant'Anna School of Advanced
Studies, Italy
Baojun Chen,
Tianjin University, China
Matthias Basil Näf,
Vrije University Brussel, Belgium

*Correspondence:

Tommaso Poliero
tommaso.poliero@iit.it

Specialty section:

This article was submitted to
Biomedical Robotics,
a section of the journal
Frontiers in Robotics and AI

Received: 03 July 2020

Accepted: 05 October 2020

Published: 09 December 2020

Citation:

Poliero T, Lazzaroni M, Toxiri S, Di Natali C, Caldwell DG and Ortiz J (2020) Applicability of an Active Back-Support Exoskeleton to Carrying Activities. *Front. Robot. AI* 7:579963. doi: 10.3389/frobt.2020.579963

Occupational back-support exoskeletons are becoming a more and more common solution to mitigate work-related lower-back pain associated with lifting activities. In addition to lifting, there are many other tasks performed by workers, such as carrying, pushing, and pulling, that might benefit from the use of an exoskeleton. In this work, the impact that carrying has on lower-back loading compared to lifting and the need to select different assistive strategies based on the performed task are presented. This latter need is studied by using a control strategy that commands for constant torques. The results of the experimental campaign conducted on 9 subjects suggest that such a control strategy is beneficial for the back muscles (up to 12% reduction in overall lumbar activity), but constrains the legs (around 10% reduction in hip and knee ranges of motion). Task recognition and the design of specific controllers can be exploited by active and, partially, passive exoskeletons to enhance their versatility, i.e., the ability to adapt to different requirements.

Keywords: exoskeleton, occupational exoskeleton, versatility, lifting, carrying, task recognition, human activity recognition

1. INTRODUCTION

In the 1970s, the scientific community began addressing the relationship between musculoskeletal disorders (MSDs) and work ergonomics. Since then, many studies have been published regarding this topic (Bernard and Putz-Anderson, 1997; Cohen, 1997; Fujishiro et al., 2005; Hamberg-van Reenen et al., 2008). Yet, in the most recent EU-OSHA report de Kok et al. (2019), MSDs are still cited as the most common work-related health problem in the EU. Indeed, 60% of workers still experience such disorders, in the majority of the cases due to back pain. MSDs affect not only the workers, but also the enterprises that, in turn, have to cope with absenteeism and productivity losses. To have an idea of the economic impact, in 2012, the total annual cost related to MSDs to the European Community represented 2% of the GDP (Bevan, 2012).

Workers performing manual material handling (MMH) activities (e.g., package loading and unloading in a warehouse or luggage handling in airports) are among the most exposed to risks and injuries. To try to reduce MSDs associated with MMH, NIOSH has developed a method for the ergonomic assessment of a task, defining whether or not it is classified as risky (Waters et al., 1993). Potentially harmful tasks should be mitigated via adoption of different solutions such as the introduction of limits for handled masses, frequencies, and task duration. Additionally, companies

have tried to mitigate MSDs by re-designing the workplace according to the newer ergonomic guidelines or by resorting to plant automation and to the introduction of industrial manipulators. However, the cost associated with these solutions and the lack of adoption of external tools by the users prevents the problem of MSDs from being completely solved.

1.1. Back-Support Exoskeletons and Lifting

The ability of back-support exoskeletons to reduce the physical loading on the lumbar spine while performing lifting tasks suggests that they may present a possible novel solution to back pain-related MSDs. Indeed, a 2016 review on occupational exoskeletons reported that usage of back-support exoskeletons yielded a 10–40% reduction in back muscle activity during repetitive lifting and static holding tasks (de Looze et al., 2016). The primary consequence of muscle activity reduction is the de-compression of the lumbar spine. Such results are confirmed by a more recent review (Theurel and Desbrosses, 2019) that stresses the clear potential of exoskeletons in limiting muscular demand. However, this report also warns that there is insufficient current knowledge to justify an unreserved adoption of this technology. Fox et al. (2019) elaborate on these devices to improve manufacturing processes. Moreover, focusing on three aspects, namely (a) actuators, (b) structures and physical attachments, and (c) control strategies employed, Toxiri et al. (2019) report on the technical development of back-support exoskeletons meant for occupational use. According to the actuator choice, an exoskeleton can be defined as active or passive. A passive exoskeleton exploits its wearer's movements to store and then release energy. Energy storage is achieved by means of passive elements such as gas/coil springs, flexible beams or elastic bands (Abdoli-e et al., 2006; Lamers et al., 2017; Näf et al., 2018). In contrast to passive exoskeletons, active devices have the ability to deliver additional energy to the user exploiting electrical motors or pneumatic actuators. Such active elements, rather than relying onto the users' movement, are powered by batteries or external supplies. Properly controlling the active actuators allows designers to tune the assistance being provided based on different control strategies. As an example, in Toxiri et al. (2018) and Tan et al. (2019) sEMG signals are used to modulate the assistive torque, while in Lazzaroni et al. (2020), Chen et al. (2018), Ko et al. (2018), Zhang and Huang (2018), and Yu et al. (2015) the control relies on kinematics.

1.2. Manual Material Handling: Is There Only Lifting?

As reported in Grazi et al. (2019), a consensus on the methods and metrics for the evaluation of back-support exoskeletons is still lacking. Indeed, the analyzed signals, the testing conditions, and the performance metric vary across the many available studies. However, all these studies have in common that the exoskeleton evaluation only considers static bending and symmetric lifting tasks. Yet, risk of overload for workers arises not only from lifting: workers may find themselves performing many different activities in the same workplace. As an example, in logistics, it is possible to imagine a quite simple task where

a worker *walks* to the shelf, *picks* the required object, *carries* it back to the cargo area, and, eventually, *lowers* it in the appropriate container. A similar scenario can be pictured in other contexts where MMH is involved. In such conditions, the International Standard ISO 11228 establishes ergonomic guidelines not only for lifting but also carrying, pushing, and pulling. Therefore, the analysis of the exoskeleton usage effects should not be limited to lifting tasks, but importantly should also tackle other activities such as carrying, pushing, pulling, and walking. This extension can capture the complexity of *out-of-the-lab* environments more reliably. As an example, an interesting study presented in Baltrusch et al. (2019) focuses on the versatility of a passive exoskeleton, studying its performance not only related to lifting but also walking. As might be expected, it emerges that passive exoskeletons provide benefits during lifting and do restrict the movement during walking. From this point of view, active exoskeletons, even if more complex and heavier, are expected to perform better, because of the possibility of tuning and customizing the assistance according to the task.

1.3. Contribution of This Study

Recent works on exoskeletons have discussed about the opportunity of exploiting human activity recognition to discriminate between different tasks such as lifting, walking, carrying, or sitting (Chen et al., 2018, 2019; Poliero et al., 2019a; Jamšek et al., 2020). For passive exoskeletons, this implies that, by using clutches for the engagement and disengagement of passive elements, as in Endo et al. (2006), Walsh et al. (2007), Ortiz et al. (2018), Jamšek et al. (2020), and Di Natali et al. (2020a), it is possible to assist only when needed, i.e., deactivate the passive elements when they create a restriction such as in the walking case. Active exoskeletons, on the other hand, thanks to their actuators versatility, could implement specific controllers for any of the previous tasks.

In the study presented hereafter, the investigation focuses on carrying activities, given their relevance to MMH and to the ISO 11228-1 standard. In particular, the authors want to elaborate more on (i) *the impact that a non-lifting activity might have on lower-back loading* and on (ii) *the need to select different controllers based on the performed task*.

First, a comparison is made between the spinal loading during lifting and carrying activities to investigate the impact of the task on this latter parameter. In particular, spinal loading, which is closely associated with risk of injuries, is caused by the activation of deep back muscles—related to back extension—generating compression on lumbar discs. When a worker is carrying a load, back extensors activate to keep the trunk stable and straight, thus, this situation also presents risks to the user.

Second, to better understand the need of different controllers according to the task, it might be useful to report a consideration. To date, the vast majority of available occupational back-support exoskeletons are designed and programmed to provide assistive torques that contribute *simultaneously* to the extension of the back and both hips, regardless of their actuation principles and control strategies. This assistance principle is derived from and replicates the typical movements observed during



FIGURE 1 | Example of luggage handling in an airport performed with the usage of XoTrunk. Written informed consent was obtained from the individual pictured in the figure.

symmetric lifting activities. Indeed, in this situation, every time there is back flexion or back extension, there is also a corresponding flexion or extension of the hips, respectively. Therefore, the presented assistance principle seems appropriate. In this study, the soundness of applying this strategy in carrying activities is investigated. Indeed, the inclusion of gait shows a different situation with respect to symmetric lifting. In particular, during carrying, contributing to back extension is appropriate, but simultaneously pushing both hips toward extension might interfere with their natural movement. More specifically, the support could be beneficial during hip extension (associated with the leg in stance phase), but may result in restriction of the hip flexion (forward swing, characteristic of the leg not in contact with the ground). Hence, to understand the need of different controllers according to the task, the effects that assisting with carrying—adopting an assistance principle derived from observation of symmetric lifting activities—has on the users are studied. The effects will be assessed in terms of muscle activity, gait kinematics, and subjective perceptions.

In the following, details on how the experimental testing was devised are reported in Section 2. Section 3 presents the results that are then discussed in Section 4. Finally, Section 5 summarizes and concludes this work.

2. MATERIALS AND METHODS

We devised an experiment, approved by the Ethics Committee of Liguria¹, that is detailed following the description of *XoTrunk*, the active back-support exoskeleton used in this study. Finally, information on data processing and outcome measures are reported.

2.1. XoTrunk: An Active Back-Support Exoskeleton

XoTrunk (see **Figure 1**) is a 6kg improved version of the *Robo-Mate* prototype, presented in Toxiri et al. (2018). Its aluminum frame houses the control and electronics box, the actuation units, and the anchoring points. These points are situated close to the thighs and the shoulders, allowing the device to transmit the torques—produced by its two brushless DC motors—to the wearer. These torques are used to help the user perform lifting, by partially contributing to hip and back extension. Additional anchoring on the waist provides more stability and comfort. More details on the actuators and low level control can be found in Di Natali et al. (2020b), whereas kinematics and physical attachments are reported in Sposito et al. (2020).

¹protocol reference number: CER Liguria 001/2019.

The versatility provided by its two electrical motors allows to test and study different control strategies. In particular, in Toxiri et al. (2018), three control strategies are presented to modulate the torque proportionally to (a) the torso inclination angle, (b) the forearm muscle activity, and (c) a combination of torso inclination and forearm muscle activity. Regardless of the selected control strategy, the motors always provided assistive torques that contribute simultaneously to the extension of the back and both hips. The backwards push on the back is the combination of the assistance provided by the left and right sides. As introduced in Section 1.3, this assistance principle is inspired by observation of symmetric lifting movements. This study concerns whether or not this assistance principle can be beneficial also for assisting carrying. The control strategy selected here was based on a constant extension torque provision. Indeed, for the sake of simplicity, during carrying the torso inclination can be neglected, whereas the forearm muscle activity can be assumed to be constant during load handling. Such simplifications were introduced to facilitate the analysis of the effects that assistance during carrying has on the users. In the following, this control mode is referred to as the Exoskeleton On (*Exo-on*) condition. Each motor generates a constant torque of 10 Nm, resulting in an overall assistance of 20 Nm.

2.2. Experimental Set-Up and Protocol

Nine healthy male subjects ($N = 9$, 1.78 ± 0.04 m, 76.55 ± 8.22 kg, 31 ± 3.46 years old) were asked to wear sporting clothes and informed they would have to perform the following tasks:

- **Lifting:** The sequence of: standing upright, reaching for a box lying 0.30 m from the ground, grasping and lifting it, reaching upright posture again, then putting the box back down on the ground and returning to the upright posture. Each sequence was repeated three times at a self-selected speed and with a freestyle lifting technique, meaning no specific instructions on lifting motion were given (Burgess-Limerick, 2003).
- **Carrying:** Straight level walking for 7.5m, while holding a box close to the trunk at self-selected speed.

Each test subject performed lifting with the box (1.2 kg) housing three different payloads, namely 0, 7, and 15 kg. In the following, the different weights are referred to as *light* (*L*), *medium* (*M*), and *heavy* (*H*). All the conditions were repeated three times for a total of 9 tests per subject. Carrying tasks were performed not only varying the loads (light, medium and heavy, as for lifting), but also the supplied assistance. In particular, two conditions were tested:

- a) No Exoskeleton (*No-exo*): carrying without the exoskeleton;
- b) Exoskeleton On (*Exo-on*): carrying while wearing the exoskeleton in the *on-mode*. The exoskeleton provides an angle independent constant torque of 20 Nm to provide support for the extension of the back and of both hips (see Section 2.1).

Each load and assistance condition was repeated three times for a total of 18 tests per subject. The task execution order, the handled weights, and the supplied assistance were randomized between subjects.

TABLE 1 | Overview of the testing protocol and the selected metrics.

Tasks	Lifting; Carrying
Loads	Light 1.2 kg (<i>L</i>), Medium 8.2 kg (<i>M</i>), Heavy 16.2 kg (<i>H</i>)
Conditions	Without exoskeleton (<i>No-exo</i>); with exoskeleton (<i>Exo-on</i>)
Repetitions	3x
Metrics	M , P , RoM_h , RoM_k , $\bar{\delta}$
Statistical analysis	for each ρ^x , α , iqr , and γ were analyzed (x being any of the above metrics)

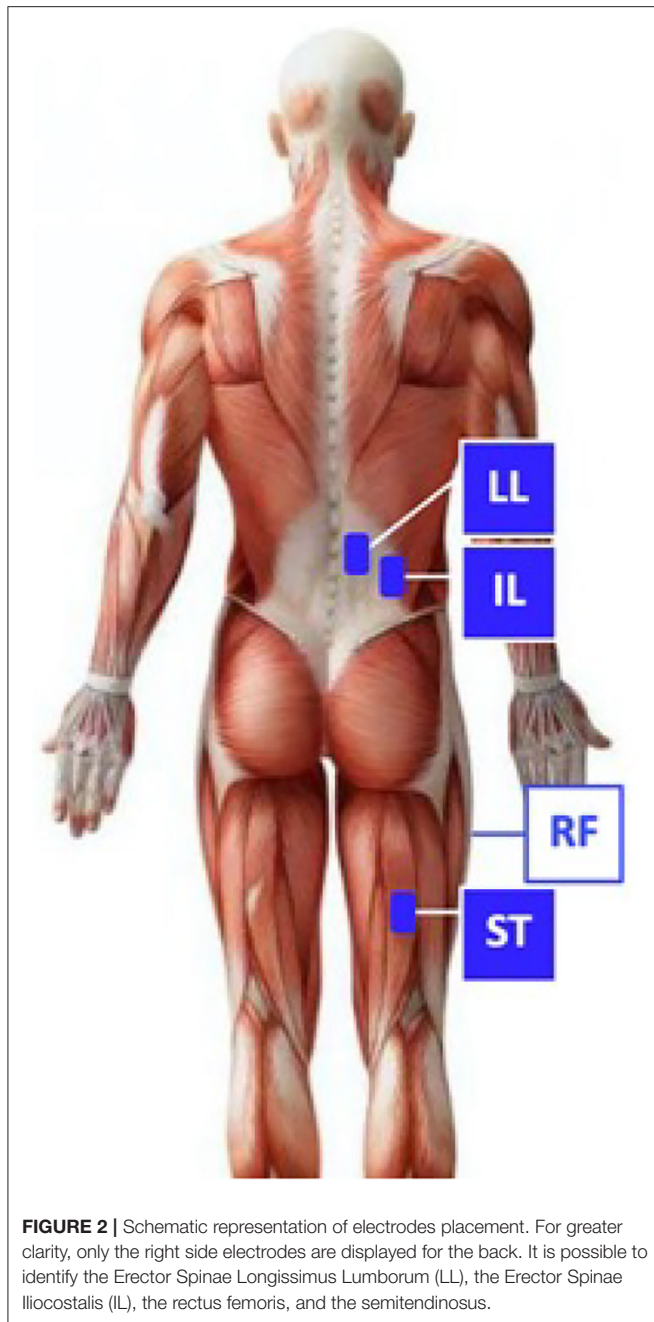
At the end of the experimental protocol, the subjects were asked to fill in a simplified version of an RPE (Rate of Perceived Exertion) questionnaire to rate the differences between carrying in the *No-exo* and in the *Exo-On* condition (Huysamen et al., 2018).

Table 1 summarizes the protocol and its independent variables.

2.3. Measurements and Data Processing

To collect muscular activity data, the subjects were asked to wear surface EMG (sEMG) electrodes (BTS FREEEMG, BTS Bioengineering, Italy). These latter were placed, according to SENIAM guidelines, to measure the bilateral activation of the muscles responsible for trunk extension, namely the Erector Spinae Longissimus Lumborum (LL) and the Erector Spinae Iliocostalis (IL). Additionally, due to the symmetry of the task, only the subjects' right leg was instrumented to measure the activation of two muscles responsible for hip flexion and extension, i.e., the rectus femoris (RF) and the semitendinosus (ST). Back and leg muscles were chosen based not only on their relevance when performing lifting activities but also on the number of studies that analyze them in order to allow comparisons of findings across different protocols (Grazi et al., 2019). Figure 2 illustrates the locations of the chosen muscles. Prior to attaching the electrodes onto the skin, the site was cleaned with alcohol, as suggested in Stegeman and Hermens (2007). Muscular activity information was acquired at a sampling frequency of 1 kHz. Extraction of metrics from the sEMG signals requires data post-processing. The common approach reported in Pons (2008) consists of filtering the amplified raw sEMG signals (BTS FREEEMG output), rectifying the output, and, eventually, computing the linear envelope (low-pass frequency filter at 2.5 Hz, Potvin et al., 1996). EMG data were normalized to maximum voluntary contractions (MVC) (McGill, 1991). Overall, lumbar extensor activity (averaged IL and LL muscle activity, right and left side) was computed prior to performing deep-back muscles analysis as in Koopman et al. (2019).

To collect motion data, the subjects were also equipped with a 3D motion tracking system (MTw Awinda, Xsens, The Netherlands). 7 Xsens IMUs were attached to the feet, shanks, thighs, and pelvis in order to reconstruct lower limb kinematics and gait phase events. The Xsens software can reconstruct motion data at a 60Hz sampling frequency. Using IMU trackers and biomechanical models, the software also provides gait phase information that can be used to perform data segmentation (Di Natali et al., 2020a). Two consecutive *heel strike* events



generated by the same foot are used to identify the start and finish of the stride.

Before data recording, Xsens calibration and MVC acquisition routines were performed for each subject (Vera-Garcia et al., 2010; Halaki and Ginn, 2012).

2.4. Outcome Metrics and Analysis

In the following, the metrics used for the assessment of the effects of assisting with carrying are reported along with the metrics used for comparing carrying and lifting tasks. This section also

introduces how the statistical analysis was performed. **Table 1** summarizes what presented hereafter.

2.4.1. The Effects of Assistance During Carrying

As previously introduced in Section 1.3, it is hypothesized that the exoskeleton will positively influence the back and hips extension, whereas the hip flexion would be hindered. To explore the effects of assisting with carrying, this task was analyzed in the *No-exo* condition (control group) and in the *Exo-on* state (test group). To be consistent with studies focusing on lifting, the effect of the exoskeleton on the back is analyzed in terms of muscle activation. For the lower limbs, on the other hand, gait inclusion suggests also adding gait kinematics analysis to the muscle activation. In the following, first the muscle analysis metrics are presented and, then, the gait kinematics are considered.

Muscle fatigue may be experienced as symptoms or signs of reduced motor control such as localized discomfort or decreased strength. Generally, physical exertions can cause fatigue that lasts for just a few hours. If fatigue persists, it may cause tissue damage and yield MSDs (ACGIH, 2008). In Jonsson (1982), the 50th percentile/median of the muscle activity distribution (M) is selected to reflect how the muscle has been working during the whole recording period. Based on this reasoning, in this work, M was chosen to monitor the risk associated with repetitive/cumulative fatigue both for the back and the lower limb muscles. Additionally, ergonomic guidelines for industry define the maximum allowed spinal compression. If this threshold is exceeded, traumatic damages in the inter-vertebral discs may result (Moore and Garg, 1995). Biomechanical models can be used to show how this compressive force is directly linked to muscle activity (Chaffin, 1969; Toxiri et al., 2015). In Jonsson (1982), the 90th percentile of muscle activity distribution (P) is indicated as being more informative than the maximum muscle activity. For such reasons, in this work, P was chosen to monitor the risk associated with traumatic damages in the inter-vertebral discs. P was analyzed also for the lower limb muscles, even though there is no clear traumatic damage associated with those sites.

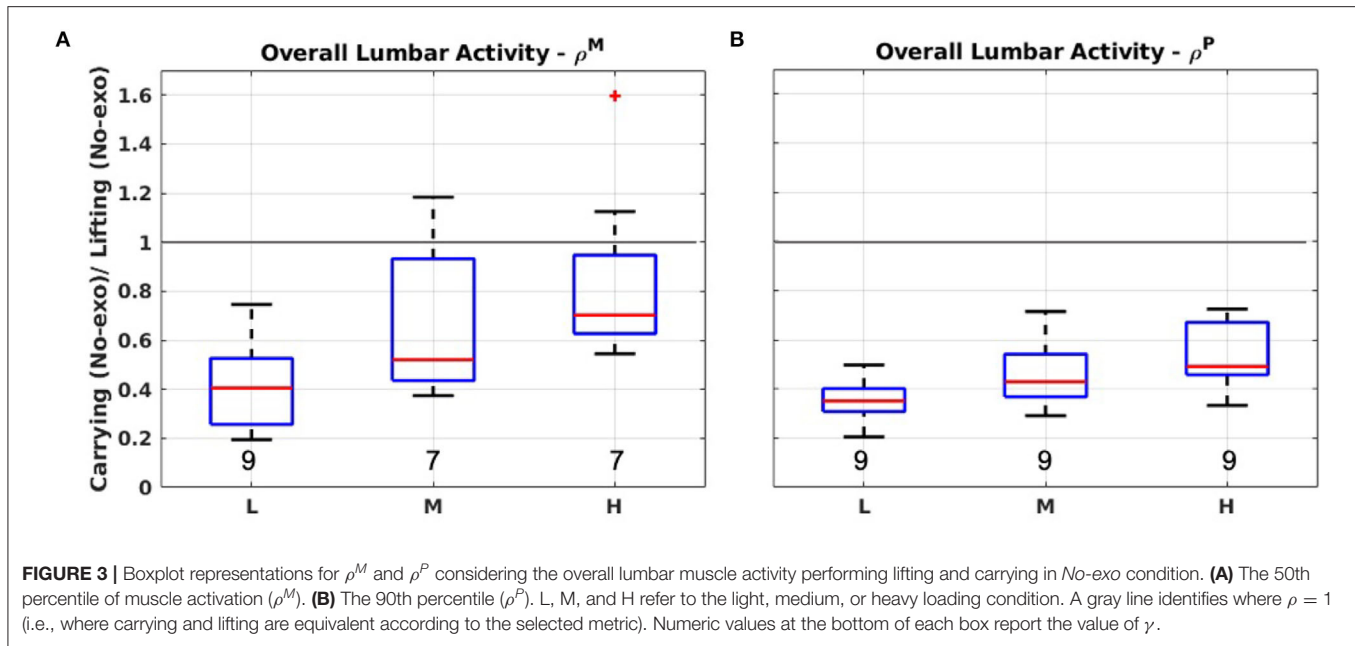
The gait kinematics is focused on the hip and knee ranges of motion (RoM_h and RoM_k , respectively) that are defined as the difference between the 90th and the 10th percentile of the lower limbs trajectory distribution during carrying. Since users were instructed to walk at a self-selected speed, an analysis on the average stride time ($\bar{\delta}$) per condition is conducted. $\bar{\delta}$ is defined as in Equation (1)

$$\bar{\delta} = \frac{1}{S-1} \sum_{k=1}^{S-1} H_{k+1} - H_k, \text{ for } k=1,2,\dots,S-1 \quad (1)$$

where S represents the number of strides in a test and H is a vector collecting all the right heel strike time events.

2.4.2. Comparing Carrying and Lifting Tasks

To report on the impact that carrying has on spinal loading compared to lifting, a simple comparison of lifting in the *No-exo* condition (control group) and carrying in the *No-exo* one



(test group) is presented. This analysis was focused on the overall lumbar extensor activity and on the same metrics presented in Section 2.4.1.

2.4.3. Statistical Analysis

Kinematic data were analyzed applying a standard one-way analysis of variance (ANOVA) with significance level set at $p < 0.05$. Such analysis was performed for both hip and knee angles. Initially, the same approach was meant to be adopted also for the stride duration examination and the muscle activity one. However, due to large variability in inter-subject walking speed and muscle activation signals (even after normalization with respect to the MVC), the choice was made to center the analysis around intra-subject variability. Indeed, big data variability implies that standard statistical analysis would not be very informative. For this reason, ratios between the test and control conditions (specified in Sections 2.4.1, 2.4.2) were adopted as an alternative form of intra-subject normalization, prior to comparison with the results obtained by other subjects. In the following, we define ρ_i^x as the ratio computed considering metric x (either M , P , RoM_h , RoM_k , or δ) in the control and test condition for a subject i .

$$\rho_i^x = \frac{X_i^{\text{control}}}{X_i^{\text{test}}} \quad (2)$$

The vector collecting ρ_i^x for all the nine healthy subjects is referred to as ρ^x . To deepen the analysis of ρ^x , and to better highlight trends in the data, the following values are taken into account for each ρ^x distribution:

- the median value (α);
- the inter-quartile range (iqr), defined as the difference between the 75th and the 25th percentile of the ρ^x distribution;

- the number of subjects for which $\rho_i^x < 1$ (γ).

2.4.4. Subjective Evaluation

The subjective evaluation forms, filled in by each subject at the end of the experimental protocol, allow a comparison to be made on whether or not the perceived effect is consistent with the objective data. Based on their relevance in this study, only the answers referring to back, waist, and legs are analyzed.

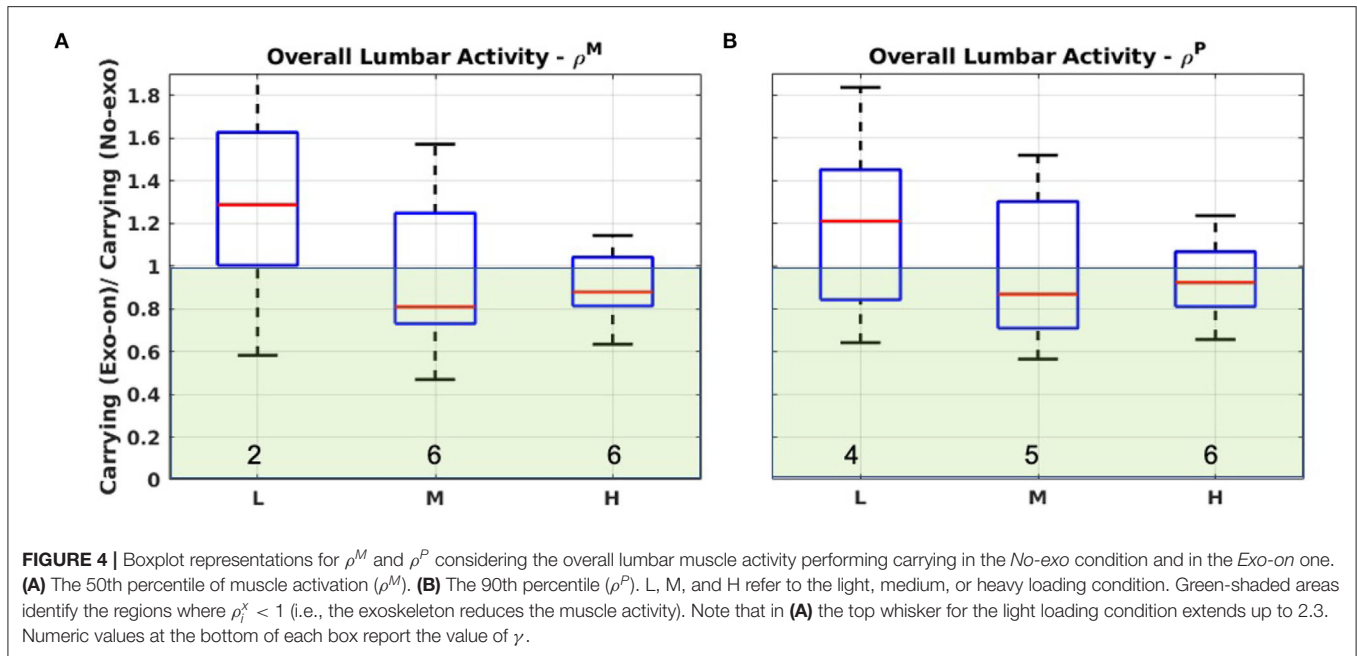
3. RESULTS

In the following, results referring to spinal loading during carrying are presented, followed by those associated with the effects of the assistance during carrying. In particular, these latter results are split into muscle analysis and gait kinematics.

3.1. Spinal Loading During Carrying

Figures 3A,B present the boxplot of the distribution of ρ^M and ρ^P when comparing the overall lumbar muscle activity during carrying and lifting activities.

Lower-back muscle activation is in the same order of magnitude, but generally lower during carrying compared to lifting, according to the reported measurements. This is true in all cases for ρ^P , whereas ρ^M shows a few subjects for which $\rho_i^M > 1$, meaning that the lumbar muscle median activation (50th percentile) was higher in carrying than lifting. In the heavy load test, one of the subjects is considered an outlier (represented by a red cross). For light loads, considering both ρ^M and ρ^P , the median (α) is around 0.40, while this number increases to around 0.60 for heavier loads, showing an overall trend. It is worth highlighting that γ is always quite close to $N = 9$, indicating a shared trend among all the subjects.



3.2. Effects of Assistance During Carrying

The results are reported focusing first on the muscle activation and, then, on the gait kinematics.

3.2.1. Muscle Activation

Figure 4 reports the boxplot associated with ρ^M and ρ^P for the overall activation of the lumbar muscles when comparing carrying activities with and without the exoskeleton. Overall, the population distributions are around the unit value and the *iqr* range is quite large (up to 0.62). However, the *iqr* has a trend to reduce as the payload increases, both for mean and peak. Indeed, the variability in the heavy load condition is about one-third of that recorded for the lighter loads.

Light and heavy load tests display opposite behaviors, with the first (light load) belonging almost entirely to the $\rho^x > 1$ region (i.e., the exoskeleton produced an increase of the metric) and the second (heavy load) to the $\rho^x < 1$ region (i.e., the exoskeleton produced a reduction of the metric). This is more evident for ρ^M rather than ρ^P . An additional interesting observation is that for both metrics the lowest value is for the intermediate weight. For both ρ^M and ρ^P , γ indicates that the majority of the subjects experienced a reduction of muscle activation in the *Exo-on* condition, with respect to the control case. Moreover, as the payload increases, the value of γ increases as well.

Figure 5 refers to the lower limb muscles activation analysis. Similarly to above, the distributions are centered around the unit value. The *iqr* still displays large variability (up to 0.71) and there is no longer a clearly narrowing trend as the payload increases. Indeed, in the case of the RF, the *iqr* is smaller for the intermediate loads than it is for heavier loading condition. Red crosses identify outliers in the ST ρ^M , and in the RF and ST ρ^P . Also in this case, it is possible to identify an increasing trend for γ as the payload increases.

3.2.2. Gait Kinematics

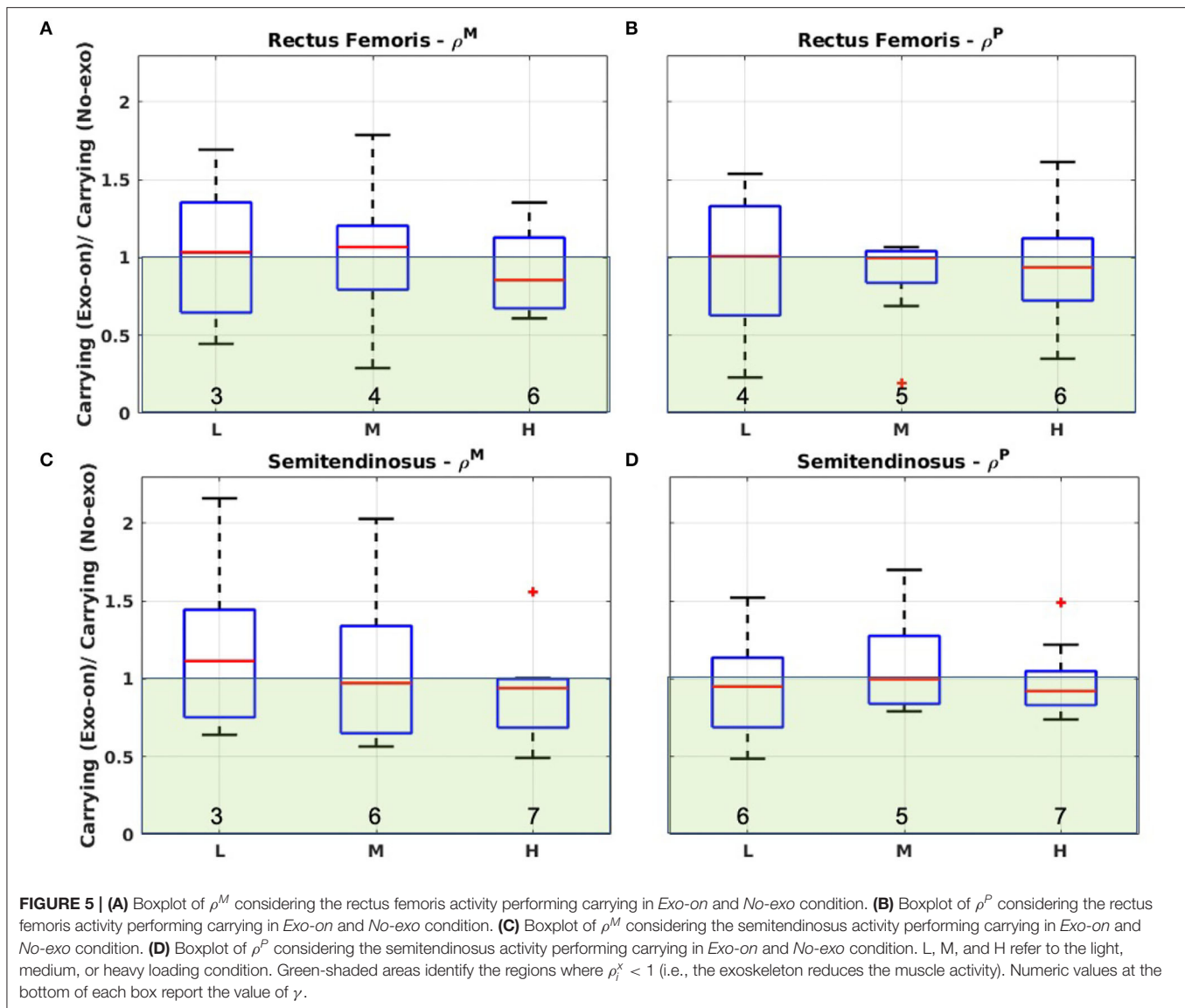
How the RoM changed between the two conditions is reported in **Figure 6**, revealing a clear trend for both the hip and the knee joints. Indeed, for both hip and knee RoM it almost always holds that $\rho^{RoM_k} < 1$ and $\rho^{RoM_h} < 1$ (see also γ values). On average, the median values (α) are around 0.90 indicating that there is a reduction in the RoMs of about 10% due to the exoskeleton action. The *iqr* values are much lower than in the muscle analysis (maximum *iqr* is 0.12 with respect to 0.71).

Significance levels obtained comparing the *Exo-on* and the *No-exo* condition are reported in **Table 2**. Bold values indicate where significance was reached ($p < 0.05$). In each condition, at least one joint had a significant RoM reduction between the test and control condition.

Moreover, by inspection of **Figure 7**, it is possible to see how the *Exo-on* condition yielded an increase of stride duration (δ), as all the distributions lie in the $\rho^{\delta} > 1$ region. The trend indicates a median increase in cycle time duration of about 6%. Outliers can be identified in the light and medium load conditions. The values of γ indicate a clear effect for all the subjects.

3.2.3. Subjective Perception

Finally, **Figure 8** summarizes, for each body region under analysis, how many users reported a benefit or hindrance/discomfort when comparing the *Exo-on* and the *No-exo* conditions. The majority of the subjects (8 out of 9) experienced a positive exoskeleton effect on the back/trunk region, whereas 7 out of 9 subjects felt hindered in the lower limbs. Interestingly, 3 users reported benefit also on the waist, where the exoskeleton is anchored. As the users were instructed to report benefit



or hindrance only if actually perceived, for a given body region, the sum of hindrance and benefit does not have to be $N = 9$.

4. DISCUSSION

In the following, the discussion is presented starting from the analysis of the carrying impact on spinal loading compared to the lifting case. The authors' assumption was that such loading would be comparable between the two activities. This supports and validates the assertion that an occupational back-support exoskeleton is needed/valuable in providing assistance during carrying. Therefore, the first assessment is followed by an evaluation of the effects of an exoskeleton assisting with carrying while applying a constant extension torque provision. A control strategy of this type is a simplification of what happens if an exoskeleton, programmed to assist lifting, is also used during

carrying. Here, the authors' hypothesis was that for carrying this strategy would turn out to be sub-optimal, namely being beneficial for the back but hindering the lower limbs. As a consequence, Section 4.3 focuses on the need to implement back-support exoskeleton versatility. Finally, the limitations of this study are discussed in Section 4.4.

4.1. The Impact on Spinal Loading

The results summarized in Figure 3 confirm that—from an ergonomic viewpoint—carrying activities can be associated with risk. Indeed, compared to lifting, muscle activity, although less during carrying, is in the same order of magnitude. In particular, as the handled payload increases, the differences between lifting and carrying are reduced and become less pronounced. This trend is particularly evident if the 50th percentile of the muscle activity distribution is considered. Generally, this value can be associated with repetitive/cumulative fatigue, whereas the 90th

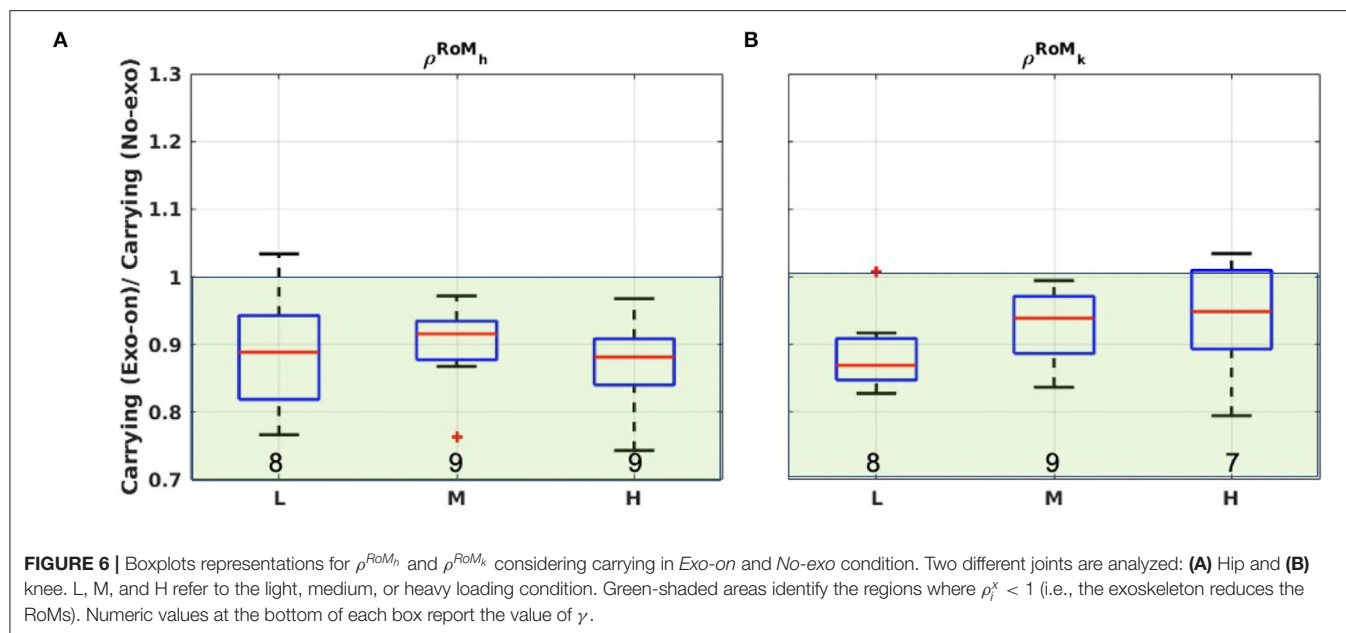


TABLE 2 | Gait kinematics—Statistical significance for the considered loading conditions.

	<i>L</i>	<i>M</i>	<i>H</i>
Hip	0.0534	0.0970	0.0396
Knee	0.0040	0.0441	0.1582

The table reports the p-values obtained from the one-way ANOVA test. Bold values indicate where statistical significance was met ($p < 0.05$).

percentile is related to traumatic damages of the inter-vertebral discs. Despite traumatic damage is seen as more concerning, it is clear that damage can occur in both lifting and carrying and, thus, should be prevented/limited. The results found in section 3.1 are consistent with the ISO 11228-1 standard that establishes ergonomic guidelines for performing both lifting and carrying, identifying the latter activity as equally worthy of attention.

Therefore, it makes sense to try to assist also the carrying activities by means of an active occupational exoskeleton.

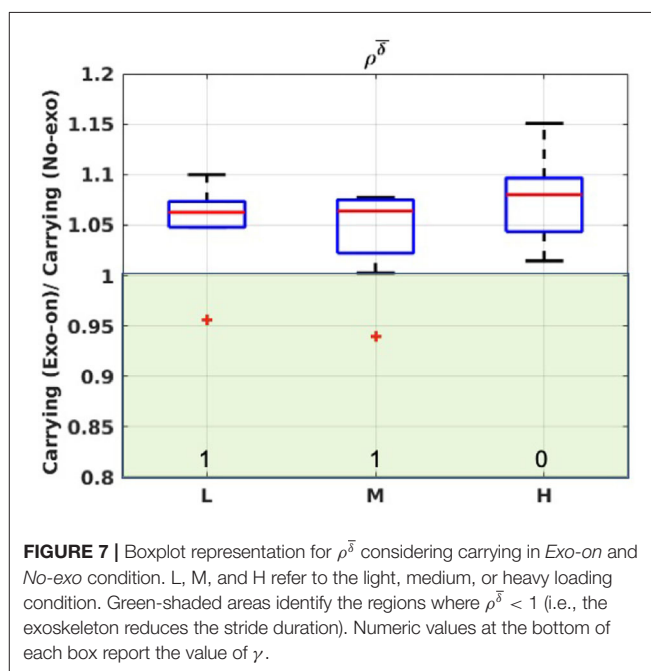
4.2. The Effects of Assistance During Carrying

The analyzed assistance principle implies that the delivered torques simultaneously support the extension of back and both hips. It was assumed that such assistance would be beneficial for the back, whereas it might hinder the natural movement of the hips, particularly in the swing phase.

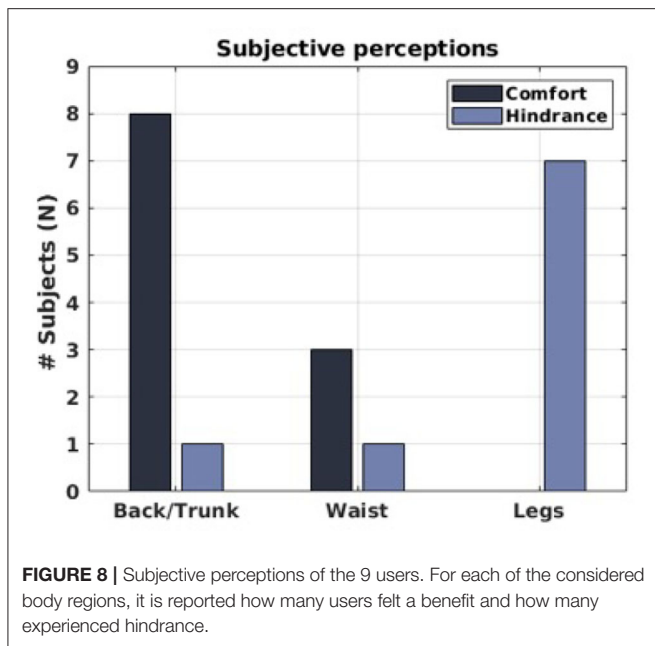
The following discussion is separated according to the two body regions under analysis.

4.2.1. The Lower Back

The experimental results do not indicate a clear polarity on the data and, thus, it is not possible to confidently conclude that, with respect to the conditions of this study, the exoskeleton is



providing a reduction in the activation and work intensity of the lower-back muscles. Nevertheless, it is worth highlighting how the data variability shows a general trend to reduce as the payload increases and that the heavy load condition has a much clearer trend toward the $\rho^M, \rho^P < 1$ region, i.e., where the exoskeleton has a benefit on the muscle activation. This suggests that conclusions drawn for this condition are more reliable than those drawn for lighter loads. In particular, for the heavier load condition, α values for ρ^M and ρ^P suggest that the exoskeleton effect is beneficial, reducing the overall lumbar activity by 12.08



and 7.99%, respectively. It is also important and encouraging that the exoskeleton is seen to have the greatest effect with the heaviest loading, as this is the circumstance that is most in need of assistance. Also, a comparison of objective and subjective data confirm the beneficial effect of the exoskeleton. Indeed, as outlined in **Figure 8**, 8 out of 9 users reported benefit on the back and only 1 out of 9 reported discomfort or hindrance on the same body segment. On the other hand, a part from the light load condition, lower-back muscle analysis showed that, out of 9, 5–6 subjects (according to the analyzed metric) had a reduction of muscle activation (see γ values in **Figure 4**). These values are not so far from those reported by the subjective evaluation forms. Therefore, the consistency between objective and subjective data suggest that, considering spinal loading, there is some evidence that the exoskeleton effect is somehow beneficial for most of the population.

Contrary to the authors' expectations, for the medium and high payload handling, the overall lumbar activity reduction is not in line with the potential of the device used in the assessment. In particular (Toxiri et al., 2018), the experiment showed significant back muscle activation reduction (around 30%), whereas a clear reduction was not obtained in this study, even though sound bio-mechanical models supported the authors' hypothesis. This, along with the negative exoskeleton effect for the light load condition, suggests that there is room for improving the constant torque strategy used in this study.

One upgrade is to modulate the delivered torque according both to the handled payload and to the user's body mass. In particular, the analysis of both α and γ supports the need to modulate the assistance according to the handled payload. Indeed, considering the lightest loading condition, the exoskeleton does not clearly reduce spinal loading, as highlighted by α . On the other hand, as the handled weight increases, the

exoskeleton assistance results in reductions of α values both for ρ^M and ρ^P ($\alpha < 1$). To this extent, it is interesting to note that, even if very slightly, the intermediate condition seems to be a minimum and might indicate that the amount of assistance provided is best around that payload range. Moreover, the number of subjects that show a benefit from the additional torque provided by the exoskeleton increased as the weight of the carried load increased (see **Figure 4**). For the light payload test, the muscle activity increase may be interpreted by subjects adopting abdominal and back-extensors co-contraction, stiffening the upper body to counteract the backwards push of the exoskeleton and to regain stability. Further experimentation could help clarifying this phenomenon and if modulating the torque according to the payload would, as expected, reduce it. Finally, the large variability in the results further suggests the possibility of modulating the delivered torque not only according to the payload, but also to the subjects' body mass. Indeed, despite body masses variability (76.55 ± 8.22 kg), the delivered torque was kept constant, and so, it is possible that subjects with different body mass experience and react differently to the same amount of assistance.

4.2.2. The Lower Limbs

The exoskeleton assistance on the lower limbs resulted in hindrance clearly affecting the gait kinematics of all the users. This hindrance is evident both as subjective perception of the users (7 out of 9 users felt hindered on the legs) and from the kinematic analysis. Indeed, hip and knee RoMs were reduced by up to 12%. Stride speed was also reduced due to a corresponding increase in stride duration (between 6 and 8%). In addition, a study conducted on the effects of load carriage on energy cost of walking (Abe et al., 2004) showed no significant differences in the energy cost associated with walking for values between the control condition (empty backpack) and the test one (backpack with a 6 kg load). This suggests that the differences noted in this study are related more to the exoskeleton torque provision, rather than the exoskeleton weight itself (6 kg). These elements suggest that simultaneously pushing both hips toward extension appears not to be the best assistive strategy.

Furthermore, although the kinematic analysis and the subjective perceptions are clearly polarized, this does not happen in the muscle analysis. There may be two main reasons that explain this lack of a clear trend.

The first reason being the non-ideal choice of the muscles. Indeed, partially due to the exoskeleton fitting and partially due to the difficulty in assessing via sEMG the hip flexor activity, in the proposed protocol it was not possible to measure the muscle activity of the Iliopsoas (hip flexor) and of the Gluteus Maximus (hip extensor) (Byrne et al., 2010). For these reasons, the activities of the RF and ST were chosen as representative of hip flexion/extension muscle activation. Problems in assessing the proper flexors and extensor are reported also in Baltrusch et al. (2019), where muscle activity did not show any significant differences between conditions.

The second reason why no trend emerges in the selected muscles might be related to the changes in the gait trajectory, as reported above. Analyzing both hip and knee joints, for each load

condition, the exoskeleton assistance resulted in a reduced RoM. Indeed, almost all of the population lies in the $\rho^{RoM_h}, \rho^{RoM_k} < 1$ region. It is interesting to note the little data variability (*iqr*), suggesting its reliability.

Moreover, the one-way ANOVA test, significance level = 0.05, conducted to compare the *Exo-on* and the *No-exo* condition, found statistically significant differences at least for one joint in all of the conditions (see **Table 2**). In the case of the hip joint, the RoM reduction is due both to smaller flexion angles, hindered by the constant torque, and to smaller extension angles, possibly due to a compensation for the unwanted/unexpected backwards push of the exoskeleton. Differences in the knee trajectory can be explained as a consequence of the hip changes. Delving a bit more into the kinematic analysis, **Figure 7** shows that the *Exo-on* condition caused a speed reduction in the users walking speed: all the population, apart from an outlier, lies within the $\rho^{\delta} > 1$ region. Therefore, reduced RoMs and slower stride durations show an evident hindrance confirming the authors' expectations.

4.3. On (the Need of) Back-Support Exoskeleton Versatility

To fully exploit back-support exoskeleton versatility, the standard control strategies can be expanded by including task awareness. This implies that, at first, the activity being performed by the user is recognized (high level), then, in accordance with the task the appropriate assistive strategy is selected (mid-level) and, finally, actuators are controlled to ensure that the provided torque is properly delivered (low-level). Such a distinction of control levels was presented in Tucker et al. (2015).

Now that data have been presented and discussed, there are more elements to debate on the need to recognize different tasks and the opportunity of selecting the controller according to the one being performed. Passive exoskeletons, generally lighter, simpler, and cheaper than active ones, can avoid the lower limb hindrance found in walking activities (Baltrusch et al., 2019). This is achieved by resorting to manual clutches, spring offsets, and automatic engage or dis-engage of passive elements, like in the commercial products by Laevo² and Ottobock³, or in research prototypes (Jamšek et al., 2020). On the other hand, due to mechanical design limitations, passive devices cannot provide support in carrying activities. This means that there is no need to discriminate among *walking* or *carrying*.

Unlike passive devices, active exoskeletons are more versatile and, so, are able to exploit the functionality and flexibility of their actuators to create assistance profiles that can be tailored to the demands of the assistive task, like carrying in this case. Not all the active exoskeletons, however, have the same “degree of versatility.” As an example, the H-WEX exoskeleton presented in Ko et al. (2018) cannot provide support differently from the approach presented in this study. This is due to the choice of a single motor for the actuation, resulting in a more compact, efficient, and lightweight exoskeleton. However, the single motor can only modulate the delivered amount of torque and cannot assist the legs independently, according to gait phase. Instead,

as an example, the APO exoskeleton (Chen et al., 2018) and the XoTrunk exoskeleton used in this study have two motors, one on each side. This design choice can be exploited to develop new assistance strategies, more appropriate for carrying. Indeed, in the previous sections, it has been discussed how a better strategy could improve the effectiveness of the exoskeleton for the back region and reduce the hindrance in the lower limbs (as seen in the data analysis). Hence, considering active exoskeletons, distinguishing among walking, carrying, and lifting is supported both by the relevance of carrying activities and by the need to switch between different controllers.

As a final comment, it is useful to note that in Poliero et al. (2019b) the distinction between lifting and walking only takes into account kinematic variables, whereas specific sources of information (like forearm muscle activity, sensorized gloves/insoles, or vision) are used to discriminate among walking and carrying. This final consideration highlights that not only mechanical choices but also control ones can affect the versatility of back-support exoskeletons.

4.4. Limitations

In the designed testing protocol, MVC calibration was performed adopting a single posture. However, this procedure is more prone to variability in the MVC normalization as subjects might exhibit differences in the posture to obtain maximum muscle activity (McGill, 1991). The large inter-subject variability did not allow us to always apply standard statistical analysis such as the analysis of variance. For this reason, the authors have decided to perform intra-subject normalization between the control and test conditions. As a consequence, the results are discussed taking into consideration trends. The proposed testing protocol was carried out in a lab setting. This might present substantial differences to the conditions found in a workplace where users may be required to walk on undulating or sloped surfaces in addition to level ground. Therefore, our findings cannot be directly generalized to out-of-the-lab scenarios. Additionally, the indication to perform the carrying task at a self-selected speed might be a further simplification of actual working conditions. Indeed, for given tasks, the workers could be required to walk as fast as possible so as not to limit productivity. Also, the relatively short duration of the activities performed during the testing protocol does not allow us to observe fatigue effects, or the effects of prolonged exoskeleton usage.

5. CONCLUSION

In the context of manual material handling and, more specifically regarding the ISO 11228-1 standard, carrying can have an impact on the spinal loading comparable to lifting. Back-support exoskeletons are generally used to assist lifting and, thus, mitigate the ergonomic risks associated with this activity. The applicability of these devices to other activities, such as carrying, is still an open issue.

This paper investigates first the effects of carrying on spinal loading and, then, the effects of assisting carrying with an exoskeleton designed for lifting tasks support. An experimental campaign involving 9 users and three different payloads (1.2, 8.2,

²<http://en.laevo.nl/>

³<https://paexo.com/paexo-back/?lang=en>

and 16.2 kg) was designed to assess the relevance of carrying and the benefits arising from providing assistance for this task, in the same way it is done for symmetric lifting, i.e., synchronously supporting back and both hips extension.

The findings indicate that carrying, from an ergonomic viewpoint, is a relevant activity because the corresponding spinal loading is comparable to lifting.

Contrary to the expected outcome, the experimental results do not provide clear evidence on the effectiveness of the analyzed strategy in supporting the lower-back. However, the overall lumbar activity shows a promising trend when carrying heavy objects as for muscle activation is reduced by up to 12%. Large data variability invites caution when interpreting it. In agreement with the expectations, the strategy yielded hindrance for the lower limbs. This is supported by reduction in hip and knee RoMs (around 10%) and an increase of stride duration (between 6 and 8%). Due to changes in gait kinematics and difficulties in assessing the proper hip flexor and extensor, muscular analysis for the lower limbs did not provide significant findings.

Finally, there has been a discussion on how a better control strategy could improve the effectiveness of the exoskeleton. As control strategies for back-support exoskeletons start addressing tasks differing from lifting, the capability of recognizing which activity is being performed and, thus, triggering the appropriate controller, becomes a relevant feature, promoting active exoskeletons versatility.

REFERENCES

- Abdoli-e, M., Agnew, M. J., and Stevenson, J. M. (2006). An on-body personal lift augmentation device (PLAD) reduces EMG amplitude of erector spinae during lifting tasks. *Clin. Biomech.* 21, 456–465. doi: 10.1016/j.clinbiomech.2005.12.021
- Abe, D., Yanagawa, K., and Niihata, S. (2004). Effects of load carriage, load position, and walking speed on energy cost of walking. *Appl. Ergon.* 35, 329–335. doi: 10.1016/j.apergo.2004.03.008
- ACGIH, C. O. (2008). “TLVS and BEIS based on the documentation of the threshold limit values for chemical substances and physical agents, and biological exposure indices,” in *American Conference of Governmental Industrial Hygienists Cincinnati* (Cincinnati, OH).
- Baltrusch, S., van Dieën, J., Bruijn, S., Koopman, A., van Bennekom, C., and Houdijk, H. (2019). The effect of a passive trunk exoskeleton on metabolic costs during lifting and walking. *Ergonomics* 1–14. doi: 10.1080/00140139.2019.1602288
- Bernard, B. P., and Putz-Anderson, V. (1997). *Musculoskeletal Disorders and Workplace Factors; A Critical Review of Epidemiologic Evidence for Work-Related Musculoskeletal Disorders of the Neck, Upper Extremity, and Low Back*. Centers for Disease Control and Prevention.
- Bevan, S. (2012). *The Impact of Back Pain on Sickness Absence in Europe*. Lancaster: The Work Foundation.
- Burgess-Limerick, R. (2003). Squat, stoop, or something in between? *Int. J. Indus. Ergon.* 31, 143–148. doi: 10.1016/S0169-8141(02)00190-7
- Byrne, D. P., Mulhall, K. J., and Baker, J. F. (2010). Anatomy & biomechanics of the hip. *Open Sports Med. J.* 4, 51–57. doi: 10.2174/1874387001004010051
- Chaffin, D. B. (1969). A computerized biomechanical model-development of and use in studying gross body actions. *J. Biomech.* 2, 429–441. doi: 10.1016/0021-9290(69)90018-9
- Chen, B., Grazi, L., Lanotte, F., Vitiello, N., and Crea, S. (2018). A real-time lift detection strategy for a hip exoskeleton. *Front. Neurobot.* 12:17. doi: 10.3389/fnbot.2018.00017
- Chen, B., Lanotte, F., Grazi, L., Vitiello, N., and Crea, S. (2019). Classification of lifting techniques for application of a robotic hip exoskeleton. *Sensors* 19:963. doi: 10.3390/s19040963
- Cohen, A. L. (1997). *Elements of Ergonomics Programs: A Primer Based on Workplace Evaluations of Musculoskeletal Disorders*. Cincinnati, OH: DIANE Publishing.
- de Kok, J., Vroonhof, P., Snijders, J., Roullis, G., Clarke, M., Peereboom, K., et al. (2019). Work-related MSDs: prevalence, costs and demographics in the EU. European risk observatory. Executive Summary.
- de Looze, M. P., Bosch, T., Krause, F., Stadler, K. S., and O’Sullivan, L. W. (2016). Exoskeletons for industrial application and their potential effects on physical work load. *Ergonomics* 59, 671–681. doi: 10.1080/00140139.2015.1081988
- Di Natali, C., Sadeghi, A., Mondini, A., Bottenberg, E., Hartigan, B., De Eyto, A., et al. (2020a). Pneumatic quasi-passive actuation for soft assistive lower limbs exoskeleton. *Front. Neurobot.* 14:31. doi: 10.3389/fnbot.2020.00031
- Di Natali, C., Toxiri, S., Ioakeimidis, S., Caldwell, D. G., and Ortiz, J. (2020b). *Systematic Framework for Performance Evaluation of Exoskeleton Actuators*. Cambridge: Wearable Technologies. doi: 10.1017/wtc.2020.5
- Endo, K., Paluska, D., and Herr, H. (2006). “A quasi-passive model of human leg function in level-ground walking,” in *2006 IEEE/RSJ International Conference on Intelligent Robots and Systems (Beijing)*, 4935–4939. doi: 10.1109/IROS.2006.282454
- Fox, S., Aranko, O., Heilala, J., and Vahala, P. (2019). Exoskeletons. *J. Manufact. Technol. Manage.* 31, 1261–1280. doi: 10.1108/JMTM-01-2019-0023
- Fujishiro, K., Weaver, J. L., Heaney, C. A., Hamrick, C. A., and Marras, W. S. (2005). The effect of ergonomic interventions in healthcare facilities on musculoskeletal disorders. *Am. J. Indus. Med.* 48, 338–347. doi: 10.1002/ajim.20225

DATA AVAILABILITY STATEMENT

The raw data supporting the conclusions of this article will be made available by the authors, without undue reservation.

ETHICS STATEMENT

The studies involving human participants were reviewed and approved by Comitato Etico Regione Liguria. The patients/participants provided their written informed consent to participate in this study. Written informed consent was obtained from the individual(s) for the publication of any potentially identifiable images or data included in this article.

AUTHOR CONTRIBUTIONS

TP, ML, ST, CD, and JO devised the experiment. TP led the experiment and performed data analysis. ML and ST helped run the experiment. ST, ML, CD, and JO helped with data analysis. All authors contributed to the manuscript drafting. JO and DC obtained funding and resources.

FUNDING

This work was supported by the Italian Workers’ Compensation Authority (INAIL) and Istituto Italiano di Tecnologia (IIT) within the project Sistemi Cibernetici Collaborativi (SCC).

- Grazi, L., Chen, B., Lanotte, F., Vitiello, N., and Crea, S. (2019). "Towards methodology and metrics for assessing lumbar exoskeletons in industrial applications," in *2019 II Workshop on Metrology for Industry 4.0 and IoT (MetroInd4.0&IoT)*, 400–404. Naples: IEEE. doi: 10.1109/METROInd4.2019.8792877
- Halaki, M., and Ginn, K. (2012). "Normalization of EMG signals: to normalize or not to normalize and what to normalize to?," in *Computational Intelligence in Electromyography Analysis-A Perspective on Current Applications and Future Challenges*, eds G. R. Naik (London, UK: IntechOpen), 175–194. doi: 10.5772/49957
- Hamberg-van Reenen, H. H., Van Der Beek, A. J., Blatter, B. M., Van Der Grinten, M. P., Van Mechelen, W., and Bongers, P. M. (2008). Does musculoskeletal discomfort at work predict future musculoskeletal pain? *Ergonomics* 51, 637–648. doi: 10.1080/00140130701743433
- Huysamen, K., Power, V., and O'Sullivan, L. (2018). Elongation of the surface of the spine during lifting and lowering, and implications for design of an upper body industrial exoskeleton. *Appl. Ergon.* 72, 10–16. doi: 10.1016/j.apergo.2018.04.011
- Jamšek, M., Petrič, T., and Babič, J. (2020). Gaussian mixture models for control of quasi-passive spinal exoskeletons. *Sensors* 20:2705. doi: 10.3390/s20092705
- Jonsson, B. (1982). Measurement and evaluation of local muscular strain in the shoulder during constrained work. *J. Hum. Ergol.* 11, 73–88.
- Ko, H. K., Lee, S. W., Koo, D. H., Lee, I., and Hyun, D. J. (2018). Waist-assistive exoskeleton powered by a singular actuation mechanism for prevention of back-injury. *Robot. Auton. Syst.* 107, 1–9. doi: 10.1016/j.robot.2018.05.008
- Koopman, A. S., Toxiri, S., Power, V., Kingma, I., van Dieën, J. H., Ortiz, J., et al. (2019). The effect of control strategies for an active back-support exoskeleton on spine loading and kinematics during lifting. *J. Biomech.* 91, 14–22. doi: 10.1016/j.jbiomech.2019.04.044
- Lamers, E. P., Yang, A. J., and Zelik, K. E. (2017). Feasibility of a biomechanically-assistive garment to reduce low back loading during leaning and lifting. *IEEE Trans. Biomed. Eng.* doi: 10.1109/TBME.2017.2761455
- Lazzaroni, M., Toxiri, S., Caldwell, D. G., De Momi, E., van Dijk, W., de Looze, M. P., et al. (2020). *Evaluation of an Acceleration-Based Assistive Strategy to Control a Back-Support Exoskeleton for Manual Material Handling*. Cambridge: Wearable Technologies. doi: 10.1109/ICORR.2019.8779392
- McGill, S. M. (1991). Electromyographic activity of the abdominal and low back musculature during the generation of isometric and dynamic axial trunk torque: implications for lumbar mechanics. *J. Orthop. Res.* 9, 91–103. doi: 10.1002/jor.1100090112
- Moore, P. V., and Garg, A. (1995). Revised niosh equation for manual lifting: a method for job evaluation. *AAOHN J.* 43, 211–218. doi: 10.1177/216507999504300408
- Näf, M. B., Koopman, A. S., Baltrusch, S., Rodriguez-Guerrero, C., Vanderborght, B., and Lefebvre, D. (2018). Passive back support exoskeleton improves range of motion using flexible beams. *Front. Robot. AI* 5:72. doi: 10.3389/frobt.2018.00072
- Ortiz, J., Poliero, T., Cairoli, G., Graf, E., and Caldwell, D. G. (2018). Energy efficiency analysis and design optimization of an actuation system in a soft modular lower limb exoskeleton. *IEEE Robot. Autom. Lett.* 3, 484–491. doi: 10.1109/LRA.2017.2768119
- Poliero, T., Mancini, L., Caldwell, D. G., and Ortiz, J. (2019a). "Enhancing back-support exoskeleton versatility based on human activity recognition," in *2019 Wearable Robotics Association Conference (WearAcon)* (Phoenix, AZ), 86–91. doi: 10.1109/WEARRACON.2019.8719625
- Poliero, T., Toxiri, S., Anastasi, S., Monica, L., and Ortiz, D. G. C. J. (2019b). "Assessment of an on-board classifier for activity recognition on an active back-support exoskeleton," in *2019 IEEE 16th International Conference on Rehabilitation Robotics (ICORR)* (Toronto, ON), 559–564. doi: 10.1109/ICORR.2019.8779519
- Pons, J. L. (2008). *Wearable Robots: Biomechatronic Exoskeletons*. Hoboken, NJ: John Wiley & Sons. doi: 10.1002/9780470987667
- Potvin, J. R., Norman, R. W., and McGill, S. M. (1996). Mechanically corrected EMG for the continuous estimation of erector spinae muscle loading during repetitive lifting. *Eur. J. Appl. Physiol. Occup. Physiol.* 74, 119–132. doi: 10.1007/BF00376504
- Sposito, M., Di Natali, C., Toxiri, S., Caldwell, D. G., De Momi, E., and Ortiz, J. (2020). *Exoskeleton Kinematic Design Robustness: An Assessment Method to Account for Human Variability*. Cambridge: Wearable Technologies. doi: 10.1017/wtc.2020.7
- Stegeman, D., and Hermens, H. (2007). *Standards for Surface Electromyography: The European Project Surface EMG for Non-Invasive Assessment of Muscles (SENIAM)*. Enschede: Roessingh Research and Development, 108–112.
- Tan, C. K., Kadone, H., Miura, K., Abe, T., Koda, M., Yamazaki, M., et al. (2019). Muscle synergies during repetitive stoop lifting with a bioelectrically-controlled lumbar support exoskeleton. *Front. Hum. Neurosci.* 13:142. doi: 10.3389/fnhum.2019.00142
- Theurel, J., and Desbrosses, K. (2019). Occupational exoskeletons: overview of their benefits and limitations in preventing work-related musculoskeletal disorders. *IIEE Trans. Occup. Ergon. Hum. Fact.* 1–17. doi: 10.1080/24725838.2019.1638331
- Toxiri, S., Koopman, A. S., Lazzaroni, M., Ortiz, J., Power, V., de Looze, M. P., et al. (2018). Rationale, implementation and evaluation of assistive strategies for an active back-support exoskeleton. *Front. Robot. AI* 5:53. doi: 10.3389/frobt.2018.00053
- Toxiri, S., Näf, M. B., Lazzaroni, M., Fernández, J., Sposito, M., Poliero, T., et al. (2019). Back-support exoskeletons for occupational use: an overview of technological advances and trends. *IIEE Trans. Occup. Ergon. Hum. Fact.* 7, 237–249. doi: 10.1080/24725838.2019.1626303
- Toxiri, S., Ortiz, J., Masood, J., Fernández, J., Mateos, L. A., and Caldwell, D. G. (2015). "A wearable device for reducing spinal loads during lifting tasks: biomechanics and design concepts," in *2015 IEEE International Conference on Robotics and Biomimetics (ROBIO)* (Zhuhai), 2295–2300. doi: 10.1109/ROBIO.2015.7419116
- Tucker, M. R., Olivier, J., Pagel, A., Bleuler, H., Bouri, M., Lambercy, O., et al. (2015). Control strategies for active lower extremity prosthetics and orthotics: a review. *J. Neuroeng. Rehabil.* 12:1. doi: 10.1186/1743-0003-12-1
- Vera-Garcia, F. J., Moreside, J. M., and McGill, S. M. (2010). MVC techniques to normalize trunk muscle EMG in healthy women. *J. Electromyogr. Kinesiol.* 20, 10–16. doi: 10.1016/j.jelekin.2009.03.010
- Walsh, C. J., Endo, K., and Herr, H. (2007). A quasi-passive leg exoskeleton for load-carrying augmentation. *Int. J. Human. Robot.* 4, 487–506. doi: 10.1142/S0219843607001126
- Waters, T. R., Putz-Anderson, V., Garg, A., and Fine, L. J. (1993). Revised niosh equation for the design and evaluation of manual lifting tasks. *Ergonomics* 36, 749–776. doi: 10.1080/00140139308967940
- Yu, H., Choi, I. S., Han, K.-L., Choi, J. Y., Chung, G., and Suh, J. (2015). Development of a stand-alone powered exoskeleton robot suit in steel manufacturing. *ISIJ Int.* 55, 2609–2617. doi: 10.2355/isijinternational.ISIJINT-2015-272
- Zhang, T., and Huang, H. (2018). A lower-back robotic exoskeleton: industrial handling augmentation used to provide spinal support. *IEEE Robot. Autom. Mag.* 25, 95–106. doi: 10.1109/MRA.2018.2815083

Conflict of Interest: The authors declare that the research was conducted in the absence of any commercial or financial relationships that could be construed as a potential conflict of interest.

The reviewer MBN declared a past co-authorship with several of the authors (TP, MZ, ST, DC, JO) to the handling Editor.

Copyright © 2020 Poliero, Lazzaroni, Toxiri, Di Natali, Caldwell and Ortiz. This is an open-access article distributed under the terms of the Creative Commons Attribution License (CC BY). The use, distribution or reproduction in other forums is permitted, provided the original author(s) and the copyright owner(s) are credited and that the original publication in this journal is cited, in accordance with accepted academic practice. No use, distribution or reproduction is permitted which does not comply with these terms.



Evaluation of Motor Primitive-Based Adaptive Control for Lower Limb Exoskeletons

Polyana F. Nunes*, Icaro Ostan and Adriano A. G. Siqueira

Rehabilitation Robotics Laboratory, Department of Mechanical Engineering, São Carlos School of Engineering, University of São Paulo, São Carlos, Brazil

OPEN ACCESS

Edited by:

Eduardo Rocon,
Consejo Superior de Investigaciones
Científicas (CSIC), Spain

Reviewed by:

Cristina Bayón-Calderón,
University of Twente, Netherlands
Luciano Luporini Menegaldo,
Federal University of Rio de
Janeiro, Brazil

*Correspondence:

Polyana F. Nunes
polyananunes@usp.br

Specialty section:

This article was submitted to
Biomedical Robotics,
a section of the journal
Frontiers in Robotics and AI

Received: 22 June 2020

Accepted: 24 November 2020

Published: 16 December 2020

Citation:

Nunes PF, Ostan I and Siqueira AAG
(2020) Evaluation of Motor
Primitive-Based Adaptive Control for
Lower Limb Exoskeletons.
Front. Robot. AI 7:575217.
doi: 10.3389/frobt.2020.575217

In order to assist after-stroke individuals to rehabilitate their movements, research centers have developed lower limbs exoskeletons and control strategies for them. Robot-assisted therapy can help not only by providing support, accuracy, and precision while performing exercises, but also by being able to adapt to different patient needs, according to their impairments. As a consequence, different control strategies have been employed and evaluated, although with limited effectiveness. This work presents a bio-inspired controller, based on the concept of motor primitives. The proposed approach was evaluated on a lower limbs exoskeleton, in which the knee joint was driven by a series elastic actuator. First, to extract the motor primitives, the user torques were estimated by means of a generalized momentum-based disturbance observer combined with an extended Kalman filter. These data were provided to the control algorithm, which, at every swing phase, assisted the subject to perform the desired movement, based on the analysis of his previous step. Tests are performed in order to evaluate the controller performance for a subject walking actively, passively, and at a combination of these two conditions. Results suggest that the robot assistance is capable of compensating the motor primitive weight deficiency when the subject exerts less torque than expected. Furthermore, though only the knee joint was actuated, the motor primitive weights with respect to the hip joint were influenced by the robot torque applied at the knee. The robot also generated torque to compensate for eventual asynchronous movements of the subject, and adapted to a change in the gait characteristics within three to four steps.

Keywords: rehabilitation robotics, motor primitives, exoskeleton, lower limbs, biomechanics

1. INTRODUCTION

According to the World Health Organization (WHO), population aging is a fact and by 2050 the number of people aged 60 and over will reach 2 billion (World Health Organization, 2015) representing one fifth of the planet's population (Castles et al., 2013). The incidence of gait disorders can reach a prevalence of 35 and 60% in people over 70 and 80 years old, respectively, and the most common disorder among these people is stroke. Worldwide, stroke is the second leading cause of death and the third biggest cause of long-term disability, with approximately 33 million surviving individuals (Lozano et al., 2012; Murray et al., 2015). Among the various anomalies caused by it, stroke can originate severe sequelae to the neural areas that control upper and lower limbs movements, since it leads to a lack or an excess of blood supply in the brain, which affects about

50% of survivors (Mackay et al., 2004). As a consequence, most post-stroke individuals do not have a balance and support phase defined as in the gait of a normal individual, leading to a greater risk of falls, as movements are uncontrolled, and balance and proprioception are impaired (Sommerfeld et al., 2004).

To improve the quality of life of these individuals is only possible because the cerebral cortex is formed by a set of interconnected neuronal cells, which, in response to changes in the environment, are able to adapt. This adaptation occurs due to the fundamental property of the nervous tissues that form the basis of learning (or relearning), called neuroplasticity. This depends exclusively on repetitive experiences that will contribute to motor recovery after stroke or any other injury to the central nervous system (CNS) (Wieloch and Nikolich, 2006; Pekna et al., 2012). CNS neuroplasticity contributes to the development of motor primitives (muscle activity pattern), which combine with flexibility to produce motor behaviors (d'Avella et al., 2003; Ting and McKay, 2007; Bizzi et al., 2008; Tresch and Jarc, 2009; Bizzi and Cheung, 2013).

In view of the difficulties faced by these individuals after the stroke and with the objective of recovering lost or impaired movements, thus improving the quality of life of these people, several studies on rehabilitation have been carried out by researchers in the field of robotics, which aim to develop new strategies to recover gait symmetry with the aid of adaptive robots (Krebs et al., 2008; Contreras-Vidal et al., 2016; Zadavec et al., 2017). In a recent study with post-stroke individuals using a lower limbs exoskeleton, it was possible to observe an increase in lateral symmetry of muscle synergies during walking and a significant evolution in gait kinematics after 3 weeks of training (Tan et al., 2018).

In the rehabilitation process, one of the most important tasks has been to accurately determine the levels of assistance that will act on human joints during gait and a recent study published by Fricke et al. (2020) showed apparent advantages of automatic adjustment over manual adjustment performed by therapists during clinical practice. Therefore, it is possible to develop an adaptive control strategy based on the knowledge of the user's kinetic characteristics, so that the exoskeleton can react intuitively to the movement intended by the user, providing coherent, collaborative and effective assistance, which has been the objective of several recent researches (Diaz et al., 2011; Yan et al., 2015; Alibeji et al., 2018; Bayon et al., 2018; Maggioni et al., 2018).

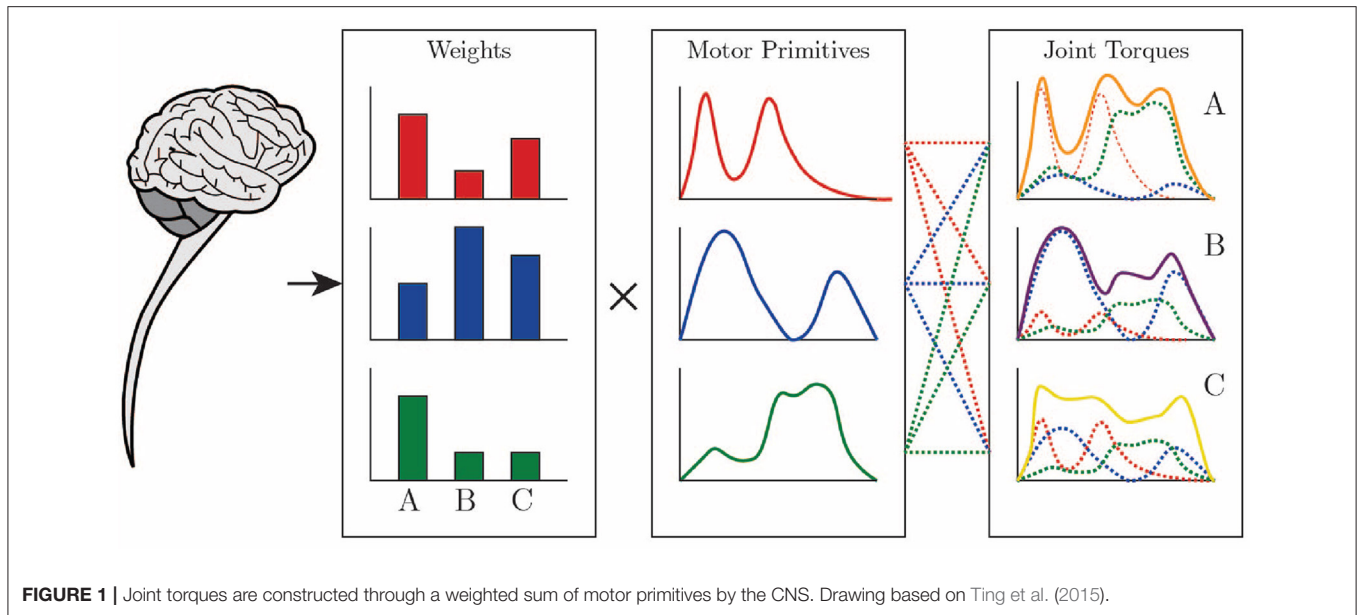
The use of motor primitives, as depicted in **Figure 1**, can significantly reduce the computational load during motor control over the CNS, since, with a basic set of primitives, it is possible to reconstruct different conditions and tasks related to a movement, just by defining when and how much to recruit from each primitive within the movement segment of each individual (Ruckert and d'Avella, 2013). The movement of the musculoskeletal system is influenced by the neural and biomechanical systems of the body and their interaction with the environment. Controlling this system is a complex task due to the abundance of degrees of freedom, with which the central nervous system is not in a position to deal initially (Bernstein, 1967).

Neuroplasticity is the neurobiological basis of the ability to adapt and learn in a manner dependent on experience, through repetitions (Wieloch and Nikolich, 2006), generating new movement patterns and new motor primitives (Bizzi et al., 2008). Such primitives have been associated with biomechanical functions necessary for walking, producing in response a specific motor output with specific patterns of muscle activity that restore previously lost functions. There is no correct or ideal motor pattern for each type of movement. The ability to choose between different solutions is implicit in the adaptability and robustness of biological systems, that is, different primitives can perform, in an equivalent way, the same type of motor task (Netune et al., 2009; Chvatal et al., 2011; Allen and Netuno, 2012).

The kinematic primitives were called sub-movements in studies carried out by Rohrer et al. (2002) about changes in the smoothness of movements in the recovery of post-stroke patients. In the same study, robotic therapy devices were used to analyze five measures of smoothness of hemiparetic movement in 31 patients recovering from stroke. The kinematic and dynamic adaptability to variations in precision, strength, and speed of movement under different conditions were analyzed in Grinyagin et al. (2005). In this last study, the kinematic variables were used to calculate the inverse dynamics, in order to obtain the torques between the articulations. To quantify the contributions of the joints individually in dynamic and kinematic primitives, the joint angles and torques were calculated by Principal Component Analysis (PCA).

In Garate et al. (2016), the concept of assistance based on primitives using an assistive exoskeleton was explored using two different approaches. In the first approach, to produce the desired assistive torque profiles, a combination of the primitives with the weights was made, and in the second approach, the motor primitives are identified to be inserted as neural stimuli in a virtual model of the musculoskeletal system. Kinematic variables of hip, knee, and ankle joint positions were used in the processing of data obtained with Inertial Measurement Units (IMU) in Nunes et al. (2018). Using the inverse dynamics of OpenSim, kinetic data (hip, knee, and ankle torques) were calculated to assess the influence of the exoskeleton structure on kinetic and muscle characteristics, using the relationships between motor primitives and their respective weights for the different conditions of use of the exoskeleton.

Herein, a bio-inspired controller for locomotion of wearable robots based on the concept of motor primitives is presented. The robot torque is calculated considering the particular kinetic motor primitives of a user, generating a force at the user's joint. A modular lower limb exoskeleton, presented in dos Santos et al. (2017a), was used to evaluate the control proposal. The device was configured to provide partial support during gait, in knee flexion and extension, applying precise torques calculated automatically by the control algorithm. As the torque of the exoskeleton is based on the primitives, it will always assist in order to compensate for the primitives with less weight, i.e., the ones which reflect some sort of lack of strength at the joint. The robot torque was applied to healthy subjects wearing the right leg of lower limbs exoskeleton, while walking on a treadmill. The healthy subjects walked actively, following



the treadmill speed, and, in order to simulate a gait with a lack of torque, the subjects were later instructed to walk at a slower pace. The user's joint torques are provided by an estimation algorithm based on a generalized momentum-based disturbance observer (DOB) approach along with an extended Kalman filter, as described in dos Santos and Siqueira (2019). The hip and ankle joints are not actuated whereas the knee joint, which comprises a rotary series elastic actuator (rSEA), is actuated.

This work is organized as follows: the next section provides more details with respect to the equipment and control algorithm. In sequel, section 3 refers to the test procedure, which is followed by the test results in section 4. Section 5 discusses the results and is followed by the conclusion.

2. METHODS

2.1. Lower Limbs Exoskeleton

The exoskeleton utilized in this work is the ExoTao (dos Santos et al., 2019). This robotic device comprises six rotary, one-degree-of-freedom joints, which can track the hip, knee, and ankle joint movement on the sagittal plane, with the aid of magnetic encoders. For the time being, only the right leg of the robot is considered. The only active joint is the knee, whereas the hip and the ankle work passively. The knee joint consists of a module with a rotary Series Elastic Actuator (SEA), as presented in dos Santos et al. (2017a), which can be configured to work in impedance and force control modes. Its motor is connected to an EPOS controller board, which communicates with the control algorithm running on a desktop computer via Controller Area Network (CAN) ports. In order to prevent the subject from slipping while walking, and to compensate for part of weight of the exoskeleton, a mechanical structure was installed as depicted in Figure 2.

The joints were designed to attend different ranges of motion with respect to different tasks. However, they can be limited by adjustable end-stops to prevent hyperextension of the joints. The exoskeleton contains Velcro® straps and telescopic links, which make it adjustable to different body heights from 1.60 to 1.90 m, in order to align the exoskeleton and the subject joints (dos Santos et al., 2017b).

2.2. Reference Values Extraction

To extract the primitives and analyze the data, aiming at the reduction of dimensionality and elimination of unnecessary characteristics, the Principal Component Analysis (Person, 1901) was employed. The PCA was chosen because it proved to be an accurate estimate to obtain a linear combination of primitives and their respective weights, in order to minimize the difference between the original and reconstructed signals (Nunes et al., 2020).

In the literature, primitives are usually calculated as the sum of the product between them, $\mathbf{p} = [\mathbf{p}_1, \mathbf{p}_2, \dots, \mathbf{p}_n]$ where $\mathbf{p} \in \mathbb{R}^{t \times n}$, and their respective weights, $\mathbf{w} = [\mathbf{w}_1, \mathbf{w}_2, \dots, \mathbf{w}_n]$ where $\mathbf{w} \in \mathbb{R}^{n \times n}$ as in Equation (1) (Cheung et al., 2009; Bizzi and Cheung, 2013; Berger and d'Avella, 2014; Roh et al., 2015). This calculation extracts a linear combination between primitives and their corresponding weights to minimize the difference between the original and reconstructed signals, which, in this case, are torque profiles $\tau \in \mathbb{R}^{n \times t}$:

$$\tau = \mathbf{p} \cdot \mathbf{w} \quad (1)$$

The motor primitives of four healthy subjects (1 female, 3 male, 30 ± 6 years, 73 ± 6 kg, 1.78 ± 0.04 m) were extracted in order to be further used by the control algorithm as reference. To extract these motor primitives, the subjects walked on a treadmill using the right leg of the exoskeleton for 2 min at 1.0 km/h. The knee

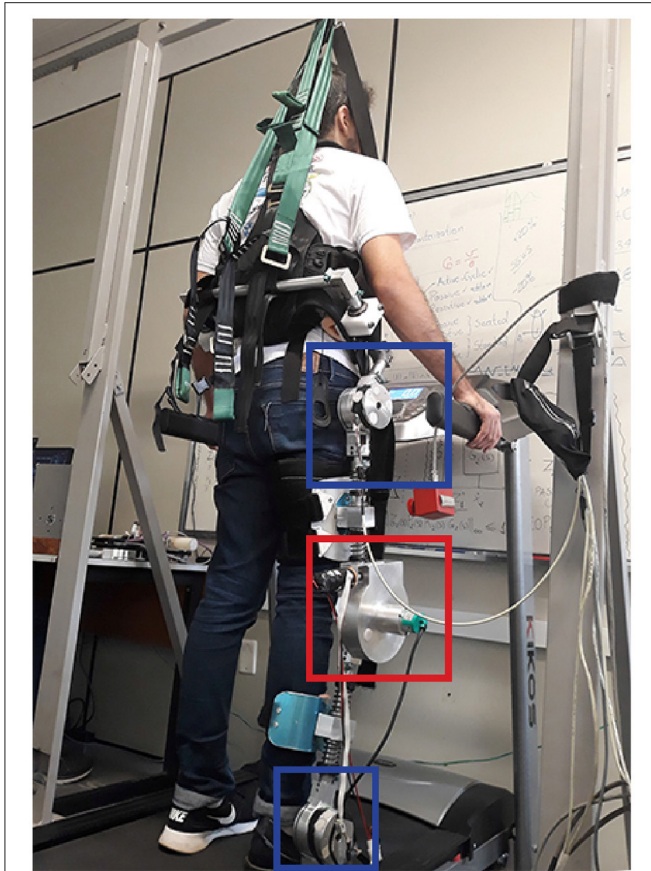


FIGURE 2 | Test setup with healthy subject wearing the right leg of the lower limbs exoskeleton ExoTao. The red box delimits the rotary SEA at the knee joint. The blue boxes depict the hip and ankle joints, which are not actuated. The robot is suspended by a mechanical structure in order to compensate for part of its weight, which leads to a more comfortable walk on the treadmill.

joint of the robot was adjusted to impedance mode, thus, the knee of the subjects followed a desired pre-recorded trajectory, according to the control law:

$$\tau_{r,imp} = K_v(\theta^d - \theta), \quad (2)$$

where K_v is the virtual stiffness of the impedance controller (set to 20 N.m/rad), $\tau_{r,imp}$ is the torque of the robot, while θ^d and θ are the desired trajectory and the knee joint measurement, respectively. An inner Proportional-Integral (PI) torque controller ensures that the robot torque is exerted at the joint.

The torque exerted by the subject's hip and ankle joints is estimated by means of an estimation algorithm that employs a generalized momentum-based disturbance observer (DOB) approach along with an Extended Kalman Filter. The Kalman Filter returns a time-varying gain at the end of every iteration, which ensures robustness with regards to the time-varying characteristics of the patient-exoskeleton model, as described by

dos Santos and Siqueira (2019). The knee torque is obtained directly from the SEA.

This procedure yields the motor primitives, \mathbf{p}_h , and their respective weights, \mathbf{w}_h , with respect to each joint. Further auxiliary data that is also considered by the control algorithm are also generated, such as maximum primitive torque, $\tau_{h,max}$, and constant torque offset values, $\tau_{h,dc}$. The subscript h denotes the word healthy.

2.3. Control Algorithm

In summary, at the end of every step, the control algorithm computes the subject's motor primitive weights, based on the primitive torques extracted beforehand and on the joint torque measurements during the last swing phase. The subject's weights that are below the reference value are identified and, during the next swing phase, the robot actuates in order to compensate for the lack of weight. The following paragraphs explain in details the calculations performed by the control algorithm.

The algorithm is provided with the data from the procedure described in section 2.2, i.e., the reference or healthy values. After the right leg of the subject has performed the k^{th} swing, his torque curves, τ_{pat} , with respect to the hip, knee, and ankle joints are obtained by the estimation algorithm and the SEA. These torque curves are treated before being employed to compute the subject motor primitive weights. First, their constant offset value, $\tau_{pat,dc}$, is subtracted. Afterward, they are divided by the extreme torque value obtained from the reference, $\tau_{max,h}$, resulting in a normalized torque profile, $\tau_{pat,n}$. This extreme value is the maximum value within each torque curve, and among torque curves. Due to the characteristic of the torque curves during the swing phase, it is known beforehand that this value is positive and related to the hip joint. However, in case other gait phases or tasks are analyzed, the algorithm handles the circumstance in which this value is a global minimum instead.

The aforementioned manipulations are summarized by the following equation:

$$\tau_{pat,n}^k = \left(\frac{1}{\tau_{h,max}} \right) (\tau_{pat}^k - \tau_{pat,dc}^k). \quad (3)$$

Therefore, the motor primitive weights of the subject, \mathbf{w}_{pat} , are extracted as in:

$$\mathbf{w}_{pat}^k = \mathbf{p}_h^\dagger \tau_{pat,n}^k, \quad (4)$$

where \mathbf{p}_h^\dagger denotes the Moore-Penrose inverse of the motor primitives extracted from the gait used as reference.

The subject weights, \mathbf{w}_{pat} , are compared with the reference weights, \mathbf{w}_h , element-by-element. The relative error between these weights provides a measurement of how distant the subject's gait is from the reference gait. This disparity, $\Delta \mathbf{w}$, should be addressed by the robotic device during the next swing phase and is denoted simply as:

$$\Delta \mathbf{w}^k = \mathbf{w}_h - \mathbf{w}_{pat}^k \quad (5)$$

The difference between the constant offset values is also addressed by the robot. Thus, the torque to be exerted by the

robot in the swing phase of the next stride of the right leg, τ_r^{k+1} , in given by:

$$\tau_r^{k+1} = \tau_{h,max} \mathbf{p} \mathbf{h} \Delta \mathbf{w}^k + (\tau_{h,dc} - \tau_{pat,dc}^k) \quad (6)$$

All quantities related to the subject are denoted by the subscript **pat**, which refers to the word patient. Though no patient was subjected to the test, the variables were named after this word to illustrate the purpose of the control algorithm, which is aimed at people with some sort of motor impairment, e.g., stroke survivors.

To avoid abrupt oscillations, the effective torque to be exerted by the robot, $\tau_{r,e}$, considers the weight deficiency from the last step and the step before the last one. This approach leads to the computation of an exponentially weighted moving average (EWMA). A diagonal matrix, α , composed of α_i factors, $i = 1, 2, 3$ weights the robot torque as in:

$$\tau_{r,e}^{k+1} = \alpha \tau_r^{k+1} + (\mathbf{I} - \alpha) \tau_r^k. \quad (7)$$

During the first step, no robot torque is applied, as there is no previous step. During the second step onward, the robot torque is applied. Exceptionally during the second swing, α is set to unit. Afterward, α is set to 0.15, a value found empirically.

This robot torque is exerted at the robot joint with the aid of an inner PI torque controller, whose gains were set to $k_p = 370$ and $k_i = 3.5$ based on previous works with the robotic device. The robot only acts during the swing phase. During the stance phase transparency is aimed, so the robot torque is set to zero and only the inner torque control loop takes place. The phase detection is hard-coded within the control algorithm and is based on pre-recorded trajectories.

All operations are shown in matrix notation because the control algorithm is proposed to work on three joints of each leg. However, because only the knee joint is actuated, here only this component of the robot torque is used.

The robot exerts torque only when the subject weights are not greater than the reference weights. Otherwise, the robot would restrain the subject's movement, applying an opposing torque. This would lead to a control strategy focused on replicating a reference torque curve, which is not the aim of this work. The same is true for the constant component of the torques when they are greater than the reference values.

However, when the subject exerts more torque than necessary, but in the opposing direction, which in practice results in opposed-sign weights of greater magnitude than the reference, the robot does act in order to correct the gait. **Figure 3** shows the complete block diagram of the proposed adaptive control algorithm.

3. TEST PROTOCOL

Two tests were performed with 5 healthy subjects (1 female, 4 male, 30 ± 6 years, 73 ± 6 kg, 1.77 ± 0.05 m) in order to evaluate the control algorithm and the motor primitive weights behavior, and one test was performed with one healthy subject

(male, 25 years old, 71 kg and 1.76 m) to evaluate the algorithm convergence and adaptability to changes in the mode of walk.

In the first test, the subjects were instructed to walk at 1.5 km/h on a treadmill for 2 min. This yields data for approximately 50 steps. In this test, the subjects walk in an active manner, as if they were without the exoskeleton. The expected robot torque is small, as the subjects produce all the necessary torque to perform the walk, dispensing further assistance. The joints trajectories and torques are expected to match, to a certain extent, the ones obtained during the procedure to extract motor primitives. Further, the behavior of all weights are analyzed.

In the second test, the subjects walked at 1.0 km/h on a treadmill for 2 min. This time, they were instructed to walk slower and also to keep the right leg passive during the swing phase, i.e., to offer no resistance in case the robot tried to move it. Hence, the motor primitive weights relative to the knee joint are expected to result in values lower than the reference, causing the robot to exert an assistive torque over the swing phase. Further, the behavior of all weights are analyzed.

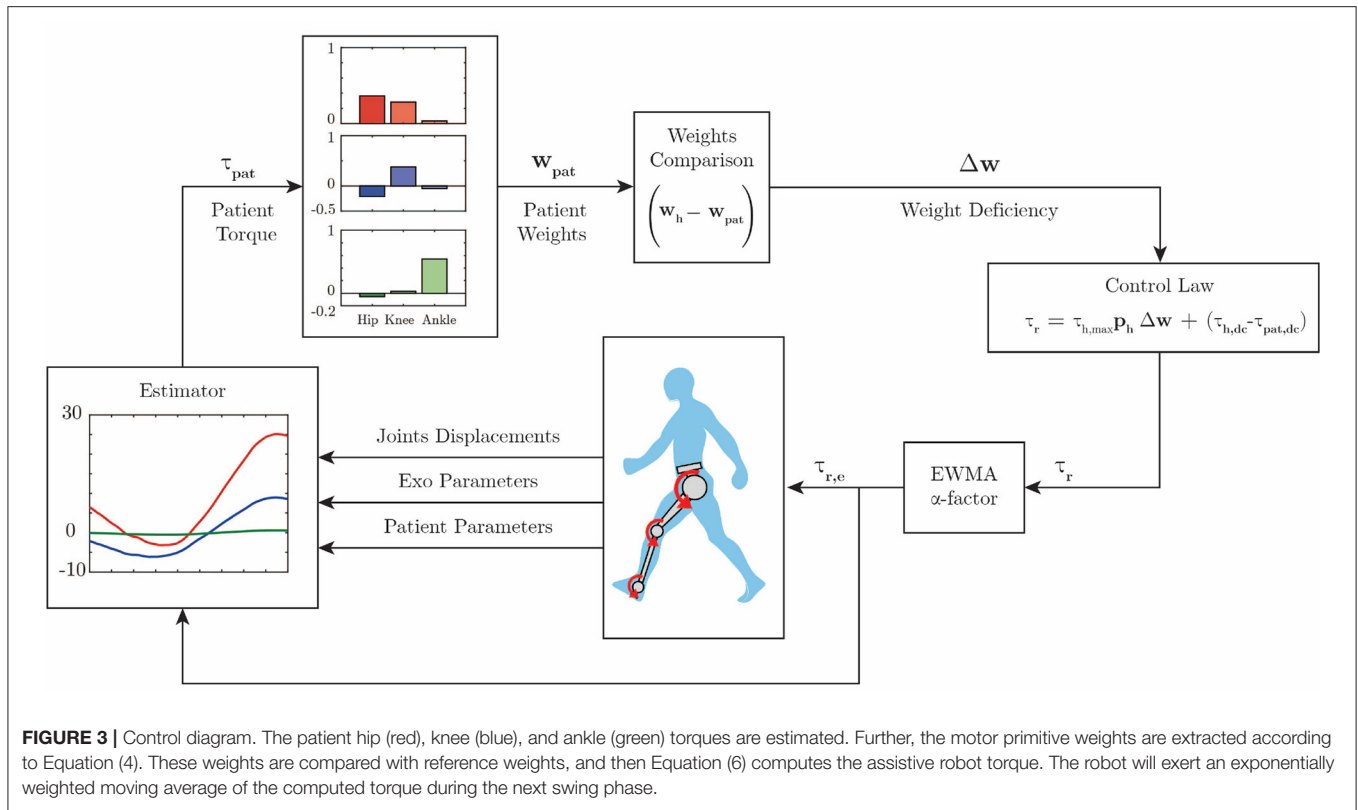
The third test consisted of a combination of the first and the second test and was performed with one healthy subject. He was instructed to walk actively for 30 s at 1.0 km/h, and passively for 30 s at the same speed, completing 1 min of walk. This yields data for 25 steps. Therefore, it could be evaluated whether the control algorithm would adapt to different patient behaviors in real time.

During all tests, the joint displacements, torques, and the motor primitive weights of the subjects were stored for further analysis. The extracted weights of the subject were divided into three categories. The weights could be considered *healthy* weights, which comprised weights with equal or greater magnitude and same direction as the reference weights. In this case, the robot did not actuate. The weights could also be considered *deficient*, which comprised weights below the absolute reference value, regardless of their direction. These weights and their behavior over the first two tests is analyzed. In this case, the robot produced torque during the next swing, in order to assist the subject. Last, the weights could be considered *asynchronous*, which comprised weights with greater magnitude as the reference, but with opposing sign. Although the robot exerted torque in order to correct the subject's gait, these weights are not considered deficient, as their occurrence is rather consequence of a lack of synchrony between the actual gait phase and the phase of the control algorithm, than the consequence of an impaired walk, in which there is a lack of weight to perform the movement.

The primitive extraction procedure and the analysis of data yielded from all tests are processed by means of routines programmed in MATLAB® software (2015a, The MathWorks, Inc., Natick, Massachusetts, United States).

4. RESULTS

Herein the experimental results obtained from the motor primitive extraction procedure are shown. These data are further used as reference values within the control algorithm. In the sequence, the results of a set of simulated patient conditions as



defined in the previous section are presented (active, passive, and a combination of these two).

4.1. Reference Primitive Torques and Weights

Figure 4A shows the average measured joint displacements (solid lines) during the swing phase. **Figure 4B** shows the average estimated joint torque profiles (solid lines). The shaded region denotes the standard deviation of the measurements.

Figure 5 shows the average primitive torque profiles from the extraction method described in section 2.2 along with the respective weight regarding each joint. The shaded region denotes the standard deviation of the measurements.

The reference weights employed as reference for the control law are described by the following matrix:

$$\mathbf{w}_h = \begin{bmatrix} \mathbf{w}_{h,hip} \\ \mathbf{w}_{h,knee} \\ \mathbf{w}_{h,ankle} \end{bmatrix} = \begin{bmatrix} 0.8784 & -0.4750 & -0.0539 \\ 0.4768 & 0.8786 & 0.0282 \\ 0.0340 & -0.0505 & 0.9981 \end{bmatrix} \pm \begin{bmatrix} 0.0097 & 0.0142 & 0.0044 \\ 0.0140 & 0.0087 & 0.0574 \\ 0.0284 & 0.0498 & 0.0015 \end{bmatrix}.$$

If one multiplies each primitive curve by the respective joint weight and sum all the three components, the average profile torque can be reconstructed for all joints. It is important to notice that each primitive is strictly related to a specific joint. The first primitive, for instance, is tight to the hip joint, which can be noted

by the fact that the hip weight of this primitive (0.8784) is greater when compared with the other two weights (0.4768 and 0.0340).

These weights ponder the influence of each primitive on the torque observed at each joint. A negative weight means that the primitive torque must have its direction changed before being multiplied by the weight and being summed to the other primitives that compose the joint torque. The control algorithm will not provide assistance in the case the subject's weights are at least equal to the reference ones. If his weights are greater than the reference, the subject is exerting more torque than necessary. If the weights are greater in magnitude but with an opposing sign, the subject is exerting more torque than necessary and in the wrong direction. In this case, the subject is not considered necessarily in need of assistance to perform the movement, as he is capable of exerting torque of greater or same magnitude as the reference.

It can be noted that during the swing phase the ankle joint exerts almost no torque. This is due the fact that the exoskeleton shoe is rigid to a certain extent, in order to aid post-stroke patients with foot-drop to perform the walk properly. Therefore, the ankle joint can be left out for this application. Hence, the reference weights matrix is further simplified as

$$\mathbf{w}_h = \begin{bmatrix} \mathbf{w}_{h,hip} \\ \mathbf{w}_{h,knee} \end{bmatrix} = \begin{bmatrix} 0.8784 & -0.4750 \\ 0.4768 & 0.8786 \end{bmatrix} \pm \begin{bmatrix} 0.0097 & 0.0142 \\ 0.0140 & 0.0087 \end{bmatrix}$$

The data extraction also provides an average of the maximum torque, which is the maximum hip torque:

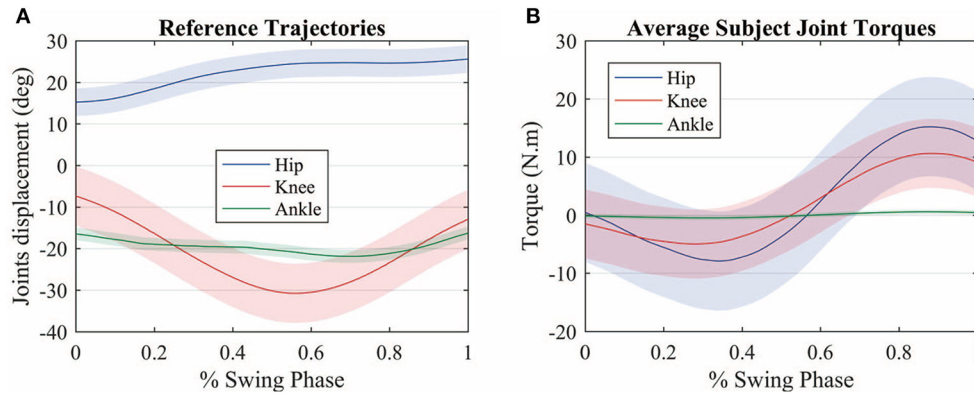


FIGURE 4 | (A) Average measured joint displacements (solid lines) during the swing phase. **(B)** Average estimated joint torque profiles (solid lines). The shaded region denotes the standard deviation of the measurements.

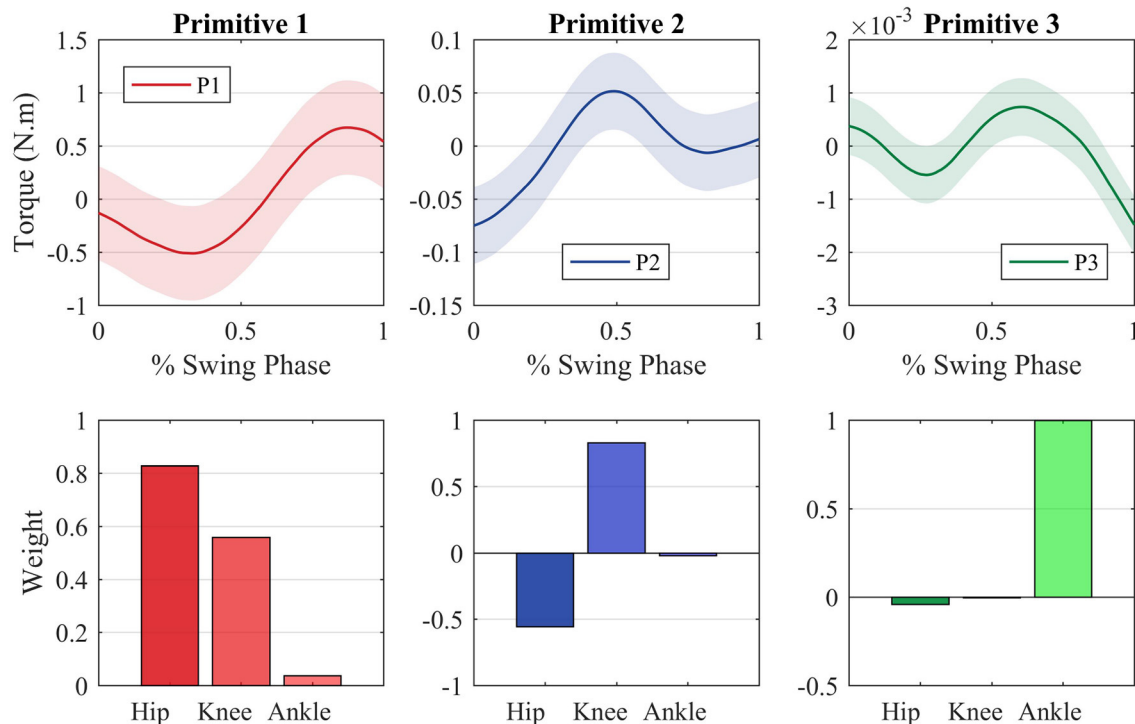


FIGURE 5 | Motor primitives extracted through the PCA method and the motor primitive weights regarding each joint. The joint torques can be reconstructed by making a weighted sum of each primitive with regards to each joint.

$$\tau_{h,max} = 25.8798 \text{ Nm.}$$

The constant component regarding the average torque of each joint is given by

$$\tau_{dc} = [\tau_{dc,hip} \quad \tau_{dc,knee}] = [12.4015 \quad 4.2152] \\ \pm [9.7966 \quad 1.2715] \text{ Nm.}$$

It can be noted that there is considerable variation among the torque offset values. This is due to the nuances in the gait pattern of the individuals, as well as their characteristics, such as body mass and leg length.

The constant components of the knee and ankle torques are small when compared with the hip component. Moreover, a steadier robot behavior was achieved when these constant values were not considered, since the robot would abruptly raise its torque to this constant value as soon as the swing phase started. Thus, they were not considered for this test, in order to obtain a

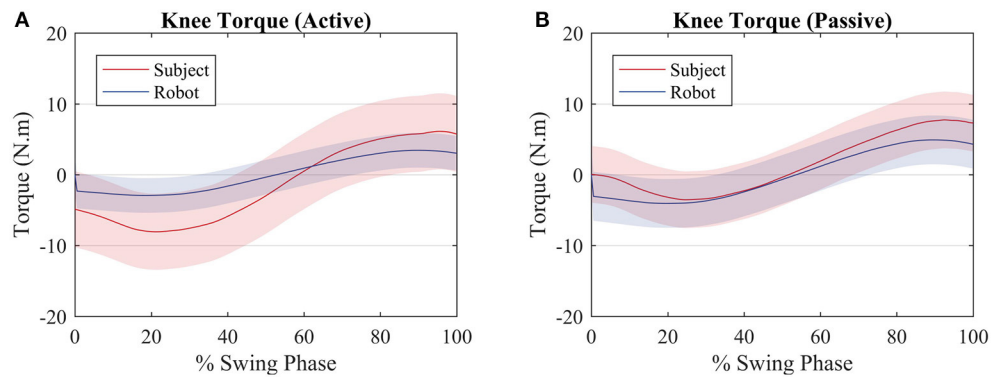


FIGURE 6 | Average torque exerted by the subjects (red) and by the robot (blue) for an **(A)** active walk and a **(B)** passive walk. Shaded regions denote the standard deviation of the measurements.

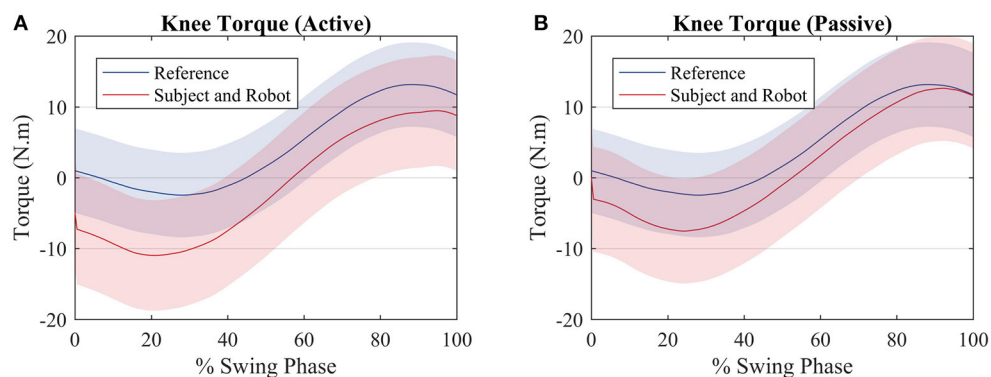


FIGURE 7 | Average torque exerted by the subjects (red) and average torque value used to compute the reference (blue) for an **(A)** active walk and a **(B)** passive walk. Shaded regions denote the standard deviation of the measurements.

smoother robot assistance and steadier gait. To extract the patient weights, \mathbf{w}_{pat} , and compare with the reference ones, the algorithm must receive the pseudo-inverse of the primitive torques, \mathbf{p}_h^+ . To reduce computation time, the pseudo-inverse is calculated beforehand and provided to the algorithm. Once the healthy parameters were set, the tests were performed.

4.2. Test Results

Though there is not an explicit torque reference value to be tracked by the control algorithm, it is expected that, for the first test, in which the subjects walked actively, the robot exerts less torque than the subject, when compared with the second test, in which the subjects walked passively. In the first case, **Figure 6A** (active), the robot produces a torque with a RMS value of 2.5 Nm, whereas the user produces a torque with a RMS value of 7.3 Nm, equal to the reference value of 7.3 Nm RMS. In the second case, **Figure 6B** (passive), the robot produces more torque (RMS = 3.5 Nm) since the user is producing less torque at the knee joint (RMS = 5.6 Nm). It must be noted that it is not possible to prevent the user from exerting torque at the knee joint. When the results of each subject are considered rather than the average among them, for the active walk the minimum RMS torque produced

by the robot was 1.2 Nm RMS, when the user was producing a torque of 10.5 Nm RMS. With respect to the passive walk, the maximum torque of the robot was 4 Nm RMS and the subject, 4.4 Nm RMS.

When the subject and the robot torque are compared with the reference, it can be noted that for both scenarios the two torques sum up in order to get closer to the reference torque as depicted by **Figure 7A** (active) and **Figure 7B** (passive).

Figure 8 shows a comparison between the hip joint positions of the subject during the primitive extraction procedure (blue) and during the tests (red). Despite an offset value, which is due to the position of the exoskeleton around the subject's hip, the trajectories are similar among all subjects, and they relate to the reference profile, though, in the active walk, the amplitude of the movement is greater.

Figure 9 shows a comparison between the knee joint positions of the subject during the primitive extraction procedure (blue) and during the tests (red). The trajectories are similar among all subjects, and they relate to the reference profile, regardless of the mode of walk, since there is robot actuation at the knee joint. It can be noted that the knee joint is closer to the reference during the passive mode of walk.

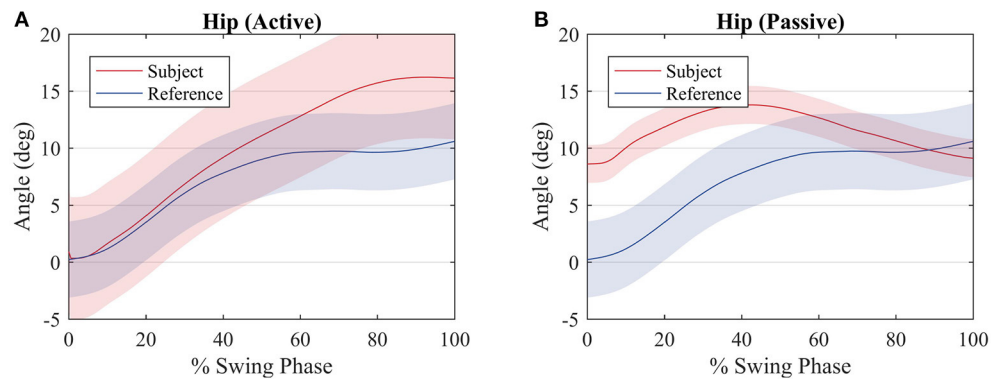


FIGURE 8 | Average hip joint displacement of the subjects (red) and average hip joint displacement during the procedure to compute the reference values (blue) for an (A) active walk and a (B) passive walk. Shaded regions denote the standard deviation of the measurements.

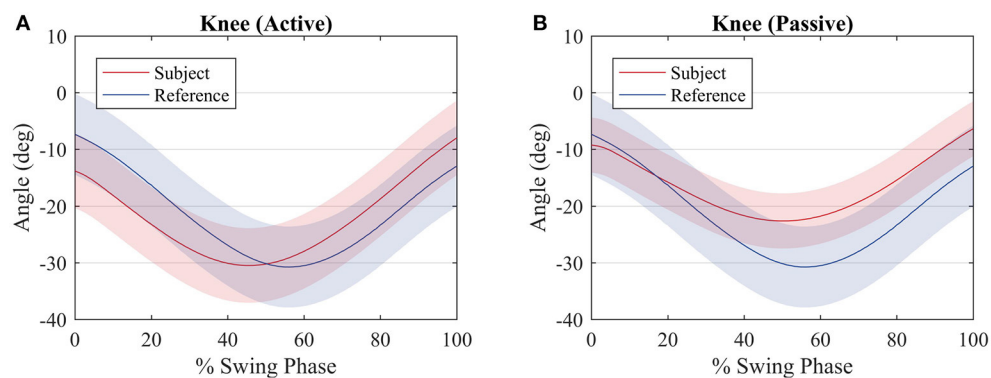


FIGURE 9 | Average knee joint displacement of the subjects (red) and average hip joint displacement during the procedure to compute the reference values (blue) for an (A) active walk and a (B) passive walk. Shaded regions denote the standard deviation of the measurements.

With respect to the motor primitive weights, only the weights that were below the reference value, regardless of their signal, were analyzed, in order to evaluate the influence of the robot actuation between the two modes of walk. To simplify this analysis, these weights were summarized in a boxplot and compared with the other subjects, as depicted in **Figure 10**.

The third test evaluated the algorithm performance during gait with oscillating characteristic. Hence, the user walked actively for 30 s and passively for more 30 s. Results are depicted in **Figure 11**.

5. DISCUSSION

As seen in **Figure 6**, the robot produces less torque during an active mode of walk when compared with the passive mode of walk. However, the robot torque is still present because even though the subjects produce torque when they walk actively, not always their torques have the exact primitive weights as the reference ones. A better clarification on why the robot acted as such is given further through an analysis of the patient weights in **Figure 10**. Therefore, the robot torque is present so that the sum

of the subject and the robot torque gets closer to the reference torque value, as in **Figure 7**.

The hip joint trajectory is depicted in **Figure 8** for an active and passive mode of walk. The trajectory is not tracked so accurately when compared to the knee joint, due to the lack of actuation on this joint. This will reflect on deficient weights with respect to the hip joint and the first motor primitive.

With respect to the knee joint trajectory, it can be noted in **Figure 9** that for both modes of walk the trajectory is close to the reference. In fact, for the passive mode of walk, the trajectory is closer when compared with the active mode of walk, due to the fact that most of the movement is performed by the robot. During the active walk, the user walks at a faster pace and the robot, sensing that the knee joint torque of the subject is sufficient or greater to perform the movement, does not oppose to the user movement. This is expected since the robot is supposed to only provide assistance rather than make the user follow strictly a pre-recorded trajectory.

One can notice that no explicit trajectory or torque tracking is included in the control algorithm. Still, torque and trajectory could still be tracked, indirectly, to a certain extent, so that it matched the reference values.

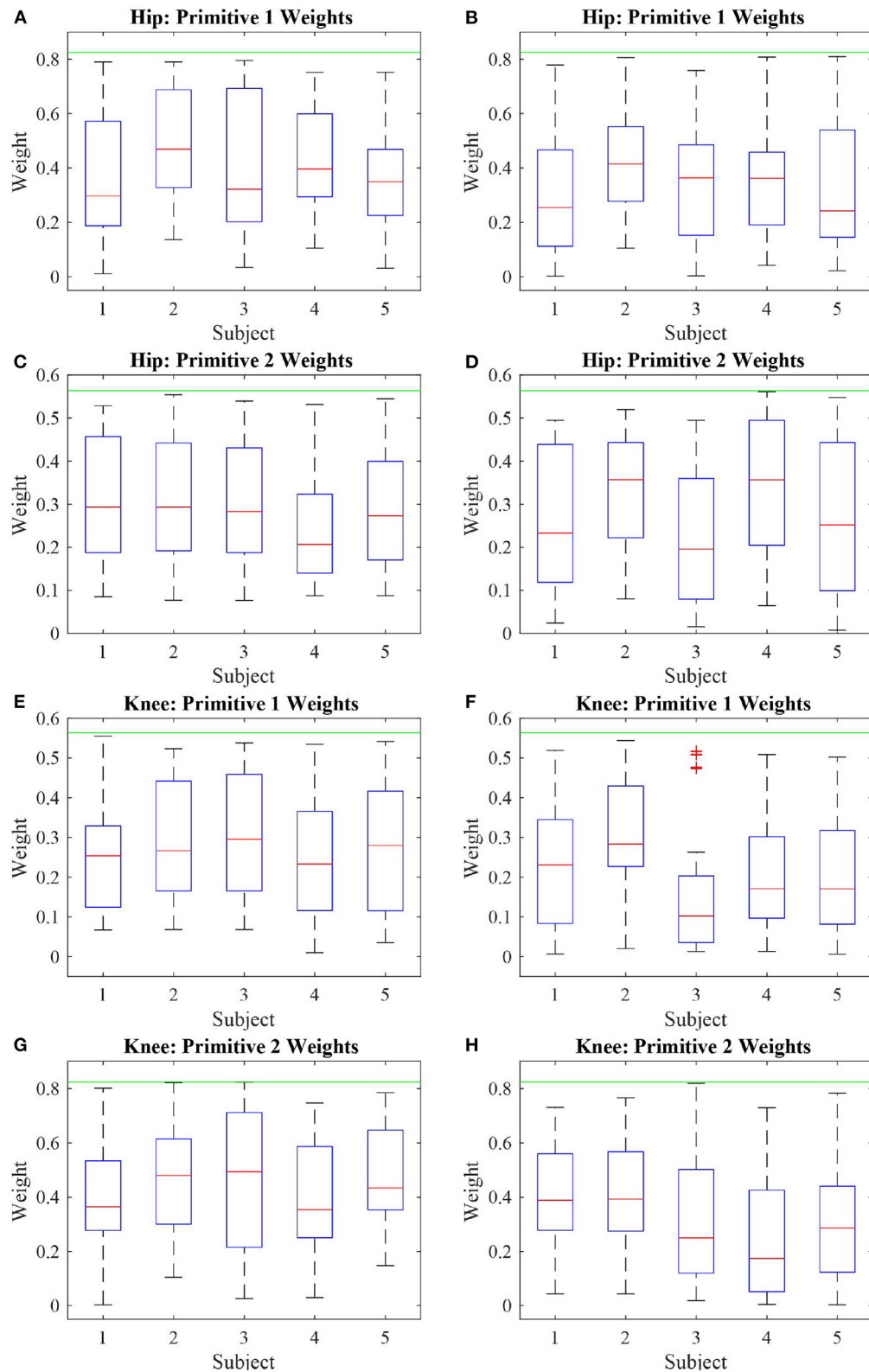


FIGURE 10 | Boxplot of the absolute value of the deficient weights of five subjects performing two modes of walk: active (A,C,E,G) and passive (B,D,F,H). It can be noted that the weights with respect to the first primitive are more affected than the weights related to the second primitive, due to the knee actuation and the absence of actuation at the hip joint.

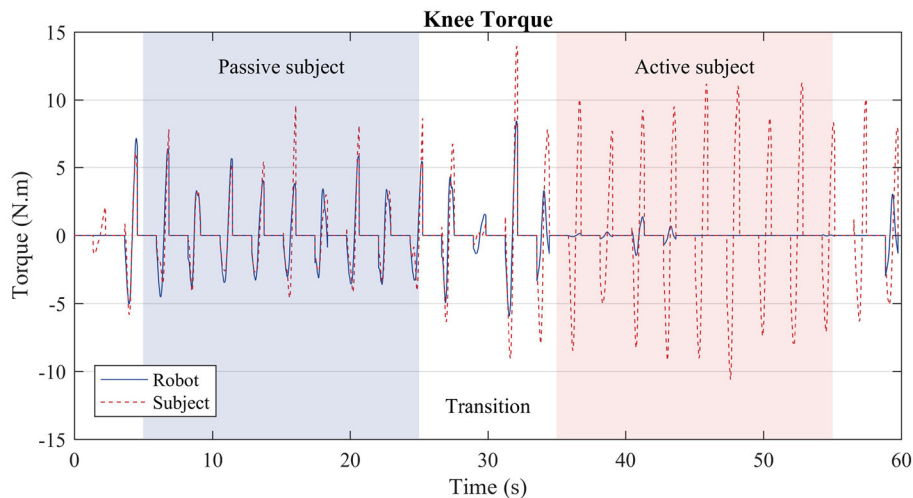


FIGURE 11 | Subject torque (red dashed lines) and robot torque (solid blue line) in the third test. During the first stage (blue region), the user was instructed to walk passively, i.e., the treadmill slowed down, and the subject prevented from moving more than necessary the knee joint of the right leg. During the second stage (red region), the user walked actively, i.e., as if he were not wearing the robot exoskeleton; thus, the robot produced considerably less torque.

As the hip joint was not actuated, most hip weights were expected to fall within the range of deficiency. However, due to the knee actuation, the weights of the hip regarding the second primitive were kept at steady values of magnitude during most of the walk.

During the active and passive mode of walk, 58% of the hip weights relative to the first primitive were deficient. With respect to the hip weight relative to the second primitive, during the active walk they were deficient 45% of the test, and, in the passive case, 51%. The knee weights with respect to the first primitive were deficient over 40% of the active walk, as 51% for the passive walk. The knee weights with respect to the second primitive were deficient 53% of the active walk, and 63% of the passive walk. Even though the weights with respect to the knee joint were deficient, the trajectory and torque tracking were ensured by the algorithm. The same is not true with respect to the hip joint, as it was not actuated.

Figure 10 shows the behavior of these weights considered deficient. It is important to analyze the deficient weights with more detail because anything below the threshold value established by the reference value is considered deficient. However, due to the antropomorphic characteristics of each person, if the primitive torques are considered to be the same, the weights must vary in order to account for the gait particularities of each person. It can be noted that most weights during the active phase are located above the median (particularly truth for most subjects in **Figures 10A,C,E,G**) whereas, for the passive walk, most weights are located below the median (**Figure 10B**) or the median values are lower when compared to the Figure beside it (**Figures 10D,F,H**).

In the third test the algorithm acted in a way that replicated what was observed in the first and second tests separately. During the transitions, i.e., the white regions of **Figure 11**, the robot torque is prone to oscillations, as the subject behavior was

changing from a passive mode of walk to an active one. Over three to four steps, the robot converges to the expected behavior. During the passive stage (blue region), the robot torque (solid blue line) complements the subject's torque (dashed red line), whereas during the active stage (red region), the robot exerts almost no torque, since the subject is capable of producing the necessary torque by himself.

The hip weights with regards to the first primitives, **Figures 10A,B**, presented a behavior similar to the weights of the knee joints regarding the same primitive (**Figures 10E,F**). Likewise, there was similarity between the behavior of the hip and knee weights with relation to the second primitive (**Figures 10C,D,G,H**). This shows that the joint weights share characteristics with other joint weights with respect to the same primitives rather than with the weights of the same joint. As a consequence, it can be inferred that the first primitive relates to the hip joint the same way the second primitive relates to the knee joint. Therefore, at the same time it seems rather convenient that the actuation over one joint is capable of propagating its effects over the other joints, which could imply that a smaller number of actuators could be used, the results also suggest that the sole actuation of one joint is not capable of compensating for all weight deficiencies pertaining the actuated joint itself.

The results also show that the sole actuation of the knee could guarantee indirectly, through motor primitive analysis, that the reference joint trajectory was tracked to a certain extent. On the other hand, a position control strategy may not guarantee that the motor primitive weights are close to a reference, though it still may result in functional patient trajectories.

Regarding the convergence and adaptability experiment, the results suggest that the algorithm converges within three to four steps to a steady behavior, once the gait characteristics of the subject are analyzed in terms of primitive weights. The robot ceases to actuate once the user produces enough torque, thus

sufficient weights, automatically. This ability to adapt guarantees a more comfortable and safe walk, and prevents the scenario in which the subject produces less torque because the robot produces all the necessary torque instead.

The current setup shall be improved in order to extend the results for different modes of walk and before doing tests with impaired individuals. For instance, the actuation of the hip joint is crucial to compensate for weight deficiencies not only at the hip joint, but also at other joints, as concluded with the results exposed here. Extending the number of healthy subjects is important for comparing different motor primitive curves to be used as reference values. The analysis of motor primitives of impaired subjects is also a subject of study, in order to evaluate over therapy how the robotic device assistance affects their primitives. Moreover, a better comprehension of the motor primitives of an impaired subject may lead to better clues on how to approach the weight deficiency problem. Finally, extensive testing with a greater number of healthy subjects is fundamental to later pursue the validation of the control algorithm with impaired subjects, affected either by stroke, SCI or other types of motor impairments which compromise the lower limbs movement.

6. CONCLUSION

This work presents a bio-inspired control algorithm based on motor primitives for a modular lower limbs exoskeleton, in order to aid the rehabilitation of individuals with motor impairment, especially post-stroke victims. First, the motor primitives along with their weights were extracted from healthy subjects. To perform this task, a torque estimation algorithm together with the Principal Component Analysis were employed. Thereafter, tests with healthy subjects wearing the right leg of the exoskeleton were executed to evaluate the controller performance in three scenarios: when the subject walks actively; when the subject shows some torque deficiency, by walking slower than expected; and when there is a combination of these two cases. In all cases, the algorithm evaluates the motor primitive weights of the current subject comparing them with the weights of a healthy subject. When deficiency is observed, the robot properly exerts a complementary torque during the swing phase, to assist the subject to perform this movement. It could be noted a relation between weights of different joints with regards to the same

primitive. This shows that even though the sole actuation of one joint has influence on the weights of other joints, it is unable to compensate for all the weight deficiencies of the same joint. Moreover, the results suggest that the knee joint trajectory could be tracked indirectly at some extent solely based on the primitive weights analysis. These results are part of the ongoing effort to develop adaptive control strategies for rehabilitation robots taken into account the specific characteristics and current conditions of a patient. To perform tests with more healthy subjects and with a greater number of actuated joints of the exoskeleton are two crucial steps in order to refine the control algorithm, in order to later perform tests with impaired subjects.

DATA AVAILABILITY STATEMENT

The original contributions generated for the study are included in the article/supplementary material, further inquiries can be directed to the corresponding author/s.

ETHICS STATEMENT

The studies involving human participants were reviewed and approved by Ethics Committee of the Federal University of São Carlos (Number 26054813.1.0000.5504). The patients/participants provided their written informed consent to participate in this study.

AUTHOR CONTRIBUTIONS

PN and IO contributed to the conception and design, acquisition of data, analysis, interpretation of data, and the drafting of the manuscript. AS contributed to the conception, design, interpretation of data, and revision of the manuscript. All authors contributed to the article and approved the submitted version.

FUNDING

This work was financed in part by the Coordenação de Aperfeiçoamento de Pessoal de Nível Superior—Brazil (CAPES)—Finance Code 001, Support Program for Graduate Studies and Scientific and Technological Research for Assistive Technology in Brazil (PGPTA), under grant 3457/2014, and São Paulo Research Foundation (FAPESP) under grant 2019/05937-7.

REFERENCES

- Alibej, N. A., Molazadeh, V., Dicianno, B. E., and Sharma, N. (2018). A control scheme that uses dynamic postural synergies to coordinate a hybrid walking neuroprosthesis: theory and experiments. *Front. Neurosci.* 12:159. doi: 10.3389/fnins.2018.00159
- Allen, J. L., and Netuno, R. R. (2012). Three-dimensional modular control of human walking. *J. Biomech.* 45, 2157–2163. doi: 10.1016/j.jbiomech.2012.05.037
- Bayon, C., Fricke, S., Rocon, E., van Der Kooij, H., and Van Asseldonk, E. H. (2018). "Performance-based adaptive assistance for diverse subtasks of walking in a robotic gait trainer: description of a new controller and preliminary results," in *2018 7th IEEE International Conference on Biomedical Robotics and Biomechanics (Biorob)* (Enschede), 414–419. doi: 10.1109/BIOROB.2018.8487189
- Berger, D. J., and d'Avella, A. (2014). Effective force control by muscle synergies. *Front. Comput. Neurosci.* 8:46. doi: 10.3389/fncom.2014.00046
- Bernstein, N. A. (1967). The co-ordination and regulation of movements: conclusions towards the study of motor co-ordination. *Biodyn. Locomot.* 104–113.
- Bizzi, E., Cheung, V., d'Avella, A., Saltiel, P., and Tresch, M. (2008). Combining modules for movement. *Brain Res Rev.* 57, 125–133. doi: 10.1016/j.brainresrev.2007.08.004
- Bizzi, E., and Cheung, V. C. (2013). The neural origin of muscle synergies. *Front. Comput. Neurosci.* 7:51. doi: 10.3389/fncom.2013.00051

- Castles, S., De Haas, H., and Miller, M. J. (2013). *The Age of Migration: International Population Movements in the Modern World*. London: Palgrave Macmillan.
- Cheung, V. C., Piron, L., Agostini, M., Silvoni, S., Turolla, A., and Bizzi, E. (2009). Stability of muscle synergies for voluntary actions after cortical stroke in humans. *Proc. Natl. Acad. Sci. U.S.A.* 106, 19563–19568. doi: 10.1073/pnas.0910114106
- Chvatal, S. A., Torres-Oviedo, G., Safavynia, S. A., and Ting, L. H. (2011). Common muscle synergies for control of center of mass and force in nonstepping and stepping postural behaviors. *J. Neurophysiol.* 106, 999–1015. doi: 10.1152/jn.00549.2010
- Contreras-Vidal, J. L., Bhagat, N. A., Brantley, J., Cruz-Garza, J. G., He, Y., Manley, Q., et al. (2016). Powered exoskeletons for bipedal locomotion after spinal cord injury. *J. Neural Eng.* 13:031001. doi: 10.1088/1741-2560/13/3/031001
- d'Avella, A., Saltiel, P., and Bizzi, E. (2003). Combinations of muscle synergies in the construction of a natural motor behavior. *Nat. Neurosci.* 6, 300–308. doi: 10.1038/nn1010
- Diaz, I., Gil, J. J., and Sanchez, E. (2011). Lower-limb robotic rehabilitation: literature review and challenges. *J. Robot.* 2011:759764. doi: 10.1155/2011/759764
- dos Santos, W. M., Caurin, G. A., and Siqueira, A. A. (2017a). Design and control of an active knee orthosis driven by a rotary series elastic actuator. *Control Eng. Pract.* 58, 307–318. doi: 10.1016/j.conengprac.2015.09.008
- dos Santos, W. M., Nogueira, S. L., de Oliveira, G. C., na, G. G. P., and Siqueira, A. A. G. (2017b). "Design and evaluation of a modular lower limb exoskeleton for rehabilitation," in *IEEE-RAS-EMBS International Conference on Rehabilitation Robotics* (London), 447–451. doi: 10.1109/ICORR.2017.8009288
- dos Santos, W. M., and Siqueira, A. A. G. (2019). "Design and control of a transparent lower limb exoskeleton," in *Wearable Robotics: Challenges and Trends*, eds M. C. Carrozza, S. Micera, and J. L. Pons (Cham: Springer International Publishing), 175–179.
- dos Santos, W. M., and Siqueira, A. A. G. (2019). Optimal impedance via model predictive control for robot-aided rehabilitation. *Control Eng. Pract.* 93, 1–8. doi: 10.1016/j.conengprac.2019.104177
- Fricke, S. S., Bayón, C., Van Der Kooij, H., and van Asseldonk, E. H. (2020). Automatic versus manual tuning of robot-assisted gait training in people with neurological disorders. *J. Neuroeng. Rehabil.* 17:9. doi: 10.1186/s12984-019-0630-9
- Garate, V. R., Parri, A., Yan, T., Muni, M., Lova, R. M., Vitiello, N., et al. (2016). A novel bioinspired framework using motor primitives for locomotion assistance through a wearable cooperative exoskeleton. *IEEE Robot. Autom. Mag.* 1070, 83–95. doi: 10.1109/MRA.2015.2510778
- Grinyagin, I. V., Biryukova, E. V., and Maier, M. A. (2005). Kinematic and dynamic synergies of human precision-grip movements. *J. Neurophysiol.* 94, 2284–2294. doi: 10.1152/jn.01310.2004
- Krebs, H. I., Dipietro, L., Levy-Tzedek, S., Fasoli, S. E., Rykman-Berland, A., Zipse, J., et al. (2008). A paradigm shift for rehabilitation robotics. *IEEE Eng. Med. Biol. Mag.* 27, 61–70. doi: 10.1109/EMEMB.2008.919498
- Lozano, R., Naghavi, M., Foreman, K., Lim, S., Shibuya, K., Aboyans, V., et al. (2012). Global and regional mortality from 235 causes of death for 20 age groups in 1990 and 2010: a systematic analysis for the global burden of disease study 2010. *Lancet* 380, 2095–2128. doi: 10.1016/S0140-6736(12)61728-0
- Mackay, J., Mensah, G. A., and Greenlund, K. (2004). *The Atlas of Heart Disease and Stroke*. Geneva: World Health Organization.
- Maggioni, S., Reinert, N., Lünenburger, L., and Melendez-Calderon, A. (2018). An adaptive and hybrid end-point/joint impedance controller for lower limb exoskeletons. *Front. Robot. AI* 5:104. doi: 10.3389/frobt.2018.00104
- Murray, C. J., Barber, R. M., Foreman, K. J., Ozgoren, A. A., Abd-Allah, F., Abera, S. F., et al. (2015). Global, regional, and national disability-adjusted life years (dalys) for 306 diseases and injuries and healthy life expectancy (hale) for 188 countries, 1990–2013: quantifying the epidemiological transition. *Lancet* 386, 2145–2191. doi: 10.1016/S0140-6736(15)61340-X
- Netune, R. R., Clark, D. J., and Kautz, S. A. (2009). Modular control of human walking: a simulation study. *J. Biomech.* 42, 1282–1287. doi: 10.1016/j.jbiomech.2009.03.009
- Nunes, P. F., Ostan, I., Santos, W. M. d., and Siqueira, A. A. (2020). "Analysis of matrix factorization techniques for extraction of motion motor primitives," in *XXVII Edição do Congresso Brasileiro de Engenharia Biomédica (CBEB 2020)* (Espírito Santo), 1–9.
- Nunes, P. F., Santos, W. M. d., and Siqueira, A. A. (2018). Control strategy based on kinetic motor primitives for lower limbs exoskeletons. *IFAC-PapersOnLine* 51, 402–406. doi: 10.1016/j.ifacol.2019.02.003
- Pekna, M., Pekny, M., and Nilsson, M. (2012). Modulation of neural plasticity as a basis for stroke rehabilitation. *Stroke* 43, 2819–2828. doi: 10.1161/STROKEAHA.112.654228
- Person, K. (1901). On lines and planes of closest fit to system of points in space. *Philos. Mag.* 2, 559–572. doi: 10.1080/14786440109462720
- Roh, J., Rymer, W. Z., and Beer, R. F. (2015). Evidence for altered upper extremity muscle synergies in chronic stroke survivors with mild and moderate impairment. *Front. Hum. Neurosci.* 9:6. doi: 10.3389/fnhum.2015.00006
- Rohrer, B., Fasoli, S., Krebs, H. I., Hughes, R., Volpe, B., Frontera, W. R., et al. (2002). Movement smoothness changes during stroke recovery. *J. Neurosci.* 22, 8297–8304. doi: 10.1523/JNEUROSCI.22-18-08297.2002
- Ruckert, E., and d'Avella, A. (2013). Learned parametrized dynamic movement primitives with shared synergies for controlling robotic and musculoskeletal systems. *Front. Comput. Neurosci.* 7:138. doi: 10.3389/fncom.2013.00138
- Sommerfeld, D. K., Eek, E. U.-B., Svensson, A.-K., Holmqvist, L. W., and von Arbin, M. H. (2004). Spasticity after stroke: its occurrence and association with motor impairments and activity limitations. *Stroke* 35, 134–139. doi: 10.1161/01.STR.0000105386.05173.5E
- Tan, C. K., Kadone, H., Watanabe, H., Marushima, A., Yamazaki, M., Sankai, Y., et al. (2018). Lateral symmetry of synergies in lower limb muscles of acute post-stroke patients after robotic intervention. *Front. Neurosci.* 12:276. doi: 10.3389/fnins.2018.00276
- Ting, L. H., Chiel, H. J., Trumbower, R. D., Allen, J. L., McKay, J. L., Hackney, M. E., et al. (2015). Neuromechanical principles underlying movement modularity and their implications for rehabilitation. *Neuron* 86, 38–54. doi: 10.1016/j.neuron.2015.02.042
- Ting, L. H., and McKay, J. L. (2007). Neuromechanics of muscle synergies for posture and movement. *Curr. Opin. Neurobiol.* 17, 622–628. doi: 10.1016/j.conb.2008.01.002
- Tresch, M. C., and Jarc, A. (2009). The case for and against muscle synergies. *Curr. Opin. Neurobiol.* 19, 601–607. doi: 10.1016/j.conb.2009.09.002
- Wieloch, T., and Nikolic, K. (2006). Mechanisms of neural plasticity following brain injury. *Curr. Opin. Neurobiol.* 16, 258–264. doi: 10.1016/j.conb.2006.05.011
- World Health Organization. (2015). *World Health Statistics 2015*. World Health Organization.
- Yan, T., Cempini, M., Oddo, C. M., and Vitiello, N. (2015). Review of assistive strategies in powered lower-limb orthoses and exoskeletons. *Robot. Auton. Syst.* 64, 120–136. doi: 10.1016/j.robot.2014.09.032
- Zadavec, M., Olenšek, A., Rudolf, M., Bizovičar, N., Goljar, N., and Matjačić, Z. (2017). "A novel robot-assisted training approach for improving gait symmetry after stroke," in *2017 International Conference on Rehabilitation Robotics (ICORR)* (London), 222–227. doi: 10.1109/ICORR.2017.8009250

Conflict of Interest: The authors declare that the research was conducted in the absence of any commercial or financial relationships that could be construed as a potential conflict of interest.

Copyright © 2020 Nunes, Ostan and Siqueira. This is an open-access article distributed under the terms of the Creative Commons Attribution License (CC BY). The use, distribution or reproduction in other forums is permitted, provided the original author(s) and the copyright owner(s) are credited and that the original publication in this journal is cited, in accordance with accepted academic practice. No use, distribution or reproduction is permitted which does not comply with these terms.



Analysis of Compensatory Movements Using a Supernumerary Robotic Hand for Upper Limb Assistance

Martina Rossero^{1,2*}, Andrea S. Ciullo¹, Giorgio Grioli¹, Manuel G. Catalano¹ and Antonio Bicchi^{1,2}

¹ Soft Robotics for Human Cooperation and Rehabilitation, Italian Institute of Technology, Genoa, Italy, ² Centro "E. Piaggio" and Dipartimento di Ingegneria dell'Informazione, University of Pisa, Pisa, Italy

OPEN ACCESS

Edited by:

Jan Veneman,
Hocoma, Switzerland

Reviewed by:

Camilla Pierella,
École Polytechnique Fédérale de
Lausanne, Switzerland
Bouri Mohamed,
École Polytechnique Fédérale de
Lausanne, Switzerland

*Correspondence:

Martina Rossero
martiross227@gmail.com

Specialty section:

This article was submitted to
Biomedical Robotics,
a section of the journal
Frontiers in Robotics and AI

Received: 27 July 2020

Accepted: 24 November 2020

Published: 17 December 2020

Citation:

Rossero M, Ciullo AS, Grioli G,
Catalano MG and Bicchi A (2020)
Analysis of Compensatory Movements
Using a Supernumerary Robotic Hand
for Upper Limb Assistance.
Front. Robot. AI 7:587759.
doi: 10.3389/frobt.2020.587759

Recently, extratheses, aka Supernumerary Robotic Limbs (SRLs), are emerging as a new trend in the field of assistive and rehabilitation devices. We proposed the SoftHand X, a system composed of an anthropomorphic soft hand extrathesis, with a gravity support boom and a control interface for the patient. In preliminary tests, the system exhibited a positive outlook toward assisting impaired people during daily life activities and fighting learned-non-use of the impaired arm. However, similar to many robot-aided therapies, the use of the system may induce side effects that can be detrimental and worsen patients' conditions. One of the most common is the onset of alternative grasping strategies and compensatory movements, which clinicians absolutely need to counter in physical therapy. Before embarking in systematic experimentation with the SoftHand X on patients, it is essential that the system is demonstrated not to lead to an increase of compensation habits. This paper provides a detailed description of the compensatory movements performed by healthy subjects using the SoftHand X. Eleven right-handed healthy subjects were involved within an experimental protocol in which kinematic data of the upper body and EMG signals of the arm were acquired. Each subject executed tasks with and without the robotic system, considering this last situation as reference of optimal behavior. A comparison between two different configurations of the robotic hand was performed to understand if this aspect may affect the compensatory movements. Results demonstrated that the use of the apparatus reduces the range of motion of the wrist, elbow and shoulder, while it increases the range of the trunk and head movements. On the other hand, EMG analysis indicated that muscle activation was very similar among all the conditions. Results obtained suggest that the system may be used as assistive device without causing an over-use of the arm joints, and opens the way to clinical trials with patients.

Keywords: compensatory movements, kinematic analysis, soft robotics, supernumerary robotic limbs, robotic assistance

1. INTRODUCTION

One of the main symptoms of neuro-muscular diseases consists of partial or total loss of motor functions, such as walking or manipulating objects (Wade, 1992; Mozaffarian et al., 2015). Considering the upper extremities, the functional reduction of the hand-arm may drastically compromise the independence of the subject, hampering the ability in performing many Activities of Daily Living (ADL) (Mondiale de la Santé and Organization, 2001). In the last decades, to flank standard medical therapy, many robotic devices have been proposed in an attempt to counteract these issues and promote motor recovery (Maciejasz et al., 2014). Recently, a new trend is emerging in the robotic field: Supernumerary Robotics Limbs (SRLs). Initially developed to improve the user's ergonomics and capacity in industrial applications (Llorens-Bonilla et al., 2012; Parietti and Asada, 2017; Ciullo et al., 2018a), they consist of additional artificial limbs that can perform tasks in close coordination with the subject wearing them. Their clinical use was pioneered by Hussain et al. (2016) where an additional robotic finger (the Sixth finger) was used for compensating hand missing abilities in chronic stroke subjects. Another device for clinical application can be found in Ciullo et al. (2020) where the SoftHand X (SHX) system is described and tested with ten post-stroke chronic subjects. It consists of an anthropomorphic artificial hand, a passive gravity compensator and an input interface used by the subject to control the device. Results showed that this system significantly improved the performances of the patients in the proposed tasks and, more in general, their autonomy in ADL. Nine out of ten patients were able to perform the whole task proposed and asserted that they would use the system in their daily life. However, it must be noted that the use of such devices may induce some side effects that can be harmful, limiting the recovery of normal movement patterns or even promoting pathological conditions, such as spasticity (Ada et al., 1994). In Ciullo et al. (2020), spasticity before and after use was measured by the Modified Ashworth Scale (MAS). Seven patients exhibited a reduction of the MAS (no statistical relevance was proven, however). Another issue can be the onset of some compensatory movements in which alternative muscles and motor strategies are used to complete a task (Levin et al., 2009). Due to the impairment, most of the patients are used to run into these strategies, so it is essential that robotic systems do not worsen this situation. In literature, some discussions and analysis have been already proposed to evaluate compensatory movements in post-stroke subjects (Cirstea and Levin, 2000; Roby-Brami et al., 2003; Michaelsen et al., 2004). These compensatory strategies most prominently involve the use of the trunk, the shoulder or proximal residual muscles capabilities to perform the requested tasks (Metzger et al., 2012; Hussaini et al., 2017). Similar investigations have been conducted also for upper limb prosthesis users (Carey et al., 2008; Metzger et al., 2012; Major et al., 2014). In Carey et al. (2008) the compensatory movements of transradial prosthesis users without wrist motion have been compared to that of non-amputees under an unrestricted and restricted forearm rotation conditions. In tasks requiring a larger forearm rotation and wrist flexion, persons with transradial amputation



FIGURE 1 | Example of head and trunk compensatory movements performed by a subject during the execution of a task of the ARAT test (pouring task).

compensated predominantly with movements of the torso side bending toward the affected side and with elbow flexion. In tasks not requiring as much forearm rotation, such as drinking from a cup, the location of compensation was not determined. This study has been extended including transhumeral prosthesis and body-powered devices users (Metzger et al., 2012) confirming the presence of compensatory movement for the trunk and proximal upper limb.

SRLs, due to their encumbrance and position with respect to the natural limbs, may have a higher predisposition to induce compensatory movements. No work has been conducted to analyze this compensation but it is important to quantify them before approaching clinical trials. This work aims at providing a detailed description of these compensatory movements (see an example in **Figure 1**) arising while using the SHX system to assist upper limb motion during the execution of some exemplary tasks.

Inspired by the methodologies adopted in the previous investigations cited, this work compares the performance of eleven right-handed healthy subjects executing grasping tasks with and without the robotic system. During the experiment, kinematic data of the upper body and EMG signals of the arm have been acquired. Results show a reduction on the arm joints Ranges of Motion, compensated by trunk and head movements. This suggests the possibility of using the SHX to assist impaired subject without over-stressing the impaired arm. However, the increase in the use of trunk and head can be harmful in the long term so a new version of the human arm interface will be developed to counteract these effects.

2. MATERIALS AND METHODS

Eleven right-handed healthy subjects (five males, six females, mean age 27) were involved within an experimental procedure approved by the Institutional Review Board of the University

of Pisa, in accordance with the Declaration of Helsinki. Each subject signed the informed consent before starting the experimental session.

2.1. Experimental Setup

Kinematic data of the upper body and EMG signals of the arm were acquired during tasks¹ using two acquisition systems, as shown in **Figure 2A**.

The Xsens MVN system, composed of 17 IMU sensors placed on the subject body (as shown in **Figure 2B**), was used to obtain kinematic data recorded with a sampling frequency of 60 Hz. For each body segment, the data acquired were the position, the orientation, the velocity, and the acceleration. Moreover, the joint angles of the shoulder, the elbow, the wrist, the trunk, and the neck were measured by the system.

A Trigno Delsys wireless system was used to record the electromyographic signal (sampling frequency 2 kHz) of the following muscles of the right arm: trapezius, lateral deltoid, biceps, triceps lateral head, ulnar flexor and extensor. Additionally, the commanded and the real pose of the robotic hand were registered. To obtain a time consistent description of the movements, all the data were synchronized with a unique custom C++ interface.

The SHX system used (shown in **Figure 3A**) is a modular robotic system for the upper limb support with anthropomorphic characteristics and inspired by neuroscientific theories of motor control (Santello et al., 1998; Della Santina et al., 2017). It is designed to be used for clinical investigation, either for the rehabilitation and for the assistance of patients with neuromuscular diseases (e.g., stroke patient) or of elder people with weak muscles in the upper limb. It is composed of single separated sub-parts that are conveniently assembled for the user's needs. In particular, it consists of an end effector that is a Pisa/IIT SoftHand implementing the function of the human hand and a passive gravity compensator. These two parts are integrated by a human-arm interface with a wrist-like structure designed as additional component with the basic function of connecting them and allowing the robotic hand to be used as an extra thesis [from which the name SoftHand eXtrathesis (SoftHand X)]. An input interface, connected to the SHX thanks to a workstation, is used by the subject to control the robotic hand. In this study, the robotic hand is activated with a hand-held handle controlled by the right natural hand of the subject. This could be considered as a limitation for the supernumerary system since the natural hand is not free to move. However, the system is thought to be used by impaired subject that can use the additional hand to recover the lost hand functions and at the same time train the movement of the natural one. Moreover, other input interfaces have been designed to control the opening and closing of the SoftHand with feet and facial muscles to leave all the hand free to be used (Ciullo et al., 2020). To investigate if the position of the robotic hand could influence the compensatory movements exploited by the subjects, two different configurations have been tested. Such configurations are the result of a previous optimization study, where the manipulability and workspace of the system

where analyzed (Ciullo et al., 2018b). The first configuration has the robotic hand in front of the natural one, aligned with the user's arm (Dorsal Distal Central, DDC), while the second has the robotic hand below the natural one (Palmar Middle Central, PMC) (**Figure 3B**). In the PMC configuration, the misalignment of the robotic hand introduces an additional gravity torque that may lead to annoying rotations of the human arm and a major force requested to the subject. The same happens for the DDC configuration due to the distance of the robotic hand with respect to the natural one. Another aspect that is worth considering is that the robotic hand in the PMC configuration can hide the object to grasp forcing the user to move head and trunk to better see the item.

2.2. Experimental Tasks

Subjects were asked to perform a modified version of the Action Research Arm Test (mARAT). This test (Lyle, 1981) is traditionally used in clinic to assess upper extremity performance in post-stroke patients. It involves the manipulation of objects differing in size, weight and shape (as shown in **Figure 4A**) starting from the same predefined position [(2) in **Figure 4B**]. For this study, the test has been modified with respect to the standard version. The gross movements (e.g., place hand behind head or to mouth) were not executed due to the encumbrance of the system. In addition, some items and activities were removed (e.g., the biggest wood cube, the washer and the ball bearing), since not compatible with the dimension and grasping capacity of the robotic hand. In details, the executed tasks, in order of execution, were the following:

- Lifting objects from a starting position [(2) in **Figure 4B**] to a higher one: in order 3 wood cubes (2.5, 5, 7.5 cm³), a sharpening stone (10 × 2.5 × 1 cm), a ball (7.5 cm diameter), and a marble (1.5 cm diameter);
- Moving two metal tubes (2.25 × 11.5 and 1.0 × 16.0 cm) from a hole [(7) in **Figure 4B**] to a peg [(8) in **Figure 4B**];
- Pouring the content of a glass [positioned in (9) in **Figure 4B**] into another one [positioned in (10) in **Figure 4B**].

Photo sequences showing some of the task executions are reported in **Figure 5**. The single task was considered accomplished when the object reached the target and the right hand came back to the starting position [(1) in **Figure 4B**]. In order to explore the whole reachable workspace, both the ipsilateral and the contralateral side with respect to the robotic system placement were explored. The objects were first moved from the starting position to the ipsilateral target (see **Figures 5A,B,E**) and then to the contralateral target (see **Figures 5B,D,F**). Each task was repeated three times in a row, positioning every time the object at the starting point.

2.3. Experimental Procedure

First, the experiment was introduced to the subject, describing him/her both the SHX system, including the data acquiring systems, and the aim of the study. Then, all the sensors were placed on the subject's body, as shown in **Figure 2B**. IMU sensors placements were done as suggested by the Xsens User's Manual. Muscles for the EMG electrodes, instead, were manually

¹ All raw data acquired are accessible on the open access repository, Hand Corpus.

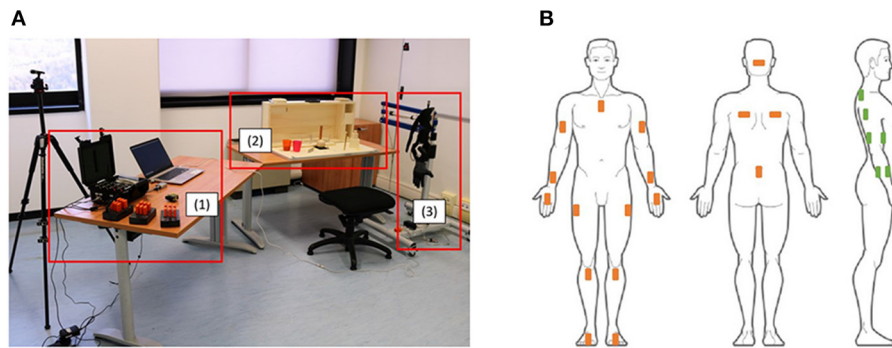


FIGURE 2 | (A) Shows a view of the experimental setup where (1) shows the data acquisition systems, (2) shows the ARAT test and (3) shows the SHX system. (B) Shows the positioning of the Xsens sensors (in orange) and of the EMG electrodes on the right arm (in green).

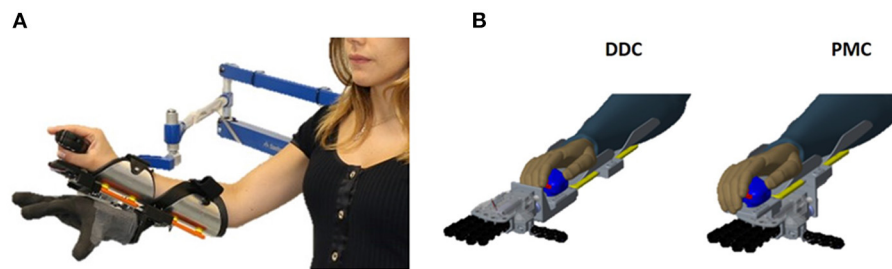


FIGURE 3 | (A) Shows the SoftHand X system used by the subjects during the experiments. (B) Shows the two configuration tested. The first has the robotic hand in front of the natural one, aligned with the user's arm (Dorsal Distal Central, DDC), while the second has the robotic hand below the natural one (Palmar Middle Central, PMC).

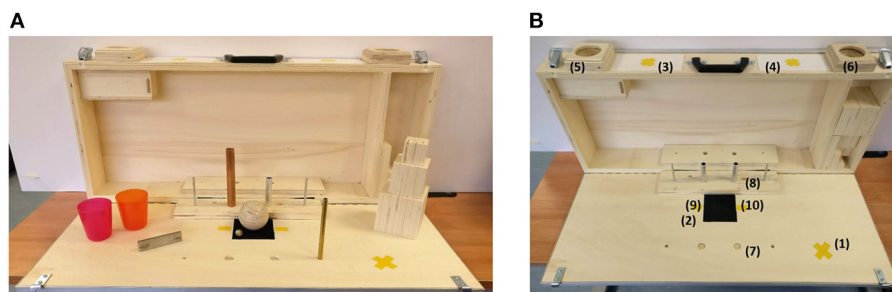


FIGURE 4 | (A) Shows the kit of items for the Action Research Arm Test, while (B) the ARAT case. In particular, (1) is the hand starting position; (2) is the object starting position; the target position for the contralateral side is in (3) while for the ipsilateral side in (4); (5) and (6) are the target positions for the ball and the marble in the contralateral side and ipsilateral side, respectively; (7) and (8) are the starting hole and the ending peg for the tube tasks; (9) and (10) are the positions of the glasses for the pouring task.

identified by the experimenter. In addition, body measurements of the subjects (e.g., legs and arms length) were inserted into the Xsens software to reconstruct the virtual body model and estimate the joint movements. A phase of calibration was then executed. To calibrate the Xsens system, he/she was asked to stay still in a stand position called N-pose (**Figure 6A**). He/she had to stand upright, feet parallel, back straight, arm straight alongside the body (vertically), thumbs and face forwards. To assess the starting position (shown in **Figure 6B**), the height

of the chair was set so that the subject could touch the table with his/her fingers, with the elbow flexed at 90° , while the distance from the table had to allow the subject touching the high back of the ARAT case. During the execution of the test with the SHX system, the robotic hand was positioned at the same starting position of the right natural hand and both the height and the distance were re-set to fit the new configuration adopted. These calibration procedures were conducted before each experimental condition tested (natural hand, DDC, and



FIGURE 5 | Photo sequences of the tasks. **(A)** Shows the lifting of the sharpening stone in the ipsilateral side, **(B)** the lifting of the sharpening stone in the contralateral side, **(C)** the lifting of the ball in the ipsilateral side, **(D)** the lifting of the ball in the contralateral side, **(E)** the moving of the tube in the ipsilateral side, **(F)** the moving of the tube in the contralateral side, and **(G)** the pouring of the content of a glass into another.

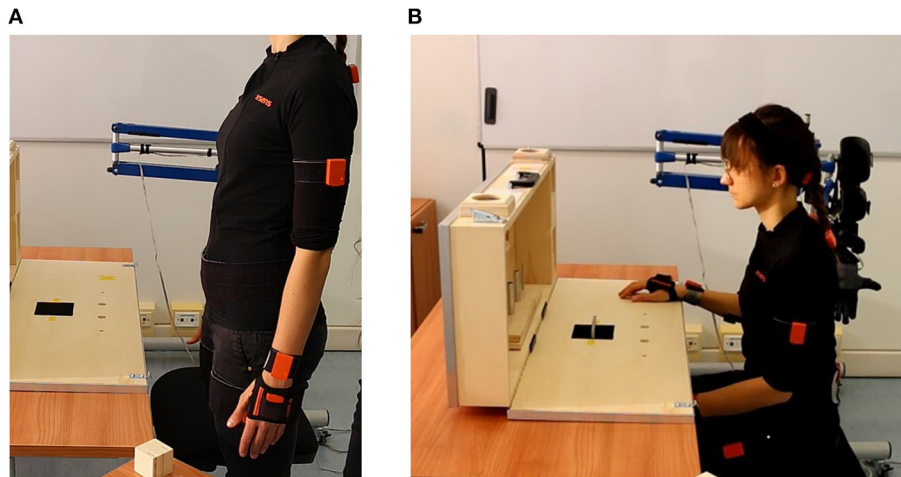


FIGURE 6 | (A) Shows the N-pose for the Xsens calibration while **(B)** shows the starting position of the experiment.

PMC). The subject executed the tasks first with his/her own hand, then using the SHX system in the two configurations cited. We asked them to keep the left arm at rest during execution since no bimanual tasks needed to be performed. Before starting the experiment, all the subjects had some minutes of training and during configuration changes they were given a few minutes to rest and the calibrations were repeated. In these experiments, we did not ask the subject to execute the tasks as fast as possible to avoid the rush to influence movements. We decided not to evaluate the performances of execution since this aspect has been already investigated in Ciullo et al. (2018b) obtaining that the execution with the DDC configuration resulted longer in most of the tasks.

2.4. Data Analysis

To quantitatively evaluate compensatory movements, a comparison between the tasks execution with the natural hand and the execution with the SHX system was performed, considering the first as reference of optimal behavior. Moreover, a comparison between the two different configurations of the SHX system was performed. After the acquisition, the kinematic data and the EMG signals obtained were exported in Matlab 2018b and different indices were computed (see **Table 1**). Taking inspiration from literature (Carey et al., 2008; Metzger et al., 2012; Hussaini et al., 2017), the Range of Motion (RoM) of the joints was calculated as the difference between the maximum and the minimum measured angles (Equation 1).

$$RoM = \max(\text{angle}) - \min(\text{angle}) \quad (1)$$

The movements considered are the abduction/adduction, the flexion/extension and the rotation of the right shoulder, head and trunk, the pronation/supination of the wrist and the flexion/extension of the right elbow. For the wrist, the other degrees of freedom were not considered since they were limited by the human-arm interface of the SHX system.

TABLE 1 | Variables calculated to evaluate the compensatory movement performed by the subject.

	Abduction/adduction
	Rotation
	Flexion/extension
RoM of the shoulder	
RoM of the elbow	Flexion/extension
RoM of the wrist	pronation/supination
	Abduction/adduction
RoM of the trunk	Rotation
	Flexion/extension
	Abduction/adduction
RoM of the head	Rotation
	Flexion/extension
Accuracy index	Intra-subject accuracy
	Inter-subject accuracy
Efficiency index	Intra-subject efficiency
	Inter-subject efficiency
RMS value of the EMG signals	

An accuracy index and an efficiency index were computed, as described in de los Reyes-Guzmán et al. (2017), to give a measure of the differences between the natural hand trajectory and the hand path length exploited by the subjects during the tasks execution with and without the robotic system. In particular, two different comparisons were conducted: *inter-subjects* and *intra-subjects*. The main difference consists of the way evaluating the reference hand trajectory (s_{ref}) (see Equations 2, 3):

$$s_{ref}^{inter} = \sum_{i=1}^N \frac{s_i}{N} \quad (2)$$

where N is the number of subjects, and s_i represents the single subject trajectory obtained during the execution of the test with

the natural hand. For intra-subject comparison:

$$s_{ref}^{intra} = \arg \min_{s_j} |s_j - s_{mean}| \quad (3)$$

where $j = 1, 2, 3$ is the number of the trial and s_{mean} is the mean hand trajectory among the three repetitions obtained during the execution of the test with the natural hand. Trajectories of different lengths have been resampled with the Matlab function *interp1* (Matlab 2018b) with a linear interpolation to allow comparisons.

Then, the accuracy index (A) was defined as the product of three different terms (Equation 4) and then normalized (A_{norm} in Equation 5).

$$A = \alpha \cdot \rho \cdot BN \quad (4)$$

$$A_{norm} = \frac{A}{A_{ref}} \cdot 100 \quad (5)$$

The term α is a sigmoid function (see de los Reyes-Guzmán et al., 2017) depending on the mean distance between the reference hand trajectory (inter or intra) and the analyzed one, the term ρ is the Pearson correlation coefficient between these two trajectories and, lastly, the term BN was defined as the percentage of the analyzed trajectory within a dispersion band around the reference hand trajectory considered acceptable. This dispersion band for the inter-subject comparison (DB^{inter}) was calculated as:

$$DB^{inter} = s_{ref}^{inter} \pm 2 \cdot std \quad (6)$$

where std is the standard deviation around the reference trajectory. For the intra-subject comparison, the dispersion band (DB^{intra}) was:

$$DB^{intra} = s_{ref}^{intra} \pm 2 \cdot \sum_{i=1}^3 \frac{s_{ref}^{intra} - s_i}{3} \quad (7)$$

The constant ($c = 2$) multiplying the standard deviation was chosen following the same procedure of de los Reyes-Guzmán et al. (2017). In particular, the dispersion band DB was calculated using $c = 1$ and $c = 1.5$ obtaining very low values of the accuracy and efficiency indices (< 10) and using $c = 2.5$ and $c = 3$ obtaining too high values (in some cases > 100). So the good solution was to choose the intermediate value that was $c = 2$.

The efficiency index (E_{norm}) was defined by normalizing the hand path length p with respect to the reference one p_{ref} (inter or intra):

$$E_{norm} = \frac{p}{p_{ref}} \cdot 100 \quad (8)$$

In de los Reyes-Guzmán et al. (2017), authors inverted the equation (see Equation 9) because the hand path length of patients was always longer than the healthy one.

$$E_{norm} = \frac{p_{ref}}{p} \cdot 100 \quad (9)$$

In our case, the hand path length without the SHX system was not always shorter than the one with the system so both Equations (8) and (9) were used.

For each robotic configuration we considered the mean values, over the three trials, of the accuracy and efficiency indices. These indices were computed also for the natural hand in order to evaluate both how much the single subject behavior was different from the mean of all the subjects and how different were the trajectories during the three repetitions of the task.

EMG signals were exported in Matlab 2018b and band-pass filtered (10–500 Hz; Butterworth 9th order), note that this has also the effect of removing the signal mean value. The signals obtained were rectified and normalized. In literature, the normalization is often performed on the maximum contraction level. Since our task caused a really small effort, it was not convenient to normalize in this way, so the maximum value obtained all the tasks was used. Finally the envelope was extracted by filtering the signal with a Butterworth low-pass filter of the 5th order with a cut-off frequency of 10 Hz. To evaluate the muscles activation, the RMS value was calculated for each subject and for each task as the mean value between the ones obtained for the three repetitions in the interval in which the muscle was activated.

For the statistical analysis, a one-sample Kolmogorov-Smirnov test was performed to assess if the data came from a standard normal distribution. This hypothesis was rejected so a non-parametric version of classical one-way ANOVA was necessary. Kruskal-Wallis test was used to statistically compared the configurations with the hand and between each other. The significance level for all statistical comparisons was set at $p < 0.05$. The comparison was performed, for all the variables and for each task, between the three different configurations considering the values obtained from the 11 subjects.

In the end, to simplify the comparison, the tasks executed were divided in five functional groups, as shown in **Table 2**. This division was done since it was noticed that, due to the similarity of movement, tasks of the same group showed similar values for the variables extracted. Then for each task, the median value of all the variables and indices was obtained among the values of all the subjects.

3. RESULTS

3.1. Kinematic Analysis

Figure 7 shows the median values of the Ranges of Motion obtained from the execution with and without the robotic hand.

3.1.1. RoM of the Wrist

For the pronation/supination, statistically significant differences have been obtained in tasks 1, 2, 7, 8, 9, 10, 12, 13, 14, 15, 16, 17 (more than 10° lower), 3, 4, 5, 6, and 11 ($< 10^\circ$ lower) for the DDC configuration with respect to the free execution, in none of the tasks for the PMC configuration with respect to the free execution and in tasks 2, 3, 4, 5, 12, and 13 ($< 10^\circ$ lower) for the DDC configuration with respect to the PMC configuration.

TABLE 2 | Functional division of the tasks.

Group 1—Contralateral lifting tasks	
Task 1	Lifting of the ball
Task 3	Lifting of the smaller cube
Task 5	Lifting of the middle cube
Task 7	Lifting of the bigger cube
Task 9	Lifting of the marble
Task 11	Lifting of the sharpening stone
Group 2—Ipsilateral lifting tasks	
Task 2	Lifting of the ball
Task 4	Lifting of the smaller cube
Task 6	Lifting of the middle cube
Task 8	Lifting of the bigger cube
Task 10	Lifting of the marble
Task 12	Lifting of the sharpening stone
Pouring task	
Task 13	Pouring the content of a glass
Group 4—Contralateral tube tasks	
Task 14	Lifting of the bigger tube
Task 16	Lifting of the smaller tube
Group 5—Ipsilateral tube tasks	
Task 15	Lifting of the bigger tube
Task 17	Lifting of the smaller tube

3.1.2. RoM of the Elbow

For the flexion/extension, statistically significant differences have been obtained in tasks 1, 2, 4, 10, 11, 14, 15, 16 (more than 10° lower), 3, 9 (more than 20° lower), 12, 17 (more than 5° lower), and 13 (more than 5° higher) for the DDC configuration with respect to the free execution, in tasks 9, 16, 17 (more than 10° lower), 10, 14, 15, (more than 20° lower), and 13 (more than 5° higher) for the PMC configuration with respect to the free execution and in none of the tasks for the DDC configuration with respect to the PMC configuration.

3.1.3. RoM of the Shoulder

For the abduction/adduction, statistically significant differences have been obtained in tasks 13, 14, 16, 17 (more than 10° higher), and 15 (more than 20° higher) for the DDC configuration with respect to the free execution, in tasks 6, 12 (<10° higher), 13, 14, 15, 16, and 17 (more than 10° higher) for the PMC configuration with respect to the free execution and in tasks 2 (more than 10° higher), 6, 8, and 12 (<10° higher) for the DDC configuration with respect to the PMC configuration. For the flexion/extension, no statistically significant differences have been obtained. For the rotation, statistically significant differences have been obtained only in task 13 (more than 20° higher) for the DDC configuration with respect to the free execution, in tasks 9, 14, 15 (more than 10° lower), 13 (more than 20° higher), and 17 (more than 5° lower) for the PMC configuration with respect to the free execution and in none of the tasks for the DDC configuration with respect to the PMC configuration.

3.1.4. RoM of the Trunk

For the abduction/adduction, statistically significant differences have been obtained in tasks 8, 10, 11, 12, 13, 14, 15, 16, and 17 (<10° higher) for the DDC configuration with respect to the free execution, in tasks 1, 2, 4, 5, 6, 7, 8, 9, 10, 11, 12, 13, 14, 15, 16, and 17 (<10° higher) for the PMC configuration with respect to the free execution and only in task 2 (<10° lower) for the DDC configuration with respect to the PMC configuration. For the flexion/extension, statistically significant differences have been obtained in tasks 10, 13, 14, 15, 16, and 17 (<10° higher) for the DDC configuration with respect to the free execution, in tasks 2, 4, 5, 9, 10, 12, 13, 15, 16, and 17 (<10° higher) for the PMC configuration with respect to the free execution and in none of the tasks for the DDC configuration with respect to the PMC configuration. For the rotation, statistically significant differences have been obtained in tasks 4, 6, 8, 10, 11, 12, 13, 14, 15 and 17 (<10° higher) for the DDC configuration with respect to the free execution, in tasks 2, 4, 6, 8, 10, 11, 12, 13, 14, 15, 16, and 17 (<10° higher) for the PMC configuration with respect to the free execution and only in task 2 (<10° higher) for the DDC configuration with respect to the PMC configuration.

3.1.5. RoM of the Head

For the abduction/adduction, statistically significant differences have been obtained in tasks 10, 12, 13, 14, 15, and 17 (<10° higher) for the DDC configuration with respect to the free execution, in tasks 10, 12, 13, and 17 (<10° higher) for the PMC configuration with respect to the free execution and in none of the tasks for the DDC configuration with respect to the PMC configuration. For the flexion/extension, statistically significant differences have been obtained in tasks 4, 10, 13, 14, 15, 16, and 17 (<10° higher) for the DDC configuration with respect to the free execution, in tasks 2, 5, 9, 10, 11, 12, 13, 14, 15, 16, and 17 (<10° higher) for the PMC configuration with respect to the free execution and in none of the tasks for the DDC configuration with respect to the PMC configuration. For the rotation, no statistically significant differences have been obtained.

3.1.6. Accuracy Index

Figure 8 shows the median values of the (A) intra-subject and (B) inter-subjects accuracy index obtained from the execution with and without the robotic hand. For the intra-subject index, statistically significant differences have been obtained in tasks 2, 4, 9, 10, 12, 13, 14, 15, 16, and 17 for the DDC configuration with respect to the free execution, in tasks 1, 2, 4, 9, 10, 12, 13, 14, 15, 16, and 17 for the PMC configuration with respect to the free execution and in none of the tasks for the DDC configuration with respect to the PMC configuration. For the execution with the natural hand the values are in the range 73–81%, for the DDC configuration the values are lower than 50% in six tasks and lower than 75% for the other tasks while for the PMC configuration the values are lower than 50% in seven tasks and lower than 70% for the other tasks. For the inter-subject index, statistically significant differences have been obtained in tasks 1, 2, 3, 4, 5, 6, 7, 8, 9, 10, 11, 12, 13, 15, 16, and 17 for the DDC configuration with respect to the free execution, in tasks 1, 2, 3, 4, 5, 6, 7, 8, 9, 10, 11, 12, 13, 15, and 17 for the PMC configuration with respect to the free

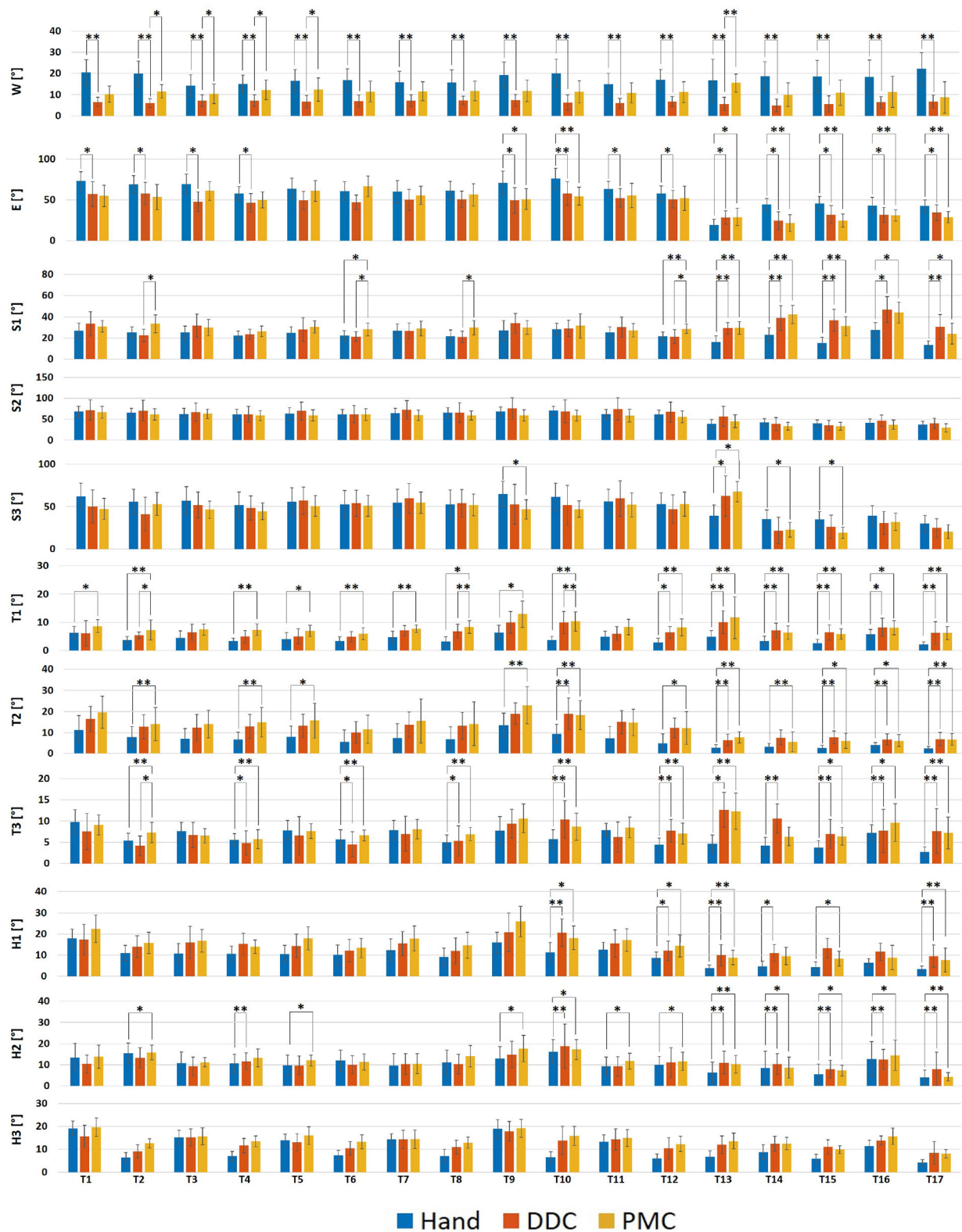
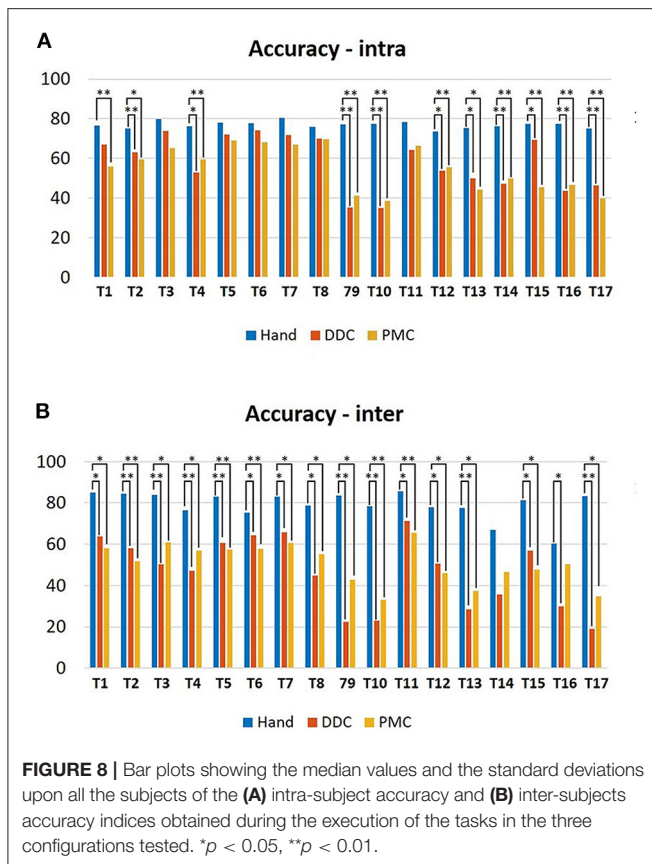


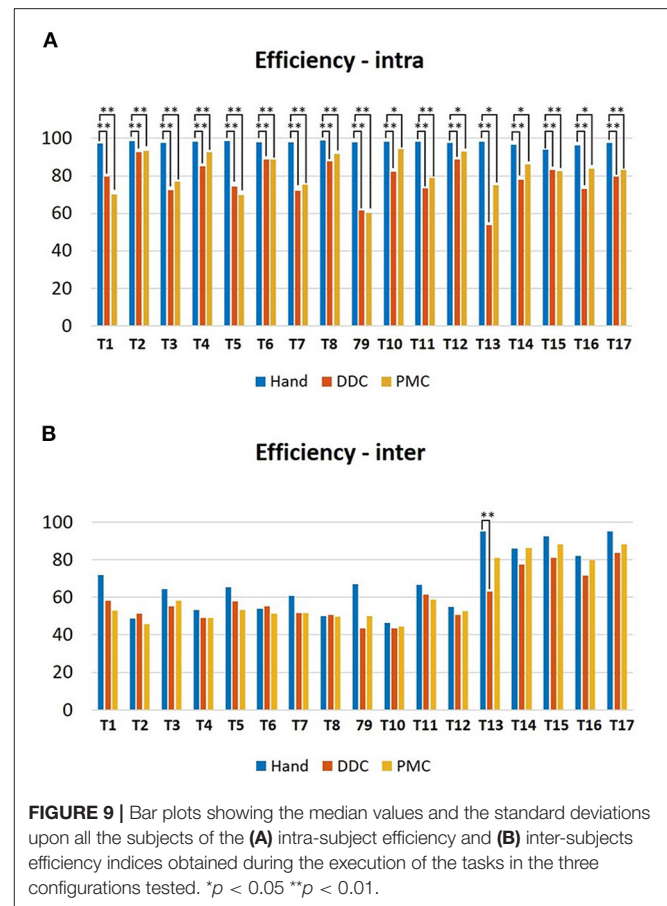
FIGURE 7 | Bar plots showing the median values and the standard deviations upon all the subjects of the RoM obtained during the execution of the tasks in the three configurations tested. S1, Shoulder abduction/adduction; S2, Shoulder flexion/extension; S3, Shoulder rotation; E, Elbow flexion/extension; W, Wrist pronation/supination; T1, Trunk abduction/adduction; T2, Trunk flexion/extension; T3, Trunk rotation; H1, Head abduction/adduction; H2, Head flexion/extension; H3, Head rotation. * $p < 0.05$, ** $p < 0.01$.



execution and in none of the tasks for the DDC configuration with respect to the PMC configuration. For the free execution the values are in the range 60–86%, for the DDC configuration the values are lower than 50% in eight tasks and lower than 72% for the other tasks while for the PMC configuration the values are lower than 50% in seven tasks and lower than 66% for the other tasks.

3.1.7. Efficiency Index

Figure 9 shows the median values of the (A) intra-subject and (B) inter-subjects efficiency index obtained from the execution with and without the robotic hand. For the intra-subject index, statistically significant differences have been obtained in all the tasks for the DDC configuration with respect to the free execution, in all the tasks for the PMC configuration with respect to the free execution and in none of the tasks for the DDC configuration with respect to the PMC configuration. For the free execution the values are in the range 93–99%, for the DDC configuration the values are in the range 53–93% while for the PMC configuration the values are in the range 60–95%. For the inter-subject index, statistically significant differences have been obtained only in task 13 for the DDC configuration with respect to the free execution, in none of the tasks for the PMC configuration with respect to the free execution and in none of the tasks for the DDC configuration with respect to the PMC configuration. For the free execution the values are lower than



50% in three tasks and lower than 95% for the other tasks, for the DDC configuration the values are lower than 50% in three tasks and lower than 84% for the other tasks while for the PMC configuration the values are lower than 50% in four tasks and lower than 89% for the other tasks.

3.2. EMG Signal Analysis

The execution of the tasks with the robotic system was always longer than the one with the natural hand, resulting in a longer activation period of the muscles. However, the values of the RMS resulted very similar between the three executions of the tasks. For the clarity of the results, only the RMS values of the deltoid, the trapezius and the triceps were reported in **Supplementary Table S6** since only for this muscles some statistical differences have been found. In particular, they have been found for the deltoid between the natural hand and the DDC configuration in tasks 10 and 13, between the natural hand and the PMC configuration in tasks 1, 2, 3, 4, 10, 11, 12, 13, 15, and between the two configurations in tasks 1, 2, for the trapezius between the natural hand and the PMC configuration in task 6 and for the triceps between the natural hand and the DDC configuration in task 13. It is also interesting to analyse the fact that the muscle activity resulting from the natural hand shows always a relaxing period between the different repetitions when the hand came back to the starting position while during the

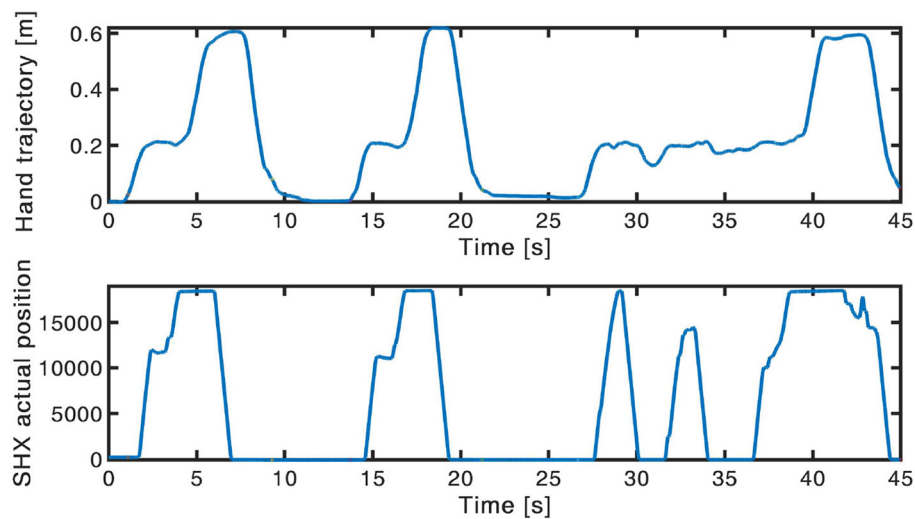


FIGURE 10 | Example of hand trajectory exploited (up) and of the consequent SHX position (down) during the lifting of the marble in the contralateral side. In the third repetition the subject needed more attempts to accomplish the task, thus resulting in a more irregular trajectory.

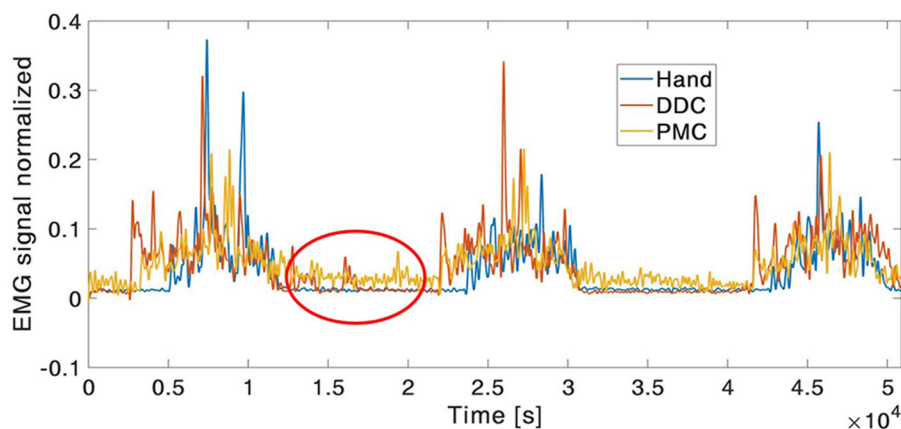


FIGURE 11 | Example of EMG envelope signal of the wrist flexor. In the red circle, it can be noticed the presence of muscle activity also during the relaxing period between trial during the execution with robotic system.

execution with the SHX system the muscle activity is higher also in this phase (example in **Figure 11**).

4. DISCUSSION

Most of the supernumerary robotic systems presented in literature have been specifically designed for augmenting workers' abilities in industrial applications (Llorens-Bonilla et al., 2012; Ciullo et al., 2018a). Most recently, the use of this technology has been also proposed for impaired assistance (Hussain et al., 2016). This can be an interesting opportunity for subjects with a permanent disability due to neuromuscular diseases, like post-stroke subjects, or injuries. In this scenario, the use of a supernumerary robotic hand can compensate for the missing functionalities by acting in charge of the natural impaired one (Ciullo et al., 2020). However, some considerations

and analyses need to be done for safety in using this novel robot-assisted approach. Differently from other assistive robotic systems (Wu et al., 2013; Nordin et al., 2014; Grimm et al., 2016), where variations on movement patterns are mainly due to the subject's impairments, in supernumerary robotic hand such alteration can be introduced by the encumbrance of the additional robotic hand itself. To verify the presence and estimate the size of these compensatory movements, with this work a quantitative analysis has been conducted involving healthy subjects.

According to the kinematic results, we observed that the use of the apparatus reduces the range of motion of the wrist, elbow and shoulder, while it increases the range of the trunk and head movements. Regarding the shoulder joint, for the tasks of groups 1 and 2 (12 tasks in total), statistically significant differences have been found only for the abduction/adduction in 3/12 tasks for the

DDC configuration and in 2/12 tasks for the PMC configuration. This shows that, for these tasks involving only grasping of objects, the shoulder movements were similar during the execution with and without the robotic system. However, a different situation can be seen in the pouring task (task 13) and in the lifting of the tubes (task 13, 14, 15, 16, and 17, so 5 in total) which required a major precision, forcing the subject to use more this joint. Indeed, for these tasks, statistically significant differences have been found for the abduction/adduction in 5/5 tasks for the DDC configuration and in 5/5 tasks for the PMC configuration, while for the flexion/extension in 3/5 tasks for the DDC configuration and in 1/5 tasks for the PMC configuration. Regarding the elbow joint, the RoM obtained during the execution with the robotic hand resulted lower with respect to the natural execution for all the tasks. This can be attributed to the presence of the gravity compensator helping the subject to move the arm without exploiting the elbow movement. The only task in which the RoM of the elbow was higher was task 13 (pouring). This is in line with the fact that, as previously said, this task also required a larger movement of the shoulder. Concerning the wrist pronation/supination, the RoM during the execution with the natural hand was higher for all the tasks. This was due to the fact that using the robotic system, the natural hand was fixed for grasping the handle controller, thus limiting the wrist movements. However, statistically significant differences have been obtained only for the DDC configuration. This aspect may prove that the execution with the PMC configuration was very similar to the execution with the natural hand. In this configuration, the robotic hand is below the natural one. This reduce the visual feedback, since the object is hidden by the robotic hand, requesting a major wrist pronation/supination. The RoM obtained from the trunk and the head movements are higher during the execution with the robotic hand, thus indicating that subjects used these movements to compensate the reduced exploitation of the arm joints. Also for trunk and head joints, the biggest differences are shown for the pouring task, the lifting of the marble and the smaller tube. This could be due both to the fact that these tasks required more dexterity, and because of the occlusion of the robotic hand pushing the subject to move the head and the trunk to better look at the object (Ciullo et al., 2018b). This was more evident with the PMC configuration for which, as already said, most of the subjects asserted that the object was hidden by the system. To solve this problem, a haptic feedback system could be added as proposed by Schofield et al. (2014) and Svensson et al. (2017).

Considering the accuracy and efficiency indices, the values were lower in the tasks requiring more dexterity (e.g., lifting of the marble and of the smallest tube). Moreover, in some cases, subjects needed more attempts to accomplish these tasks, thus resulting in more irregular hand trajectories (example in **Figure 10**). Nevertheless, also the values obtained during the executions with the natural hand were low (average 79.11% for the inter-subject accuracy and 67.79% for the inter-subject efficiency), reflecting an high variability between the subjects to accomplish the same task. This variability can explain the very low values (average 46.59% for the inter-subject accuracy in the DDC configuration, 50.76% for the inter-subject accuracy in the

PMC configuration, 59.04% for the inter-subject efficiency in the DDC configuration, and 61.18% for the inter-subject efficiency in the PMC configuration) obtained for the two configurations of the SHX. In fact, it can be caused not only by the encumbrance of the robotic system but also by the difference in the strategy and trajectory used by different subjects.

For what concerns the muscles activity, the values of the RMS resulted similar between the three conditions and few statistically significant differences have been found. This could be justified by the fact that all the tasks proposed were quite short and easy to be executed for healthy subjects, and all the items had a light weight (the heaviest was <250 g). None of the subjects experienced evident level of fatigue and no evident differences among the natural hand and the robotic configurations were found. However, the execution with the robotic system was always longer than the one with the natural hand, resulting in a longer activation period of the muscles. Moreover, the muscle activity resulting from the natural hand shows always a relaxing period between the three repetitions of the tasks, when the hand come back to the starting position. During the execution with the SHX system the muscle activity was present also in this phase (see **Figure 11**). This was more evident for the wrist muscles in the DDC configuration. Two main reasons could justify this evidence: first the subject contracted the wrist muscles to maintain the position and hold the handle. The other reason is that, as already said, even if the subject is helped by the gravity compensator, during the use of the robotic system, the misalignment and the distance of the robotic hand, with respect to the subject's arm, introduces an additional gravity torque. This situation leads to annoying rotations of the human arm and a major force requested to the subject. The same problem was highlighted by stroke patients, using this human-arm interface during previous pilot studies. To counteract these effects, a new prototype of the human-harm interface may be developed with reduced weight and encumbrance and with the addition of a counter-mass.

For what concerns the comparison between the two robotic configurations no relevant differences have been obtained in the values of the indices considered so they can be selected in accordance to the subjects' preference or need. However, it was noticed that, as said in section 2.1, the annoying rotations caused by the misalignment and the distance of the robotic hand requested higher movements exploited to accomplish the task. This was true mostly for the DDC configuration. In particular, in the tube tasks in which the object were closer to the subjects trunk RoM resulted higher with respect to the other two executions. Also the problem of occlusion caused by the position of the hand in the PMC configuration was reported by subjects. Larger movement of the head have been reported during the execution with this configuration, in particular in tasks of group 1 and 2 involving the grasping of subjects.

Although the absence of impaired subjects may represent a limit for this work, the normal condition of the involved ones ensures that any movement variations is mainly related to the system design. Another subject-related factor that may alter the movement execution, inducing compensation with trunk

and head movements, can be the muscular fatigue. However, data analysis on the EMG signals have reported no differences on muscle activities during the whole experimental procedure, excluding in this way the fatigue as possible cause for movement compensations. For this reason, we did not consider muscle synergies even though they can provide interesting outcomes. Due to the ease of the tasks, very low variance among the different synergies would have been obtained. Another limit of this study could be the lack of a metric considering all the joints together, such as kinematic synergies. The huge amount of data acquired and the selected indices provide enough information for our analysis but future works will be designed to analyze the correlation between joints and include additional and more general indices.

5. CONCLUSION

This work provides a detailed description of the compensatory movements exploited by subjects using a supernumerary robotic hand for upper limb assistance. No relevant differences have been found between the two configurations tested so they can be selected in accordance to the subjects preference or need. By comparing the joints movement during the use of the robotic system with respect to the free execution, it has also been demonstrated that, the SHX system can be useful to reduce the stress on the wrist, elbow and shoulder joints, since the RoM exploited was very similar or decreased in the majority of the tasks. However, the use of the trunk and of the head increased. Moreover, from the EMG signals analysis, the muscles activity resulted very similar during the use of the system, thus demonstrating that this device is not detrimental from the point of view of the muscular fatigue. This work suggest that the system may be used as assistive device without causing an over-use of the arm joints and also opens the way to clinical trials with patients. Results may help to upgrade the system with a more comfortable and suitable human-arm interface to avoid occlusion of objects and larger movements of trunk and head. Future work will be oriented to the evaluation of the compensatory movements also with post-stroke patients.

REFERENCES

- Ada, L., Canning, C., Carr, J., Kilbreath, S., and Shepherd, R. (1994). Task-specific training of reaching and manipulation. *Adv. Psychol.* 105, 239–265. doi: 10.1016/S0166-4115(08)61281-9
- Carey, S. L., Highsmith, M. J., Maitland, M. E., and Dubey, R. V. (2008). Compensatory movements of transradial prosthesis users during common tasks. *Clin. Biomech.* 23, 1128–1135. doi: 10.1016/j.clinbiomech.2008.05.008
- Cirstea, M., and Levin, M. F. (2000). Compensatory strategies for reaching in stroke. *Brain* 123, 940–953. doi: 10.1093/brain/123.5.940
- Ciullo, A. S., Catalano, M. G., Bicchi, A., and Ajoudani, A. (2018a). “A supernumerary soft robotic hand-arm system for improving worker ergonomics,” in *International Symposium on Wearable Robotics* (Pisa: Springer), 520–524. doi: 10.1007/978-3-030-01887-0_101
- Ciullo, A. S., Felici, F., Catalano, M. G., Grioli, G., Ajoudani, A., and Bicchi, A. (2018b). Analytical and experimental analysis for position optimization of a grasp assistance supernumerary robotic hand. *IEEE Robot. Autom. Lett.* 3, 4305–4312. doi: 10.1109/LRA.2018.2864357

DATA AVAILABILITY STATEMENT

The original contributions presented in the study are included in the article/**Supplementary Material**, further inquiries can be directed to the corresponding author/s.

ETHICS STATEMENT

The studies involving human participants were reviewed and approved by Institutional Review Board of the University of Pisa. The patients/participants provided their written informed consent to participate in this study. Written informed consent was obtained from the individual(s) for the publication of any potentially identifiable images or data included in this article.

AUTHOR CONTRIBUTIONS

MR designed the experimental protocol and drafted the manuscript. ASC participated in the design of the experimental setup and revised the manuscript. MGC and GG supervised the engineering process and data analysis. AB supervised the research.

FUNDING

This work has received funding from the ERC Synergy grant Natural Bionics (Grant Agreement No. 810346).

ACKNOWLEDGMENTS

The authors would like to thank Manuel Barbarossa, Michele Maimeri, and Mattia Poggiani for their help in the development of the setup, and all the subject who participated in the study.

SUPPLEMENTARY MATERIAL

The Supplementary Material for this article can be found online at: <https://www.frontiersin.org/articles/10.3389/frobt.2020.587759/full#supplementary-material>

- Ciullo, A. S., Veerbeek, J. M., Temperli, E., Luft, A. R., Tonis, F. J., Haarman, C. J., et al. (2020). A novel soft robotic supernumerary hand for severely affected stroke patients. *IEEE Trans. Neural Syst. Rehabil. Eng.* 28, 1168–1177. doi: 10.1109/TNSRE.2020.2984717
- de los Reyes-Guzmán, A., Dimbwadyo-Terrer, I., Pérez-Nombela, S., Monasterio-Huelin, F., Torricelli, D., Pons, J. L., et al. (2017). Novel kinematic indices for quantifying upper limb ability and dexterity after cervical spinal cord injury. *Med. Biol. Eng. Comput.* 55, 833–844. doi: 10.1007/s11517-016-1555-0
- Della Santina, C., Piazza, C., Gasparri, G. M., Bonilla, M., Catalano, M. G., Grioli, G., et al. (2017). The quest for natural machine motion: An open platform to fast-prototyping articulated soft robots. *IEEE Robot. Autom. Mag.* 24, 48–56. doi: 10.1109/MRA.2016.2636366
- Grimm, F., Naros, G., and Gharabaghi, A. (2016). Compensation or restoration: closed-loop feedback of movement quality for assisted reach-to-grasp exercises with a multi-joint arm exoskeleton. *Front. Neurosci.* 10:280. doi: 10.3389/fnins.2016.00280
- Hussain, I., Salvietti, G., Spagnoletti, G., and Praticchizzo, D. (2016). The soft-sixthfinger: a wearable EMG controlled robotic extra-finger for grasp

- compensation in chronic stroke patients. *IEEE Robot. Autom. Lett.* 1, 1000–1006. doi: 10.1109/LRA.2016.2530793
- Hussaini, A., Zinck, A., and Kyberd, P. (2017). Categorization of compensatory motions in transradial myoelectric prosthesis users. *Prosthet. Orthot. Int.* 41, 286–293. doi: 10.1177/0309364616660248
- Levin, M. F., Kleim, J. A., and Wolf, S. L. (2009). What do motor “recovery” and “compensation” mean in patients following stroke? *Neurorehabil. Neural Repair* 23, 313–319. doi: 10.1177/1545968308328727
- Llorens-Bonilla, B., Parietti, F., and Asada, H. (2012). “Demonstration-based control of supernumerary robotic limbs,” in *RSJ International Conference on Intelligent Robots and Systems (IROS), 2012* (Vilamoura: IEEE), 7–12. doi: 10.1109/IROS.2012.6386055
- Lyle, R. C. (1981). A performance test for assessment of upper limb function in physical rehabilitation treatment and research. *Int. J. Rehabil. Res.* 4, 483–492. doi: 10.1097/00004356-198112000-00001
- Maciejasz, P., Eschweiler, J., Gerlach-Hahn, K., Jansen-Troy, A., and Leonhardt, S. (2014). A survey on robotic devices for upper limb rehabilitation. *J. Neuroeng. Rehabil.* 11:3. doi: 10.1186/1743-0003-11-3
- Major, M. J., Stine, R. L., Heckathorne, C. W., Fatone, S., and Gard, S. A. (2014). Comparison of range-of-motion and variability in upper body movements between transradial prosthesis users and able-bodied controls when executing goal-oriented tasks. *J. Neuroeng. Rehabil.* 11:132. doi: 10.1186/1743-0003-11-132
- Metzger, A. J., Dromerick, A. W., Holley, R. J., and Lum, P. S. (2012). Characterization of compensatory trunk movements during prosthetic upper limb reaching tasks. *Archiv. Phys. Med. Rehabil.* 93, 2029–2034. doi: 10.1016/j.apmr.2012.03.011
- Michaelsen, S. M., Jacobs, S., Roby-Brami, A., and Levin, M. F. (2004). Compensation for distal impairments of grasping in adults with hemiparesis. *Exp. Brain Res.* 157, 162–173. doi: 10.1007/s00221-004-1829-x
- Mondiale de la Santé, O., and Organization, W. H. (2001). *International Classification of Functioning, Disability and Health: ICF*. Geneva: World Health Organization.
- Mozaffarian, D., Benjamin, E. J., Go, A. S., Arnett, D. K., Blaha, M. J., Cushman, M., et al. (2015). Executive summary: heart disease and stroke statistics—2015 update: a report from the american heart association. *Circulation* 131, 434–441. doi: 10.1161/CIR.0000000000000157
- Nordin, N., Xie, S. Q., and Wünsche, B. (2014). Assessment of movement quality in robot-assisted upper limb rehabilitation after stroke: a review. *J. Neuroeng. Rehabil.* 11:137. doi: 10.1186/1743-0003-11-137
- Parietti, F., and Asada, H. H. (2017). “Independent, voluntary control of extra robotic limbs,” in *2017 IEEE International Conference on Robotics and Automation (ICRA)* (Marina Bay Sands: IEEE), 5954–5961. doi: 10.1109/ICRA.2017.7989702
- Roby-Brami, A., Feydy, A., Combeaud, M., Biryukova, E., Bussel, B., and Levin, M. (2003). Motor compensation and recovery for reaching in stroke patients. *Acta Neurol. Scand.* 107, 369–381. doi: 10.1034/j.1600-0404.2003.00021.x
- Santello, M., Flanders, M., and Soechting, J. F. (1998). Postural hand synergies for tool use. *J. Neurosci.* 18, 10105–10115. doi: 10.1523/JNEUROSCI.18-23-10105.1998
- Schofield, J. S., Evans, K. R., Carey, J. P., and Hebert, J. S. (2014). Applications of sensory feedback in motorized upper extremity prosthesis: a review. *Expert Rev. Med. Dev.* 11, 499–511. doi: 10.1586/17434440.2014.929496
- Svensson, P., Wijk, U., Björkman, A., and Antfolk, C. (2017). A review of invasive and non-invasive sensory feedback in upper limb prostheses. *Expert Rev. Med. Dev.* 14, 439–447. doi: 10.1080/17434440.2017.1332989
- Wade, D. T. (1992). Measurement in neurological rehabilitation. *Curr. Opin. Neurol. Neurosurg.* 5, 682–686.
- Wu, C., Yang, C., Chen, M., Lin, K., and Wu, L. (2013). Unilateral versus bilateral robot-assisted rehabilitation on arm-trunk control and functions post stroke: a randomized controlled trial. *J. Neuroeng. Rehabil.* 10:35. doi: 10.1186/1743-0003-10-35

Conflict of Interest: The authors declare that the research was conducted in the absence of any commercial or financial relationships that could be construed as a potential conflict of interest.

Copyright © 2020 Rossero, Ciullo, Grioli, Catalano and Bicchi. This is an open-access article distributed under the terms of the Creative Commons Attribution License (CC BY). The use, distribution or reproduction in other forums is permitted, provided the original author(s) and the copyright owner(s) are credited and that the original publication in this journal is cited, in accordance with accepted academic practice. No use, distribution or reproduction is permitted which does not comply with these terms.



Suitability of the Openly Accessible 3D Printed Prosthetic Hands for War-Wounded Children

John-John Cabibihan^{1*}, Farah Alkhatib², Mohammed Mudassir¹, Laurent A. Lambert³, Osama S. Al-Kwif⁴, Khaled Diab⁵ and Elsadig Mahdi¹

¹ Department of Mechanical and Industrial Engineering, Qatar University, Doha, Qatar, ² School of Mechanical Engineering, University of Western Australia, Perth, WA, Australia, ³ School of Public Administration and Development Economics, Doha Institute for Graduate Studies, Doha, Qatar, ⁴ Department of Management and Marketing, Qatar University, Doha, Qatar, ⁵ Qatar Red Crescent Society, Doha, Qatar

OPEN ACCESS

Edited by:

Carlos A. Cifuentes,
Escuela Colombiana de Ingeniería
Julio Garavito, Colombia

Reviewed by:

Jose Gonzalez-Vargas,
Otto Bock, Germany
Mehran Moazen,
University College London,
United Kingdom

*Correspondence:

John-John Cabibihan
john.cabibihan@qu.edu.qa

Specialty section:

This article was submitted to
Biomedical Robotics,
a section of the journal
Frontiers in Robotics and AI

Received: 12 August 2020

Accepted: 04 December 2020

Published: 11 January 2021

Citation:

Cabibihan J-J, Alkhatib F, Mudassir M, Lambert LA, Al-Kwif OS, Diab K and Mahdi E (2021) Suitability of the Openly Accessible 3D Printed Prosthetic Hands for War-Wounded Children. *Front. Robot. AI* 7:594196. doi: 10.3389/frobt.2020.594196

The field of rehabilitation and assistive devices is being disrupted by innovations in desktop 3D printers and open-source designs. For upper limb prosthetics, those technologies have demonstrated a strong potential to aid those with missing hands. However, there are basic interfacing issues that need to be addressed for long term usage. The functionality, durability, and the price need to be considered especially for those in difficult living conditions. We evaluated the most popular designs of body-powered, 3D printed prosthetic hands. We selected a representative sample and evaluated its suitability for its grasping postures, durability, and cost. The prosthetic hand can perform three grasping postures out of the 33 grasps that a human hand can do. This corresponds to grasping objects similar to a coin, a golf ball, and a credit card. Results showed that the material used in the hand and the cables can withstand a 22 N normal grasping force, which is acceptable based on standards for accessibility design. The cost model showed that a 3D printed hand could be produced for as low as \$19. For the benefit of children with congenital missing limbs and for the war-wounded, the results can serve as a baseline study to advance the development of prosthetic hands that are functional yet low-cost.

Keywords: prosthetics, assistive technologies, war-wounded, 3D printing, grasping

1. INTRODUCTION

The loss of upper limbs has significant impact on the functional activities and social interactions of a person. The loss of upper limbs can be classified according to congenital limb loss or acquired limb loss. There is a 2:1 incidence ratio of congenital limb loss to acquired limb loss (Masada et al., 1986; Vannah et al., 1999; Vasluian et al., 2013). Congenital limb loss is attributed to malformations that have structural abnormalities of prenatal origin (Czeizel, 2005). The prevalence of upper limb loss is twice that of the lower limbs (Hirons et al., 1991). Acquired limb loss can be due to various reasons, including diseases or traumatic amputations from machinery, vehicular accidents, electrical injuries, or weaponry (Krebs et al., 1991).

In recent years, the acquired loss of the upper limbs have further increased due to warfare. Children are the most vulnerable victims of wars. Like other civilians, they can suffer a range of war-related injuries. Improvised explosive devices (IEDs), landmines, mortars, and air strikes are more likely to kill or permanently impair a child due to their inclination for outdoor activities.

In 2017 alone, the United Nations General Assembly Security Council (2018) reported that there were around 9,624 children who were killed or maimed in armed conflicts worldwide (Table 1).

In the Syrian Civil War (2011-present), Handicap International (Bevington, 2015) estimated that one million people were injured and around 8% of them require prosthesis or orthosis. That translates to a latent demand of around 80,000 individuals who need such devices in one country alone. The vulnerability of the war-wounded is usually worsened by the collapse of the healthcare system. The Physicians for Human Rights (2015) have documented the systematic attacks on healthcare providers in Syria. To compensate for the lack of healthcare services, Qatar Red Crescent Society (a member of the Red Cross Red Crescent Societies), the International Committee of the Red Cross, Humanity and Inclusion (formerly Handicap International), and Médecins Sans Frontières (MSF) have come to the forefront of humanitarian assistance. For them, however, the provision of prosthetic limbs has become problematic because of the prohibitive prices in the context of international donor fatigue.

The price of commercially-available body-powered prostheses ranges from \$4,000 to \$10,000 (Resnik et al., 2012; ten Kate et al., 2017) while the electrically-powered ones cost between \$25,000 and 75,000 (Resnik et al., 2012; van der Riet et al., 2013; ten Kate et al., 2017). For government-compliant upper extremity prosthesis, the American Orthotic and Prosthetic Association (2015) estimated that the price was between \$1,500 and 5,000. All these amounts render the purchase of a prosthesis unaffordable for most of those who live in difficult living conditions, such as in the war zones, refugee camps, or low-income countries. The statistics in Table 1 are miniscule as compared to the

demand for mass-produced consumer goods like mobile phones or athletic shoes. Due to the various levels of limb loss or amputations among the patients and the various preferences for functionality or other features (Korkmaz et al., 2012), a mass production approach for prosthetics is not feasible. There is patient-specificity for each prosthetic device.

An emerging technology for the fast production of low-cost prosthetics is three-dimensional (3D) printing (Cabibihan et al., 2015; Cabibihan et al., 2018; Alhaddad et al., 2017; Alturkistani et al., 2020). The 3D printing process is the additive deposition of material in a layer-by-layer manner to construct parts from a 3D computer-aided design (CAD) model (Hull, 1986). Consumer-grade desktop 3D printers, cost between \$250 and 2,500. There are advantages of using 3D printing for prosthesis fabrication. First, the process does not need the numerous constraints imposed by changing the tools and switching manufacturing processes for each part. Secondly, 3D printing allows free-form shape, which can replicate the contours of human limbs. It allows the fabrication of prosthesis that is specific to the shape and size of each patient. Lastly, because the fabrication of parts is at low volume, the inventory of parts is minimized, thus, further minimizing the production costs.

In this paper, we ask whether the openly accessible, body-powered 3D printed prosthetic hands are suitable for the use of children (i.e., under 18 years old) with missing hands in low-resource settings. First, we evaluated all the published designs of openly accessible 3D printed prosthetic hands for their suitability to those with congenital loss of hands or war-related amputation. Next, we investigated the grasping postures of a representative design of a prosthetic hand. There were a few available designs but their cable-driven mechanisms and the materials used for 3D printing were similar. Third, we investigated the probable design aspects where failure can occur: the cables could break and the grasp could become compromised, the material in the fingers could break due to the high stresses from the cables that were under tensile forces, or the fingers' joints could fail due to the cyclic loads during the grasping and carrying of objects. Fourth, we developed a cost model to approximate the minimum price of each 3D printed hand. Lastly, we discussed the implications of this work for children with congenital limb loss and the war-wounded.

2. OPENLY ACCESSIBLE 3D PRINTED PROSTHETIC HANDS

As a baseline study, we investigated the body-powered 3D printed hands that were available online. Prosthetic hands that were controlled using pattern recognition of electromyographic (EMG) signals and other sensory feedback strategies were excluded in the investigation (Kuiken et al., 2016; Resnik et al., 2019).

Some of the available designs are shown in Table 2. These hands are anthropomorphic consisting of five fingers, each featuring two or three phalanges. One joint links the wrist to the harness, which is mounted to the stump of the amputated part of the arm. These types of mechanisms are considered

TABLE 1 | Number of children affected worldwide by armed conflicts in 2017 (Adapted from United Nations General Assembly Security Council, 2018).

Country	Killed	Maimed	Total
Afghanistan	861	2,318	3,179
Central African Republic	61	43	104
Columbia	18	35	53
Democratic Republic of Congo	156	178	334
Iraq	279	438	717
Israel and State of Palestine	15	1,165	1,180
Lebanon	8	12	20
Libya	40	38	78
Mali	19	15	34
Myanmar	196	24	220
Somalia*	–	–	931
South Sudan	36	57	93
Sudan	19	75	94
Syrian Arab Republic	910	361	1,271
Yemen	552	764	1,316
Total	3,170	5,523	9,624

*Data for killed or maimed were not provided.

as underactuated because the number of degrees of actuation is lower than the degrees of freedom (DOFs) on the whole mechanism (Birglen et al., 2008). For the hands in Table 2, there are at least 10 DOFs and a single mode of actuation, which is the flexing of the joint between the wrist and the harness.

The fingers are actuated by the cables that are connected to the wrist. To control the body-powered prosthetic limb, cables are used to transfer the movements exerted from the body part to the prosthesis. This movement could be from the chest, shoulder, elbow, or wrist depending on the level of amputation. The flexion of the fingers depends on the tension force of the non-elastic cables, while the extension of the fingers depends on the restorative effect of the elastic cord that has a certain amount of flexibility, which then allows the return of the fingers to their natural pose (Alkhatib et al., 2019b).

Among these designs, the Raptor Reloaded Hand (Figure 1) from the e-NABLE community has proven to be popular and is currently being used by more than 1,500 amputees from 40 countries because of its simple assembly and fairly acceptable appearance (Owen, 2017). This design has been reported in previous works (Arabian et al., 2016; Burn et al., 2016; Greene et al., 2016; Sullivan et al., 2017; ten Kate et al., 2017; Vujaklija and Farina, 2018). Further studies are needed to evaluate the technical integrity and functionality of this hand. We used this design to evaluate the movement, grasping forces, failure modes, and associated costs to produce a prosthetic hand for those with congenital limb loss or for the war-wounded.

3. MATERIALS AND METHODS







3.1. Grasping Poses

The human hand is capable of various grasp types. It is capable for full-hand grasping (i.e., power grasps) or for dexterous grasping (i.e., precision grasps) of various objects. There are 15 joints and 20 DOFs in the human hand (Jones and Lederman, 2006; Kapandji, 2016). The human hand has been shown to perform 33 grasp postures (Feix et al., 2013; Feix et al., 2016). In that study, the 33 grasps were achieved using 17 objects. Among those objects were a ball, a coin, cylinders of various diameters, and others that are representative of objects in daily life. The full list of grasp postures can be found at the link.

3.1.1. Materials

The Raptor Reloaded 3D design was downloaded and was used at the default scale of the original file (e-NABLE Community, 2014; Alkhatib et al., 2019a). The CAD file was 3D printed using Polylactic Acid (PLA; MakerBot, USA) filament on a desktop 3D Printer (Replicator 5th Generation, MakerBot Industries LLC, Brooklyn, NY, USA; build table: 29.5×19.5×16.5 cm³). The following settings were used: 215°C printing temperature, 0.2 mm layers, 2 shells, 35% infill, and the cooling fan was set to active mode. The printing was completed after 17 h. To complete the assembly, non-elastic and elastic cords were needed for the grasp and release mechanism. The non-elastic cables (super Dyneema strong braided fishing line, SeaKnight, China) were required to flex the fingers. Elastic cords (3 mm dia, Polypropylene Shock Cord, Sgt. Knots Supply Co, NC, USA) were used to return the

TABLE 2 | Openly accessible 3D printed prosthetic hands: structural material and the types of cables for flexion and extension.

Prosthetic hand	Design	Joints	Material	Flexion	Extension
Cyborg Beast (Zuniga, 2015)		10	ABS ^a or PLA ^b	Non-elastic cables	Elastic cords
Falcon Hand (Arabian, 2014)		11	ABS	Non-elastic cables	Orthodontic rubber bands
FlexyHand (Wood, 2014)		14	PLA or Filaflex	Non-elastic cables	Flexible joints
K1 Hand (Keuster, 2015)		14	ABS or PLA	Non-elastic cables	Elastic cords
Phoenix Hand (Bryant, 2016)		10	ABS or PLA	Non-elastic cables	Elastic cords
Raptor Reloaded (e-NABLE Community, 2014)		10	PLA	Non-elastic cables	Elastic cords

^aAcrylonitrile butadiene styrene.

^bPolylactic acid.

fingers to their default pose. A knotting technique, known as the improved clinch knot, was used to firmly secure the cables and cords.

3.1.2. Selection of Grasp Poses

The prosthetic hand is a transcarpal prosthetic hand. As such, a user dons the prosthetic hand and has to flex the wrist so that the grasping can be done. The protocol to find the grasping set was conducted as follows. First, a healthy child (8 years old) wore the transcarpal prosthetic hand through straps. The straps within the prosthetic hand simulated the grasping of a child amputee. Second, the images of the 33 grasps (Feix et al., 2016) were displayed on the screen, which the child repeated. In accordance to the procedure in Deimel and Brock (2016), the last step was to judge the quality of the grasp by moving the grasped object. Three consecutive trials were done for repeatability. We then shortlisted the grasp poses that the prosthetic hand was capable of.

3.2. Grasping Range of Motion

For an underactuated hand, all fingers wrap around the surface of an object. In cases where an object is smaller than the enclosing volume of the fingers, the fingers that are not touching the object will continue to flex until the structural limits are reached. For the representative sample (i.e., the Raptor Reloaded Hand), we investigated the limits imposed by the structural constraints. In this section, we asked whether the range of motion of the fingers was similar to that of the human hand. Additionally, we wanted to know how much flexion force on the wrist was required to achieve the prosthetic hand's range of motion.

3.2.1. Data Analysis

The positions of the fingertip were determined according to its X and Y coordinates. A geometrical scheme was then developed to understand the grasping relationship between the finger's joints

and links with its geometry. Forward kinematics was carried out by determining the Denavit-Hartenberg (D-H) parameters (Corke, 2017).

Figure 2A shows the link frame of the index finger. The two-dimensional Cartesian coordinates system (x, y) defines the origin point (0,0) at the wrist joint where $\theta_1 = 0$. The D-H convention was used to create the transformation matrices based on four parameters, which can be obtained from the link frame of the prosthetic hand. These parameters are the link lengths, a_i , link twists, α_i , link offsets, d_i , and joint angles, θ_i (**Table 3**). The transformation matrices are shown in Equations (1)–(4).

$${}^0T_1 = \begin{pmatrix} \cos \theta_1 & -\sin \theta_1 & 0 & L_1 \cos \theta_1 \\ \sin \theta_1 & \cos \theta_1 & 0 & L_1 \sin \theta_1 \\ 0 & 0 & 1 & 0 \\ 0 & 0 & 0 & 1 \end{pmatrix} \quad (1)$$

$${}^1T_2 = \begin{pmatrix} \cos \theta_2 & -\sin \theta_2 & 0 & L_2 \cos \theta_2 \\ \sin \theta_2 & \cos \theta_2 & 0 & L_2 \sin \theta_2 \\ 0 & 0 & 1 & 0 \\ 0 & 0 & 0 & 1 \end{pmatrix} \quad (2)$$

$${}^2T_3 = \begin{pmatrix} \cos \theta_3 & -\sin \theta_3 & 0 & L_3 \cos \theta_3 \\ \sin \theta_3 & \cos \theta_3 & 0 & L_3 \sin \theta_3 \\ 0 & 0 & 1 & 0 \\ 0 & 0 & 0 & 1 \end{pmatrix} \quad (3)$$

$${}^0T_3 = {}^0T_1 {}^1T_2 {}^2T_3 \quad (4)$$

The fingertip's posture can be expressed as position and orientation quantities, $[X, Y, \phi]^T$. The X and Y positions of the fingertip with respect to the wrist joint angle (θ_1),

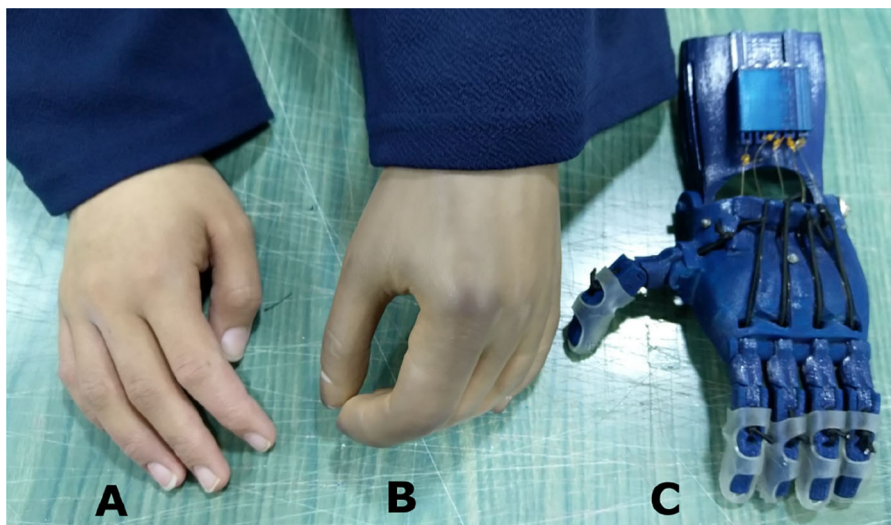


FIGURE 1 | An amputee with a cosmetic prosthetic hand in one of our field interviews. **(A)** The non-affected hand. **(B)** A cosmetic hand with a darkened complexion due to the aging of the silicone material and smudging from dark clothes. **(C)** The Raptor Reloaded 3D printed prosthetic hand as a representative design of openly accessible 3D printed hands.

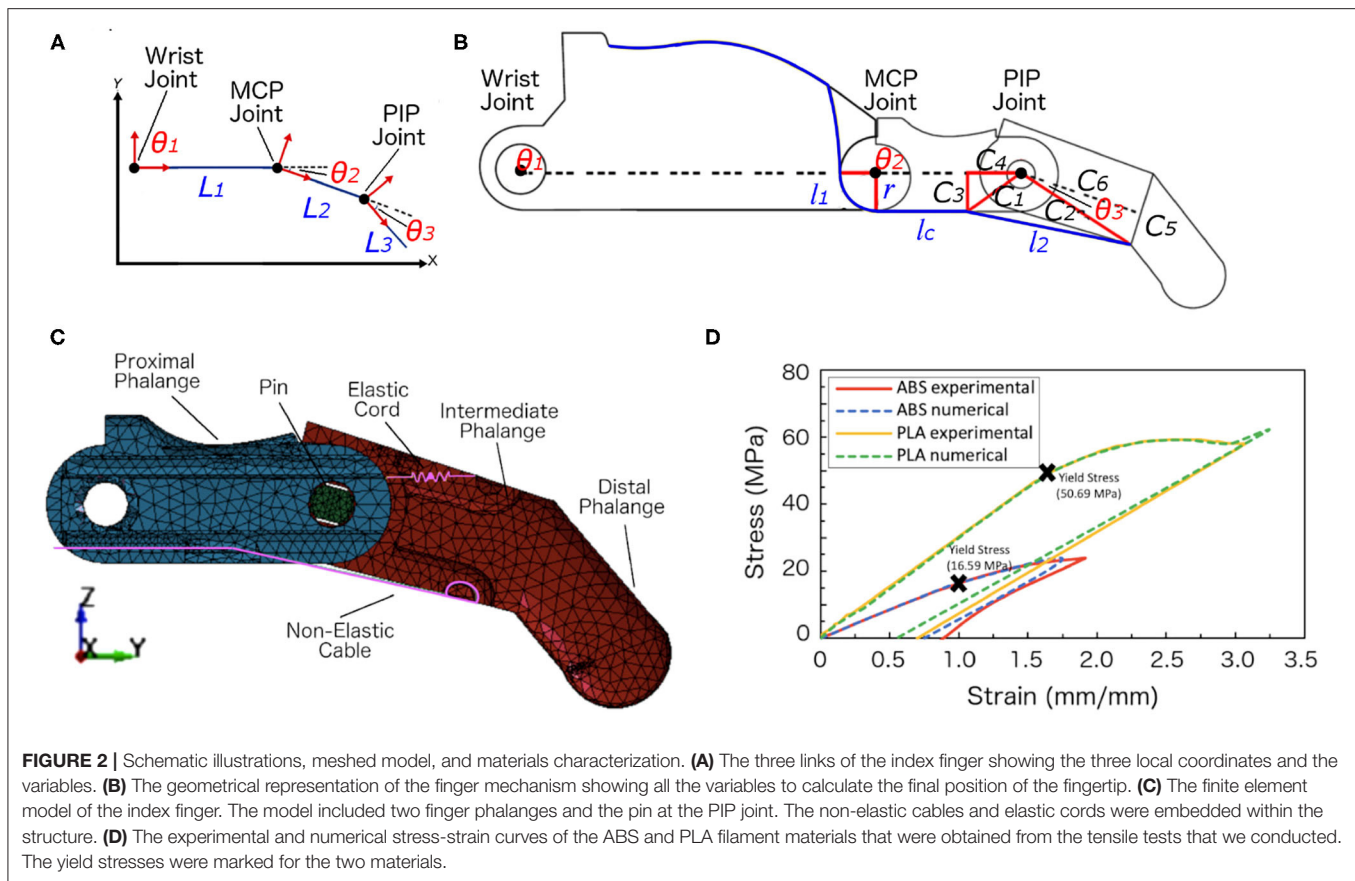


TABLE 3 | Denavit-Hartenberg parameters of the 3D printed prosthetic index finger.

Link number, L_i	Link length, a_i	Link twist, α_i	Link offset, d_i	Joint angle, θ_i
1	L_1	0	0	θ_1
2	L_2	0	0	θ_2
3	L_3	0	0	θ_3

metacarpophalangeal (MCP) joint angle (θ_2) and the proximal interphalangeal (PIP) joint angle (θ_3) were calculated by the following forward kinematics equations (Equations 5 and 6). The finger's orientation, ϕ , can be represented as the sum of the joint angles, θ_1 , θ_2 , and θ_3 (Equation 7).

$$X = L_1 \cos \theta_1 + L_2 \cos(\theta_1 + \theta_2) + L_3 \cos(\theta_1 + \theta_2 + \theta_3) \quad (5)$$

$$Y = L_1 \sin \theta_1 + L_2 \sin(\theta_1 + \theta_2) + L_3 \sin(\theta_1 + \theta_2 + \theta_3) \quad (6)$$

$$\phi = \theta_1 + \theta_2 + \theta_3 \quad (7)$$

A mathematical relationship between the fingertip position and the applied grasping force was developed to calculate the X and Y positions of the fingertip. The geometry of the prosthetic index finger is shown in **Figure 2B**. The finger's

grasping motion (flexion) was actuated by the tension of the cables, while the return motion (extension) was actuated by the elastic cords.

The flexion and extension resulted into changes in the MCP joint angle (θ_2) and PIP joint angle (θ_3). The Raptor Reloaded hand simplified the design by combining the DIP joint to the PIP joint. Henceforth, the DIP joint will not be mentioned. The value of these angles depended on the cable length, l_{Cable} , which is in contact with the pulleys, the length of the cable along the phalanges, and the length until the fixed pin joint where the cable is attached (Equation 8). In other words, the more tension force is applied to the cable, the shorter the cable length will become. Consequently, more flexion will be achieved by the fingers. The cable's length has a maximum value at the natural pose ($\theta_1 = \theta_2 = \theta_3 = 0^\circ$) and it has the minimum length at the full tension ($\theta_1 = 0^\circ; \theta_2 = \theta_3 = 90^\circ$). It is worth to mention that θ_3 will never be zero in the actual design. The minimum value of θ_3 can be assumed to be zero for simplification and this will not affect the finger analysis.

The cable length (l_{Cable}) and the tension force applied on the cable ($F_{tension}$) has a proportional relationship. This relationship was experimentally obtained by applying tension forces on the finger and measuring the values. A force gauge (DFS50, Nextech Global Company Limited, Thailand) was used for measuring the tension force and a Vernier caliper (part 530-118, Mitutoyo, Japan) was used for taking the length measurements.

The relationship between the cable's length and the MCP joint angle, θ_2 , and PIP joint angle, $\theta_3 = 0^\circ$, can be calculated from Equations (9) to (12).

$$l_{Cable} = l_1 + l_2 + l_c \quad (8)$$

$$l_1 = r \left(\frac{\pi}{2} - \theta_2 \right) \quad (9)$$

$$l_2 = \sqrt{C_1^2 + C_2^2 - 2C_1C_2 \cos(90^\circ - \theta_3)} \quad (10)$$

$$C_1 = \sqrt{C_3^2 + C_4^2} \quad (11)$$

$$C_2 = \sqrt{C_5^2 + C_6^2} \quad (12)$$

where l_c is a constant, while l_1 and l_2 are calculated from Equations (9) and (10), respectively. C_1 and C_2 can be obtained from actual measurements by using Equations (11) and (12). The variables l_c , C_3 , C_4 , C_5 , C_6 , and r are constant lengths that can be measured directly from the design (Table 4). These constants will only be applicable if the downloaded design is not subjected to the scaling of the default dimensions.

3.3. Finite Element Modeling

Non-linear finite element (FE) analysis was implemented using the software LS-DYNA (mmmps R8.1.1, Livermore Software Technology Corporation, USA) to predict the maximum load applied on the prosthetic index finger before failure or breakage. The FE method divides the system into smaller parts (i.e., finite elements) and uses algorithms to solve the partial differential equations (PDEs). This numerical method approximates the system solution under the given initial and boundary conditions (Biddis et al., 2004; Mollica and Ambrosio, 2009). The FE method was earlier used in the analysis of prosthetic fingers and structures (Cabibihan et al., 2006a,b, 2014). In the current work, the locations with potentially high stress concentration were predicted to be at the distal finger phalange, proximal finger phalange, and at the pin. An FE model was created to determine the stresses at the critical components of the prosthetic hand. The various conditions and assumptions are described henceforth.

3.3.1. Geometry

The open-source CAD files were downloaded from e-NABLE Community (2014), and the original design was modeled as it is. The model included the proximal phalange, the combined intermediate and distal phalanges, the non-elastic cable, the elastic cord, and the pin at the PIP joint (Figure 2C). For the

purpose of saving computational time, the wrist, palm, and the pin at the MCP joint were not modeled since the direct contact with the objects comes from the distal and proximal finger phalanges.

3.3.2. Geometry Meshing

To create the FE model, the finger geometry was subdivided into small 3D quadratic tetrahedron solid elements. Each element has four nodes and one nodal rotation to eliminate the probability of rotational deformation. For the non-elastic cable, the beam elements were used to model the cable because it has constant cross-sectional properties, its length is larger than its width, and it handles a load, which is distributed along its length. The beam elements consisted of three nodes in three-dimensional space. Two nodes were used for the identification of the geometry and the third node was for the orientation of the beam element. To model the elastic cords, one discrete element was used with one degree of freedom and two nodes. This discrete element has a spring behavior to simulate the elasticity of the elastic cord. A spring constant of 1,000 N/m was assumed, based on the elastic linear relationship between the force applied and displacement created (Hooke's law). In our study the applied force did not exceed 25 N and the extended displacements were relatively small (measured in mm), thus the spring constant was assumed on average.

H-refinement test was used to conduct the convergence study. With this process, the number of elements were increased in the model by reducing the element size. The initial mesh size ranged between 2.0 and 2.4 mm. The maximum value of von Mises stress was selected with respect to the number of elements. For computational time savings and because the maximum von Mises stress was almost constant after having 53,198 elements, we used the current model, with the element size ranging between 1.2 and 1.8 mm.

3.3.3. Materials

Two types of filament materials were evaluated in the analysis: Acrylonitrile Butadiene Styrene (ABS; MakerBot ABS) and Polylactic Acid (PLA; MakerBot PLA). Both materials were compatible with the 3D printer (MakerBot Industries LLC, NY, USA). The piecewise linear plasticity material model (MAT_024) (Hallquist, 1993) from LS-DYNA material library was used to model the ABS and PLA distal finger phalange, the combined intermediate and proximal finger phalange, and the pin. The modeled non-elastic cable was a braided fishing line cable (super Dyneema strong braided fishing line, SeaKnight, China). The plastic kinematic material model (MAT_003) was used to model the non-elastic cable with very low strain rate because the cable was assumed to have no deformation with respect to time.

3.3.4. Materials Verification

To verify the selected material model MAT_024, experimental tensile tests for ABS and PLA filaments were simulated numerically using LS-DYNA. The experimental tensile tests were performed using a universal testing machine (5969 Series Universal Testing Systems, Instron, USA). The loading rate for the tensile test was set to 5 mm/min. The samples of ABS and

TABLE 4 | Design constants of the geometry as measured from the Raptor Reloaded Hand (dimensions in mm).

l_c	C_3	C_4	C_5	C_6	r
15.75	6.00	7.25	6.00	20.00	2.25

PLA materials were printed according to ASTM D638 standard (ASTM D638-14, 2014) and the same printer and printing conditions were used as described in section 3.1.1. **Table 5** shows the obtained material properties of the two filament materials from our experimental test.

Elasto-plastic materials were defined as materials that achieve their elastic and plastic behaviors after reaching the yield stress of the material. On the contrary, metals undergo plastic deformation after reaching their yield stresses. The resulting stress-strain curves from the experimental tests were used to define the effective plastic strain of the material. The effective plastic strain is a value that increases whenever the material is actively yielding. This value was calculated incrementally over a period of time to characterize the plastic deformation. **Figure 2D** showed good agreement in the stress-strain curves between the experimental and numerical results. The yield stresses obtained from the experimental tensile tests for the ABS and PLA materials were 16.59 and 50.69 MPa, respectively.

3.3.5. Boundary Conditions

Three important conditions were taken into account in modeling the prosthetic finger. First, the hole at the proximal phalange was supported in all directions (i.e., in translation and rotation), with the exception of the rotational movement around the x-axis. Second, the pin was fully supported in all directions (i.e., all the degrees of freedom of the pin nodes were constrained). Third, no support was applied on the intermediate phalange, which means that it was free to move in any direction. To constrain the intermediate phalange, a frictional contact between the pin nodes and intermediate phalange node was applied with a friction constant of 0.3. The same contact was applied between the proximal phalange and the intermediate phalange.

3.3.6. Loading

Tension force was applied on one node of the cable. The ABS finger model was subjected to 5 and 15 N, while the PLA finger model was subjected to 5, 15, and 25 N. These values were close to the 22.2 N maximum force limit to single-handedly grasp, pinch, or twist objects (Standards for Accessible Design; United States Department of Justice, 2010; std. no. 309.4).

3.4. Production Cost Analysis

In evaluating the cost for each 3D printed hand, the following components were considered: the equipment cost (i.e., 3D printer), material cost (i.e., filament, cables, and elastic cords), labor cost of the technician, the cost of maintaining the 3D printer, and the energy cost (**Table 6**). The equipment, filament,

and maintenance costs were obtained from the manufacturer of the 3D printer (Replicator+, MakerBot Industries LLC, NY, USA). The cable (super Dyneema strong braided fishing line, SeaKnight, China) and elastic cord Polypropylene Shock Cord, Sgt. Knots Supply Co, NC, USA) were sourced from industrial suppliers. The labor and energy costs were based on local costs in Doha, Qatar.

The life expectancy of the 3D printer was estimated to be 10,000 h or around 3.5 years. The extruder was approximated to be replaced at the half life expectancy of the 3D printer. The labor cost came from the university's salary guidelines and the energy cost was based on the electricity consumption of the machine where the unit price was based on the data provided by the local energy supplier.

The total cost to produce one 3D printed hand consisted of the following cost components:

$$C = C_{EQ} + C_{RM} + C_{LA} + C_{MA} + C_{EN} \quad (13)$$

where C_{EQ} is the equipment cost per hour, C_{RM} is the raw material cost per hand, C_{LA} is the labor cost per hour, C_{MA} is the maintenance cost per hour, and C_{EN} is the energy cost per hour.

The equipment cost per hour was calculated as: $C_{EQ} = (2,800/10,000) = \$0.28/\text{hour}$, which was based on the life expectancy of the 3D printer of 10,000 h and the initial equipment cost. The raw material cost for every printed hand was calculated as the sum of the filament (\$5.59), non-elastic cable (\$0.019), and elastic cord (\$0.09) for a total of \$5.70. The labor cost was calculated from the time to assemble the various parts of the printed hand. The assembly was around 1 h for each hand. The labor cost, C_{LA} , is equal to:

$$C_{LA} = \frac{1,000(\frac{\$}{\text{month}})}{8(\frac{\text{hours}}{\text{day}}) \times 5(\frac{\text{days}}{\text{week}}) \times 4(\frac{\text{weeks}}{\text{month}})} = \frac{\$6.25}{\text{hour}} \quad (14)$$

The maintenance cost per hour, C_{MA} , was calculated based on a 2-year maintenance cost over the life expectancy of the 3D printer: $C_{MA} = 400/10,000 = \$0.04/\text{hour}$. The energy cost, C_{EN} , is equal to \$0.078 per hour. The total time to complete 3D printing of

TABLE 5 | Mechanical properties obtained experimentally from the tested 3D printed ABS and PLA samples.

Material	Mass density (g/cm ³)	Young's modulus (GPa)	Ult. tensile stress (MPa)	Failure strain (%)
ABS	1.10	1.40	32.00	1.05
PLA	1.30	3.90	54.00	2.20

TABLE 6 | Elements and prices for the cost model calculations.

Cost model element	Item	Unit cost	Note
Equipment cost	3D Printer	\$2,800/unit	10,000 h life expectancy (approx.)
Material cost	PLA Filament	\$43/kg	130 g/hand
	Cables	\$15/spool of 500 m	0.625 m/hand
	Elastic cords	\$9/spool of 50 m	0.5 m/hand
Labor cost	Technician's Salary	\$1,000/month	Monthly part-time salary
Maintenance cost	3D Printer Extruder	\$200/unit	5,000 h life expectancy (approx.)
Energy cost	Power	\$0.47/kWh	167 W; 17 h printing/hand

one hand was 17 h. The cost equation for producing one hand is as follows:

$$C = (0.28 \times 17) + 5.70 + 6.25 + (0.04 \times 17) + (0.078 \times 17) \quad (15)$$

4. RESULTS

4.1. Limited Grasping Poses

From the 33 total grasps that a human hand can do (cf. section 3.1), there were only three grasping postures that can be achieved using the 3D printed hand that was considered in this study (i.e., the Raptor Reloaded Hand). **Figures 3A–C** shows the grasp poses and representative objects: palmar pinch of a coin (7.7 g), lateral grasp of a credit card (10 g), and an inferior pincer grasp of a golf ball (46.4 g).

4.2. Cable Tension Analysis

The range of motion of the finger with respect to θ_1 , θ_2 , and θ_3 are shown in **Figure 3D**. From the initial conditions, the joints θ_2 and θ_3 flexed to 22.5° when the cable applied a force of 4.4 N. The variable cable length, l_{VC} , was only 1.2 mm ($l_{VC} = l_{Cable, experimental}$

- 41.45, where 41.45 mm was the total cable length measured experimentally when $\theta_1 = \theta_2 = \theta_3 = 0^\circ$). When a force of 8.9 N was applied, the joints θ_2 and θ_3 flexed to 45° and the variable cable length recorded was 5.7 mm. It took more tensile force to achieve a higher flexion angle. To flex both joints to 67.5° , a force of 17.8 N was required. The variable cable length to achieve that was 14 mm. The full flexion angle of 90° required that a user needs to exert a force of 22.2 N and an engagement of the cable to 15 mm in length. **Table 7** compares the experimental total cable length from the theoretical total cable length calculated in Equation (8) and the experimental tests described earlier. The errors were calculated to be from 1.75 to 7.61%.

4.3. Failure Analysis

The yield stresses of the ABS and PLA materials were defined (**Figure 2D**). The yield point indicates the end of the elastic behavior and the start of plastic behavior of the materials (i.e., the finger will deform and fail beyond this value). Two different loads were applied on the ABS finger, and three loads on the PLA finger for investigating the material failure. **Figure 4A** shows

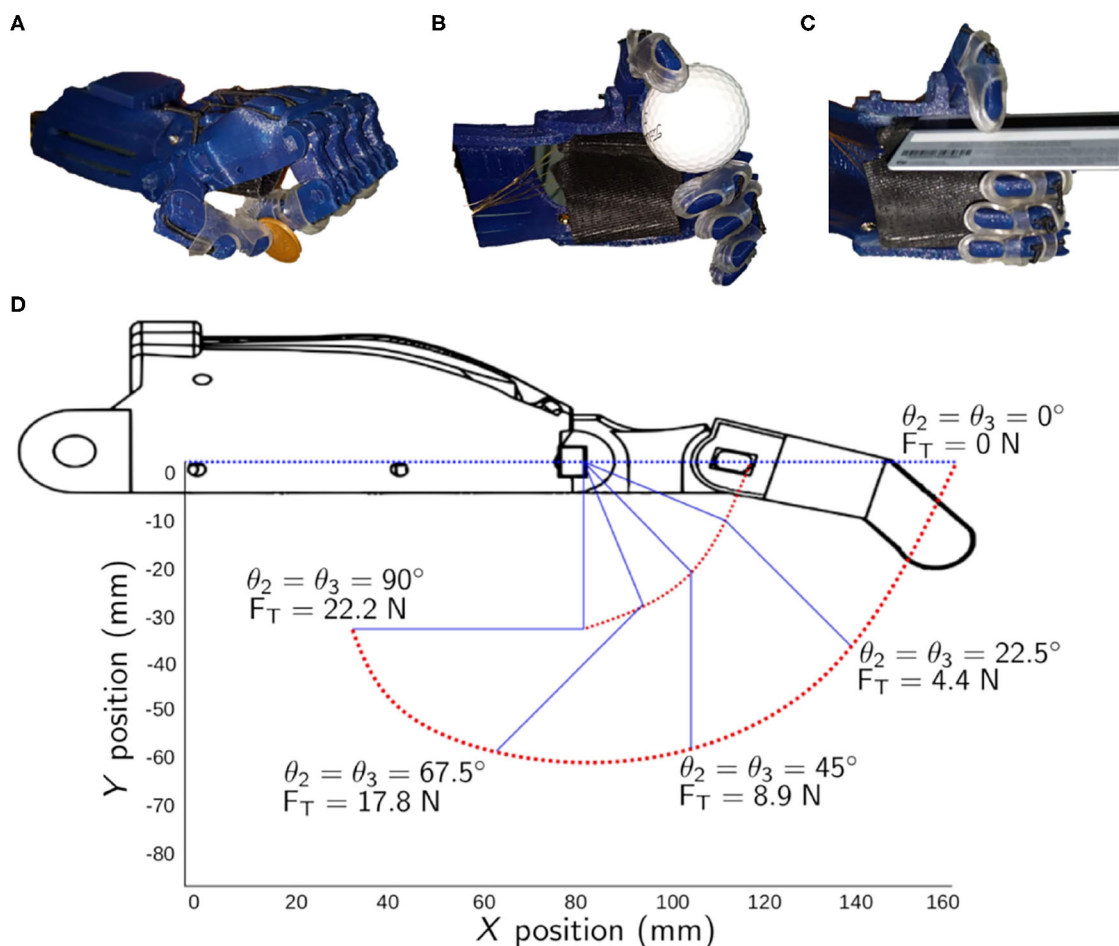
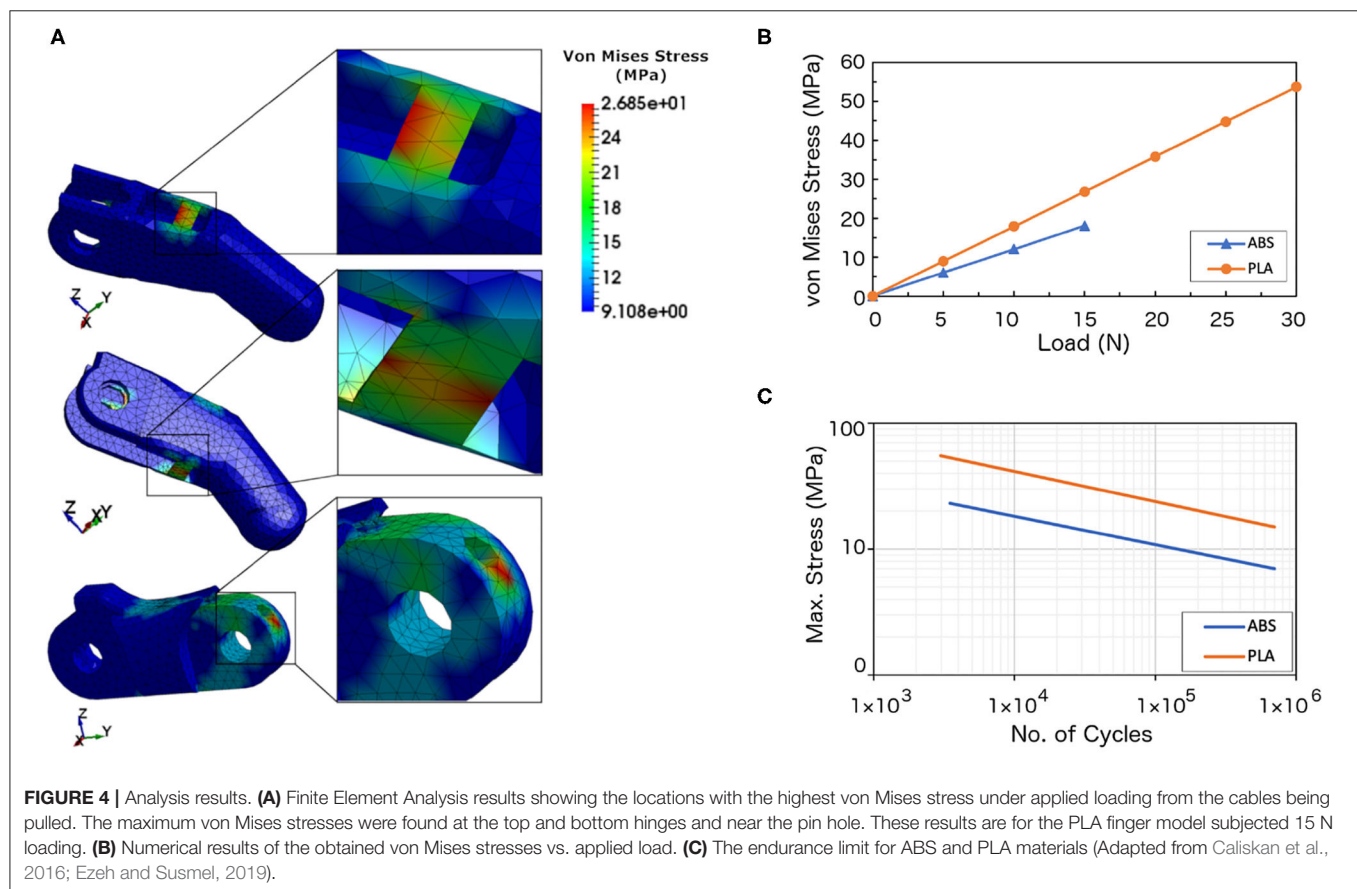


FIGURE 3 | Grasping movements that can be achieved by the representative body-powered 3D printed prosthetic hand. **(A)** Palmar pinch. **(B)** Inferior pincer grasp. **(C)** Lateral grasp. **(D)** The positions of the index finger of the 3D printed prosthetic hand in the X and Y axes with respect to the MCP and PIP joint angles.

TABLE 7 | Relationships between the grasping posture angles, forces, total cable lengths, errors, and the variable cable length.

Angle, $\theta_2 = \theta_3$ (deg)	Cable tension force (N)	Total cable length, theoretical, (mm)	Total cable length, experimental, (mm)	Error (%)	Variable cable length (mm)
0	0	42.19	41.45	1.75	0
22.5	4.2	37.74	40.45	7.17	1.2
45	8.9	33.22	35.75	7.61	5.7
67.5	17.8	29.34	27.45	6.44	14.0
90	22.2	27.22	26.45	2.83	15.0



the contour plots for the von Mises stresses of the PLA finger under 15 N loading (also see animations). It can be seen from the figure and animations that the highest stress concentration areas can be found at the hinges and at the pin holes in both the proximal and distal finger phalanges. From these results, it can be concluded that the initial failure can occur at these high stresses regions.

From the numerical results, the maximum stresses achieved at 10 N load for the ABS and at 25 N load for the PLA were 12.04 and 44.76 MPa, respectively. **Figure 4B** shows the von Mises stresses of the ABS and PLA with respect to the applied forces. The ABS material registered a maximum von Mises stress of 6.02 and 12.04 MPa when loaded with a 5 and 10 N forces, respectively. In comparison, the PLA material has higher maximum stresses

as compared with the ABS material. The PLA have maximum stresses of 8.95, 26.85, and 44.76 MPa when loaded with forces of 5, 15, and 25 N, respectively. The von Mises criterion was used to determine whether the material will yield or fracture. If the value of the von Mises stress is equal or greater than the material's yield stress then the material will yield. As seen from **Figure 4B**, the stresses have increased linearly with the increase in the applied force. The estimated failure stresses were 13.75 N for the ABS material and 28.3 N for the PLA material.

When a 10 N load was applied to the PLA finger, the maximum stress obtained from the numerical analysis was 17.90 MPa (cf. **Figure 4B**). If we assume that the finger will have 50 cyclic movements per day, the finger will experience 18,250 cycles per year. Using the endurance limit for the PLA material (**Figure 4C**),

this finger can withstand 3×10^5 cycles before failure, which is equivalent to 16 years (Table 8).

In the FE modeling, the tension force was applied to the non-elastic cable. Numerical results showed that the maximum stress obtained on the non-elastic cable was 100 MPa at 28 N of tension loading. The other stresses obtained at each load were tabulated in Table 9. However, from the product's specification sheet, the cable can hold up to 1,570 MPa at 440 N of tension loading. It can be concluded that no failure will occur at the cable unless there are other external conditions, such as tearing from the friction developed between the cable and the plastic material.

4.4. Production Cost

The total cost for producing one unit of a 3D printed hand was calculated to be \$18.72. The three major contributors to the total cost were the equipment cost per hour (C_{EQ}), raw material cost per hand (C_{RM}), and labor cost per hour (C_{LA}). The maintenance cost per hour (C_{MA}) and energy cost per hour (C_{EN}) have minimal contribution to the overall cost. The C_{EQ} can be reduced by producing multiple hands at the same time (cf. Rickenbacher et al., 2013; Piili et al., 2015). The C_{RM} cost can be decreased by ordering large quantities directly from key suppliers.

5. DISCUSSION AND CONCLUSION

5.1. The Importance of 3D Printing for Prosthesis

The absence of limbs from congenital reasons or from warfare can have devastating physical, psychological and socio-economic consequences (McKechnie and John, 2014; Griffet, 2016). For the war-wounded children, the consequences go beyond their impaired capacity to play, perform chores, and to care for oneself. Their loss of limbs can leave them with various social issues as well as mental disorders: post-traumatic stress disorders, generalized anxiety disorder, depression, and cognitive disorders (Betancourt et al., 2011; Hemmati et al., 2015). The thousands of children maimed by war each year have limited access to prosthesis services and it may take up to 10 years before a prosthetic limb can be fitted (Santa Barbara, 2006).

TABLE 8 | The life cycle of the ABS and PLA prosthetic fingers with respect to the load.

Material	5 N	10 N	15 N	20 N	25 N
ABS	1×10^6 (no failure)	7×10^4 (4 yrs)	Fail	Fail	Fail
PLA	5×10^6 (no failure)	3×10^5 (16 yrs)	7×10^4 (4 yrs)	2×10^4 (1 yr)	7.5×10^3 (0.5 yr)

TABLE 9 | Axial stresses from the applied load on the cable.

Applied load (N)	5	10	15	20	25	28
Axial stress (MPa)	17.8	35.7	53.6	71.4	89.3	100.0

The emergence of 3D printing has opened many opportunities for artificial hands for assistive purposes (Tian et al., 2017; Negrello et al., 2020). This paper endeavored to answer whether the openly accessible designs of body-powered 3D printed prosthetic hands are suitable and affordable for the harsh environmental conditions of the war-wounded. There were four aspects that were evaluated: grasping poses, the range of motion of the grasps and the analysis of the corresponding cable lengths, the failure analysis in the various critical components of the 3D printed hand, and the cost of production.

5.2. Human vs. Prosthetic Hand: Differences in Grasping Movements

The human hand can perform 33 grasp types due to the various combination of movements that it can do (Figure 5). The human hand is capable of the adduction/abduction of the five fingers with the radial adduction/abduction of the thumb, the flexion/extension of the five fingers with adduction/abduction of the palm, and the reposition/opposition of the thumb with the bending/flattening of the palm. On the contrary, the fingers of the 3D printed hand are only capable of flexion and extension on a flat palm design. It is noteworthy to mention that the four fingers of the 3D printed hand can achieve the flexion and extension angles of up to 90° in both of the PIP and MCP joints, which are similar to the human hand (cf. Figure 3D). While the thumb can perform extension and flexion, the thumb is unable to perform reposition/opposition in addition to the palm's inability to flex. The current 3D printed hand and similar prosthetic hand designs were limited to perform only 3 out of 33 grasps (i.e., palmar pinch, inferior pincer grasp and lateral grasp). The grasping postures of the investigated 3D printed hand were severely limited by the hand's structural design.

However, it may not be necessary to aim for a complete replication of the 33 grasps due to the cost constraints. An increase in the degrees of freedom and functionality has an implication on the increased complexity of the prosthetic hand. A complicated prosthetic hand can lead to an increase in the non-usage rate. In a future work, we can ask children with missing upper limbs on the priority of tasks that they wish they can do, a matter so far poorly taken care of in the literature. Thus, a balance for optimal design and affordable cost needs to be further investigated.

5.3. Robustness of 3D Printed Hands for Environments With Limited Resources

A mechanical apparatus that serves as a user's interface to various objects in the environment on a daily basis will tend to fail. A failure analysis of this interface (i.e., a prosthetic hand) becomes more relevant when the filament materials used for the 3D printing process are polymers. Ideally, prosthetic hands should be able to perform the basic grasping activities of daily living without failure.

Based on our results, the average life expectancy was found to be 4 years under light daily activities. Small, lightweight items like paper, ball, and cards are within the expected loading cycles (Table 8). Usually, such prostheses are designed for children who

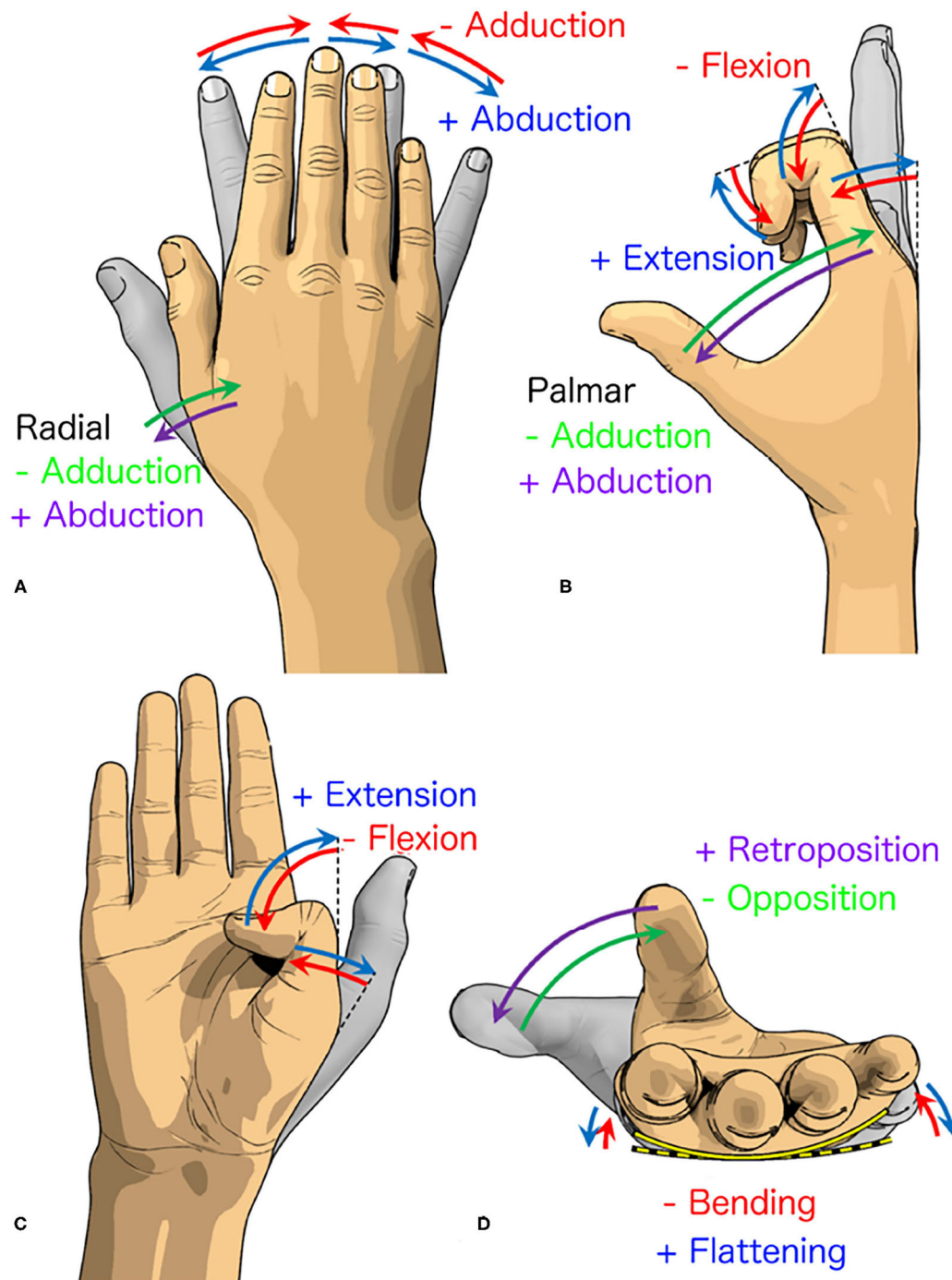


FIGURE 5 | Various movements of the fingers. **(A)** The radial abduction/adduction of the thumb and the relative abduction/adduction of the remaining fingers. **(B)** The palmar abduction/adduction of the thumb and the flexion/extension of the remaining fingers. **(C)** The flexion/extension of the remaining thumb joints. **(D)** The opposition/retroposition of the thumb and the bending/flattening of the palm. The blue/purple and red/green arrows indicate the positive and negative directions, respectively.

are still in the development stage and a continuous size upgrade is needed. Thus, the durability of these hands may not be crucial. Our results showed that the PLA material cannot be subjected to heavy loads (i.e., more than 28 N).

From a consumer psychology perspective, it can be argued that the repeated replacement of a device might decrease the trust in a device's functionality and reliability. To mitigate this issue, we anticipate to use a better structural materials, which

can last longer and require less replacement. New materials with high strength (e.g., thermoplastic elastomers, nylon, polyvinyl alcohol) are expected to boost the confidence in this device. With improved designs of 3D printing extruders to process new materials, more improvements can be added to enhance the load capacity, grasping ability, and the appearance of this type of prosthetic hand.

The non-elastic cable's load capacity is high and is unlikely to fail (**Table 9**). On the other hand, the elastic cables are more likely to lose their elasticity with time, which makes the return motion slower or unreachable. The periodic replacement of these low-cost cables can solve this issue. The condition on the failure of the cables due to friction was not conducted. Simulating this condition will depend on the surface finish of the printed hand (i.e., related to the 3D printer's quality) and this cannot be considered in our analysis because we would not be able to predict which 3D printer will be used by those in the war zones. Spare cables and elastic cords can be provided to the users so they can make the replacements when necessary.

5.4. Cost Considerations for Low-Resource Countries and Host Countries for Refugees

The design characteristics of conventional upper limb prosthesis are incompatible to the design requirements in locations where there is a lack of power supply, scarce resources, and zero options for warranties. The on-site production of prosthesis parts would significantly reduce the cost and time of shipping and delivery, and provide a higher level of accuracy.

The emergence of 3D scanning and printing is minimizing the dependence on highly-trained prosthetists in conflict zones. In the traditional prosthesis fabrication process, which rely on molding and casting, there needs to be some adjustments on fitting the resulting prosthesis to the amputee. The reason for that additional process was that the procedure to obtain the measurements was already flawed at the start. In the conventional process, the amputee would be asked to submerge the stump in gypsum plaster (plaster of Paris) or alginate. The stump, due to its compliant tissue, has already been deformed in the process (Cabibihan, 2011; Cabibihan et al., 2011). The ideal procedure is a non-contact way to obtain the data (i.e., 3D scanning). The 3D scanning approach is compatible with the 3D printing procedure.

In developed countries, the cost for conventional upper limb prostheses is from \$1,500 to as high as \$75,000. For such amount, there is the risk that the materials used in the prosthesis can be repurposed or bartered in case they are provided freely in conflict zones. With a basic 3D printed prosthetic hand costing as low as \$19, prosthesis providers in developing countries and in those countries hosting refugees could find such options to be attractive.

5.5. Limitations and Future Work

The primary use of an upper limb prosthetic device is to let the user live without stigma. Both the prosthesis user and the people around the user give importance to the appearance of the prosthesis (Scotland and Galway, 1983). The current paper did not address the appearance of the prosthesis. Amidst a healthcare sector that is facing economic difficulties due to donor fatigue

after almost a decade of conflict in areas like in Syria, the focus of the paper was in the technical evaluation of the benefits and limitations of the current 3D printed prosthetic hand designs. The current designs were intended to be affordable alternatives to the more expensive, traditional methods of manufacturing. Future work can address the fitting of a glove and its coloration.

In war-affected and low-resources countries, the main advantages of 3D printed prosthetic hands are in the portability of the 3D printers, the cost-effectiveness of the material, the possibility of on-site production, the amputee-specific design, and the low maintenance cost. These prosthetic hands are still not satisfactory for functional tasks for a user's daily activities and are not replacements for other improved and advanced designs. This type of prosthetic design and production technique must not be media-hyped because the users might expect too much. This is a temporary solution, but 3D printed prosthetics can still help the users in their basic daily activities and improve their self-confidence. With the exception of the motors, some of the elements we investigated here are also present in other mechatronic prosthetic hands. If resources are available and if the users so desire, further enhancements can be done by the inclusion of robotic elements in the prosthetic hand. The results presented herein serve as a baseline study to advance the development of prosthetic hands that are functional yet low-cost.

DATA AVAILABILITY STATEMENT

The original contributions presented in the study are included in the article/**Supplementary Material**, further inquiries can be directed to the corresponding author/s.

AUTHOR CONTRIBUTIONS

J-JC, FA, and EM conceived and designed the study. FA and MM performed the experiments. LL and KD arranged and conducted the field interviews and analyzed the users' feedback. OA-K developed the cost model. J-JC, FA, MM, and EM analyzed the data and interpreted the results. All authors wrote and contributed to the final version of the manuscript and approved the submission.

FUNDING

This work was supported by a research grant from Qatar University under the grant no. IRCC-2019-001.

ACKNOWLEDGMENTS

We wish to thank AM El Noamany for the illustrations of the human hand poses.

SUPPLEMENTARY MATERIAL

The Supplementary Material for this article can be found online at: <https://www.frontiersin.org/articles/10.3389/frobt.2020.594196/full#supplementary-material>

REFERENCES

- Alhaddad, A. Y., Alkhatib, S. E., Khan, R. A., Ismail, S. M., Shehadeh, A.-S. S., Sadeq, A. M., et al. (2017). "Toward 3D printed prosthetic hands that can satisfy psychosocial needs: grasping force comparisons between a prosthetic hand and human hands," in *International Conference on Social Robotics* (Cham: Springer), 304–313. doi: 10.1007/978-3-319-70022-9_30
- Alkhatib, F., Cabibihan, J. J., and Mahdi, E. (2019a). Data for benchmarking low-cost, 3D printed prosthetic hands. *Data Brief* 25:104163. doi: 10.1016/j.dib.2019.104163
- Alkhatib, F., Mahdi, E., and Cabibihan, J. J. (2019b). "Design and analysis of flexible joints for a robust 3D printed prosthetic hand," in *2019 IEEE 16th International Conference on Rehabilitation Robotics (ICORR)* (Toronto, ON), 784–789. doi: 10.1109/ICORR.2019.8779372
- Alturkistani, R., A., K., Devasahayam, S., Thomas, R., Colombini, E. L., Cifuentes, C. A., Homer-Vanniasinkam, S., et al. (2020). Affordable passive 3D-printed prosthesis for persons with partial hand amputation. *Prosthet. Orthot. Int.* 44, 92–98. doi: 10.1177/0309364620905220
- American Orthotic and Prosthetic Association (2015). *AOPA Statement on 3-D Printing in Prosthetics*. AOPA, VA.
- Arabian, A. (2014). *Falcon Hand V2*. Available online at: <https://www.thingiverse.com/thing:603039> (accessed December 05, 2018).
- Arabian, A., Varotsis, D., McDonnell, C., and Meeks, E. (2016). "Global social acceptance of prosthetic devices," in *Global Humanitarian Technology Conference (GHTC)* (Seattle, WA), 563–568. doi: 10.1109/GHTC.2016.7857336
- ASTM D638-14 (2014). *Standard Test Method for Tensile Properties of Plastics*. West Conshohocken, PA: ASTM International.
- Betancourt, T. S., Borisova, I. I., de la Soudière, M., and Williamson, J. (2011). Sierra leone's child soldiers: war exposures and mental health problems by gender. *J. Adolesc. Health* 49, 21–28. doi: 10.1016/j.jadohealth.2010.09.021
- Bevington, M. (2015). *Syrian Crisis Situation Update January 2015*. Handicap International, MD.
- Biddis, E., Bogoch, E., and Meguid, S. (2004). Three-dimensional finite element analysis of prosthetic finger joint implants. *Int. J. Mech. Mater. Des.* 1, 317–328. doi: 10.1007/s10999-005-3308-3
- Birglen, L., Lalibert, T., and Gosselin, C. M. (2008). *Underactuated Robotic Hands, 1st Edn*. Berlin: Springer Publishing Company, Inc. doi: 10.1007/978-3-540-77459-4
- Bryant, J. (2016). *Phoenix Hand V2*. Available online at: <http://enablingthefuture.org/phoenix-hand/> (accessed December 05, 2018).
- Burn, M. B., Ta, A., and Gogola, G. R. (2016). Three-dimensional printing of prosthetic hands for children. *J. Hand Surg.* 41, e103–e109. doi: 10.1016/j.jhbs.2016.02.008
- Cabibihan, J.-J. (2011). Patient-specific prosthetic fingers by remote collaboration—a case study. *PLoS ONE* 6:e19508. doi: 10.1371/journal.pone.0019508
- Cabibihan, J.-J., Joshi, D., Srinivasa, Y. M., Chan, M. A., and Muruganantham, A. (2015). Illusory sense of human touch from a warm and soft artificial hand. *IEEE Trans. Neural Syst. Rehabil. Eng.* 23, 517–527. doi: 10.1109/TNSRE.2014.2360533
- Cabibihan, J.-J., Pradipta, R., and Ge, S. S. (2011). Prosthetic finger phalanges with lifelike skin compliance for low-force social touching interactions. *J. NeuroEng. Rehabil.* 8:16. doi: 10.1186/1743-0003-8-16
- Cabibihan, J. J., Abubasha, M. K., and Thakor, N. (2018). A method for 3-d printing patient-specific prosthetic arms with high accuracy shape and size. *IEEE Access* 6, 25029–25039. doi: 10.1109/ACCESS.2018.2825224
- Cabibihan, J. J., Carrozza, M. C., Dario, P., Pattofatto, S., Jomaa, M., and Benallal, A. (2006a). "The Uncanny Valley and the search for human skin-like materials for a prosthetic fingertip," in *2006 6th IEEE-RAS International Conference on Humanoid Robots* (Genova), 474–477. doi: 10.1109/ICHR.2006.321315
- Cabibihan, J. J., Chauhan, S. S., and Suresh, S. (2014). Effects of the artificial skin's thickness on the subsurface pressure profiles of flat, curved, and braille surfaces. *IEEE Sensors J.* 14, 2118–2128. doi: 10.1109/JSEN.2013.2295296
- Cabibihan, J. J., Pattofatto, S., Jomaa, M., Benallal, A., Carrozza, M. C., and Dario, P. (2006b). "The conformance test for robotic/prosthetic fingertip skins," in *IEEE/RAS-EMBS International Conference on Biomedical Robotics and Biomechanics, 2006* (Pisa), 561–566.
- Caliskan, S., Lekesiz, H., Karaca, A., and Yildiz, A. (2016). "Fatigue properties of ABS thermoplastics used in exterior lighthing," in *17th International Conference on Machine Design and Production* (Bursa).
- Corke, P. (2017). *Robotics, Vision and Control: Fundamental Algorithms in MATLAB, Vol. 118*. Springer. doi: 10.1007/978-3-319-54413-7
- Czeizel, A. E. (2005). Birth defects are preventable. *Int. J. Med. Sci.* 2, 91–92. doi: 10.7150/ijms.2.91
- Deimel, R., and Brock, O. (2016). A novel type of compliant and underactuated robotic hand for dexterous grasping. *Int. J. Robot. Res.* 35, 161–185. doi: 10.1177/0278364915592961
- e-NABLE Community (2014). *Raptor Reloaded Hand*. Available online at: <http://enablingthefuture.org/upper-limb-prosthetics/raptor-reloaded/> (accessed December 05, 2018).
- Ezeh, O., and Susmel, L. (2019). Fatigue strength of additively manufactured polylactide (pla): effect of raster angle and non-zero mean stresses. *Int. J. Fatigue* 126, 319–326. doi: 10.1016/j.ijfatigue.2019.05.014
- Feix, T., Romero, J., Ek, C. H., Schmiedmayer, H., and Kragic, D. (2013). A metric for comparing the anthropomorphic motion capability of artificial hands. *IEEE Trans. Robot.* 29, 82–93. doi: 10.1109/TRO.2012.2217675
- Feix, T., Romero, J., Schmiedmayer, H., Dollar, A. M., and Kragic, D. (2016). The grasp taxonomy of human grasp types. *IEEE Trans. Hum. Mach. Syst.* 46, 66–77. doi: 10.1109/THMS.2015.2470657
- Greene, S., Lipson, D., Soe, A. H., and Mercado, A. (2016). *Design and Manufacture of a Scalable Prosthetic Hand Through the Utilization of Additive Manufacturing*. Undergraduate Thesis for Worcester Polytechnic Institute, Worcester, MA.
- Griffet, J. (2016). Amputation and prosthesis fitting in paediatric patients. *Orthop. Traumatol.* 102, 161–175. doi: 10.1016/j.otsr.2015.03.020
- Hallquist, J. O. (1993). *LS-DYNA3D Theoretical Manual*. Livermore, CA: Livermore Software Technology Corporation.
- Hemmati, M. A., Shokoohi, H., Masoumi, M., Khateri, S., Soroush, M., Modirian, E., et al. (2015). Mental health disorders in child and adolescent survivors of post-war landmine explosions. *Milit. Med. Res.* 2:30. doi: 10.1186/s40779-015-0052-3
- Hirons, R. R., Williams, K. B., Amor, R. F., and Day, H. J. B. (1991). The prosthetic treatment of lower limb deficiency. *Prosthet. Orthot. Int.* 15, 112–116. doi: 10.3109/03093649109164645
- Hull, C. (1986). *Apparatus for Production of Three-Dimensional Objects by Stereolithography*. Google Patents. US Patent 4,575,330, Arcadia, CA.
- Jones, L. A., and Lederman, S. J. (2006). *Human Hand Function, Vol. 1*. New York, NY: Oxford University Press. doi: 10.1093/acprof:oso/9780195173154.001.0001
- Kapandji, I. A. (2016). *The Physiology of the Joints, Vol. 1*. New York, NY: Churchill Livingstone.
- Keuster, E. (2015). *K-1 Hand*. Available online at: <http://enablingthefuture.org/k-1-hand/> (accessed December 05, 2018).
- Korkmaz, M., Erbahçeci, F., Ulger, O., and Topuz, S. (2012). Evaluation of functionality in acquired and congenital upper extremity child amputees. *Acta Orthop. Traumatol. Turcica* 46, 262–268. doi: 10.3944/AOTT.2012.2631
- Krebs, D. E., Edelstein, J. E., and Thornby, M. A. (1991). Prosthetic management of children with limb deficiencies. *Phys. Ther.* 71, 920–934. doi: 10.1093/ptj/71.12.920
- Kuiken, T. A., Miller, L. A., Turner, K., and Hargrove, L. J. (2016). A comparison of pattern recognition control and direct control of a multiple degree-of-freedom transradial prosthesis. *IEEE J. Transl. Eng. Health Med.* 4, 1–8. doi: 10.1109/JTEHM.2016.2616123
- Masada, K., Tsuyuguchi, Y., Kawabata, H., Kawai, H., Tada, K., and Ono, K. (1986). Terminal limb congenital malformations: analysis of 523 cases. *J. Pediatr. Orthop.* 6, 340–345. doi: 10.1097/01241398-198605000-00015
- Mckechnie, P. S., and John, A. (2014). Anxiety and depression following traumatic limb amputation: a systematic review. *Injury* 45, 1859–1866. doi: 10.1016/j.injury.2014.09.015
- Mollica, F., and Ambrosio, L. (2009). *The Finite Element Method for the Design of Biomedical Devices*. Milan: Springer Milan, 31–45. doi: 10.1007/978-88-470-1195-3_3
- Negrello, F., Stuart, H. S., and Catalano, M. G. (2020). Hands in the real world. *Front. Robot. AI* 6:147. doi: 10.3389/frobt.2019.00147

- Owen, J. (2017). *Cam's 3D Printed Hand Journey*. Available online at: <http://enablingthefuture.org/2017/08/20/cams-3d-printed-hand-journey/> (accessed December 02, 2018).
- Physicians for Human Rights (2015). *Syria's Medical Community Under Assault*. New York, NY.
- Piili, H., Happonen, A., Vaisto, T., Venkataramanan, V., Partanen, J., and Salminen, A. (2015). Cost estimation of laser additive manufacturing of stainless steel. *Phys. Proc.* 78, 388–396. doi: 10.1016/j.phpro.2015.11.053
- Resnik, L., Acluche, F., Borgia, M., Latlief, G., and Phillips, S. (2019). EMG pattern recognition control of the Deka arm: Impact on user ratings of satisfaction and usability. *IEEE J. Transl. Eng. Health Med.* 7, 1–13. doi: 10.1109/JTEHM.2018.2883943
- Resnik, L., Meucci, M. R., Lieberman-Klinger, S., Fantini, C., Kelty, D. L., Disla, R., et al. (2012). Advanced upper limb prosthetic devices: implications for upper limb prosthetic rehabilitation. *Arch. Phys. Med. Rehabil.* 93, 710–717. doi: 10.1016/j.apmr.2011.11.010
- Rickenbacher, L., Spierings, A., and Wegener, K. (2013). An integrated cost model for selective laser melting (SLM). *Rapid Prototyp. J.* 19, 208–214. doi: 10.1108/13552541311312201
- Santa Barbara J. (2006). Impact of war on children and imperative to end war. *Croat. Med. J.* 47, 891–894.
- Scotland, T., and Galway, H. (1983). A long-term review of children with congenital and acquired upper limb deficiency. *J. Bone Joint Surg.* 65-B, 346–349. doi: 10.1302/0301-620X.65B3.6841409
- Sullivan, M., Oh, B., and Taylor, I. (2017). *3d Printed Prosthetic Hand. Mechanical Engineering Design Project Class*, 65. Available online at: <https://openscholarship.wustl.edu/mems411/65> (accessed October, 2018).
- ten Kate, J., Smit, G., and Breedveld, P. (2017). 3D-printed upper limb prostheses: a review. *Disabil. Rehabil.* 12, 300–314. doi: 10.1080/17483107.2016.1253117
- Tian, L., Magnenat Thalmann, N., Thalmann, D., and Zheng, J. (2017). The making of a 3d-printed, cable-driven, single-model, lightweight humanoid robotic hand. *Front. Robot. AI* 4:65. doi: 10.3389/frobt.2017.00065
- United Nations General Assembly Security Council (2018). *Children and Armed Conflict — Report of the Secretary-General*. New York, NY: United Nations.
- United States Department of Justice (2010). *Guidance on the 2010 ADA Standards for Accessible Design ADA*. Available online at: https://www.ada.gov/regs2010/2010ADASTandards/Guidance_2010ADASTandards_prt.pdf (accessed December 02, 2018).
- van der Riet, D., Stopforth, R., Bright, G., and Diegel, O. (2013). “An overview and comparison of upper limb prosthetics,” in *2013 Africon* (Pointe-Aux-Piments), 1–8. doi: 10.1109/AFRCON.2013.6757590
- Vannah, W. M., Davids, J. R., Drvaric, D. M., Setoguchi, Y., and Oxley, B. J. (1999). A survey of function in children with lower limb deficiencies. *Prosthet. Orthot. Int.* 23, 239–244. doi: 10.3109/03093649909071640
- Vasluian, E., van der Sluis, C. K., van Essen, A. J., Bergman, J. E. H., Dijkstra, P. U., Reinders-Messelink, H. A., et al. (2013). Birth prevalence for congenital limb defects in the northern Netherlands: a 30-year population-based study. *BMC Musculoskel. Disord.* 14:323. doi: 10.1186/1471-2474-14-323
- Vujaklija, I., and Farina, D. (2018). 3D printed upper limb prosthetics. *Expert Rev. Med. Dev.* 15, 505–512. doi: 10.1080/17434440.2018.1494568
- Wood, S. (2014) *Flexy Hand 2*. Available online at: <http://enablingthefuture.org/upper-limb-prosthetics/the-flexy-hand/> (accessed December 02, 2018).
- Zuniga, J. (2015). *Cyborg Beast with Increased Wrist Movement*. Available online at: <http://www.cyborgbeast.org/devices/> (accessed December 02, 2018).

Conflict of Interest: The authors declare that the research was conducted in the absence of any commercial or financial relationships that could be construed as a potential conflict of interest.

Copyright © 2021 Cabibihan, Alkhatib, Mudassir, Lambert, Al-Kwafi, Diab and Mahdi. This is an open-access article distributed under the terms of the Creative Commons Attribution License (CC BY). The use, distribution or reproduction in other forums is permitted, provided the original author(s) and the copyright owner(s) are credited and that the original publication in this journal is cited, in accordance with accepted academic practice. No use, distribution or reproduction is permitted which does not comply with these terms.



3D Scanning of the Forearm for Orthosis and HMI Applications

Joel C. Perry*, Jacob R. Brower, Robert H. R. Carne and Melissa A. Bogert

Department of Mechanical Engineering, University of Idaho, Moscow, ID, United States

OPEN ACCESS

Edited by:

Carlos Rodriguez-Guerrero,
Vrije University Brussel, Belgium

Reviewed by:

Kevin Langlois,
Vrije University Brussel, Belgium
Jacopo Zenzeri,
Italian Institute of Technology (IIT), Italy

*Correspondence:

Joel C. Perry
jperry@uidaho.edu

Specialty section:

This article was submitted to
Biomedical Robotics,
a section of the journal
Frontiers in Robotics and AI

Received: 27 June 2020

Accepted: 26 February 2021

Published: 14 April 2021

Citation:

Perry JC, Brower JR, Carne RHR and
Bogert MA (2021) 3D Scanning of the
Forearm for Orthosis and HMI
Applications.
Front. Robot. AI 8:576783.
doi: 10.3389/frobt.2021.576783

The rise of rehabilitation robotics has ignited a global investigation into the human machine interface (HMI) between device and user. Previous research on wearable robotics has primarily focused on robotic kinematics and controls but rarely on the actual design of the physical HMI (pHMI). This paper presents a data-driven statistical forearm surface model for designing a forearm orthosis in exoskeleton applications. The forearms of 6 subjects were 3D scanned in a custom-built jig to capture data in extreme pronation and supination poses, creating 3D point clouds of the forearm surface. Resulting data was characterized into a series of ellipses from 20 to 100% of the forearm length. Key ellipse parameters in the model include: normalized major and minor axis length, normalized center point location, tilt angle, and circularity ratio. Single-subject (SS) ellipse parameters were normalized with respect to forearm radiale-styilion (RS) length and circumference and then averaged over the 6 subjects. Averaged parameter profiles were fit with 3rd-order polynomials to create combined-subjects (CS) elliptical models of the forearm. CS models were created in the jig as-is (CS1) and after alignment to ellipse centers at 20 and 100% of the forearm length (CS2). Normalized curve fits of ellipse major and minor axes in model CS2 achieve R^2 values ranging from 0.898 to 0.980 indicating a high degree of correlation between cross-sectional size and position along the forearm. Most other parameters showed poor correlation with forearm position ($0.005 < R^2 < 0.391$) with the exception of tilt angle in pronation (0.877) and circularity in supination (0.657). Normalized RMSE of the CS2 ellipse-fit model ranged from 0.21 to 0.64% of forearm circumference and 0.22 to 0.46% of forearm length. The average and peak surface deviation between the scaled CS2 model and individual scans along the forearm varied from 0.56 to 2.86 mm (subject averages) and 3.86 to 7.16 (subject maximums), with the peak deviation occurring between 45 and 50% RS length. The developed equations allow reconstruction of a scalable 3D model that can be sized based on two user measures, RS length and forearm circumference, or based on generic arm measurements taken from existing anthropometric databases.

Keywords: 3D arm scanning, standardized orthosis design, physical human-machine interface, ellipse-fit forearm model, 3D point cloud, exoskeleton robotic interface

INTRODUCTION

The prevalence of robotic devices in upper extremity stroke rehabilitation has risen significantly in the last decade. Devices include end-effector designs where a patient is connected to a robot at the hand and/or forearm, and exoskeleton designs where the robot may connect to the user at multiple points along the arm and hand. Exoskeletons mimic the length and structure of human

limb segments in order to move synchronously with the segments during tasks. This requires an intimate human-to-robot connection, also known as a physical human-machine interface (pHMI), in order to distribute loading safely to adjacent biological tissues.

The main goal of a pHMI is to ensure synchronous movement between the user and robot through a comfortable and safe connection. Misalignment between a user and robot are potential comfort and safety issues that can increase the risk of injury (Amigo et al., 2011; Gopura et al., 2016) and lower system performance. Furthermore, misalignment from an offset or improperly sized pHMI can induce high concentrations of load on the skin, resulting in localized oxygen deprivation or cell death. In addition to safety concerns, prolonged discomfort from the physical connection to a robotic device can reduce motivation to train, and impair range of motion as well as robot tracking accuracy, all of which can degrade the performance and effectiveness of the device.

Despite the importance of pHMI design on device function, the methods and specifications associated with developing pHMI components have been largely ignored in published literature. An extensive review reveals that details on the pHMI tend to fall into one of three categories: (a) authors refer to an orthosis but the design is either not described or only briefly described in terms of appearance (Perry et al., 2007; Jarrassé et al., 2008; Klein et al., 2008; Pylatiuk et al., 2009; Gmerek, 2012; Ohnishi et al., 2013; Rohm et al., 2013; Vaca Benitez et al., 2013; Herrnsstadt and Menon, 2016; Sangha et al., 2016); (b) authors describe a generic orthosis design with added compliance to mitigate forces due to misalignment or dissimilarities in anthropometric shape, in which case the design elements focus on kinematics (Jarrassé and Morel, 2012); or (c) authors explain human interface details but do not report on the shape of their orthosis design (Jackson et al., 2007; Rocon et al., 2007; Gupta et al., 2008; Vanderniepen et al., 2009; Ragonesi et al., 2010; Vitiello et al., 2013; Alavi et al., 2017; Ates et al., 2017). In other words, most papers present the mechanical design and/or controller design, but very little content, if any, is focused on the design of the physical interface with the user. In many cases, the design of the pHMI connection to the robot is addressed as an afterthought in comparison to the extensive effort that goes into the kinematic, mechanical, and control system design. However, inadequate attention to the interface components can greatly hamper effectiveness and usability of a wearable or collaborative robot design.

A well-designed pHMI for the forearm should safely and comfortably support the arm throughout the desired range of motion, minimize tracking error, be easy to don and doff, and have reasonable manufacturability. In the traditional approach to orthosis design, an individual's arm is cast and the cast orthosis is then modified to improve comfort in vulnerable regions (Jacobs and Austin, 2014; Coppard and Lohman, 2015; Webster and Murphy, 2018). Although the process achieves an intimate fit with arm geometry, it requires the user's arm during casting, produces a model that may not fit comfortably on other individuals, and takes skilled time to develop. In contrast, a standardized orthosis approach requires an intimate knowledge of the anthropomorphic topology and variations within the target

population. Ideally, a single orthosis that performs well with all users would simplify design, reduce cost, and improve alignment consistency. However, a single standardized orthosis means that some level of fit (e.g., tightness and coverage) must be sacrificed in order to accommodate a wider range of individuals.

In order to develop a design tool to assist in the development of standardized orthoses, knowledge of arm shape, deformation, and movement patterns throughout the desired range of motion are needed. Existing data on forearm shape, including effects of pronation and supination movements, were not found in the literature. Therefore, a set of experiments were designed and conducted as outlined in Section Materials and Methods. The aim of the experiments was to gather scanned point cloud data of the forearm with the arm in two poses: (1) a nearly extreme supination pose, and (2) a nearly extreme pronation pose. Point cloud data was normalized, curve-fit with an elliptical model, combined, and used to generate a model of the human forearm for orthosis design purposes. The normalized results, presented in Section Results, characterize the general shape of the forearm and develop a nondimensionalized, thus scalable, model of the human arm.

MATERIALS AND METHODS

The protocol followed in this study has been approved by the University of Idaho Institutional Review Board (IRB#:19-087). The study involves digital and analog collection of anthropometric forearm data from human subjects ($N = 6$) that represent a convenience sample of the population. The approach taken to quantify arm geometry is based on white-light scanning and ellipse-fit modeling of the human forearm. A commercial white-light scanner was used to capture arm geometry from 6 healthy participants while their upper arm, forearm, and hands were supported in a desired posture using a custom testing apparatus. To evaluate the error of the 3D scanner, an easily measurable base object, a coffee cup, was chosen to have measurements taken by both 3D scanning methods and using Vernier calipers for comparison. Two forearm poses, pronation and supination, were examined with participants attached to the apparatus. The scanned data measurements were fit with ellipses using a least-squares ellipse-fitting code and compared to anthropometer measurement databases.

Testing Apparatus

The relationship between anthropometric landmarks and the rotation axis of the forearm was not found in literature, so a testing apparatus was constructed for this purpose. The apparatus contains a forearm jig, consisting of a support structure and a swiveling handle (**Figure 1**) that mimics the rotational axis commonly used in upper-limb robots to support pronation and supination. The testing structure was composed of two (upper and lower) extruded aluminum beams extending out from a wall. These beams were used to secure the hand and elbow of subjects while allowing line-of-sight access around subject forearms during scanning. The jig setup (**Figure 1**) consisted of a rotational handle with the grip angled 12° from horizontal, as recommend by Tilley (2001). A 12.70-mm diameter ($\frac{1}{2}$ -inch)

steel rod was attached to the handle, aligned vertically through its center, and extended upward through each of two brackets mounted to the upper extruded aluminum beam. A second extruded aluminum beam, directly below the first, held a humeral cradle made of a 12.70-mm ($\frac{1}{2}$ -inch) thick piece of profile-cut plywood covered in 6.35-mm ($\frac{1}{4}$ -inch) thick medical foam. The profile of this cradle was taken from a section of scanned arm and offset to provide clearance for larger arms. A rigid bar, that will be referred to as a “flag,” was clamped to the vertical rod, and two bump stops were fixed to the upper aluminum beam. The flag contacted one stop in supination and the other stop in pronation to provide consistent rotations between subjects. The aluminum beam of the testing structure extended from the wall roughly one meter to allow space to walk around the subject during the scanning process. The interface of the aluminum structure was designed to secure the elbow in the apparatus while enabling wrist pronation and supination. The supination stop was set at roughly 80° of supination and the pronation stop at 40° of pronation representing a functional forearm ROM (Figure 1).

Scanning Procedure

The testing apparatus and forearm was scanned using a Go!SCAN 50, 3D scanner from Creaform. (Creaform Inc, 2015). The object and targets are recognized by the scanner from a coded pattern of light projected from a white light (LED) source and target 3D locations of stickers are reported to the scanning software to further improve accuracy of intra-scan feature alignment (Creaform Inc, 2015). The use of positioning targets reduces scan error by providing a rigid and accurate locating feature. An initial scan of the apparatus marked with adhesive targets provided a starting template to which subsequent arm scans were located by the scanner software. This automatically placed all scans in the same location and orientation with respect to the setup. Targets were placed on the aluminum beams and the scanning aid wand to assist in scan capture. The scanner could not capture targets on both beams at the same time, so the scanning aid wand targets gave the scanner a rigid reference as it scanned down the arm to improve scanner registration. These targets were first scanned without a subject and saved as a template from which subject scans were later run. In this template, a coordinate system was placed with the Z-direction pointing upward through the handle pronosupination rotation axis (defined as the axis of a cylinder made from sampled scan points of the rod). The origin was located on the bottom side of the upper aluminum beam, and the positive X-direction was placed normal to the side face of the aluminum beam toward the subject (Figure 1B).

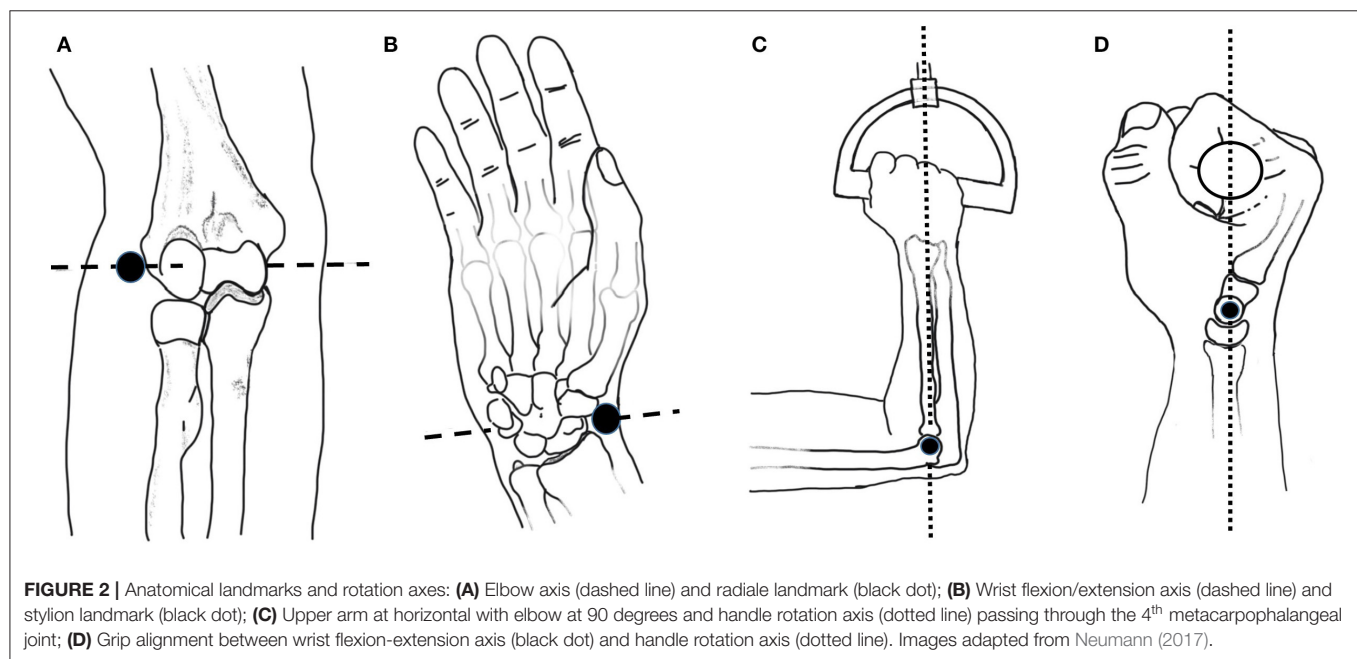
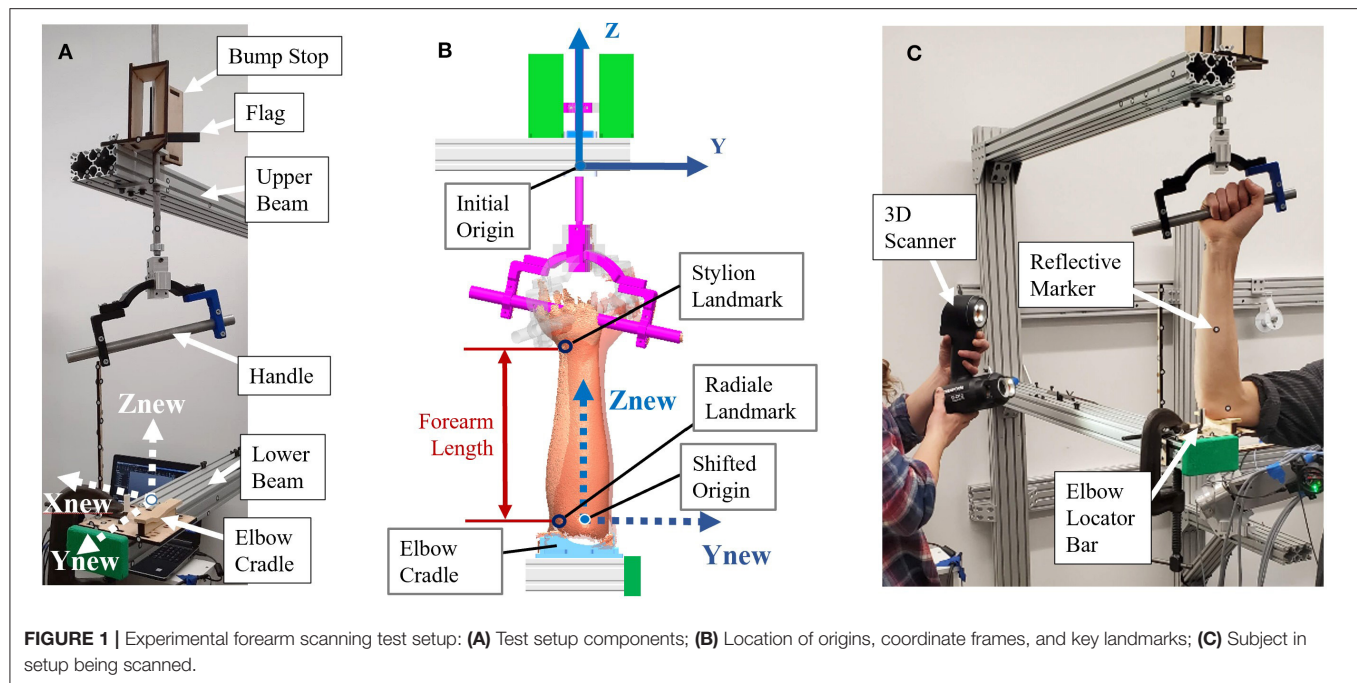
Five males and one female between the ages of 22 and 41 participated in the arm scan study and represent a convenience sample of the general population. During a pre-scanning procedure, optical positioning targets were placed on the subject's arm at the subject's wrist flexion and extension rotational axis, and elbow rotational axis as estimated by the radiale and stylium landmarks, respectively (Figure 2). These landmarks were chosen to lie along the radial and ulnar centerlines in supination, which have good palpable features and therefore have good

identification and repeatability. The targets were placed in the supination pose with the subject's arm bent to 90° and the palm facing posteriorly to reduce target movement due to skin sliding relative to bone structure between anatomical positions. Radiale-stylium length measures were taken from these landmarks, and forearm circumference measures were taken at the elbow crease in this same pose. Subject anthropometric measures are reported in Table 1. Positioning target stickers placed on the subject's skin in these key locations provide reference points for data analysis. The origin of this system is located at the Z location of the positioning sticker placed on the radiale landmark. The positioning target placed on the stylium landmark was used to trim the dataset. The elbow crease, as determined visually, was also a dataset trimming location.

Each subject scan was performed with the subject's forearm placed in the apparatus in the desired pose. Once positioned, each subject was instructed how to perform the desired movements and encouraged to get comfortable in the jig and swivel between both poses to check for comfort. The subject was also questioned on the comfort of the rotational constraint imposed by the jig. The wrist was left unrestrained and the subject was instructed to try to keep their wrist angle (i.e., flexion/extension) the same during the experiment while maintaining a consistent elbow location between scans. The chair height was adjusted to allow the upper arm to be horizontal and the elbow at 90° in the setup (Figure 2C). In the coronal plane, the subject's wrist and elbow rotational centers were aligned with the rotational axis (Figure 2D). The subject's upper arm was placed in the humeral cradle to help maintain elbow position. A locator bar was adjusted to contact the subject's anterior elbow surface, and the subject was directed to maintain contact with the bar during scanning.

Scanning was done in two stages to allow the operator to completely scan the forearm. One stage swept from the left side of the subject clockwise to the aluminum beam, and the other stage swept from subject side of the aluminum beam to the right side of the subject. Each stage started with scanning setup targets to initialize the new stage and then was swept continuously from top to bottom. Coverage from each stage was overlapped to ensure a complete surface was captured. The handle of the setup jig was set at a fixed value of $\sim 12^\circ$, so the orientation of the wrist deviation axis was considered to remain constant. Subjects were scanned once in supination and once in pronation. One subject participated in a repeated scan study in which supination was scanned twice, then pronation twice, and then supination and pronation were each scanned a final time. During the repeated scan study, the subject remained in the setup the whole time, alternating between poses when instructed. Subjects were instructed to maintain a pose while the scan data was visually checked for holes and completeness and rescanned as needed before the being allowed to move.

Scans were taken and processed using a proprietary software for Creaform scanners (VXElements VX8). The “semi-rigid positioning” and “use natural features” settings within the VXElements software were selected to normalize data point spread and improve scan registration. The



“semi-rigid positioning” setting allows extra error in the scanner registration algorithm to accommodate scanning people because people move slightly even when trying to remain still (Crennen, 2017). The “use natural features” setting lets the scanner use features it scans as registration landmarks (Creaform Inc, 2015). Scanner resolution was set at 0.500 mm. 3D mesh geometry of the object is created in VXmodel by the software from each camera frame captured by the scanner.

Anthropometric Measurements

Numerous anthropometric databases are available that provide general measures of size, shape, and composition for particular populations (National Center for Health Statistics, 2011; Gordon et al., 2014; Fryar et al., 2016; Löffler-Wirth et al., 2016). However, the data provided lacks the information necessary to design for a close fit with arm topography. Bone, muscle, skin, and subcutaneous tissue are the main components that make up the resulting peripheral shape. As the arm and underlying bones

TABLE 1 | The anthropometric data collected from the six subjects in the study.

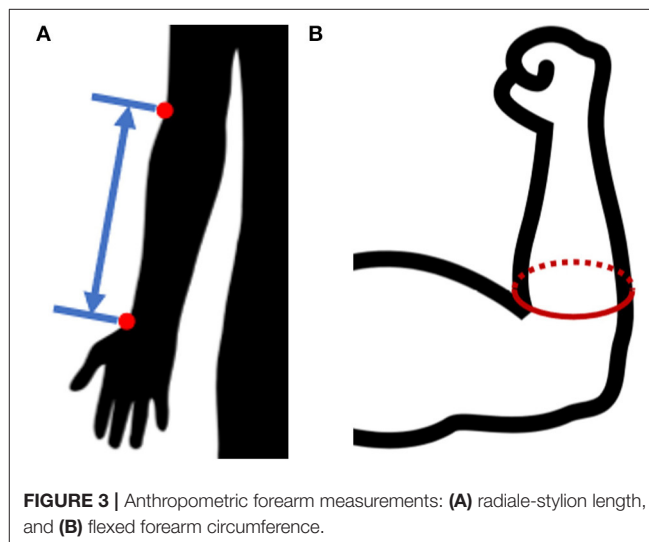
Subject no.	Height (m)	BMI (kg/m ²)	Radiale-Stylelon length (mm)	Relaxed forearm circumference (mm)	Flexed forearm circumference (mm)	Wrist circumference (mm)
1	1.778	24.0	251	296	306	-
2	1.562	24.7	239	269	269	162
3	1.575	28.1	228	279	279	150
4	1.702	19.9	243	268	272	161
5	1.807	22.8	233	268	275	161
6	1.949	20.2	275	283	286	171

(i.e., radius and ulna) move, the muscles involved in their movement change shape and location. These structures play an integral part in determining how well a user's arm will fit a particular orthosis.

The present study collected basic anthropometric measures in conjunction with 3D scan data to allow correlation with databases like the 2011-2014 NHANES 3 study by the CDC (Fryar et al., 2016) and the 2012 ANSUR 2 study by the US Army (Gordon et al., 2014). Measures recorded included: age, gender, height, weight, radiale-styilion length (**Figure 3A**), flexed forearm circumference, relaxed forearm circumference, and wrist circumference. Measures were taken following to the procedures laid out in the ANSUR 2 manual (Gordon et al., 2014), using a combination of a measuring tape and a set of jumbo-sized Vernier calipers. Throughout the remainder of the paper, radiale-styilion length, or RS length, will be used to represent forearm length (**Figure 3A**), and forearm circumference will be measured as the circumference around the forearm just above the junction between the upper arm and the forearm (**Figure 3B**). The forearm circumference measure is taken with the upper arm extended horizontally forward, elbow flexed to 90°, and fist clenched with palm facing the head (as outlined in Gordon et al., 2014). All subject data was anonymized by a subject number.

Ellipse Fitting

Scanner datasets are unorganized point clouds and therefore make inefficient surface models. Noise and superfluous data points in the data set have been reduced or removed through regional downsampling and fitting elliptical profiles to the downsampled datasets. Downsampling was achieved by moving the ellipse center to the origin, converting to polar coordinates, and then averaging values within 10° windows around the scan. Once downsampled, elliptical profiles were fit to transverse slices of point cloud scan data along the length of the forearm rotation axis. The ellipse fitting method uses a least-squares ellipse-fitting code written by Gal (2003). Ellipse parameters from fitted ellipses convert 3D coordinates into meaningful 2D shape characteristics as illustrated in **Figure 4**. This 2D approach was continued down the length of the arm modeling thin slices of arm scan data at each of 17 forearm locations from 20 to 100% RS length. At each interval, an ellipse was fit to data spanning a $\pm 1\%$ RS length band. Together, ellipses at normalized arm locations from each subject (**Figure 4A**)

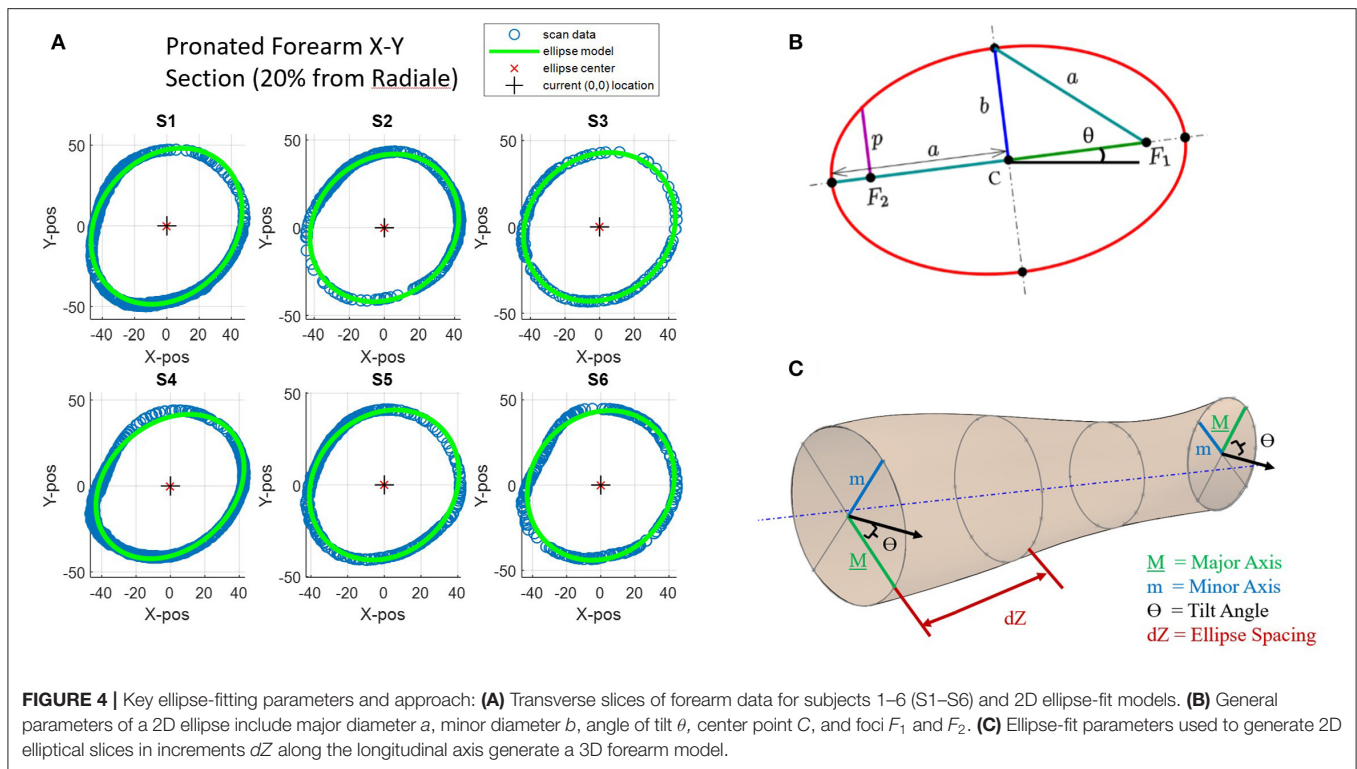


produce a set of ellipse parameters (**Figure 4B**) at each slice that can be used to recreate a 3D surface of forearm geometry (**Figure 4C**). Ellipse parameters were normalized, curve-fit with 3rd-order polynomials as a function of axial distance from the radiale landmark.

Ellipses are conics defined by a common quadratic polynomial and appear many places in nature including planetary orbits. The circle is a special case of an ellipse where the major and minor axes are equal in length. Key parameters of an ellipse (**Figure 4B**) are the center point location (point C), the major axis (dimension a), the minor axis (dimension b), and the foci (points F_1 , F_2) (Downs, 2003). For this experiment, a tilted ellipse is considered, so tilt angle (θ) is also included. A major characteristic not found in **Figure 4** is circularity. Circularity is defined for this study as the ratio of minor axis length (b) to major axis length (a). A circularity value of 1 indicates that the ellipse has equal major and minor axes and is therefore a circle. As the circularity of the ellipse nears 1, the ellipse tilt angles become unstable as small errors in axis lengths can cause large angular errors.

Single-Subject vs. Combined-Subjects Models

Ellipse-fit models were created first for individual subjects, a single-subject (SS) model, based on individual scan data.



Longitudinal slice locations and ellipse center locations for each SS model are normalized based on subject RS length, while ellipse major and minor axes are normalized based on forearm circumference. At each cross-sectional slice, ellipse parameters include: (1) normalized major axis length, (2) normalized minor axis length, (3) normalized center point location in X, (4) normalized center point location in Y, (5) ellipse tilt angle, and (6) circularity ratio. The six normalized SS models were then combined by averaging ellipse parameters into combined-subjects (CS) models.

Two CS models were developed. A first model was based on averaged SS models from the setup as-is (i.e., using the elbow cradle and the self-selected wrist orientation). A second model was developed based on averaged SS models after each SS model had first been re-aligned to common centers near the wrist and elbow. The first combined-subjects model (CS1) assumes the jig rotation axis of the experimental setup represents the anatomical pronosupination axis of each subject and averages out variations in wrist placement to arrive at a general population model. The second combined-subjects model (CS2) first aligns the scans of individuals to common centers at each end of the forearm before averaging ellipse parameters. These alignment locations were chosen at 20 and 100% RS length, as a distance of 20% RS length was reliably above the forearm crease, thereby avoiding scan artifacts from the biceps.

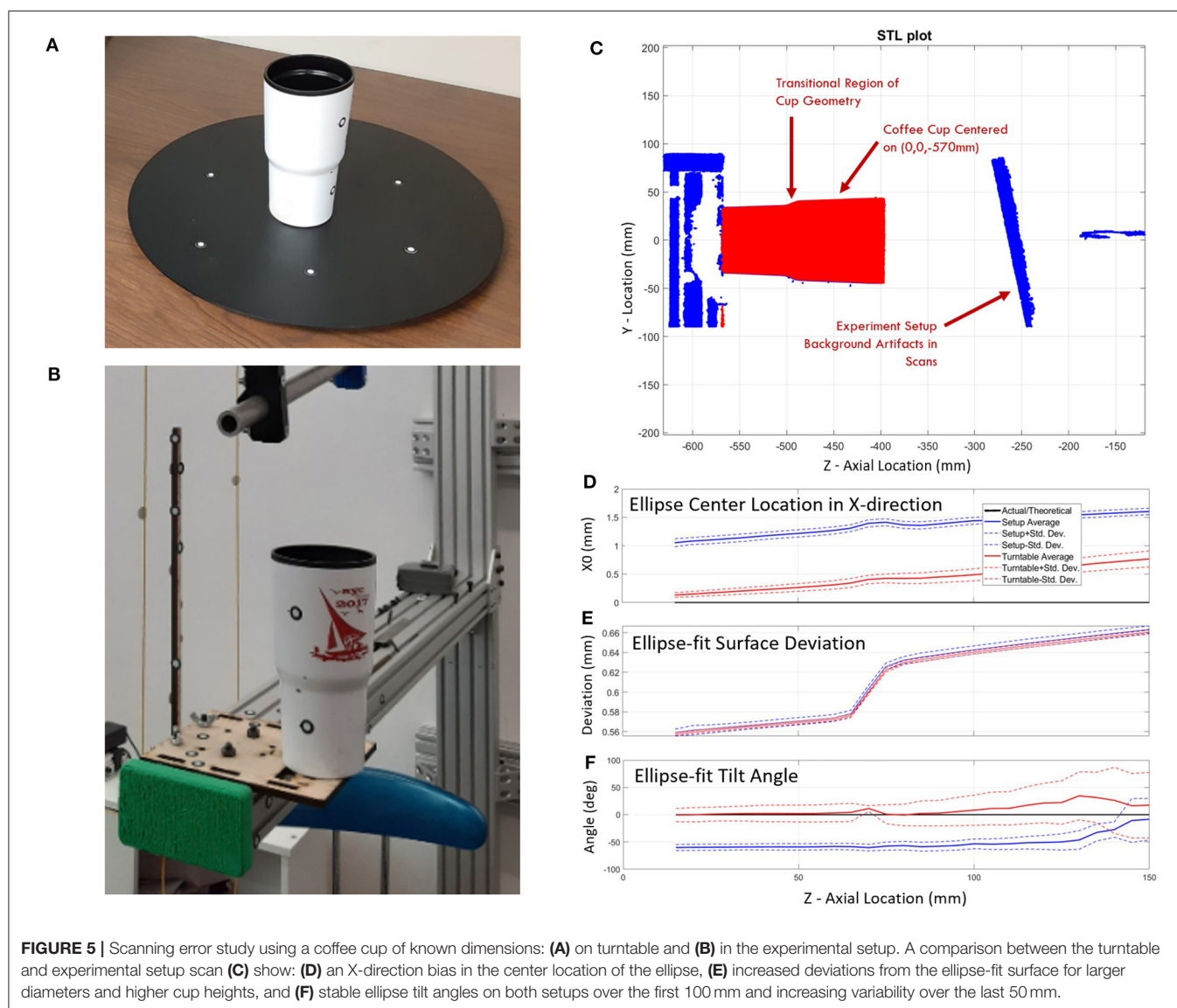
Although the two CS models are largely similar, a significant difference lies in the location of the ellipse center points and their standard deviations. Standard deviations in CS1 provide insight into the variability in self-selected arm placement within

the setup, while the overall model of CS2 provides the best overall representation of normalized forearm shape for development of a generalized forearm model and for use in orthosis design.

Scanning Error Evaluation

The Go!SCAN 50 takes 550,000 measurements per second at a resolution of 0.500 mm with a reported accuracy up to 0.100 mm and a volumetric accuracy of 0.300 mm/m if positioning targets are used and the object presents adequate geometry or color texture (Creaform Inc). Details on how this error was evaluated were not specified, so a static rigid object of measurable size was used to evaluate measurement error in the scanning setup.

Scanner registration error can be largely affected by object shape and visible positioning targets. A test was performed to evaluate the error of the 3D scanner using a stationary object with known dimensions. A coffee cup was chosen for this study as it has a roughly cylindrical shape similar to a human arm. Two scanning methods were used to create the point mesh data of the coffee cup: (1) a traditional scanning method using a turntable, and (2) the experimental setup (Figure 5). The turntable (Figure 5A) represented a well-controlled traditional scanning environment that had six positioning targets with at least three visible to the scanner throughout the scan. The experiment setup (Figure 5B) was less controlled and involved the operator walking around the coffee cup to complete the scan. This setup had obstacles that interrupted the scanner path and limited positioning target visibility. Data points from both studies were run through the ellipse-fitting code



to evaluate the error of the scanner in each environment. Dimensions were also recorded manually from the coffee cup using Vernier calipers.

RESULTS

The results are split into five sections: Error Evaluation, Single-Subject Modeling, Combined-Subjects Modeling, Shape Changes between Pronation and Supination, and Application of the Ellipse-Fit Model. Section Error Evaluation provides the expected error using our proposed method. Section Single Subject (SS) Forearm Modeling illustrates the form of raw data from single subjects and the presence of misalignments. Section Combined-Subjects (CS) Forearm Modeling presents: (a) two types of combined-subjects models, with and without additional alignment, and (b) the primary results of this research in the form of a set of equations that construct a scalable 3D

model of the human forearm. The fourth topic (Section Shape Changes between Pronation and Supination) emphasizes the variation in forearm shape during pronation and supination. Section Application of the Ellipse Fit provides an example of using the forearm model in analyzing the model performance with respect to the scan data and implications on the design of orthoses from the tabulated equations and data from the ANSUR 2 database.

Error Evaluation

Error evaluation included consideration of different scanning approaches and inconsistencies between repeated scans. Error introduced by different scanning methods was evaluated by capturing a static object (a coffee cup) with two different scanning methods, whereas error introduced by the scanner and subject were evaluated by taking repeated scans of the same subject with a single scanning method.

Scanning Method Comparison

The error evaluation study compared scanning accuracy of a plastic coffee cup using two different scanning methods: the traditional turntable scanning method and the experimental scanning method. In the coffee cup experiment, it was assumed that the cup had a perfectly circular cross-section due to perceived quality of manufacturing tolerances. This near perfect circularity would cause unstable ellipse tilt values where small length errors can cause large tilt angle errors. This was seen in the datasets of all experiments as the major-to-minor axis ratio neared 1. Ellipse center coordinates in the X direction showed an average starting bias of 0.13 mm that drifted 0.65 mm over the 150 mm cup length for the turntable setup while the experimental setup showed an average starting bias of 1.06 mm that drifted 0.55 mm over the same distance (**Figure 5D**). Y -direction center coordinates started with average biases of 0.05 and 0.07 mm and drifted to 0.43 and 0.72 mm for the turntable and experimental setup, respectively. The maximum mean deviation between the raw data and the fit ellipses is <0.68 mm (**Figure 5E**). The mean deviation of the data cloud from ellipse-fit is minimal at the lower side of the transitional section of the cup and maximal farthest from the base plane. Deviation grew sharply at the transition feature. The standard deviation of distance from raw data to ellipse fits shows a similar pattern but stays below 0.39 mm. Ellipse axis lengths of both setups were within 2% of diameters found using calipers. The ellipse tilt angle remained relatively stable in both setups (0° for the turntable and -60° for the experimental setup) over the first 100 mm of the cup's axial location and displays a pronounced increase in variability over the last 50 mm (**Figure 5F**).

Error in Repeated Scans

Experimental data captured using a 3D scanner includes scanner instrument error (precision and accuracy), scanning registration errors from arm geometry and positioning target spacing, and inclusion of erroneous data points captured during both voluntary and involuntary human movement (e.g., breathing). A repeatability check measured the error between successive scans of the same individual in the same session (i.e., without leaving the setup). In this check, a randomly selected subject was scanned three times in each pronated and supinated pose to evaluate scanner errors. The subject stayed in the setup the entire time, while attempting to hold the pose and alternate between poses when instructed. Subtle shifts were noticed in targets between repeat scans down the length of the arm. Ellipse parameter data was curve-fit with 3rd-order polynomials, and goodness-of-fit statistics were found for the resulting curve fits to quantify data variation. R^2 values are above 0.93, and root mean square error (RMSE) range from 0.66 to 0.97 mm for distance measurements. Tilt angle RMSE range from 2.5° to 4.0° . These represent baseline variations of the scanner experiment and ellipse-fit method. The study has a mean deviation between raw and ellipse-fit data of <1.5 mm with a standard deviation of <0.8 mm. These values are obtained from an SS model without additional data manipulation for scan alignment.

Single Subject (SS) Forearm Modeling

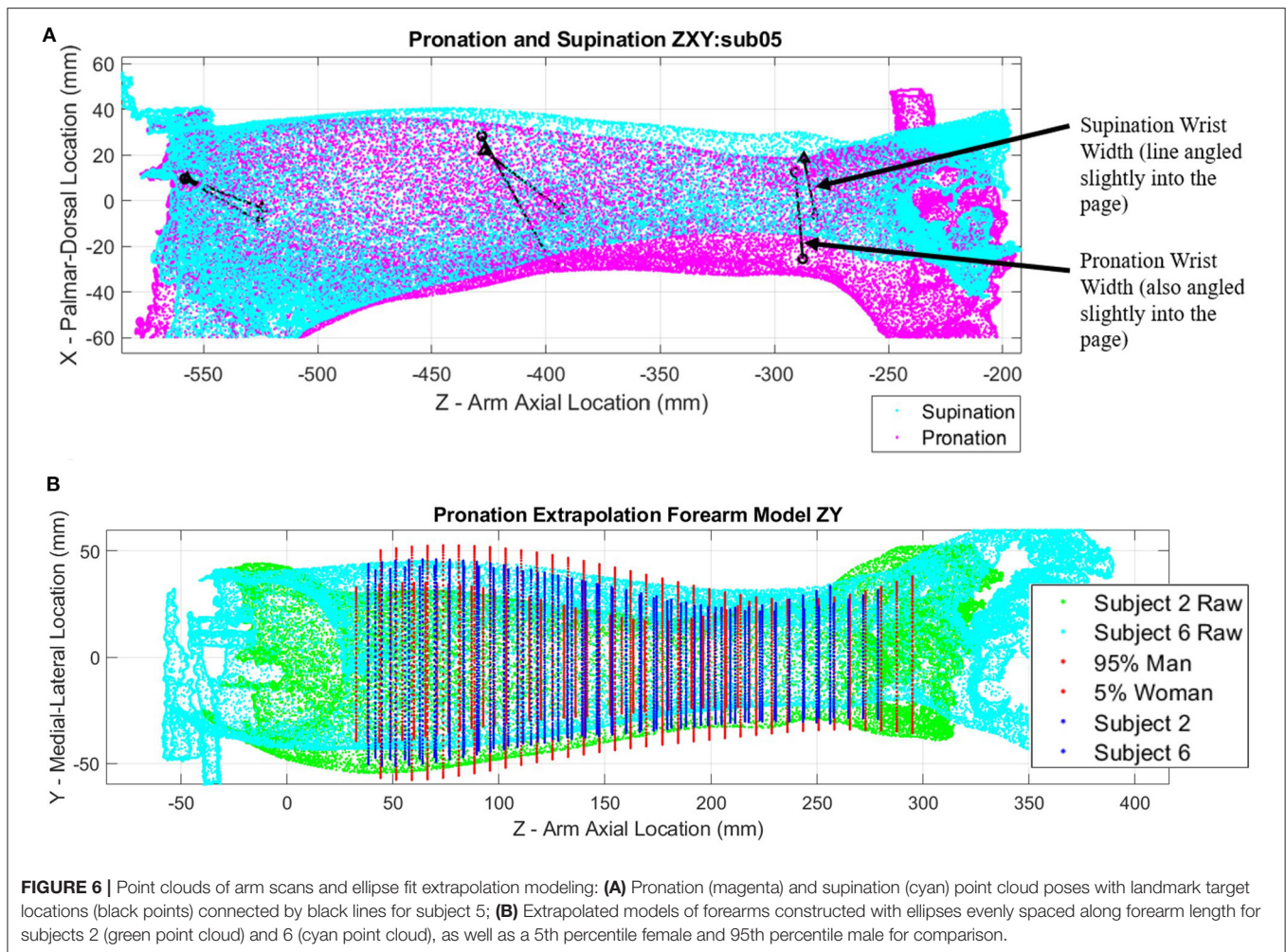
The right forearms of six subjects were scanned in the testing apparatus in 40° of pronation and 80° of supination. Raw arm surface data including target positions for different poses and subjects were plotted and overlaid for visual inspection. Scans from Subject 5 show relatively large shifts in target positions near the wrist indicating a large misalignment with the rotation axis of the apparatus (**Figure 6A**). Differences are illustrated by black lines that connect common pairs of medial and lateral scanning targets in each pose. Similar plots of raw scan data for each subject are available in **Supplementary Figures SF1.1 through SF1.6**.

Figure 6B shows a relative comparison of two arm scans for subjects of differing stature alongside estimates of 5th percentile female and 95th percentile male models. The shape of each forearm scan is represented by a series of ellipses at 5 mm spacing along the length of the forearm, with each ellipse being fit through a cross-sectional slice of forearm data points. Ellipse parameters without normalization are compared side by side in **Supplementary Figures SF2.1–SF2.3** (pronation) and **Supplementary Figures SF3.1–SF3.3** (supination).

Heatmap plots of the deviation values of the raw data points were plotted in Cartesian coordinates (**Figure 7**) to visualize how well the SS ellipse-fit models described the actual arm scan data. Yellow regions indicate places where the arm structure deviates the most from the ellipse fit. Most arms show regions of highest deviation near muscle bellies between the elbow and mid-arm in both poses and at bony prominences near the wrist in pronation. The subject with the most pronounced deviations, subject 6, is shown in **Figure 7**. Comparisons of single-subject models to raw data are provided for the remaining subjects in **Supplementary Figures SF4.1–SF4.6** (pronation) and **Supplementary Figures SF5.1–SF5.6** (supination).

Combined-Subjects (CS) Forearm Modeling

Scan data from all six subjects were normalized and combined into a combined-subjects (CS1) elliptical model for comparison. Normalized major and minor axis lengths, tilt angle, normalized center point coordinates, and circularity for all subjects are illustrated in **Figure 8** for supination (**Figures 8A–F**) and pronation (**Figures 8G–L**). Average and maximum error at each slice along the forearm are shown in **Figures 8M,N**. As seen in the figure, parameters are highly consistent between the models for all but the location of ellipse centers. Despite having similar overall profiles, shifts in the data both at the elbow and the wrist indicate variations in alignment between subjects. Misalignment of ellipse centers results in average deviations of 1–12 mm and peak deviations of 8–18 mm between the CS1 model and individual subject scans. CS1 alignment, ellipse parameters, and maximum model error are provided in **Supplementary Figures SF6, SF10, SF14** for pronation, and **Supplementary Figures SF7, SF11, SF15** for supination, respectively. CS1 scan data, ellipse fit, and downsampled data along the arm from 20 to 100%RS length are available in **Supplementary Figures SF18.1 through SF18.17** (pronation) and **SF19.1 through SF19.17** (supination). Average model error

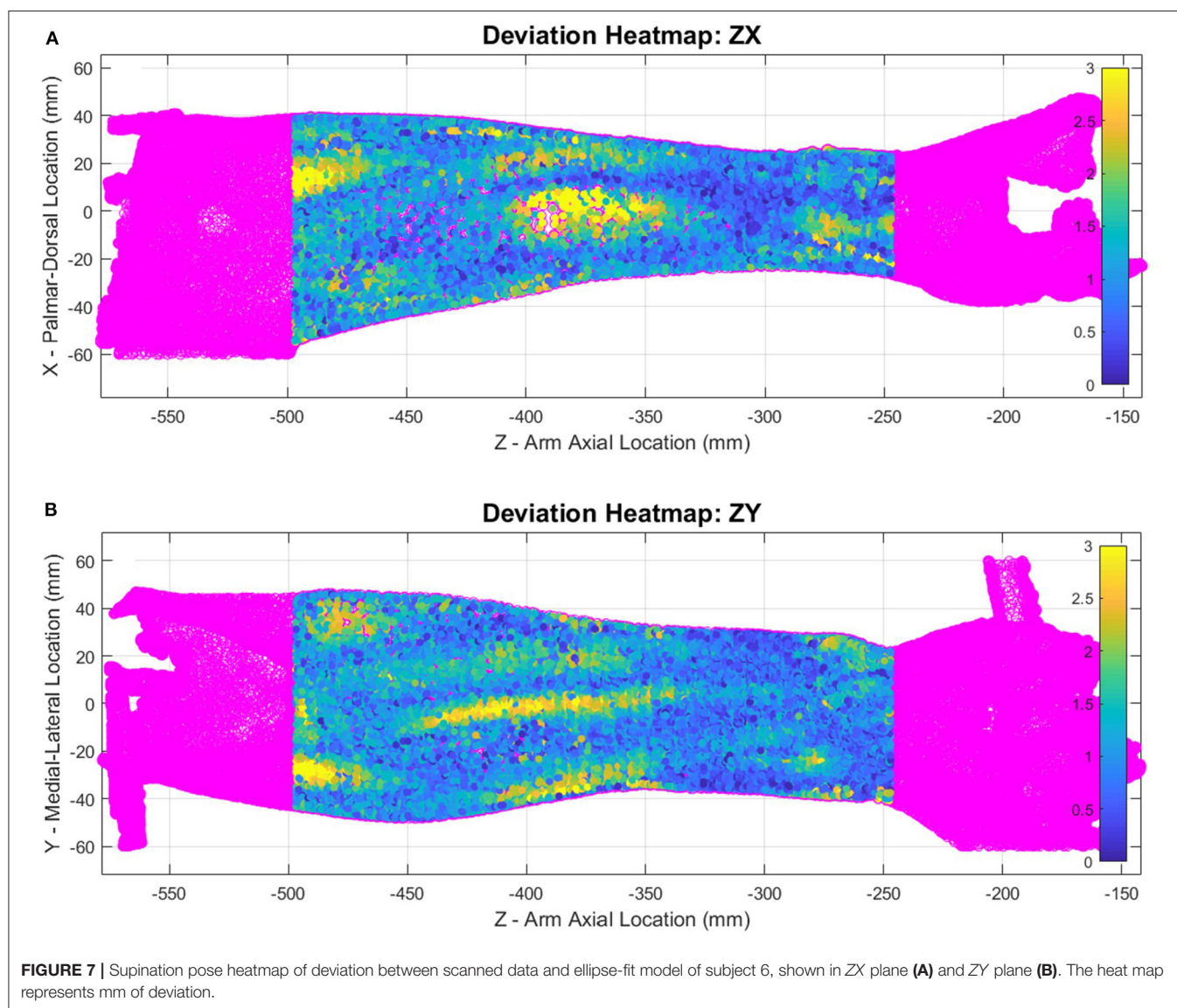


for each subject is plotted in **Supplementary Figure SF22** (pronation), and **Supplementary Figure SF23** (supination).

A second combined-subjects model (CS2) was developed after alignment of the forearm scan with a common vertical axis. Scans were aligned based on the ellipse centers of slices at normalized forearm locations of 0.2 mm/mm (i.e., 20% RS length from the radiale) and 1 mm/mm (i.e., at the styloid). A comparison between forearm alignment in CS1 and CS2 is shown in **Figure 9** for subject 4, a subject with one of the largest misalignments to the rotation axis of the apparatus. CS1 (**Figure 9A**) represents the average of arm locations in the apparatus based on a self-selected wrist placement. The aligned model of CS2 (**Figure 9B**) provides a more accurate representation of average arm geometry. The resulting ellipse parameters and model error for each subject over the length of the forearm are provided for CS2 in **Figure 10**. Alignment of the ellipse centers in CS2 lowered average deviations to 1–3 mm and peak deviations to 4–7 mm between the CS2 model and individual subject scans. CS2 alignment, ellipse parameters, and maximum model error are provided in **Supplementary Figures SF8, SF12, SF16** for pronation, and SF9, SF13, and SF17 for supination, respectively. CS2 scan data, ellipse fit, and downsampled data along the arm from 20 to 100%RS

length are available in **Supplementary Figures SF20.1–SF20.17** (pronation) and **Supplementary Figures SF21.1–SF21.17** (supination). Average model error for each subject is plotted in **Supplementary Figure SF24** (pronation), and **Supplementary Figure SF25** (supination).

The statistical R^2 correlations of fit and root-mean-squared error (RMSE) between 3rd-order models and average CS2 ellipse parameters along the normalized forearm axial length are provided in **Table 2**. The best-fit polynomial equations for CS2 ellipse parameters are given in **Table 3**. Equations from the table, and two inputs (forearm RS length and circumference), are sufficient to construct a mathematical model of the forearm. The input values can be obtained from a specific individual or from the ANSUR 2 dataset to represent a particular percentile of the population. Similarly, an orthosis model can be generated using these same inputs over the desired region where the orthosis is to be placed. For example, an individual whose RS length is 250 mm with a desired orthosis location along the forearm from 50 to 100 mm from the radiale, would use values for x of 0.2 and 0.4 to generate ellipses at either end of the orthosis. An orthosis could then be made in a computer-aided design software by lofting a surface between subsequent elliptical sketches. Additional model



resolution can be achieved by generating additional ellipses between the two end sketches, further refining the lofted orthosis surface. It is important to note that the equations use normalized forearm dimensions based on radiale-styloid length and flexed forearm circumference, as described in section Ellipse Fitting.

Shape Changes Between Pronation and Supination

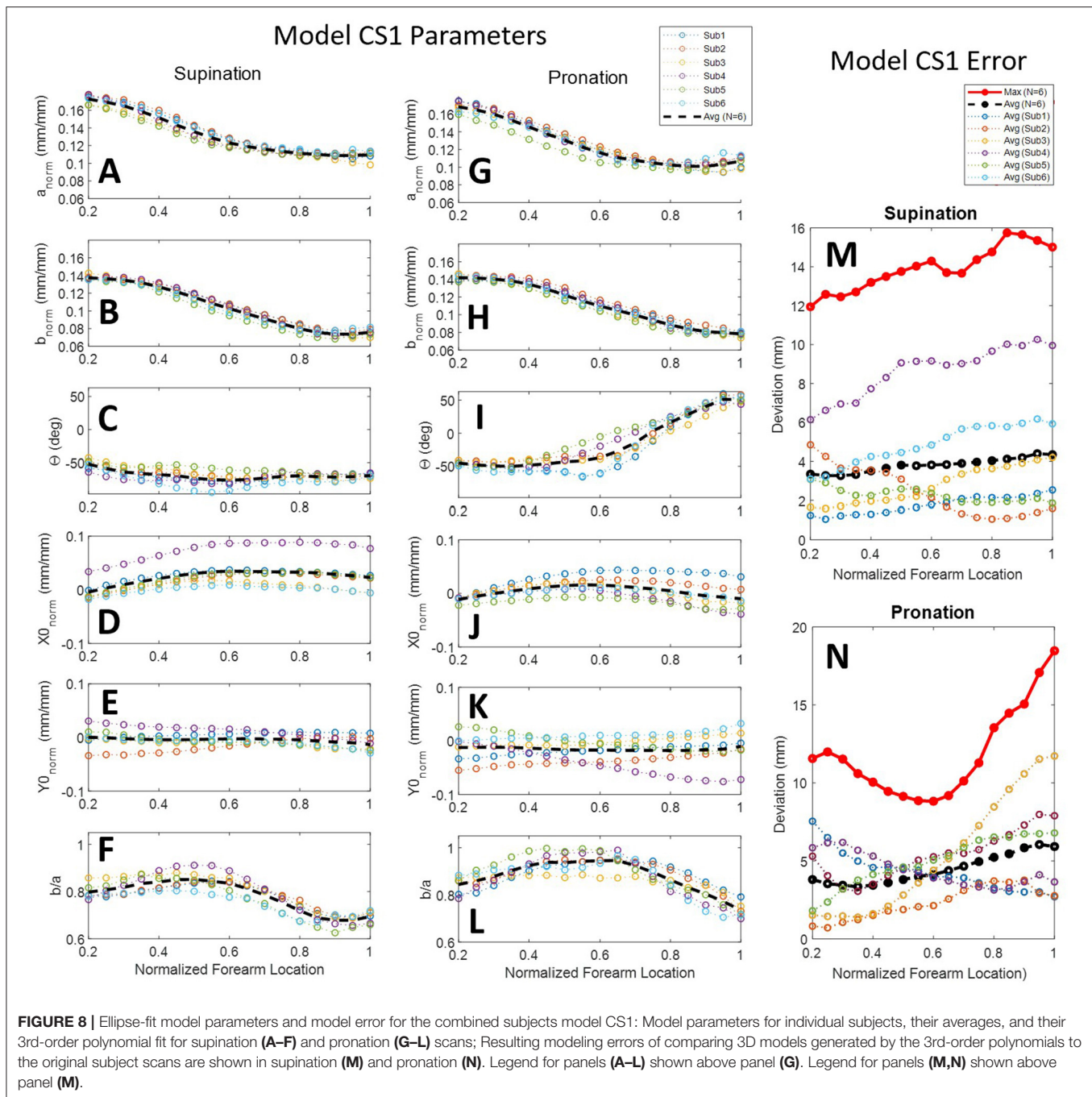
The forearm shape changes significantly between pronation and supination poses. The size of deviations for a single subject (subject 2) are illustrated with heatmaps in **Figure 11**. Blue regions show where there is little positional change of the arm surface between poses, while yellow regions show where the shape changes by at least 8 mm. Data was trimmed using the origin X and Y planes to remove far side data points from view. Each view (palmar, dorsal, ulnar, and radial) was named by hand

directions and forearm bone landmarks to indicate which surface is shown.

Another major difference between poses can be seen in the tilt angle, θ , of **Figure 10**. The angle varies substantially between pronation and supination poses, staying relatively constant from 20 to 60% RS length around -50° , but in pronation increases almost linearly from 60 to 100% RS length to $+50^\circ$. Circularity is also lower in supination indicating a more elliptical shape with larger major axis and smaller minor axis.

Application of the Ellipse Fit

To illustrate current upper-limb rehabilitation robot practices and the importance of pHMI fit with the user, a single thermoplastic C-channel orthosis of a mean individual was designed in SolidWorks. The orthosis was built using the proposed pronation extrapolation model for use with a robotic exoskeleton system called Blue Sabino. The orthosis attaches to

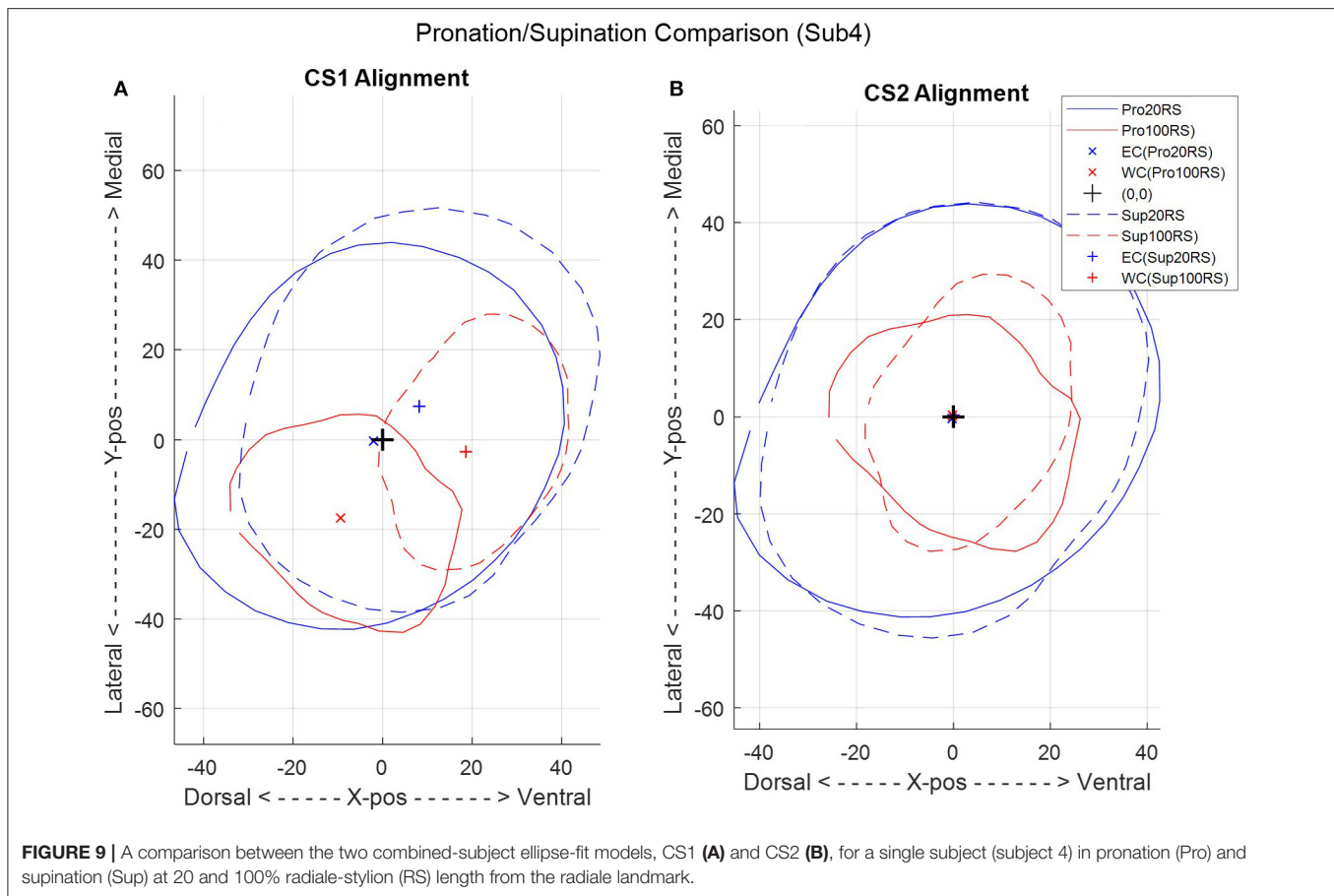


the robot via the inferior side of the cuff, and would secure to the user via a set of hook-and-loop Velcro straps. The orthosis was designed with 165° of wrap on the medial side of the cuff and 120° on the lateral side. The large angle of wrap around the forearm has been used to illustrate the shape provided to support the arm under a wide array of model orientations. However, it should be noted that a cuff of this geometry would not allow easy donning and doffing by users, particularly if rigid. Extrapolation models for both the smallest (i.e., 5th percentile female) and largest (i.e., 95th percentile male) individuals were placed in the model to

visualize the geometric performance of the concept (Figure 12). Although a medium-sized cuff has been designed based on the ellipse-fit model, subject evaluations of fit and comfort have not yet taken place.

DISCUSSION

Geometric analysis of the proposed forearm model provides insight into the design of a standardized orthosis. Forearm scans show significant change in shape



between supination and pronation poses. The ellipse-fit model proves useful in constructing a mathematically-driven, scalable, generalized surface model of the human forearm for use in sizing and developing orthosis designs.

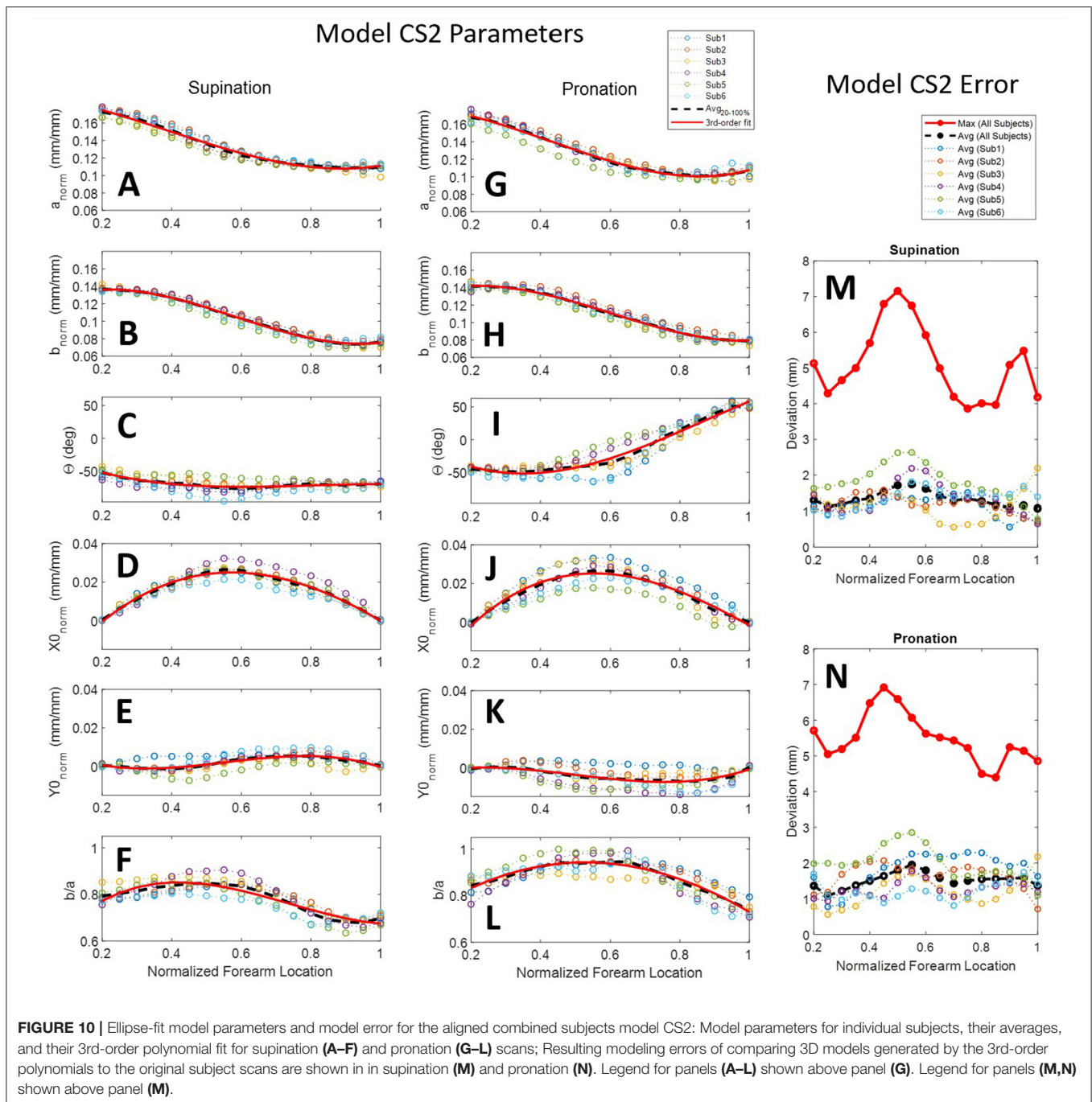
Scanner Error

The coffee cup experiment provides a relatively controlled reference study to quantify the error of the scan and compare scanner error to traditional caliper measurements. The turntable and experiment setup scans were manually aligned to caliper measurements which introduced small errors in dataset location, but has no net effect on each dataset relative to itself. Both setups produced a similar increase in error as the scanner moved away from the turntable or experiment frame where most of the position targets were located.

The experimental setup showed a pronounced ellipse center-point shift in the X direction (**Figure 5D**) that was not present in the Y direction nor the turntable data. This 1.06–1.61 mm bias is likely an artifact of the experimental setup and is expected to slightly influence data collection. Turntable data aligns slightly better with the measured data plot, which is expected from a more controlled scan environment. The experiment setup had a pronounced ovalization with a consistent bias to ellipse tilt angle averaging about -60° for the first 100 mm of the cup's length

(**Figure 5F**) suggesting a consistent shape bias due to scanner sensor readings, scanner software, and experiment procedure. This is likely related to the X-direction shift. Such a bias was not noticed in the turntable results, which more closely follow the axis ratio of 1 expected from the perfectly circular cross-section assumption. Similar or greater deviations than the discovered 0.39 mm between the raw data and the ellipse-fit cup are to be expected from forearm scans. The error of the ellipse best-fit model in our cup study is 2–3.5 times larger than the error found in other studies of static objects using similar scanners (Dickinson et al., 2016; Kersten et al., 2018; Polo et al., 2019). This is likely due to two of these studies using objects with better fit-locking geometric features, and the third using an abundance of positioning targets on the reference object. This identifies the importance of having tracking stickers close to the geometries being scanned and provides key insight into developing a forearm scanning environment. This supports the addition of the vertical wand with tracking stickers behind the arm that allows for additional visual reference points as the scanner moves along the forearm and away from tracking stickers attached to the extruded aluminum beam.

The one-subject repeatability check highlights the presence of variance in the data. Subtle shifts were seen between subsequent scans of the same subject in the same session. This phenomenon is expected due to a variety of potential causes, one



being involuntary movement by the subject, such as breathing. Placement of positioning stickers, scanner movement patterns, and scanning speed are other potential sources that could contribute to the observed error. Identifying the contributions from each source would require an intensive study to isolate their effects. Contributions from involuntary human movement could be further reduced through immobilization of wrist flexion/extension. However, these shifts in the CS1 model were removed from the CS2 model through pre-alignment of the scans.

Forearm Scans

The forearm is a highly dynamic and deformable mechanism, making it much more complicated to obtain repeatable measurements as compared to more traditional engineering objects. Variability studies using 3rd-order polynomial regression fits and statistics were used to characterize trends and indirectly comment on the quality of the study data in addition to the error studies previously discussed. The 3rd-order polynomial fit with normalized and averaged ellipse parameters of model CS2 have R -squared (R^2) values that range from 0.941 to

TABLE 2 | RMSE of CS2 3rd-order ellipse-fit model parameter with six-subject averages and R^2 correlation with normalized forearm location.

Pose	Variable	3rd-order fit with averaged ($N = 6$) ellipse parameter profiles			R^2 correlation with normalized forearm location (Z)
		R^2	RMSE (Units)	Normalized w.r.t.	
Pronation	Normalized Major Axis	0.998	0.0041 (mm/mm)	Forearm Circumference	0.898
Supination		0.995	0.0064 (mm/mm)	Forearm Circumference	0.926
Pronation	Normalized Minor Axis	0.999	0.0029 (mm/mm)	Forearm Circumference	0.980
Supination		0.999	0.0021 (mm/mm)	Forearm Circumference	0.972
Pronation	Tilt Angle	0.988	0.285 (rad)	n/a	0.877
Supination		0.941	0.106 (rad)	n/a	0.381
Pronation	Normalized X Center	0.985	0.0046 (mm/mm)	RS length	0.020
Supination		0.991	0.0031 (mm/mm)	RS length	0.005
Pronation	Normalized Y Center	0.941	0.0028 (mm/mm)	RS length	0.369
Supination		0.951	0.0022 (mm/mm)	RS length	0.391
Pronation	Circularity	0.983	0.0334	n/a	0.279
Supination		0.942	0.0609	n/a	0.657

Pronation fits highlighted in blue for clarity.

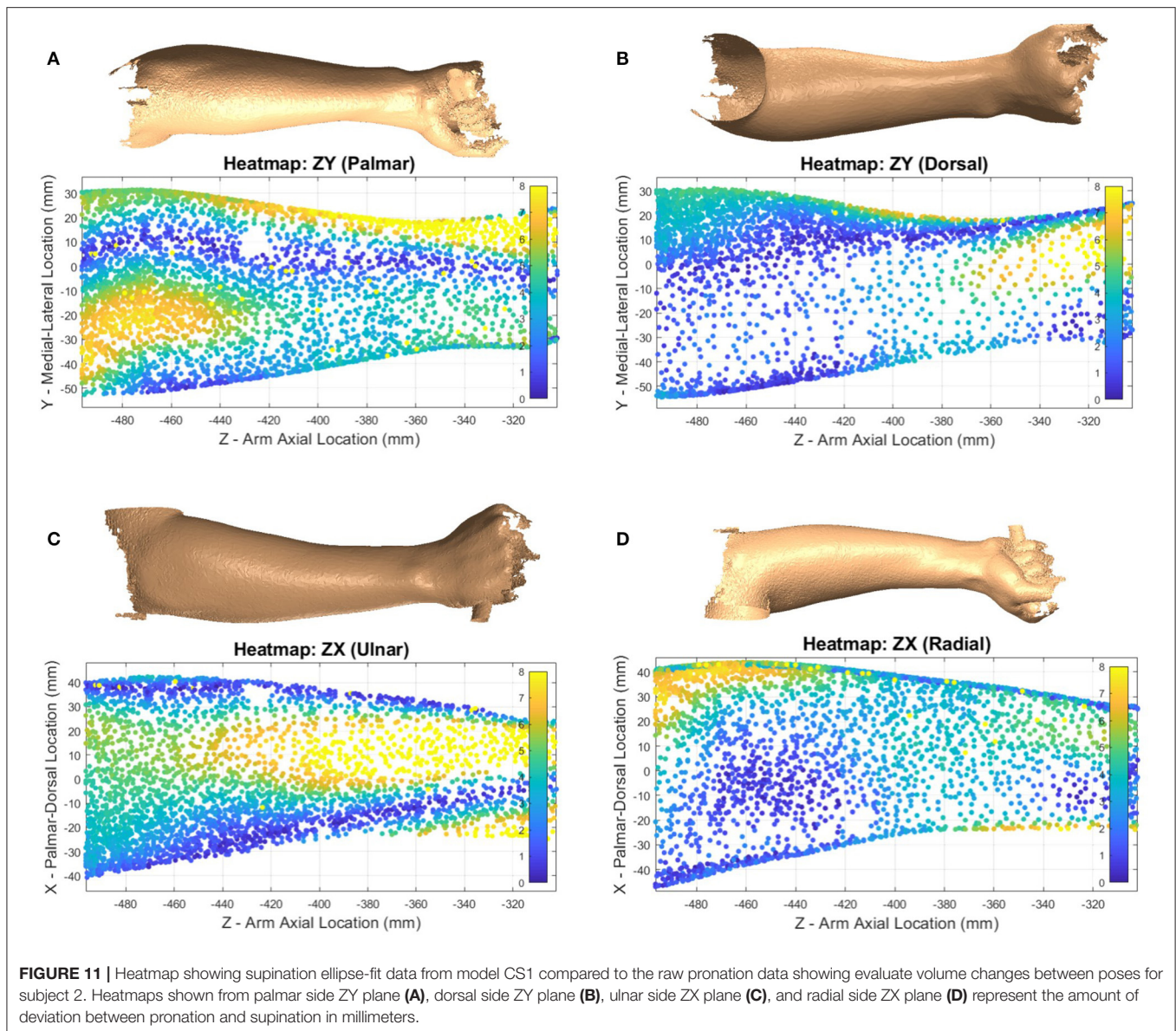
TABLE 3 | Forearm model equations include elliptical parameter best-fit equations from a 3rd-order polynomial fit through the CS2 ellipse parameters, Y , vs. normalized axial location, x .

Pose	Dependent variable (Y)	Independent variable (x)	Equation
Pronation	Normalized Major Axis, a_{norm}	Normalized Forearm Location	$Y = 0.2536 x^3 - 0.3264 x^2 - 0.0004 x + 0.1808$
	Normalized Minor Axis, b_{norm}	Normalized Forearm Location	$Y = 0.2882 x^3 - 0.5210 x^2 + 0.1894 x + 0.1225$
	Tilt Angle, θ	Normalized Forearm Location	$Y = -4.8876 x^3 + 12.8539 x^2 - 7.1845 x + 0.2399$
	Normalized X Center, $X_{0,norm}$	Normalized Forearm Location	$Y = 0.1019 x^3 - 0.3504 x^2 + 0.2942 x - 0.0475$
	Normalized Y Center, $Y_{0,norm}$	Normalized Forearm Location	$Y = 0.1085 x^3 - 0.1620 x^2 + 0.0588 x - 0.0062$
	Circularity, b/a	Normalized Forearm Location	$Y = 0.0977 x^3 - 1.1571 x^2 + 1.1395 x + 0.6501$
Supination	Normalized Major Axis, a_{norm}	Normalized Forearm Location	$Y = 0.1713 x^3 - 0.1990 x^2 - 0.0535 x + 0.1922$
	Normalized Minor Axis, b_{norm}	Normalized Forearm Location	$Y = 0.3329 x^3 - 0.5798 x^2 + 0.2068 x + 0.1156$
	Tilt Angle, θ	Normalized Forearm Location	$Y = -2.3585 x^3 + 5.6793 x^2 - 4.2738 x - 0.2692$
	Normalized X Center, $X_{0,norm}$	Normalized Forearm Location	$Y = 0.0573 x^3 - 0.2607 x^2 + 0.2423 x - 0.0390$
	Normalized Y Center, $Y_{0,norm}$	Normalized Forearm Location	$Y = -0.1361 x^3 + 0.2266 x^2 - 0.1043 x + 0.0135$
	Circularity, b/a	Normalized Forearm Location	$Y = 1.4204 x^3 - 3.1362 x^2 + 1.8798 x + 0.5104$
Both	Actual major axis, a	Normalized major axis, a_{norm}	$Y = (\text{User Forearm Circumference in mm}) \cdot x$
	Actual minor axis, b	Normalized minor axis, b_{norm}	$Y = (\text{User Forearm Circumference in mm}) \cdot x$
	Actual X center, X_0	Normalized X center, $X_{0,norm}$	$Y = (\text{User Radiale-Stylen Length in mm}) \cdot x$
	Actual Y center, Y_0	Normalized Y center, $Y_{0,norm}$	$Y = (\text{User Radiale-Stylen Length in mm}) \cdot x$
	Actual forearm location	Normalized forearm location	$Y = (\text{User Radiale-Stylen Length in mm}) \cdot x$
	Circularity, b/a	Circularity, b_{norm}/a_{norm}	$Y = x$

The last six equations provide parameters for both poses based on forearm measures of circumference or radiale-stylen length. Equations corresponding to pronation, supination, and both poses are separated by blue highlight for clarity.

0.999 with a root-mean-square error (RMSE) of 0.21 to 0.64% of their respective reference measurement used for normalization. R^2 values of CS2 ellipse parameter correlations with normalized forearm location on the other hand have a much wider range. Ellipse axis lengths are highly correlated with forearm location having R^2 values from 0.898 to 0.980. This suggests that forearm circumferential variability is well-explained by location along the length of the forearm and is likely due to a general shared arm structure among the sample population.

In addition to major and minor axes, arm shape is described by ellipse tilt angle and center location. Ellipse tilt angle elicited the most significant difference between pronation and supination, where the tilt angle in pronation was highly correlated with forearm location ($R^2 = 0.877$) while supination was not ($R^2 = 0.381$). Not surprisingly, circularity is only moderately correlated with forearm location ($R^2 = 0.657$) in supination, and very poorly in pronation ($R^2 = 0.279$). All other ellipse parameters are very poorly correlated with position along the forearm. Pronation generally had a more circular shape to its cross-sections than



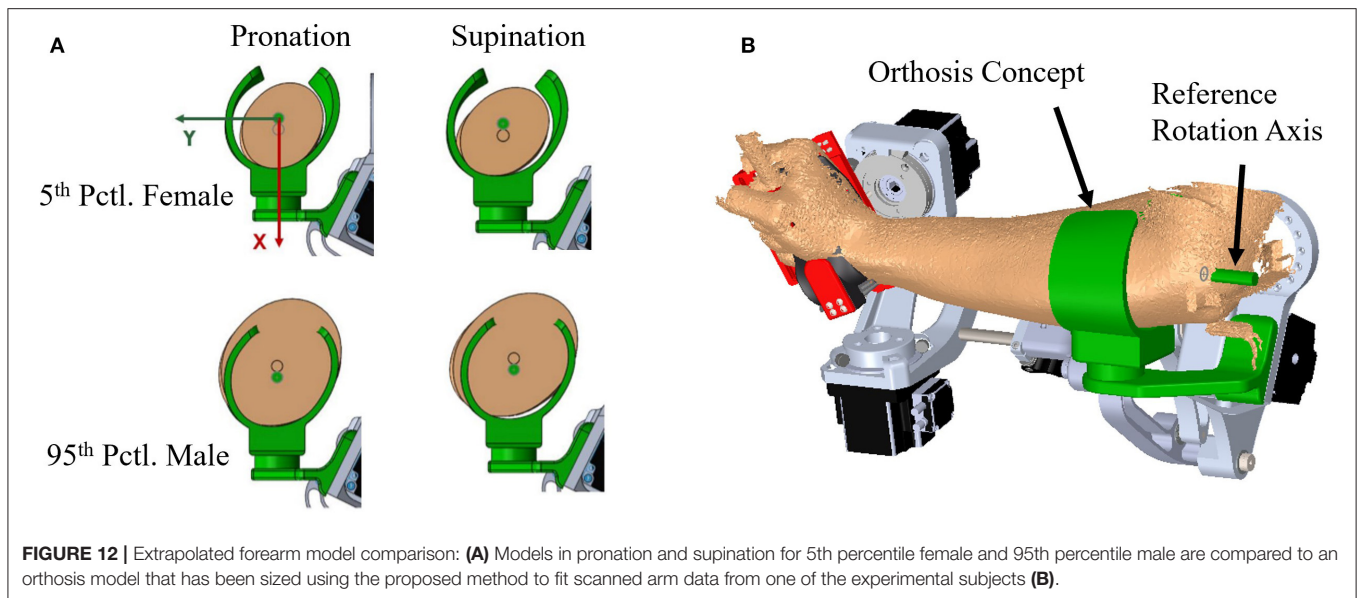
supination and was nearly circular for two of the subjects between 45 and 65% RS length, measured from the radiale. This resulted in significantly less data points in the scanned point cloud in these regions due to complications in tilt angle as the axis ratios neared 1, an artifact of using ellipses to fit nearly circular objects. The center point position RMSE varied from 0.31 to 0.46 % of RS length in the X direction and 0.22 to 0.28% of RS length in the Y direction. This equates to a center-to-center RMSE of 0.38–0.54% RS length between the model and the average subject, or 1.0–1.4 mm RMSE for a 50th percentile male.

The model parameters from model CS1 provide insight into the variability in subject positioning relative to a forearm rotation axis by an untrained technician that may be useful in estimating alignment error encountered in upper-limb robot donning. It was noticed that verbal direction to the subject to keep a consistent posture between poses was not sufficient. As a result, the forearm

alignment of subjects widely varied. For this reason, the second aligned model CS2 was developed. This second model provides a close approximation of the average arm shape across the subject pool. Model CS2 should be used in developing forearm models for close-fitting orthoses. Model CS1 can be used to see the effects of subject misalignment in a semi-constrained environment. Adapting the handle assembly to use mechanical indexing features to constrain the ulnar and radial epicondyles of the wrist could be used to further reduce variability in alignment between supination and pronation pose scans in the experimental setup. A similar use of indexing features could be used at the elbow to reduce alignment variability of the humeral epicondyles.

Forearm Deformation

Shape change can have major impacts on orthosis fit and comfort. Modeling the human arm based on optical scanning of tracking



stickers is complicated by movement of the bones and muscles through pronosupination under the surface of the skin. Bones move relative to the surface and relative to one another causing subtle changes in location of surface markers. Skin artifacts in axial rotation tend to cause under-rotation of the wrist flexion-extension axis markers, as skin stretches. Mid-arm markers show relative motion of the skin but have little to do with underlying movements. It is also evident from scan geometry that the forearm shortens in length from the supination pose to pronation pose with wrist breadth changing as well. Wrist markers moved an average of 4.84 mm closer together in pronation than in supination, which indicates that the wrist changes size during forearm rotation. Measured distances between lateral pairs of skin markers averaged changes of 0.49 to 5.1 mm suggesting position targets affixed to the skin should not be treated as rigid landmarks if high accuracy is needed. For accurate deformation data and determination of actual rotation centers, skin markers are unsuitable with mid-arm targets especially prone to skin effects. These events suggest two things: (1) alignment of the anatomical rotation center to the fixture rotation axis was accommodated by wrist joint movement, as well as global arm movement instead of pure forearm rotation, and (2) using targets to find the rotation center of the arm is complicated by skin effects and bone topology.

Heatmap plots of a supinated forearm in **Figure 7** identify the portions of scan data that deviate most from the SS ellipse-fit model. This particular subject had a low body fat percentage which may have contributed to the larger localized deviations. The deviation patterns in the figure suggest that, at least for thin subjects, bony prominences, superficial tendons, and muscle bellies may be the primary sources of model deviation. Similarly, heatmap plots of a pronated forearm in **Figure 11** illustrate regions of largest difference between pronation and supination. The particular subject was fairly well-aligned in the setup and thus would produce a similar heatmap using either of alignments

CS1 or CS2. From the figure, it appears that most of the difference near the elbow is caused by the pronator muscles, and most of the difference near the wrist is caused by the ulna and radius. The location of largest changes show regions where rigid orthoses would need the most padding to accommodate misalignment. Conversely, the regions of lowest change indicate regions where rigid orthoses may feasibly support the forearm comfortably during pronosupination movements. The specific regions of high and low change depend heavily on model alignment, thus appropriate selection of rotation axis placement is important.

Ellipse Fit Application

Skin loading has a critical design limit for user comfort and safety. As illustrated in **Figure 12A**, a standardized HMI cannot intimately fit all users. A compensation mechanism is needed to ensure high fidelity force transmission to the robot while keeping forces on the user within safe limits. Example compensation mechanisms may include thermoplastic walls of the orthosis that are deformed by tightening Velcro straps until the orthosis fits the user snugly, orthosis walls that linearly slide to contact the user's arm, or a pneumatic cuff that is inflated until adequate contact with the user's arm is achieved. The difference between extreme individuals is a key design criteria that drives the requirements of foam or skin compression to achieve a proper fit. Multiple HMI sizes are commonly used to narrow the band of deviations that the compensation mechanism must accommodate. However, the accommodation bandwidth for any size can be increased by using an HMI profile that more closely matches the subject's anatomical form such as the mathematical forearm model of **Table 3**.

Figure 12B shows a simple concept of a thermoplastic C-channel-shaped orthosis based off the pronation model of **Table 3**. Similar designs with Velcro straps are used in other upper limb rehabilitation robots. The figure shows extreme users in a one-size-fits-all design based on the average model in a pronation pose. Several design issues are immediately apparent.

First, the smallest and largest users are not aligned to the rotation axis because arm diameters are too small or too large for the designed orthosis. Second, the orthosis walls must be strained in order to contact each user. The model presented in this study allows these deflections to be estimated and included in the design. A third issue arises when the orthosis user rotates his/her arm from pronation to supination, in which case the orthosis no longer matches the user's arm shape. In a rigid shell, this could result in pressure concentrations, gaps, and/or arm alignment changes with potential consequences on arm tissue loading. If the user and robot kinematics stay aligned, this results in an enforced displacement problem where the geometric mismatch represents the desired design condition, and reaction forces can be solved if component material properties are known. Foam is commonly used in standardized orthoses to add comfort and soften the interaction of the orthosis on the user. In an enforced displacement scenario, a foam layer between the orthosis and the user can be used to reduce reaction forces. While the ellipse-fit model shows promise as a means to represent arm topology for arms in pronation and supination, the resulting performance of the model in terms of comfort and support in customized applications needs further evaluation by subjects during both static and non-static tasks.

The effectiveness of this model has yet to be evaluated for resulting fit and comfort with subjects. This model is purely a geometric comparison and neglects deformation and compliance in the human-to-robot system that will likely have impacts on comfort and tracking accuracy. Human variation in size and shape as well as skin properties require a larger sample size. Further refinement of the forearm rotation axis location is also likely needed to optimize performance over a wider range of forearm rotation. This should both improve the exoskeleton performance and patient comfort during rehabilitation. Although the model was implemented virtually through CAD, a physical model in a clinical environment will allow for feedback from patients. The patient feedback will both validate the model and outline areas of potential improvement. A more expansive study with a larger subject pool would also further refine the model to better represent the general population.

CONCLUSION

This study provides a tool for assisting in the design of standardized orthoses for use in exoskeleton robotic applications. It establishes a closed-form, scalable model for the interface between the surface of the forearm and a physical human-machine interface. It provides data on both supination and pronation arm shapes allowing for the design of orthoses that accommodate a full functional range of forearm rotations. It

also highlights the importance of considering the effects of pronosupination on arm size and shape in designing orthoses for exoskeletons. The developed model can be resized in length and width with a few simple measurements of arm geometry to quickly create a potential pHMI design for a user of arbitrary arm size. This data-driven model of the "average" forearm shape could help designers fabricate orthoses that provide a reasonable fit to a wider array of individuals and improve the generalized fit of prototype pHMIs in rehabilitation robotics research.

DATA AVAILABILITY STATEMENT

The raw data supporting the conclusions of this article will be made available by the authors, without undue reservation.

ETHICS STATEMENT

The studies involving human participants were reviewed and approved by University of Idaho Institutional Review Board. The patients/participants provided their written informed consent to participate in this study.

AUTHOR CONTRIBUTIONS

JP is the senior researcher who guided developments, revised processing scripts, and prepared the final manuscript for submission. JB took the lead on drafting the preliminary manuscript. RC assisted JB with drafting the methods section. MB was the lead graduate student during experimental design, data collection, and initial processing, and provided periodic guidance to JB and RC throughout preparation of the preliminary manuscript. All authors contributed to and approved the final manuscript.

FUNDING

This work was funded by the National Science Foundation (Award#1532239) and the Eunice Kennedy Shriver National Institute of Child Health and Human Development of the National Institutes of Health (Award#K12HD073945). The content is solely the responsibility of the authors and does not necessarily represent the official views of the National Science Foundation nor the National Institutes of Health.

SUPPLEMENTARY MATERIAL

The Supplementary Material for this article can be found online at: <https://www.frontiersin.org/articles/10.3389/frobt.2021.576783/full#supplementary-material>

REFERENCES

- Alavi, N., Zampierin, S., Komeili, M., Cocuzza, S., Debei, S., and Menon, C. (2017). A preliminary investigation into the design of pressure cushions and their potential applications for forearm robotic orthoses. *Biomed. Eng. Online* 16:54. doi: 10.1186/s12938-017-0345-8
- Amigo, L. E., Casals, A., and Amat, J. (2011). Design of a 3-DoF joint system with dynamic servoadaptation in orthotic applications. *IEEE Int. Conf. Robot. Autom.* 3700–3705. doi: 10.1109/ICRA.2011.5980173
- Ates, S., Haarman, C. J. W., and Stienen, A. H. A. (2017). SCRIPT passive orthosis : Design of interactive hand and wrist exoskeleton for rehabilitation at home after stroke. *Auton. Robots* 41, 711–723. doi: 10.1007/s10514-016-9589-6

- Coppard, B. M., and Lohman, H. (2015). *Introduction to Orthotics: A Clinical Reasoning and Problem Solving Approach*, 4th edn. St. Louis, MO: Elsevier.
- Creaform Inc (2015). *Understanding Portable 3D Scanning Technologies*. Quebec: Creaform Inc.
- Creaform Inc. (n.d.). *Go!SCAN 3D G2 Scanner*. Retrieved from: <https://www.creaform3d.com/en/goscan-3d-g2-scanner> (accesses March 12, 2019).
- Crennen, T. (2017). *Creaform 3D Scanning: How to Scan the Human Body With the GoScan50*. Retrieved from CATI website: <https://www.cati.com/blog/2017/09/how-to-scan-the-human-body-with-the-creaform-goscan50>
- Dickinson, A. S., Steer, J. W., Woods, C. J., and Worsley, P. R. (2016). Registering a methodology for imaging and analysis of residual-limb shape after transtibial amputation. *J. Rehabil. Res. Dev.* 53, 207–218. doi: 10.1682/JRRD.2014.10.0272
- Downs, J. W. (2003). *Practical Conic Sections: The Geometric Properties of Ellipses, Parabolas and Hyperbolas*. Mineola, NY: Dover Publications, Inc.
- Fryar, C. D., Gu, Q., Ogden, C. L., and Flegal, K. M. (2016). *Anthropometric Reference Data for Children and Adults: United States, 2011–2014*. Vital and Health Statistics. Retrieved from: <https://lccn.loc.gov/2016032998>
- Gal, O. (2003). *Fit_ellipse Version 1.0.0.0*. Retrieved from MATLAB Central File Exchange website: https://www.mathworks.com/matlabcentral/fileexchange/3215-fit_ellipse (accessed September 10, 2019).
- Gmerek, A. (2012). “The virtual reality system used for upper extremity rehabilitation,” in: *Proceedings of the International Conference on Methods and Models in Automation and Robotics* (New York, NY), 312–314.
- Gopura, R. A. R. C., Bandara, D. S. V., Kiguchi, K., and Mann, G. K. I. (2016). Developments in hardware systems of active upper-limb exoskeleton robots: a review. *Robot. Autonom. Syst.* 75, 203–220. doi: 10.1016/j.robot.2015.10.001
- Gordon, C. C., Blackwell, C. L., Bradtmiller, B., Parham, J. L., Barrientos, P., Paquette, S. P., et al. (2014). *2012 Anthropometric Survey of U.S. Army Personnel: Methods and Summary Statistics*. U.S. Army Natick Soldier Research Development & Engineering Center.
- Gupta, A., O'Malley, M. K., Patoglu, V., and Bugar, C. (2008). Design, control and performance of RiceWrist: A force feedback wrist exoskeleton for rehabilitation and training. *Int. J. Robot. Res.* 27, 233–251. doi: 10.1177/0278364907084261
- Herrnstadt, G., and Menon, C. (2016). Voluntary-driven elbow orthosis with speed-controlled tremor suppression. *Front. Bioeng. Biotechnol.* 4:29. doi: 10.3389/fbioe.2016.00029
- Jackson, A., Culmer, P., Makower, S., Levesley, M., Richardson, R., Cozens, A., et al. (2007). “Initial patient testing of iPAM—a robotic system for stroke rehabilitation,” *Proceedings of IEEE* <https://ieeexplore.ieee.org/xpl/conhome/4428348/proceeding> International Conference on Rehabilitation Robotics (Noordwijk: IEEE), 250–256.
- Jacobs, M., and Austin, N. (2014). *Orthotic Intervention for the Hand and Upper Extremity*, 2nd edn. Philadelphia, PA: Lippincott Williams and Wilkins.
- Jarrassé, N., and Morel, G. (2012). Connecting a human limb to an exoskeleton. *IEEE Trans. Robot.* 28, 697–709. doi: 10.1109/TRO.2011.2178151
- Jarrassé, N., Robertson, J., Garrec, P., Paik, J., Pasqui, V., Perrot, Y., et al. (2008). “Design and acceptability assessment of a new reversible orthosis,” in: *2008 IEEE/RSJ International Conference on Intelligent Robots and Systems*, 1933–1939 (Nice), 1933–1939.
- Kersten, T. P., Lindstaedt, M., and Starosta, D. (2018). Comparative geometrical accuracy investigations of hand-held 3D scanning systems - An update. *Int. Arch. Photogrammetry Remote Sens. Spatial Inf. Sci.* 42, 487–494. doi: 10.5194/isprs-archives-XLII-2-487-2018
- Klein, J. S. J., Spencer, Allington, J., Minakata, K., Wolbrecht, E. T., Smith, R., et al. (2008). “Biomimetic orthosis for the neurorehabilitation of the elbow and shoulder (BONES),” in: *Proceedings of the 2nd Biennial IEEE/RAS-EMBS International Conference on Biomedical Robotics and Biomechatronics* (Scottsdale, AZ), 535–541.
- Löffler-Wirth, H., Willscher, E., Ahnert, P., Wirkner, K., Engel, C., Loeffler, M., et al. (2016). Novel anthropometry based on 3D-body-scans applied to a large population based cohort. *PLoS One* 11:e0159887. doi: 10.1371/journal.pone.0159887
- National Center for Health Statistics (2011). *Vital and Health Statistics, Series 3, Number 39*, (08/2016). Retrieved from: <https://lccn.loc.gov/2016032998>
- Neumann, D. A. (2017). *Kinesiology of the Musculoskeletal System: Foundations for Rehabilitation*. 3rd Edn. St. Louis, MI: Elsevier, Inc.
- Ohnishi, K., Saito, Y., Oshima, T., and Higashihara, T. (2013). Powered orthosis and attachable powerassist device with Hydraulic Bilateral Servo System. *Annu. Int. Conf. IEEE Eng. Med. Biol. Soc.* 2013, 2850–2853. doi: 10.1109/EMBC.2013.6610134
- Perry, J. C., Rosen, J., and Burns, S. (2007). Upper-limb powered exoskeleton design. *IEEE/ASME Trans. Mechatronics* 12, 408–417. doi: 10.1109/TMECH.2007.901934
- Pollo, M.-E., Cuartero, A., and Felicísimo, Á. M. (2019). Study of uncertainty and repeatability in structured-light 3D scanners. *arXiv [Preprint]* arXiv:1910.13199.
- Pylatiuk, C., Kargov, A., Gaiser, I., Werner, T., Schulz, S., and Bretthauer, G. (2009). “Design of a flexible fluidic actuation system for a hybrid elbow orthosis,” in: *2009 IEEE International Conference on Rehabilitation Robotics* (Kyoto), 167–171.
- Ragonesi, D., Rahman, T., Sample, W., and Agrawal, S. (2010). “Dynamic simulation and experimental validation of an upper extremity powered orthosis,” in: *IEEE/ASME International Conference on Advanced Intelligent Mechatronics*, AIM (Montreal, QC), 1–6.
- Rocon, E., Belda-Lois, J. M., Ruiz, A. F., Manto, M., Moreno, J. C., and Pons, J. L. (2007). Design and validation of a rehabilitation robotic exoskeleton for tremor assessment and suppression. *IEEE Trans. Neural Syst. Rehabil. Eng.* 15, 367–378. doi: 10.1109/TNSRE.2007.903917
- Rohm, M., Schneiders, M., Müller, C., Kreiling, A., Kaiser, V., Müller-Putz, G. R., et al. (2013). Hybrid brain-computer interfaces and hybrid neuroprostheses for restoration of upper limb functions in individuals with high-level spinal cord injury. *Artif. Intell. Med.* 59, 133–142. doi: 10.1016/j.artmed.2013.07.004
- Sangha, S., Elnady, A. M., and Menon, C. (2016). “A compact robotic orthosis for wrist assistance,” *Proceedings of the IEEE RAS/EMBS International Conference on Biomedical Robotics and Biomechatronics* (Singapore), 1080–1085.
- Tilley, A. R. (2001). *The Measure of Man and Woman: Human Factors in Design*, revised edn. Hoboken, NJ: John Wiley and Sons.
- Vaca Benitez, L. M., Tabie, M., Will, N., Schmidt, S., Jordan, M., and Kirchner, E. A. (2013). Exoskeleton technology in rehabilitation: Towards an EMG-based orthosis system for upper limb neuromotor rehabilitation. *J. Robot.* 2013, 610589. doi: 10.1155/2013/610589
- Vanderniepen, I., Ham, R., Van, D. amme, M., Van, Versluys, R., and Lefeber, D. (2009). “Orthopaedic rehabilitation: a powered elbow orthosis using compliant actuation,” *2009 IEEE 11th International Conference on Rehabilitation Robotics* (Kyoto), 172–177.
- Vitiello, N., Lenzi, T., Roccella, S., De Rossi, S. M. M., Cattin, E., Giovacchini, F., et al. (2013). NEUROExos: a powered elbow exoskeleton for physical rehabilitation. *IEEE Trans. Robot.* 29, 220–235. doi: 10.1109/TRO.2012.2211492
- Webster, J. B., and Murphy, D. P. (2018). *Atlas of Orthoses and Assistive Devices*, 5th edn. Philadelphia: Elsevier.

Conflict of Interest: The authors declare that the research was conducted in the absence of any commercial or financial relationships that could be construed as a potential conflict of interest.

Copyright © 2021 Perry, Brower, Carne and Bogert. This is an open-access article distributed under the terms of the Creative Commons Attribution License (CC BY). The use, distribution or reproduction in other forums is permitted, provided the original author(s) and the copyright owner(s) are credited and that the original publication in this journal is cited, in accordance with accepted academic practice. No use, distribution or reproduction is permitted which does not comply with these terms.

Advantages of publishing in Frontiers



OPEN ACCESS

Articles are free to read
for greatest visibility
and readership



FAST PUBLICATION

Around 90 days
from submission
to decision



HIGH QUALITY PEER-REVIEW

Rigorous, collaborative,
and constructive
peer-review



TRANSPARENT PEER-REVIEW

Editors and reviewers
acknowledged by name
on published articles

Frontiers

Avenue du Tribunal-Fédéral 34
1005 Lausanne | Switzerland

Visit us: www.frontiersin.org

Contact us: frontiersin.org/about/contact



REPRODUCIBILITY OF RESEARCH

Support open data
and methods to enhance
research reproducibility



DIGITAL PUBLISHING

Articles designed
for optimal readership
across devices



FOLLOW US

@frontiersin



IMPACT METRICS

Advanced article metrics
track visibility across
digital media



EXTENSIVE PROMOTION

Marketing
and promotion
of impactful research



LOOP RESEARCH NETWORK

Our network
increases your
article's readership